CONFERENCE SERIES

Contributions

15th Symposium on
Atomic and Surface Physics and Related Topics

Editors: V. Grill, T. D. Märk

innsbruck university press

CONFERENCE SERIES

Series Editors: K. Habitzel, T. D. Märk, B. Stehno

universität
innsbruck

*i*up • ***innsbruck*** university press

www.uibk.ac.at/iup

© 2006 *innsbruck* university press
1st edition
All rights reserved.

Vizerektorat für Forschung
Leopold-Franzens-Universität Innsbruck
Christoph-Probst-Platz, Innrain 52
A-6020 Innsbruck
www.uibk.ac.at/iup

Book editors: Verena Grill, Tilmann Märk
Cover design: Carmen Drolshagen
Produced: Fred Steiner, Rinn – Book on Demand

ISBN: 3-901249-82-6

***innsbruck* university press** in Conference Series:
Series Editors: K. Habitzel, T. D. Märk, B. Stehno

Also available by ***i**up* in this series:
Contributions – 2nd International Conference on Proton Transfer Reaction Mass Spectrometry and Its Applications – ISBN: 3-901249-78-8
Editors: A. Hansel, T. D. Märk

41st Symposium on Theoretical Chemistry – Innsbruck, Austria September 5-7, 2005
ISBN: 3-901249-80-X
Editors: Bernd M. Rode, Bernhard R. Randolf

XV Symposium on
Atomic and Surface Physics and Related Topics

Contributions

Editors:
Verena Grill
Tilmann Märk

Institut für Ionenphysik und Angewandte Physik
Der Leopold-Franzens-Universität Innsbruck
Technikerstr. 25
6020 Innsbruck

Obergurgl, Austria
February 4 – 9, 2005

15th SYMPOSIUM ON ATOMIC AND SURFACE PHYSICS AND RELATED TOPICS 2006
Obergurgl - Austria - February 4-9, 2006

International Scientific Committee:

Davide Bassi, Universitá degli Studi di Trento
Piero Casavecchia, Perugia
Tilmann D. Märk, Leopold Franzens Universität Innsbruck
Martin Quack, Eidgenössische Technische Hochschule Zürich

Local Organizing Committee:

Institut für Ionenphysik, Leopold Franzens Universität Innsbruck:
Wolfgang Grabmer
Verena Grill (Chairperson)
Tilmann Märk
Sandra Naschberger (Conference secretary)
Projektservicebüro, Leopold Franzens Universität Innsbruck:
Sara Matt-Leubner
W-INN:
Gundula Weingartner
Erminald Bertel

SASP Erwin Schrödinger Gold Medal 2006

In 1992 the ‚SASP Award for Outstanding Scientific Achievements’ was initiated by the SASP International Scientific Committee. This award is granted during the biennial SASP meeting to one or two scientists, chosen amongst those who have strong connections to the activities of SASP. So far the award was granted to

1992	David Smith, Birmingham
1994	Zdenek Herman, Praha
1996	Werner Lindinger and Tilmann Märk, Innsbruck
1998	Eldon Ferguson, Boulder, and Chava Lifshitz, Jerusalem
2000	Jean H. Futrell, Richland
2002	Eugen Illenberger, Berlin
2004	Anna Giardini-Guidoni, Roma

Recipients of the SASP Award 2006 – in the form of the ‘Erwin Schrödinger Gold Medal’ designed by Zdenek Herman – will be

Davide Bassi, Trento

Martin Quack, Zürich

Davide Bassi from the University of Trento, Italy, will receive the award for his outstanding contributions to the field of Ion-molecule Reactions a subject that has been in the center of interest of SASP since its beginning and his continuous commitment for SASP.

Martin Quack from the ETH Zürich, Switzerland, will receive the award for his exceptional achievements in the field of Spectroscopy a subject that has been in the center of interest of SASP since its beginning and his continuous support for SASP.

Foreword

In 1978 SASP was founded as a biennial winter conference by members of the Institute for Atom Physics (then the Institute for Ion Physics, and since 2006 the Institute for Ion Physics and Applied Physics) of the Leopold Franzens University Innsbruck, Austria.

Since the beginning the format of SASP has been similar to that of a Gordon Conference, with invited lectures, poster presentations with ample time for discussion and indoor and outdoor activities. The attendance of the symposium has been kept to about 100 participants.

This international symposium seeks to promote the growth of scientific knowledge and effective exchange of information among scientists in the field of atomic, molecular, and surface physics. A special emphasis of this conference will be to focus on nano particles and biomolecules and to provide room for discussion between academics and industry. The symposium deals in particular with collisional interactions involving different types of collision partners, i.e. electrons, photons, molecules, nano particles, and surfaces.

SASP usually takes place in Austria, but every second time it may be held in another alpine country.

So far the SASP conferences were held at the following locations:

1978	Zirog, Italy
1980	Maria Alm
1982	Maria Alm
1984	Maria Alm
1986	Obertraun
1988	La Plagne, France
1990	Obertraun
1992	Pampeago, Italy
1994	Maria Alm
1996	Engelberg, Switzerland
1998	Going
2000	Folgaria, Italy
2002	Going
2004	LaThuile, Italy
2006	Obergurgl

We would like to thank Zdenek Herman, Praha for the permission to use his marvellous drawing. We thank the FFG/Austrian nano initiative and the W INN, west Austrian initiative for nano networking, for financial support.

Contents

Invited Papers

Contributed Papers (Posters)

Invited Papers

(Trans)formation of carbon nanotubes: Role of electronic and thermal excitations

David Tománek

[1]*Physics and Astronomy Department, Michigan State University,*
East Lansing, MI 48824-2320, USA
tomanek@pa.msu.edu

Due to the important effect of defects on the physical properties of nanotubes, it is imperative to obtaining microscopic insight into the formation and transformation of defects during nanotube growth [1]. Owing to their structural flexibility, carbon nanotubes and related nanostructures show an unprecedented capability of self-healing at defect sites. The combination of *ab initio* density functional electronic structure calculations with molecular dynamics simulations is a powerful tool to demonstrate the ability of narrow nanotubes to heal out vacancies at high temperatures and in the photo-excited state. Photo-excitations can be used to identify and even non-destructively remove other defects, including chemisorbed oxygen. Large-scale morphology changes in graphitic nanostructures can be initiated at Stone-Wales defects, and may propagate throughout the structure by a sequence of Generalized Stone-Wales transformations. Large-scale computer simulations offer valuable insight into the transition states of this process, capable of large-scale morphology changes, including fusion of nanotubes.

[1] David Tomanek, Carbon-based nanotechnology on a supercomputer, Topical Review, J. Phys.: Condens. Matter 17, R413-R459 (2005).

Spectroscopy of cold, gas-phase biomolecular ions

Anthi Kamariotis, Oleg V. Boyarkin, Sébastien Mercier and Thomas R. Rizzo

*Laboratoire de chimie physique moléculaire, École Polytechnique Fédérale de Lausanne,
EPFL SB ISIC LCPM, Station 6, CH-1015 Lausanne*

ABSTRACT

We measure photofragment spectra of gas-phase biomolecular ions in a home-built tandem quadrupole mass spectrometer containing a 22-pole ion trap that can be cooled to less than 10K. Infrared photofragment spectra of protonated and lithiated amino acids solvated by selected numbers of water molecules provide insight into the structure of these species and hence the nature of the solvation process. Electronic photofragment spectra of solvated, aromatic amino acids provide information on the excited state dynamics that occur in these biological chromophores.

1. Introduction

Spectroscopic studies of biological molecules in the gas phase have largely focused on neutrals produced by simple heating or laser desorption techniques and cooled in a supersonic free jet. While a wealth of information has resulted from such studies, at physiological pH, most biological molecules exist as closed-shell molecular ions, where the competition between charge solvation by water and by the molecule itself helps determine the subtle energetic balance that leads to the stabilization of a particular conformation.

Despite the relative ease of volatilizing closed-shell biological ions, their low number density in the gas phase make performing spectroscopic studies of these species a challenging task. We produce ions by electrospray, collect them in a hexapole ion trap, mass select them, and then irradiate them by an IR or UV laser pulse (or a combination of the two) in either a 0.6 meter octopole ion guide or in a cooled, 22-pole linear ion trap. We generate photofragment spectra by monitoring the appearance of fragment ions as a function of the laser wavelength.

This talk will focus on two kinds of photofragment spectroscopy. In one case, we use infrared photofragment spectroscopy in the light-atom stretch region to investigate salt-bridge formation in solvated, amino acids. We have extensively studied $\text{Valine}\bullet\text{H}^+(\text{H}_20)_n$ and $\text{Valine}\bullet\text{Li}^+(\text{H}_20)_n$ clusters, since dissociation studies in an ICR cell have suggested that the latter form a gas-phase salt-bridge.

In a second type of experiment, we perform UV photofragment spectroscopy on bare aromatic amino acid ions cooled to ~10 K in a 22-pole ion trap. Collisional cooling in such a trap greatly simplifies the spectroscopy by reducing both rotational and vibrational temperatures. Our most recent results on protonated tryptophan and tyrosine and their clusters with water will be presented.

Ionization of water and biomolecules by protons in the bragg peak energy range : separation of direct ionization and electron capture processes

S. Eden[1], J. Tabet[1], S. Ouaskit[1,2], B. Farizon[1], M. Farizon[1], P. Scheier[3] and T. D. Märk[3]

[1] *Institut de Physique Nucléaire de Lyon, IN2P3-CNRS et Université Claude Bernard Lyon 1, 4 rue Enrico Fermi, F-69622 Villeurbanne Cedex, France*

[2] *Université Hassan II, Faculté des Sciences II, B.P. 6621-sidi Othermane, Casablanca, Morocco*

[3] *Institut für Ionenphysik, Leopold Franzens Universität, Technikerstr. 25, A-6020 Innsbruck, Austria*

Mass analyzed product ion signals of water [1], Uracil and DNA Basis upon proton impact ionization were measured in coincidence with the projectile. The charge state of this hydrogen atom is analyzed and facilitates the identification of the ionization process, i.e. direct ionization for H^+, single electron capture for H^0 and double electron capture for H^-. Partial and total cross sections for both direct ionization and electron capture processes was determined. The total and partial cross sections for direct ionization after proton impact are compared with corresponding cross sections for electron impact ionization giving further evidence for polarization and kinetic energy effects leading to higher cross sections at lower velocities for proton ionization.

[1] F. Gobet, S. Eden, B. Coupier, J. Tabet, B. Farizon, M. Farizon, M. J. Gaillard, M. Carré, S. Ouaskit, T. D. Märk, and P. Scheier, *Phys. Rev. A* **70**, 062716 (2004)

Low energy electron impact on gas phase cytosine and adenine: vibrational, electronic excitations, negative ions

Robert Abouaf and Henri Dunet

Laboratoire des Collisions Atomiques et Moléculaires (UMR 8625) Bâtiment 351 Université Paris Sud 91405 Orsay Cedex, France (abouaf@lcam.u-psud.fr)

ABSTRACT

The low lying excited states of cytosine, adenine and 9methyladenine are studied by electron energy loss spectroscopy with angular analysis. Besides the dipole allowed transitions to singlet states, the lowest triplet states are also observed. The vibrational excitation is recorded in the π* resonances energy regions, showing the excitation of various vibrational modes. Dissociative electron attachment cross sections are presented for $(M\text{-}H)^-$ anions produced after the loss of an H atom.

1. Introduction

After several cascades following the action of an ionizing radiation, among many other processes, it has been demonstrated that the low energy electrons (0-20eV) produced can efficiently damage the DNA material (1). In this energy range, the electrons can induce excitation the low lying electronic states of the molecule, ionization or dissociation. Below about 10eV, the collision process is dominated by the formation of "resonances", i.e. very short lived anions states produced by the temporary capture of an electron by the target at selected energies. The decay occurs via two competing processes leading either to rejection of the electron (vibrational excitation), or to dissociation via the dissociative electron attachment process (DEA), giving rise to a stable anion and one or several fragments. DEA may have in some cases very large cross sections ($>10^{-16}cm^2$) and is well known to efficiently break molecular bonds well below the bond energy, even at zero energy if the electron affinity of the fragment is large enough. In cytosine and adenine we have studied electronic excitation of the low lying states, resonant vibrational excitation and negative ions produced by DEA.

2. Results

Electronic excitation is studied by electron energy loss spectroscopy with angular analysis. Varying the residual energy and the observation angle may allow to distinguish the dipole allowed transitions from the spin or symmetry forbidden transitions. For singlet states, our measurements in the gas phase are in good agreement with UV-visible absorption results (solutions or films) or with various calculations. Evidence of triplet states is observed at 3.5eV and 4.25eV (± 0.1eV) for cytosine and at 3.80eV (adenine) in good agreement with quantum chemical calculations.

The vibrational excitation has been recorded in the energy region where several resonances have been located by electron transmission (2), mainly assigned to the capture of the electron into π* antibonding orbitals. The energy loss spectra recorded with 0.025eV resolution FWHM show the excitation of various vibrational modes.

The main anions produced by DEA are obtained by the loss of an H atom leading to $(C\text{-}H)^-$ for cytosine and $(A\text{-}H)^-$ anions for adenine. The cross sections are peaking around 1.3eV for cytosine and 0.95eV for adenine; they show several structures. Using 9methyladenine it is shown that the H ablation occurs for adenine on the N_9 site. For cytosine the spectrum is reminiscent of the results obtained in uracil and thymine (3) and the H ablation is likely to occur on the N_1 site.

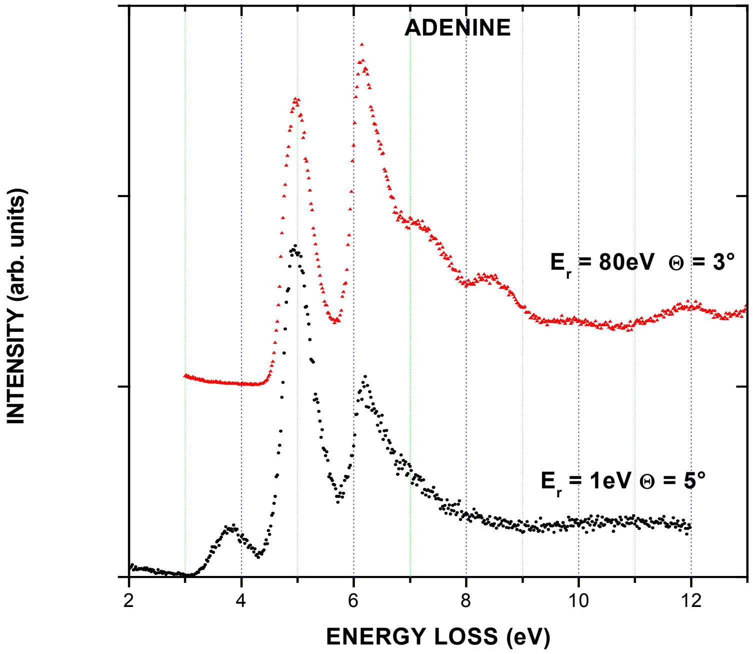

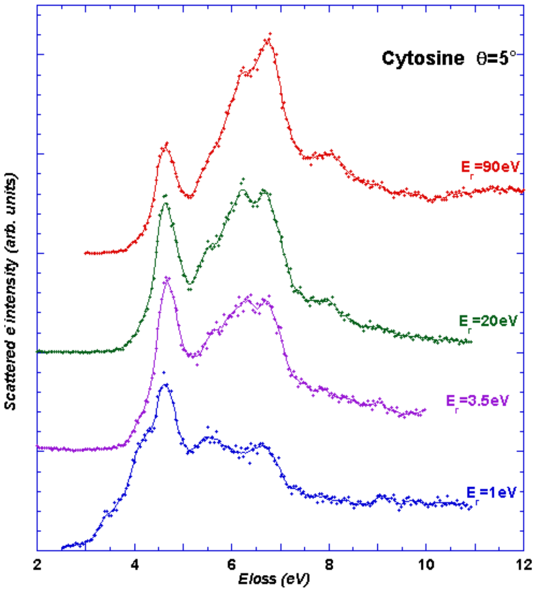

1. B. Boudaïffa, P. Cloutier, D. Hunting, M.A. Huels, L. Sanche Science **287**, 1658 (2000)
2. K. Aflatooni, G.A. Gallup, P.D. Burrow J. Phys. Chem. A102, 6205 (1998)
3. S. Ptasinska, S. Denifl, P. Scheier, E. Illenberger, T.D. Märk Angew. Chem **44**, 2 (2005) and references therein.

Site selectivity in dissociative free-electron attachment to gas phase nucleobases.

F. Zappa[1,3], S. Ptasinska[1], S. Denifl[1], V. Grill[1], P. Scheier[1], T.D. Märk[1,2]

[1] *Institut für Ionenphysik, Leopold-Franzens Universität Innsbruck, Technikerstr. 25, A-6020 Innsbruck, Austria*

[2] *Also Adjunct Professor at Department of Experimental Physics, Comenius University, 84248 Bratislava (Slowakia).*

[3] *on leave from UNESA, Rio de Janeiro, Brasil.*

ABSTRACT

In this presentation we will show the results of a series of experiments[1-4] concerning free-electron attachment to 2 nucleobases, namely thymine and uracil, and partially deuterated or methylated derivatives, in the gas phase. Negative ion yields as a function of the electron energy, for all molecules studied, exhibit common resonances for two major channels, i.e., at sub-excitation energies (<3 eV) for the formation of the closed-shell heavy fragment anion $(M\text{-}H)^-$, and at electron energies above 5 eV for the complementary channel leading to the formation of H^-. By careful analysis of the experimental results, we are able to explain each of the resonances observed to the cleavage of an H atom from a specific site in these molecules. Furthermore, by comparing our results with DNA strand-breaks produced by low-energy electron irradiation [5], we tentatively attribute the 10 eV resonance in the H^- anion yield to be an important intermediate step for DNA double strand breaks.

1. Introduction

The interaction of low energy electrons with DNA has been demonstrated to be an important mechanism in the production of both single and double strand breaks, even at sub-ionization energies [5]. Furthermore, the yield of such DNA damage shows a resonant behaviour with energy which is an indication of transient negative ion formation. Indeed, the authors of ref [5] have demonstrated also the effective resonant H^- production from thin layers of DNA and its building blocks such as thymine, water and deoxyribose.

In order to deepen the understanding of DNA damage at the molecular level experiments in the gas phase with increased electron energy resolution have been performed by several groups [1-4, 6, 7]. Parallel to the experiments numerous theory groups devoted their work to the investigation of low-energy electron interactions with biomolecules [8-10]. Experiments using partially deuterated thymine clearly demonstrated that energetic constraints lead to a bond selectivity in the formation of the closed shell anion $(T\text{-}H)^-$ accompanied by the loss of a neutral H atom [7]. Subsequent experiments with the same molecules where D replaces the H atoms in thymine in Innsbruck with increased sensitivity and resolution accompanied by high-level quantum chemical calculations revealed additional bond selective dissociative electron attachment (DEA) channels and enabled the unambiguous assignment of the reaction paths leading to the formation of several fragment anions including ring dissociation [2]. In the present work we demonstrate that in DEA to methylated uracil and thymine (where selectively one hydrogen atom attached to a nitrogen atom of the ring is replaced with a CH_3 group) all resonances leading either to $(M\text{-}H)^-$ or H^- can unambiguously be assigned to a specific site.

2. Experimental apparatus

Fig. 1 Schematic view of experimental apparatus.

The experimental set-up is depicted in fig.1. In short, a powder sample of the molecules of interest is vaporized in an oven, at temperatures up to 190°C, producing an effusive beam through a capillary. This molecular beam is crossed perpendicularly by a beam of electrons produced by an electrostatic hemispherical monochromator. In the present study the energy of the electron beam is varied from ~0 up to typically 15 eV with an electron energy resolution between 60 and 140 meV. Anions produced in the interaction chamber are mass analyzed by a quadrupole mass filter and detected by a channeltron type secondary-electron multiplier operated in a single count mode.

2. Results and discussion

Anion efficiency curves for the production of $(M-H)^-$ fragments are presented in fig 2a for uracil (dotted line) and 3-methyl-uracil (solid line), and in fig 2b for thymine (dotted line) and 1-methyl-thymine (solid line). All resonances observed occur below an incident energy of 3 eV, and from the figures one can immediately see a strong similarity between the curves for uracil and thymine. In fact, the two molecules differ only by a methyl group at the C5 position of the central ring, and previous results with partially-deuterated uracil [7] showed that H-loss from the carbon positions does not contribute to the $(M-H)^-$ signal in this energy range.
3-methyl-uracil (3mU) is an isomer of thymine where the CH_3 group is attached to the N3 position. Thereby, the only hydrogen atom of m3U that is attached to a nitrogen atom is the one at the N1 site. The anion yield above 1.5 eV of $(3mU-H)^-$ is strongly suppressed compared to uracil. In contrast, in the case of 1-methyl-thymine (m1T), the H atom at the N1 position is replaced by CH_3. The anion yield of $(m1T-H)^-$ is a smooth asymmetric Gaussian like curve that starts at about 1.4 eV and reaches its maximum at 1.8 eV. According to high-level quantum chemical calculations the energy that is required to generate $(U-H)^-$ via loss of the N3 hydrogen atom is 1.4 eV and thus in perfect agreement with the present experiment. In contrast to all the other anion yields shown in Fig. 2 all narrow features are missing in the case of m1T. Therefore, one can conclude that all narrow resonances at low electron energy of both uracil and thymine are due to H loss from the N1 position, while a smooth contribution at higher electron energies is due to H loss from the N3 position.

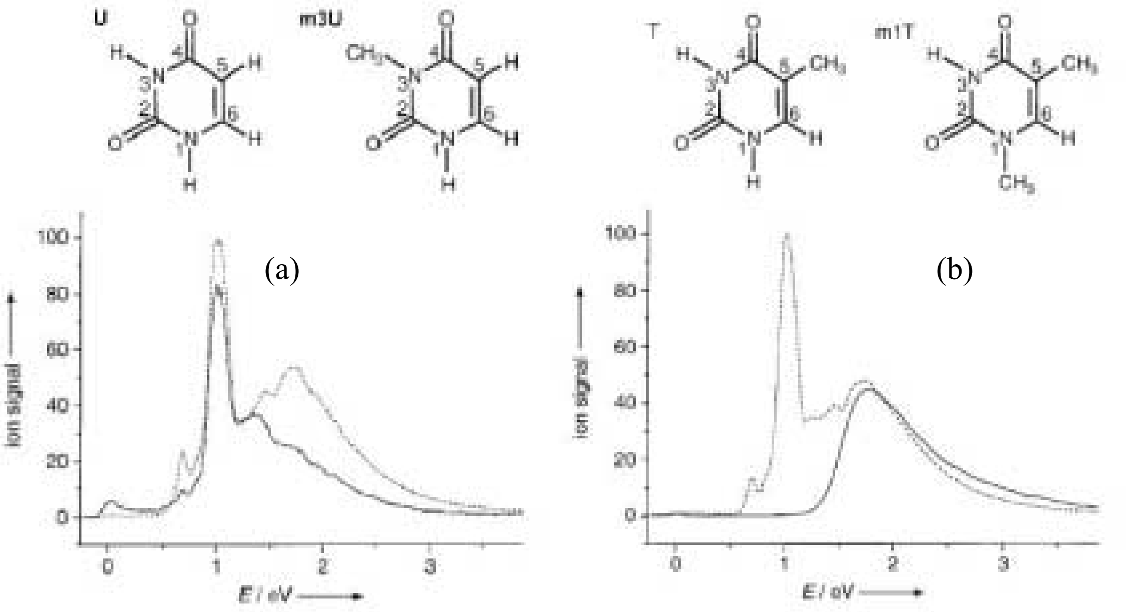

Fig. 2 (a) Yeld plots of the fragment anion (Molecule-H)$^-$ as a function of impacting electron energy on molecules uracil (dotted line) and 3.methyl uracil (full line) (b) Same as (a) in the case of thymine (dotted line) and 1 methyl thymine (full line).

In the case of the production of H$^-$, we could make use of the same strategy, and the results are summarized in figure 3. Four distinct resonances can be identified, in the energy range between 5 and 12 eV. Once more the lowest energy feature can be attributed to the N1 position, followed by the N3 position, but this time the carbon position C6 contribute, as well as the methyl groups.

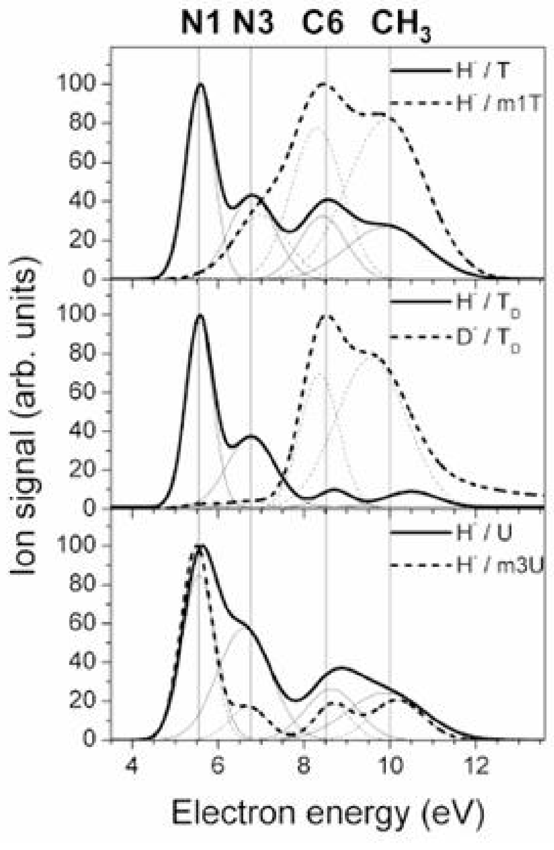

Fig. 3 H$^-$ yeld plots, as function of impacting electron energy on thymine (T), 1-methyl-thymine (m1T), partially deuterated thymine (T_D), uracil (U) and 3-methyl-uracil (m3U).

In plasmid DNA both SSBs and DSBs have been observed recently in the energy range between about 6 and 12 eV [5]. The present results show that in the energy range below about 6 eV H$^-$ loss exclusively occurs from the N1 site. In DNA, thymine is coupled to the sugar by the (N1-C) bond. The present findings show that H$^-$ loss is inhibited at electron energies below 6 eV when

N1-H is replaced by N1-CH_3, and this should also apply if a sugar molecule is connected to the N1 site. Thus the present results rather point to the fact that the strongest H^- resonance observed in the pyrimidines (i.e., at about 5.5 eV) is suppressed in plasmid DNA and may not contribute to strand breaks. Conversely, at energies above about 7 eV H^- loss from the C atoms dominates. Moreover, from the present results information on the relative contribution of H^- originating from CH_3 and the C6 position can be derived. In the first case a C-centered radical is formed, which in organic chemistry is known to be very reactive and hence is expected to lead to strand breaks.

3. References

[1] S. Ptasinska, S. Denifl, P. Scheier, E. Illenberger and T.D. Märk, *Bond- and Site-Selective Loss of H Atoms from Nucleobases by Very-Low-Energy Electrons (<3 eV)*. Angew. Chem. Int. Ed. **44** (2005) 6941–6943;

[2] S. Ptasinska, S. Denifl, B. Mroz, M. Probst, V. Grill, E. Illenberger, P. Scheier and T.D. Märk, *Bond selective dissociative electron attachment to thymine*. J. Chem. Phys. **123** (2005) 124302-1-8;

[3] S. Ptasinska, S. Denifl, V. Grill, T.D. Märk, E. Illenberger and P. Scheier, *Bond- and Site-Selective Loss of H^- from Pyrimidine Bases*. Phys. Rev. Lett. **95** (2005) 093201;

[4] S. Ptasinska, S. Denifl, V. Grill, T.D. Märk, P. Scheier, S. Gohlke, M.A. Huels and E. Illenberger, *Bond-Selective H^- Ion Abstraction from Thymine*. Angew. Chem. Int. Ed. **44** (2005) 1647–1650;

[5] M. A. Huels, B. Boudaiffa, P. Cloutier, D. Hunting, L. Sanche, J. Am. Chem. Soc. 125(2003) 4467;

[6] R. Abouaf,J . Pommier,H. Dunet, Int. J. Mass Spectrom. **226** (2003) 397;

[7] H. Abdoul-Carime, S. Gohlke, E. Illenberger, Phys. Rev. Lett. **92** (2004)168103;

[8] R. Barrios, P. Skurski, J. Simons, J. Phys. Chem. B **106** (2002) 7991;

[9] X. Li, M. D. Sevilla, L. Sanche, J. Am. Chem. Soc. **125** (2003) 13668;

[10] A. Grandi, F. A. Gianturco, N. Sanna, Phys. Rev. Lett. **93** (2004) 048103;

4. Acknowledgments

This work was supported by FWF (Wien), the EU commission (Brussels, through the EPIC network and the COST Action P9). F.Z gratefully acknowledges a post-doc grant from the Brazilian agency CNPq.

Electron attachment to selected amino acids

Š. Matejèík

Department of experimental physics, Comenius University, 84248 Bratislava, Slovakia

ABSTRACT

The interaction of ionizing radiation with matter tends to the production of secondary reactive species along the track of the radiation. These secondary species may undergo subsequent reactions with the medium. Secondary electrons with kinetic energies below 20 eV [1] belong to the most abundant secondary particles with a yield of 5x104 per MeV deposited. Dissociative electron attachment is an efficient reaction in the energy range of the secondary electrons. This reaction is responsible for formation of negative ions and radicals in the gas (and aggregate) phase and may play important role in the radical formation in the alanine.

The DEA to a molecule in the gas and condensed phase is a resonant process which proceeds via two steps:

$$e + M \rightarrow (M^-)^{\#} \rightarrow \text{negative ions + neutral fragments} \qquad (1)$$

The first step is the formation of the transient negative ion (TNI) $(M^-)^{\#}$ which may subsequently (in the second step) dissociate into negative ions and neutral fragments or radicals. The resonant character of the DEA reactions is represented by the form of the cross sections. The position and width of the DEA resonances are characteristic for the molecule and given ion. Using the crossed electron/molecule beams technique combined with the mass analysis of the negative ions we were able to measure the ion yields for the formation of particular negative ions.

Aflatooni et al. [2] measured the temporary anion states of selected amino acids including L-Alanine in the electron energy range from about 0 to 6 eV. Using the electron transmission spectroscopic technique they were able to detect a resonance at an electron energy of 1.80 eV which has been assigned to the electron attachment into the empty π* orbital of the –COOH group of alanine. Recently several studies on DEA to amino acids glycine, alanine and valine [3,4,5,6] have been published. These studies revealed some characteristic dissociation patterns in the DEA to aminoacids. The dominant DEA channels in all molecules were the $(M\text{-}H)^-$ ions, where M denotes the amino acid molecules. According to these studies the $(M\text{-}H)^-$ ions have been formed via low energy π * (COOH) resonance peaking below 2 eV. The π*(COOH) resonance is typical feature for the molecules containing the COOH (carboxyl) functional group. The DEA studies of glycine and alanine [3,4,5,6] showed that besides the π* resonance additional resonances at higher electron energies (around 5-6 and 8-10 eV) exist. These resonances are associated with the excitation of the molecules.

Acknowledgments

This work was supported by the Slovak Grant agency APVT project Nr. 20-007504

References

[1] International Comission on Radiation Units and Measurements, ICRU Report 31 (1979)

[2] K. Aflatooni, B. Hitt, G. A. Gallup, P. D. Burrow, J. Chem. Phys., 115 (2001) 6489

[3] S. Gohlke, A. Rosa, E. Illenberger, F. Brüning, M. Huels, J. Chem. Phys., 116 (2002)10164

[4] S. Ptasinska, S. Denifl, A. Abedi, P. Scheier, T. D. Märk, Anal. Bioanl. Chem., 377 (2003) 1115

[5] S. Ptasinska, S. Denifl, P. Scheier, T.D. Märk, S. Matejcik, Chem. Phys. Lett., 403 (2005) 107

[6] J. Koèíšek, D. Kubala, O. Ingolfsson, Š. Matejèík, in preparation

Combining mass-spectrometry and infrared spectroscopy for the determination of structures of molecules of biological interest

Jean Pierre Schermann[1], Charles Desfrançois[1], Gilles Grégoire[1], Frédéric Lecomte[1], Jean Christophe Gillet[1], Mahamadou Seydou[1] and Joël Lemaire[2]

[1] Laboratoire de Physique des lasers Institut Galilée, Université Paris Nord, Villetaneuse, F-93430, France (scherman@galilee.univ-paris13.fr)

[2]Laboratoire de Chimie physique, Faculté des Sciences d'Orsay, Université Paris Sud, Orsay, F-91405 , France

ABSTRACT

The combination of the widely tunable infrared beam of a free-electron laser (CLIO, Orsay) coupled to high-resolution mass spectrometers (a home-built ICR cell or a modified commercial quadrupole trap) allow the determination of structures of molecular systems of biological interest in the gas-phase. After a presentation of the experimental technique and of the procedure used for interpretation of spectra, examples are given concerning peptides and drugs.

1. Introduction

Mass-spectrometry allows the selection of perfectly identified ionized systems. Infrared (IR) spectroscopy is a widely used method for the determination of molecular structures. However, IR spectra of molecular systems isolated in the gas-phase can be obtained by direct monitoring of the IR absorption only in the case of neutral molecules in very intense beams [1] or deposited on helium clusters [2]. In the case of ions, the densities are so low that direct absorption cannot be observed. Fortunately, a recent improvement of a method known since more than 20 years allows to by-pass this problem. Infrared multiphoton dissociation (IRMPD) of ions is currently used by mass-spectroscopists in order to fragment mass-selected ions. In those experiments, non-tunable lasers are used and no structural information can be derived. The fragmentation is brought by sequential absorption of IR photons and is similar to that obtained by fragmentation obtained by collision-induced dissociation (CID) [3]. With the advent of widely tunable free electron lasers, CLIO in Orsay [4] and FELIX at FOM [5] and pulsed IR OPO lasers [6], it is now possible to get structural information from resonant IRMPD. The striking difference between experiments using non-tunable lasers and those using tunable lasers is that the first step becomes resonant. Fragmentation of ions is then only observable when there is a coincidence between the laser frequency and a vibrational frequency of the studied system. By confrontation between experimental spectra and simulated spectra calculated for the different possible conformations of the investigated system, one can deduce structural information. Experiments have been performed in our group on free or protected peptides, cyclic peptide and anti-malaria (artemisine) drugs, protonated neuromediators and their agonists.

2. Experimental procedure

In IRMPD experiments, ions are submitted to the continuously tunable IR radiation issued from the free electron laser (FEL) CLIO. The ions absorb a first IR photon while they are still in a low-lying internal energy state where the density of vibrational states is rather low. This first step is resonant and its spectral dependence is thus characteristic of the initial ion conformations at room temperature, as usual in IR absorption spectroscopy. This first amount of added energy is then rapidly redistributed over the different coupled modes by internal vibrational relaxation (IVR) and further absorption of many IR photon leads to fragmentation, due to progressive heating, in a very similar fashion to multiple collision activation (CID).

The resonant infrared absorption of ions is monitored through the observation of fragment ions due to the sequential absorption of several IR photons, which increases the internal energy and induces the dissociation. The studied ions here presented are protonated and are produced either by MALDI (Matrix Assisted Laser Desorption Ionization) and injected into a compact Fourier Transform Ion Cyclotron Resonance mass spectrometer, or by electrospray and injected in a commercial quadrupole mass-spectrometer with a hole drilled for illumination by the FEL radiation. Ions with the mass of interest are selectively isolated before IR irradiation by the free electron laser beam during a few seconds. The laser is then continuously tuned in the 800 to 2000 cm^{-1} region, with a bandwidth of about 10 cm^{-1}, and it is often attenuated in order to avoid saturation effects (average power ca. 200 mW). The ion fragment yields, induced by IRMPD, are then monitored as a function of the IR laser wavelength.

3. Interpretation of IR spectra

For calculating fragmentation spectra, it is assumed for simplicity that only the resonant initial excitation step has to be taken into account. Absorption frequencies are independently determined with a reasonable accuracy by means of DFT (Density Functional Theory), which is the most accessible method for such mid-size molecular systems. The different possible configurations are first evaluated by means of a systematic or Monte Carlo search procedure and then optimized at the B3LYP/6-31G* level, which proves to be sufficiently accurate. The IR spectra corresponding to the different protonation sites are quite different but, for the most energetically favourable protonation site, only one or two configurations are populated although experiments are run at room temperature.

4. Examples of structural determinations

The case of the dialanine peptide is characteristic of protonated peptides [7]. Two sites of protonation are possible, one (A) on the N-terminal amino group or one (O) on the carbonyl oxygen of the amide C=O group. In the former case, the configurations can be *cis* or *trans*, but a very large barrier exists between those two possibilities and only the *trans* configurations are populated in the gas-phase. The comparison between experimental and calculated absorption spectra clearly shows that only A configurations are populated and that only two configurations must be considered at room temperature.

When the N-terminal amino group is “protected” by replacement of one hydrogen by an acetyl group, a similar study shows that the O (on C=O) protonation site indeed becomes the most favorable. When alanine is replaced by histidine [8], the most favorable protonation site moves on the nitrogen of the imidazole side chain. It is thus possible to directly determine protonation sites that were otherwise inferred either by basiciy considerations or lengthy kinetic methods.

It is interesting to compare the behavior of free peptides and cyclic peptides. Peptides corresponding to recognition sites of proteins are frequently used as drugs. For example, receptors situated at the surface of cells and called integrins specifically recognize the arginine-glycine-aspartic acid (RGD) sequence. Some drugs designed for inhibition of inflammation or cancer thus contain this RGD sequence which is essential for communication between cells. In a free peptide, an extremely large number of configurations are possible and the drug may not necessarily adopt the configuration which is biologically active, i.e. recognized by the receptors. Pharmacologists thus design cyclic peptides which contain the RGD sequence but the constraints imposed by the cycle strikingly diminish the number of possible configurations. This is verified by comparing the IRMPD spectra of the free RGD tripeptide and the cyclic RGDFV pentapeptide.

[1] Tailor-made aggregates of α-hydroxy esters in supersonic jets N.Borho, M.Suhm Phys.Chem.Chem.Phys.6 2885-2890 (2004)
[2] IR-IR double resonance spectroscopy in helium nanodroplets: photoinduced isomerization G.E.Douberly, J.M.Merritt, R.E. Miller Phys.Chem.Chem.Phys. 7 463-468 (2005)
[3] Activation of large ions in FT-ICR mass spectrometers J.Laskin, J.Futrell Mass Spectrom.Rev.24 135-167 (2005)
[4] Vibrational signature of charge solvation vs. salt bridge isomers of sodiated amino acids in the gas phase. C. Kapota, J. Lemaire, P. Maitre, G. Ohanessian, *J A C S* 126, 1836 (2004)
[5] Charge-state resolved mid-infrared spectroscopy of a gas-phase protein: G von Helden et al *PCCP* 7 1345 (2005)
[6] Infrared photodissociation spectroscopy of electrosprayed ions in a Fourier transform mass spectrometer K.Brueker, F.W.McLafferty et al JACS 127 4076-4083 (2005)
[7] Investigation of the protonation sites in the dialanine peptide by infrared multiphoton dissociation spectroscopy B. Lucas, G. Grégoire, J. Lemaire, P. Maitre, J.M. Ortega, A. Rupenyan, B. Reimann, J.P. Schermann, C. Desfrançois Phys. Chem. Chem. Phys. 6, 2659 (2004)
[8] Infrared multiphoton dissociation spectroscopy of protonated N-actyl-alanine and alanyl-histidine G.Grégoire et al Int.J.Mass Spectrom. 243 105-113 (2005)

Environmental and Biological Applications of Microplasmas

K. Becker[1], A. Koutsospyros[2], C. Christodoulatos[3], N. Abramzon[4], and G. Brelles-Mariño[5]

[1] Dept. of Physics and Engineering Physics and Center for Environmental Systems, Stevens Institute of Technology, Hoboken, NJ 07030, USA (e-mail: kbecker@stevens.edu)
[2] Center for Environmental Systems, Stevens Institute of Technology, Hoboken, NJ 07030, and Dept. of Civil & Environmental Engineering, Univ. of New Haven, New Haven, CT 06516, USA
[3] Dept. of Civil, Environmental and Ocean Engineering and Center for Environmental Systems, Stevens Institute of Technology, Hoboken, NJ 07030, USA
[4] Physics Dept., California State Polytechnic University, Pomona, CA 91768, USA
[5] Biological Sciences Dept., Calif. State Polytechnic University, Pomona, CA 91768, USA

Abstract

Stable glow discharge plasmas at elevated pressures can be generated and maintained easily when the plasma is spatially confined to cavities with dimensions below 1 mm (“microplasmas”). We studied the use of several atmospheric-pressure microplasmas in the remediation of volatile organic compounds (VOCs) and in biological decontamination. VOCs studied include prototypical aliphatic and aromatic compounds. The biological systems under study included individual bacteria as well as bacterial biofilms, which are highly structured communities of bacteria that are very resistant to antibiotics, germicides, and other conventional forms of destruction.

I. Introduction

Discharge plasmas at high pressures, where collisional and radiative processes beyond binary collisions involving ground-state species become important, are used in many applications such as high power lasers, opening switches, novel plasma processing applications and sputtering, EM absorbers and reflectors, remediation of gaseous pollutants, medical sterilization and biological decontamination, and excimer lamps and other non-coherent vacuum-ultraviolet (VUV) light sources [1]. However, self-sustained diffuse discharges tend to be unstable at high pressure due to their susceptibility to filamentation and transition to an arc. We explored the generation and maintenance of stable, high-pressure plasmas in cavities with dimensions below 1 mm, so-called “microplasmas” [2]. While the “pd” values of high-pressure microplasmas are similar to those of larger plasmas operating at low pressure (around 1 Torr · cm), the current and energy densities that can be realized in a microplasma are much higher. Here we present recent data on the use of microplasmas in selected environmental and biological applications.

II. Experimental Details

Most of the results described in this paper were obtained with plasma reactors based on the Capillary Plasma Electrode (CPE) discharge. The CPE discharge utilizes dielectric capillaries that cover one or both electrodes of the discharge device [3]. Figure 1 shows schematically the three plasma reactors that were used in the present VOC destruction experiments. The top left diagram shows a rectangular reactor with solid pin electrodes, which is operated in the cross-flow regime (CF-CPE reactor). The use of metallic pins minimizes energy losses in the system and improves plasma generation and stability. The top right diagram shows a rectangular plasma reactor with hollow-pin electrodes, which is operated in the flow-through regime (FT-CPE reactor). The gas stream is introduced through the hollow pin electrodes and the capillaries. This maximizes the exposure of the contaminants to the region of highest plasma density. The bottom diagram shows an annular (A-CPE) reactor. The contaminant streams are fed axially into the reactor. This mode of operation allows the contaminated gas stream to flow through the entire annulus of the reactor where exposure to the plasma occurs.

Fig.1: Schematic diagrams of 3 CPE discharge configurations used for environmental applications. Top left: Cross-flow CPE (CF-CPE) reactor with solid pin electrodes; Top right: Flow-through CEP (FT-CPE) reactor with hollow pin electrodes; Bottom: Annular CPE (A-CPE) reactor with a solid center electrode.

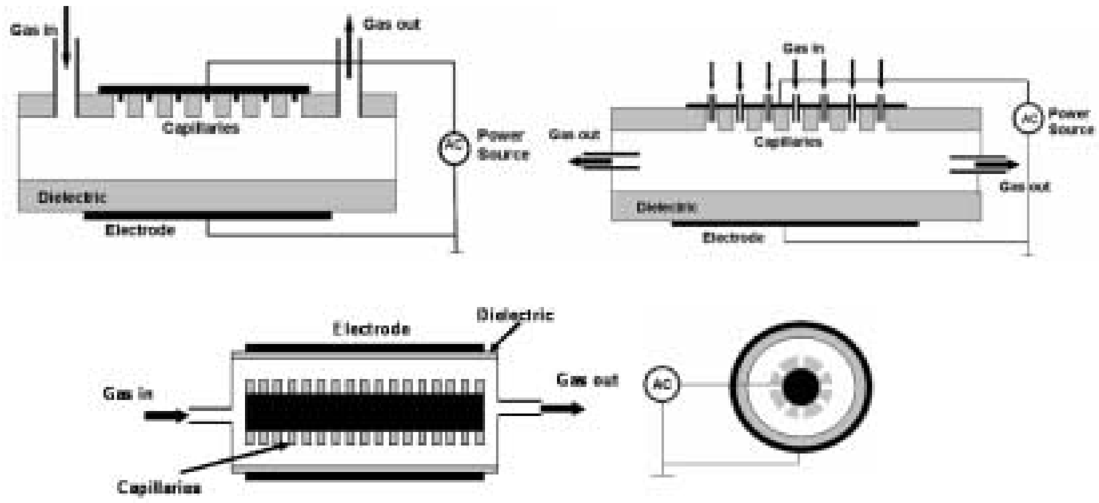

III. Results and Discussion

III.1. Environmental Applications of CPE Microplasmas

Non-thermal plasmas in environmental applications such as remediation of gaseous waste streams have been studied for more than 20 years [4]. While much research has been carried out using laboratory-scale remediation system, the transition to industrial prototypes and commercial pilot units has been slow because the plasma chemistry involved in the destruction processes is not well understood and we lack a detailed understanding of how to couple the discharge physics to the plasma chemistry. Ideally, the destruction of VOCs would lead to CO_2 and H_2O as the only reaction products. However, that goal is rarely, if ever achieved in practice.

III.1.1 VOC Destruction Efficiency

Koutsospyros et al. [5] studied VOC destruction of prototypical aliphatic (ethylene, heptane, octane) and aromatic (benzene, toluene, ethylbenzene, xylene) VOCs in the context of exploring non-thermal plasmas for use in Advanced Life Support (ALS) systems. Initial contaminant concentrations varied between 75 and 1500 ppm(v) in air with gas flow rates between 1 and 10 l/min. Destruction efficiencies were determined as a function of plasma energy density, initial contaminant concentration, residence time in the plasma volume, and reactor volume, and a kinetic model was developed to determine the relevant rate constants for contaminant destruction. Input powers ranging from 10 - 100 W were used to generate plasma volumes between 3 and 20 cm^3. This resulted in energy densities (J/cm^3) between 0.5 and 10 J/cm^3 and residence times in the range of 0.2–2 s. For all compounds, operating conditions could be identified that guaranteed destruction efficiencies of 95-100%. Fig. 2 shows the destruction efficiency for benzene in two CPE plasma reactors, an annular reactor and a cross-flow, solid-pin-electrode reactor. Essentially complete destruction can be achieved in the annular reactor for specific energies of 3 J/cm^3 and above. On the other hand, specific energies approaching 10 J/cm^3 are required to achieve comparable destruction in the cross-flow reactor. This indicates that optimization of the reactor geometry is a critical component in achieving maximum destruction efficiency.

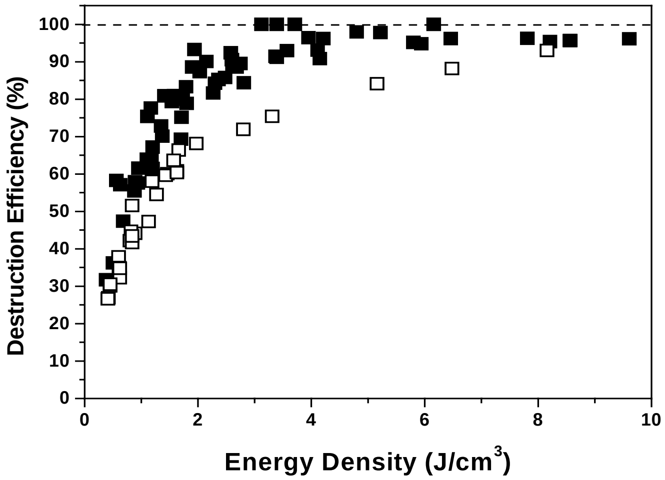

Fig. 2: Benzene destruction efficiency in an annular CPE plasma reactor (solid squares) and in a cross-flow CPE plasma reactor (open squares). For both reactors, data are shown for initial contaminant concentrations varying between 200 and 1200 ppm(v) and flow rates varying between 2 and 8 l/m; in all cases, the residence was chosen to be sufficiently long to ensure maximum destruction efficiency.

III.1.2 By-Product Formation

By-product formation is another important consideration of the VOC destruction process. Ultimately, one needs to measure the concentrations of all identified by-products and the gaseous carbon oxides, CO and CO_2. We analyzed the plasma-treated gas stream leaving the reactor using a variety of standard techniques. "Carbon closure", i.e. the complete accounting of all carbon in the influent, can be determined by evaluating the carbon mass balances for the reactants and all identified products. We found that carbon closure for benzene and ethylene was essentially 100% and ranged from 70-90% for toluene, heptane, octane, and ethylbenzene.

III.2. Biological Applications of Microplasmas.

The use of plasmas interacting with biological systems has mainly focused on using lethal plasma intensities for inactivation, bio-decontamination, and sterilization.

III.2.1 Inactivation of Individual Microorganisms by Plasmas

The inactivation of individual microorganisms by plasmas has received much attention in recent years [6]. Particular emphasis has been on the use of atmospheric-pressure plasmas as they do not require costly vacuum enclosures and thus facilitate the convenient and low-cost treatment of large surface areas. Spore-forming bacteria are among the most resistant microorganisms. A convenient measure for the effectiveness of a decontamination method is the so-called D-value (decimal reduction factor), which is the time that it takes to reduce a certain concentration of microorganisms by one order of magnitude. In the case of *Bacillus subtilis* spores, typical D-values for conventional inactivation methods such as the use of dry or steam heat or chemicals such as ethylene oxide (EtO) or chlorine dioxide (ClO_2) are in the range of a few minutes [6]. Plasma-based inactivation using non-equilibrium plasmas can achieve similar D-values with the added advantages that heat-sensitive material can be decontaminated and without generating environmentally hazardous, contaminated chemicals as by-products.

We have studied the inactivation of several spore-forming bacteria such as *Bacillus subtilis* spores and *Bacillus stearothermophilus* spores using atmospheric-pressure CPE plasma reactors in various gas mixtures. The following observations are noteworthy:

1. The inactivation curves are well-described by a single-exponential decay law which extends over many orders of magnitude of cell reduction.
2. D-values below 2 min were achieved for spore-forming bacteria; D-values for the inactivation of bacteria in the vegetative state are significantly shorter [6].

3. The single-exponential decay holds for high initial spore concentrations (> 10^6 colony forming units (CFU) per ml) and for dilute concentrations (< 10^4 CFU/ml).

III.2.2 Inactivation of Biofilms by Plasmas

Biofilms are highly structured communities of bacteria with complex structures. Biofilm formation is initiated when planktonic bacteria adhere to surfaces and begin to excrete exopolysaccharide that can anchor them to the surface. Among the most notable differences between planktonic cells and biofilms is the much higher resistance of biofilms to antibiotics, germicides, and other conventional sterilization and inactivation methods.

A He-stabilized capacitive discharge plasma was used in the present studies. The biofilms were produced in 96-well polystyrene microplates using a bacterial suspension of *Chromobacterium violaceum* CV026. The biofilms were then subjected to the plasma for various exposure times. After the plasma treatment, the biofilms were removed and evaluated for the presence of colony forming units (CFU). Figure 3 shows the number of *C. violaceum* biofilm-forming cells as a function of plasma exposure time for a 4-day old biofilm. The number of biofilm-forming cells is reduced rapidly by more than two orders of magnitude after a plasma exposure of 5 minutes. For longer exposure times (5-60 min), the inactivation curve is well described by a single-exponential decay. After an exposure to the plasma for about 60 min, the number of biofilm-forming cells has been reduced by about 3.5 orders of magnitude. It is apparent from the result that the plasma-initiated inactivation of biofilms is a more complex process than the inactivation of individual microorganisms.

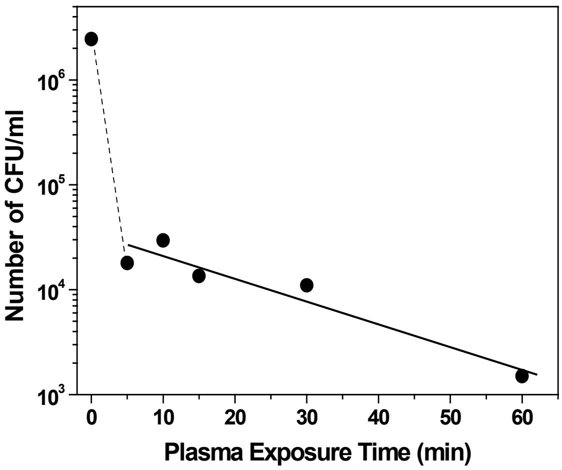

Fig.3: Plasma-induced inactivation of biofilm-forming cells. The number of colony forming units (CFU) per ml is plotted vs. the plasma exposure time. The solid line is a single-exponential decay curve through the data points in the range from 5-60 min exposure time. The dashed line is just a guide to the eye.

We acknowledge the financial support from NASA, NSF, ARO, AFOSR, and CSuperb.

References

[1] "Non-equilibrium Air Plasmas at Atmospheric Pressure", editors: K Becker et al., IOP Publ., Bristol, UK (2004), chapter 9 "Applications of Atmospheric-Pressure Air Plasmas" and references therein

[2] K.H. Becker et al, J. Phys. D (2006), in press; R. Foest et al, Int. J. Mass Spectrom. (2006), in press

[3] E.E. Kunhardt and K. Becker, US Patents 5872426, 6005349, 6147452, 6879103, and 6900592.

[4] B.M. Penetrante and S.E. Schultheiss, "Non-thermal Plasma Technologies for Pollution Control", Proc. NATO-ASI, Vol. 34A/B, Plenum Press, New York (1993)

[5] A. Koutsospyros et al., Int. J. Mass Spectrom. 233, 305 (2004); IEEE Trans. Plasma Sci, 33, 42 (2005)

[6] M. Laroussi, in ""Non-equilibrium Air Plasmas at Atmospheric Pressure", editors: K. Becker et al, IOP Publ., Bristol, UK (2004), section 9.9 "Biological Decontamination Using Non-equilibrium Atmospheric Air Plasmas" and references therein

Recent Developments in Proton-Transfer-Reaction Mass Spectrometry

Armin Wisthaler, Armin Hansel, Tilmann D. Märk

Institut für Ionenphysik, Leopold-Franzens-Universität Innsbruck, Technikerstraße 25, A-6020 Innsbruck (armin.wisthaler@uibk.ac.at)

Proton-Transfer-Reaction Mass Spectrometry (PTR-MS) is a highly sensitive, real-time analytical technique for detecting volatile organic compounds (VOCs) in air, which was developed in the mid-1990's in the laboratories of the Institute of Ion Physics at the University of Innsbruck. PTR-MS combines the concepts of soft, nonfragmenting chemical ionization (via proton transfer reactions with H_3O^+ reagent ions) and of highly sensitive and quantitative product ion formation in an ion flow drift tube. Since its inception PTR-MS has become a leading technology in the on-line VOC analysis, spanning a number of research fields that include predominantly atmospheric chemistry, increasingly food science, and most recently in the emerging field of medical and life sciences.

A series of recent technical improvements that will be outlined in this talk have greatly improved the instrument's capabilities. A 5 to 10-fold increase in sensitivity has been obtained with current detection limits ranging from 10 to 100 pptV (3σ, 1 sec signal integration). The PTR-MS response time has been lowered to about 150 ms, making it one of the fastest currently available VOC sensors. The implementation of sophisticated mass spectrometric equipment (ion traps, time-of-flight) has led to a gain in duty cycle and in analyte specificity (MS/MS capability).

Optimized modes of PTR-MS operation have broadened the spectrum of measurable species. Previous attempts to measure formaldehyde which is a key species for studies of photochemical oxidation pathways in the troposphere had yielded discouraging results. Here, we will present modifications to the PTR-MS technique by which the instrument's performance for formaldehyde detection can be significantly improved. Results from intercomparison measurements with other formaldehyde measurement techniques (Hantzsch monitor, DOAS, DNPH/HPLC/UV-VIS) will be presented. In this context we will also show results that compare PTR-MS measurements of a broad spectrum of oxygenated VOCs with data from a variety of other state-of-the-art instruments, confirming a superior PTR-MS performance.

Classification of strawberry cultivars by PTR-MS fingerprinting: from standard multivariate analysis to innovative data mining techniques

F. Biasioli[1], P. Granitto[1], E. Aprea[1], D. Mott[1], T. D. Märk[2], F. Gasperi[1]

[1]*Istituto Agrario di S. Michele a/A, Via E. Mach, , 38010 S. Michele a/A, Italy (franco.biasioli@iasma.it)*

[2]*Institut für Ionenphysik, Leopold Franzens Universität Innsbruck, Technikerstr. 25, 6020 Innsbruck, Austria*

ABSTRACT

Mass spectrometric methods based on chemical ionization, Proton Transfer Reaction-Mass Spectrometry (PTR-MS) in particular, often allow the direct introduction of complex mixtures of volatile compounds into the ion source of the analyzer and they produce reliable mass spectra that preserve a lot of chemical information about the sample because of the reduced fragmentation in comparison to other methods. In practical applications these spectra, providing a genuine image of the volatile profile, can be used for a rapid and non-invasive characterization of products and processes. However, the multivariate nature of the data, the high variability often associated with real samples (for instance foodstuff or biological samples) and the need to provide the user with fast and straightforward data analysis methods limit at present the widespread use of these techniques in industry.

Thus, in the last years we have investigated the possibility to apply data mining methods data obtained by PTR-MS in order to allow for rapid characterizations of agroindustrial products. Among the various applications studied we discuss here, as an illustrative case study, the classification of strawberry cultivars.

In preliminary studies we demonstrated that even unsupervised methods, like Principal Component Analysis (PCA), indicate the possibility to identify cultivars by direct and rapid sampling of the headspace of single whole fruits. We found evidence that PTR-MS data reflect also the influence of other agronomic parameters like the ripening degree or the cultivation methods. However, an unambiguous classification of cultivars on the basis of PCA data compression was not possible in these first studies.

Based on this first exploratory study we extended in the present investigation the data analysis methods to supervised chemometric approaches like Neural Network and discriminant Partial Least Squares that are probably the most used classification methods for spectrometric and spectroscopic data. Results thus obtained demonstrate, as far as we know for the first time, the possibility to clearly identify the cultivar of single strawberry fruits by non-destructive measurements.

Moreover, quite recently we further extended our study considering, on the one side, fruits produced and measured over several years (2002, 2003, 2004) and, on the other side, introducing new and innovative data mining methods that should provide optimum performance in classification reducing, at the same time, the risk of overfitting, i.e., Random Forest, Support Vector Machine and Penalized Discriminant Analysis. We thus confirmed conclusions from our preliminary studies.

We also have been able for the first time to relate successfully PTR-MS fingerprinting data with results of other characterizations of agroindustrial products, i.e., genetics and sensory analysis in particular.

Besides the applied relevance of the proposed approach indicating a practical example for the implementation of PTR-MS analysis, we believe that our work can also be a useful example of the application of innovative methods of data analysis. These methods may be applied in many other fields thus providing a valuable link between the activity of academia and the needs of industry.

PTR-MS: A new technique for trace VOC detection in the atmosphere

Armin Hansel and Armin Wisthaler

Institut für Ionenphysik, Leopold-Franzens Universität Innsbruck, Technikerstrasse 25, 6020 Innsbruck, Austria, (armin.hansel@uibk.ac.at)

Ten years ago we built the first Proton Transfer Reaction Mass Spectrometer instrument (PTR-MS) at the Institute of Ion Physics of the University of Innsbruck. In PTR-MS we use H_3O^+ ions to ionise volatile organic compounds (VOC) present in air. With this technique a variety of organic species in complex matrices can be monitored in real-time with detections limits as low as a few pptv (part per trillion). This review covers the main principle of PTR-MS and shows examples of chemical field measurements in the atmosphere and in the laboratory.

VOC are emitted into the atmosphere from biogenic and anthropogenic sources and have a significant impact on tropospheric ozone formation and the hydroxyl radical (OH) concentration, and on secondary organic aerosol formation. The global anthropogenic VOC flux is estimated as 1 x 10^{14} g C per year, while biogenic emissions may be higher by at least a factor of ten (1.2 x 10^{15} g C per year). Reactive biogenic volatile organic compounds (BVOC) include the quantitatively dominant group of isoprenoids (isoprene and terpenes). Isoprene emissions contribute to the regulation of OH concentration, though influence the residence time of methane in the atmosphere an important greenhouse gas. Photooxidation of terpenes result in condensable products which play an important role in secondary aerosol formation. Thus, BVOC emissions into the atmosphere influence the production of ozone and aerosols, which both have adverse effects on health, and are significant factors for the Earth's climate.

Within the plant kingdom only certain plant species emit isoprenoids. Generally, isoprene emission is more frequently reported for deciduous plants whereas monoterpene emission is common for evergreen leaves. Both isoprene and monoterpene emission rates are strongly regulated by light and temperature. The complex regulation processes of the emission of an ecosystem as a result of the interaction of biochemistry, ecology, air chemistry and meteorology still remains to be elucidated. Questions related to the fate of BVOC both in physiological processes and in the atmosphere have been addressed. In this paper we will present recently obtained results from field measurements concerning eddy correlation flux measurements of BVOC above a temperate forest using PTR-MS. In addition plant enclosure measurements utilising PTR-MS and ^{13}C labelled CO_2, glucose and starch will be presented. These laboratory based investigations support the idea that besides photo synthetically fixed CO_2 other carbon sources are used for isoprene and monoterpene formation.

The Spectroscopy of Astrochemical Ices; A Study in Ice Morphology

N. J. Mason, A. Dawes, R. Mukerji, P. Holtom, M. P. Davis and B. Sivaraman

Interdisciplinary Centre of Astrobiology; Department of Physics and Astronomy, The Open University, Walton Hall, Milton Keynes, MK7 6AA, United Kingdom; n.j.mason@open.ac.uk

ABSTRACT

Over 130 molecules have been observed in the InterStellar Medium (ISM) ranging from the simplest diatomics to complex hydrocarbons including acetic acid, glycine and glucose, molecules that are believed to be the precursors of life. The formation of many of these 'prebiotic' molecules is now believed to arise from the chemical processing of ice layers on the surface of micron sized dust grains found in the ISM. The morphology of the ice is expected to play a key role in such heterogeneous chemistry however, to date, the morphology of most molecular ices is unknown at temperatures below @ 100K, temperatures typical of the ISM. In this article we report the results of the first studies of the morphology of astrochemical ices using synchrotron radiation, studies that reveal the complex nature of ices at low temperatures.

1. Introduction

During the last century, the presence of icy particles throughout the universe has been confirmed by numerous ground and space based observations. Thin icy layers are known to cover dust particles within the cold regions of the interstellar medium (ISM), and drive a rich chemistry in energetic star-forming regions. The polar caps of terrestrial planets, as well as most of the outer-solar-system satellites, are covered with by ice (which may be several metres thick). Smaller solar system bodies, such as comets and Kuiper Belt Objects (KBOs), contain a significant fraction of icy materials. Icy particles are also present in planetary atmospheres and play an important role in determining the climate and the environmental conditions on our own planet, surface chemistry on ice particles in the Earth's stratosphere playing a key role in ozone chemistry.

Such ices can exist in a number of crystalline or amorphous phases, and the links between these solid, gas and liquid phases may be typically represented on a pressure-temperature phase diagram. At the low temperatures of the ISM is expected that most ices will be amorphous in nature. Amorphous ices resemble liquids, in that they exhibit no long-range molecular order and, provided that the temperature is low enough to prevent molecular rearrangement from occurring, such amorphous ices are metastable with respect to the crystalline forms. In contrast the presence of crystalline ices infers that the pressure and temperature conditions under which the ices formed were somewhat higher than the prevailing conditions during amorphous ice formation. It can also be an indicator of pressure, stress or elevated temperature on the ice itself, driving the phase change from amorphous to a crystalline form, hence crystalline ice might suggest some processing of the nascent ice has occurred (or is occurring) suggesting that the morphology of the ice might be a maker of their physical and chemical history.

However, at present, we know remarkably little about the morphology of low temperature molecular ices (<100K) and even less about the structure of ice mixtures as might be formed under astrochemical conditions. Nor do we have much quantitative details of the physical and chemical processing of such ices by typical astronomical radiation (photons, electrons and ions). We have started a detailed experimental programme to characterise the morphology of such astrochemical ices using infrared and UV spectroscopy and study the physical and chemical processing of such ices under irradiation. Here we give two examples for pure SO_2 and NH_3 ice.

2. Morphology of SO_2 ice

Sulphur dioxide (SO_2), has recently been observed for the first time in the extragalactic medium, five SO_2 transitions being detected towards NGC 253 with a total column density of 7 x 10^{13} cm^{-1}. Infrared observations and microwave studies have revealed that SO_2 is found in most regions of the interstellar medium and is a common species in the solar system. SO_2 plays a major role in the atmospheric chemistry of Venus and is present on the volcanically active Jovian moon, Io, in solid, liquid and gaseous forms. It has also been found on the surface of the Jovian moon, Europa.

The VUV photoabsorption spectrum of solid SO_2 condensed at a rate of 2.8 μm/hr onto the CaF_2 substrate (precooled to 25 K) [so called 'fast deposition'] is shown in Figure 1a and is compared with SO_2 deposited at 80K and SO_2 deposited at 25 K and annealed to 80 K. The "slow deposition" of SO_2 deposited on the precooled substrate at 25 K at a rate of 0.21 μm/hr shown in Figure 1b.

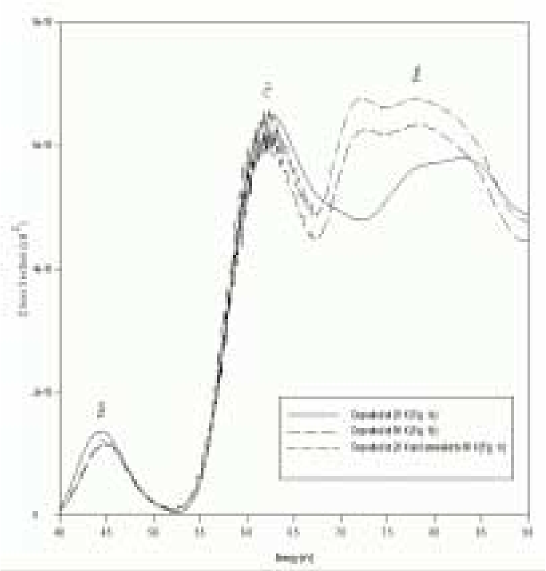

Figure 1a Spectra of "Fast deposited" SO_2

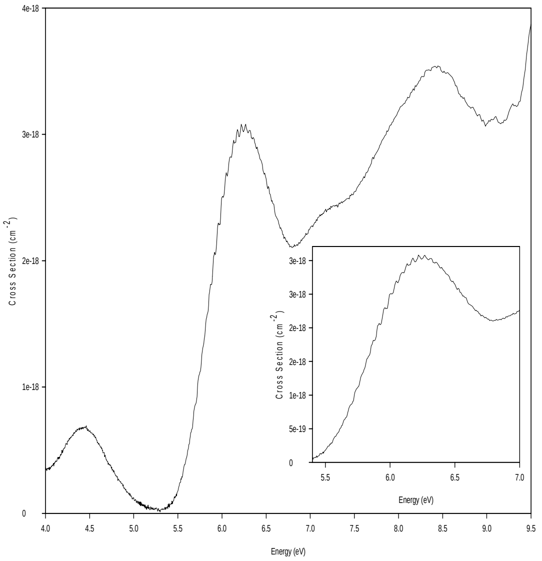

Figure 1 b Spectra of "slow deposited" SO_2

Our initial rapid deposition of SO_2 at low temperatures (25 K) is most likely to form a glassy, amorphous structure as the rapid deposition and low temperatures will not allow the incident sulphur dioxide molecule time or mobility to convert to the more stable crystalline form. Upon heating, the additional input of energy should allow the ice to rearrange and form an ordered crystalline structure which, as it is more thermodynamically stable, is retained upon further cooling.

In an amorphous solid there is no long range order but some short range order may still exist. The order in any solid depends on the orientation and distribution of the molecules. No long range order in an amorphous solid suggests that random orientations and distributions are possible. The statistical distribution of the molecular environments of such a disordered solid can explain the broadening out and loss of vibrational structure.

In contrast in a crystalline state we have a greater coupling between the molecules. It has been stated that coupling can increase the intensity of infrared features (and thus we assume their UV counterparts) by propagating a particular vibration through the crystal lattice. From this argument it seems clear that when we observe vibrational structure in our ice we must be viewing a crystalline structure.

3. Morphology of NH_3 ice

Ammonia was the first polyatomic molecule to be detected in space and is a constituent of the Gas Giants: Jupiter, Saturn, Uranus and Neptune. Observational studies reveal the possible presence of ammonia or ammonia hydrate on a number of satellites of the outer planets including Saturn's satellite Enceladus, Charon, a satellite of Pluto and Miranda, a satellite of Uranus. Condensed phase ammonia is also believed to be an abundant constituent of cometary ices. However rapid photodissociation of ammonia by solar UV makes it difficult to detect, and most knowledge about NH_3 in comets comes from optical spectra of NH_2. Ammonia has also been identified in meteorites, the Kuiper belt object Quaoar and interstellar grain mantles.
The spectrum of pure solid NH_3 deposited at 25 K shows a broad, smooth band with a maximum at 177 nm (7.0 eV) lacking any vibrational structure (Figure 2). The first absorption band is due to the $\tilde{A}^1A_2'' \leftarrow \tilde{X}^1A_1'$ molecular transition of NH_3. In the solid this band is blueshifted from the gas phase by 15 nm with the shape and the intensity of the band appears to trace the outline of the vibrational minima in the gas phase. Ammonia forms hydrogen bonds in the solid phase. In its crystalline cubic form it hydrogen bonds to six nearest neighbours where the lone pair on the nitrogen atom is shared between hydrogens of three molecules and each hydrogen atom bonds to three separate molecules. The hydrogen bonding is believed to be responsible for the blueshift in the spectrum from the gas to the solid phase. The further shift as the sample is annealed above 70 K is indicative of higher degree or more ordered hydrogen bonding as would be expected if the solid changes phase from a disordered to an ordered structure. The blueshift may be related to the fact that the electrons that are involved in the $\tilde{A}^1A_2'' \leftarrow \tilde{X}^1A_1'$ molecular transition also participate in the hydrogen bonding. A distortion of the non-bonding orbital is expected as hydrogen bonds are formed.

For samples deposited between 25 and 75K spectra remained unchanged from that of the 25K deposit. However all spectra deposited above 75K exhibit a relatively sharp feature at 194 nm. The intensity of this band decreases with increased sample temperature. The shape of the bands below 190 nm is also very different at the different temperatures. At 75K there is a broad feature around 183 nm and a relatively narrow feature at 173 nm. At 85 K two overlapping bands peaking at 178 nm and 172 nm dominate the spectrum. At 95K as the intensity of the 194 nm band decreases a high intensity band centred at 170 nm dominates the spectrum. Annealing each of the samples deposited at the different temperatures showed no change in the spectra other than a slight sharpening of the bands.

In the excited state of a free NH_3 molecule an electron is promoted to an extended atomic-like Rydberg orbital. In the solid these orbitals are greatly perturbed by surrounding molecules and may have conduction band properties. In a molecular crystal with a large dielectric constant, promotion of an electron from a valence to a conduction band and the subsequent electron-hole pairing results in a ***Wannier exciton***. The question that then arises is what is so unique about the structure of solid NH_3 between 65 and 80 K? The structure is thermodynamically stable and is hence not believed to be a metastable phase, furthermore this structure cannot be formed by annealing sample deposited at lower temperatures. One possible explanation for the origin of the exciton transition may be related to the formation of ***crystallites*** in the crystalline solid ammonia, that is islands of crystalline material embedded in amorphous ice. It is expected that the size, shape and density of crystallites may affect the intensity of the exciton transition, the larger the number of grain boundaries the stronger the exciton.

It is then possible to relate the temperature profile of solid ammonia to its morphology as summarised in figure 2.

1) Samples *deposited below 50 K* are amorphous. This is a thermodynamically unstable structure that reorders upon annealing.

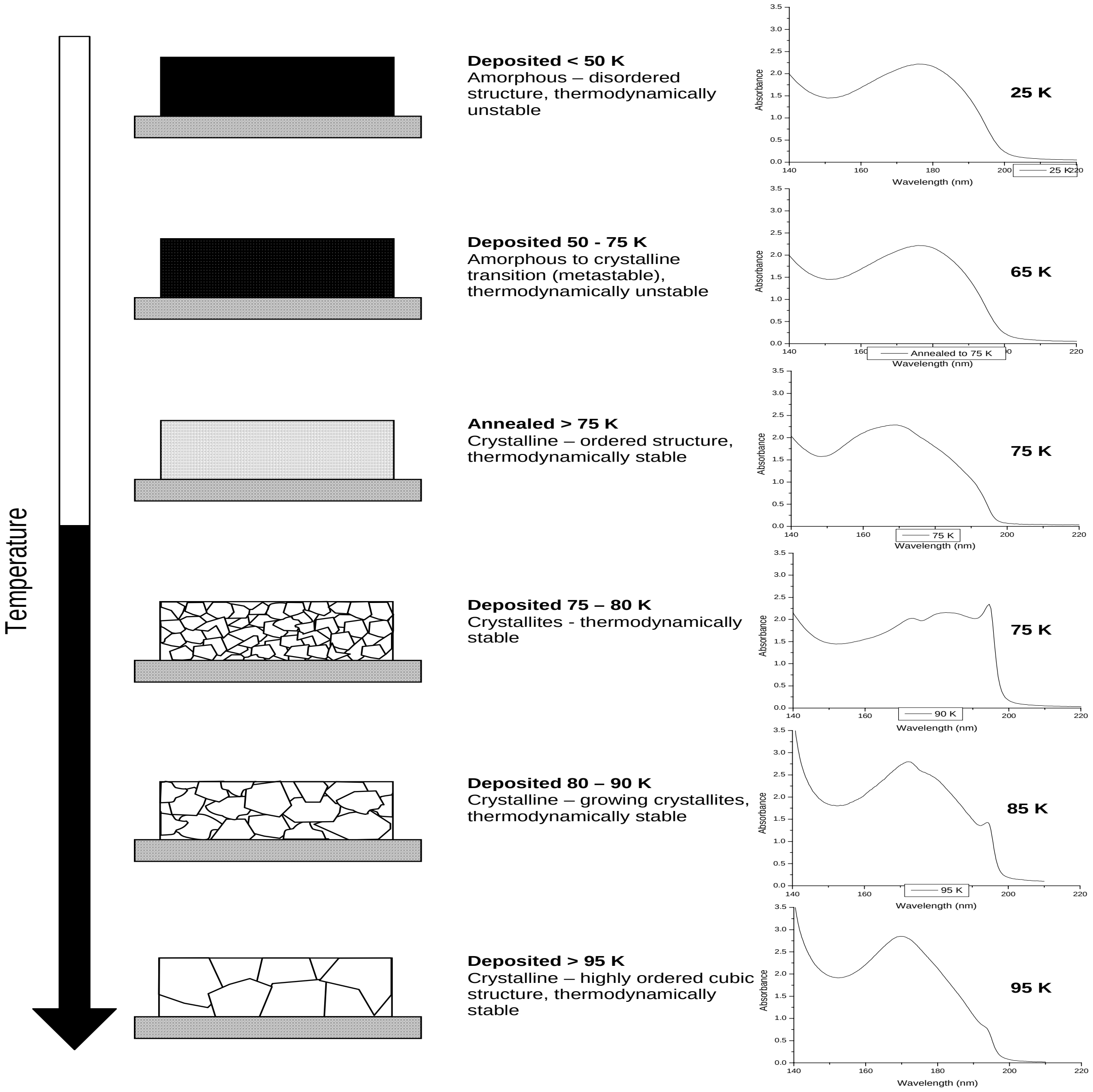

Figure 2: An illustration of the ice morphology structure as interpreted from VUV spectra of NH_3 ice.

2) When *annealed above 75 K* the solid crystallises forming an ordered, hydrogen bonded structure that is thermodynamically stable.
3) The spectra of all samples *deposited between 65 and 80K* exhibit an intense ‘exciton’ peak, with the highest intensity observed in a narrow temperature range between 65 and 80 K.
4) In samples *deposited at temperatures higher than 85K* the exciton peak diminishes with increasing temperature. Crystallites are few and probably large such that the sample is an ordered cubic crystal with a thermodynamically stable structure.

Further details of the experimental arrangements and their importance in astrochemistry may be found in forthcoming publications (1,2).

1. VUV photoabsorption spectroscopy of sulphur dioxide ice P D Holtom, A Daes, R J Mukerji, S M Webb , S V Hoffman and N J Mason PCCP (2005) in press

2. An investigation into the temperature dependence on the photoabsorption spectrum of pure solid ammonia A Dawes, R J Mukerji, M P Davis, P D Holtom, S M Webb, S V Hoffman, D A Shaw and N J Mason PCCP (2005)

Electron-beam lithography with molecular monolayers: fabrication of molecular surface nanostructures and unimolecular nanosheets

Armin Gölzhäuser

Physics of Supramolecular Systems, University of Bielefeld, Universitätsstr. 25, 33615 Bielefeld (goelzhaeuser@physik.uni-bielefeld.de)

A major goal in nanotechnology is the preparation and manipulation of supramolecular objects with nanometer dimensions. It is generally believed that future biotechnological and molecular electronics applications will heavily rely on molecular self-assembly as a major fabrication scheme. However, to perform molecular self-assembly in a controlled manor, one requires molecular resolution surface templates. For this task, it is essential to develop tools that can build nanoscale surface templates. The modification of surface bound self-assembled monolayers (SAMs) can do this and is therefore a very active field of research [1]. Low energy electrons are particularly well suited for the patterning of SAMs. First, electron-beam lithography can fabricate high-resolution (<6 nm) structures in a controlled manor. Second, the response of self assembled monolayers to electron irradiation can be tailored. Whereas the hydrocarbon chains in aliphatic SAMs are destroyed by electron beams [2], aromatic SAMs show an enhanced stability after electron bombardment [3], cf. Fig. 1. Functionalized aromatic self-assembled monolayer are particularly useful for e-beam patterning, as the impinging electrons dehydrogenate and cross-link the underlying aromatic cores, and chemically convert the terminal group, for example from nitro to amino [4,5], cf. Fig. 2. Hence, electron beam lithography creates localized surface groups to which other molecules may be coupled. The molecular patterns can be transferred into metals [6] and semiconductors [7], and molecular patterns can be utilized for the laterally controlled electrochemical deposition [8,9]. More generally, molecular templates can be used to immobilize various molecular entities (dyes, polymers [10], biomolecules [11]) on surfaces, cf. Fig. 3.

Finally, the controlled preparation of individual *nanosheets*, i.e. free-standing membranes which have the thickness of a single biphenyl molecule, is demonstrated [12]. These sheets can be prepared by electron-induced cross-linking of self-assembled monolayers and subsequent release of the material from its substrate.

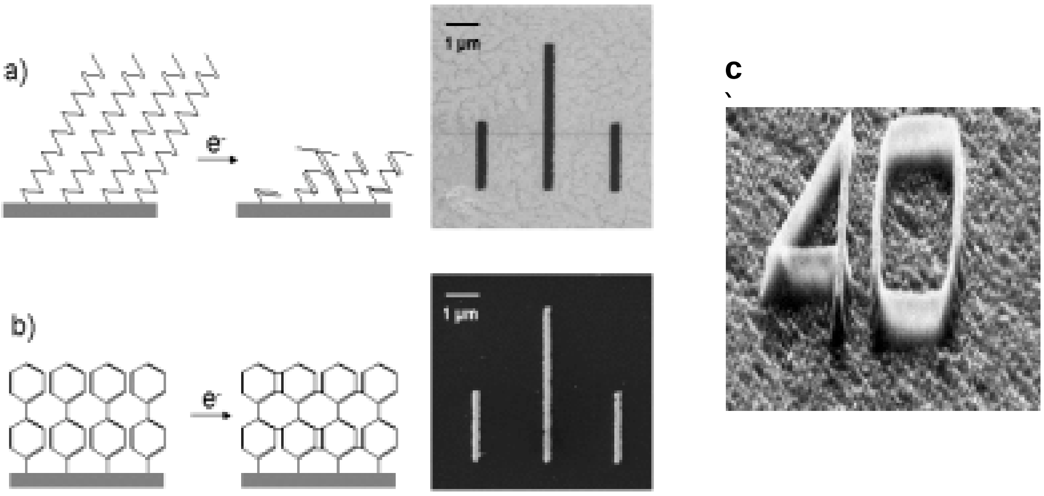

Fig. 1: Upon irradiation with electrons aliphatic SAMs, such as hexadecanethiol on gold, are destroyed and the monolayer acts as a positive resist (a). In aromatic SAMs, such as biphenylthiol, the molecules are laterally cross-linked and the SAM is a negative resist (b). The scanning electron micrographs to the right of the schematics show gold lines patterns that were produced with the respective SAMs. (c) A 40 nm line width pattern in Si produced with a cross-linked hydroxybiphenyl SAM

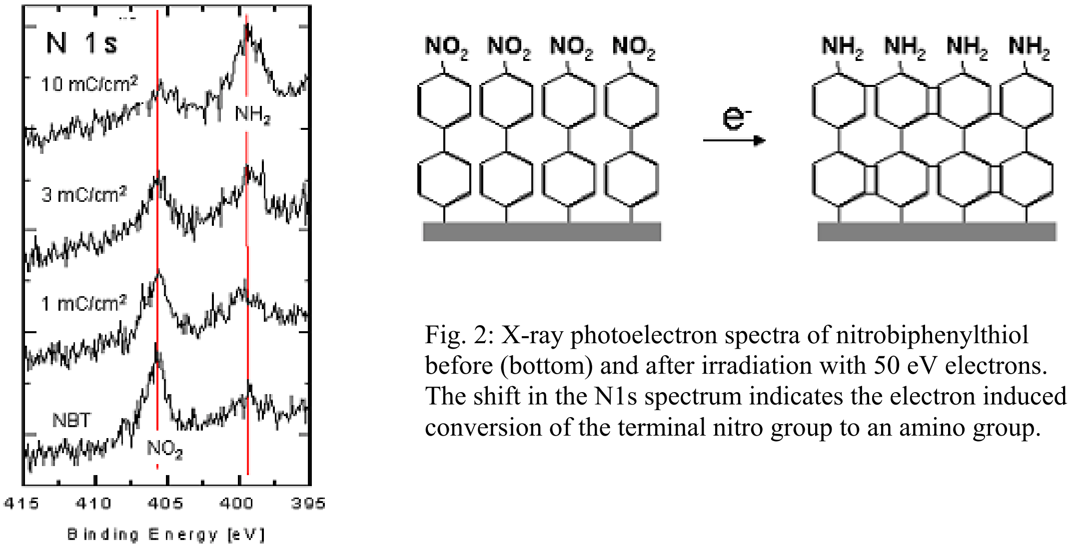

Fig. 2: X-ray photoelectron spectra of nitrobiphenylthiol before (bottom) and after irradiation with 50 eV electrons. The shift in the N1s spectrum indicates the electron induced conversion of the terminal nitro group to an amino group.

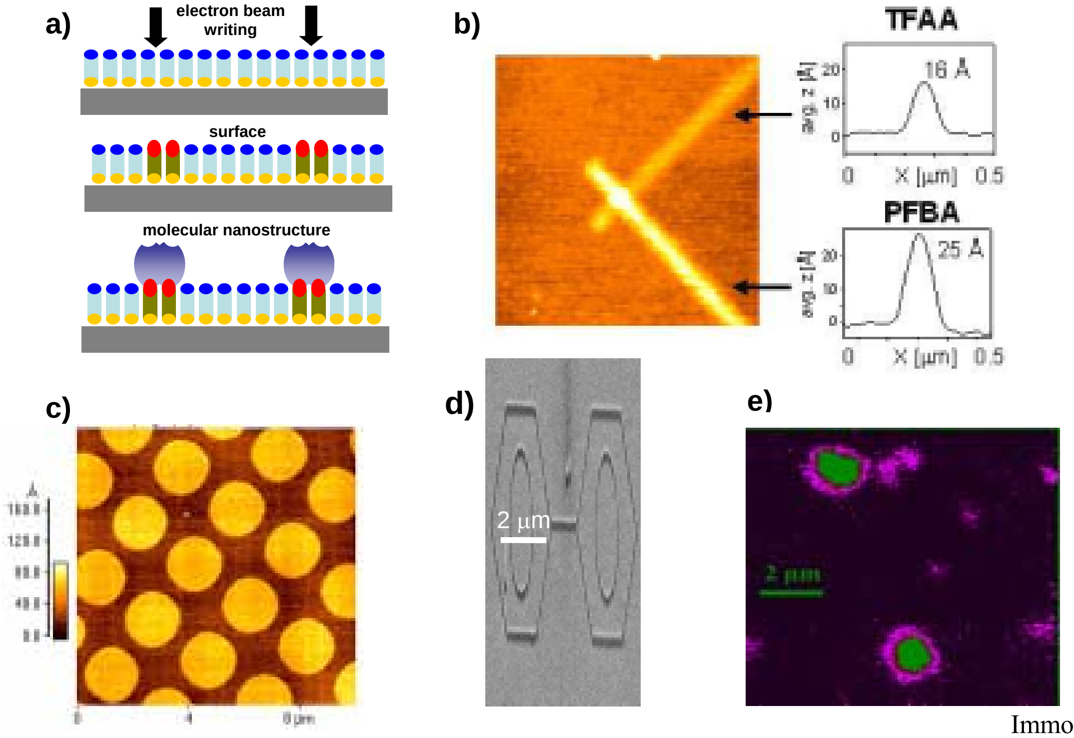

Fig. 3: Immobilization of different molecular entities on SAM-templates patterned by chemical nanolithography: a) schematic representation; b) AFM image and profiles of perpendicular trifluoroacetic acid anhydride (TFAA) and perfluorobutyric acid anhydride (PFBA) lines; c) AFM image of avidin molecules on a circular (d=1.5 µm) pattern; d) SEM image of a "biphenyl" pattern made by surface directed polymerization (linewidth 100nm); e) fluoresce micrograph of surface immobilized dyes.

References:

1. Here are two recent reviews on the field : R.K. Smith, P.A. Lewis, P.S. Weiss: Patterning self-assembled monolayers, Prog. Surf. Sci. 75, 1-68 (2004); J.C. Love. L.A. Estroff, J.K. Kriebel, R.G. Nuzzo, G.M. Whitesides: Self-assembled monolayers of thiolates on metals as a form of nanotechnology, Chem. Rev. 105,1103-1169 (2005).

2. M. Zharnikov, W. Geyer, A. Gölzhäuser, S. Frey, M. Grunze: Modification of alkanethiolate monolayers on Au-substrates by low energy electron irradiation: Alkyl chains and the S-Au interface, Phys. Chem. Chem. Phys. 1, 3163-3171 (1999).

3. W. Geyer, V. Stadler, W. Eck, M. Zharnikov, A. Gölzhäuser, M. Grunze: Electron induced cross-linking of aromatic self-assembled monolayers: negative resists for nanolithography, Appl. Phys. Lett. 75, 2401 (1999).

4. W. Eck, V. Stadler, W. Geyer, M. Zharnikov, A. Gölzhäuser, M. Grunze: Generation of surface amino groups on aromatic self-assembled monolayers by low energy electron beams – A first step towards chemical lithography, Adv. Mater. 12, 805 (2000)

5. A. Gölzhäuser, W. Eck, W. Geyer, V. Stadler, Th. Weimann, P. Hinze, and M. Grunze: Chemical Nanolithography with Electron Beams, Adv. Mater. 13, 806 (2001).

6. A. Gölzhäuser, W. Geyer, V. Stadler, W. Eck, M. Grunze, K. Edinger, Th. Weimann, P. Hinze: Nanoscale-Patterning of self-assembled monolayers with electrons, J. Vac. Sci. Technol. B, 18(6), 3414 (2000).

7. A. Küller, W. Eck, V. Stadler, W. Geyer, A. Gölzhäuser: Nanostructuring of silicon by electron beam lithography of self-assembled hydroxybiphenyl monolayers, Appl. Phys. Lett., 82, 3776 (2003).

8. T. Felgenhauer, C. Yan, W. Geyer, H.-T. Rong, A. Gölzhäuser, M. Buck: Electrode modification by electron-induced patterning of aromatic self-assembled monolayers, Appl. Phys. Lett., 79, 3323 (2001).

9. G. Kaltenpoth, B. Völkel, C.T. Nottbohm, A. Gölzhäuser, M. Buck: Electrode Modification by electron-induced patterning of self-assembled monolayers, J. Vac. Sci.Technol. B 20, 2734 (2002).

10. U. Schmelmer, R. Jordan, W. Geyer, W. Eck, A. Gölzhäuser, M. Grunze, A. Ulman: Oberflächeninitiierte Polymerisation auf selbstorganisierten Monoschichten: strukturierte Polymerbürsten auf Makrometer- und Nanometerskala, Angewandte Chemie, 115, 577 (2003).

11. A. Biebricher, A. Paul, P. Tinnefeld, A. Gölzhäuser, M. Sauer: Controlled three-dimensional immobilization of biomolecules on chemically patterned surfaces. Journal of Biotechnology, 112, 97 (2004)

12. W. Eck, A. Küller, M. Grunze, B. Völkel, A. Gölzhäuser: Free-standing nanosheets from cross-linked biphenyl self-assembled monolayers, Adv. Mat., 17, 2583-2587*,* (2005)

Organic nanofibers from functionalised oligophenylenes: new materials for nanophotonic devices

Katharina Al-Shamery

Carl v. Ossietzky University Oldenburg, Institute of Pure and Applied Chemistry, Oldenburg, Germany, katharina.al.shamery@uni-oldenburg.de

ABSTRACT

Growth of mutually aligned, several tens to hundreds of µm long organic nanofibers is demonstrated on mica under ultra high vacuum conditions. The fibers from functionalised para-phenylenes are grown by vacuum sublimation. Atomic force microscopy shows typical heights of the fibers of a few ten nanometers and typical widths of a few hundred nanometers. The length and morphology of the well organized nanofibers is depending on the functionalisation and the length of the para-phenylene building block. For example the well organized growth of long nanofibers from 4,4```-Dimethoxy-1,1`:4`,1``:4``,1```-quaterphenyl (MOP4) is more similar to the growth of long para-hexaphenyl (p-6P) nanofibers than to the rather unorganized growth of short para-quaterphenyl (p-4P) aggregates. The fibers emit intense blue light with well resolved higher order vibronic peaks and exhibit dichroitic non linear responses comparable to common inorganic compounds used for frequency doubling.

1. Introduction

Future information technology will be based on nanophotonic devices. In this context the interest in growing and manipulate selectively inorganic or organic nanowires has grown immensely. One very promising class of materials consists of short-chain para-phenylenes (p-nP, n=4-6) which can form semi-conducting films, aggregates or nanofibers with rather delocalised π-electrons. The most important property is that they emit blue light after excitation with either UV light (around 360 nm) or electrons which makes them well-suited candidates for building up active layers in organic light-emitting diodes (OLEDs), organic field effect transistors (OFETs) and other electronic and optoelectronic devices. Depending on the growth conditions oriented needle growth is observed on mica.

2. Results

The growth mechanism of the needles is influenced by strong electric dipole fields on mica which induce a dipole moment in the polarizable organic molecules, leading to an attraction via dipole-induced dipole forces and thus an alignment of the individual organic molecules along the surface dipole orientation. If the molecules possess enough surface mobility (i.e. if the surface is warm enough), aligned, needle-like aggregates of hundreds of µm can be grown with very well defined molecular orientations and widths between 50-400 nm [1]. Fig. 1 shows a fluorescence microscope image (500 x 500 μm^2) of two domains, consisting of parallel oriented, non contacting p-6phenylene nanofibers (nominal mass thickness 11 nm, inset: atomic force microscopy image (20 x 20 μm^2) of the same area). The growth of organic nanofibers is strongly depending on the functional groups of the para-phenylenes [2,3]. Their optical properties are highly anisotropic exhibiting linear waveguiding properties because of their high refractive index. If one increases the intensity of the excitation light, nonlinear optical effects can be observed in the nanofibers [4]. Due to the low photobleaching threshold of the aggregates, femtosecond laser pulses had to be employed as the excitation source. At excitation wavelengths between 770 and 786 nm contributions to the two-photon signal intensity from both two-photon luminescence (TPL) and second harmonic generation (SHG) have been observed, where $I_{SHG} / I_{TPL} \approx 0.015$.

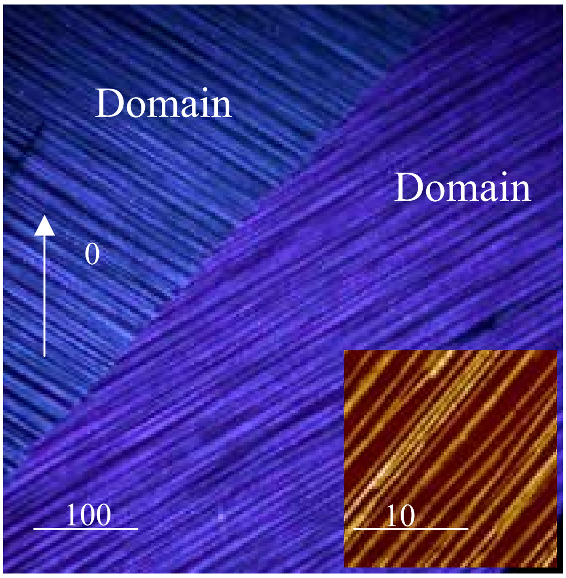

Fig. 1 fluorescence microscope image (500 x 500 µm^2) of two domains, consisting of parallel oriented, non contacting p-6phenylene nanofibers (nominal mass thickness 11 nm, inset: atomic force microscopy image (20 x 20 µm^2) of the same area).

Information about the position of the nonlinear transition dipole moment with respect to the long axis of the needles is obtained by rotationg the polarization vector of the exciting light around the surface normal. Fig. 2 exhibits the non linear response of a bunch of oriented para-hexa-phenylene fibers in two different domains rotated by 120° grown on mica as a function of the polarization of the incoming and outcoming laser beam (signal recorded at λ = 394 nm).

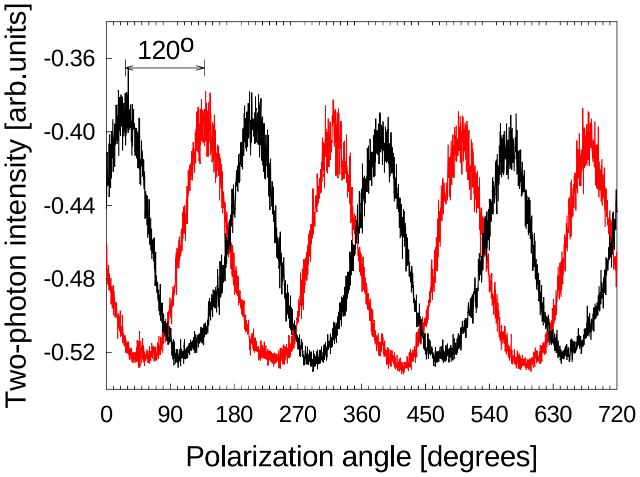

Fig. 2: Polarisation angle dependent two-photon signal intensity of nanofibers grown from p-6-phenylene from two different domains as a function of polarization of the laser light (signal recorded at λ = 394 nm). The polarisation angle is counted clockwise [4].

A χ(2) has been obtained which is only half of that for KDP (potassium dihydrogen phosphate), a common material for frequency doubling laser light [4].

[1] F. Balzer, H.-G. Rubahn, Appl.Phys.Lett. **79** (2001) 3860.
[2] M. Schiek, A. Luetzen, K. Al-Shamery, F. Balzer, R. Frese, H.-G. Rubahn, Appl. Phys. Lett., **86** (2005) 153107, Selected for Virtual Journal of Nanoscale Science & Technology, April 2005
[3] M. Schiek, A. Lützen, K. Al-Shamery, F. Balzer, H.-G. Rubahn, Surf. Sci., submitted
[4] F. Balzer, K. Al-Shamery, R. Neuendorf, H.-G. Rubahn, Chem.Phys.Lett. **368** (2003) 307.

Molecular clusters as reaction medium: Aqueous chemistry of transient species

Martin K. Beyer[1,2], O. Petru Balaj[2,3], Mirko Gruber[2], Stephan J. Reitmeier[2], Brigitte S. Fox-Beyer[2], Zheng Sun[2,4], Chi-Kit Siu[2,5], Vladimir E. Bondybey[2]

[1]Institut für Chemie, Sekr. C4, Technische Universität Berlin, Straße des 17. Juni 135, 10623 Berlin, Germany; martin.beyer@mail.chem.tu-berlin.de

[2]Department Chemie, Physikalische Chemie 2, Technische Universität München, Lichtenbergstraße 4, 85747 Garching, Germany

[3]Ecole Polytechnique, Departement de Chimie, UMR 7651 - Laboratoire DCMR, Route de Saclay - 91128 Palaiseau CEDEX, France

[4]Institute of Chemistry, Chinese Academy of Sciences, Zhongguancun, Haidian, Beijing 100080, P.R. China

[5]Department of Chemistry, York University, 4700 Keele Street, Toronto, Ontario, Canada M3J 1P3

ABSTRACT

Reactions of ionic water clusters, or hydrated ions, studied by Fourier transform ion cyclotron resonance (FT-ICR) mass spectrometry, proceed analogous to solution phase reactions [1,2]. This idea is applied to study aqueous chemistry of species which are short-lived in aqueous solution. Examples of such transient species are the hydrated electron and monovalent transition metal ions. In the gas phase experiment, individual reaction steps are identified unambiguously, since the nature of the reactive species is defined, in contrast to bulk solutions. Recent results suggest that also thermochemical information can be directly inferred from the experiment via the quantitative analysis of the number of evaporating water molecules. This approach is exemplified with the reactions of formic acid with hydrated electrons $(H_2O)_n^-$.

Monovalent vanadium is metastable in the cluster, and is oxidized to V(II) or V(III) with formation of atomic or molecular hydrogen, respectively [3]. These reactions are strongly size-dependent. Temperature resolved experiments with a nitrogen-cooled ICR cell, controlling the black-body radiation temperature experienced by the clusters between 86 – 300 K, reveal new insight into the reaction mechanism. At the lowest temperature studied, 86 K, H_2 formation is still efficient, while loss of water molecules is exceedingly slow and probably collisionally activated, at a rate of less than 1×10^{-3} s^{-1}. This shows that the barrier for the redox reaction is small, and that the $V(H_2O)_n^+$ clusters are only observable on the ICR time scale because the H_2 formation pathway is very complicated, making the reaction highly improbable. Temperature resolved measurements of the rate constants of the black body radiation induced processes allow the extraction of activation energies via master equation modelling as implemented in VARIFLEX [4].

[1] G. Niedner-Schatteburg and V.E. Bondybey, *Chem. Rev.* **2000**, 100, 4059.

[2] V.E. Bondybey and M.K. Beyer, *Int. Rev. Phys. Chem.* **2002**, 21, 277.

[3] B.S. Fox, I. Balteanu, O.P. Balaj, H.C. Liu, M.K. Beyer and V.E. Bondybey, *Phys. Chem. Chem. Phys.* **2002**, 4, 2224.

[4] S.J. Klippenstein, A.F. Wagner, R.C. Dunbar, D.M. Wardlaw and S.H. Robertson; VARIFLEX, A Program for Flexible Transition State Theory; VS. 1.00, **1999**.

Surface Processing of Nano-Crystalline Diamond Films for Different Applications

H. Drexel[1], D. Steinmüller-Nethl[1], L.A. Francis[2], C. Van Hoof[2]

[1] Rho-BeSt coating GmbH, Erlach 165, 6150 Steinach a.B., AUSTRIA
(h.drexel@rhobest.com)

[2] IMEC, Kapeldreef 75, B-3001 Leuven, BELGIUM

ABSTRACT

Nano-crystalline diamond (NCD) films are offering the same outstanding physical properties as natural diamond and hence provide a tremendous rich field of new applications. The **Na**no – crystalline **Di**amond **Ne**twork (NaDiNe) was founded by Rho-BeSt coating in order to utilize the provided opportunities at its best. Several results which could be achieved within the framework of NaDiNe will be presented. The applications range from bio-functionalisation over nano - electro-mechanical systems (NEMS) as far as pancreatic cell - growth on specially treated diamond films.

1. Introduction

Since 1994 a modified CVD process which allows deposition of extremely smooth nano-crystalline diamond (NCD) films on various substrates has been developed. The main features of the ρ-BeSt coating diamond films are: high purity (more than 98 % sp^3-hybridisation), randomly oriented crystallites with a grain size of 5-15 nm, closed layer at 200 nm, three dimensional growth on large area and moreover strong adhesion at substrates like silicon, glass, sapphire, ceramics, titanium etc.. These special features are complemented by the intrinsic properties of diamond. The most important for the applications described here are: highest hardness, high Young's Modulus, high chemical stability, large electrochemical potential window for functionalisation with bio-molecules, surface termination either hydrophilic or hydrophobic, biocompatibility and conductivity controllable by doping. Taking advantage of the tremendous capability offered by the combination of the intrinsic properties of diamond and the features of the NCD films we were able to realise new and promising applications.

2. ρ-BeSt and the **Na**no–Crystalline **Di**amond **Ne**twork (NaDiNe)

In past ρ-BeSt coating technique was manly applied for cutting tools and also for luxury goods in recent years. However beside these applications NCD is also well suited for electronic devices and for several bio-applications. To cope with the challenges in these fields it is essential to bring together interdisciplinary expertise. Therefore ρ-BeSt coating collaborated with universities, research institutes and private companies. These partners are combined in the network project NaDiNe financially supported by the Austrian Nano Initiative and organisationally by Kompetenzzentrum Medizin Tirol (KMT) and West Austrian Initiative for Nano Networking (W_INN). The aim of this consortium is to establish new products based upon nano-crystalline diamond coatings. Together with our partners we were able to grow Langerhans cells for transplantation and to produce NEMS (nano-electro-mechanical-system) devices by means of lithographic methods as well as to functionalise diamond coatings for different applications like bio-sensors.

3. Surface termination and functionalisation

Building up a diamond lattice carbon has to hybridise in sp^3–configuration. Consequently each carbon atom sitting at the surface exhibits one unsaturated dangling bond at the surface. These dangling bonds provide the opportunity to terminate and moreover to functionalise the diamond surface very easily. Inherently the diamond surface is saturated with hydrogen due to the production process leading to a hydrophobic surface behaviour.

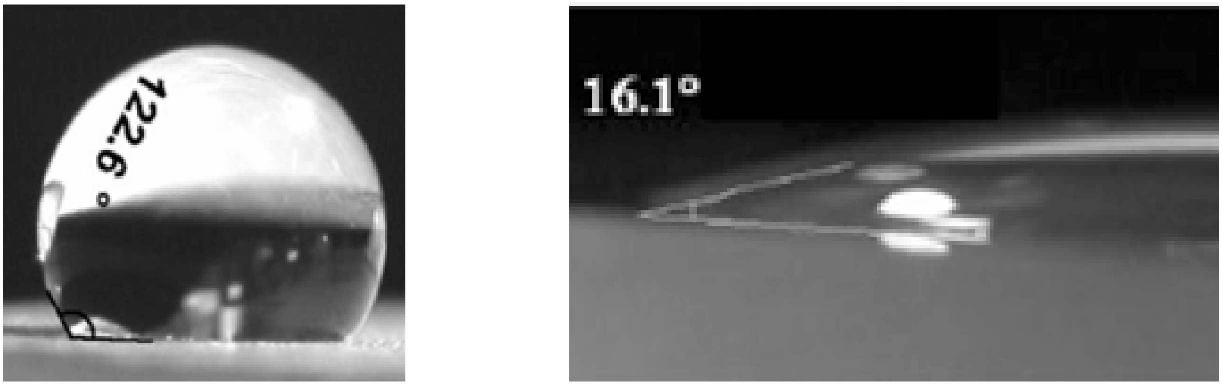

Figure 1: water droplet sitting on a nano-crystalline diamond surface as produced (left) and after termination of the surface with oxygen (right)

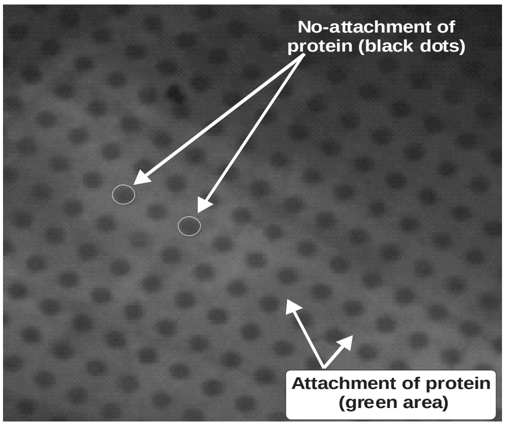

Simply by heating up the diamond surface in oxygen atmosphere the hydrogen atoms are replaced by oxygen - containing groups thus leading to a hydrophilic surface termination (see figure 1). Both the hydrogen as well as the oxygen termination are long term stable under ambient conditions. The hydrogen and oxygen - containing groups bounded to the surface can be used as functional group for covalently binding of various molecules. Hence they are offering an easy way to functionalise the surface (see figure 2).

Figure 2: Protein-modified nano-crystalline diamond films for biosensor applications, Nature Mat. **3** (2004), 736-742

4. Growth of Pancreatic Cells for Transplantation on NCD-films

People being afflicted with diabetes mellitus typ 1 (T1DM) suffer from an autoimmune process that destroys the insulin producing beta cells of the Islets of Langerhans. To cure this disease the whole pancreas has to be replaced by a pancreas from a donor. In year 2000 Shapiero et al. [New Engl. J. Med., **343**, (2000) 230-238] succeed in curing T1DM by just transplanting pancreatic islets cells but for one patient two or three donors are necessary (10.000 cells/kg). Cultivation and cell proliferation in vitro on promising substrates, such as diamond, would allow an acceleration of growth of islet cells and hence significantly reduce the number of donors needed. We have tested the growth of islet cells on hydrogen as well as on oxygen terminated - thus hydrophobic respectively hydrophilic - diamond substrates. The results had been compared with quartz glass which is known to be very biocompatible. We have been able to achieve the same adhesion and spreading of the Langerhans cells as on quartz glass and additionally found that the cells on diamond stay fitter. However the advantage of diamond is that it is not only bio compatible but also can be chemically modified very easily. These modifications can be performed either with special growth factors, amino acids, peptides or DNA and enhanced cell attachment, structured cell growth, influence on cell function etc. are expected.

5. NEMS Devices

Photo lithography and etch processes are the most commonly used methods for the production of nano-structured devices. Even though this technique is normally used for silicon we were able to apply it successfully to diamond substrates too. We have realised freestanding membranes, cantilevers and bridges in the nanometer range. These devices can be used not only as sensors or detectors but also as actuators. In combination with the bio-functionalisation these systems represent the very first prototypes for biosensors.

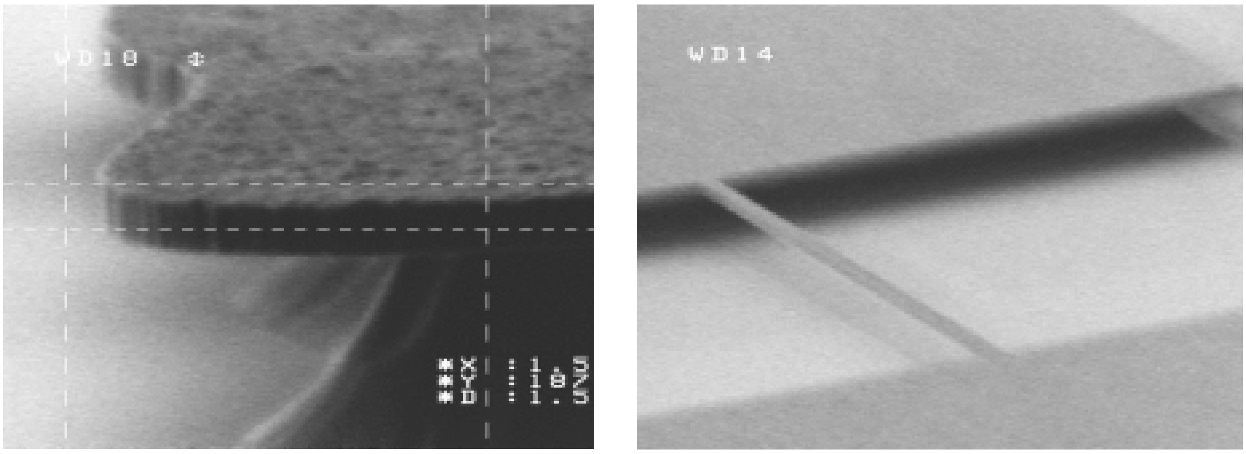

Figure 3: nanostructures etched out of a 200 nm thick nano - crystalline diamond film; cantilever (left) and catwalk with a 200 times 200 nm cross section and a length of 10 µm (right)

6. Conclusions and Outlook

Nano-crystalline diamond films have been processed and structured in order to meet various electronic and bio applications. First prototypes for cell culturing as well as for bio-sensors have been realised. The results achieved encourage further investigations which in turn will lead to tremendous contributions for various new and sophisticated applications.

Supported by:

nano
austrian nano initiative

winn
west austrian initiative
for nano networking

NADINE
nano diamond network

Cold Electron Collisions in Plasmas

David Field[1], Nykola Jones[1], Peter Cicman[1], Richard Balog[1], Roman Curik[1,2], Jean Pierre Ziesel[3], Tom Field[4]

[1]Dept. of Physics and Astronomy, University of Aarhus, 8000 Aarhus C, Denmark
dfield@phys.au.dk

[2]Heyrovsky Institute, Czech Academy of Sciences, Prague 8, Czech Republic

[3] Laboratoire Collisions Agrégats Réactivité, Université Paul Sabatier, 31062 Toulouse, France

[4] Dept. of Pure and Applied Physics, Queen's University Belfast, UK ...

ABSTRACT

The significance of the electron energy distribution in reactive plasma discharges is outlined. Rotationally inelastic cross-sections for electron-polar molecule collisions are essential data to calculate this energy distribution. However reliable data do not exist in the literature and constitute the most outstanding area of ignorance in the field of electron-molecule scattering. We present a method for extracting these data from experimental results and at the meeting we will present state-to-state cross-sections for H_2O and other species.

1. Introduction

One of the most important means of forming nanostructures is through the use of reactive radiofrequency (RF) plasmas, with production lines presently working at below the 100nm level. The aim is to improve etch definition by a factor of ten within the next decade. RF chemical plasmas run at a pressure <100 mtorr, $[e^-] \sim 10^{10}$-10^{11} cm^{-3} and a power density: a few W/cm^2. Electron-molecule collisions produce reactive species in plasmas. Here we stress very low energy "cold electron" collisions below 100 meV. The electron chemistry depends on the electron energy and cold electrons can be particularly efficient in attachment and dissociative attachment to form reactive radicals and negative ions[1]. The electrical characteristics of the RF discharge also depend on the electron energy distribution (EED). For example the time averaged value of the plasma potential is approximately proportional to the electron temperature[2,3]. Moreover if electrons are tied up as negative ions through electron attachment, the electrical properties of the discharge will undergo major changes. At all events the chemical, physical and electrical properties of the discharge are intimately connected and the EED is an essential characteristic for plasma modelling. Modelling may only be reliably conducted with a knowledge of electron-molecule inelastic and reactive cross-sections.

If there are polar molecules or polar molecular fragments in the plasma, electrons rapidly tend to equilibrate to the temperature of the neutral. The processes to which we refer are typified by hot $e^- + CHCl_3\ (J_{low}) \rightarrow$ cooler $e^- + CHCl_3\ (J_{high})$ and cool $e^- + CHCl_3\ (J_{high}) \rightarrow$ hot $e^- + CHCl_3\ (J_{low})$ leading to rapid temperature equilibration through rotational energy transfer. If there are concurrently

---

[1] e.g. Ziesel, Jones, Field&Madsen JCP **122** 24309 (2005)

[2] Song, Field&Klemperer J. Phys. D Appl. Phys **23** 673 (1990)

[3] May, Field, Klemperer J.Appl.Phys. **73** 1634 (1993)

electron-attaching species in the plasma, these suck out the low energy electron tail. A continuous process of electron temperature equilibration, through rotationally inelastic scattering, may therefore be coupled to removal of the low energy population of electrons through attachment. To include this process in plasma modelling, cross-sections are evidently required for rotationally inelastic scattering of electrons by polar molecules. This is the subject of the present work.

There are no experimentally based data in the literature for cross-sections for processes which change the rotational state of polar molecules through electron collisions in the most important regime at low energy. In this connection such cross-sections are large at low energy (e.g. [[4]]) and can exceed one thousand $Å^2$. Up to the present the only available general method of obtaining cross-sections has been through theoretical calculations based on the Born approximation(see [4]), at the simplest level of first order point dipole. This ignores for example the presence of elastic scattering and the reliability of the cross-sections available is questionable.

We report here the first reliable near-threshold cross-sections for rotationally inelastic scattering. This is based on novel theory which we use to fit to very low energy electron scattering data. Since this method is new, for the present we have data only for the water molecule. This illustrates how the method works and the state-to-state data that are forthcoming. Water was chosen for its inherent importance in other fields and also because rigorous ab initio calculations have recently been performed on this molecule[5],[6]. Other species of more importance to plasma etching will be analyzed shortly and some data may be available at the time of the meeting.

2. Experimental Considerations

The experimental apparatus has been described in detail elsewhere[7]. Suffice it to say that we use a photoionization source of electrons, employing synchrotron radiation from the ASTRID storage ring (ISA, Aarhus) to photoionize Ar at threshold at 15.75 eV. We form high resolution low energy beams, whose energies may extend down to a few meV with an energy resolution of typically 1 meV. Electron beam gas-cell scattering experiments yield total integral scattering cross-sections as a function of electron energy. Note that for experimental reasons a known proportion of the forward scattering is not included in the measurements. In independent experiments in the presence of a 20G magnetic field, axial to the electron beam, we measure scattering cross-sections into the backward hemisphere.

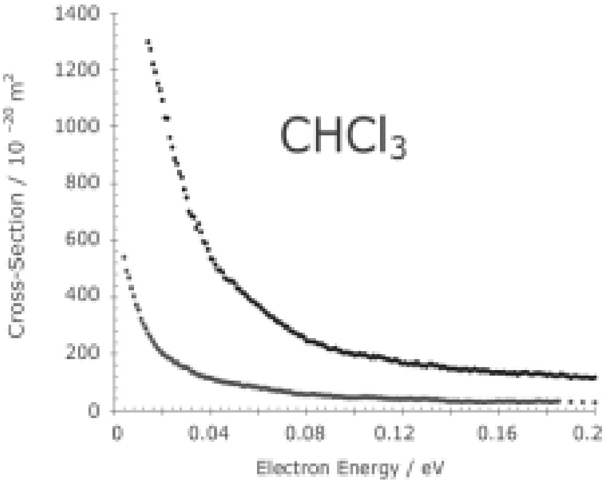

Typical experimental data for the variation of the scattering cross-section for electrons by polar molecules are shown below, for $CHCl_3$. The upper curve shows the integral scattering cross-section and the lower the scattering cross-section into the backwards hemisphere.

Significant points are (i) the energy of the electrons extends to very low values of 10 meV and below, (ii) the scattering cross-sections rise very rapidly at low energy, (iii) measured cross-sections are for the sum total of all types of events.

---

[4] Lunt, Field, Hoffmann, Gulley&Ziesel J.Phys.B At.Mol.Opt.Phys. **32** 2707 (1999)

[5] Faure, Gorfinkiel &Tennyson Mon.Not.R.Astrr.Soc. **347** 323 (2004)

[6] Faure, Gorfinkiel &Tennyson J.Phys.B At.Mol.Opt.Phys. **37** 801 (2004)

[7] Hoffmann, Lunt, Jones, Field&Ziesel Rev.Sci.Instr. **73** 4157 (2002)

At these energies the cross-section is overwhelmingly due to elastic scattering and rotationally inelastic scattering, with a few Å^2 of dissociative attachment for $CHCl_3$.[8]

We seek to obtain rotational state-to-state cross-sections from these and similar data, for example for H_2O. The outstanding problem is that the cross-sections involve a superposition of elastic and inelastic events. There was until recently very little indication in the literature of the relative magnitude of these cross-sections. However the sophisticated theoretical work by the University College London (UCL) group[5,6] shows that a significant proportion - perhaps 50% at lower energies - of the total scattering cross-section can be due to elastic scattering, at any rate in the case of H_2O.

2. Comments on the theory of rotationally inelastic scattering

The inherent theoretical difficulties in treating an electron-dipole system in which the potential varies as r^{-2} are well documented[9]. The potential combines with the centrifugal term $\ell(\ell+1)/r^2$ and, by the same token, the dipole dominated potential mixes partial waves and a partial wave decomposition is not feasible. The essential difficulty in the classical analogue is that of a particle suffering a collision of sufficiently small impact parameter that the deflection angle of the incoming particle becomes infinite. If small changes are made to the potential in the vicinity of $r=0$ to obviate this, effectively cutting off the r^{-2} behaviour near the origin, then the resulting deflection angle and the scattering cross-section are very sensitive to these changes. Hence in scattering calculations a very careful description must be made of the target wave functions in order that the electron-molecule potential is accurately estimated. The long range attraction also requires that many partial waves be involved, compounding the computational problem. In addition, the scattering problem should naturally be treated as a many channel problem, involving close coupling. For example, as noted, the interaction leads not only to rotationally inelastic scattering but also elastic scattering in which the target molecular species remains in the same rotational state after the collision as before.

The theoretical apparatus developed by one of us (RC) involves recasting the problem in terms of the scattering of waves which have already undergone mixing by a pure dipole potential. These so-called ‘dipole partial waves’ are then subjected to the action of the remaining part of the potential. This may be described as a ‘two potential’ model, combining r^{-2} with an unknown V^{int} which contains all the complicated electron-electron and electron-nucleus interactions which one would normally have to compute in an ab initio theory. However here we fit to the experimental data, using phase shifts for the dipole partial waves as parameters. In this way we do not need to have any knowledge of V^{int}. Because the dipole partial waves contain the effects of the long range r^{-2} potential, it turns out that at low energy only two such waves, analogous to s- and p-waves, but now called σ- and π-waves, are required to fit the data. Thus for every energy we have two values of cross-section - integral and backward - and two unknown phase shifts, η_σ and η_π. Thus phase shifts and the corresponding cross-sections may be extracted from the data. At the lower energies, η_π is effectively zero and both integral and backward data can be fitted with the single parameter η_σ.

This procedure turns out to be very successful in fitting the experimental data with high precision. We are able to verify the theoretical result of the UCL group that elastic scattering plays an important role in electron-H_2O encounters. Rotational state-to-state cross-sections are also derived which agree well with the UCL theory.[5,6] These results will be discussed in the presentation.

3. Concluding Comments

---

[8] Matejcik, Senn, Scheier, Kiendler,Stamatovic&Märk. J.Chem.Phys. **107** 8955 (1997)

[9] e.g. Newton *Scattering Theory of Waves and Particles* Springer 2nd Ed. Verlag New York 1982

The work reported here and the results to be presented at the meeting represent the very first experimentally based rotationally inelastic scattering cross-sections for electron molecule collisions with polar molecules. There is a great deal of work to be done in this field in the future, in the first place analyzing the substantial quantity of data, similar to that for $CHCl_3$ shown here, which we have obtained in recent years for a variety of species. These include numerous halogenated species of interest in plasma based etching.

The next step for theory is to be able to build a structure which deals with the three coupled channels of elastic, rotationally inelastic and reactive scattering. Recent work was able to extract absolute values of attachment cross-section[1], but only for non-polar molecules. In the future we would seek to extract reactive cross-sections for polar species also.

Strategies and Pitfalls in the Quantitative Analysis of Thin Films

Peter Wilhartitz

Plansee AG Postfach 74 A-6600 Reutte, Austria,
e-mail: Peter.Wilhartitz@plansee.com

A wide variety of analytical techniques is available today for the characterisation of thin films. Although qualitative information can be achieved in a very straight forward manner it is extremely difficult to gain precise quantitative information about chemical composition, structure and speciation.

Commonly used analytical techniques such as XPS, SIMS, EPMA, RBS and ERDA bear several pitfalls when applied to thin films with heterogeneous structure or graded composition. For quantitative analysis almost no calibration samples are available if the application is not related to semiconductor industry. Thus it can happen that even so called absolute methods like RBS and ERDA are misleading.

Based on selected examples possible strategies to avoid disappointing results will be discussed.

Nanostructures for cryoelectronics

A. Plecenik[1], M. Gregor[2], T. Plecenik[1], P. Kúš[1], V. Gašparík[1, 2], M. Štefečka[2], and A. Zeleňák[2]

[1] Department of Experimental Physics FMFI, Comenius University, Mlynská dolina F2, 84248 Bratislava, Slovak Republic, e-mail: plecenik@fmph.uniba.sk

[2] BIONT a.s., Karloveská 63, 842 55 Bratislava 4, Slovak Republic

We report preparation of Single Electron Tunneling Transistor (SETT) based on titanium thin films. The titanium dioxide was formed onto titanium thin films by Atomic Force Microscope (AFM) local oxidation nanolithography [1, 2]. Non conductive titanium dioxide regions determined titanium conductive area for SETT. A few tens of nanometers wide oxidized titanium lines were used for formation of island between source and drain.

The titanium thin films were deposited on unheated single crystalline Si (001) and Al_2O_3 (r-sapphire) substrates by a planar DC magnetron sputtering. The thickness of titanium thin films were below 10 nm and roughness less than 2 nm. The initial pressure into the vacuum chamber was 10^{-4} Pa and the pressure during deposition was 0, 5 Pa. The voltage between the anode and the cathode was 400 V and the current was 500 mA. After the deposition, the chemical composition of titanium films was analysed by Auger Electron Spectroscopy (AES). Surface topography was measured by Atomic Force Microscope Solver P-47 (Fig. 1).

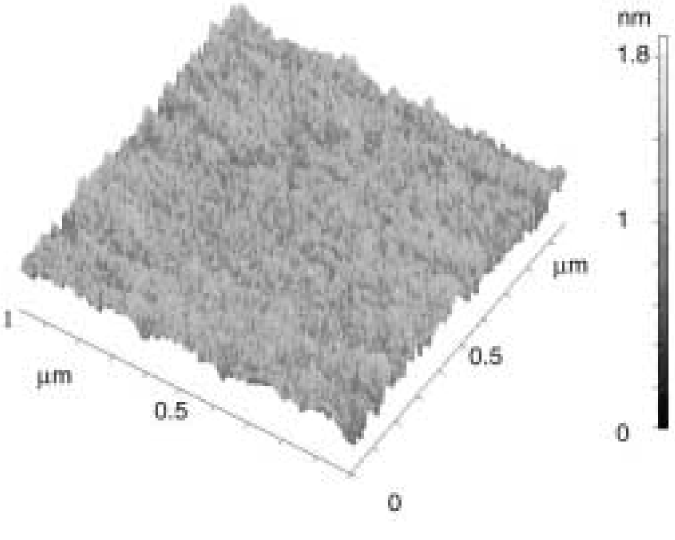

Fig. 1 Topography of titanium thin film on silicon substrate measured by AFM microscope

Process of the nanostructure fabrication consisted from several steps. First of all, the structures with micrometer dimension were fabricated using the optical lithography technique. Lithographic pattering was achieved by selective irradiation of photoresist deposited onto a titanium thin film. It was necessary to prepare the structures of micrometer dimensions before the nanolithography process, because the maximum operating area of SPM nanolithography is less than 50x50 μm^2. For determination of the micro-structures the physical Ar^+ ion etching with energy of ions 500 eV and chemical wet etching in HF solution were used. The strips with thickness about 5 nm and width 10 μm were obtained (see Fig. 2) after stripping of photoresist. On such stripes the SPM nanolithography was applied.

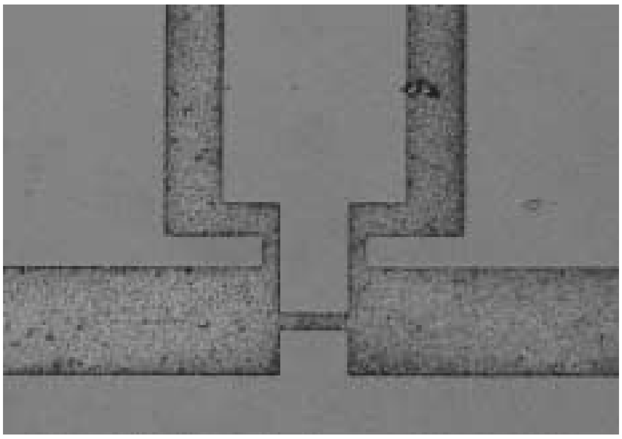

Fig. 2 Microstrip prepared by optical lithography on titanium thin films and etched by Ar^+ ion beam. The width of central strip is 10 μm.

Titanium thin films with thickness below 5 nm were completely oxidized down to the substrate by AFM nanolithography. In air or humid atmosphere, the probe and the surface of the sample are covered by thin film of absorbed water. When a tip approaches the surface, these absorbed layers come in contact and a water bridge is produced. Electrochemical reaction is initiated through the bridge upon application of corresponding electric strength. The height of the oxide depends on the applied voltage, the writing speed, the current between the tip and the sample, and the humidity. We used an atomic force microscope operating in tapping mode. The voltage between AFM tip and the surface was 10 V, the oscillation amplitude of the tip was 2-3 nm and the writing speed was 1000 nm/s. All modifications were done at room temperature and ambient air with relative humidity 50 – 90 %.

The main aim of our work is preparation of Single Electron Tunnelling devices, which can detect charges and manipulate the motion of individual electron with high precision. The fabrication of these nanostructure devices has to be perfect, and it requires development of extremely precise measurement techniques. Single electron devices shall find significant application in the digital electronics, in fabrication of memory chips or shift registers. [3, 4].

All structures were produced using combination of the optical lithography technique and the AFM oxidation process. Figure 3 shows a tree-dimensional image by AFM of the Single electron tunneling transistor design. At the centre region of the Ti layer, the island region is formed which is surrounded by the two parallel narrow TiO_x lines that will work as tunneling junctions for the SET and the two large TiO_x barrier regions which work as an insulator betwee

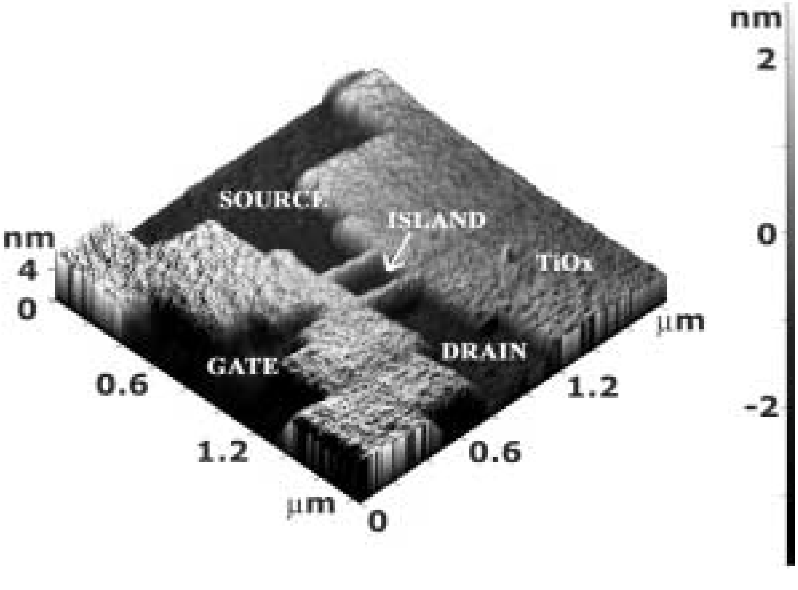

Fig. 3 Design of the Single Electron Tunneling Transistor prepared by AFM local oxidation nanolithography on the titanium central strip.

The measurements of the prepared SETT structures at temperatures 20 mK are in the progress.

Acknowledgement

All works were done under the facilities of laboratories of the Department of Experimental Physics, FMFI Comenius University and the Laboratory of nanotechnology, BIONT, a.s. The authors thanks to the Ministry of Education of the Slovak Republic for support of the grant "Nanostructures for nanometrology, sensors and cryoelectronics". This work was also partially supported by the VEGA project No. 1/2011/05 and APVT project No. APVT-51-016604.

References

[1] Vullers, M., Ahlskog, M., Haesendonck, V. C. Titanium nanostructures made by local oxidation with the atomic force microscope, Applied Surface Science 144-145, 1999. p. 584-588.

[2] Matsumoto, K., Ishii, M., Segawa, K., Oka, Y., Vartanian, B. J., and Harris, J. Room Temperature Operation of Single Electron Transistor made by STM Nano-Oxidation Process for TiOx/Ti System, Applied Physics Letters, 68 (1),1995, p. 34-36.

[3] Matsumoto, K. Application of scanning tunneling/atomic force microscope nanooxidation process to room temperature operated single electron transistor and other devices, Scanning Microscopy Vol. 12, No. 1, 1998, p. 61-69.

[4] Gregor, M., Plecenik, A., Metrology and testing 1/2003; p.3-9

Optical emission spectroscopy of a hollow cathode sputtering source

C. Ionita[1], R. Apetrei[2], D. Alexandroaei[2], D. Luca[2], P. Balan[1], R. Schrittwieser[1], G. Popa[2]

[1] Institute for Ion Physics, Leopold-Franzens University Innsbruck, A-6020 Innsbruck, Austria (Codrina.Ionita@uibk.ac.at)

[2] Faculty of Physics, Alexandru Ioan Cuza University, RO-700506 Iaşi, Romania

ABSTRACT

Experimental results on a cavity-hollow cathode post-discharge sputtering source are presented. For the sputtering regimes of magnetic (Ni) and non-magnetic targets (Cu, Ti) the following discharge parameters were used: Ar-pressure $6\times10^{-2} \div 1\times10^{-1}$ mbar and discharge current $5 \div 60$ mA. The spatial distribution of the relative electron density in front of the nozzle was measured by emission spectroscopy in order to correlate the optical and electrical diagnostic data. The radial and axial distributions of the emission spectra were mapped in the 340 to 650 nm wavelength range. By applying an Abel transformation to the radial distribution of the light intensity, the proportionality factor to the electron plasma density was calculated. Also the spectra of the discharge for using Ni, Cu and Ti as sputtering materials were measured.

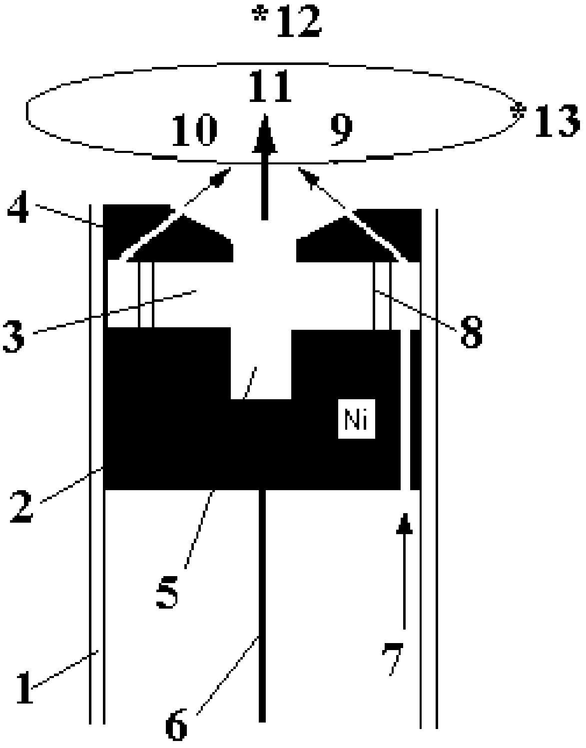

Fig. 1. Schematic diagram of the cavity-hollow cathode: 1: cylindrical glass tube, 2,4: Ni-disks, 3: cylindrical cathode cavity, 5: cylindrical hole, 6: electrical cathode lead, 7,9,10: Ar-gas inlets, 8: glass spacer, 11: plasma jet, 12: position of the substrate, 13: anode ring.

1. Introduction

Thin films growth by plasma-assisted sputtering is a well-established technique. However, the search for specific sputtering source geometries is still pending. A simple low cost high-efficiency sputtering source operated in the $10^{-1} \div 10^{-2}$ mbar regime was proposed recently, which utilizes the so-called cavity-hollow cathode post-discharge [1]. Unlike magnetron sputtering sources, there are no problems with sputtering of ferromagnetic materials since there is no magnetic field. Due to intense substrate ion bombardment good quality ferromagnetic films can be grown [2]. Although there is a lot of experience with hollow cathode discharges, their use as sputtering sources requires further research. This has been carried out previously mainly by electrical diagnostic methods. Here we present results of emission spectroscopy investigations.

2. Experimental set-up

Fig. 1 shows a schematic of the sputtering source. In a cylindrical glass tube (1), two

25-mm diameter Ni-disks (2) and (4) are used to enclose a 1.4 cm^3 cylindrical cathode cavity (3) within the glass spacer of 6 mm height (8). The lower electrode (2) has a central 5 mm diameter cylindrical hole (5) to enhance the ionization rate inside the cathode chamber. A 3 cm diameter ring anode (13) is co-axially inserted at a distance of 1.8 cm from the nozzle, close to the film substrate (located in position 12).

Argon gas was introduced in front of the nozzle through three inlets (7, 9, 10), while power was applied to the cathode via the electrode (6). Under normal operation, a conically shaped glowing plasma jet (11) occurs in front of the cathode, where the particle motion is controlled by electrical and pressure gradients.

Optical measurements were performed using an optical fibre, a monochromator and a photomultiplier. The radial distribution of the light intensity was measured at different axial positions between the two electrodes and in front of the exit nozzle of the hollow-cathode source. The light intensity was measured for 434.8 nm wavelength. This line of the optical emission spectrum corresponds to the de-excitation of singly ionized argon between the energy levels of 19.49 eV and 16.64 eV [3]. To determine the plasma emissivity, which is proportional to the electron plasma density, we use an Abel inversion. In the case of cylindrical symmetry of the light source the observed projected intensities can be transformed into a radial distribution within the plasma [4].

3. Results and discussion

If $I(y)$ is the measured intensity of the radiation integrated over the line of sight at a distance y from the centre and $\varepsilon(r)$ the local emissivity of the plasma at a distance r from the centre, then $I(y)$ *is* related to $\varepsilon(r)$ by the equation:

$$I(y) = 2\int_0^{(R^2-y^2)^{1/2}} \varepsilon(r)dx = 2\int_y^R \frac{\varepsilon(r)rdr}{(r^2-y^2)^{1/2}} \qquad (1)$$

R is the radius at which $\varepsilon(r)$ becomes zero. An inversion yields the desired quantity $\varepsilon(r)$:

$$\varepsilon(r) = -\frac{1}{\pi}\int_r^R \frac{dI(y)}{dy}\frac{dy}{(y^2-r^2)^{1/2}} \qquad (2)$$

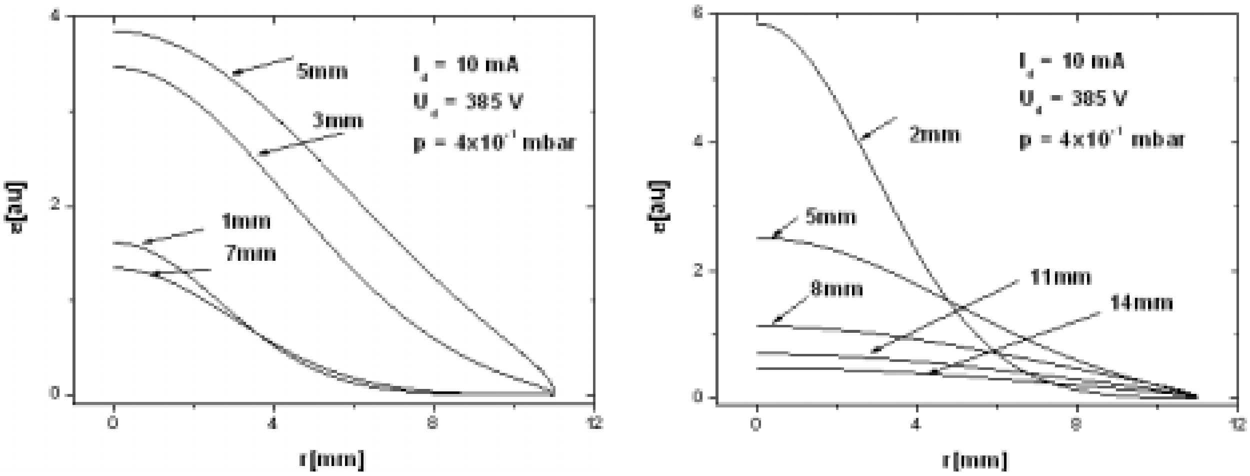

(a) (b)

Fig. 2. Radial profile of plasma emissivity at different locations on the z-axis axis between the cathode and the anode. (a) between the two cathode parts, (b) between the upper cathode and the anode.

Since Eq. (1) is of the Abel type, Eq. (2) is the corresponding Abel inversion.

Optical diagnostics was performed under the following pressure and current conditions: 0.4 - 0.95 mbar and 10 mA, respectively. The radial distribution of the light intensity of 434.8 nm wavelength was monitored at different position along the distance between the electrodes (2) and (3) and along the distance between the upper electrode (3) and the ring anode (13), (see Fig. 1).

Different positions on the symmetry axis (i.e. the *z*-axis), are considered going from the lower cathode to the upper one (when we are between the cathodes), and going from the upper cathode to the anode (when we are between the upper cathode and the anode). The obtained curves were fitted using Gaussian functions. The correlation coefficients R^2 were more than 0.99. These Gaussian functions were used in the Abel inversion to obtain the plasma emissivity, ε(*r*). As shown in Fig. 2(a), the plasma emissivity and the corresponding plasma density are smaller near the electrodes. It was observed that plasma was more confined near the electrodes, while inside the glass spacer the emissivity is larger and the plasma expands into the whole glass spacer. Between the upper cathode and the anode, Fig. 2(b), the emissivity decreases drastically while approaching the anode. In the same time, the plasma is more dense and confined near the upper cathode.

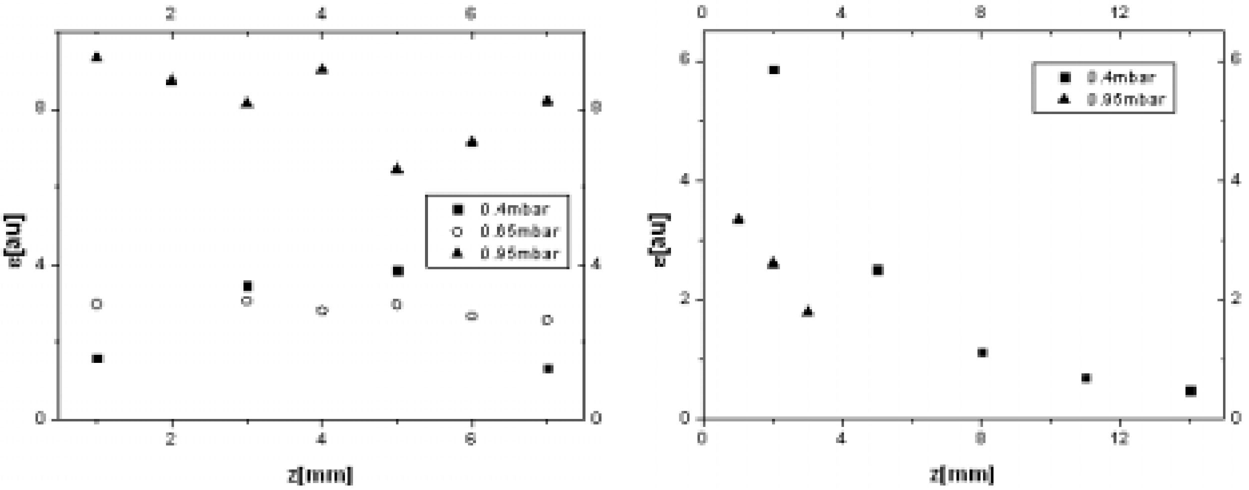

(a) (b)

Fig. 3. Axial profile of plasma emissivity at different locations on the z-axis axis between the cathode and the anode. (a) between the two cathode parts, (b) between the upper cathode and the anode.

If we monitor the plasma emissivity along the symmetry axis for different pressures, we observe the following facts: Between the electrodes, the emissivity reaches a maximum at the mid-distance between the electrodes (2) and (4) for $p = 0.4$ mbar. It is almost constant along the *z*-axis for $p = 0.65$ mbar, while for $p = 0.95$ mbar it shows a minimum in the middle of the inter-electrode distance. As shown in Fig. 3, the emissivity is decreasing with increasing pressure at a certain location between the anode and cathode. The emissivity decreases while approaching the anode for all pressures that were investigated. A decrease of the length of the plasma jet with increasing pressure is also noticed.

Fig. 4 shows typical optical emission spectra taken from the space between cathode and anode of the cavity hollow-cathode post-discharge for various materials such as Cu, Ti and Ni. The appropriate experimental values of the pressure and discharge current are essential for the sensitivity of OES diagnostics.

4. Conclusion

Optical measurements were performed to diagnose the post-discharge Ar plasma jet in front of a cavity-hollow cathode post-discharge and between the electrodes. There are clear similarities between electrical and optical diagnostics. It was observed that the plasma emissivity shows a rapid monotonous decrease along 2 cm on the hollow-cathode axis, which is correlated to the evolution of the electron temperature, the plasma density, and the ion velocity distribution functions. This evolution was observed also by electrical methods [2]. Optical diagnostics of the plasma inside the glass spacer shows that the radial distribution of the plasma density is almost Gaussian while axially it is rather constant. Further optical emission spectroscopy experiments are in progress to monitor the distribution of the atomic species both inside the hollow cathode and in the anode-cathode interval to get data for the design of a suitable geometry for film deposition.

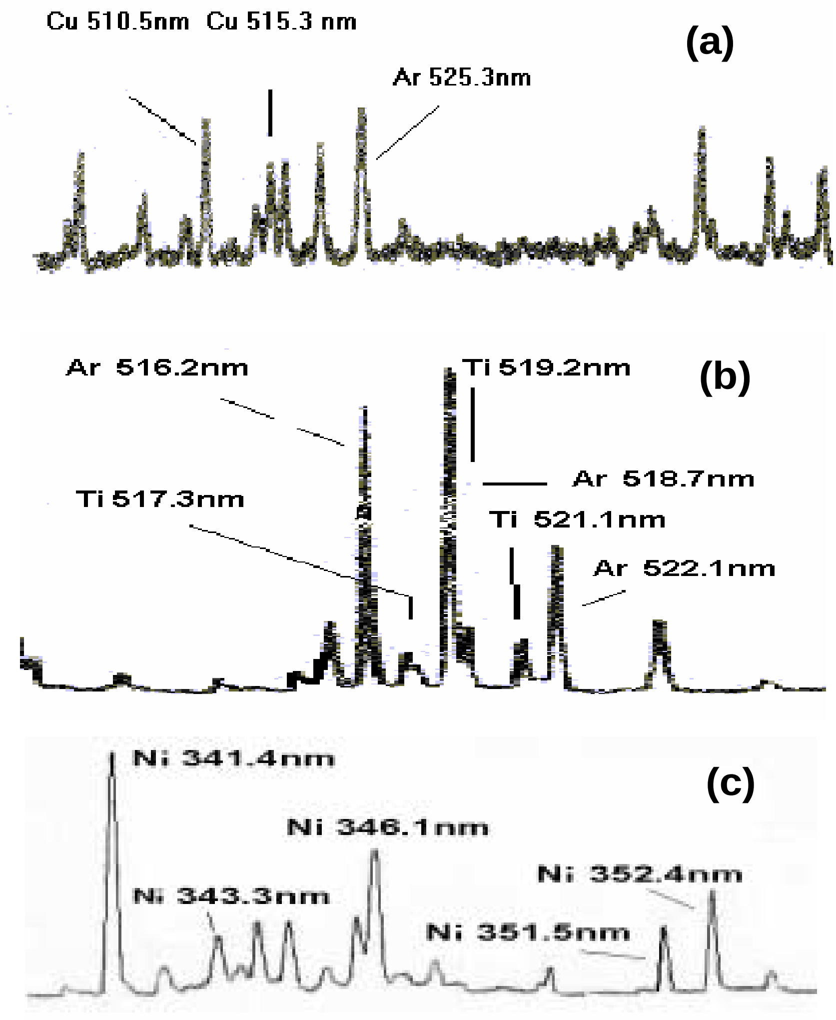

Fig. 4 OE spectra for three different cathode materials (a) Cu at p = 0.3 mbar; (b) Ti at p = 0.09 mbar; (c) Ni at p = 0.2mbar; I = 40mA.

Acknowledgement

The financial support by the Romanian CERES contract no 4-100/2004 is acknowledged. This work was partly performed in the framework of the CEEPUS network A103 and of a Socrates-Erasmus exchange programme.

References

[1] M. H. Kazemeini, A. A. Berezin, N. Fukuhara, *Thin Solid Films* **372** (2000) 70.

[2] P. C. Balan, R. Apetrei, D. Luca, C. Ionita, R. Schrittwieser, G. Popa, J. Optoel. *Adv. Mater.* **7** (2005) 2459.

[3] NIST Physics Laboratory, *Handbook of Basic Atomic Spectroscopic Data*, http://physics.nist.gov/.

[4] W. Lochte-Holtgreven, *Plasma Diagnostic*, North-Holland, Amsterdam, 1968, p 134.

Chemistry of organic molecules in non thermal plasmas

P. Franceschi, G. Guella, D. Ascenzi, L. Penasa, P. Tosi

Department of Physics, University of Trento, Via Sommarive 14, I -38050 Povo, Trento, ITALY
(pfranc@science.unitn.it)

ABSTRACT

Chemistry occurring in non thermal plasmas at atmospheric pressure have been studied by combining gas chromatography, mass spectrometry and guided ion beam experiments. In the case of benzene – air mixtures, several ionic products containing nitrogen and oxygen atoms have been observed. In particular an interesting ion of molecular formula $C_6H_5N_2^+$ has been produced. Ion trap MS-MS measurements and guided ion beam (GIB) experiments on the reaction of the phenyl cation with nitrogen molecules allowed us to establish that the detected $C_6H_5N_2^+$ is the benzenediazonium ion. In the case of acetonitrile (CH_3CN) – air mixtures, we observed several cluster ions ($C_4H_5N_2^+$, $C_4H_7N_2^+$, $C_5H_7N_2^+$, $C_6H_{10}N_2^+$). In contrast to a widely accepted assumption, we have shown that they are covalent molecules rather than electrostatically bound adducts.

1. Introduction

Non-thermal plasmas constitute high energy environments that can effectively promote chemical rearrangements in the gas phase. The chemistry is dominated by the presence of atoms and molecules in excited states, radicals and ions, whose interaction can result in chemical reactions, electron transfer and excitation/relaxation of internal degrees of freedom.

A growing interest on atmospheric pressure non thermal plasmas has been registered in recent years. Atmospheric plasma reactors have been successfully applied (in some cases coupled with solid state catalysers [1]) for removing pollutants such as polyciclic aromatic hydrocarbons (PAHs) and volatile organic compounds (VOCs) (gas clean-up) [2]. In addition they have been proposed for promoting the reforming process for hydrogen production [3], opening interesting perspectives on biomass and biogas exploitation.

The chemistry of atmospheric pressure plasmas is very complex since chemical rearrangements proceed through complex reaction pathways involving both charged and neutral species. The ion chemistry can be directly probed by Atmospheric Pressure Chemical Ionization Mass Spectrometry ion-sources (APCI – MS). Even if it is widely accepted that APCI produces ions with just gentle fragmentation it has been recently shown that it can promote a rich ionic chemistry [4, 5]. Besides APCI-MS, gas chromatography (GC-MS) can be used for analyzing stable neutral molecules produced in non equilibrium plasmas.

The simultaneous knowledge of ionic and neutral products is a key step in understanding the overall chemistry of the plasma system.

From a fundamental point of view, the resulting chemical complexity derives from the microscopic details of molecular reactivity. In the case of ion population this connection can be directly investigated by studying key reactions under controlled conditions (single collision with well defined reagent kinetic energy and internal state) in a guided ion beam apparatus.

2. APCI-MS ion chemistry

The APCI technique is highly sensitive [6] and very selective towards stable ions since chemical equilibrium conditions are usually achieved within the atmospheric pressure ion source [7]. In these conditions fast exothermic ion/molecule reactions occur effectively channelling the charge into the most stable species.

The primary reactions, leading to hydronium ion formation have been recognized and investigated by Carroll et al.[8].The principal ions present in the carrier gas are cluster ions of the type $H^+(H_2O)_n$ even at temperature above 200°C. In these conditions, protonated molecular ions are the most common ions observed [9]. A similar behaviour occurs also in an atmospheric pressure photoionization (APPI) system [10] where the efficiency of ionization has been found to be much higher for compounds with good proton affinity.

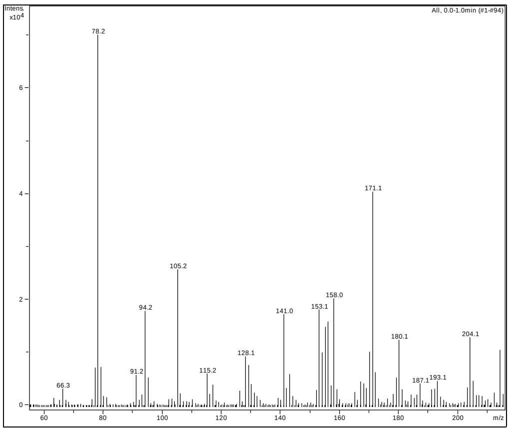

Figure 1: Positive ion mode APCI spectrum of benzene

3. Experimental

APCI - MS

Atmospheric Pressure Chemical Ionization sources consists of a small size corona discharge. In our case the experiments were performed in a Bruker Esquire-LCTM quadrupole ion trap mass spectrometer (Bruker-Daltonics, Milano, Italy) equipped with an APCI interface (HP/Agilent Technologies). Instrumental parameters were optimized to obtain the highest molecular ion abundance for each analyte studied.

Guided Ion Beam (GIB)

Our home built Guided Ion Beam apparatus consists of a tandem mass spectrometer equipped with a radiofrequency octopole scattering cell for trapping reagent an product ions. Selected elementary processes involving ionic species can be investigated under controlled conditions (single collision with well defined reagent kinetic energy).

Barrier discharges + GC-MS analyzer

The non thermal plasma reactor consists of an atmospheric pressure Dielectric Barrier Discharge (DBD) connected to a GC-MS analyzer (Thermo-Finnigan Trace DSQ). In this set-up, stable products can be analyzed as a function of the discharge parameters.

4. Ion Chemistry of nitrogen-benzene APCI

Several reasons motivate the investigation of the plasma chemistry of benzene-air mixtures. From an analytical point of view, it has been recently shown that charge exchange from benzene ion increases the sensitivity of APCI-MS toward hydrophobic compounds [11]. Moreover, the ion chemistry of benzene and polycyclic aromatic hydrocarbons (PAHs) has attracted great interest from fundamental research aimed at understanding reaction mechanisms and their implications in the chemistry of various ionized environments (e.g. combustion systems and planetary ionospheres) [12]. An up to date example is given by the recent discovery of benzene in the upper atmosphere of Titan by the Cassini probe [13].

APCI spectra

As shown in the figure 1, relevant peaks in the positive ion mode APCI full-scan spectrum of benzene are also detected at m/z 78, 94, 105, 153-158, 171 and 187.

The peaks at m/z 78 and 94 can be directly attributed to benzene ($C_6H_6^+$) and a benzene oxidized ion ($C_6H_6O^{+\cdot}$) respectively. The 105 ion will be discussed in the next paragraph while the heavier ions result from benzenoid self-condensation. in diphenyl-like “covalent-dimers”. A similar electrophilic reaction involving benzene-oxidized forms is responsible for 171 and 187 ions production.Such pattern of ions has been recently observed [14] in the APPI spectrum of benzene. In particular, the formation of the dimeric non-covalent ion at m/z 156 has been explained as originating from a gas-phase clustering reaction between $C_6H_6^{+\cdot}$ ions and neutral benzene.

Is worth noting that, with the exclusion of m/z = 105, the major molecular peaks has been observed in the GC-MS analysis of the DBD treatment of benzene–air mixtures. In this case, the major chromatographic peaks have been assigned to phenol (C_6H_5OH), diphenil ($C_{12}H_{10}$) and products deriving from the further oxidation of phenol/phenol-like dimers.

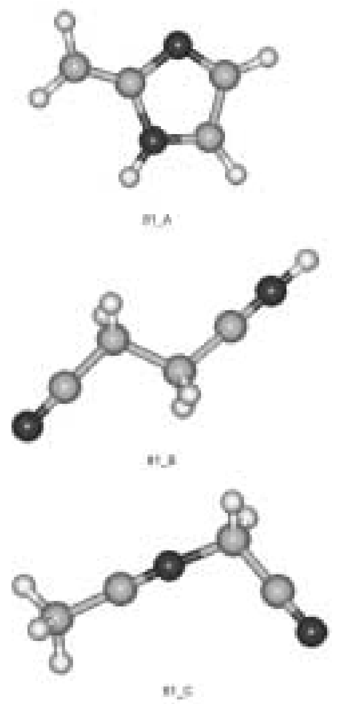

Figure 3: Selected optimized geometries for the C4H5N2+

Benzenediazonium ion

We have detected $C_6H_5N_2^+$ ions in the APCI mass spectrum of benzene. The identification of the ion at m/z 105 as benzenediazonium ion is supported by measurements performed with isotopically labelled reactants, and by MS^2 experiments.

In addition, we have investigated the possible ion-molecule reactions leading to $C_6H_5N_2^+$ in a guided ion beam tandem mass spectrometer. We have shown that the $C_6H_5N_2^+$ ion can be formed in the addition reaction of $C_6H_5^+$ and N_2. The adduct is collisionally stabilized, as demonstrated by the quadratic dependence of the product signal on the N_2 pressure in the scattering cell. The energetics of this reaction has been characterized by *ab initio* calculations.

5. Acetonitrile clusters

Acetonitrile, CH_3CN, is a dipolar aprotic solvent widely used in a variety of chemical processes in organic synthesis and in physical organic chemistry investigations for its capacity to dissolve both hydrophilic and hydrophobic substances Biomass burning has been identified as the dominant natural source of acetonitrile, which has been therefore proposed as a tracer for biomass burning emissions.

As in the case of benzene, we investigated APCI ion chemistry of acetonitrile combining mass spectrometry and *ab-initio* methods. In particular we focussed on the oligomeric structures related to acetonitrile dimers and trimers.

Considering the overwhelming number of isomeric forms we deduced the basic structural information by careful inspection of the isotopical exchange reactions. On these bases we calculated the structures and the energetics of the most relevant cluster ions $C_4H_5N_2^+$, $C_4H_7N_2^+$, $C_5H_7N_2^+$, $C_6H_{10}N_2^+$.

Up to now, only elemental formulas have been proposed for such ionic species [15] and often they have been tacitly assumed to be electrostatically bound adducts. On the contrary that they arise from covalent bond rearrangements leading to intriguing oligomeric covalent structures.

6. References

[1] S. Futamura,H.Einaga,H.Kobashima,L.Y.Hwan, Catalysis Today 89 (2004) 89.

[2] S.A. Nair, A.J.M. Pemen, K. Yan, F.M. van Gompel, H.E.M. van Leuken, E.J.M. van Heesch, K.J. Ptasinski, A.A.H. Drinkenburg, Fuel. Proc. Technol. 84 (2003) 161.

[3] Y. Sekine, K. Urasaki, S. Kado, M. Matsukata, E. Kikuchi, Energy and Fuels 18 (2004) 455.

[4] G.Guella, D. Ascenzi, P. Franceschi, P. Tosi, Rapid Communications in Mass Spectrometry 19 (2005) 1.

[5] G.Guella, P. Franceschi, P. Tosi, Chemical Physics Letters 415 (2005) 265.

[6] S.N. Ketkar, J.G. Dulak, W.L. Fite, J.D. Buchner and S. Dheandhanoo, Anal. Chem. 61 (1989) 260.

[7] D.R. Zook and E.P. Grimsrud, J. Phys. Chem. 92 (1988) 6374.

[8] I. Dzidic, D.I. Carroll, E.C. Horning, Anal. Chem. 48 (1976) 1763.

[9] J. Sunner, G. Nicol, P. Kebarle, Anal. Chem. 60 (1988) 1300.

[10] D.B. Robb, T.R. Covey, A.P. Bruins, Anal. Chem. 72 (2000) 3653.

[11] C. Perazzolli, I. Mancini, G. Guella, Rapid Commun. Mass Spectrom. 19 (2005) 461.

[12] D. Ascenzi, D. Bassi, P. Franceschi, O. Hadjar, P. Tosi, M. Di Stefano, M. Rosi, A. Sgamellotti, J. Chem. Phys. 121 (2004) 6728.

[13] Seewww.nasa.gov/mission_pages/cassini

[14] M. Tubaro, E. Marotta, R. Deraglia, P. Traldi Rapid Commun. Mass Spectrom. 17 (2003) 2423.

[15] B.M. Kolakowski, J.S. Grossert, L. Ramaley, Journal of the American Society of Mass Spectrometry 15 (2004) 312.

Gas-phase Catalysis by Atomic and Cluster Metal Ions: The Ultimate Single-Site Catalysts

H. Schwarz

Institut für Chemie, Technische Universität Berlin, Straße des 17.Juni 135,D-10623 Berlin, Germany, FAX: +49 30 314 21102, E-mail: Helmut.Schwarz@mail.chem.tu-berlin.de

Gas-phase experiments, employing state-of-the-art techniques of mass spectrometry, provide detailed insights into numerous elementary processes. The focus of this review will be on elementary reactions of ions that achieve complete catalytic cycles at thermal energies. The examples chosen cover aspects of catalysis pertinent to areas as diverse as atmospheric chemistry and surface chemistry. We will describe how oxygen-atom transfer, bond-activation and fragment-coupling processes can be mediated by atomic or cluster metal ions. In some instances truly unexpected analogies of the idealized gas-phase ion catalysis can be drawn with related chemical transformations in solution or the solid state and so improve our understanding of the intrinsic operation of a practical catalyst at a strictly molecular level.

The Prospect of Designer Materials via Cluster Assembly: The Next Frontier in Nanoscale Science

A.W. Castleman, Jr.

Departments of Chemistry and Physics, Penn State University, 104 Chemistry Building, University Park, PA 1680, email: awc@psu.edu

ABSTRACT

Systems of finite size often give rise to unique properties that differ from those of an extended solid or the individual molecular constituents of which they are comprised. Particularly interesting are ones of nanoscale dimensions whose composition can be selectively chosen, and ones whose individual characteristics can be retained when assembled as an extended material. A major long-term goal of our research in this area is to develop ways of tailoring the design and formation of new nanoscale materials of desired electronic, optical and catalytic properties. A major theme of this lecture will be devoted to a discussion of our efforts to produce superatoms, selected on the basis of the electron shell model, that enable the development of clusters which mimic elements of the periodic table. Recent success has been obtained in producing alloy cluster species of specific size and composition that simulate various elements such as rare gases, halogens, alkaline earth metals and other multivalent species. Focus on the reactivities of these species demonstrates the role that such cluster assembled materials may have in effecting desired reactions. It is becoming increasingly recognized that cluster science can help elucidate the physical and chemical properties of condensed phase catalysts and can provide detailed information on the mechanisms of reactions and the nature of various reaction sites that enable certain catalytic materials to be especially effective. In this context, our latest findings on various metal and metal compound cluster systems will be presented.

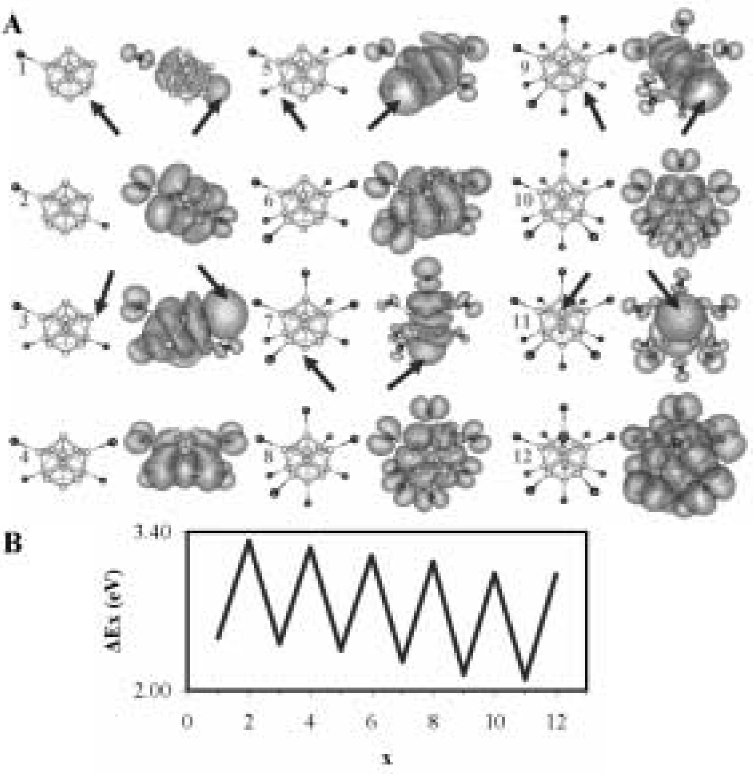

(A) Lowest energy structures and charge maps for $Al_{13}I_x^-$ (x values from 1 to 12). The areas of high charge density, or active sites, are indicated by arrows. (B) ΔE_x, the energy to remove one 1 atom from $Al_{13}I_x^-$ for x values form 1 to 12. Figure taken from "Al Cluster Superatoms as Halogens in Polyhalides and as Alkaline Earths in Iodide Salts", *Science*, **307**, p. 231 (2005).

Crossed molecular beam studies of radical-molecule and radical-radical reaction dynamics

P. Casavecchia

Dipartimento di Chimica, Università degli Studi di Perugia, Via Elce di Sotto, 8, 06123 Perugia, Italy, E-mail: piero@dyn.unipg.it

ABSTRACT

In this talk, the recent progress in dynamical studies of radical-molecule and radical-radical reactions using the crossed molecular beam scattering technique will be presented. It will be shown that, by exploiting the novel implementation of (i) the *soft* electron-ionization (EI) method for product detection and (ii) of variable beam crossing angle set-ups, the identification of the primary products, the determination of the branching ratios and the dynamics of virtually all channels of polyatomic multichannel reactions have now become amenable to the CMB technique with *universal* EI mass spectrometric detection. Examples will focus on the polyatomic reactions of acetylene and ethylene with oxygen and carbon atoms, of great relevance in areas ranging from combustion to astrochemistry, and on the reactions of atomic oxygen with alkyl radicals, such as methyl and allyl, of great importance in combustion chemistry.

1. Introduction

Our understanding of the dynamics of bimolecular reactions has benefited greatly of the "*universal*" capability of the Crossed Molecular Beams (CMB) scattering technique with Electron Ionization (EI) mass spectrometric detection and time-of-flight analysis [1]. Up to date, however, all CMB instruments with EI detection have featured "hard" EI (using 60-200 eV electrons) and a geometry of the two crossing beams of fixed 90° angle. Although in principle all reactions products can be detected by this technique, in practice there are some significant limits. One of the main limitations is known to reside in the dissociative ionization under hard EI of reagents, products, and background gases, that can greatly complicate and even prohibit the identification of primary products, particularly for polyatomic reactions exhibiting multiple channels and involving hydrocarbon molecules or radicals. In addition, when one increases the collision energy (by increasing the beam velocities), a significant loss of angular and velocity resolution arises. Furthermore, it is often not possible to cover with the rotating detector a wide enough angular range to capture the entire angular distribution of the products, especially for strongly exoergic or kinematically unfavored reaction channels.

In the aim of overcoming most of these traditional difficulties, very recently we have improved our CMB apparatus in several ways [2]. Specifically, to overcome the problem of the dissociative ionization we have introduced, for the first time, the *soft* EI ionization for product detection by using low-energy tunable electrons. This is an attractive alternative to the use of photo-ionization by VUV synchrotron radiation, and offers the bonus that branching ratios can be derived, because EI ionization cross sections are known or can be estimated. We have also implemented the possibility of crossing the two reactant beams at 45°, 90°, and 135°. These new settings allow us to vary the collision energy, E_c, in a much wider range than previously possible, when also exploiting the seeded beam technique. In general, the low E_c values are of particular interest for studies of reactions relevant to interstellar and extraplanetary chemistry environments, while the high E_c values are more relevant for combustion reactions. Furthermore, higher kinematic resolution and wider angular capability are attained with the 135° and 45° configurations, respectively.

While reactive differential cross sections (DCSs) have been measured using the CMB technique for a very large variety of radical-molecule reactions [1], little has been done on radical-radical systems despite their importance. This is mainly due to the difficulty of generating radical beams of sufficient intensity to carry out DCS measurements. In our laboratory we are generating since a number of years *continuous* supersonic beams of a variety of simple radicals (O, N, C, Cl, OH, CN) by using a high-pressure radio-frequency discharge beam source [1], and these beams have been used for investigating a variety of radical-molecule reactions. Recently, we have also developed a new source, based on *flash pyrolysis* in a SiC nozzle, for generating *continuous* supersonic beams of alkyl radicals (CH_3, C_2H_5, C_3H_3, etc.). The availability of these sources, coupled with a sensitive CMB instrument exploiting the "*soft*" electron ionization [2], has very recently permitted us to undertake, for the first time, the investigation of the dynamics of a variety of radical-radical reactions.

In this talk, we will discuss some results of recent studies on the dynamics of polyatomic multichannel reactions, as those of oxygen and carbon atoms with acetylene and ethylene for which, by exploiting the above instrumental improvements, it has been possible to essentially detect all reaction products, determine their branching ratios and characterize the dynamics of the competing reaction pathways [3-6]. We will also report on the first measurements of product angular and velocity distributions for the reactions of methyl (CH_3) and allyl (C_3H_5) radicals with oxygen atoms, of great relevance in combustion chemistry [7] .

2. Radical-molecule reactions

The reactions of $O(^3P)$ with acetylene and ethylene play a key role, besides in the combustion of acetylene and ethylene themselves, in the overall mechanisms for hydrocarbon combustion. The reactions of $C(^3P)$ with acetylene and ethylene are of great relevance in the chemistry of interstellar clouds, hydrocarbon synthesis and combustion.

The reaction $O(^3P)+C_2H_2$

The reaction $O(^3P)+C_2H_2$ is used as an example to illustrate the capability of the simple and, yet, powerful method of *soft* EI. By exploiting soft EI it has been possible to detect, for the first time, the CH_2 (methylene) product from the CH_2+CO forming channel, as well as the HCCO (ketenyl) product from the competing HCCO+H pathway. From product angular and velocity distributions, the reaction dynamics and the branching ratio of the two channels have been elucidated [3,6]. It is found that under truly single-collision conditions HCCO formation accounts for 80% of the overall reaction, and this corroborates the results of recent kinetic determinations and theoretical predictions.

The reaction $O(^3P)+C_2H_4$

The reaction $O(^3P)+C_2H_4$ constitutes another excellent example of the capabilities of CMB reactive scattering experiments with soft EI detection. There are five exoergic channels:

$$O(^3P) + C_2H_4 \rightarrow H + CH_2CHO \qquad \Delta H^\circ_0 = -71 \text{ kJ mol}^{-1} \qquad (1a)$$

$$\rightarrow H + CH_3CO \qquad \Delta H^\circ_0 = -114 \text{ kJ mol}^{-1} \qquad (1b)$$

$$\rightarrow H_2 + CH_2CO \qquad \Delta H^\circ_0 = -356 \text{ kJ mol}^{-1} \qquad (1c)$$

$$\rightarrow CH_3 + HCO \qquad \Delta H^\circ_0 = -113 \text{ kJ mol}^{-1} \qquad (1d)$$

$$\rightarrow CH_2 + HCHO \qquad \Delta H^\circ_0 = -29 \text{ kJ mol}^{-1} \qquad (1e)$$

Since the pioneering work of Cvetanovic in the mid 1950s, many research groups have investigated this reaction, employing a variety of experimental techniques under different conditions of pressure and temperature, identifying only some of the possible products, which has given rise to uncertainties and controversy. By using *soft* EI we have been able to unambiguously detect the following radical and molecular products: CH_2CHO, CH_3CO, CH_2CO, CH_3, and CH_2, corresponding to the five reaction pathways (1a-e). From a detailed series of angular and velocity distribution measurements at *m/e*=42, 15, and 14 using different electron energies, and from measurements of fragmentation patterns, we have characterized the reaction dynamics of all five competing channels and determined their branching ratios [4,6].

The reaction $C(^3P)+C_2H_2$

The reaction $C(^3P) + C_2H_2$ is known as a key process in the chemistry of the interstellar medium (ISM) and in particular of dense interstellar clouds (ISCs). The H elimination channel synthesises the C_3H radical, observed under its cyclic (*c*) and linear (*l*) forms with different *c*/*l* concentration ratios in various astrophysical objects, whereas the H_2 elimination channel produces the C_3 radical which is also detected in the ISM. Elucidating the dynamics of this reaction in a wide range of relative collision (translational) energies, E_c, including those relevant of ISCs is thus of high interest. Despite considerable experimental and theoretical work over the past 10 years, the detailed mechanism and dynamics of this reaction are still not well understood [8-10]. In particular, several important issues are still open, namely: (a) what are the precise exoergicities of the *l*-C_3H + H and *c*-C_3H + H pathways and (b) what are the branching ratios between *l*-C_3H, *c*-C_3H and C_3 and how do they vary with E_c?

From measurements of product angular and velocity distributions at different masses (*m/e*=37 and 36) in a wide range of collision energies (E_c~3.5-50 kJ/mol), we have identified the primary products (*l-,c*-C_3H+H and C_3+H_2), determined the branching ratios of the C_3H and C_3 forming channels, derived their center-of-mass angular and translational energy distributions, characterized the reaction micromechanisms, and obtained information on the potential energy surfaces (PESs) [5].

The reaction $C(^3P)+C_2H_4$

The reaction $C(^3P)+C_2H_4$ has been investigated at four different E_c. H-atom elimination, H_2-elimination, and C-C bond fission processes from the initially formed C_3H_4 intermediate can occur. From product angular and velocity distributions in the laboratory frame, product angular and translational energy distributions in the center-of-mass have been determined; the primary reaction products and their branching ratios have been obtained [11]. At the lowest E_c of 9.1 kJ mol^{-1} formation of $HCCCH_2$ (propargyl) + H is observed to be the dominant channel; formation of less stable C_3H_3 isomer(s) is minor (2%). As E_c increases, formation of appreciable, increasingly larger fractions of less stable propyn-1-yl and/or cyclopropenyl isomers is also observed. In contrast, the H_2 elimination channels leading to C_3H_2 formation have not been found to occur. The occurrence of C-C bond fission channels are possibilities that initially [11] could not be explored because of a too high background signal arising from dissociative ionization of elastically scattered C_2H_4 at the corresponding *m/e* of the products. Very recently, however, by employing the new approach of soft EI, it has become possible to also look at these channels. In fact, we have been able to detect both CH_2 (at *m/e*=14) and C_2H_2 (at *m/e*=25) products by using 19 eV electrons, which is close to the threshold for dissociative ionization of C_2H_4 to CH_2^+ (~18 eV) and C_2H^+ (~19 eV). This would have been impossible using *hard* EI.

3. Radical-radical reactions: $O(^3P) + CH_3$ and C_3H_5

We will also report on the first direct measurements of product angular and velocity distributions for two important radical-radical reactions: $O(^3P)+CH_3$ (methyl) and $O(^3P)+C_3H_5$ (allyl), which are of great relevance in combustion chemistry. These reactions have been investigated extensively from the kinetic standpoint, and also theoretically [12-14]; recently, OH product rovibrational distributions were determined by laser-induced-fluorescene for $O(^3P)$+allyl in pulsed jets [13]. In our CMB study, the primary products and their dynamics of formation are derived. Formaldehyde and acrolein are found to be the main products of the $O(^3P)$ reaction with methyl and allyl, respectively. By exploiting soft EI, C-C bond fission channels have also been observed in the O+C_3H_5 reaction. The results are interpreted at the light of the available electronic structure calculations of the potential energy surfaces [7].

Acknowledgments

This work was supported by the Italian MIUR (Ministero Istruzione, Università, Ricerca) via COFIN 2003 and 2004 and FIRB 2001. The European Commission is also gratefully acknowledged for support through contracts MRTN-CT-2004-512302 (MOLECULAR UNIVERSE) and Coordination Action 001637 (EuroPlanet).

References

[1] P. Casavecchia, *Rep. Prog. Phys.* ***63** (2000) 355, and references therein.*

[2] P. Casavecchia, G. Capozza, and E. Segoloni, "Crossed molecular beam reactive scattering: towards *universal* product detection by *soft* electron-impact ionization", in "Modern Trends in Chemical Reaction Dynamics: Experiment and Theory" Part 2, *Adv. Ser. Phys. Chem.* Vol. 14, X. Yang & K. Liu, Eds. (World Scientific, Singapore, 2004), Ch. 7.

[3] G. Capozza, E. Segoloni, F. Leonori, G. G. Volpi, P. Casavecchia, *J. Chem. Phys.* **120**, 4557 (2004) (Communication); and in preparation.

[4] P. Casavecchia, G. Capozza, E. Segoloni, F. Leonori, N. Balucani, G. G. Volpi, *J. Phys. Chem.* A **109**, 3527 (2005) (Letter, Front Cover); and in preparation.

[5] M. Costes, C. Naulin, F. Leonori, A. Bergeat , G. Capozza, E. Segoloni, N. Balucani, P. Casavecchia, *Faraday Discuss.* **133** (2006), in preparation.

[6] P. Casavecchia, F. Leonori, E. Segoloni, N. Balucani, G. Capozza, *J. Phys. Chem A* (Feature Article), in preparation. N. Balucani, F. Leonori, E. Segoloni, G. Capozza, and P. Casavecchia, *Int. Rev. Phys. Chem.*, in preparation.

[7] F. Leonori, N. Balucani, E. Segoloni,, A. Bergeat, R. Petrucci, D. Stranges, P. Casavecchia, in preparation.

[8] R. I. Kaiser, W. Sun, A. G. Suits, and Y. T. Lee, *J. Chem. Phys.* **107**, 8713 (1997); R. I. Kaiser, *Chem. Rev.* **102**, 1309 (2002)

[9] D. C. Clary, E. Buonomo, I. R. Sims, I.W.M. Smith, W. D. Geppert, C. Naulin, M. Costes, L. Cartechini, and P. Casavecchia, *J. Phys. Chem. A* **106**, 5541 (2002); L. Cartechini, A. Bergeat, G. Capozza, P. Casavecchia, G. G. Volpi, W. D. Geppert, C. Naulin, M. Costes, *J. Chem. Phys.* **116,** 5603 (2002); P. Casavecchia, N. Balucani, L. Cartechini, G. Capozza, A. Bergeat, G.G. Volpi, *Faraday Discuss.* **119**, 27 (2001).

[10] T. Takayanagi, *Chem. Phys. Lett.* **312**, 61 (2005).

[11] W. D. Geppert, C. Naulin, M. Costes, G.- Capozza, L. Cartechini, P. Casavecchia, and G. G. Volpi, *J. Chem. Phys.* **119**, 10607 (2003).

[12] W. Hack, M. Hold, K. Hoyermann, J. Wehmeyer, and T. Zeuch, *Phys. Chem. Chem. Phys.* **7**, 1977 (2005), and references therein.

[13] S.-K. Joo, L.-K. Kwon, H. Lee, J.-H. Choi, *J. Chem. Phys.* **120**, 7976 (2004); and refs. therein.

[14] T. P. Marcy, R. R. Diaz, D. Heard, S. R. Leone, L. B. Harding, S. J. Klippenstein, J. Phys. Chem. A 105, 8361 (2001).

Photoionisation and ion-molecule reaction studies involving radical species of planetary interest

C. Alcaraz[1], C. Nicolas[1], R. Thissen[1], O. Dutuit[1], J. Zabka[2], P. Franceschi[3], T. Schüßler[4], W. Roth[4], H.-J. Deyerl[5], M.Elhanine[6], T. Gerber[7], and I. Fischer[4]

[1]LCP, Centre Universitaire Paris-Sud, Bât. 350, 91405 ORSAY Cedex, France (christian.alcaraz@lcp.u-psud.frr)

[2]J. Heyrovsky' Institute of Physical Chemistry, Academy of Sciences of the Czech Republic, Prague, Czech Republic

[3]Dept. of Physics, University of Trento, Via Sommarive 14, 38050 Povo (TN), Italy

[4]Institute of Physical Chemistry, University of Würzburg, Am Hubland, D-97074 Würzburg, Germany

[5]Faculty of Natural Science, TU Chemnitz, D-09107 Chemnitz, Germany

[6]Lab. Francis Perrin, SPAM, CEA/Saclay, F-91191 Gif-sur-Yvette, France

[7]Paul-Scherrer-Institute, Reaction Analysis Group, CH-5332 Villigen, Switzerland

ABSTRACT

Studies of bimolecular and unimolecular processes involving radical species $R^{\cdot}$ or their cations R^+, particulary important for the chemistry of Titan, Mars, or Venus ionosphere, are reported. In this work, we have focussed on the dependance of the ion reactivity on their internal excitation using synchrotron radiation excitation and photoelectron - photoion coincidence techniques. In a first part, we present reactions of state-selected N^+ and O^+ atomic ions with CH_4 and CO_2 respectively, for which the reactivity of ground state ions, $N^+(^3P)$ or $O^+(^4S)$, is found to be very different than the reactivity of metastable states, $N^+(^1D)$, $O^+(^2D)$ or $O^+(^2P)$. In a second part, we report on the photoionisation and dissociative photoionisation of allyl ($C_3H_5^{\cdot}$), propargyl ($C_3H_3^{\cdot}$) and ethyl ($C_2H_5^{\cdot}$) hydrocarbon radicals produced with a flash pyrolysis source.

1. Introduction

In planetary atmospheres, photodissociation, photoionisation and dissociative photoionisation processes of neutral molecules by the solar radiation lead to the formation of many well known neutral and ionic stable molecules, but also to very particular species like neutral radicals, $R^{\cdot}$, excited metastable ions, R^{+*}, and dications R^{++}. For instance in the Titan atmosphere, which is essentially constituted of molecular nitrogen, N_2, and small hydrocarbons, in particular methane, CH_4, the photoexcitation processes not only lead to N_2^+ and CH_4^+ molecular ions but also to $N^{\cdot}$ and $CH_3^{\cdot}$ radical, N^+ or CH_3^+ ions and N_2^{++} dications. As these primary species then react with molecules of the neutral atmosphere to lead to secondary products, it is very important to well caracterize their production and reactivity which can be very particular. In general, less is known on this subject than for stable molecules as it is more difficult to prepare these species, especially if one wants to control their internal energy. In recent years, we have been involved [1-9] in studies of the photoexcitation processes that lead to these species and in studies of their reactivity. Few examples of this work [1-3, 9] are presented here.

2. Reactions of N^+ and O^+ atomic ions

N^+ / O^+ ions are formed in planetary ionospheres by dissociative or non dissociative photoionisation or electron impact of neutral molecules (N_2 / O_2, CO_2) and radicals (N / O) . In these processes, excited states of these ions can also be produced. Depending on their radiative lifetimes and on the neutral atmosphere density, the reactivity of these excited state has to be considered. This is the case for $N^+(^1D)$, $O^+(^2D)$ and $O^+(^2P)$ metastable states whose lifetimes are about 270 s, 2-9 hours and 5-6 s respectively and which lie 1.9, 3.3 and 5.0 eV above their respective ground state . We have used dissociative photoionisation ($M_2 + h\nu \rightarrow M^+ + M + e^-$) of N_2 (Fig.1a) and O_2 (Fig.1b) and TPEPICO coincidence techniques to produce state-selected N^+ and O^+ ions. At the particular photon energies (labels 2 on Fig.1a and 3 and 5 on Fig.1b) corresponding to selected asymptotes $M^{+*} + M^*$, almost pure excited state selection is achieved by discrimination of the atomic ion fragments which have recoil translational energy. For instance, at about 26.2 eV (label 2 in Fig.1a), corresponding to the $N^+(^1D) + N(^4S)$ asymptote, only metastable $N^+(^1D)$ ions are produced. The state-selected atomic ion reactions have been then studied at these photon energies.

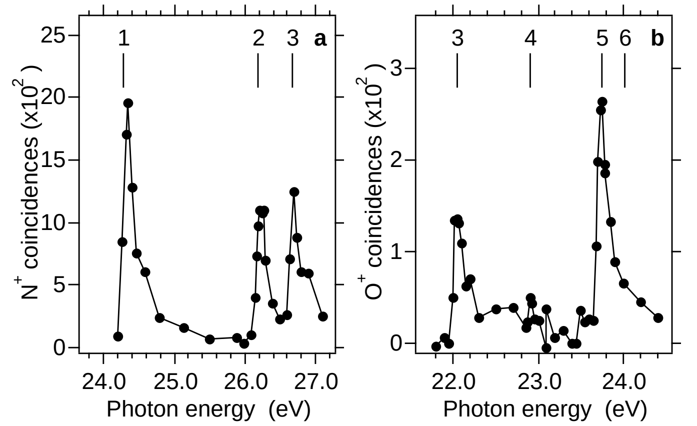

Figure 1. TPEPICO spectra of N^+ (**a**) and O^+ (**b**) in the dissociative photoionization of N_2 and O_2 respectively, recorded as a function of photon energy with strong kinetic energy discrimination of the atomic fragment ions.

a. $N^+ + CH_4$ reaction

To our knowledge, no reaction of pure metastable N^+ state has been reported in the literature yet. In several N^+ reaction studies, dissociative ionization of N_2 by electron impact is used to produce excited N^+, but only a fraction of the N^+ population is in a metastable state. The main channels of the reaction are:

$N^+(^3P) + CH_4 \rightarrow CH_3^+ + NH \quad \Delta H = -3.4$ eV (N1)
$\rightarrow CH_3^+ + H + N \quad \Delta H = -0.2$ eV (N1')
$\rightarrow CH_4^+ + N \quad \Delta H = -1.9$ eV (N2)
$\rightarrow HNC^+ + H_2 + H \quad \Delta H = -2.4$ eV (N3)
$\rightarrow HCNH^+ + H_2 \quad \Delta H = -8.8$ eV (N4)

Only one result, the branching ratio between the main products CH_3^+, CH_4^+, HNC^+, and $HCNH^+$, will be discussed here. Note that we have used $^{15}N_2$ and deuterated methane CD_4 to avoid mass overlaps. The branching ratio between these products measured in an ion cyclotron resonance (ICR) study [10], 0.53 : 0.05 : 0.10 : 0.32 for CH_3^+ : CH_4^+ : HNC^+ : $HCNH^+$ are in good agreement with other published values [11-14]. Note that in a very recent experiment [15], in order to be more representative of the ions present in Titan atmosphere, higher pressures of the methane target gas were used to allow the primary product ions to undergo further chemistry. The numeric modeling of the data which includes consecutive reactions leads to a 0.38:0.03:0.15:0.44 branching ratio for the primary $N^+ + CH_4$ reaction quite different from the lower pressure studies previously reported [10-14]. Figure 2 shows our measured branching ratio as a function of collision energy for the ground state $N^+(^3P)$ and excited state $N^+(^1D)$ [1]. One notes first that our measured branching ratio in the coincidence experiments at low collision energy for the ground state reaction, 0.51:0.11:0.09:0.29, are very close from the 300 K values of McEwan et al [10] which are used in planetary ionospheric models.

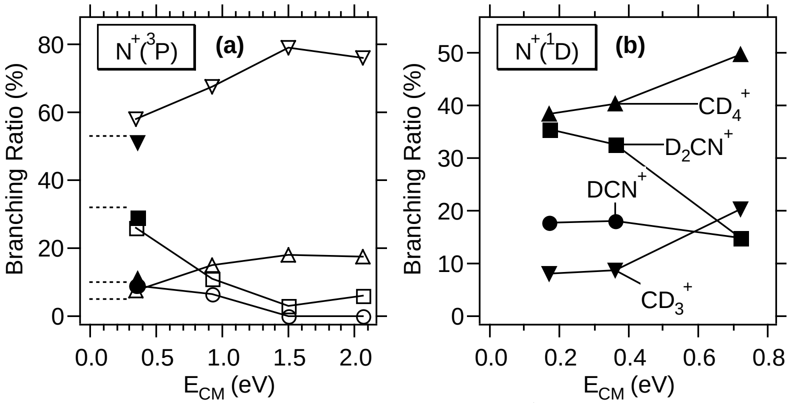

Figure 2. Product branching ratio for the $^{15}N^+ + CD_4$ reaction (same notation in (**a**) and (**b**)). Full and Open symbols: coincidence and non-coincidence measurements respectively. The non-deuterated values evaluated in the literature [10], for the $^{14}N^+(^3P) + CH_4$ reaction at a temperature 300 K, are shown at low energies by a dashed line in (**a**).

What is remarkable is the very different branching ratio for the reaction of the excited state $N^+(^1D)$ which is now 0.09:0.40:0.18:0.33 for CD_3^+ : CD_4^+ : DNC^+ : $DCND^+$. One can especially note the complete inversion of the ratio between CD_3^+ and CD_4^+ products. CD_4^+, coming from the non dissociative charge transfer is now the major product though about 1.9 eV more energy is available.

We will see that this surprising behaviour can be explained when spin-orbit selection rule is considered for the N^+ recombination process occuring in the charge transfer between N^+ and CH_4.

b. $O^+ + CO_2$ reaction

The first main channels that will be discussed here are:

$O^+(^4S) + CO_2$ → $O_2^+ + CO$ ΔH = -1.2 eV (O1)

→ $CO_2^+ + O$ ΔH = +0.16 eV (O2)

For this reaction, extensive efforts have been done to characterize the effects of all the forms of energy including O^+ electronic energy [16-19] and translational energy [16, 18-22] (see [1] for a more complete discussion). Viggiano et al. [22] have noted that all types of energy seem to be equally efficient in promoting the endothermic charge transfer channel which becomes rapidly the dominant channel. To produce pure population of O^+ metastable states, other methods have been already used [23, 24], but none of them to probe the O_2^+ and CO_2^+ productions in the present $O^+ + CO_2$ reaction. We have measured the absolute cross section for O_2^+ and CO_2^+ production in each $O^+(^4S)$, $O^+(^2D)$ and $O^+(^2P) + CO_2$ reactions [1]. The cross sections shown in Fig.3 confirm the predominence of CO_2^+ production for the two excited metastable states. Isotope distribution of $^{32}O_2^+$, $^{34}O_2^+$ and $^{36}O_2^+$ products observed in ion-molecule reactions occurring in an equimolar $C(^{16}O)_2 + C(^{18}O)_2$ mixture have suggested that the form of the complex is $(OO...CO)^+$ rather than a CO_3^+ form where all oxygen are equivalent [25]. We have recently used $^{18}O_2$ to prepare $^{18}O^+$ parent ions and have studied the $^{18}O^+ + CO_2$ reaction. We observe almost exclusively the $^{18}O^{16}O^+$ and $C^{16}O_2^+$ products also implying the same form of the intermediate complex. This was recently confirmed by recent calculations [26].

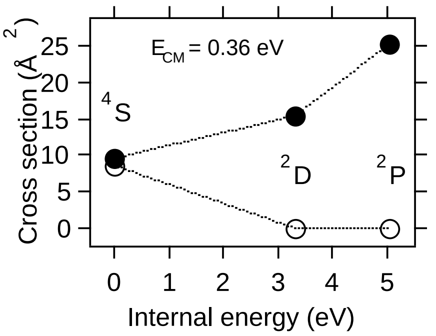

Figure 3. Absolute cross sections for O_2^+ (open circle) and CO_2^+ (full circle) production in the $O^+(^4S,^2D,^2P) + CO_2$ reaction

3. Photoionisation of hydrocarbon radicals

We have measured the photoionisation and dissociative photoionisation of small hydrocarbon radicals: allyl ($C_3H_5^{\cdot}$) [3], propargyl ($C_3H_3^{\cdot}$) and ethyl ($C_2H_5^{\cdot}$) [2] that were produced in a flash pyrolysis source which is known to be well suited for these radicals [27, 28]. Threshold photoelectron spectroscopy and photoion yield were recorded as a function of photon energy as well as TPEPICO technique to probe the fragmentation processes, essentially the loss of H or H_2.

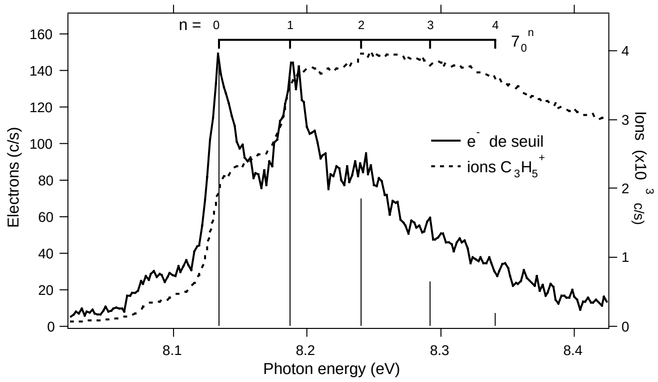

Figure 4. TPES and photoion yield of allyl radical $C_3H_5^{\cdot}$ produced by flash pyrolysis of 1,5-hexadiene precursor

[1] C. Alcaraz, C. Nicolas, R. Thissen, J. Zabka, O. Dutuit, *J. Phys. Chem.* **2004**, *108*, 9998.

[2] T. Schussler, W.Roth, T. Gerber, C. Alcaraz, I. Fischer, *Phys. Chem. Chem. Phys.* **2005**, *7*, 819.

[3] T. Schussler, H. J. Deyerl, S. Dummler, I. Fischer, C. Alcaraz, M. Elhanine, *J. Chem. Phys.* **2003**, *118*, 9077.

[4] C. Simon, J. Lilensten, O. Dutuit, R. Thissen, O. Witasse, C. Alcaraz, H. Soldi-Lose, *Annales Geophysicae* **2005**, *23*, 781.

[5] J. Lilensten, O. Witasse, C. Simon, H. Soldi-Lose, O. Dutuit, R. Thissen, C. Alcaraz, *Geophys. Res. Lett.* **2005**, *32*, L03203.

[6] J. Lilensten, C. Simon, O. Witasse, O. Dutuit, R. Thissen, C. Alcaraz, *Icarus* **2005**, *174*, 285.

[7] O. Witasse, O. Dutuit, J. Lilensten, R. Thissen, J. Zabka, C. Alcaraz, P.-L. Blelly, S. W. Bougher, S. Engel, L. H. Andersen, K. Seiersen, *Geophys. Res. Lett.* **2003**, *30*, 1360.

[8] O. Witasse, O. Dutuit, J. Lilensten, R. Thissen, J. Zabka, C. Alcaraz, P.-L. Blelly, S. W. Bougher, S. Engel, L. H. Andersen, K. Seiersen, *Geophys. Res. Lett.* **2002**, *29*, 104.

[9] C. Nicolas, C. Alcaraz, R. Thissen, M. Vervloet, O. Dutuit, *J. Phys. B: At. Mol. Opt. Phys.* **2003**, *36*, 2239–2251.

[10] M. J. McEwan, G. B. I. Scott, V. G. Anicich, *Int. J. Mass Spec. Ion Proc.* **1998**, *172*, 209.

[11] V. G. Anicich, W. T. Huntress Jr., J. H. Futrell, *Chem. Phys. Letters* **1977**, *47*, 488.

[12] D. Smith, N. G. Adams, T. M. Miller, *J. Chem. Phys.* **1978**, *69*, 308.

[13] M. Tichy, A. B. Raskshit, D. G. Lister, N. D. Twiddy, N. G. Adams, D. Smith, *Int. J. Mass. Spectrom. Ion Phys.* **1979**, *29*, 231.

[14] N. G. Dheandhanoo, R. Johnsen, M. A. Biondi, *Planet. Space Sci.* **1984**, *32*, 1301.

[15] V. G. Anicich, P. Wilson, M. J. McEwan, *J. Am. Soc. Mass Spectrom.* **2004**, *15*, 1148.

[16] T. F. Moran, J. B. Wilcox, *J. Chem. Phys.* **1978**, *69*, 1397.

[17] A. A. Viggiano, R. A. Morris, J. F. Paulson, *J. Chem. Phys.* **1990**, *93*, 1483.

[18] B. G. Lindsay, D. R. Sieglaff, K. A. Smith, R. F. Stebbing, *J. Phys. B: At. Mol. Opt. Phys.* **1999**, *32*, 4697.

[19] C. Y. Ng, *J. Phys. Chem. A* **2002**, *106*, 5953.

[20] D. E. Hunton, A. A. Viggiano, R. A. Morris, J. F. Paulson, D. Smith, N. G. Adams, *J. Geophys. Res.* **1991**, *96*, 13881.

[21] G. D. Flesch, C. Y. Ng, *J. Geophys. Res.* **1991**, *96*, 21403.

[22] A. A. Viggiano, R. A. Morris, J. M. Vandoren, J. F. Paulson, *J. Chem. Phys.* **1992**, *96*, 270.

[23] M. Lavollee, G. Henri, *J. Phys. B: At. Mol. Opt. Phys.* **1989**, *22*, 2019.

[24] X. Li, Y. L. Huang, G. D. Flesch, C. Y. Ng, *Rev. Sci. Instrum.* **1995**, *66*, 2871.

[25] J. F. Paulson, R. L. Mosher, F. Dale, *J. Chem. Phys.* **1966**, *44*, 3025.

[26] H. Ndome, M. Hochlaf, **(in preparation)**.

[27] D. W. Kohn, H. Clauberg, P. Chen, *Rev.Sci.Instrum.* **1992**, *63*, 4003.

[28] J.A.Blush, H.Clauberg,D.W.Kohn,D.W.Minsek,X.Zhang,P.Chen, *Acc. Chem. Res.* **1992**, *25*, 385.

Collisions of slow C_1-C_3 hydrocarbon ions with room-temperature and heated carbon surfaces: A summary

Zdenek Herman

V. Cermák Laboratory, J,. Heyrovský Institute of Physical Chemistry, Academy of Sciences of the Czech Republic, Dolejškova 3, 182 23 Prague 8, Czech Republic

Studies of surface collisions of ions provide information of interest for both chemistry and physics. Considerable attention had been devoted during the last decade to collisions of slow molecular ions of energies 10 –100 eV [1-3]. Besides the basic interest of describing details of elementary processes in single ion-surface encounters, there are two areas of research, where these studies are of importance. One is activation of polyatomic molecular projectile ions in surface collisions, energy transfer at surfaces, and dissociation pathways of the projectile ions, all relevant to novel methods of analysis of organic and bioorganic ions [4]. The other is information on collision processes relevant to plasma-wall interaction in low temperature plasmas and fusion systems. In this respect, the importance of interaction of molecular ionic species in the gaseous phase and in collisions with surfaces in fusion devices has been recognized and demand for data on collisions of slow molecular ions, diatomic and simple polyatomic, has been repeatedly emphasized [5]. The list of ions relevant to this problem includes ions of hydrocarbons C_1 - C_3, CO, CO_2, Be and Si hydrides [6].

This contribution summarizes a part of our systematic effort to study interaction of slow hydrocarbon ions CH_n^+ (n=3-5), $C_2H_n^+$ (n=2-5), $C_3H_n^+$ (n=2-8) and their isotopic (D, ^{13}C) variants with carbon surfaces (highly-oriented pyrolytic graphite, samples of Tokamak tiles) at room-temperature and heated to about 600^0 C. Experiments showed that at room temperature the carbon surfaces were covered by a layer of background hydrocarbons. Heating the surface to or above 600^0C effectively removed this hydrocarbon layer so that collisions of the projectile ions occurred with a “naked”, hydrocarbon-free carbon surface. Ion survival probability, energy transfer, fragmentation and chemical reactions of the projectile ions at surfaces were studied in dependence on the incident energy of the projectile ions and incident angle.

1. EXPERIMENTAL

Mass spectra, translational energy and angular distributions of the product ions were measured in the scattering experiments using the Prague apparatus EVA II modified to study ion collisions with surfaces (Fig. 1). Briefly, projectile ions were formed by bombardment by 120 eV electrons of methane, acetylene, ethylene, ethane, propene, cyclopropane, and propane (or their deuterated or ^{13}C-labelled variants) at an ion source pressure of about 3.10^{-5} Torr. The ions were extracted, accelerated to about 150- 200 eV, mass analyzed by a 90^0 permanent magnet, and decelerated to a required energy in a multi-element deceleration lens. The narrow beam was directed towards the carbon target surface under a pre-adjusted incident angle Φ_N. Ions scattered from the surface passed through a

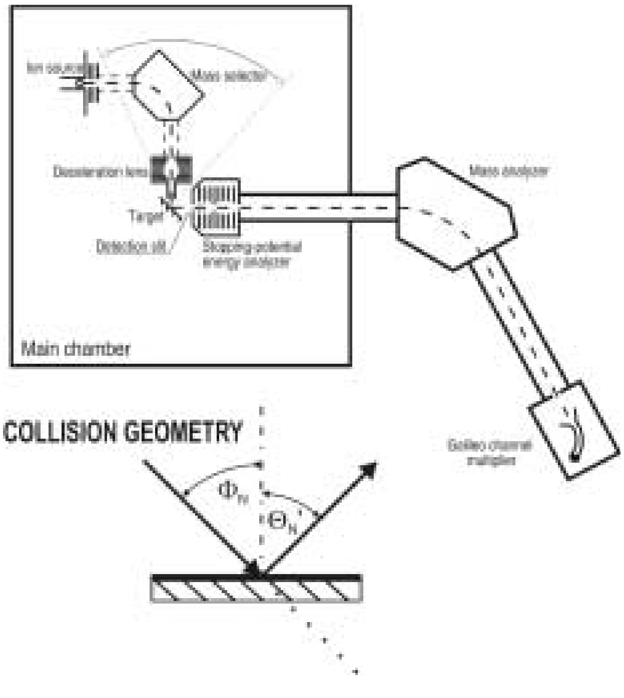

detection slit into a stopping potential energy analyzer. After energy analysis the ions were focused and accelerated into a detection mass spectrometer (a magnetic sector instrument), and detected with a Galileo channel multiplier. The primary beam - target section could be rotated about the scattering center with respect to the detection slit to obtain angular distributions.

2. RESULTS

Scattering studies of C_1 *hydrocarbon ions (*CD_5^+*,* $CD_4^{+\bullet}$*,* CD_3^+ *and their H or* ^{13}C *isotopic variants) [7] impinging on room-temperature HOPG surfaces showed both surface-induced dissociation of the projectiles and chemical reactions with the surface material (Fig. 2). The projectiles showed formation of* $C_2X_3^+$ *(X=H,D) in interaction of the projectiles with terminal* CH_3*-groups of surface-adsorbed hydrocarbons, as shown by analysis of the results with labeled projectile ions, and formation of a small amount of* C_3 *product ions. Collisions of* $CD_4^{+\bullet}$ *led, in addition, to the formation of* CD_4H^+ *in a H-atom transfer reaction with hydrogen of surface hydrocarbons. The surface collisions were inelastic, with 41-55% of the incident energy in product ion translation. Heating of the surface to* 600^0 *C practically removed the surface hydrocarbon layer as indicated by the absence of products of the efficient H-atom transfer*

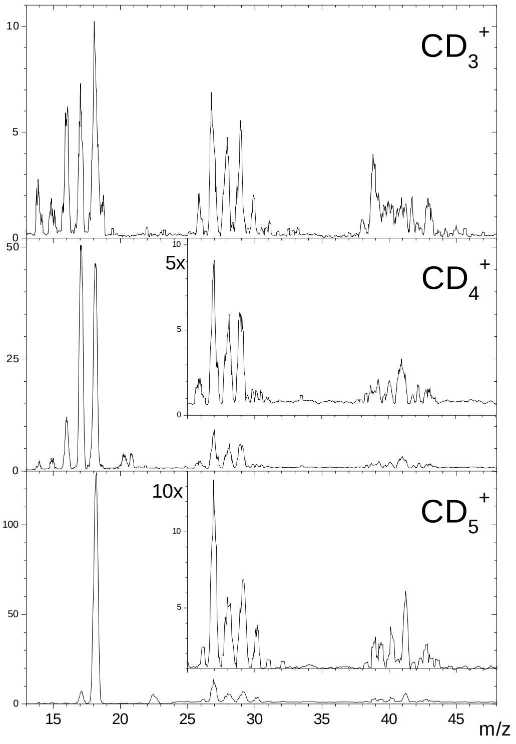

Fig. 2

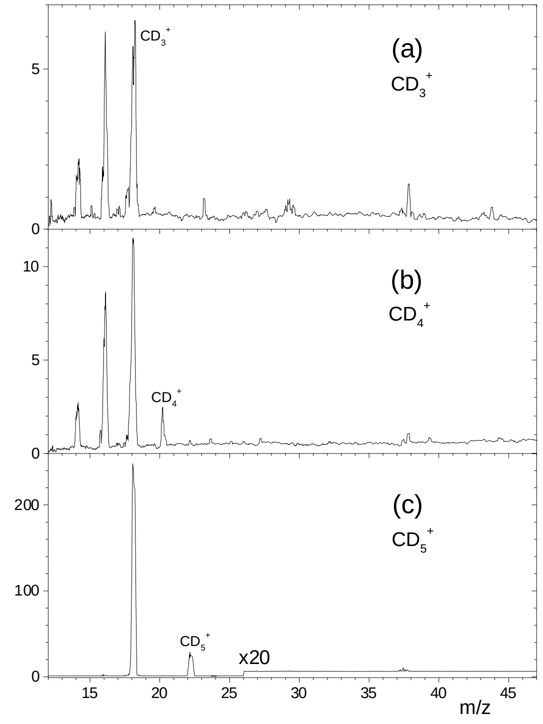

Fig. 3

reaction. Interactions of the projectiles with the heated surface showed only fragmentation of the projectile ions (no chemical reactions) in inelastic collisions with about 75 % of the incident energy in product ion translation. The absolute survival probability was defined as the sum of intensities of all product ion, scattered from the surface, to the intensity of the incident projectile ion beam. It varied from a few tenths of percent for ions CH_3^+ *and* CH_4^+ *to several tens of percent for closed shell ions* CH_5^+ *(Table I).*

Interaction of $C_2H_n^+$ (n= 2-5) hydrocarbon ions and some of their isotopic variants with room-temperature and heated HOPG surfaces [8] was investigated over the range of incident energies 11 – 46 eV and an incident angle of 60^0 with respect to the surface normal. Collisions with the heated HOPG surface showed only partial or substantial dissociation of the projectile ions; translational energy distributions of the product ions peaked at about 50% of the incident energy. Interactions with the HOPG surface at room temperature showed both surface-induced dissociation of the projectiles and – in case of radical cation projectiles $C_2H_2^{+\bullet}$ and $C_2H_4^{+\bullet}$ – chemical reactions with the hydrocarbons on the surface. These reactions were, analogously as with the ion CH_4^+, (i) H-atom transfer to the projectile, formation of protonated projectiles, and their subsequent fragmentation, and (ii) formation of a carbon chain build-up product in reactions of the projectile ion with a terminal CH_3-group of the surface hydrocarbons, and subsequent fragmentation of the product ion to $C_3H_3^+$. This mechanism was elucidated by the analysis of the results of experiments in which D-labelled compounds were used. The product ions were formed in inelastic collisions in which the translational energy of the surface-excited projectile peaked at about 32 % of the incident energy. Examples of the translational energy distribution of product ions from collisions with both the heated (dashed curves) and room-temperature (solid lines) carbon surfaces are shown in Fig. 4. Angular distributions of reaction products showed peaking at sub-specular angles close to 68^0 (heated surfaces) and 72^0 (room-temperature surfaces). The absolute survival probability at the incident angle of 60^0 was about

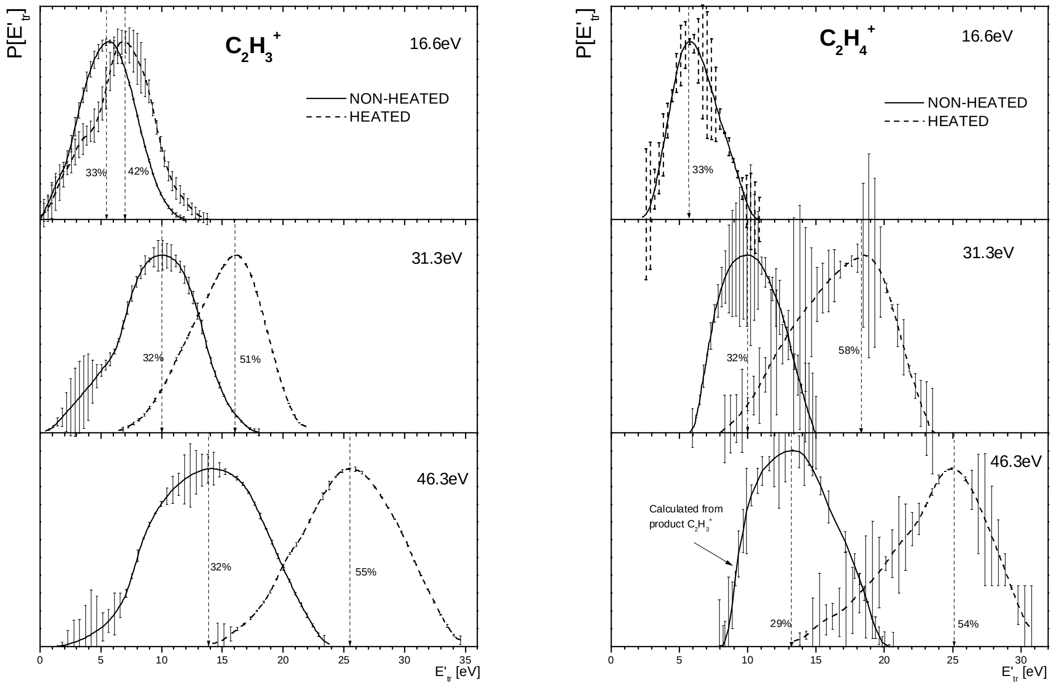

Fig. 4

0.1% for $C_2H_2^{+\bullet}$,close to 1% for of $C_2H_4^{+\bullet}$ and $C_2H_5^+$, and about 3-6 % for $C_2H_3^+$. The data on survival probabilities are summarized in Table 1.

Studies of collisions of the $C_3H_n^+$ (n=3-8) projectile ions led to analogous results as those of CH_n^+ and $C_2H_n^+$ ions: only fragmentation of the projectiles on heated surfaces was observed, while on room-temperature carbon surfaces both fragmentation and chemical reaction of H-atom transfer were observed. However, no measurable amount of carbon-chain build-up reactions (formation of C_4 hydrocarbons) could be observed.

TABLE I. PERCENTAGE OF SURVIVING IONS, S_A(%), IN COLLISIONS OF CH_n^+ AND $C_2H_n^+$ IONS WITH ROOM-TEMPERATURE AND HEATED HOPG SURFACES [7,8]

projectile	E_{inc}=11.7 eV S_a(%)	E_{inc}= 16.3 eV S_a(%)	E_{inc}=31.3 eV S_a(%)	E_{inc}=46.3 eV S_a(%)
NON-HEATED				
CD_3^{+} (a)		0.12±0.03	0.22±0.04	0.26±0.16
$CD_4^{+\bullet\,(a)}$		0.37±0.06	0.34±0.2	0.27±0.26
$CD_5^{+(a)}$		12.5±5	12.0±5	18±7
$C_2H_2^{+\bullet}$	0.1±0.03		0.1±0.03	0.06±0.01
$C_2D_2^{+\bullet}$				0.08±0.02
$C_2H_3^{+}$		6.4±0.4	4.1±0.7	2.4 ±
$C_2H_4^{+\bullet}$		2.3±0.6	1.2	0.7±o.1
$C_2D_4^{+\bullet}$			1.0±0.4	0.9±0.2
$C_2H_5^{+}$	0.3±0.03	1.1±0.03	1.0±0.1	0.3±0.03
HEATED				
$CD_3^{+(a)}$		0.09		0.1
$CD_4^{+\bullet\,(a)}$		(5)	2.3	
$CD_5^{+(a)}$				23
$C_2H_2^{+\bullet}$	0.1±0.04		0.1±0.04	0.36±
$C_2D_2^{+\bullet}$			0.07±0.2	
$C_2H_3^{+}$			3.6±0.2	5
$C_2H_4^{+\bullet}$			0.2±0.05	0.8±0.2
$C_2D_4^{+\bullet}$			0.4±0.05	

ACKNOWLEDGEMENTS

Partial support of the described research by the Association EURATOM-IPP.CR in cooperation with Association EURATOM-ÖAW, by a CRP (2001-2005) of the I.A.E.A., Vienna, by the Grant Agency of the Academy of Sciences of the Czech Republic, and by the Grant Agency of the Czech Republic is gratefully acknowledged. The author appreciates collaboration of J. Žabka, J. Roithová, Z. Dolejšek, J. Jašík, A. Pysanenko (Prague) and T.D. Märk and L. Feketeová (University of Innsbruck) in this work and wishes to express his thanks to them.

REFERENCES

1. Cooks, R. G.; Ast, T.; Mabud, M. D. Int. J. Mass Spectrom. **100** (1990) 209.
2. Hanley, L., Ed., Polyatomic Ion-Surface Interactions, Int. J. Mass Spectrom. **174** (1998).
3. Grill, V., Shen, J.; Evans, C.; Cooks, R. G. Rev. Sci. Instr. **72** (2001) 3149.
4. 15th Sanibel Conference on Mass spectrometry (Ion Activation in Chemistry and Biochemistry), Sanibel Island, FL, USA, 2003; Z. Herman, J.A.Soc. Mass Spectrom. **14** (2003) 1360.
5. Hofer, W.O.; Roth, J. Eds. Physical Processes of the Interaction of Fusion Plasmas with Solids; Academic Press, San Diego, CA, 1996
6. “Data for molecular processes in edge plasmas”, I.A.E.A. TechDoc, I.A.E.A., Vienna (in print)
7. Roithová, J.; Žabka, J; Dolejšek, Z.; Herman, Z. J. Phys. Chem. B **106** (2002) 8293.
8. Jašík, J.; Žabka, J.; Feketeová, L.; Pysanenko, A.; Ipolyi, I.; Märk, T.D.; Herman, Z. J. Phys. Chem. A **109** (2005) 10208.

Fullerenes: Electron Attachment and Detachment

Olof Echt [1,2], S. Ptasinska [2], S. Denifl [2], M. Stano [2], P. Sulzer [2], F. Zappa [2], P. Scheier [2], T. D. Märk [2], J. U. Andersen [3], E. Bonderup [3], B. Concina [3], P. Hvelplund [3], B. Liu [3], S. Brøndsted Nielsen [3], J. Rangama [3], J. S. Forster [4], K. Hansen [5]

[1] *Physics Department, University of New Hampshire, Durham, USA*

[2] *Institut für Ionenphysik, Leopold Universität Innsbruck, Technikerstr. 25, A-6020 Innsbruck, Austria*

[3] *Dept. of Physics and Astronomy, University of Aarhus, Aarhus C, DK-8000, Denmark*

[4] *Dept. de Physique, Université de Montréal, Quebec, H3C 3J7, Canada*

[5] *Dept. of Physics, Göteborg University, SE-41296 Gothenburg, Sweden*

ABSTRACT

One or even two electrons may be attached to gas-phase fullerenes thanks to their large electron affinity, and the large number of degrees of freedom which suppresses autodetachment. In this contribution we discuss two entirely different experiments pertaining to anions. At the Institute of Ion Physics in Innsbruck, fullerene anions are formed by electron attachment to C_{60}, C_{70}, C_{76}, C_{78}, C_{80}, $Sc_3N@C_{80}$, C_{82}, C_{84}, and C_{86}. While the overall shape of the spectra is quite similar for all species, with a pronounced resonance at 0 eV and a broad maximum around 4 to 6 eV electron energy, there are some differences in detail, in particular for $Sc_3N@@C_{80}$. Also noticeable are differences in the stabilization against autodetachment which reflects, last not least, differences in the adiabatic electron affinity.

In experiments performed at the Aarhus Centre for Atomic Physics, C_{60}^- anions are formed in an electrospray source; another electron may be attached by charge exchange with sodium vapor. The ions are injected into a storage ring where they are exposed to a pulsed, tunable IR laser. Details about the electronic structure, including the Jahn Teller distortion, are deduced from the anion lifetime with respect to autodetachment, and their response to light from a laser pulse that is scanned across the HOMO-LUMO gap.

1. Introduction

Formation of anions by attachment of free electrons to gas-phase C_{60} has received considerable attention (see ref. [2, 3] and references therein). A controversial issue was the nature of the resonance in the C_{60}^- yield at low energies. It is now widely accepted that s-wave capture is possible for C_{60}, leading to a strong resonance at exactly 0 eV. At higher energies some structure is observed in the anion yield whereas above 8 to 10 eV the yield drops off rapidly due to thermally activated autodetachment. However, few fullerenes other than C_{60} have been investigated so far, and some findings are quite surprising. For example, C_{84}^- was reported to show no evidence for resonant formation at 0 eV [3]. Moreover, in spite of the recent availability of endohedral fullerenes in milligram quantities, no attempt had been reported to compare the attachment spectra of empty and filled fullerenes. Here we report such a comparison for C_{80} with $Sc_3N@C_{80}$ [4].

In solution, anions with as many as six bound electrons may be stabilized [5]. A myriad of measurements have been performed on these species in solution and in matrices to determine their electronic and optical properties. However, perturbation by the surroundings is always a concern in the interpretation of these data. This complication is safely avoided in gas-phase experiments. We have applied action spectroscopy to determine absorption spectra of C_{60} mono- and dianions stored in an ion ring. The ions are exposed to light from a tunable laser, and the electron emission is monitored as a function of time elapsed since the laser pulse. In addition to recording spectra by scanning the laser wavelength, we have probed the dependence of spectral features on the internal energy of the anions [6-8]

2. Electron Attachment to Fullerenes

The experiments were carried out with a crossed electron/molecular beam apparatus. The electron beam was formed in a custom-designed hemispherical electron monochromator with an energy resolution of about 90 –120 meV. C_{60}, C_{70} and a mixture of higher fullerenes (mostly C_{76}, C_{78}, and C_{84}) were obtained from MER Corporation. $Sc_3N@C_{80}$ was obtained from Luna nanoWorks. The powder was, without further treatment, vaporized from a stainless steel oven. Negative ions formed in the reaction chamber were extracted by a weak electric field towards the entrance of a quadrupole mass spectrometer. The mass selected negative ions were detected by a channeltron detector. The electron energy scale was calibrated using electron attachment to SF_6 which has a narrow resonance in the SF_6^- yield at 0 eV due to s-wave scattering.

Figure 1 displays some spectra. They show a pronounced resonance at 0 eV, including C_{84} for which Abouaf and coworkers [3] (see top panel) did not report a resonance. However, above 1 eV their spectrum agrees reasonably well with ours.

The bottom panel reveals excellent agreement between our C_{60} spectrum and the one reported by Vasil'ev et al. [9]. The only difference is in the strength of the 0-eV resonance relative to the high-energy part. However, this ratio critically depends on the electron resolution. Also, in the present work we have not normalized the ion yield to the electron current. This does not impact energies above 0.5 eV where the electron current is constant within ±10 %.

We also note good agreement with data which Kresin and coworkers recorded below 2.5 eV by a method that is particularly well suited for low electron energies, namely depletion of a beam of neutral C_{60} [10]. Overall, the agreement of our data with literature data for electron energies lends credence to their accuracy, especially for energies above 1 eV.

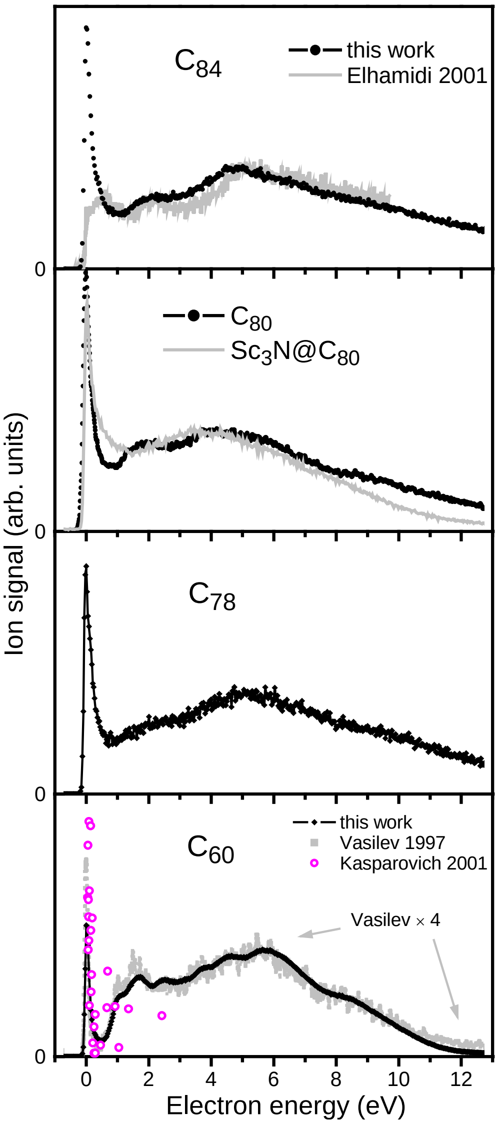

Fig. 1: Electron attachment to fullerenes. Note the comparison of C_{80} and $Sc_3N@C_{80}$. The bottom and top panels compare current data with literature data.

The two middle panels in figure 1 afford a comparison of $Sc_3N@C_{80}$ with C_{78} and C_{80}. The $Sc_3N@C_{80}^-$ yield peaks at 4 eV, less than that of any of the empty fullerenes. Furthermore, the minimum between this maximum and the 0-eV resonance is unusually shallow. It is tempting to relate these differences to the very special properties of $Sc_3N@C_{80}$. According to calculations, the encapsulation of the Sc_3N unit is a strongly exothermic process that is accompanied by a formal transfer of six electrons from the scandium atoms to the fullerene cage [11]. Moreover, whereas C_{80} has either D_2 or D_{5d} symmetry, the Sc_3N unit strongly stabilizes the icosahedral isomer of C_{80} which has a moderately large HOMO-LUMO gap and an electron affinity slightly less than similarly sized empty fullerenes [12].

Our spectra do, indeed, provide evidence for the reduced electron affinity. The anion yield of $Sc_3N@C_{80}$ falls off more quickly than for any other fullerene, save C_{60}. We have modeled the thermal autodetachment along the lines described in [2], however we also take into account the width of the vibrational energy distribution of the fullerenes that emerge from the oven. Although the modeled ion yield falls off more abruptly than the one observed, the shift between the endohedral and the empty C_{80} can be rationalized by the ≈0.36 eV difference in their electron affinities (see [12] and references therein).

3. Infrared Spectroscopy of C_{60}^- and C_{60}^{2-}

The experiments are carried out at the electrostatic ion storage ring ELISA in Aarhus, see figure 2. C_{60}^- is sprayed from a solution of C_{60} and tetrathiafulvalene in toluene and dichloromethane. The ions are thermalized in a linear ion trap with a He trapping gas. After ejection from the trap, acceleration to 22 keV, and mass selection with a magnet, ion bunches may be passed through a cell containing Na vapor, where dianions are formed by electron transfer. The ions are stored in the ring with a revolution time of 108 μs.

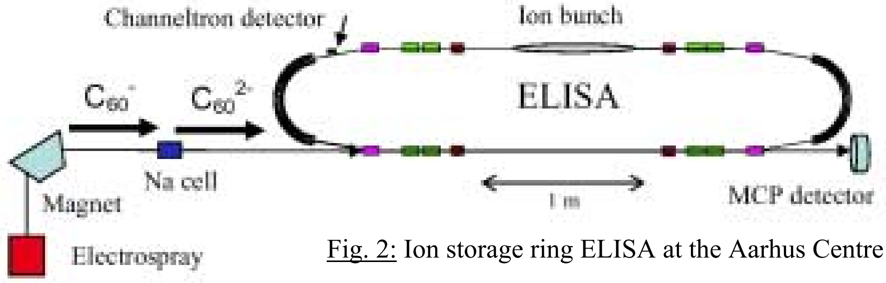

Fig. 2: Ion storage ring ELISA at the Aarhus Centre for Atomic Physics.

We apply action spectroscopy to determine the absorption spectrum in the near-infrared. The laser is an optical parametric oscillator, pumped by the third harmonic from a Nd-doped yttrium-aluminum garnet (Nd:YAG). The time dependence of products from excited C_{60}^{z-} (neutrals for $z = 1$, or monoanions for $z = 2$) are detected by a particle detector as a function of time after the laser pulse. For C_{60}^-, the adiabatic detachment energy is about twice as large as the photon energy. The signal is found to scale with the laser pulse energy to the power 3.5; all results have been normalized accordingly.

The situation is different for dianions. C_{60}^{2-} decays, even without laser excitation; its lifetime strongly depends on the internal energy of the species. On the other hand, C_{70}^{2-} is essentially stable on the time scale of 1 s. We conclude that the adiabatic detachment energy of C_{60}^{2-} is negative, whereas it is positive for C_{70}^{2-}. The electrons are confined by a large Coulomb barrier, and from modeling the time evolution of C_{60}^{2-} with and without a laser, we conclude that electron detachment proceeds via tunneling from a thermally populated triplet state at about 0.12 eV above the singlet ground state. The adiabatic detachment energy of C_{60}^{2-} is obtained as -0.20 ± 0.03 eV [7].

Additional information is gleaned from the wavelength dependence of the product yield. We have recorded absorption spectra of C_{60}^- [6] and C_{60}^{2-} [8]. In figure 3 (top) we display a spectrum of C_{60}^{2-} recorded 3 ms after injection of the ions into the ring. The monoanions were thermalized in the ion trap at 225 K. For comparison we show an absorption spectrum recorded in a gamma-irradiated MTHF solution by Hase et al. [1]. A variation of the measurement relative to the injection time makes it possible to probe the dianion at different degrees of thermal excitation, showing that the feature labeled I in figure 3 is composed of two lines separated by 22 meV; the splitting arises from the Jahn Teller distortion of the ground state.

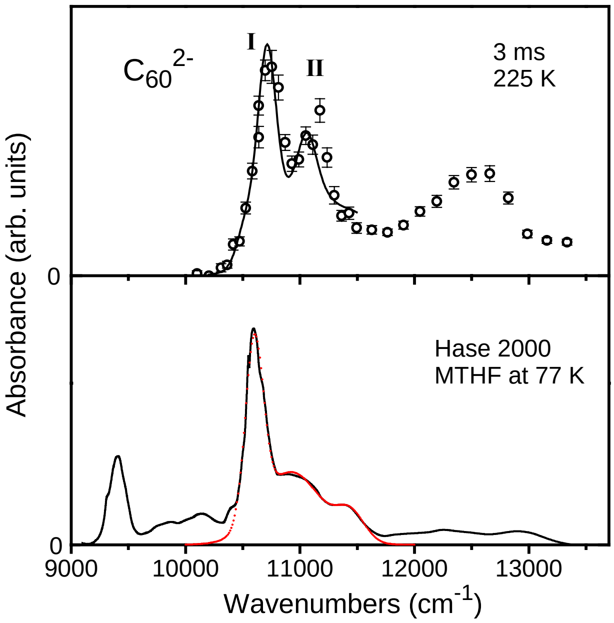

Fig. 3: Comparison of absorption spectra of C_{60}^{2-} recorded in the gas phase (this work, approximate ion temperature 225 K) and in gamma-irradiated MTHF solution at 77 K [1].

4. Acknowledgements

We thank Luna Innovations, Inc. (www.lunainnovations.com) for supplying the $Sc_3N@C_{80}$ compound. This work was partially supported by the FWF, Wien, the European Commission, Brussels, the Danish National Research Foundation, and the EU Research Training Network. The Aarhus collaboration was initiated by the European network LEIF.

5. References

[1] H. Hase, Y. Kitajima, Y. Miyamoto, Y. Miyatake, Y. Tajima, M. Hoshino, Chem. Phys. Lett. 326 (2000) 186.
[2] S. Matejcik, T. D. Märk, P. Spanel, D. Smith, T. Jaffke, E. Illenberger, J. Chem. Phys. 102 (1995) 2516.
[3] O. Elhamidi, J. Pommier, R. Abouaf, Int. J. Mass Spectrom. 205 (2001) 17.
[4] S. Ptasinska, O. Echt, S. Denifl, M. Stano, P. Sulzer, F. Zappa, P. Scheier, T. D. Märk, J. Phys. Chem. A, submitted (2006).
[5] C. A. Reed, R. D. Bolskar, Chem. Rev. 100 (2000) 1075.
[6] S. Tomita, J. U. Andersen, E. Bonderup, P. Hvelplund, B. Liu, S. B. Nielsen, U. V. Pedersen, J. Rangama, K. Hansen, O. Echt, Phys. Rev. Lett. 94 (2005) 053002.
[7] S. Tomita, J. U. Andersen, H. Cederquist, B. Concina, O. Echt, J. S. Forster, K. Hansen, B. A. Huber, P. Hvelplund, J. Jensen, B. Liu, B. Manil, L. Maunoury, S. Brøndsted Nielsen, J. Rangama, H. T. Schmidt, H. Zettergren, S. Tomita, J. Chem. Phys. in print (2006).
[8] S. Tomita, J. U. Andersen, E. Bonderup, B. Concina, O. Echt, J. S. Forster, K. Hansen, P. Hvelplund, B. Liu, S. B. Nielsen, J. Rangama, submitted for publication (2006).
[9] Y. V. Vasil'ev, R. F. Tuktarov, V. A. Mazunov, Rapid Commun. Mass Spectrom. 11 (1997) 757.
[10] V. Kasperovich, G. Tikhonov, V. V. Kresin, Chem. Phys. Lett. 337 (2001) 55.
[11] J. M. Campanera, C. Bo, M. M. Olmstead, A. L. Balch, J. M. Poblet, J. Phys. Chem. A 106 (2002) 12356.
[12] L. N. Sidorov, Physics of the Solid State 44 (2002) 413.

Real-time Experiments of Doped Helium Nanodroplets: Coherence and Relaxation

Patrick Claas[2], Georg Droppelmann[2], Marcel Mudrich[1], Claus-Peter Schulz[3] and Frank Stienkemeier[1,2]

[1]Physikalisches Institut, Universität Freiburg, Hermann-Herder-Str.3, D-79104 Freiburg, Germany (frank.stienkemeier@physik.uni-freiburg.de)

[2]Fakultät für Physik, Universität Bielefeld, Universitätsstr. 25, D-33615 Bielefeld, Germany

[3]Max-Born-Institut, Max-Born-Str. 2a, D-12489 Berlin, Germany

Real-time dynamics in superfluid helium nanodroplets is studied by means of femtosecond pump-probe techniques. In particular, a beam of helium droplets is doped with alkali atoms. The formation of alkali-helium exciplexes upon electronic excitation of the alkalis is followed in real time. Formation times are determined, especially comparing superfluid ^{4}He and normalfluid ^{3}He droplets [1]. Furthermore, we observe quantum interference structures both in the ionization rates of desorbed single atoms as well as exciplex molecules. Analysis of the interference oscillations reveals a detailed view of the level structure of the molecules, providing a novel approach to characterize vibrational structures and dynamics of transient species. Moreover, in this way even the time evolution of energies can be studied.

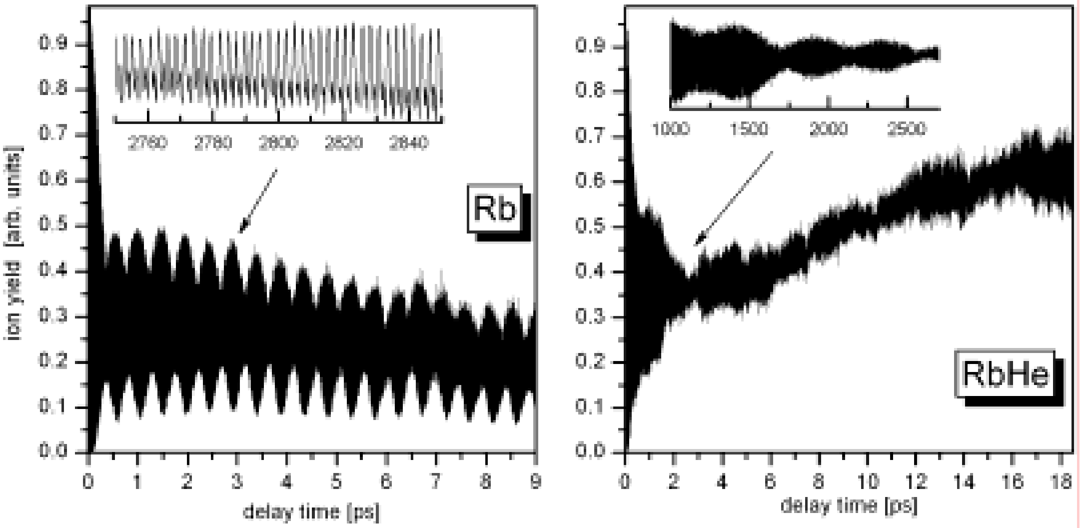

Fig.1: Quantum interferences of Rb atoms as well as Rb*He exciplex molecules. Rb atoms were attached to helium nanodroplets, electronically excited (5p ← 5s) by a femtosecond laser and detected mass selectively. The insets show the resolution of the optical frequency and the structure of the amplitude modulation.

[1] G. Droppelmann, O. Bünermann, C.P. Schulz and F. Stienkemeier, Phys.Rev.Lett. 93, 023402 (2004).

Intramolecular Primary Processes: Recent Results and New Questions

Martin Quack

Physical Chemistry, ETH Zürich, CH-8093 Zürich, Switzerland,
email: Martin@Quack.ch ; web: www.ir.ethz.ch

ABSTRACT

We outline the Zürich approach to derive intramolecular primary processes from high resolution spectroscopy. We then review recent results on intramolecular vibrational redistribution (IVR) and on tunneling processes. Time scales for fast intramolecular energy redistribution range from less than 100 femtoseconds (fs) to many nanoseconds (ns). Tunneling processes for hydrogen bond dynamics in hydrogen bonded clusters such as $(HF)_2$ fall in the picosecond (ps) to nanosecond ranges, where both rearrangement and predissociation of the hydrogen bonds occur. Fast stereomutation tunneling processes in chiral molecules such as H_2O_2 can be observed in the picosecond to nanosecond time ranges. All these processes are highly nonstatistical showing extreme "non-RRKM" behaviour. Certain slow tunneling processes for stereomutation cover times exceeding many times the age of the Universe. However, well before this limit is reached, tunneling between enantiomers is suppressed by asymmetry arising from the parity violating weak nuclear force. Measurements of the processes of time dependent parity violation on the time scale of milliseconds to seconds could indirectly provide information on properties of the standard model of high energy physics including lifetimes and masses of the short lived heavy particles such as the Z-Boson with a sub-yoctosecond (ys) lifetime and the still hypothetical Higgs-particle. In a speculative final part of the paper we present possible consequences of a hypothetical CPT violation on the one hand and of a molecular theory of thought and decision making on the other hand.

1. Introduction

Intramolecular motions and the related fast primary processes are at the origin of all chemical reactions. Fig. 1 outlines two different prototypes of important intramolecular reactions:

The first type is a unimolecular rearrangement by passing over a potential "barrier" in a one dimensional picture or more generally a saddle point on a multidimensional potential hypersurface. Thermal rate constants

$$k(T) = A\exp(-E_A / RT) \tag{1}$$

or specific, energy dependent rate constants

$$k(E, J, \Gamma ...) = \frac{W(E, J, \Gamma ...)}{h\rho(E, J, \Gamma ...)} \tag{2}$$

with further dependencies on angular momentum J and other constants of the motion Γ, may cover a very wide range of values from years (up to the age of the universe, some Giga-years) to picosecond and perhaps subpicosecond time ranges. However, in the traditional theoretical description by statistical theories consistent with Eqs (1) and (2) there is actually no dynamical primary process associated with these large variations in times. Rather, the variations in rate constants are entirely derived from statistical factors that arise in appropriate, generalized formulations of quasiequilibrium theories (QET) or transition state theory (TST, also "RRKM" theory [1, 2]). Even vibrational preionization of C_{60} after infrared multiphoton excitation has been described by such a generalized statistical theory [3] (also called "thermionization").

However, it is conceivable that intramolecular primary processes of vibrational energy redistribution, indeed, become important in determining the rate of unimolecular reactions [4, 5] and in the first part of our short review we shall deal with such processes of intramolecular vibrational redistribution.

In the second part of our paper we shall deal with tunneling processes of intramolecular rearrangements in hydrogen bonded clusters but in particular also stereomutation of chiral molecules (see Fig 1). Such processes open interesting avenues of investigation ranging from the biochemistry of evolution to high energy physics, which will lead us to many new questions. If space, time and matter permit, we shall conclude with some remarks on a hypothetical molecular theory of thought and decision making related to various aspects of these molecular primary processes.

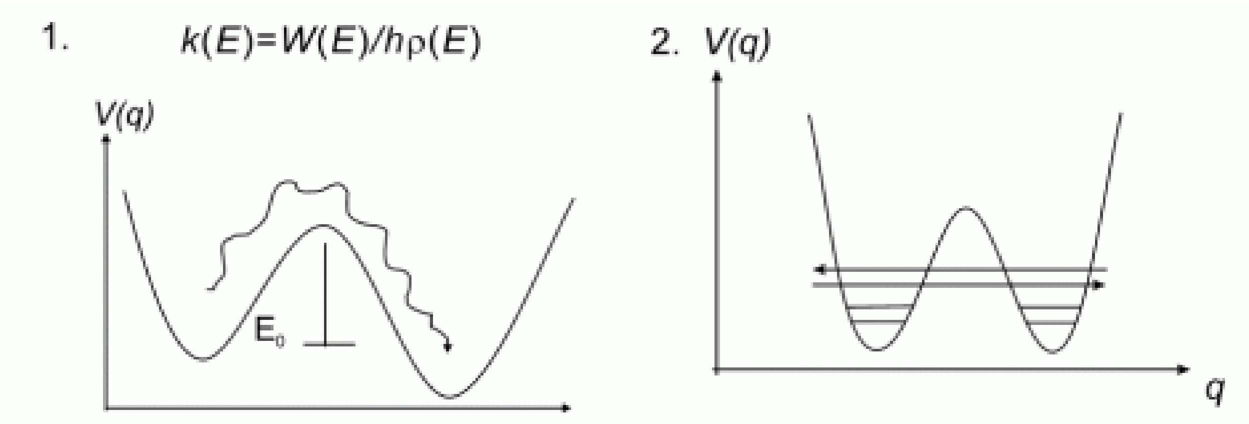

Fig. 1: Schematic representation of two prototypical primary processes for intramolecular reactions: 1. Reaction by internal excitation and barrier crossing. 2. Reaction by tunneling.

2. Outline of the Zürich Group Approaches to Intramolecular Kinetics

Fig 2 provides a survey of the alternative approaches to study kinetic primary processes as they are both pursued by the Zürich group. However, while the approach by kinetic spectroscopy, often with fs pump-probe techniques, finds wide use in many groups worldwide, the approach by stationary very high resolution molecular spectroscopy, largely developed by the Zürich group over the last decades, has found much less attention.

It consists essentially in a spectral eigenstate analysis of the solution to the time dependent Schrödiger equation [5-8]

$$i\frac{h}{2\pi}\frac{\partial\Psi(q,t)}{\partial t}=\hat{H}\Psi(q,t) \tag{3}$$

$$\Psi(q,t)=\sum_{n=0}^{\infty}c_n\varphi_n(q)\exp(-2\pi i E_n t/h) \tag{4}$$

High resolution spectroscopy essentially provides the energies E_n (with respect to some reference level) and, by appropriate analysis, the energy eigenfunctions $\varphi_n(q)$, where q stands for the whole set of space and spin coordinates under consideration. Equivalent representations involve the Heisenberg equations of motion for observables or the statistical representation through the Liouville-von-Neumann equation for the density operator. The effective time resolution Δt of the experimental approach is related to the effective spectral band width $\Delta\nu$ over which the analysis is successfully carried out

$$\Delta t > 1/(4\pi\Delta\nu) \tag{5}$$

If $\Delta\nu = c\cdot\Delta\tilde{\nu} = c\cdot 15'000\,\mathrm{cm}^{-1}$ is inserted as a realistic case, then Δt = 200 as (attoseconds as) is obtained. One might wonder how a pure spectral energy measurement can be equivalent to a time dependent measurement. Perhaps this can be seen by an analysis of time resolved experiments. Here some time dependent observable is detected by reference to a clock. In the best limit this will be an atomic clock described by the two level case of Eq (4) with an energy difference ΔE between the levels and period τ:

$$\tau = h/\Delta E \tag{6}$$

$$\Psi(q,t)=\mathrm{d}(a+b\exp(-2\pi i\Delta E t/h) \tag{7}$$

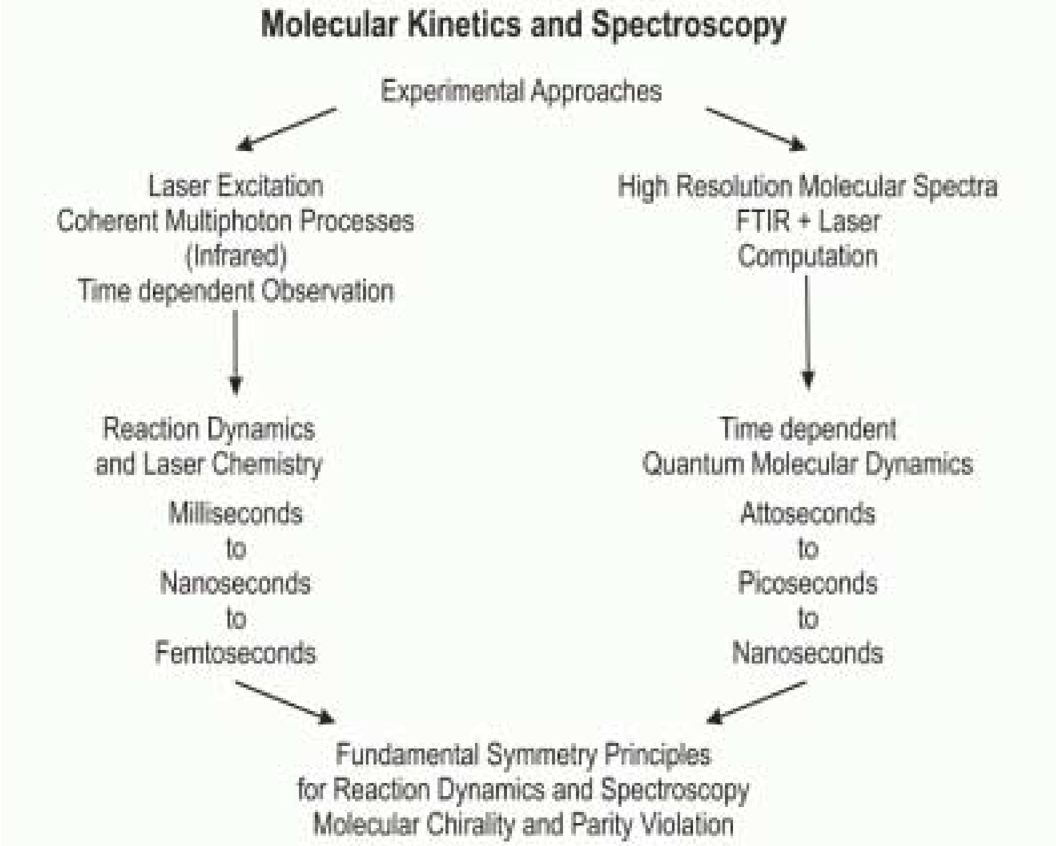

Fig 2: The alternative approaches to intramolecular primary kinetic processes. On the left hand side, the widely used approach by kinetic spectroscopy with either continuous, time resolved detection or pump-probe techniques is shown. On the right hand side the alternative approach using high resolution spectroscopy without essential time resolution as developed by the Zürich group is shown. Fundamental symmetry principles are a particular important study objective.

Thus in essence, the time resolved experiment is analyzed with Eqs (6) and (7) by reference to an energy difference in the atomic clock. The spectroscopic energy resolved experiment analyses the energy-time properties of Eq (4) directly by reference to Eqs (6) and (7). Even though much abbreviated, this contains the essence of the two approaches. Of course the equivalence does not imply an identity, as often the analysis following Eq(4) cannot be carried out, nor can the time resolved experiment always be done (for instance not on the yoctosecond (ys) timescale, where the 0.26 ys lifetime of the Z-Boson is determined by an energy resolved experiment). For more detail we refer to refs. [5, 6]. An interesting general question concerns the overlap and agreement or disagreement between results from the two approaches outlined in Fig 2. This question is subject to current investigations in our work and the example of CF_3CHIF is discussed below.

3. Intramolecular Vibrational Redistribution

After extensive investigations of the spectroscopy and short time dynamics of the CH-chromophore in organic molecules [9], which is effectively a 2- or 3-coupled vibrational modes system, there have been recent extensions to four effectively coupled mode systems in the case of CDFClBr [10, 11] and CF_3CHFI [12]: The new questions which arise here are: Which is the extra mode that couples to the CH-chromophore and on what time scale does this coupling become important? In both CDFClBr and CF_3CHFI the extra mode is a CF-stretching mode, which is coupled to CD/CH by Fermi resonances [10, 12]. In the case of CF_3CHFI there are, of course, several CF-stretching modes and interestingly it is the mode which mostly corresponds to stretching the CF-bond in β-trans position to the CH-bond, which is involved in this coupling and becomes importantly excited after about 200 fs, where the CH-stretch-bend redistribution is already fairly complete. This provides us with an interesting picture of initial energy flow in this molecule. We may note that an important β-trans OH-CH-stretching coupling has been observed also in methanol (H_3C-OH), although the nature of the coupling is different, in detail [13, 14].

The obvious new question is, of course, which modes are coupled next and at which time the CI-stretching mode, which leads to the lowest dissociation channel [15], becomes excited. This last question has been addressed in recent work from our group using fs pump probe spectroscopy, where the infrared pumping excites two quanta of CH-stretching and the probing in the UV is sensitive to C-I excitation because of Franck-Condon effects in the transition to a repulsive excited state potential along the CI bond. It is found that CI stretching in CF_3CHFI is importantly excited after about 2 ps and more. The results and the general technique are also outlined in a paper at this meeting [16, 17].

While the interesting D/H isotope effect on IVR in CHFClBr is easily studied by synthesizing CDFClBr [10] often one wishes to investigate such isotope effects in natural abundance or in mixtures of isotopomers, which are not easily separated. The ideal technique to do so has been developed in our laboratory (ISOS/IRSIMS) and has been extensively reviewed recently [18]. Results include primary processes in $CHCl_3$ (with isotope effects for $^{35}Cl/^{37}Cl$), Aniline $C_6H_5NH_2$ (with H/D isotope effects), and benzene C_6H_6 (with ^{13}C isotope effects in natural abundance [19]). We may note also a paper on high resolution spectroscopy of aromatic compounds at this meeting [20].

Another question concerns the nature of irreversibility and the increase of entropy in these processes. In a sense this is a very old question, which can, however, be asked now for the quantum dynamics of single individual molecules in a new light [21, 22]. This question is related to the much more general question of fundamental symmetry breakings in physics, which we shall address in the following chapter.

4. Tunneling Processes in Hydrogen Bond Rearrangement and Stereomutation Processes, and Related Symmetry Breakings including Parity Violation in Chiral Molecules

The spectroscopic approach is ideally suited for investigation of tunneling processes and for ground state tunneling it has been used for a very long time with the aid of microwave spectroscopy, ammonia inversion being the “classic” case. The new aspect in high resolution infrared spectroscopy is the possibility of studying mode selective catalysis and inhibition of such processes by exciting specific vibrational modes in molecules and hydrogen bonded clusters. We may mention here hydrogen bond rearrangement and predissociation processes, in $(HF)_n$ clusters, in particular $(HF)_2$ isotopomers, which show a rich variety of such mode selective tunneling reactions reviewed in [6, 23] (see references therein). Another class of highly mode selective tunneling reactions are stereomutations of chiral molecules of the general type

$$\mathrm{R} \rightleftarrows \mathrm{S} \tag{8}$$

H_2O_2 is a case in question, which has been studied by spectroscopy and using „exact“ full dimensional quantum dynamics on a complete 6-dimensional potential hypersurface [24, 25]. This work has been extended to a wider range of X–Y–Z–X’ molecules with various compositions, which are all axially chiral at their equilibrium geometry [26]. In these systems a new question arises: At which magnitude of the tunneling barrier and reduced mass and below which size of tunneling splittings will one see dominant effects from the fundamentally new, parity violating weak nuclear force? It turns out that for molecules such as Cl–S–S–Cl [27] and Cl–O–O–Cl [28] the conditions are actually met that parity violation becomes the dominant effect. In these systems, there exists an in principle measurable [29] energy difference $\Delta_{pv}E$ between enantiomers (R and S, with $N_A \cdot \Delta_{pv}E = \Delta_R H_0^{\ominus}$ being the enthalpy of the reaction (8). The finding a decade ago that such parity violating potentials are larger [30-32] by 1 – 2 orders of magnitude than previously anticipated led to a rebirth of the field of “electroweak quantum chemistry” [30] and a completely new outlook on the possibility of proving and analyzing the resulting effects experimentally [33, 34]. If this is successful, this opens new avenues towards fundamental symmetries in physics from experiment and theory in molecular physics, including new possibilities of testing CPT symmetry (see [5, 21, 22, 33] for reviews). Two papers at this conference discuss aspects of recent progress in this field. [28, 35]. These studies show that investigations of intramolecular primary processes provide many exciting research opportunities, including an approach towards a hypothetical molecular theory of thought outlined in more detail elsewhere [36].

Acknowledgement

Our work is supported by the ETH Zürich and the Schweizerischer Nationalfonds as well as the Miller Institute for Basic Research in Science. I am very grateful to my coworkers, mentioned in the list of references, for their essential contributions towards the work reviewed here briefly.

References:

[1] M. Quack, J. Troe, *Statistical methods in scattering,* in *Theoretical chemistry: Advances and perspectives (Theory of scattering, papers in honor of Henry Eyring), Vol. 6B,* pp. 199-276, (Ed.: D. Henderson), Academic Press, New York, **1981**.

[2] M. Quack, J. Troe, *Statistical Adiabatic Channel Model,* in *Encyclopedia of Computational Chemistry, Vol. 4,* pp. 2708-2726, (Eds.: P. von Ragué Schleyer, N. Allinger, T. Clark, J. Gasteiger, P. A. Kollman, H. F. I. Schaefer, P. R. Schreiner), John Wiley & Sons, **1998**.

[3] M. Hippler, M. Quack, R. Schwarz, G. Seyfang, S. Matt, T. Märk, *Chem. Phys. Lett.*, **1997**, *278*, 111-120.

[4] M. Quack, *Nuovo Cimento Soc. Ital. Fis. B*, **1981**, *63B*, 358-377.

[5] M. Quack, *Molecular femtosecond quantum dynamics between less than yoctoseconds and more than days: Experiment and theory,* in *Femtosecond Chemistry, Proc. Berlin Conf. Femtosecond Chemistry, Berlin (March 1993)*, Chapt. 27, pp. 781-818, (Eds.: J. Manz, L. Woeste), Verlag Chemie, Weinheim, **1995**.

[6] M. Quack, *Chimia*, **2003**, *57*, 147-160.

[7] M. Quack, *Chimia*, **2001**, *55*, 753-758.

[8] E. Schrödinger, *Annalen der Physik IV. Folge*, **1926**, *81*, 109-139.

[9] M. Quack, *Annu. Rev. Phys. Chem.*, **1990**, *41*, 839-874.

[10] A. Beil, H. Hollenstein, O. L. A. Monti, M. Quack, J. Stohner, *J. Chem. Phys.*, **2000**, *113*, 2701-2718.

[11] S. Albert, K. K. Albert, M. Quack, *Very-high-resolution studies of chiral molecules with a Bruker IFS 120 HR: The rovibrational spectrum of CDBrClF in the range 600 - 2300* cm^{-1}*,* in *Trends in Optics and Photonics (TOPS), Vol. 84,* pp. 177-180, Optical Society of America, Washington DC, **2003**.

[12] J. Pochert, M. Quack, J. Stohner, M. Willeke, *J. Chem. Phys.*, **2000**, *113*, 2719-2735.

[13] L. Lubich, O. V. Boyarkin, R. D. F. Settle, D. S. Perry, T. R. Rizzo, *Faraday Discussions*, **1995**, *102*, 167-178.

[14] M. Quack, M. Willeke, *J. Chem. Phys.*, **1999**, *110*, 11958-11970.

[15] Y. B. He, J. Pochert, M. Quack, R. Ranz, G. Seyfang, *Faraday Discuss.*, **1995**, *102*, 275-300.

[16] V. Krylov, M. Nikitchenko, M. Quack, G. Seyfang, *Femtosecond Intramolecular Dynamics After Near-IR Excitation of* CH_3I, C_2H_5I, CF_3CHFI, *and* C_7H_8 *Molecules in the Gas Phase and in Solution,* in *Nonlinear Frequency Generation and Conversion: Materials, Devices and Applications III, Proc. SPIE, Vol. 5337,* pp. 178-189, (Eds.: K. L. Schepler, D. D. Lowenthal), SPIE, Bellingham, WA, **2004**.

[17] V. Krylov, E. Miloglyadov, M. Quack, G. Seyfang, **2006**, Paper at SASP 2006 (this issue).

[18] M. Hippler, M. Quack, *Isotope Selective Infrared Spectroscopy and Intramolecular Dynamics,* in *Isotope Effects in Chemistry and Biology, Part III, Isotope Effects in Chemical Dynamics*, Chapt. 11, pp. 305-359, (Eds.: A. Kohen, H.-H. Limbach), Marcel Dekker Inc., New York, **2005**.

[19] M. Hippler, R. Pfab, M. Quack, *J. Phys. Chem. A*, **2003**, *107*, 10743-10752.

[20] S. Albert, M. Quack, **2006**, Paper at SASP 2006 (this issue).

[21] M. Quack, *Nova Acta Leopoldina*, **1999**, *81*, 137-173.

[22] M. Quack, Paper at WATOC 2005, Cape Town (to be published).

[23] M. Quack, M. A. Suhm, *Spectroscopy and Quantum Dynamics of Hydrogen Fluoride Clusters,* in *Advances in Molecular Vibrations and Collision Dynamics, Vol. 3, Molecular Clusters,* pp. 205-248, (Eds.: Z. Bacic, J. Bowman), JAI Press Inc., Stamford, Conn. and London, England, **1998**.

[24] B. Kuhn, T. R. Rizzo, D. Luckhaus, M. Quack, M. A. Suhm, *J. Chem. Phys.*, **1999**, *111*, 2565-2587.

[25] B. Fehrensen, D. Luckhaus, M. Quack, *Chem. Phys. Lett.*, **1999**, *300*, 312-320.

[26] M. Gottselig, M. Quack, J. Stohner, M. Willeke, *Int. J. Mass Spectrom.*, **2004**, *233*, 373-384.

[27] R. Berger, M. Gottselig, M. Quack, M. Willeke, *Angew. Chem.-Int. Edit.*, **2001**, *40*, 4195-4198, Angew. Chem. **2001**, *113*, 4342-4345.

[28] M. Quack, M. Willeke, **2006**.

[29] M. Quack, *Chem. Phys. Lett.*, **1986**, *132*, 147-153.

[30] A. Bakasov, T. K. Ha, M. Quack, *Ab initio calculation of molecular energies including parity violating interactions,* in *Chemical Evolution, Physics of the Origin and Evolution of Life, Proc. of the 4th Trieste Conference (1995),* pp. 287-296, (Eds.: J. Chela-Flores, F. Raulin), Kluwer Academic Publishers, Dordrecht, **1996**.

[31] A. Bakasov, T. K. Ha, M. Quack, *J. Chem. Phys.*, **1998**, *109*, 7263-7285.

[32] R. Berger, M. Quack, *J. Chem. Phys.*, **2000**, *112*, 3148-3158, (cf. R. Berger and M. Quack, Proc. 37th IUPAC Congress Vol. 2, p. 518, Berlin, **1999**).

[33] M. Quack, *Angew. Chem., Int. Ed. Engl.*, **2002**, *114*, 4618-4630, Angew. Chem. **2002**, *114*, 4812-4825.

[34] M. Quack, J. Stohner, *Chimia*, **2005**, *59*, 530-538.

[35] J. Stohner, M. Quack, **2006**, Paper at SASP 2006 (this issue).

[36] M. Quack, *Time and Time Reversal Symmetry in Quantum Chemical Kinetics,* in *Fundamental World of Quantum Chemistry. A Tribute to the Memory of Per-Olov Löwdin, Vol. 3,* pp. 423-474, (Eds.: E. J. Brändas, E. S. Kryachko), Kluwer Adacemic Publishers, Dordrecht, **2004**.

Attosecond Measurement and Control of Electronic Motion

Matthias Lezius[1], **Markus Kitzler**[2]

[1] *Max-Planck Institute for Quantum Optics, Hans-Kopfermannstr. 1, Garching D-85741, Germany*

[2] *Photonics Intitute, Vienna Technical University, Gusshausstr. 27/387, A-1040 Vienna*

We suggest using orthogonally polarized two-color laser pulses to direct tunneling electrons with attosecond precision around the ion core. We prove that the angles of birth and recollision, the recollision energy and the temporal structure of the recolliding wave packet can be controlled without stabilization of the carrier-envelope phase of a few-cycle laser, and that the wave packet's properties can be described by classical equations of motion for a point charge. This establishes unique mapping between parameters of the laser field and attributes of the recolliding wave packet. The method presented here is capable of probing ionic bound dynamics with attosecond resolution from an adjustable direction. The method might be used as an alternative method to laser alignment of molecules. Shaping the properties of the recollision wave packet by controlling the laser field may also provide new routes for improvement of attosecond pulse generation via high harmonic radiation. In a carthesian coordinate system we assume the electric field to be of the form (atomic units are used)

$$A_x(t) = -\hat{E}_x \frac{f_x(t)}{\omega_x} \sin(\omega_x t + \varphi_{CE,x})$$

$$A_y(t) = -\hat{E}_y \gamma \frac{f_y(t+\Delta t)}{\omega_y} \sin(\kappa\omega_y (t+\Delta t) + \varphi_{CE,y})$$

Here ω_x is the laser frequency and $\hat{E}_x$ the peak electric field strength, both in x-direction, $\gamma = \hat{E}_y / \hat{E}_x$ is the ratio of the peak electric field strength in y to the one in x, $\varphi_{CE,x}$ and $\varphi_{CE,y}$ are the carrier-envelope (CE) phases in x and y direction, and $\kappa = \omega_y / \omega_x$. We have confirmed the validity of the model by comparison to data that has been published recently [1].

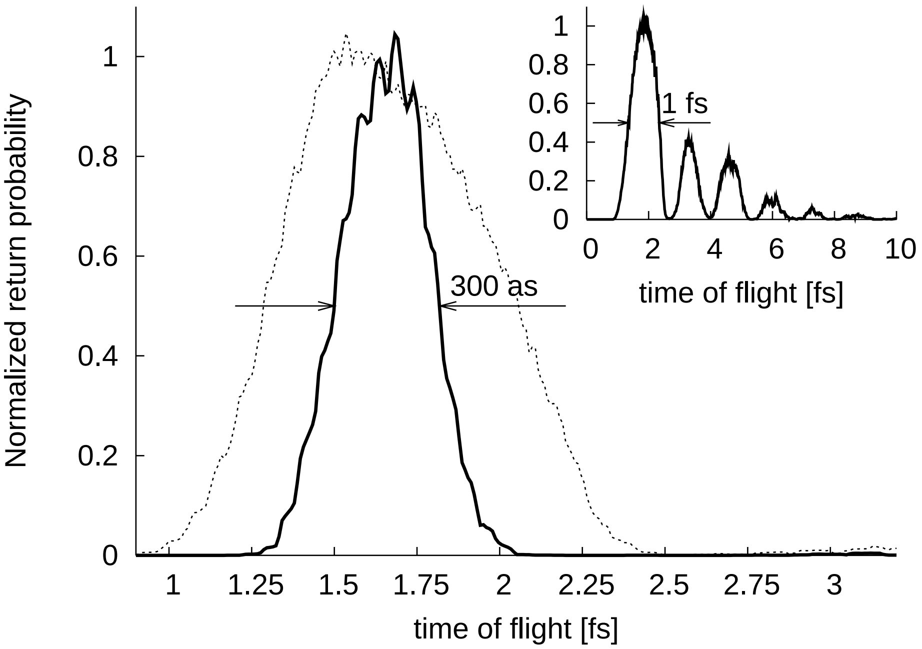

FIG. 1: Time structure of the recolliding electrons (recollision current) as seen by atomic ions in 800 nm laser field in *x*, $\kappa = 2$, $I_x = I_y = 1.65\times10^{14} W/cm^2$,$\varphi_{CE,x} = 0$, $\varphi_{CE,y} = 0.8\pi$ (thick, full line). The thick, dotted-dashed line depicts the same but for $\varphi_{CE,x} = -0.4\pi$, $\varphi_{CE,y} = 0$. The thin, dotted current was created by linearly polarized light, $\varphi_{CE,x} = 0$, $I_x = 4.34\times10^{14} W/cm^2$in Argon. Pulse durations 5 fs (FWHM). The inset shows the recollision current for H_2 with the molecular axis orthogonal to the laser polarization in linearly polarized 800 nm laser light, 4 cycles (FWHM), peak intensity $2\times10^{14} W/cm^2$.

The inset of fig. 1 shows the time structure of the recollision current experienced by a hydrogen molecule with the internuclear axis perpendicular to the laser polarization, using a linearly polarized gaussian laser pulse (800 nm, 4 cycles FWHM, $\varphi_{CE,x} = 0.2\times10^{14} W/cm^2$. The thick lines in the main part of fig. 1 show the recollision current as seen by a Argon atom when it is exposed to a field as stated in the figure caption, briefly $\gamma = 1, \kappa = 2$. Fig. 2(a) depicts the laser field in *x*- and *y*-direction for the full line. Fig. 1 demonstrates that recollision takes place only once and within a time interval of ~ 300 as, and that the recollision current for a few-cycle pulse is - apart from slight changes in the absolute value coming from the envelope due to varying times of ionization - always the same as long as the phase relation in *x* and *y* stays the same, i.e. $\Delta\varphi$= $\varphi_{CE;y}$- $\kappa\varphi_{CE;x}$ = const. Note, that all parameters used here are experimentally realistic ($\kappa = 2$) and that by tuning of the frequency ratio the duration might be decreased even further. Precise field design (cf. fig. 2(a)) imposes useful constraints for recollision in two dimensions. The dramatically improved time resolution in orthogonal two-color fields results from the fact that only selective portions of the wave packet fulfill the recollision condition.

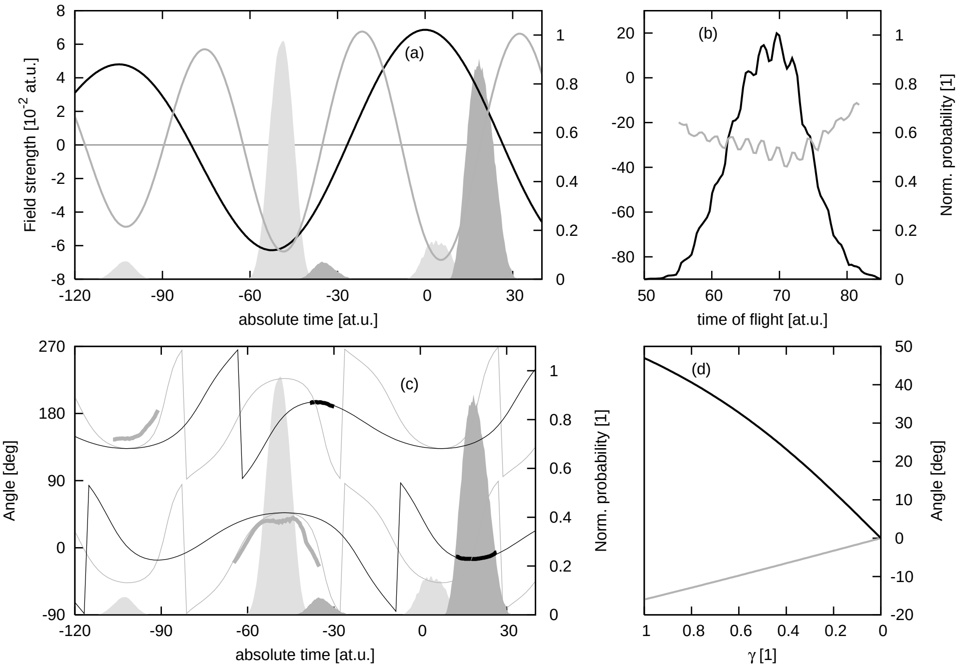

FIG. 2: Birth and recollision angle of the wave packet discussed in fig. 1: (a) Temporal structure of the ionizing part (light shaded area) and the returning ionizing part (dark shaded area) of the wave packet and the generating laser field in *x* (full line) and *y* (dashed line) over absolute time. (b) Temporal structure (black line) and recollision angle (gray line) over time of flight. (c) Birth (gray lines) and recollision angles (black lines) over absolute time. The thick lines depict the numerical data, the thin lines are calculated by relations for a point charge (see text). (d) Birth angle for a wave packet born at $t_b = -47$ (full line) and recollision angle of that wave packet (dashed line) at a recollision time of $t_r = 20$ over the intensity ratio γ, both calculated for a point charge (see text).

The wave packet can be adjusted by the parameters of the field. The angle of an electron born at time t_b to the *x*-axis at a time $t > t$ is $\vartheta_r(t,t_b) = \mathrm{atan}(\dot{y}(t)/\dot{x}(t))$. Provided an electron born at t_b recollides with the ion at time t_r, its angle to the *x*-axis is $\vartheta_r(t,t_b)$. Within the strong field approximation (SFA) $\vartheta_r(t,t_b)$ turns into:

$$\vartheta_r(t_r,t_b) = a\tan\left(\frac{\gamma f_y(t_r)\sin(\kappa\omega_x t_r+\varphi_y)-f_y(t_b)\sin(\kappa\omega_x t_b+\varphi_y)}{\kappa f_y(t_r)\sin(\kappa\omega_x t_r+\varphi_x)-f_x(t_b)\sin(\kappa\omega_x t_b+\varphi_x)}\right).$$

This means that the recolliding part can be treated like a point charge starting at the origin with zero initial velocity. This opens up the possibility to predictably probe ions from adjustable directions. Orthogonally polarized two-color pulses can also be used to control the recollision energy. Within the SFA Newton's equations allow to calculate the recollision energy $E_r(t_r,t_b)$ for an electron in a field in *x* and *y* direction which starts at t_b and recollides at t_r: $E_r(t_r,t_b) = 1/2\sum_{i=x,y}\left[\left(A_i(t_r)-A_i(t_b)+v_{b,i}\right)^2\right]$,

with $v_{b,i}$ the birth momentum in direction *i*. Comparison of $E_r(t_r,t_b)$ with the mean recollision energy over time extracted from the numerical data leads to almost perfect agreement. Our simulations show that the appearance of the distribution of those trajectories returning to the ion reflects the birth angle of the wave packet (~45° here), and that it is by a factor of about 2 narrower than the one in linearly polarized light. We found out that the high-energy part of the spectrum and the cut-off energy can be described very well. However, trajectories do not recollide within a well defined energy band, as would be desirable for the creation of single attosecond pulses without xuv filters, but the spectrum also exhibits a low energy tail originating from birth momentum spread. Experiments related to the work, which has been published recently [2, 3], are currently performed by Markus Kitzler at the Photonics Intitute of the Vienna Technical University.

This work has been supported by the Austrian science fund, FWF, F016. We thank A. Scrinzi and J. Caillat for useful inputs as well as R. Nuter and M. Ivanov for elucidating discussions.

[1] H. Niikura et al., Nature 417, 917 (2002).
[2] M. Kitzler, K. O'Keeffe, and M.Lezius, J. Mod. Optics, *in print* (2005).
[3] M. Kitzler and M. Lezius, Phys. Rev. Letters, *in print* (2005).

Influence of particle-induced electron emission on the plasma sheath voltage

N. Schupfer[1], D.D. Tskhakaya sr.[1], R. Khanal[1], F. Aumayr[2], S. Figueira da Silva[2], S. Kuhn[1], and HP. Winter[2]

[1]*Institut für Theoretische Physik, Universität Innsbruck, Austria*

[2]*Institut für Allgemeine Physik, Technische Universität Wien, Austria*

Abstract

The boundary region of magnetically confined fusion plasmas is of great relevance for the generation and transport of plasma impurities between the material boundary (first wall, divertor plates) and the hot core plasma. The concentration of impurities, including He ash in future D-T fusion reactors, determines transport of the non-neutronic part of fusion power (energetic neutral and charged particles vs. radiation) from the core plasma to the boundary, which influences the plasma-wall interaction processes. Local plasma cooling by impurity ion radiation causes steeper density and temperature gradients and thereby can support formation of internal transport barriers (ITBs) for improved plasma confinement. In this whole context the potential drop between the sheath edge and the material boundary (the so-called plasma sheath voltage, PSV) is important for desorption and sputtering from the wall material.

For modelling such boundary plasma properties, electron emission both from walls and divertor plates, induced by the plasma majority and (multiply charged) impurity ions, is commonly neglected because magnetic field lines nearly parallel to the boundary inhibit the slow ejected electrons to flow toward the plasma. However, it is still of interest to estimate its effect quantitatively. As a first step, we consider here the case with no magnetic field. For a magnetic-field free collisionless plasma without electron emission, the PSV will correspond to the floating potential Vf of an electrostatic probe [1],

$$V_f = \frac{k\ T_e}{2\ e} . \left[\ln(2\pi\ \frac{m_e}{m_i}) - 1 \right] \quad (\approx \frac{3.3\ k\ T_e}{e}\ for\ \ protons),$$

where Te, me and mi are the plasma electron temperature and the electron and ion masses, respectively. However, this relation is inadequate for typical boundary regions of magnetically confined fusion plasmas because it does not take into account impurity ions and particle induced electrons. Recently, a more general sheath theory [2] has been developed which we use here as a basis for some preliminary self-consistent PSV calculations including electron emission from the wall induced by electrons (EIEE), majority ions (IIEE) and impurity ions (ImpIEE). Partial reflection of fast electrons (ER) from the boundary surface as well as magnetic fields will be considered later. For these calculations realistic total electron yields and energy distributions are assumed as explained below.

Particle-induced electron emission and electron reflection from solid surfaces

For impact of fusion-relevant singly charged ions (D^+, T^+, C^+, O^+, etc.) on dynamically clean metal- (stainless steel, Be, W) or graphite surfaces, we need only to consider kinetic electron emission (KE) [3]. KE is subject to an impact energy threshold which depends primarily on electronic properties of the target suface. A comparative study [4] for different target surfaces as gold, HOPG (highly oriented pyrolytic graphite) and textured graphite yielded for hydrogen atomic and molecular ions a KE threshold of 50 eV/amu for graphite and of 600 eV/amu for gold. For heavier ions these thresholds become considerably lower (30 eV/amu for graphite and 75 eV/amu for gold). In general, for impact energies below 100 eV/amu, total KE yields remain below 0.1 electrons per projectile. Characteristic electron energy distributions for KE increase from zero to a maximum at typically a few eV and then gradually level off [3]. Total KE yields increase with projectile incidence angle roughly according to $1/\cos\theta$, where θ is the incidence angle with respect to the surface normal [3].

The situation is quite different for impact of multiply charged ions (MCI) where in addition to KE also potential electron emission (PE) takes place. PE is most effective at low impact energy and its electron yield depends primarily on the projectile potential energy (sum of ionisation potentials for creating the particular MCI), but only weakly on the target surface [5]. It amounts typically to one electron per 100 eV potential energy, and for conducting surfaces (metals, graphite) hardly depends on the incidence angle [6]. Total electron yields from PE and KE for impact of singly and multiply charged carbon ions on graphite have been given in [4]. Electron energy distributions for PE start from zero energy, peak at typically 5 to 10 eV and then level off [5]. Of particular interest are the He^{2+} ions („alpha particles“) in future burning fusion plasmas. Considering PE from metal surfaces, only a few widely spaced $He^+(n,l)$ states are available for electron capture from the surface. Consequently the surface density-of-states decides critically which PE processes contribute and thus the PE yield strongly depends on the target surface [7]. For fusion relevant materials, in particular graphite, PE yields between 0.5 and 1 can be expected, but reliable data are not yet available.

For electron-induced electron emission yields (δ) and fast electron reflection coefficients (η), we refer to a data collection in [8]. For instance, for a tungsten surface and electron impact energies between 10 and 100 eV, δ increases from about 0.5 to 1, whereas η stays below 0.1. Reliable data for fusion-relevant target surfaces, in particular graphite, are not yet available. Electron energy distributions $d\gamma_\alpha/dE$ are parametrized as $d\gamma_\alpha/dE = D^{e\alpha}\, E \exp(-E/E^{e\alpha})$. $E^{e\alpha}$ is the maximum of the electron energy distribution [8].

Here, α = e, p and i denote primary electrons, hydrogen and impurity ions, respectively. The quantity $D^{e\alpha} = \gamma_\alpha/(E^{e\alpha})^2$ is directly related to the respective total electron yield. All parameters have to be derived for the specific projectile-target surface combinations (see above). For electron reflection (ER) conservation of the impinging electron energy can be assumed. Preliminary self-consistent PSV calculations have been made in order to investigate the relevance of EIEE and IIEE processes (see below). In further consequence also the influences of ER and of magnetic fields on the PSV will be studied.

Plasma sheath model

The PSV is calculated in a self-consistent way based on a new plasma sheath theory [2] in the „asymptotic two-scale approximation“. A planar collisionless non-neutral space-charge sheath („Debye sheath“) is assumed between the wall and the „sheath edge“, where it joins with a quasineutral presheath extending toward the undisturbed plasma. Generally speaking, the presheath may take into account relevant collisional processes, non-planar geometry and/or ion gyromotion [9]. The non-neutral part of the plasma-wall transition region (the sheath) is described kinetically, whereas the quasineutral presheath is taken into account within a multifluid formalism. The potential decreases monotonically from the sheath edge to the wall. Primary electrons with half-Maxwellian velocity distribution from the undisturbed plasma are partially reflected in the Debye sheath region, while those reaching the wall are absorbed and will cause electron-induced emission with assumedly uniform starting velocity and total electron yield γ_e. Hydrogen (p) and impurity ions (i) are accelerated by the decreasing potential, hit the wall and give rise to ion-induced electrons with uniform velocities and total electron yields γ_p and γ_i, respectively. The starting velocities and densities of electrons at the wall are calculated from the emission energy distribution (see above), and densities and velocities at the presheath entrance result from conservation of electron flux and energy for the self-consistently calculated PSV.

First results and outlook

In table 1 we have listed „reduced PSV“ data Φ = PSV(k T_e) which were calculated for a sheath edge plasma temperature k T_e = 100 eV by taking into account the influence of EIEE, IIEE and ImpIEE with given values for γ_e, γ_p, f_i (impurity ion density in percent of the plasma density) and γ_i, respectively. The preliminary data show clearly the influence of particle-induced electron emission from the boundary surface, which is most important for EIEE, while for realistic plasma conditions the influences of IIEE and ImpIEE remain minor.
Further detailed studies will also take into account magnetic field effects which probably will reduce the here derived influence of EIEE, IIEE and ImpIEE.

Plasma and surface conditions	n_i	γ_e	γ_p	γ_i	Φ
pure without EIEE and IIEE	-	-	-	-	3.021
pure, with EIEE	-	0.3	-	-	2.699
pure with EIEE and IIEE	-	0.3	0.12	-	2.599
C^{5+} imp. without EIEE and IIEE	5 %	-	-	-	3.090
C^{5+} imp. with EIEE	5 %	0.3	-	-	2.767
C^{5+} imp., EIEE, IIEE and ImpIEE	5 %	0.3	0.12	3.8	2.594

Table 1: Reduced PSV values Φ = PSV(k T_e) from self-consistent calculations of the plasma sheath voltage under the assumption of different particle-induced electron emission processes at the material boundary (experimental data for EIEE and IIEE for a graphite surface [4]).

Acknowledgment

This work has been carried out within Association EURATOM-OEAW.

References

[1] I.H. Hutchinson, Principles of Plasma Diagnostics, Cambridge University press, New York (1987)

[2] R. Khanal, A kinetic trajectory simulation (KTS) model for boundes plasmas, Ph.D. thesis, Inst. of Theoretical Physics, University of Innsbruck (Oct. 2002)

[3] D. Hasselkamp, in Particle Induced Electron Emission II, Springer Tracts in Modern Physics, vol. 123, Springer, Berlin (1992)

[4] S. Cernusca, HP. Winter, F. Aumayr, A. Quayyum, W. Schustereder, C. Mair, P. Scheier and T.D. Märk, Int.J. Mass Spectrom. **223-224** 21 (2003)

[5] A. Arnau et al., Surface Science Reports **27** 113 (1997)

[6] C. Lemell, J. Stöckl, J. Burgdörfer, G. Betz, HP. Winter and F. Aumayr, Phys.Rev.Lett. **81** 1965 (1998)

[7] H.D. Hagstrum and G.E. Becker, Phys.Rev. B **8** 107 (1973);
A. Niehaus, p. 79 in Ionization of solids by heavy particles (edr. R. Baragiola), NATO ASI Series vol. **306**, Plenum, New York 1993

[8] E.W. Thomas, in Atomic and Plasma-Material Interaction Data for Fusion, vol 1, suppl. to Nucl. Fusion, IAEA Vienna 1991, p. 79

[9] K.-U. Riemann, Theory of the Plasma-Sheath Transition, J.Tech.Phys. **41** 89 (2000)

Parity-Pairs in Differential Cross Sections of Hexapole State-Selected NO colliding with He

A. Gijsbertsen and S. Stolte
Laser Centre and Department of Physical Chemistry, Vrije Universiteit Amsterdam,
De Boelelaan 1083, 1081 HV Amsterdam, The Netherlands

H. Linnartz
Sackler laboratory for Astrophysics, Leiden Observatory,
P.O. Box 9513, 2300 RA Leiden, The Netherlands

C.A. Taatjes and D.W. Chandler
Combustion Research Facility, Sandia National Laboratory, Livermore, CA 94550, USA

The conventional exact close coupling (CC) solution of the scattering problem of a rare gas atom R and a hetero nuclear rigid diatomic (NO) requires the expansion of the incoming plane wave e^{ikZ} into an infinite sum of Legendre polynomials $P_l(\cos\theta)$, where θ is the scattering angle. Each $P_l(\cos\theta)$ is multiplied by an incoming and outgoing spherical wave $e^{\pm i(kR-l\pi/2)}/(kR)$ to yield the proper plane wave. The absolute value of the position vector is written as R, the orbital quantum number as l and the incoming wave number as k. The semi classical impact parameter b (see Fig. 1) relates to l as

$$b \approx \frac{l+\frac{1}{2}}{k}. \tag{1}$$

The quantum number l couples with the NO rotational quantum number j to yield the total angular momentum quantum number J. Both J and the overall parity of the total wave function are conserved by the scattering Hamiltonian. Solving this scattering problem (at $E_{tr} = 500\ \mathrm{cm}^{-1}$) numerically involves a large set of coupled $(j, l, \epsilon, j', l', \epsilon')$ differential equations at each value of $J < 120.5$, which makes this treatment time-consuming. Calculating

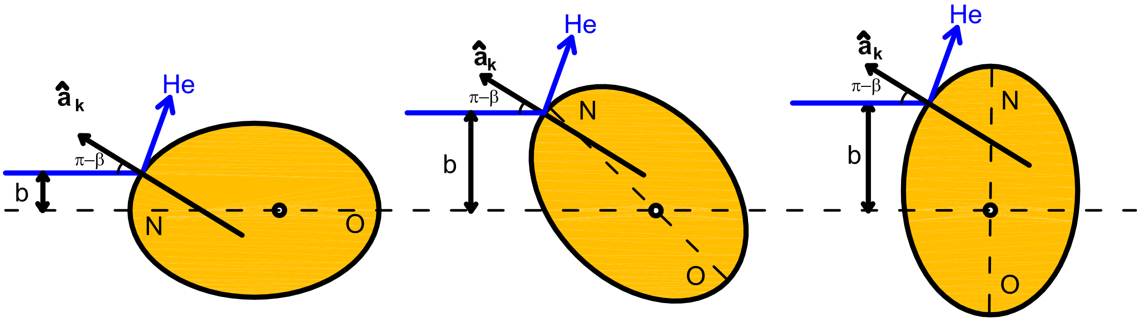

Figure 1: All orientations are present in the initial wave function. Constructive and destructive interference between these waves will occur dependent on the difference in path length. The potential can cause scattering under a certain angle for many different impact parameters. Note that for a hard shell as drawn here, the kinematic apse $\hat{\boldsymbol{a}}$ coincides with the surface normal $\hat{\boldsymbol{n}}$.

differential cross sections for He-NO with current technology takes a set of several parallel processors several days [1].

Our Quasi Quantum Treatment (QQT) aims at the simplification and approximation of exact quantum treatments. It presents an intuitive basis for understanding the physics behind the steric asymmetry [2] and - more generally - the relation between inelastic collisions and the anisotropy of the inter-molecular potential.

For scattering trajectories (rays) to interfere, the trajectories from a single initial state need to be scattered under an identical angle and into the same final molecular state. The impact parameter b gives the distance between a straight line along the the trajectory of the incoming particle long before collision and the origin of the potential (see Fig. 1). Traditionally, to calculate differential cross sections, a summation over l is made that in the classical limit can be replaced by integration over $b \approx l/k$.

In the case of an anisotropic potential, even when neglecting the attractive part, the repulsive part of the potential allows scattering into a certain angle for many impact parameters. This is demonstrated in Fig. 1 using a hard egg-shaped potential. The projection m_a of the total angular momentum $\boldsymbol{j}$ on an apse $\hat{\boldsymbol{a}}$ is approximately conserved during the collision, when the repulsive part of the potential dominates. The kinematic apse is defined as [3]:

$$\hat{\boldsymbol{a}}_k = \frac{\boldsymbol{k}' - \boldsymbol{k}}{|\boldsymbol{k}' - \boldsymbol{k}|}. \tag{2}$$

The spherical angles which define the direction of the kinematic apse in the collision frame ($\hat{\boldsymbol{Z}} \equiv \hat{\boldsymbol{k}}$) are defined as β and α. The orientation of the molecular axis with respect to the kinematic apse is given by the spherical angles γ_a and ϕ_a.

In the QQT the commonly-used sum over l (or integral over the impact parameter b) is replaced by an integral over the apse angles β and α. The scattering angle is determined fully by the angle of the kinematic apse with the incoming momentum and the final rotational state. When one integrates over b, scattering into the same angle and thus interfering contributions originate from many values of b (see Fig. 1), making the integral cumbersome to evaluate. Fig. 2 schematically shows the scattering angle of the outgoing momentum for different final rotational states at a *single* direction of kinematic apse. Note that $\frac{1}{2}\pi \le \beta \le \pi$ for scattering with $k' \le k$. No interfering contributions from different apse orientations occur as there is a direct relation between apse angle and scattering angle.

The conventional scattering amplitude $f_{j,m,\Omega\to j',m',\Omega}(\vartheta)$ can be expressed in a newly introduced scattering amplitude $g_{j,m,\Omega\to j',m',\Omega}(\beta)$. The azimuthal angles α and φ are redundant because of cylindrical symmetry; note $\alpha = \phi$. The scattering amplitudes are related via a Jacobian:

$$f_{j,m,\Omega\to j',m',\Omega}(\vartheta) = \sqrt{\frac{\sin\beta}{\sin\vartheta}\left|\frac{\partial\beta}{\partial\vartheta}\right|}\; g_{j,m,\Omega\to j',m',\Omega}(\beta). \tag{3}$$

Note that Eq. 3 does not specify the choice of the quantization axis. Recall that the projection of the total angular momentum on the apse (m_a) is (approximately) conserved during the scattering process ($m'_a = m_a$). Including m_a conservation in the calculation leads to an enormous simplification. The scattering amplitude in the apse frame (where the apse $\hat{\boldsymbol{a}}_k$ serves also as quantization axis) is defined as:

$$\begin{aligned} g_{j,m_a,\Omega\to j',m_a,\Omega}(\beta) &= C(\beta)\langle j', m_a, \Omega|\; g_{j\to j'}(\gamma_a;\beta)\; |j, m_a, \Omega\rangle = \\ C(\beta) &\int_0^{\pi}\int_0^{2\pi} \Psi^*_{j',m_a,\Omega}\; g_{j\to j'}(\gamma_a;\beta)\; \Psi_{j,m_a,\Omega}\; \sin\gamma_a\; d\phi_a d\gamma_a. \end{aligned} \tag{4}$$

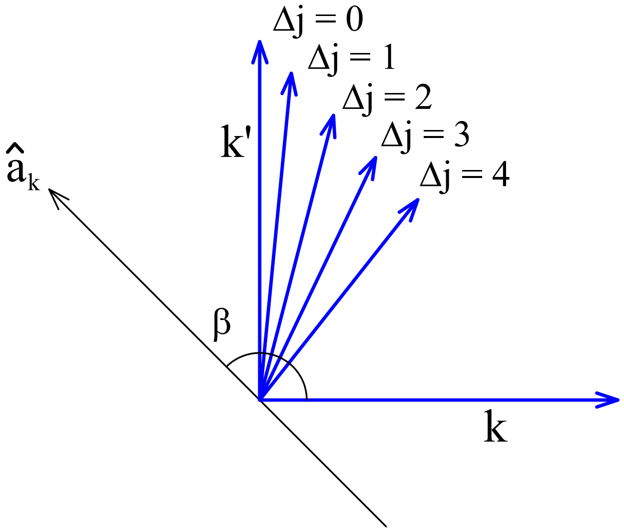

Figure 2: Part of the incoming momentum $\boldsymbol{k}$ is transformed into rotation. The orientation of the apse (β) and the translational energy loss due to rotational excitation Δj fixes the scattering angle.

The differential cross section for scattering of $j=\frac{1}{2},\overline{m}_a=\frac{1}{2},\overline{\Omega}=\frac{1}{2},\epsilon \rightarrow j',\overline{m}_a=\frac{1}{2},\overline{\Omega}=\frac{1}{2},\epsilon'$ is given by:

$$\frac{d\sigma_{j=\frac{1}{2},\epsilon\rightarrow j',\epsilon'}}{d\omega} = C(\beta)^2\frac{j'+\frac{1}{2}}{4k^2}\,\frac{\sin\beta}{\sin\vartheta}\left|\frac{\partial\beta}{\partial\vartheta}\right|\;|g_{j'-\epsilon\epsilon'/2}(\beta)|^2 \tag{5}$$

$$\text{with:}\qquad g_n(\beta)=\int_{-1}^{1} g_{j\rightarrow j'}(\gamma_a;\beta)P_n(\cos\gamma_a)d\cos(\gamma_a).$$

In Eq. 5, it can be seen that the differential cross sections for transitions from $j=\frac{1}{2},\epsilon=-1$ to two neighboring rotational states with the same parity (for example $j'=3.5,\epsilon'=1$ and $j'=4.5,\epsilon'=-1$) are similar, except for a different pre-factor $(j'+\frac{1}{2})$. This propensity rule immediately follows from Eq. 5:

$$\frac{d\sigma_{\frac{1}{2},\epsilon=-1\rightarrow\frac{3}{2},\epsilon'=1}}{d\omega} \approx \frac{2}{3}\frac{d\sigma_{\frac{1}{2},\epsilon=-1\rightarrow\frac{5}{2},\epsilon'=-1}}{d\omega} \propto \left|\int_{-1}^{1} g(\gamma_a;\beta)P_2(\cos\gamma_a)d\cos(\gamma_a)\right|^2$$

$$\frac{d\sigma_{\frac{1}{2},\epsilon=-1\rightarrow\frac{5}{2},\epsilon'=1}}{d\omega} \approx \frac{3}{4}\frac{d\sigma_{\frac{1}{2},\epsilon=-1\rightarrow\frac{7}{2},\epsilon'=-1}}{d\omega} \propto \left|\int_{-1}^{1} g(\gamma_a;\beta)P_3(\cos\gamma_a)d\cos(\gamma_a)\right|^2$$

$$\frac{d\sigma_{\frac{1}{2},\epsilon=-1\rightarrow\frac{7}{2},\epsilon'=1}}{d\omega} \approx \frac{4}{5}\frac{d\sigma_{\frac{1}{2},\epsilon=-1\rightarrow\frac{9}{2},\epsilon'=-1}}{d\omega} \propto \left|\int_{-1}^{1} g(\gamma_a;\beta)P_4(\cos\gamma_a)d\cos(\gamma_a)\right|^2$$

et cetera.

The current treatment explains the surprising observation that differential cross sections come in ”parity pairs” as seen in ion imaging (velocity mapping) experiments [4]. Differential cross sections for parity conserving He-NO collisions are plotted in Fig. 3.

The contra-intuitive result that the differential cross section to the upper j' component of each parity pair $j'-\epsilon\epsilon'/2$ is larger than that to the lower j' component opposes the

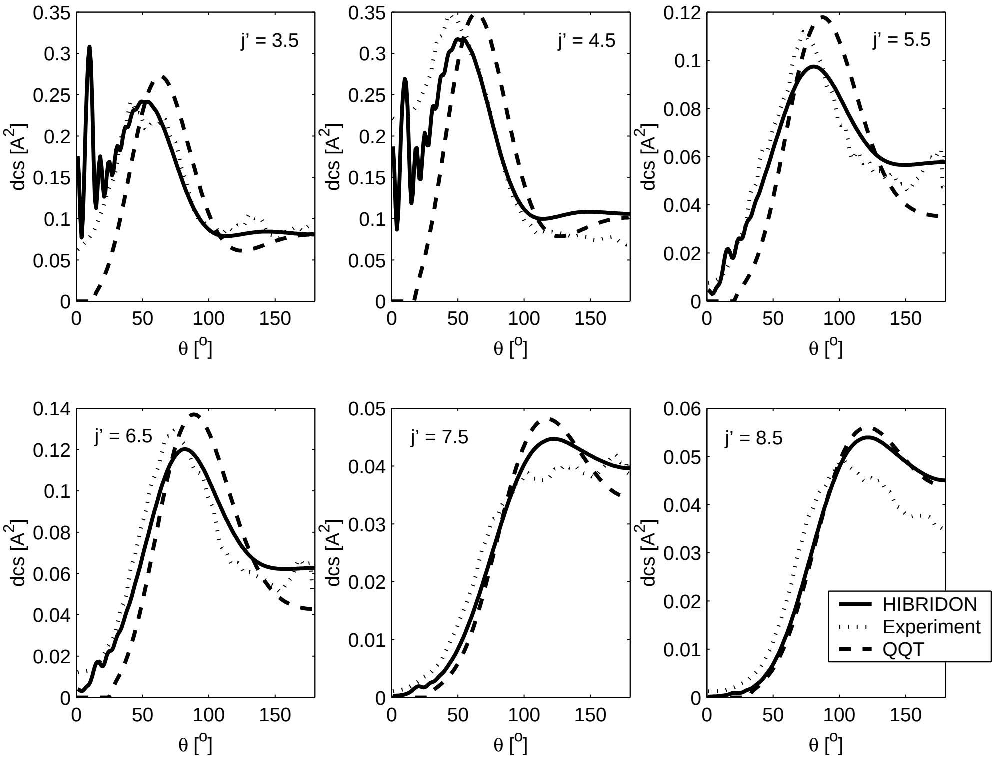

Figure 3: Several differential cross sections for parity conserving transitions ($p = p' = -1$). The parity pairs are easily seen in this figure. Both the experimental and hard shell QQT results are normalized on the total cross section from close coupling HIBRIDON results on an *ab initio* potential energy surface.

"exponential gap" model [5]. This rule of thumb predicts that the cross section for a small "gap" (the change of translational energy during collision) and thus a small j' is larger than to a higher one.

The QQT differential cross sections calculated for non-oriented NO molecules colliding with He atoms agree reasonably well to experimental results and close coupling calculations. The QQT predicts a parity propensity rule that is also seen in experimental results and results from full quantum mechanical calculations. This propensity rule was not recognized as such until now.

---

[1] G. Groenenboom (2005), private communications.

[2] A. Gijsbertsen, H. V. Linnartz, C. A. Taatjes, and S. Stolte (2005), document in preparation.

[3] V. Khare, D. J. Kouri, and D. K. Hoffmann, J. Chem. Phys. **74**, 2275 (1981).

[4] A. Gijsbertsen, J. Kłos, D. W. Chandler, G. Rus, A. E. Wiskerke, H. V. Linnartz, and S. Stolte (2005), in press, J. Chem. Phys.

[5] R. D. Levine, *Reaction Dynamics* (Cambridge University Press, 2005).

The reactivity and reaction dynamics of ionospherically relevant molecular dications

Claire L. Ricketts and Stephen D. Price

Chemistry Department, University College London, 20 Gordon Street, London, UK. WC1H 0AJ (S.D.Price@ucl.ac.uk)

ABSTRACT

A number of small molecular dications, for example N_2^{2+}, O_2^{2+}andr CO_2^{2+}, have recently been proposed as playing a significant role in the chemistry of planetary ionospheres. In this presentation we report the results of experiments to study the bimolecular reactivity of these dications, at low collision energy, using position sensitive coincidence spectroscopy. These experiments reveal the chemical reactions these species undergo in collisions with neutral molecules and also provide a powerful probe of the reaction dynamics of these reactive processes.

1. Overview

Small molecular doubly-charged ions (dications) are usually highly energy-rich and reactive metastable species.[1-4] However, despite their high internal energy content, many molecular dications have recently been shown to display considerable chemical reactivity with neutral species.[5-25] For example:

$$CF_2^{2+} + H_2 \rightarrow HCF_2^{+} + H^{+} \qquad (1)$$

Recent interest in the bimolecular reactions of small molecular dications has been heightened as atmospheric modelling has predicted that the chemistry of these species may influence the chemistry of planetary ionospheres.[24,26,27] In addition, these bimolecular dication reactions usually generate a pair of monocationic products which separate with considerable translational energy due to their electrostatic repulsion. These highly energetic (“hot”) monocations may also influence ionospheric chemistry.

Initial studies of the chemical reactions of molecular dications were prompted by the mass-spectrometric observation of products which involved the formation of new chemical bonds following dication-neutral collisions.[11,28] Since these early observations many new chemical reactions between dications and neutrals have been documented. However, more detailed investigations of the dynamics of these reactions were scarce and restricted to pioneering angular scattering measurements in Prague[5,7,15] and studies of intermolecular and intramolecular isotope effects at UCL.[9,10,17] The angularly resolved data from Prague demonstrates the continued power of such studies as a probe of ionic reaction dynamics. However, when applied to dication reactions, two short-comings in these ″conventional″ approaches to studying dicationic reactivity and dynamics are apparent. Firstly, most dication bond-forming reactions involve the formation a pair of monocationic products and often an additional neutral species:

$$CF_2^{2+} + H_2O \rightarrow OCF^{+} + H^{+} + F \qquad (2)$$

If only conventional mass spectra are recoded to detect the charged products of a dication reaction, it is often impossible to deduce which partner ions (H^+ above) accompany the formation of the bond-forming product (OCF^+ above). Considering reaction (2), H^+ ions are also formed by dissociative electron transfer reactions, and so the fact that OCF^+ ions are formed together with H^+ ions is hard to determine from a simple mass spectrum. A second problem stems from the fact, as again illustrated by reaction (2), that the chemical reactions of dications are often three-body processes; reactions which generate three products. For a three-body reaction, the measurement of the velocity of just *one* of the products, as performed in a conventional experiment, does not allow the reconstruction of the kinematics of the reaction as a whole; this is because the velocities of *two* of the products are needed for the dynamics of a three-body reaction to be reconstructed by conservation of momentum.

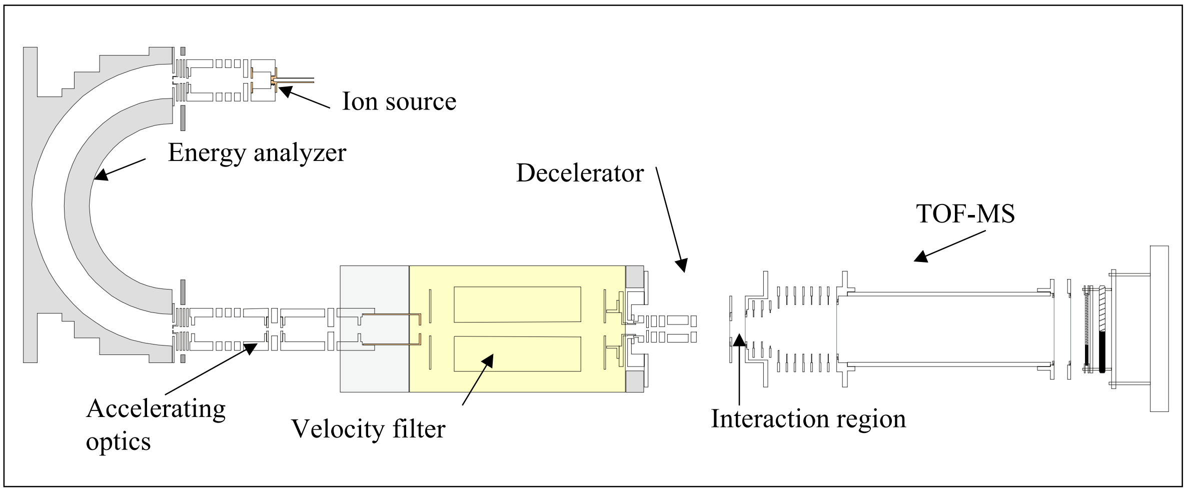

Figure 1 Schematic of the position sensitive coincidence spectrometer used to study dication reaction dynamics.

We have developed an experiment which overcomes the above two problems and generates angularly resolved data to probe the reactivity and dynamics of dication chemical reactions. Our studies employ a position sensitive coincidence (PSCO) experiment to detect, in coincidence, both of the charged products from a dication chemical reaction on an event-by-event basis.[29] This coincidence data readily identifies the pair of charged products from each reactive channel. The data also yields the initial velocity vectors of both of the charged products for each individual reactive event we detect. For a three-body reaction this data then allows the determination of the velocity of the undetected neutral species via conservation of momentum. Thus, the complete kinematics of the reactive scattering process is accessible and, hence, the experiment provides an extremely powerful insight into the dynamics of these complex processes.[30-34]

2. Experimental details[29]

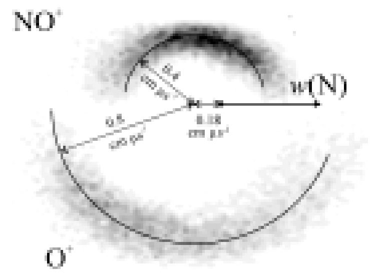

Figure 2: Internal frame scattering diagram for the reaction of N_2^{2+} with O_2 to form $NO^+ + O^+ + N$.

The position sensitive coincidence apparatus is illustrated in Figure 1. Briefly, a beam of ions is extracted from a home-built ion source. The translational energy, and energy spread, of the ions in the beam is controlled by a hemispherical energy analyser through which the beam passes. The reactant dications of interest (e.g. N_2^{2+}) are selected from the ion beam, decelerated (to 2-15 eV in the laboratory frame) and collide in the source region of a time-of-flight mass spectrometer (TOFMS) with the neutral reactant and the reactions of interest occur. We generate dication beams with excellent intensity and energy distributions. Typical beam currents are 1 pA at an energy of 4 eV in the source region with a translational energy spread of 0.1 eV. Following the interaction of the dication beam with the neutral target the ionic products are detected and analysed by pulsing an extraction voltage (30-50 kHz) in the source region of the TOFMS. The ions then fly down the TOFMS and are detected at a position sensitive detector interfaced to fast timing electronics. This position sensitive data can be interpreted to yield the initial velocity vectors of the two charged fragments from a dication reaction. From these velocity vectors the dynamics of the reaction can be determined. Experiments can be carried out with either a pulsed (~0.5 μs) or continuous beam of reactant dications. The pulsed beam produces higher quality data at the expense of longer run times.

3. Data Interpretation

The flight times of the ions we detect in pairs can be assembled into a two-dimensional mass spectrum, which readily identifies both of the ions formed in all the reactions occurring in the collision system. In addition, as described above, we can extract from our data the velocities of the ionic products for each reactive event we detect. Converting these ionic velocities to the centre-of-mass (COM) frame, and using conservation of momentum, gives the velocity of the undetected neutral product. These velocities completely define the kinematics and from them we can extract key quantities which characterise the dynamics each reactive channel.[29,30] For example:

- the angular distribution of each of the products with respect to the velocity of the COM,
- the angle between the products as they separate, the so-called internal scattering angles,
- the translational and internal energies of the products
- the scattering diagram in both the COM and the "internal" frame(Figure 2)
- the electronic states of the products and reactants from the energy balance.

Examining these pieces of information allows us to determine the details of the reactive pathway and the reaction dynamics for each reactive channel we detect from a given collision system.

4. Results

This presentation will describe the details of this new experimental approach to studying the dynamics of these complex reactions and illustrate the powerful insights into the reaction mechanisms that result.[30-34] Particular attention will be given to recent studies of the reactions of N_2^{2+}, O_2^{2+} and CO_2^{2+} with molecules relevant to the ionospheric chemistry of the Earth, Mars and Titan. These experiments show a wealth of chemical reactivity and reaction mechanisms which are, perhaps surprisingly, dominated by the formation of a doubly charged collision complex. For example, reactions between N_2^{2+} and C_2H_2 reveal several new chemical reactions, as illustrated in Figure 3.

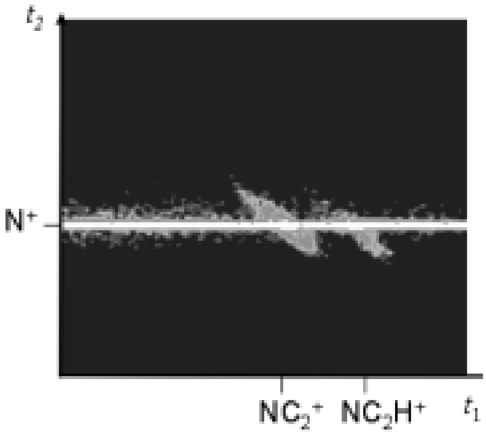

Figure 3. Two-dimensional mass spectrum showing the formation of carbon-nitrogen bonds following collisions of N_2^{2+} with acetylene.

5. Acknowledgements

The authors thank the members of MCInet, an EU research training network, for many helpful discussions. This work was supported by the EPSRC and the Leverhulme Trust.

References

1 D. Schroder *et al.*, *J. Phys. Chem. A* (1999) **103** 7385.
2 D. Mathur, *Phys. Rep.* (1993) **225** 193.
3 S. D. Price, *J. Chem. Soc. Faraday Trans.* (1997) **93** 2451.
4 S. D. Price, *Phys.Chem.Chem.Phys.* (2003) **5** 1717.
5 Z. Herman *et al.*, *Int. J. Mass Spectrom.* (1999) **192** 191.
6 Z. Herman, *Int. Rev. Phys. Chem.* (1996) **15** 299.
7 L. Mrazek *et al.*, *J. Phys. Chem. A* (2000) **104** 7294.
8 K. A. Newson *et al.*, *J. Chem. Soc. Faraday Trans.* (1998) **94** 2735.
9 K. A. Newson *et al.*, *Chem.Phys.Lett.* (1998) **294** 223.
10 K. A. Newson *et al.*, *Chem.Phys.Lett.* (1997) **269** 93.

11 S. D. Price *et al.*, *J. Am. Chem. Soc.* (1994) **116** 8673.

12 P. Tosi *et al.*, *Chem.Phys.Lett.* (1999) **310** 180.

13 P. Tosi *et al.*, *Phys. Rev. Lett.* (1999) **82** 450.

14 W. Y. Lu *et al.*, *J.Chem.Phys.* (2000) **112** 4648.

15 Z. Dolejsek *et al.*, *Chem.Phys.Lett.* (1995) **235** 99.

16 N. Tafadar *et al.*, *Int. J. Mass Spectrom.* (1999) **192** 205.

17 N. Tafadar *et al.*, *J.Chem.Phys.* (2001) **115** 8819.

18 J. Roithova *et al.*, *J. Phys. Chem. A* (2003) **107** 7347.

19 J. Roithova *et al.*, *J. Phys. Chem. A* (2003) **107** 7355.

20 J. Roithova *et al.*, *Int. J. Mass Spectrom.* (2003) **228** 487.

21 D. Kearney *et al.*, *Phys.Chem.Chem.Phys.* (2003) **5** 1575.

22 N. Lambert *et al.*, *J.Chem.Phys.* (2003) **119** 1421.

23 N. Tafadar *et al.*, *Int. J. Mass Spectrom.* (2003) **223-224** 547.

24 O. Witasse *et al.*, *Geophys. Res. Lett.* (2002) **29** Art No. 1263.

25 N. Lambert *et al.*, *J. Phys. Chem. A* (2005) DOI: 10.1021/jp052981d.

26 J. Lilensten *et al.*, *Geophys. Res. Lett.* (2005) **32** art. no. L03203.

27 C. Simon *et al.*, *Ann. Geophys.* (2005) **23** 781.

28 B. K. Chatterjee *et al.*, *Journal of Chemical Physics* (1989) **91** 1378.

29 W. P. Hu *et al.*, *Meas. Sci. Technol.* (2002) **13** 1512.

30 S. M. Harper *et al.*, *J. Phys. B.* (2002) **35** 4409.

31 S. M. Harper *et al.*, *J.Chem.Phys.* (2004) **121** 3507.

32 S. M. Harper *et al.*, *J.Chem.Phys.* (2004) **120** 7245.

33 S. W. P. Hu *et al.*, *Mol. Phys.* (2005) **103** 1809.

34 C. L. Ricketts *et al.*, *J.Chem.Phys.* (2005) **123** Art No:134322.

Clusters in intense light fields - plasma physics on the 1-nm scale

Karl-Heinz Meiwes-Broer, Tilo Döppner, Thomas Fennel, Johannes Passig, Josef Tiggesbäumker

Institute of Physics, University of Rostock, Universitätsplatz 3, 18051 Rostock, Germany

Atomic clusters in intense laser fields are a nice playground to study the coupling of strong radiation into matter. In particular, non-stationary plasma effects lead to pronounced dynamics in the optical response. Recent experiments have shown that excitation with optically delayed dual pulses provides a powerful way to control the coupling of the radiation to these finite systems. Both the yield of highly charged atomic ions [1] as well as the kinetic energy of emitted electrons [2] are strongly enhanced for a particular optimal delay. After the first pulse initiates the cluster expansion the delay-dependent impact of the second pulse can be studied. In this contribution we will present experimental results on the charging dynamics by use of the femtosecond dual-pulse technique. Special emphasis will be put onto the role of the laser focus. The significance of the temporal structure of the laser field is demonstrated by complementary Vlasov calculations [3] on model systems. We attribute the distinct maximum in the charging efficiency to plasmon-enhanced ionization of the expanding cluster which is supported by the simulations [1]. Applying this method to free clusters and those which are embedded in helium droplets [4] reveals a significant influence of charge transfer processes which will be discussed.

[1] T. Döppner, Th. Fennel, Th. Diederich et al., Phys. Rev. Lett. 94:013401, 2005
[2] T. Döppner, Th. Fennel, P. Radcliffe et al., submitted
[3] Th. Fennel, G. Bertsch and K.H. Meiwes-Broer, Eur. Phys. J. D 29:367, 2004
[4] T. Döppner, S. Teuber, Th. Diederich et al., Eur. Phys. J. D 24:157, 2003

Time resolved spectroscopy of photochemical reactions on size selected metal clusters

Gerd Ganteför, Marco Niemietz, Markus Engelke, and Young Dok Kim

Department of Physics, University of Konstanz, D-78457 Konstanz, Germany
(gerd.gantefoer@uni-konstanz.de)

ABSTRACT

Time resolved photoelectron spectra of mass-selected $Ag_nO_2^-$ cluster anions are presented. Absorption of a single pump photon populates an excited state, which decays by photodissociation via the pathway $Ag_nO_2^- \rightarrow Ag_n^- + O_2$. Each step of the reaction can be examined using a second delayed photon for photoelectron spectroscopy. The series of photoelectron spectra recorded with increasing pump-probe delay reveals the reaction pathway, which exhibits pronounced size dependence.

1. Introduction

Real-time recording of a chemical reaction process as in a movie is one of the future visions in chemistry. However, atoms and molecules are too small to be directly visualized and the time scales are so fast that a direct access is almost impossible. But with fast pulse lasers providing light pulses shorter than 100 fs it is possible to observe reactions at least indirectly, applying special spectroscopic techniques. Such data reveal the fast changes of the electronic and geometric structure of these systems.

In small nanoparticles and clusters chemistry is different in comparison to the bulk. There is new chemistry taking place in the nanoworld and the properties of clusters vary with each additional atom. Therefore, for experiments on clusters size-selection is necessary. One of the most successful concepts is experiments on ion beams, because ions allow an accurate size selection prior to the experiment. The disadvantages of low target intensity have to be compensated by the use of intense lasers.

Time-resolved photoelectron spectroscopy of size selected cluster anions has first been used to analyse the photodissociation of an I_2 molecule by a 1.5 eV photon [1]. It was possible to reveal the time-dependent change of the electronic structure in the sequence of photoelectron spectra with increasing time delay. More recently this technique has been used for detailed studies of the relaxation of hot electrons in metal clusters [2]. Up to now, very few experiments using this technique focus on chemical reactions. One experiment on the photodissociation of CO from an Au_2^- dimer was hampered by the statistical nature of this thermal dissociation process, which did not allow for a direct observation of the changing electronic structure [3].

O_2 chemisorption on various metal clusters is a first step in understanding the surprisingly effective catalytic CO oxidation taking place on Au clusters supported on oxide surfaces [4]. This discovery triggered an enormous activity studying the reaction of metal clusters with O_2. The increased catalytic activities of nano-particles seem to be not limited to Au, but also relevant for other materials: For both, Au and Ag clusters in the size regime up to $n = 20$ atoms, a pronounced even odd alternation has been found with the even numbered cluster anions being much more reactive [5,6]. According to spectroscopic results the O_2 binds molecularly to Ag_n^- and Au_n^- clusters.

Here, we present the results of time resolved photoelectron spectroscopy on the photodesorption of O_2 from $Ag_nO_2^-$ clusters. An electronic excited state populated by the pump photon decays by photodissociation. Both, the signature of the excited state and the time scales show a pronounced dependence on the cluster size n.

2. Experimental set up

The experimental set up is described in detail elsewhere [7]. Ag_n^- cluster anions are generated using a pulsed arc cluster ion source. Bulk Ag is vaporized in a pulsed electric arc and clusters grow in a He carrier gas. Charged and neutral clusters are flushed through an extender in a supersonic expansion into high vacuum. O_2 can be injected into the extender resulting in the formation of $Ag_nO_2^-$ clusters. After passing a skimmer the anions are accelerated in a pulsed electric field and mass selected using a reflectron time-of-flight mass spectrometer. The anion beam intersects the interaction volume of a time-of-flight electron spectrometer. A selected bunch of anions is irradiated by two pulses of a femtosecond laser system and the detached photoelectrons are guided using magnetic fields towards an electron detector. The kinetic energy of the photoelectrons can be determined from the time-of-flight with an energy resolution of about 5%.

The pulse width of a single pulse of the femtosecond laser is 60fs and the total time resolution of the experimental set up is 150 fs determined from the non-resonant two-photon signal of the photodetachment from Ag_3^-. The pulse energies of the pump and the probe pulse are determined for each cluster and adjusted just below the threshold of two-photon processes, which correspond to the appearance of electrons with higher kinetic energies. This procedure optimizes the yield of a true pump-probe signal and minimizes background from multiphoton processes. The procedure has to be conducted for each cluster, because the cross sections of photoexcitation and detachment vary with cluster size.

From earlier studies using a similar set up a vibrational temperature of the cluster anions corresponding to roughly room temperature has been determined [8].

3. Results and Discussion

Fig.1 displays a section of a mass spectrum of Ag_n^- clusters reacted with O_2. Ag_8^- reacts readily with O_2, while Ag_7^- and Ag_9^- are relatively unreactive. This is one example of the size dependence of the chemical properties of the Ag_n^- clusters in this size regime. As a general matter of fact the even numbered Ag and Au clusters have an odd number of electrons and are rather reactive.

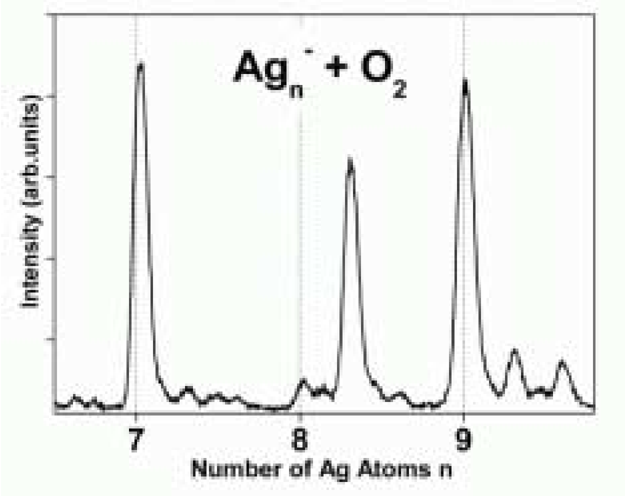

Fig.1 Mass spectrum of Ag_n^- cluster anions reacted with O_2. The dotted lines indicate the positions of the unreacted clusters. The intense maximum at a mass corresponding to 8.3 Ag atoms is assigned to $Ag_8O_2^-$. Almost all Ag_8^- cluster anions have reacted with O_2, while the clusters with even number of valence electrons are rather unreactive.

Before we focus on the analysis of the time-resolved photoelectron spectra of $Ag_2O_2^-$, it is important to discuss the photoelectron spectra of the ground states of $Ag_2O_2^-$ and Ag_2^-. Fig. 2 displays the spectra recorded with a conventional pulsed laser (Nd:YAG laser, hν = 4.66 eV). From the spectra the vertical detachment energies of the two species can be extracted: 2.3 eV for $Ag_2O_2^-$ and 1.1 eV for the bare Ag_2^- dimer. The spectrum of $Ag_2O_2^-$ shows a pronounced vibrational finestructure (denoted with arrows) indicating a molecularly bound O_2 molecule similar to the case of $Au_2O_2^-$. It is important to mention that experiments on reacted $Au_nO_2^-$ clusters are more difficult to conduct because of the much higher electron affinities. The photon energies available in our present time-resolved experiment set up are not sufficient yet, therefore the similar system $Ag_nO_2^-$ was studied.

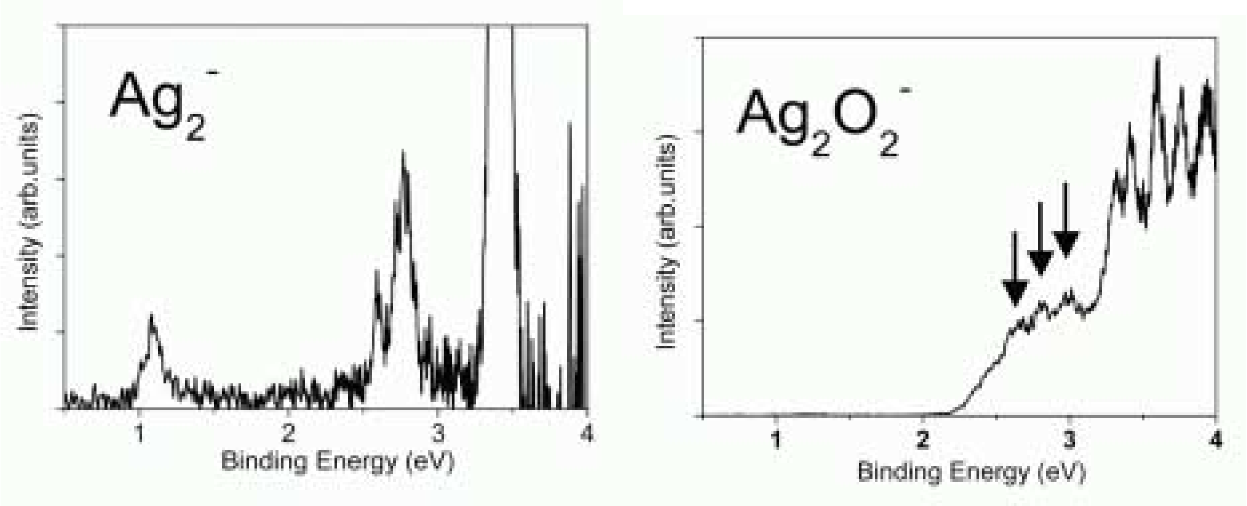

Fig.2 Photoelectron spectra of the ground states of Ag_2^- and $Ag_2O_2^-$ recorded using a photon energy of 4.66 eV. The photodissociation process $Ag_2O_2^- + h\nu \rightarrow Ag_2^- + O_2$ should correspond to a transition from the spectrum on the right hand side to the one on the left hand side with increasing delay time. The time-resolved photoelectron spectra might show the dynamics of the electronic structure during photodissociation.

Using time resolved photoelectron spectroscopy we focus on the cluster $Ag_2O_2^-$. In our set up the two photon energies 1.55 eV and 3.1 eV are available. The lower photon energy of 1.55 eV is not sufficient for photoexcitation of the $Ag_nO_2^-$ species, but using 3.1 eV photon energy as pump pulse leads to a pronounced pump-probe signal due to very effective photoexcitation. Therefore, the pump-probe series are recorded with a pump-energy of 3.1 eV and the photoelectron spectra are recorded with a relatively low photon energy of 1.55 eV only. In future experiments this energy will be increased.

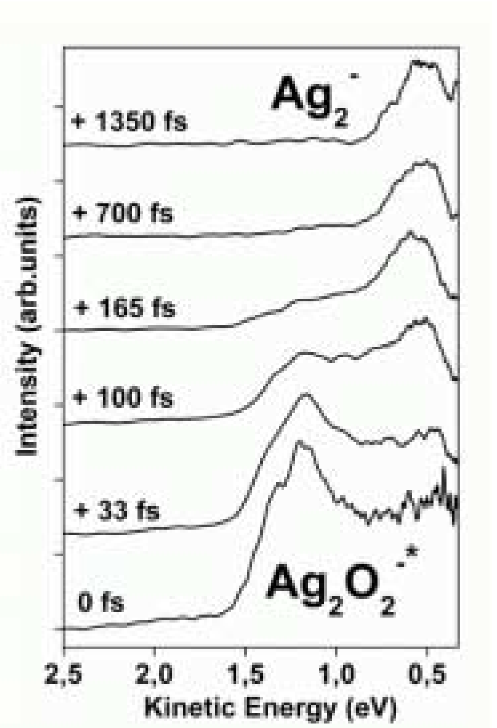

Fig.3. Series of pump probe photoelectron spectra of $Ag_2O_2^-$. At zero delay the photodetachment (probe photon 1.55 eV) from the excited species $Ag_2O_2^{-*}$ (pump photon 3.1eV) gives rise to the appearance of a broad feature at a kinetic energy of 1.2 eV. The peak disappears on a very short time scale and a feature at a binding energy of about 0.5 eV appears, which can be assigned to photodetachment from Ag_2^-, which has a vertical detachment energy (VDE) of 1.1eV (see Fig.2, $E_{kin} = VDE - h\nu_{probe}$). The error of the absolute energy calibration is ± 0.1 eV.

Fig.3 displays a series of pump-probe spectra with a pump energy of hν = 3.1 eV and a probe energy of hν = 1.55 eV. At zero delay between pump and probe pulse an intense feature at a kinetic energy of 1.2 eV is observed. This is assigned to an excited state of $Ag_2O_2^-$ which has a short lifetime of less than 100 fs, which is close to our experimental resolution. The peak vanishes with increasing pump-probe delay and a feature at lower kinetic energy appears. This feature is tentatively assigned to photodetachment from Ag_2^-. The observed kinetic energy of about 0.5eV corresponds to a binding energy (hν = 1.55eV) of about 1eV, which agrees within the experimental error with the binding energy of the first peak in the spectrum of Ag_2^-. Small shifts in binding energy could be due to uncertainties in the absolute energy calibration of the electron time of flight spectrometer and to the difference in vibrational temperature. The Ag_2^- might be vibrationally excited after the photodissociation which might cause a change in lineshape of the peak.

Similar spectra are recorded for larger $Ag_nO_2^-$ clusters with n = 2, 3, 4 and 8. In all cases an intense time-dependent pump-probe signal at comparable kinetic energies is observed, which we assign to the excitation of an excited state of the anions of similar nature. Since in the case of $Ag_2O_2^-$ this state decays by dissociation of a neutral O_2 it might have a considerable contribution from the anti-binding 2π* orbital of O_2. In most cases, a pronounced vibrational finestructure of this excited state was observed. The energetic position, the lifetime and the vibrational finestructure show a strong variation with the cluster size for the few systems studied so far.
By comparison with corresponding calculations we hope to gain a deep insight into the photodesorption process of O_2 molecules from size-selected Ag_n^- cluster anions. This insight might also help to understand the dynamics of other chemical reactions involving O_2 and coinage metal clusters.

References

[1] M. T. Zanni, B. J. Greenblatt, A. V. Davies, D. M. Neumark, J. Chem. Phys. **111**, 2991 (1999).
[2] N. Pontius, M. Neeb, W. Eberhardt, G. Lüttgens, P.S. Bechthold, Phys. Rev. B **6**7, 35425 (2003).
[3] G. Lüttgens, N. Pontius, P. S. Bechthold, M. Neeb, and W. Eberhardt, Phys. Rev. Lett. **88**, 076102 (2002).
[4] A. Sanchez, S. Abbet, U. Heiz, W.-D. Schneider, H. Häkkinen, R.N. Barnett, U. Landman, J. Phys. Chem. A **103**, 9573 (1999).
[5] D. Stolčić, M. Fischer, G. Ganteför, Y. D. Kim, Q. Sun, and P. Jena, J. Am. Chem. Soc., **125**, 2848, (2003).
[6] Y. D. Kim, G. Ganteför, Chem. Phys. Lett. **383**, 80 (2004).
[7] P. Gerhardt, M. Niemietz, Y. D. Kim, G. Ganteför, Chem. Phys. Lett. **382**, 454 (2003).
[8] C.-Y. Cha, G. Ganteför, W. Eberhardt, Rev. Sci. Instrum. **63**, 5661 (1992).

Decay Dynamics of Droplets Charged to the Rayleigh Limit

Denis Duft[1], Rene Müller[1], Bernd Huber[2] and Thomas Leisner[1]

[1] Institut für Physik, Technische Universität Ilmenau, Weimarer Straße 32,
98693 Ilmenau (thomas.leisner@tu-ilmenau.de)

[2]Centre Interdisciplinaire de Recherche Ions Lasers, rue Claude Bloch, 14070 Caen
Cedex 5, France

ABSTRACT

We investigate the dynamics of micrometer sized charged droplets as they approach the limit of Coulomb stability by slow evaporation. The Rayleigh limit of stability of charged liquid droplets is confirmed with high precision and the dynamics of the Coulomb instability is described quantitatively. Our main finding is that the droplets deform into an prolate spindle like shape before two fine jets of highly charged liquid are ejected form the apex points. In one such process about 30% of the droplet charge is expelled, but only about 0.1% of the droplet mass. For positively charged droplets this process is rather universal and does not depend on the type of the liquid. The speed of disintegration is a function of droplet size and viscosity however.

1. Introduction

The breakup of charged microdroplets is important in the charge separation in electrified clouds as well as in technical applications like electrospray ionization, fuel injection or ink jet printing. The stability of highly charged droplets has been studied theoretically as early as 1882 by Lord Rayleigh who could show that that for a drop with radius a_0, surface tension s and charge Q the spherical shape remains stable as long as the fissility $X= Q^2/(64\pi \ \varepsilon_0 \ \sigma \ a_0^3)$ is smaller than one [1]. If X approaches unity, the quadrupole deformation is the first to become unstable. Rayleigh did not discuss the dynamics of this instability at X=1 but realized that for X much larger than one, higher multipole deformations grow faster than the quadrupole mode. For such systems, he concluded that the instability proceeds via the formation of " ... fine jets, whose fineness, however, has a limit", without giving further comments. We have recently been able to take still images of charged droplets during their instability at high temporal and spatial resolution [2] (c.f. Fig. 1). Here we report the detailed dynamics of the jet formation process and discuss its dependence on droplet size and viscosity and on the polarity of the charge.

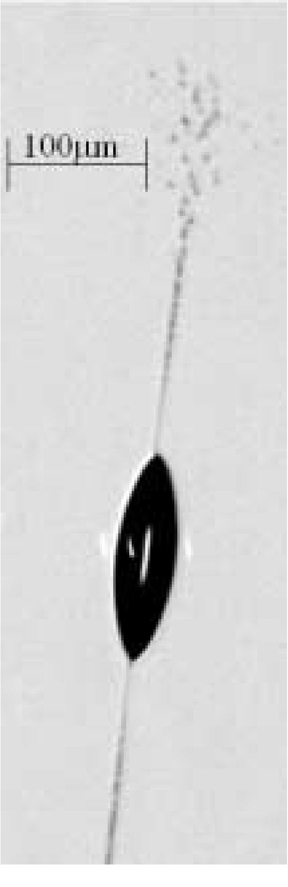

Fig. 1: Microphotograph of an liquid droplet in the moment of coulomb instability. The two Rayleigh – jets are clearly visible. The droplet is rotationally symmetric around its long axis.

2. Experimental

Individual droplets of ethylene glycol were generated with a piezo driven nozzle, charged by influence from a high voltage electrode and injected into an electrodynamic balance operating under ambient conditions. The balance is of the classical "Paul- trap" design with a hyperboloidal torus electrode and top and bottom hyperboloidal cap electrodes. A static field in vertical direction is superimposed by applying DC voltages of opposite sign to the top and bottom electrode to compensate the gravitational force on the droplet. In order to observe the droplets, the balance is placed inside a horizontally orientated long working distance microscope. This microscope is equipped with a triggerable flashlamp for illumination and a cooled CCD camera for image acquisition. A HeNe laser beam polarized under 45° with respect to the horizontal plane of scattering illuminates the droplet. Scattered light is used to image the droplet via a microscope objective onto an vertically oriented linear CCD array in order to determine its vertical position in the trap. Light scattered from the droplet is additionally detected angular resolved with a 2- dimensional CCD camera for phase function measurements. This allows a time resolved determination of the droplet size with high accuracy [reference]. Furthermore, a photomultiplier detector probes the overall intensity of the light scattered in an angular range between 80° and 100° at a much higher temporal resolution. This signal is used to detect the onset of a coulomb instability and to trigger the flashlamp for ultrafast photography, as described in more detail elsewhere [3].

3. Results

Droplets of water and ethylene glycol were injected into the levitator at an initial radius of about 45µm and were allowed to evaporate slowly. As shown in Fig. 2, their charge stays constant around 1.25 pC until the Rayleigh limit of stability is reached. In this instance, the droplet looses about 1/3 of its charge without any appreciable loss of mass. This process repeats itself several times whenever the Rayleigh limit of instability is reached again.

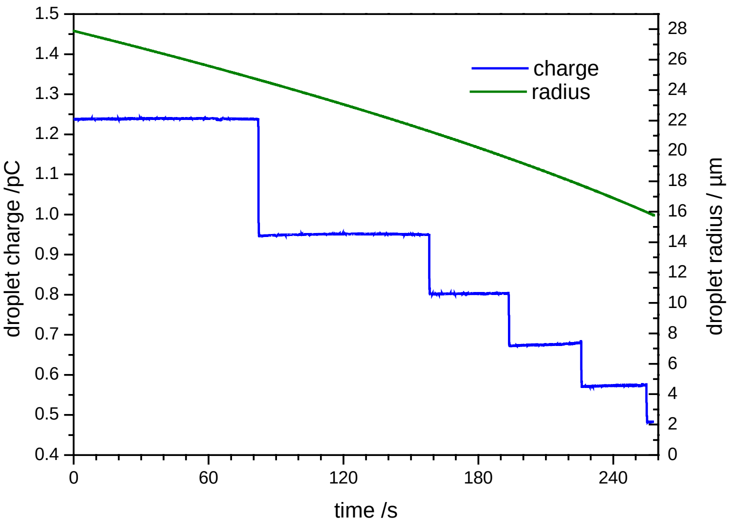

Fig. 2: Size and charge of an evaporating droplet of ethylene glycol levitated in an electrodynamic balance. Rayleigh instabilities are clearly visible.

Microscopic images of droplets of ethylene glycol and water have been taken at various times t after the onset of the coulomb instability (c.f. Fig. 1). These experiments have been repeated at different temperatures between –20°C and +50°C. It turns out that the evolution of the shape of the droplets is remarkably insensitive to these external parameters. It can be described with high accuracy by an rotating a superellipse $(x/a)^n+(z/b)^n=1$ around the z–axis. The shape is then determined by the aspect ratio $\eta = b/a$ of the superellipse and the superelliptic exponent n. An exponent n=2 yields ellipsoids, while n < 2 corresponds to spindle like - and n>2 to barrel like shapes. Typical superelliptic shapes are visible in Fig 3 as red lines around the droplet images.

In Fig. 2 we summarize the results of some thousand coulomb- instabilities by showing the motion of an droplet during the instability in the n - η plane.

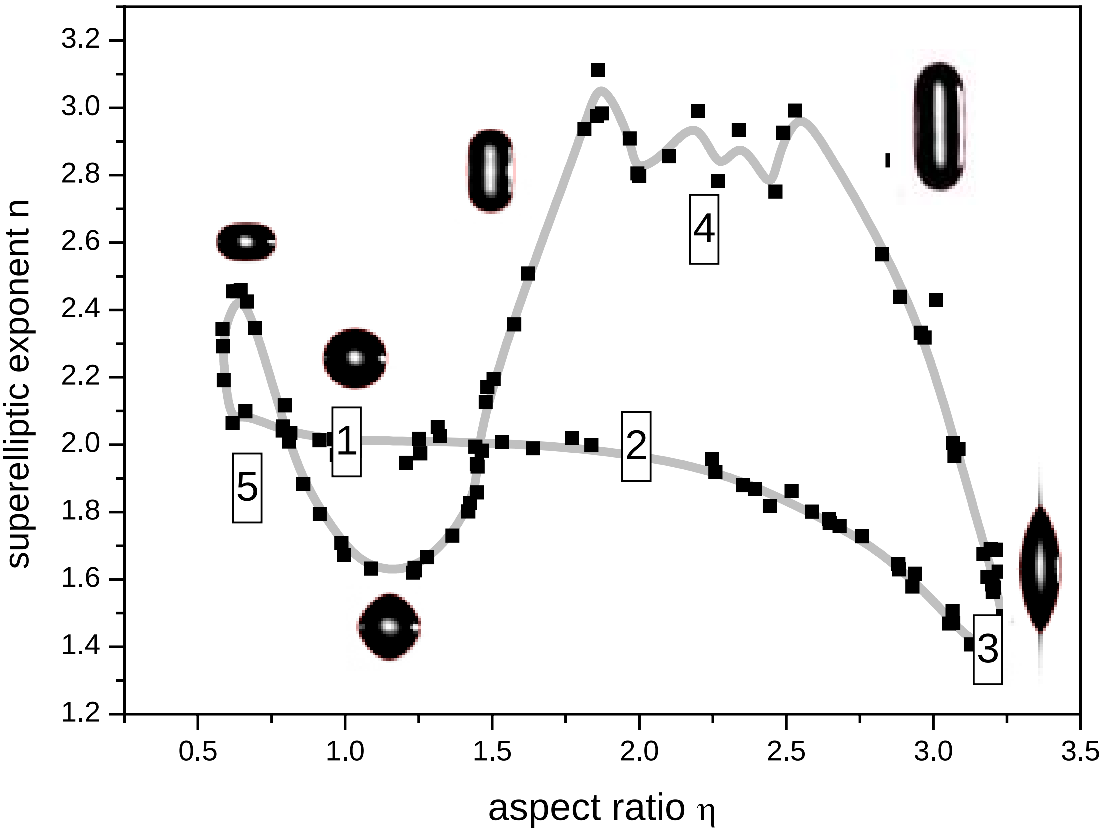

Fig. 3: The shapes of droplets during an Coulomb instability described by their aspect ratio and their superelliptic exponent. Characteristic shapes are given as inserts and numbers which are discussed in the text.

The droplets slowly starts deforming from a spherical geometry (n=2, η=1) at time t=0 (point 1), then deforms into an prolate ellipsoid (n=2, η~3, point 2) before acute tips and finally jets develop at the apexes (point 3, n=1.4, η=3.4). After the jet the tips immediately contract and the tip curvature oscillates for a few periods with high frequency (region 4). The droplet then contracts again but overshoots over the spherical shape and returns to sphericity after one more period of oscillation (region 5). For a water droplet of radius 30µm the time from point 1 to point 2 amounts to approx. 100µs, while from 2 to 3 and from 3 to 4 only abot 10 µs are needed. The time needed for the contraction back to the spherical shape amounts to about 50µs. While the form of Fig. 2 seems to be rather universal, these times do depend on droplet radius and viscosity.

In our contribution, the respective scaling laws will be presented and the dynamics of the jet itself will be discussed.

References

[1] Lord Rayleigh, Phil.Mag.14, 184, (1882)
[2] Duft, D., Achtzehn, T., Müller, R., Huber, B. A., and Leisner, T., Nature 421, 128, (2003)
[3] T. Achtzehn, R.Müller, D.Duft and T. Leisner, Eur. Phys. J. D 34 311 –313 (2005)

High-Pressure Expansion of Molecular Gases

Wolfgang Christen

Humboldt-Universität zu Berlin, Institut für Chemie, Brook-Taylor-Str. 2, 12489 Berlin, Germany; christen@chemie.hu-berlin.de

ABSTRACT

One possibility for efficient cooling of gas-phase molecules is their supersonic expansion into vacuum. Increasing the stagnation pressure will increase the number of collisions taking place during expansion, and thus affect cooling and condensation. For molecular gases such as carbon dioxide or ethene this may lead to additional effects due to the possibility of a phase transition to the supercritical state.

In this contribution we present recent results on the high-pressure expansion of supercritical fluids as a tool to produce cold, neutral beams of non-volatile or thermally labile molecules.

Water clusters: Mass spectrometry of pick-up products and effective polarizability measurements

Ramiro Moro, Roman Rabinovitch, Yanfei Ren, Vitaly Kresin

Department of Physics and Astronomy, University of Southern California,
Los Angeles, California 90089-0484, USA. E-mail: <kresin@usc.edu>

ABSTRACT

We are conducting a series of studies on water clusters, $(H_2O)_n$ and $(D_2O)_n$ ($n \leq 18$), in a molecular beam. One set of experiments investigates the pick-up and subsequent electron-impact ionization of such guests as an additional water molecule, an amino acid molecule, or a DCl molecule. Ionization-induced fragmentation pathways are explored, and implications for the pick-up process, proton exchange, and mass spectrometry analysis are considered. In a related experiment, the products of jointly embedding water and glycine molecules in a liquid helium nanodroplets are being investigated. Finally, the effective polarizabilities of water clusters have been measured in an electric-field deflection experiment, and the implications for dipole dynamics will be discussed.

1. Pick-up of water by water

Water clusters $(H_2O)_n$ and $(D_2O)_n$ are produced by supersonic expansion and pick up an additional heavy or light water molecule, respectively, while flying through a pick-up cell (a new cell design is described in [1]). The products are analyzed by electron bombardment ionization mass spectrometry [2]. Isotope substitution studies show that ionization proceeds via the well-known loss of an OH or OD group, but these have a strong predilection to come from the guest, rather than the host, molecule: ≈60% of ionization events involve the guest molecule. even for large *n* (see Fig. 1). This suggests that proton exchange is suppressed, the host clusters are frozen into rigid shapes, and the adducts reside on the surface and present a dangling OH [or OD] bond where the ionization-induced hole prefers to localize dissociatively.

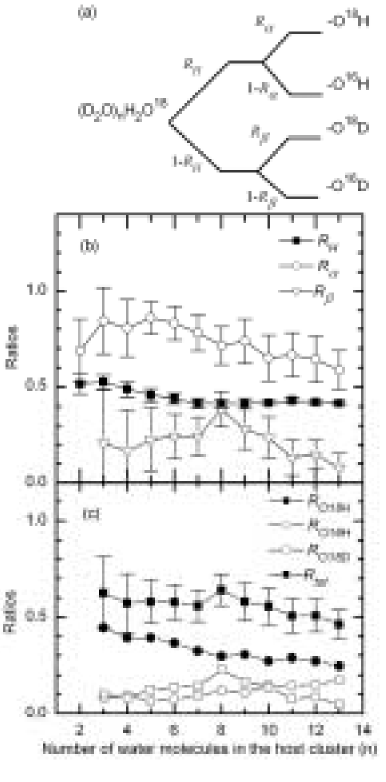

Fig. 1 (a) Diagram of the results obtained from H_2O^{18} pick-up by $(D_2O)_n$ clusters. The fractions *R* represent the relative intensities of different fragments produced upon ionization. (b) Experimental values for R_H, R_α and R_β. (c) Quantities derived from the experimental ratios: the probabilities that atoms from the picked-up molecule depart the ionized cluster either together (R_{O18H}) or paired with an atom from the substrate (R_{O16H} and R_{O18D}). The estimated experimental accuracy of these three ratios is ±6%. The high value of the sum total probability, $R_{tot} \equiv R_{O18H} + R_{O16H} + R_{O-18D}$, confirms that the ionization process strongly targets the guest molecule.

2. Pick up of acid by water

To further investigate the process of solvation at the cluster surface, we measured the mass spectrum of DCl molecules picked up by the water cluster beam [3]. We found that in all cases, electron-impact ionization induces the departure of a chlorine atom (see Fig. 2). This suggests that the acid molecule tends to dissociate upon pick-up

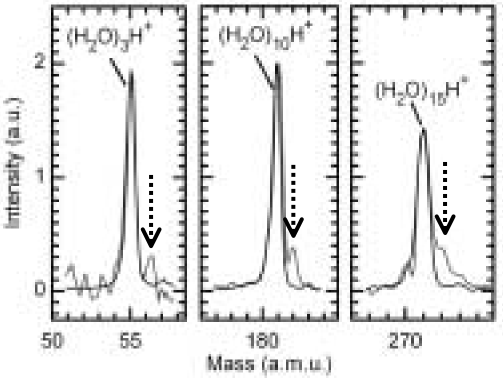

Fig. 2. Electron-ionization mass spectra of $(H_2O)_n$ clusters which have picked up a DCl molecule in flight. As a result, the mass spectrum acquires new $(H_2O)_nD^+$ peaks (marked by dotted arrows), which demonstrates that ionization is always accompanied by the departure of a chlorine atom.

3. Pick up of amino acids by water

The beam of water clusters was also used to pick up the amino acids glycine and tryptophan [2]. As in the previous cases, the guest molecule contributes a large fraction of OH loss (≈30% for Tryptophan and ≈60% for glycine), which is largely insensitive to the cluster size, see Fig. 3. It is noteworthy that no significant amino-acid fragmentation is observed beyond the hydroxyl group loss, in contrast to other measurements employing electron-impact ionization. This may have implications for mass spectrometry of organic molecules.

The observations presented here give rise to interesting questions regarding the dynamics of pick-up, solvation, and dissociative ionization processes.

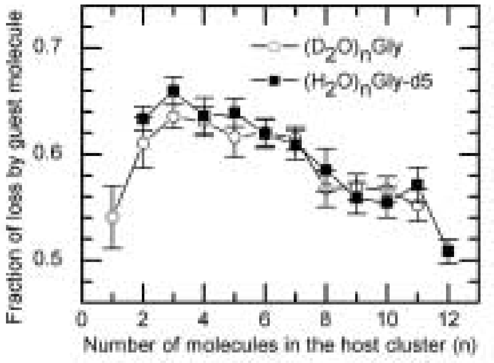

Fig. 3. Open circles: the fraction of clusters $(D_2O)_n$Gly which lose a hydroxyl group (OH) from glycine upon ionization. Filled squares: the fraction of clusters carrying deuterated glycine, $(H_2O)_n$Gly-d5 which lose a hydroxyl group (OD) from Gly-d5 upon ionization.

4. Water and amino acids jointly embedded in He_n nanodroplets.

As in the gas phase, individual glycine molecules embedded in liquid helium clusters undergo strong fragmentation during electron impact ionization [4]. Based on the results described above, it is interesting to inquire whether co-embedding a water cluster and a glycine molecule in He_n can suppress fragmentation. An experiment along these lines is in progress. Preliminary results (see Fig. 4) suggest that this is indeed possible.

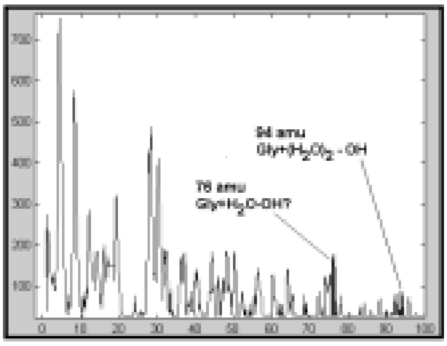

Fig. 4. A mass spectrum (preliminary data) of helium droplets carrying both a glycine molecule and a few water molecules, obtained by electron impact ionization. The peaks at 76 and 94 amu suggest that in this combination, glycine avoids significant fragmentation in the mass spectrometer.

5. Electrostatic beam deflection of water clusters.

The supersonic water cluster beam has been interrogated by deflection in an inhomogeneous electric field. The apparatus can resolve angular deflections down to ≈10µrad (Fig. 5).

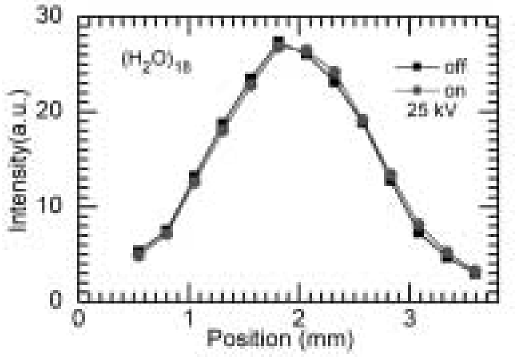

Fig. 5. The undeflected and deflected beam profiles of the $(H_2O)_{18}$ cluster.

All $(H_2O)_{n=3\text{-}18}$ clusters display uniform beam deflections characteristic of polarizable particles. The size dependence of the effective polarizabilities is shown in Fig. 6. These values exceed theoretical values of the electronic polarizability (e.g., [5]) by a large factor, and are therefore due to the thermally fluctuating permanent dipole moment of the cluster, deduced to be ≈1.5-2 Debye. The size dependence of the effective polarizability and the fluctuating behavior of the dipoles are closely connected to the question of cluster melting.

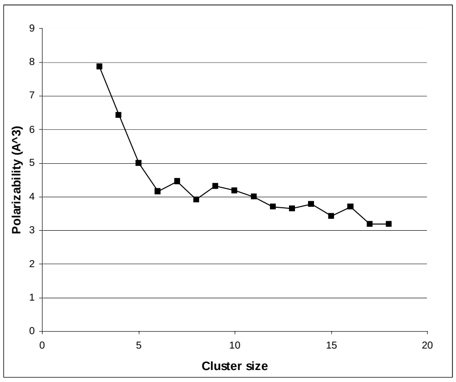

Fig. 6. Effective polarizabilities per molecule of $(H_2O)_n$ clusters from a supersonic expansion, as determined from electrostatic beam deflection measurements.

This work is supported by the U.S. National Science Foundation.

References

1 R.Moro, R.Rabinovitch, and V.V.Kresin, Rev. Sci. Instrum. 76, 056104 (2005).
2 R.Moro, R.Rabinovitch, and V.V.Kresin, J. Chem. Phys. 123, 074301(2005).
3 R.Moro, R.Rabinovitch, and V.V.Kresin, to be published.
4 F.Huisken, O.Werhahn, A.Y.Ivanov, and S.A.Krasnokutski, J. Chem. Phys 111, 2978 (1999).
5 L.Jensen, M.Swart, P.Th. van Duijnen, and J.G.Snijders, J. Chem. Phys. 117, 3316 (2002).

High-Resolution Photoelectron Spectroscopy of Radicals

S. Willitsch[1], H. J. Wörner, A. Schulenburg, E. Vliegen and F. Merkt

ETH Zurich, Physical Chemistry, CH-8093 Zurich, Switzerland
(merkt@xuv.phys.chem.ethz.ch)

[1] *present address: Physical and Theoretical Chemistry Laboratory, Oxford University,*
Oxford OX1 3QZ

A source of cold radicals in supersonic expansions is presented that is compatible with the requirements (low pressure < 10^{-6} mbar, absence of stray electric and magnetic fields, low ion densities) of a high-resolution pulsed-field-ionization zero-kinetic-energy photoelectron spectrometer [1]. Rotationally resolved photoelectron spectra of several radicals (NH_2, ND_2, CH_3, CD_3, CH_2D, CD_2H, C_5H_5 [2] and C_5D_5) have been measured to obtain information on the photoionization dynamics of the radicals and on the rovibronic energy level structure of the ions. The study of NH_2^+ provides for the first time experimental information on the bending levels and the bending potential of this quasilinear molecule. The study of the isotopomers of CH_3 illustrates how the photoionization dynamics changes when the symmetry changes from D_{3h} for the symmetric top molecules CH_3 and CD_3 to C_{2v} for the asymmetric top molecules CH_2D and CD_2H. The study of C_5H_5 and C_5D_5 offers the opportunity to investigate how antiaromaticity is reflected in the rovibronic energy levels structure of $C_5H_5^+$ and $C_5D_5^+$.
If time permits, a very recent study will be presented in which we have been able to trap the simplest of all radicals.

[1] “Generation and high-resolution photoelectron spectroscopy of small organic radicals in cold supersonic expansions”, S. Willitsch, J. M. Dyke and F. Merkt, Helv. Chim. Acta **86**, 1152-1166 (2003).
[2] “Photoelectron spectroscopic study of the first singlet and triplet states of the cyclopentadienyl cation”, H. J. Wörner and F. Merkt, Angew. Chem. Int. Ed. **44**, pp (2005).

Electron-induced chemistry in condensed molecular films

C. Jäggle[1], E. Burean[1], I. Ipolyi[3], W. Michaelis[1], D. Bankmann[2], P. Swiderek[1]

[1] *Universität Bremen, Fachbereich 2 (Chemie/Biologie), Institut für Angewandte und Physikalische Chemie, Leobener Straße / NW 2, Postfach 330 440, 28334 Bremen, Germany (swiderek@uni-bremen.de)*

[2] *Institut für Organische Chemie, Universität zu Köln, Greinstr. 4, 50939 Köln, Germany*

[3] *Department of Plasmaphysics, Comenius University, Mlynska dolina F2, 84248 Bratislava, Slovak Republic*

ABSTRACT

Electron-induced dissociation of molecules, often taking place via formation of short-lived negative ions, leads to the production of reactive fragments. When formed in a condensed phase environment, these fragments can undergo further reactions with their neighbours. If the conditions and materials are appropriately chosen, this leads to the formation of new bonds and thus larger molecular products or attachment of molecular units to a solid surface. This opens ways to new approaches for the controlled modification of surfaces once the reaction mechanisms are sufficiently understood. Recent examples of such reactions are presented and discussed in this contribution.

1. Introduction

Mass spectrometric studies of negative ion formation from molecules exposed to low-energy electrons (0-10 eV) through dissociative electron attachment (DEA) often reveal that specific products are formed within certain ranges of electron impact energies (E_0) /1-3/. Analogous measurements on electron-stimulated desorption (ESD) of negative fragments give evidence that such resonant processes are also important in condensed molecular samples but here subsequent intermolecular reactions can occur /4/.

The observed pronounced energy dependence of low-energy electron-induced reactions provides a perspective to control chemical processes at surfaces or in thin molecular films by choosing the appropriate beam energy. Electron-induced reactions already have found interesting applications in lithography /5/ thus controlling the spacial pattern of a surface modification. On the other hand, little attention has been paid to the prospect of controlling the reaction mechanism and thus the product of the modification, although examples are known. As shown previously, the functionalisation of hydrogenated amorphous silicon surfaces using H_2O and CF_4 produces oxidized or fluorinated silicon within a well-defined range of electron impact energies /6,7/.

In order to obtain a better control over electron-induced reactions at surfaces or in the condensed phase, in a first step the products have to be identified as comprehensively as possible under various conditions (temperature, film thickness and composition) and as a function of E_0. This contribution presents previous results concerning low-energy (0-20 eV) electron-induced reactions of some prototypical molecules in the condensed phase and discusses their possible application for the modification of surfaces.

2. Reaction products of prototypical molecules

Electron-induced reactions in our laboratory are monitored by high-resolution electron energy loss (HREEL) spectroscopy, thermal desorption spectroscopy (TDS), and reflection-absorption infrared spectroscopy (RAIRS). Samples studied recently include, among others, different saturated aldehydes and acetonitrile. The experiments on aldehydes are motivated by the question of the fate of reactive fragments produced under exposure to electrons.

Like other oxygen-containing molecules, aldehydes, of which acetaldehyde (CH_3CHO) is the simplest example, efficiently expel CO under exposure to electrons above roughly 8 eV:

$$CH_3CHO \rightarrow \cdot CH_3 + CO + \cdot H$$

In the condensed phase, the remaining methyl and H fragments may attack other molecules. In order to elucidate as comprehensively as possible the reactions occurring after the initial electron-molecule interaction and their mechanism, different experimental techniques are applied to identify products that are formed within the molecular film.

Acetonitrile (CH_3CN) in the gas phase undergoes specific fragmentations depending on E_0 /1/. Around 3.2 eV DEA produces CH_2CN^- with high efficiency whereas dissociation of the C-C bond is preferred above 6 eV. Again, the fate of the resulting fragments in the condensed phase has been investigated. The observed products are discussed in relation to the known gas phase reaction pathways.

3. Perspectives for the functionalisation of surfaces

Organic functionalisation of surfaces is important because it allows to tailor the properties of a material or forms the basis for more complex molecular architectures. Important materials to be functionalised comprise not only inorganic surfaces like those of semiconductors but also simple hydrocarbon layers. This provides a route to surfaces tailored according to the actual need but based on readily available starting materials. In this contribution the perspectives of electron-induced reactions for surface functionalisation will be discussed in comparison to other already established methods. Finally, recent results on the functionalisation of materials using acetonitrile will be presented. This concerns both model experiments on acetonitrile mixed with a saturated hydrocarbon but also the functionalisation of H-terminated diamond /8/. The former experiment aims at establishing conditions under which a functionalisation of simple hydrocarbon materials with acetonitrile or related compounds under exposure to low-energy electrons takes place while the latter provides direct evidence for such a process at specific E_0.

/1/ W.Sailer, A.Pelc, P.Limão-Vieira, N.J.Mason, J.Limtrakul, P.Scheier, M.Probst, T.D.Märk, Chem.Phys.Lett. **381**, 216 (2003).

/2/ M.Stepanović, Y.Pariat, M.Allan, J.Chem.Phys. **110**, 11376 (1999).

/3/ S.Ptasińska, S.Denifl, V.Grill, T.D.Märk, P.Scheier, S.Gohlke, M.A.Huels, E.Illenberger, Angew.Chem. **117**, 1673 (2005).

/4/ M.Imhoff, L.Parenteau, L.Sanche, M.A.Huels, Phys.Chem.Chem.Phys. **7**, 3359 (2005).

/5/ W.Eck, V.Stadler, W.Geyer, M.Zharnikov, A.Gölzhäuser, M.Grunze, Adv.Mat. 12, 805 (2000).

/6/ W. Di, P. Rowntree, and L. Sanche, Phys. Rev. B **52**, 16618 (1995).

/7/ D.V.Klyachko, P.Rowntree, L.Sanche, Surf.Sci. **389**, 29 (1997), Surf.Sci. **346**, L49 (1996).

/8/ A.Lafosse, M.Bertin, D.Cáceres, C.Jäggle, P.Swiderek, C.Pliszka, R.Azria, Eur.Phys.J. D **35**, 363 (2005).

Electron processing at sub-excitation energies

Eugen Illenberger

Institut fuer Chemie und Biochemie - Physikalische und Theoretische Chemie, Freie Universitaet Berlin, Takustrasse 3, D-14195 Berlin, email: iln@chemie.fu-berlin.de

Abstract

The interaction of very low energy (0-3eV) electrons with molecules exhibits unique features like specific bond cleavage creating specific ions and radicals. The underlying process is formation of a transient molecular anion by resonant electron capture and subsequent decomposition into a negative ion and one or more radicals. The general nature of such *dissociative electron attachment* (DEA) processes is characterized by a cross section which increases towards low energies. It can exceed the geometrical cross section of the corresponding molecule by orders of magnitude. We explore the evolution of such DEA reactions along a route from simple molecules (unimolecular processes in isolate molecules) to complex systems like molecular aggregates, molecular nanofims or biologically relevant systems.

Electron Driven Reactions

Electron initiated reactions play a key role in nearly any field of pure and applied science, in the gas phase as well as in condensed phases or at interfaces. We mention here (a) substrate induced photochemistry, (b) radiation damage of biological material or the molecular mechanism, how radio sensitizers (used in tumor therapy) operate, (c) reactions induced by electrons in surface tunneling microscopy (STM), or (d) any kind of plasma used in industrial plasma processing. In each of these fields the electron-molecule interaction represents a key step within an eventually complex reaction sequence.

In the photochemistry of molecules at surfaces, the transfer of photo-excited (hot) electrons from the surface to the adsorbed molecule can form a transient negative ion which may decompose [1] or initiate desorption of the neutral molecule. By this mechanism, adsorbed molecules (irre-spective of physisorption or chemisorption) can be photochemically active already at photon energies, where the molecule itself is still transparent.

On the other hand, in a direct photochemical reaction the interacting photons move electrons in the target molecule (at least for photon energies beyond the IR domain) and these excited electrons exert forces on the nuclei which initiate the reaction. We can hence consider also a *direct* photoreaction as a process which is ultimately driven by electrons. This is particularly true for any type of photon induced electron transfer reaction.

Tunneling electrons in STM can induce site selective dissociations, or excite selective vibrational modes (by biasing the voltage between tip and surface) coupled with surface hopping or desorption [2]. This field, sometimes assigned as *single molecule engineering*, opens many new and interesting prospects with respect to both basic science and application.

In the condensed phase, energy deposition by high-energy radiation produces electrons as the most abundant secondary species. The interaction of these *ballistic* secondary electrons with living cells are considered to play a crucial role in the complex reaction sequence leading to genotoxic effects like strand breaks in DNA [3].

Last but not least in any kind of plasma electrons are present in exceeding numbers which drive ionization, excitation and attachment processes. *Plasma processing* is, among others, the key technology for the fabrication of integrated circuits and hence the basis of what we now call *information technology*. Plasmas used in materials processing are usually so called cold or anisotropic plasmas. Although they contain a variety of high energy species like ions, the plasma does not heat its container, i.e., the excited species are far from equilibrium. The electron energy distribution in such cold plasmas peaks at a few electron volts. The energy supply and thus the maintenance of the plasma is nearly exclusively provided via electron-molecule collisions.

Electron Capture by Molecules

Capture of a free electron by a molecule generates a *transient negative ion* (TNI) which can be viewed as a molecular quantum state embedded in the electron - target continuum. Such compounds are formed when free electrons of particular energy interact with neutral molecules [4]. In the picture of electron scattering theory a resonance is characterized by constructive interferences of the electron wave in the area of the target. In the time dependent description the electron resides in the vicinity of the target for times longer compared to direct (unhindered) propagation across the area of the target. We can thus regard this electron scattering phenomenon as the formation of a short lived negative ion. Since the process is operative at particular energies, it is also called *a negative ion resonance* (NIR). Synonymously the term *transient negative ion* (TNI) is used since such a quantum state is principally unstable towards loss of the extra electron (autodetachment). In the approach of molecular orbitals (MOs), the extra electron resides temporarily in one of the normally unoccupied MOs. In competition to loss of the extra electron (autodetachment) a NIR can consequently also dissociate into fragments consisting of one ion and one or more neutrals. The overall process is called *dissociative electron attachment* (DEA), *viz*.,

$$e^- + M \rightarrow M^{-*} \rightarrow R + X^- \qquad (1)$$

where M^{-*} assigns the TNI formed via a Franck-Condon transition. If DEA channels are energetically accessible at low energies, the cross section for DEA in the gas phase can reach values exceeding 100 Å^2 (10^{-18} m^2) [5].

We shall consider the *formation* of such quantum states, their *energy* and also their *evolution* at different stages of aggregation, namely in single molecules under collision free conditions, in clusters formed by supersonic gas expansion, and on the surface of solids or in molecular nanofilms.

Reactions in the Gas Phase

The interaction of electrons with gas phase molecules is studied in a crossed beam experiment with an effusive molecular beam and ion analysis and detection by means of mass spectrometry. In the gas phase the large cross section for DEA towards low electron energies results from the general energy dependence of the attachment cross section. From very basic principles (Wigner threshold laws, scattering of a charged particle from a polarizable target [5]) one expects the capture cross section near threshold to increase with decreasing electron energy. These threshold laws, on the other hand, are controlled by the dominant electron-target interaction at larger distances. For neutral gas phase molecules this interaction can be approximated by the charge induced dipole potential. Due to the resonant nature of the DEA process (1) the energy deposited to the precursor ion corresponds to the incident electron energy. By that means it is straight forward and convenient to study unimolecular reactions in DEA. As an example, the DEA reaction

$$e^- (0\ \text{eV}) + C_2F_5I \rightarrow C_2F_5 + I^- \qquad (2)$$

which has a strong resonance close to 0 eV and decomposes at 100% selectivity by the cleavage of the C-I bond [6]. In this case the selectivity is simply due to energetics since any other DEA channel is inaccessible at that energy. Due to the reciprocal energy dependence of the attachment cross section (see above) this DEA reaction is not only *selective* but also very *effective*.

In this connection we mention one of the current frontiers in molecular physics and chemistry, namely the study of ultra-fast reactions in molecules (femto-chemistry). The aim is to follow the reaction on a time scale on which a direct bond rupture occurs. The second aim is to control a chemical reaction, with the prerequisite to cleave a selective bond within a polyatomic molecule. This is performed by means of particularly shaped (tailored) ultra-short laser pulses [7]. A successful transfer of this (in the gas phase so far promising) concept to solution will have an enormous technological impact. Such reactions are usually triggered by the (coherent) excitation of electrons to anti-bonding molecular orbitals (MOs). In the language of time dependent quantum mechanics, the ground state wave packet (describing the motion of the atoms in the electronic ground state) is transferred to the excited state potential energy surface on which it propagates. While in femtochemistry selectivity is obtained by coherent control, many DEA reactions are by its nature selective.

It is now well established that any of the gas phase DNA bases (thymine (T), cytosine (C), adenine (A) and guanine (G)), exhibit a very pronounced low energy resonance near 1 eV. It exclusively decomposes by the abstraction of a neutral hydrogen atom. For thymine (T) the corresponding reaction is

$$e^- (\ 1\ \mathrm{eV}) + \mathrm{T} \ \rightarrow\ (\mathrm{T-H})^- + \mathrm{H} \qquad (3)$$

which proceeds by hydrogen abstraction from the N position [8]. It has very recently been demon-strated [9], that this remarkable *bond selectivity* can even be made *site selective*: while 1.0 eV electrons induce cleavage exclusively from the N1 position, it can be switched to hydrogen loss from the N3 position by tuning the electron energy to 1.8 eV. Strong efforts are under way to study the influence of the DNA network on such resonances [10]. Apart from the aspect of radiation damage/cancer therapy, biomolecular systems offer a unique opportunity to study fundamental phenomena such as resonant bond cleavages and energy or charge transfer processes in systems of increasing complexity.

Reactions in Molecular Aggregates

The interaction of low energy electrons with *molecular clusters* is studied in a crossed beam experiment with the aggregates formed by supersonic gas expansion. The high cross section and selectivity of the DEA reaction (1) can be used to study ion molecule reactions in clusters, e.g., binary nucleophilic displacement (SN2) reactions in a *finite* system bridging the gas phase and condensed phase [11]. A further aspect concerns the respond of hydrogen bonded complexes in the supersonic beam toward low energy electron attack. From gas phase DEA experiments it is well established, that isolate DNA bases abstract neutral hydrogen atoms from sites which are involved in the coupling to the complementary strand. The hydrogen bonded dimer of formic acid (and other organc acid) can then be used as a model system to study the respond of the system with respect to hydrogen loss when going from the isolate molecule to the hydrogen bonded complex [12].

Reactions in Molecules on Surfaces and in Molecular Nanofilms

The interaction of electrons with adsorbed and condensed molecules is studied in the UHV where the molecules are condensed on a cryogenically cooled metal surface. In a *molecular film* the extra electron will generally become localized on an individual molecule, the interaction can therefore (as in clusters) be viewed on a molecular site. The TNI is then coupled to an environment and can decompose into fragments or relax into its ground state. Negative fragment ions desorbing from a molecular film can directly be observed by mass spectrometric techniques. Ion desorption from a condensed phase environment, however, is subjected to particular energy constraints and also structural constraints. Together with the pathways for of energy dissipation, the possibility to observe a resonance via fragment ion desorption [13] is strongly suppressed.

We demonstrate the potential of slow electrons to act as a soft tool for surface modification [14]. By setting the energy of a well defined electron beam to values below 3 eV, the surface of a thin film of 1,2-C2F4Cl2 molecules can completely be transformed into molecular chlorine (and byproducts, possibly perfluorinated polymers). At higher energies (above the threshold for electronic excitation, > 6 eV) some equilibrium state in the composition between product and initial molecule can be achieved, however, accompanied by a gradual overall degradation of the film. The effect of complete transformation is based on both the *selectivity* and particular *energy dependence* of the *initial* step of the reaction which is dissociative electron attachment (DEA) to C2F4Cl2 but also the fact that the initial molecule is efficiently decomposed by subexcitation electrons while the product Cl2 is virtually unaffected. The progress of the reaction during electron irradiation is followed by electron stimulated desorption.

This work has been supported by Deutsche Forschungsgemeinschaft, Volkswagen Stiftung, Humboldt Foundation and the European Union.

References

[1] St. J. Dixon-Warren, E.T. Jensen and J.C. Polanyi, Phys. Rev. Lett. 67 (1991) 2395.

[2] J. I. Pascual, N. Lorente, Z. Song, H. Conrad, and H. P. Rust, Nature 423 (2003) 535.

[3] L. Sanche, Eur. Phys. J. D 35 (2005) 367.

[4] E. Illenberger and J. Momigny, *Gaseous Molecular Ions. An Introduction to Elementary Processes Induced by Ionization*. Steinkopff Verlag, Darmstadt/Springer-Verlag, New York 1992.

[5] H. Hotop, M.-W. Ruf, M. Allan and I.I. Fabrikant, Adv. At. Mol. Opt. Phys. 49 (2003) 85.

[6] J. Langer, S. Matejcik and E. Illenberger, Phys. Chem. Chem. Phys. 4 (2002) 5105.

[7] T. Brixner, H. H. Damrauer, P. Niklaus and G. Gerber, Nature 414 (2001) 57.

[8] H. A. -Carime, S. Gohlke and E. Illenberger, Phys. Rev. Lett. 92 (2004) 168103.

[9] S. Ptasinska, S. Denifl, P. Scheier, E. Illenberger, T. D. Maerk, Angew. Chem. Int. Ed. 44 (2005) 694.

[10] S. Ptasinska, S. Denifl, P. Scheier, T. D. Maerk, S. Gohlke, E. Illenberger, Angew. Chem. Int. Ed (submitted).

[11] J. Langer, R. Balog, S. Gohlke, M. Stano, H. Abdoul-Carime and E. Illenberger, Int. J. Mass Spectrometry 233 (2004) 267.

[12] F. A. Gianturco, R. R. Luchese, J. Langer, I. Martin, M. Stano, G. Karwasz, E. Illenberger Eur. Phys. J. D 35 (2005) 399.

[13] E. Illenberger, Surf. Sci. 528 (2003) 67.

[14] R. Balog and E. Illenberger, Phys. Rev. Lett. 91 (2003) 213201.

Contributed Papers (Posters)

New Calculated and Measured Absolute Cross Section for the Electron-Impact Ionization of $C_2H_2^+$

H. Deutsch[1], K. Becker[2], P. Defrance[3], M. Probst[4], and T.D. Märk[5,6]

[1] Institut für Physik, Ernst Moritz Arndt Universität Greifswald, D-17487 Greifswald, Germany
[2] Department of Physics and Center for Environmental System), Stevens Institute of Technology, Hoboken, NJ 07030, USA (e-mail: kbecker@stevens.edu)
[3] Université Catholique de Louvain, Département de Physique, Chemin du Cyclotron, 2, B-1348 Louvain-la Neuve, Belgium
[4] Institut für Ionenphysik, Leopold Franzens Universität Innsbruck, A-6020 Innsbruck, Austria
[5] Dept. Plasmaphysics, Univerzita Komenskeho, Mlynska dolina, 842 48 Bratislava, Slovak Republic

Abstract

New measurements of the cross section for electron impact ionization of the molecular ion $C_2H_2^+$ have been carried out recently, which differ significantly from earlier data. The new data and the significant discrepancies between the earlier data and the results of various calculations, which disagreed among themselves by a factor of 3, motivated a renewed attempt to apply the semi-classical Deutsch-Märk (DM) formalism to the calculation of the absolute electron-impact ionization cross section of that molecular ion. A quantum chemical molecular orbital population analysis for both the neutral molecule and the ion revealed that in the case of $C_2H_2^+$ the missing electron is highly localized near the site of a C atom in the molecule. This information is explicitly incorporated in our formalism. The results obtained by taking the ionic character directly into account are in excellent agreement with recent experiments.

I. Introduction

Collisions between electrons and neutral molecules have been the subject of intense experimental and theoretical studies since the early days of atomic collision physics. By contrast, electron collision studies with singly and multiply charged molecular ions as targets have not nearly received as much attention despite the importance of molecular ions in many environments. Electron impact ionization of a molecular ion is a particularly challenging process for experimentalists because of the fact that both the projectile and the target are charged, which poses difficulties not encountered in experiments with neutral targets. In addition, there are competing channels for the formation of particular fragment ions involving dissociative excitation vs. dissociative ionization, which cannot be separated experimentally unless all reaction products of the collision are detected. Calculations of cross sections for the ionization of molecular ions are also challenging. Up to now, we are only aware of the application of semi-rigorous methods such as the Deutsch-Märk (DM) formalism [1] and the binary-encounter-Bethe (BEB) method of Kim and co-workers [2] to the calculation of ionization cross sections of a few selected molecular ions [3-5]. Comparisons of the calculated cross sections with available experimental data for the ions H_2^+, N_2^+, O_2^+, CD^+, CO^+, CO_2^+, H_3O^+/D_3O^+, and CD_4^+ [4,5] were in reasonable agreement only in the case of N_2^+ [3-5]. Serious disagreements for the other ions were often attributed to the inability of the experiment to separate contributions due to dissociative excitation from contributions due to dissociative ionization. However, it should also be noted that the application of the DM formalism to molecular ions requires certain assumptions and additional approximations that are not required in the case of neutral molecular targets whose validity is entirely based on plausibility arguments.

Here we present calculated electron-impact ionization cross sections for $C_2H_2^+$ using a modified variant of our formalism, which takes into account details of the ionization process obtained from a comparison of the quantum chemical molecular orbital population analyses for the neutral molecular and the molecular ion. The choice of $C_2H_2^+$ was motivated by the availability of new and improved experimental data [6]. Previous calculations disagreed among themselves by a factor of 3 and none of the calculated cross sections agreed with the earlier experimental data as shown in fig. 1.

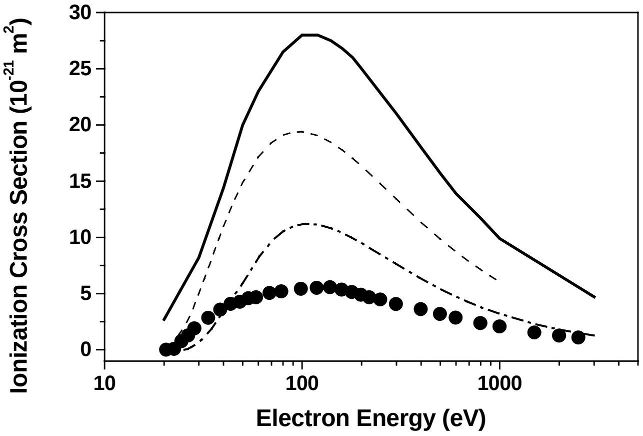

Fig. 1: Previous results for the electron-impact ionization of $C_2H_2^+$: calculated cross section using the old DM formalism (solid line) compared with the calculated BEB cross section (dashed line), the cross section of Janev and Reiter (dash-dot line) and the measured data of Defrance and co-workers (circles).

II. Background

The DM formula expresses the atomic ionization cross sections σ as the sum over all partial ionization cross sections corresponding to the removal of a single electron from a given atomic sub-shell labeled by the quantum numbers n and l as

$$\sigma(u) = \sum_{n,l} g_{nl}\, \pi\, r_{nl}^2\, \xi_{nl}\, b_{nl}^{(q)}(u)\, [\ln(c_{nl}\, u)/u] \qquad (1)$$

where r_{nl} is the radius of maximum radial density of the atomic subshell characterized by quantum numbers n and l [7] and ξ_{nl} is the number of electrons in that sub-shell. The sum extends over all atomic sub-shells labelled by n and l. The factors g_{nl} are weighting factors which were originally determined from a fitting procedure using reliable experimental cross section data for the rare gases and uranium. The quantity u refers to the “reduced” energy $u = E/E_{nl}$, where E denotes the incident energy of the electrons and E_{nl} is the ionization energy in the (n,l) sub-shell. The energy-dependent function $b_{nl}^{(q)}(u)$ has the form

$$b_{nl}^{(q)}(u) = \{(A_1 - A_2)/[1 + (u/A_3)^p]\} + A_2 \qquad (2)$$

and the 4 quantities A_1, A_2, A_3, and p are constants that were determined from reliable measured cross sections for the various values of n and l [1]. The superscript “q” refers to the number of electrons in the (nl) sub-shell. Our formula can be extended for the case of a molecular ionization cross section calculations provided one carries out a Mulliken or other molecular orbital population analysis which expresses the molecular orbitals in terms of the atomic orbitals of the constituent atoms. Orbital population analyses can be obtained routinely for a large number of molecules and radicals as well as positively charged molecular ions. The application of the DM formalism to molecular ions required several modifications as well as additional assumptions and approximations:

(i) The energy-dependent part in formulas (1) and (2), which was derived for neutral targets, was extended to ions by replacing the neutral ionization energy E_{nl} by the corresponding ionization energy of the ion. This neglects the fact that the Coulomb interaction between the incident electron and the target may affect the impact energy.

(ii) The weighting factors g_{nl} for the ionic component of the molecular ion were derived semi-empirically from a fitting procedure using well-established ionization cross sections of ions.

(iii) The data base of radii r_{nl} for atomic ions is much less developed than the corresponding data base for neutral atoms. In cases where no calculated radii for atomic ions were available, neutral radii were used. This is an acceptable substitution as the cross sections depend on the product of g_{nl} and $(r_{nl})^2$ and this product is obtained from a fitting procedure.

Therefore, the ionic character of the target was only reflected in the population analysis of the molecular orbitals as a 'missing' electron which resulted in different populations ξ_{nl} and different energies E_{nl}. In essence, the previous DM calculation for e.g. CO_2^+ treated the ion as an iso-electronic neutral BO_2 molecule with the orbitals of the CO_2^+ ion.

Here we remedy some of the limitations of the approach described above. In a first step, we carry out a Mullikan population analysis for both the molecular ion and the neutral molecule in an effort to "localize" the positive charge in the molecular ion, if possible. In the present case of $C_2H_2^+$ this means trying to identify whether the ionic character can be associated with a H^+ ion in the target or a C^+ ion. If the ionization can be localized in this fashion, the second step involves the determination of the weighting factors for the corresponding atomic ion. This can be done by applying the DM formalism to experimentally determined cross sections for the ionization of the corresponding singly charged ion. Such a comparison yields a value for the product $(r_{nl}^2 \cdot g_{nl})$ for the atomic ion, which, in turn, yields directly a value for the weighting factors g_{nl} for the atomic ion, if the ion radii r_{nl} are known. If these radii are not known, neutral radii are used (see above). With this information, the DM formalism can now be applied to the ionization of a molecular ion with far fewer assumptions and approximations compared to our previous approach.

III. Application of the DM Formalism to the Ionization of $C_2H_2^+$.

The results of the Mullikan analyses for C_2H_2 and $C_2H_2^+$ were limited to the outermost five orbitals. Two conclusions were reached, (1) the two outermost orbitals (orbital 5 and 4) are of pure C(2p) character and (2) the electron that is removed in the ionization process from orbital 5 can be attributed 100% to the C atom . This has the following consequences for the values of the parameter ξ_{nl} in equation (1):

orbital 5: ξ_{nl} to C^+ (100%)
orbital 4: ξ_{nl} to C (100%)
orbitals 3,2,1: ξ_{nl} to C^+ (50%) and to C (50%)

whereas the H atoms are not affected by the distribution of the ξ_{nl} to C and C^+.

The weighting factors for the C^+ ion were obtained by fitting a DM cross section for the process $C^+ + e^- \rightarrow C^{++} + 2\,e^-$ to measured data. This yields the following values for the so-called 'reduced weightings factors' $g_{nl} \cdot E_{nl}$: 16.64 eV for the two 2s electrons and 10.02 eV for the one 2p electron. In this derivation we used the atomic radii for the ionic orbitals.

IV. Results and Discussion

Figure 2 shows the comparison between the result of the present calculation and the new experimental data of Defrance and co-workers [6]. As can be seen, in contrast to the earlier situation (see Fig.1) the agreement for these two new data sets is quite good over the entire range of electron energies. There appears to be a minor discrepancy in the cross section shape. The calculated cross section rises somewhat faster than the measured cross section, reaches its maximum value at a slightly lower energy, and subsequently declines a little more gradual with increasing impact energy. However, the deviation at any given energy is well within the quoted error margin of the experimental data. The main effect of taking into account the details of the ionization process in terms of the exact location of the missing electron in the molecular ion as compared to the neutral molecule is a 20% reduction in the maximum value of our calculated cross section as can be seen from a comparison of our present cross section in figure 2 with our 'old' cross section shown in figure 1.

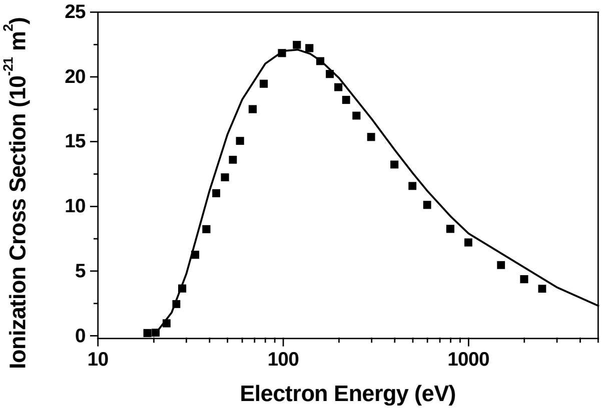

Fig. 2. Calculated cross section for the electron-impact ionization of $C_2H_2^+$ vs. electron energy using the present formalism (solid line) in comparison with the recent data of Defrance and co-workers (squares).

Acknowledgments

This work has been carried out within the Association EURATOM-ÖAW. The content of the publication is the sole responsibility of its publishers and it does not necessarily represent the views of the EU Commission or its services. It was partially supported by the FWF, Wien, Austria. One of us (KB) acknowledges partial financial support from the U.S. National Aeronautics and Space Administration (NASA) under grant NNG04GR07G.

References

[1] H. Deutsch, P. Scheier, K. Becker, and T.D. Märk, Int. J. Mass Spectrom. 233, 13 (2004) and references therein to earlier work

[2] W. Hwang, Y.-K. Kim, and M.E. Rudd, J. Chem. Phys. 104, 2956 (1996)

[3] Y.K. Kim, K.K. Irikura, and M.A. Ali, J. Res. NIST 105, 285 (2000)

[4] H. Deutsch, K. Becker, P. Defrance, U. Onthong, R. Parajuli, M. Probst, S. Matt, and T.D. Märk, J. Phys. B 35, L65 (2002)

[5] H. Deutsch, K. Becker, P. Defrance, U. Onthong, M. Probst, S Matt, P. Scheier, and T.D. Märk, Int. J. Mass Spectrom. 223/224, 639 (2003)

[6] P Defrance, private communication (2005) and to be published

[7] J.P. Desclaux, Atom. Data Nucl. Data Tables, 12, 325 (1973)

Time-Resolved Optical Emission Spectroscopy During Pulsed DC Magnetron Sputter-Deposition of Ti and TiO_2 Thin Films

A. Belkind[1], W. Zhu[1,2], J. Lopez[1,3], and K. Becker[1,4]

[1] Department of Physics and Engineering Physics, Stevens Institute of Technology, Hoboken, NJ, 07030, USA (e-mail: kbecker@stevens.edu)
[2] Present Address: Center for Bioelectrics, Old Dominion University,Norfolk, VA, 23510, USA
[3] Present Address: Department of Physics, St. Peter's College, Jersey City, NJ 07306, USA
[4] Center for Environmental Systems, Stevens Institute of Technology, Hoboken, NJ, 07030, USA

ABSTRACT

Time-resolved optical emission spectroscopy was used to analyze pulsed DC magnetron plasmas during the sputter deposition of Ti and TiO_2 thin films. The studies were focused on the temporal behavior of the emissions of selected Ti, Ar, and O lines during the "on time", when the magnetron plasma is turned on and during the "reverse time", when the magnetron plasma is turned off. Single and double exponential decays of the optical emissions were found during the "reverse time". During the "on time", we observed a rapid increase of some emission lines with a more or less pronounced overshoot and a slow increase of other emissions which followed the temporal evolution of the conduction current. The various time constants can be related to the dynamics of the fast electrons, the Ar metastables, the Ti atoms (metallic mode), and the O atoms (oxide mode).

I. INTRODUCTION

Titanium dioxide (TiO_2) has been known for a long time as a material with a high refractive index, a high transparency in the visible and near-infrared wavelength region, a high dielectric constant, and very good wear resistance and chemical stability. TiO_2 thin films are widely used in gas sensors, in solar cells, or as corrosion-protective coatings and optical coatings [1]. Titania, in the anatase phase, is also a very effective photocatalytically activated (by ultraviolet light) oxidizing agent. Sputter deposition is one of many ways to produce titania films. To assure a high deposition rate, good film adhesion, large-scale uniformity of film thickness and low temperature during film growth, reactive magnetron sputtering is usually applied. Titanium thin films are extensively used as diffusion barriers to impede the metal migration to the Si substrate in high-temperature processes such as high-temperature sputtering and reflow developed for via-filling [2] and they are used as the gate electrode and ohmic contacts in microelectronic devices.

While magnetron sputter deposition of metallic films is a well-established process, the sputter deposition of insulating films is more challenging. Pulsed DC magnetron sputtering is frequently used for the reactive sputter deposition of dielectric films due to the ability to avoid arcing. In a pulsed DC driven discharge, the negative potential on the target is periodically modulated with a pulsing frequency, typically between 5 and 350 kHz with a reverse time, during which a positive voltage (usually 10-20% of the negative voltage) is applied as a part of each duty cycle. To avoid arcing, the optimum pulsing frequency and reverse time are routinely determined empirically and are optimized for a particular application and magnetron device.

Here we report the results of time-resolved optical emission spectroscopic studies during pulsed DC magnetron sputtering of Ti and TiO_2. The work is focused on analyzing the temporal behavior of argon, oxygen, and titanium emissions during the “on-time” and the “reverse-time” of the pulsed DC magnetron plasma in Ar (metallic mode) and in an Ar/O_2 mixture (oxide mode).

II. EXPERIMENTAL DETAILS

The experiments were performed in a box coater with a planar rectangular magnetron HRC-373. Sputtering was done using a 99.999% titanium target of size $87.2 \times 202.1 mm^2$. The base pressure in the system was in the range of $4\text{-}8 \times 10^{-4}$ Pa. Sputtering of Ti was done in Ar (metallic mode), while reactive sputtering of TiO_2 was done in the oxide mode in an Ar/O_2 mixture in the pressure range of 0.4 to 1.3 Pa. The pulsed DC power was provided by a combination of an Advanced Energy® MDX-10 DC power supply and an Advanced Energy® Sparc-le V pulse generator. The DC power supply was operated in the constant current mode at currents of about 4 A. The Sparc-le V was set to operate in the constant power mode at repetition frequencies of 20 kHz with reverse pulse durations from 1 to 10 μs. The current and voltage pulse forms were recorded using a Tektronix® TDS 3034 oscilloscope connected to a Tektronix® P5205 high voltage differential probe and a Tektronix® TCP 202 current probe.

The light emission from the plasma was collected with a fiber optics cable and imaged onto the entrance slit of a 0.5 meter SPEX Model 1870 spectrometer equipped with a 1200 groove/mm grating. The optical detection system was set up in such a way that most of the light reaching the detector originated from a section of the densest part of the plasma from the race track region nearest to the fiber optics cable. The dispersed plasma emission spectra were recorded by a Roper Scientific ICCD camera and ST-133 controller. The synchronization of the CCD camera and the pulsed DC discharge was done in the following way: a voltage tapped off from the pulsed DC power supply system through a Tektronix® P5200 high voltage differential probe was fed into a BNC Model 555 pulse/delay generator, which produced 5 V TTL trigger pulses. The TTL trigger pulses were then fed into the ST-133 controller to control the electronic shutter on the ICCD camera. The camera was exposed to the discharge for 0.1-0.2 μs with 0.1-0.2 μs separation between each exposure.

The emission intensities were measured every 0.1 - 0.2 μs with an integration time of 0.2 μs, which allows us to determine decay times down to about 0.2 μs with a high level of accuracy. Fig. 1a shows the time-resolved emission of the Ti line at 399.86 nm obtained in the metallic mode together with a single exponential fit yielding a decay time of 1.76 ± 0.12 μs. Fig. 1b shows the time-resolved emission of the Ar 750.39 nm line with a decay time of $\tau = 0.29 \pm 0.04$ μs. Fig. 1c shows the time resolved emission intensity of the Ar line at 763.51 nm. Here a double exponential fit yields a decay with two time constants: $\tau_1 = 0.31 \pm 0.06$ μs and $\tau_2 = 2.5 \pm 0.3$ μs.

III. RESULTS AND DISCUSSION

III.1 Time-resolved optical emissions during the “reverse time”

Fig. 2a shows the full cycle time-resolved emission spectra of two neutral argon lines (750.39 nm, 763.51 nm) together with neutral titanium line (399.86 nm) in the metallic mode. Fig. 2b shows a view of the decay of the emission intensities from the beginning of the “reverse time”. The decay of the Ar emission line at 750.39 nm has a fast initial drop followed by a much slower decline. The initial fast decay of the Ar 750.39 nm line follows an exponential decay with a time constant of 0.29 ± 0.04 μs. The main route to populating the emitting levels of these two lines is electron impact excitation of ground-state Ar atoms, which requires electrons with energies of more than 13 eV. Those energies are primarily found in the fast beam electrons, which disappear within a microsecond into the "reverse time". Thus, the initial decay of the intensity of these emission lines is due to the rapid disappearance of the fast beam electrons and can, in fact, be used to monitor the decay of the beam electrons in the afterglow.

Fig. 2: Time-resolved intensity of (a) the Ti 400 nm line; (b) the Ar 750 nm line; (c) the Ar 763 nm line.

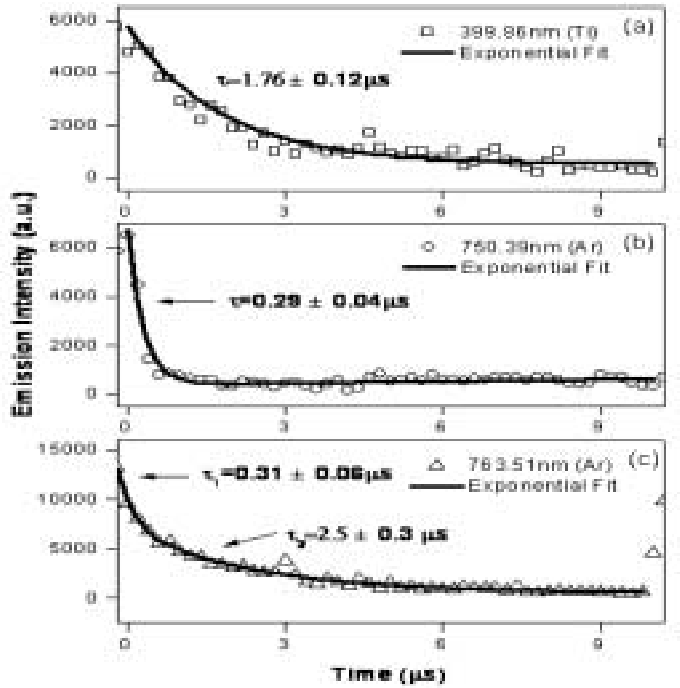

Fig. 3. Time-resolved emission spectra of two Ar lines (750.39 nm, 763.51 nm) together with the Ti line (399.86 nm) recorded in the metallic mode for (a) a full pulse cycle and (b) the "reverse time" region only.

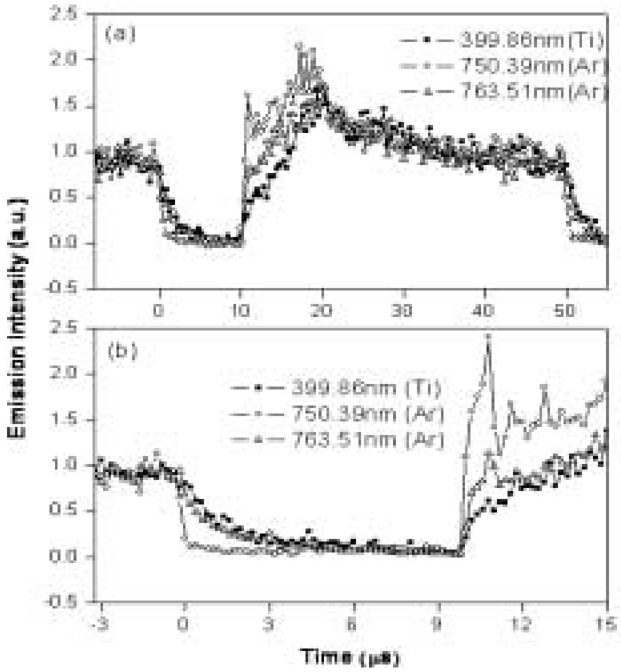

The production of Ti stops abruptly at the beginning of the "reverse time". Nevertheless, Ti emission lines are recorded during the entire duration of the "reverse time". The decay of the Ti emissions can be fit to a single-exponential decay with a time constant of about 1.7 μs. As the excitation of Ti lines requires only a minimum electron energy of slightly more than 3 eV, the slow decay constant of the Ti emissions is associated with a combination of 2 factors, the decrease of the electron temperature of the slow bulk electrons and the decay in the density of Ti atoms in the afterglow. The diffusion of Ti atoms out of the viewing region of our optical detection system takes a few microseconds depending on the kinetic energy of the atoms, which can range from a few tenths of an eV to a few eV. The presence of the decaying Ti emission during the entire "reverse time" indicates that Ti deposition does not stop abruptly (i.e. in the range of microseconds) when the power is turned off.

The optical emission spectroscopic studies in the oxide mode were focused on the same emission lines that were studied in the metallic mode (except for the Ti lines, which were very weak), but also included the O 844.63 nm line, which is not present in the metallic mode.

III.2 Time-resolved optical emissions during the "on-time"

The Ar 750.39 nm line rises rapidly and overshoots the steady-state level of the emission intensity (reached after about 10 μs). The Ar 763.51 nm line (and other Ar lines terminating in a lower metastable level) exhibits a much less pronounced overshoot. By contrast, the intensity of the Ti line increases much more slowly and does not show any overshoot. This different behavior can be understood on the basis of the temporal behavior of the voltage and discharge current when the plasma is reestablished. The initial voltage overshoot produces a significant amount of energetic electrons, which, in turn, leads to a significant population of the emitting levels of the Ar 750.39 nm and other Ar lines during that period. Since the emitting level of the Ar 763.51 nm line is not as efficiently excited from the Ar ground state as that of the 750.39 nm line, the overshoot in the emission intensity of the 763.51 nm line is less pronounced. The gradual increase of the emission intensity of the Ti 398.19 nm line is due to the slowly increasing number density of Ti atoms, which is determined by the rate at which they are sputtered at the target surface. The current at the beginning of the “on-time” is a combination of a displacement current and conduction current. The displacement current is related to the formation of the plasma sheath and disappears after the plasma sheath is formed (usually that process takes a few microseconds). The conduction current, which determines the sputter rate at the target, rise only slowly at the beginning of the “on time” and thus the Ti 398.19 nm emission line is a measure of the rise of the conduction current at the beginning of the ”on time”. During the rest of the on-time, the emission intensities of all lines follow, in a first approximation, the variation of the conduction current. The optical emission spectroscopic studies in the oxide mode show results that are similar to those in the metallic mode.

Acknowledgments

This work was supported in part by the US National Science Foundation (NSF), by the US Army TACOM/ARDEC under contract DAAE30-00-D-1011 DO#20-1 (Picatinny Arsenal).

References

1. H.K. Pulker, Coatings on glass, 4th ed. Elsevier: Amsterdam, 1996, p. 359
2. S. Li, Y. K. Lee, C. Q. Sun and M. H. Liang, Surface Review and Letters, 8, 4 (2001)

Electron Impact Ionization of $SiCl_x$ (x=1-4)

J. Mahoney[1], R. Basner[2], M. Gutkin[1], V. Tarnovsky[1], H. Deutsch[3], and K. Becker[1,4]

[1] Department of Physics and Engineering Physics, Stevens Institute of Technology, Hoboken, NJ 07030, USA (e-mail: kbecker@stevens.edu)
[2] Institut für Niedertemperatur-Plasmaphysik, Friedrich-Ludwig-Jahn-Strasse 19, D-17489 Greifswald, Germany
[3] Institut für Physik, Ernst-Moritz-Arndt-Universität, Domstr. 10a, D- 17487 Greifswald, Germany
[4] Center for Environmental Systems (CES), Stevens Institute of Technology, Hoboken, NJ 07030, USA

Abstract

We measured absolute partial cross sections for the formation of various singly charged positive ions produced by electron impact on $SiCl_x$ (x=1-4) using two different experimental techniques, a time-of-flight mass spectrometer (TOF-MS) and a fast-neutral-beam apparatus. The energy range covered was from the threshold to 900 eV in the TOF-MS and to 200 eV in the neutral beam apparatus. In the case of $SiCl_4$, the results obtained by the two different experimental techniques were found to agree very well. For the $SiCl_x$ (x=1-3) radicals, only results obtained from the fast-beam technique are available. Some of the cross section curves exhibit an unusual energy dependence with a pronounced low-energy maximum at an energy around 30 eV followed by a broad second maximum at around 100 eV. This is indicative of the presence of an indirect ionization channel and is similar to what has been observed by us earlier for $TiCl_4$ and the $TiCl_x$ (x=1-3) radicals.

I. Introduction

The electron impact ionization and dissociative ionization of a molecule are among the important fundamental collisional interactions and they also play a key role in many applications such as gas discharges and gas lasers, fusion edge plasmas, radiation and environmental chemistry and plasma processing of materials – to name just a few. $SiCl_4$ is used as an admixture in processing plasma feed gas mixtures that are used for selective reactive ion etching of GaAs on AlGaAs [1] and for other plasma-enhanced processes including the formation of self-assembled nano-crystalline silicon dots by $SiCl_4/H_2$ plasma-enhanced chemical vapor deposition and the characterization of polyester fabrics treated in $SiCl_4$ plasmas. In those applications, the electron-impact ionization and dissociative ionization cross sections for the $SiCl_4$ molecule as well as for the $SiCl_x$ radicals resulting from the collisional break-up of $SiCl_4$ are very important quantities for the understanding and modeling of the interaction of silicon-chlorine plasmas with materials.

Here, we report the results of the experimental determination of absolute partial and total electron-impact ionization cross sections for $SiCl_4$ and the $SiCl_x$ radicals.

II. Experimental Apparatus

The TOF-MS and the fast-beam apparatus used in the present experiments have been described in detail in earlier publications [2,3]. Here we only give a brief summary of some modifications made to the fast-beam apparatus.

We recently upgraded the fast-beam apparatus by replacing the electron gun and the ion detector. All other features of the apparatus and the experimental technique remain unchanged. We installed a new dispenser-type cathode, which consists of a strongly-bonded, continuous metallic phase of a refractory metal (in our case a porous tungsten matrix of about 20% porosity), interspersed uniformly with the emitting material, a mixture of barium and calcium aluminate. After installation, it is activated by indirect heating (similar to a conventional oxide coated cathode). A comparison of the electron beam current produced by the new electron emitter with the current produced by the old gun over the entire range of electron energies used here (up to 200 eV) is shown in fig. 1.

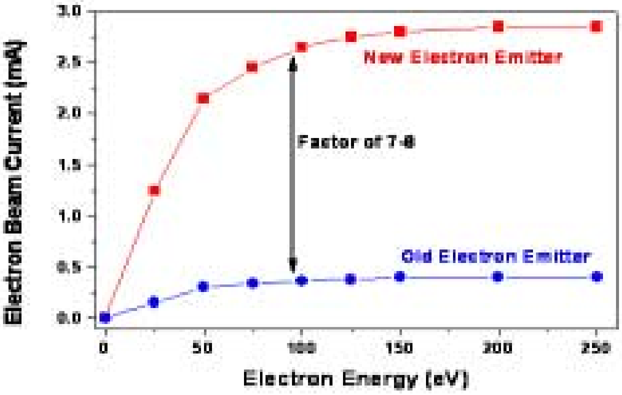

Fig. 1. Comparison of the electron beam current of the new electron gun with that of the old gun as a function of electron energy.

The new electron beam current is almost a factor of 10 higher than what was obtained with the previous gun. In addition, the interaction volume of the new electron beam and the target beam is only about 30% of the previous volume. Thus, the current density in the interaction region is higher by about a factor of 30. We also replaced the ion detector, a channel electron multiplier (CEM) with a triple multichannel plate (MCP) detector in a Z-stack arrangement for maximum gain in conjunction with a position-sensitive detection scheme. Specifically, we selected a RoentDek DLD40 MCP detector with delay-line anode capable of high-resolution 2D-imaging and fast timing for charged particle or photon detection at high rates with multi-hit capability. All signals from the detector are fed into an amplifier-discriminator (DLATR) module, which is a 6-fold differential amplifier with integrated constant fraction discriminator (CFD) circuits for each amplifier channel. It is specifically designed to read out the RoentDek delay-line detectors. The DLATR module delivers analog outputs of the amplified signal (amplification 30-150). The CFD stage provides the timing signals with a resolution below 50 ps. The CFD stages separate a pair of incoming signals with a pulse-pair resolution of about 20 ns.

The fast-beam apparatus affords the capability to measure directly all quantities that determine the absolute cross section. However, here we used the well-established Kr or Ar absolute ionization cross sections to calibrate a pyroelectric crystal. The calibrated crystal, in turn, is then used to determine the flux of the neutral target beam in absolute terms. The typical uncertainty of absolute cross sections determined in the fast-beam apparatus is ±15%.

III. Results and Discussions

The TOF-MS technique was used to determine a complete set of the partial cross sections for the formation of all singly charged ions from $SiCl_4$ from threshold to 900 eV and cross sections for the formation of five doubly charged ions, $SiCl_x^{++}$ (x=1-4) and Si^{++}. Figure 2 shows the cross sections for the formation of the singly charged ions up to an energy of 200 eV. The following observations are noteworthy:

Fig. 2. Absolute cross sections for the formation of singly charged ions by electron impact on $SiCl_4$.

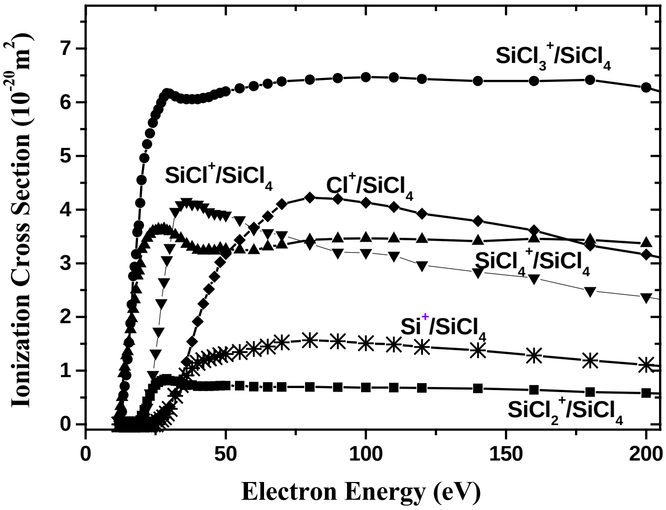

(1) In terms of their absolute magnitude, the partial ionization cross sections fall into three categories, (i) the $SiCl_3^+$ cross section, which has by far the largest absolute value of more than 6 x 10^{-20} m^2, (ii) the $SiCl_4^+$, $SiCl^+$, and Cl^+ cross sections whose maximum values are around 4 x 10^{-20} m^2, and (iii) the $SiCl_2^+$ and Si^+ cross sections with maximum values below 1.5 x 10^{-20} m^2.

(2) In terms of the cross sections shapes, the partial ionization cross sections for the three molecular ions $SiCl_x^+$ (x = 2-4) display a double-maximum structure. Such a cross section shape is unusual for molecular partial ionization cross section functions, but has been observed before in the case of other Cl-containing molecules of similar molecular structure, $TiCl_4$ [3] and CCl_4 [4,5] and also in the Cl^+ ionization cross section from Cl_2 [6]. The pronounced low-energy maximum may be indicative of the presence of indirect ionization channels such as autoionization. The fact that the low-energy maximum and the second maximum at about 100 eV are of roughly equal magnitude for these three ions suggest that the contributions to the ionization cross section arising from respectively the indirect and the direct ionization channel are of comparable magnitude. The $SiCl^+$ cross section, on the other hand, appears to be dominated by indirect ionization processes as the cross section curve declines monotonically after reaching a prominent low-energy maximum at around 35 eV. The cross sections of the two atomic fragment ions Cl^+ and Si^+ display a much more conventional molecular ionization cross section shape rising from threshold to a broad maximum around 80 eV and declining gradually towards higher impact energies.

It is difficult to identify the exact indirect ionization mechanisms mentioned above. The fact that the observed structure around 30 eV appears to be correlated to the presence of Cl atoms in several molecules suggests [7] that an autoionizing state may be produced by promoting an essentially atomic Cl(2s) electron, which has a binding energy of about 30 eV. The subsequent Auger-like decay produces several possible ions depending on which valence-orbital electrons fills the (2s) vacancy. Further experiments are needed to uniquely identify this observed indirect ionization process.

The absolute cross section values for the formation of the doubly charged molecular ions $SiCl_x^{++}$ (x=1-4) and the Si^{++} atomic ion are typically at least 1 order of magnitude smaller than the corresponding cross sections for the formation of the respective singly charged ions. The formation of $SiCl_3^{++}$ has the largest partial cross section with a maximum value of about 0.17×10^{-20} m^2. The cross section shapes for the formation of the doubly charged ions did not display the unusual shape found in the case of some singly charged ions. All cross section curves showed broad maxima at energies around or slightly above 100 eV.

The measured partial ionization cross sections indicate that dissociative ionization of $SiCl_4$ is dominant at all impact energies. The sum of the cross sections for the formation of the five singly charged fragment ions accounts for about 82% of the total single $SiCl_4$ ionization cross section at 100 eV. Furthermore, the cross section for the formation of the doubly charged $SiCl_4^{++}$ parent ions accounts for only 1.5% of the total cross section for the formation of doubly charged ions.

We also measured absolute partial electron impact ionization cross sections for the three free radicals $SiCl_3$, $SiCl_2$, and SiCl in the fast beam apparatus. The preliminary results for these radicals indicate that the importance of dissociative ionization vs. parent ionization decreases with the complexity of the target. Furthermore, as was the case before for the $TiCl_3$ (x=1-3) radicals [8], we also found evidence of the presence of the indirect ionization channel that was observed for $SiCl_4$ in some partial cross sections of the $SiCl_x$ (x=1-3) radicals.

Acknowledgments

This work was partially supported by the Chemical Sciences, Geosciences, and Biosciences Division, Office of Basic Energy Sciences, U.S. Department of Energy.

References

[1] R.J. Shul and S.J. Pearton, Handbook of Advanced Plasma Processing Techniques (Berlin Heidelberg: Springer, 2000)
[2] V. Tarnovsky and K. Becker, J. Chem. Phys. 98, 7686 (1993)
[3] R. Basner, M. Schmidt, V. Tarnovsky, H. Deutsch, and K. Becker, Thin Solid Films 374, 291 (2000)
[4] B.G. Lindsay, K.F. McDonald, W.S. Yu, and R.F. Stebbings, J. Chem. Phys. 121, 1350 (2004)
[5] K. Leiter, K. Stephan, E. Märk, and T.D. Märk, Plas. Chem. Plas. Proc. 4, 235 (1984)
[6] R. Basner and K. Becker, New J. Phys. 6, 118 (2004)
[7] T.N. Rescigno and C.W. McCurdy, private communication (2005)
[8] V. Tarnovsky, R. Basner, M. Schmidt, and K. Becker, Int. J. Mass Spectrom. 208, 1 (2001)

Pulsed Electrical Discharges in Water for Decontamination Applications

S. Gershman[1,2], O. Mozgina[2], A. Belkind[2], and K. Becker[2,3]

[1] *Department of Physics, Rutgers University, New Brunswick, NJ, USA*
[2] *Department of Physics and Engineering Physics, Stevens Institute of Technology, Hoboken, NJ, 07030, USA (e-mail: kbecker@stevens.edu)*
[3] *Center for Environmental Systems, Stevens Institute of Technology, Hoboken, NJ, 7030, USA*

Abstract

The application of a high-voltage pulse to two electrodes submerged in water triggers physical and chemical processes. Physical processes include the generation of UV light, shock waves and bubbles, which are critical for the formation of a discharge in a liquid. We have been studying various technical realizations of the pulsed electrical discharge in water (PDW) concept in the context of developing an efficient way for the in-situ, on-demand generation of oxidizing agents such as OH, H_2O_2, and O_3 for water decontamination applications. Maximum OH and H_2O_2 concentrations are obtained in water with a conductivity of about 5-10 S/cm. The formation of OH radicals increases in a sub-linear fashion with the average power input, while the rate of H_2O_2 formation increases linearly with the power input.

I. Introduction

A pulsed electrical discharge in water (PDW) can be used for sterilization (deactivation of viruses, bacteria, yeast), decolorization, oxidation and other chemical remediation processes in water and other liquids. If a short high-voltage pulse is applied between two electrodes submerged in water (or in other aqueous media), an electrical discharge is formed, which triggers various physical and chemical processes [1,2]. The physical processes include the generation of UV light, shock waves and bubbles, which are critical for the discharge formation in a liquid. The PDW produces a plasma consisting of electrons, and ions and radicals of water molecules and its fragments, e. g. OH, H, O, O_2^+, O^+, H^+, O_2^-, O^-, H_2O^+, H_2O_2, and O_3. The presence of these and other species in the bubbles created by the PDW has been confirmed by optical emission spectroscopy (OES). The concentrations of OH and H_2O_2 depend on the conductivity of the water. Maximum concentrations were obtained for conductivities of in the range of 5 - 10 S/cm. Experiments showed that the OH formation and the formation of aqueous electrons increases in a sub-linear fashion with the average power input, while the H_2O_2 formation increases approximately linearly with the average power input. The concentration of H_2O_2 in a PDW (without external bubbling) was found to be as high as 50 ppm and can exceed a few hundred ppm, if external bubbles of O_2 or air are injected into the water.

Here we report results of the use of a pulsed electrical discharge in bubbled water (PDBW) for water decontamination and sterilization. Preliminary experiments with Rhodamin WT showed that the discolorization rate depends critically on the O_2 gas flow through the system in the presence of the discharge. Using a 10 kV pulse, discolorization rates of up to 90% in less than 90 min were obtained for a gas flow of 20 ml/min, whereas the rate slowed to less than 10% in the absence of external bubbling. The data are indicative of the fact that oxidizing agents (H_2O_2, OH, and O_3) are produced in-situ, dissolved in water, and react with the water contaminants.

II. Experimental Details

Various types of PDBW reactor configurations have been used in laboratory-scale experiments such as needle-to-plane, wire-to-plane, wire-to-cylinder, ring-to-cylinder, wire-to-mesh, mesh-to-mesh, disk-to-ring and wire-to-plane configurations. Mesh-to-mesh reactors in an axial cylindrical and a plane-to-plane configuration appear to be the most energy efficient configurations [1]. Preliminary results were obtained using a plane-to-plane configuration in the system shown schematically in figure 1. The experiments were directed at monitoring electrical robustness of the system under the increased power delivered to the reactor.

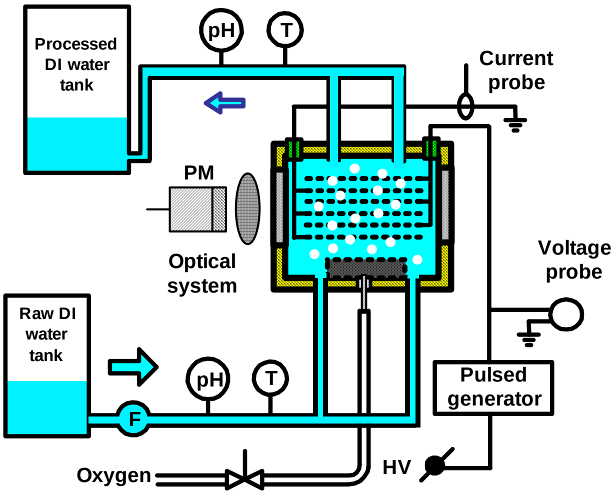

Fig. 1. Schematic diagram of the PDBW reactor system

The current system uses a power supply which employs two rotating spark-gap switches to generate the high-voltage pulses. A DC 40 kV power supply is used as a power source. Electrical diagnostics is performed by recording current and voltage oscillograms.

Another system that we developed essentially in parallel uses a single hollow capillary (needle) as one electrode and a disk-shaped plate as the opposite electrode. This system allows us to introduce single bubbles of gas through the needle and record the electrical and optical properties of the discharge generated in the bubble while it sits at the tip of the needle electrode. The electrical measurements are synchronized with optical measurements that include time-resolved and space-resolved plasma emission spectroscopic studies. The identification of various radicals generated in the discharge will be based on their characteristic emissions.

III. Results and Discussion

Here we summarize some preliminary results of the electrical (current, voltage) measurements, the Rhodamin decolorization studies and recent optical emission spectroscopic studies.

III.1 Electrical Measurements

Typical oscillograms for the current and voltage in a PDBW are shown in figure 2. The diagram on the left shows the temporal development of the voltage pulse (pulse height 6 kV) and the current (current slightly above 3 A) during the early stages (up to about 2.5 µs) when the voltage pulse is applied. The current pulse shows significant ringing and drops faster than the voltage pulse. The diagram on the right hand side shows the entire temporal structure of the current and voltage pulse (out to 40 µs when the current and voltage pulses have disappeared) for slightly different conditions (voltage pulse of about 8 kV, current of about 10 A). In both cases, we used a repetition rate of 70 Hz, but slightly different conductivities. Other noteworthy results of the electrical characterization studies of a single-bubble PDBW can be summarized as follows:

- The discharge occurs only when the bubble surrounds the needle, for voltages in the range of 8 – 20 kV; typical bubble sizes are approximately 2 mm in diameter for an electrode separation of about 4 mm.
- The discharge is limited to the gas inside the bubble.
- The current signature suggests a DBD-type discharge with one metal electrode and one electrode covered by de-ionized water.

Fig. 2. Typical voltage and current oscillograms for the PDBW.

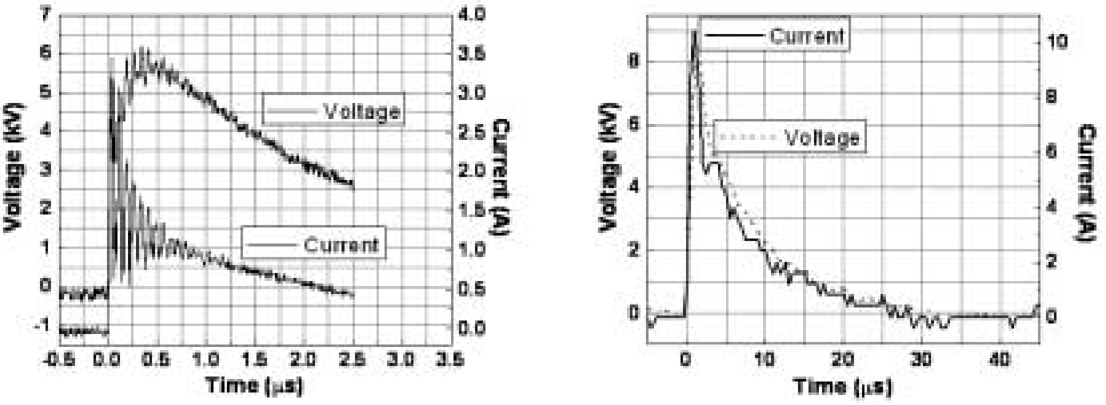

III.2 Rhodamin Decolorization

Results of our preliminary Rhodamin decolorization experiments are summarized in fig. 3. We show the reduction in rel. Rhodamin concentration as a function of discharge treatment time for various O_2 gas flow rates from no flow to 20 ml/min. The initial Rhodamin concentration was 200 ppb and the pH value of the water was 6.7. It is apparent from the results in figure 3 that the O_2 gas flow rate has a dramatic effect on the efficiency of the decolorization process.

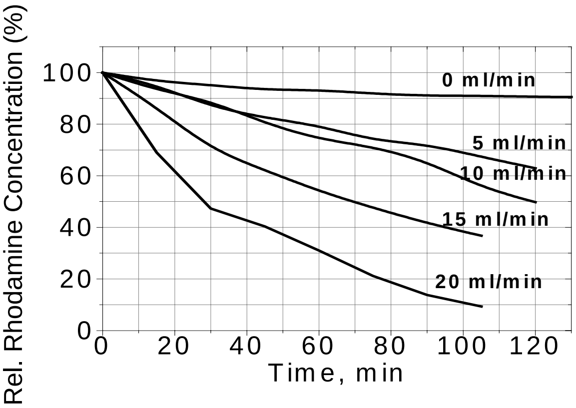

Fig. 3: Rhodamin decoloration as a function of discharge treatment time for various O_2 gas flow rates.

Without external O_2 flow, only about 10% of the Rhodamin is removed even after 2 hours. By contrast, with a flow rate of only 20 ml/min, we achieve a more than 90% removal in about 100 min.

III.3 Optical Emission Spectroscopy

We have recently begun to use the single-bubble PDBW system to obtain time resolved optical emission data in several spectral regions using optical filters. We inserted an optical fiber into the chamber, so that the tip of the fiber is close to, but does not touch the gas bubble formed on the needle electrode. The optical fiber is connected to a Hamamatsu photomultiplier tube (PMT) and the optical signal is recorded by a digital oscilloscope as shown in figure 4 (left diagram). Gas is fed through the needle and a stationary bubble forms surrounding the tip of the needle as shown on the right side of fig. 4.

Fig. 4. Optical emission spectroscopic (OES) setup to study emissions from a single-bubble PDBW (left diagram) and location of the single gas bubble at the tip of the needle electrode (right diagram).

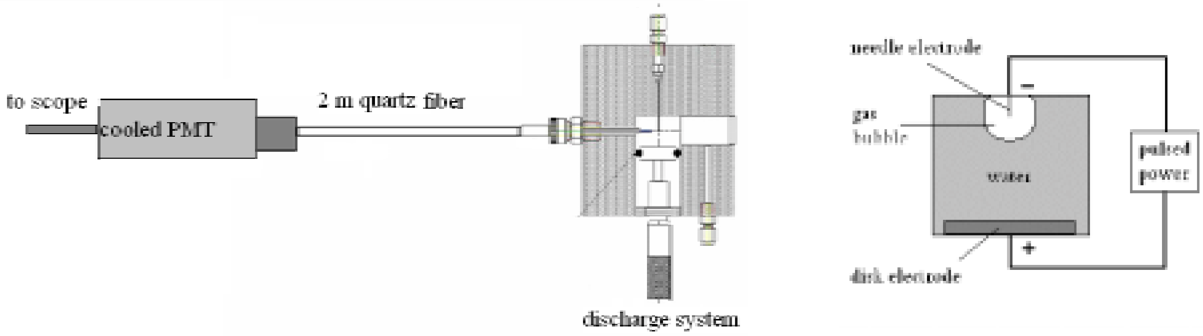

We have used both O_2 and Ar bubbles with voltages in the range of 8 – 25 kV applied to the needle relative to the disk electrode. The optical emission results using a narrow filter with a peak transmission around 310 nm (OH emission) confirm the existence of an electrical discharge process for voltages above 8 kV for Ar bubbles and above 10 kV for O_2 bubbles of approximately 2 mm in diameter for an electrode distance of about 4 mm. The light signal recorded by the PMT begins at about the same time as the conduction current can be seen on the current oscillogram. The light emission decays when the discharge is turned off, again following essentially the decay of the conduction current.

Further investigations are underway aimed at recording the entire spectrum emitted by the PDBW in conjunction with efforts to obtaining images of the bubble during the duration of the discharge.

Acknowledgments

This work was supported by the U.S. Army, Picatinny Arsenal through ARDEC Contract No. DAAE30-00-D-1011 #23-1

References

[1] P. Sunka et al., Plasma Sources Sci. Technol. 8, 258 (1999)
[2] P. Lukes et al., J. Phys. D: Appl. Phys. 38, 409 (2005)

Laser Induced Breakdown Spectroscopy at submersed target surfaces

R. Fantoni, V. Lazic, F. Colao, V. Spizzichino

ENEA FIS-LAS, V. E. Fermi 45, 00044 Frascati (RM), Italy, fantoni@frascati.enea.it

ABSTRACT

A double pulse laser excitation technique has been applied in order to generate a LIBS signal on different submersed metal surfaces, aimed for both qualitative and quantitative analysis. The mechanism of the interaction of the second laser pulse with the submersed target is shortly discussed, in order to justify the enhancement observed in LIBS signal with respect to the single pulse excitation. The occurrence of the breakdown induced by the second pulse in the rarefied atmosphere generated by the first pulse is held responsible for relatively narrow line emission observed from underwater plasma.

1. Introduction

Nowadays Laser Induced Breakdown Spectroscopy (LIBS) has developed as an analytical technique in which the broadband emission light collected from the area where an intense laser pulse is focused is utilized for the qualitative and quantitative analysis of the examined medium. The breakdown process in fact leads to a plasma formation, whose relaxation is accompanied by atomic and ionic line emissions suitable to the analytical determination. The observation of the plasma relaxation is done in a proper time window in which Local Thermal Equilibrium (LTE) is assumed to hold, then quantitative analysis can be performed once main plasma parameters (temperature and electron density) are independently estimated [1].

LIBS can be used to characterize targets at any phase (solid, liquid, gas, aerosol, nanostructure) since the same process, above described at a surface, can occur in different media (from vacuum to high density gases or liquids), either at sample surface or in the bulk liquids or gases. Thermal, mechanical and chemical properties of the medium however strongly affect the time evolution of the process and may limit its analytical applications. For example, in bulk liquid analysis the duration of the plasma emission is dramatically reduced due to high density of the surrounding medium.

In order to overcome this limitation, which initially prevented quantitative analyses in liquid phase, the possibility to use trains of laser pulses, suitably delayed, in order to initiate and sustain the process has been successfully exploited [2]. In particular the double pulse technique, consisting of focusing a pair of pulses, delayed by 1 - 100 μs, onto the target, was demonstrated for analytical applications to submersed samples [3]. The first pulse creates a bubble in the dense medium, while the second pulse, coming during bubble expansion, creates a secondary plasma in the rarefied medium formed. The main characteristics of the double pulse LIBS for application in dense media are the summarized in the following:

- The LIBS signal is detected after the second pulse, during the expansion of the secondary plasma in the low density medium generated by the first pulse, the latter causing only a strong rarefaction of the medium under study.
- The expansion of the secondary plasma contained in the low density bubble occurs on a time scale longer than the one experimentally measured in the high density medium.
- Narrower emission lines are detected after the second laser pulse, due to the relatively low pressure inside the bubble.

2. Experimental

Main constituents of a LIBS set-up, as sketched in figure 1, are a pulsed laser source and a spectrometer (dispersive element plus multichannel detector) with suitably designed optical systems (laser focusing and collecting plasma emission) and electronics (trigger and delay generators) components. The experiment is usually fully computer controlled.

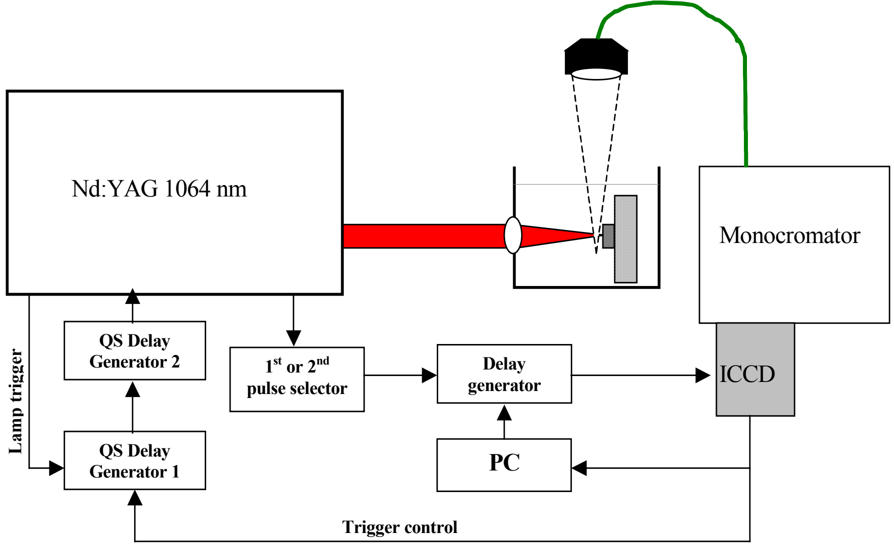

Figure 1 – Schematic of the set-up for double pulse LIBS on submersed solid samples.

The LIBS laboratory set-up for surface analysis of submersed samples is also shown in figure 1. Its peculiar optical characteristics can be summarized as follows:

- the double pulse emitted from the same laser source enters horizontally into the cuvette through the lens sealing one of its sidewalls;
- the signal collection is perpendicular to the laser beam across the solution;
- the signal is guided to the entrance of the monochromator by a fiber glass and detected at its exit by the ICCD.

The use of the double pulse LIBS technique in water is mandatory whenever the detection of minor/trace elements is required, as it allows to generate the plasma in a reduced medium density. Due to the statistic character of plasma generation in water, with a predefined probability of breakdown generation [4], filtering algorithm were developed in order to improve the signal to noise ratio after the identification and elimination of the pulses not leading to the generation of discrete plasma emission inside the observation volume [5].

3. Results and discussion

The possibility of metal (alloys) underwater recognition and analysis is of great interest in submarine archeology [6]. In fact the use of mini-spectrometers in combination with miniaturized Nd:YAG laser source is making possible the design of portable LIBS probes for in situ, and almost non destructive, underwater analysis of archaeological findings prior to they recovery. To this respect the possibility of recognition of precious and semi-precious ancient alloys from more recent iron residuals is very attractive.

The need to optimize water transparency window for both to the laser beam and the generated optical signal strongly recommends the use of visible radiation in both cases (green excitation at 532 nm, blue detection in the range 450 -500 nm). However the larger energy available supports the use of 1064 nm as excitation wavelength also in water.

In a series of laboratory experiments performed on metallic targets submersed in artificial sea-water we have demonstrated the feasibility of the technique for jewelry and copper alloys recognition, and even the possibility of underwater collection of quantitative data in the case of bronze samples whenever standards with similar composition were available for calibration curve construction.

As figure 2 shows, even the collection of the LIBS signal generated in a narrow blue wavelength range was sufficient to distinguish between commercial silver and gold alloy, made of silver and nickel the former and of gold, copper and zinc the second.

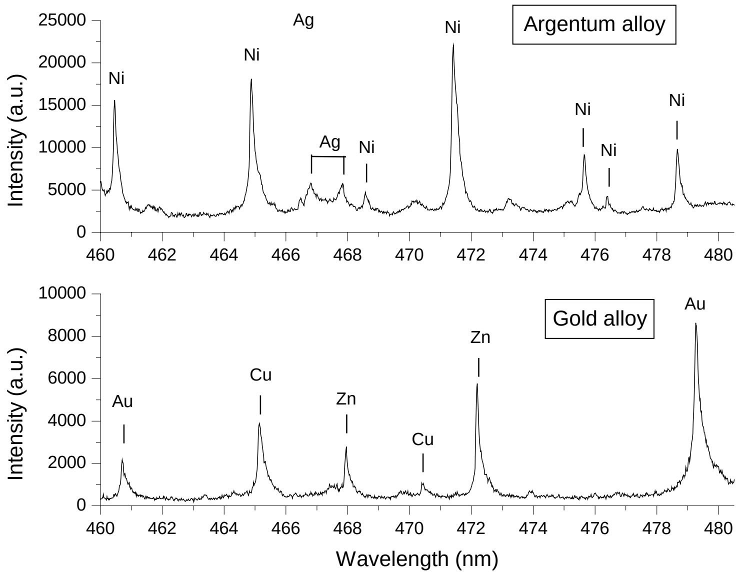

Figure 2 - Recognition of precious alloys by means of double pulse LIBS in artificial sea-water. Single shot spectra collected after the second pulse. Laser parameters: λ = 1064 nm, E1 = 120 mJ, E2=160 mJ, Spot dia. 300 μm, interpulse delay 55 μs. Acquisition parameters: Delay 100 ns, Gate width: 400 ns.

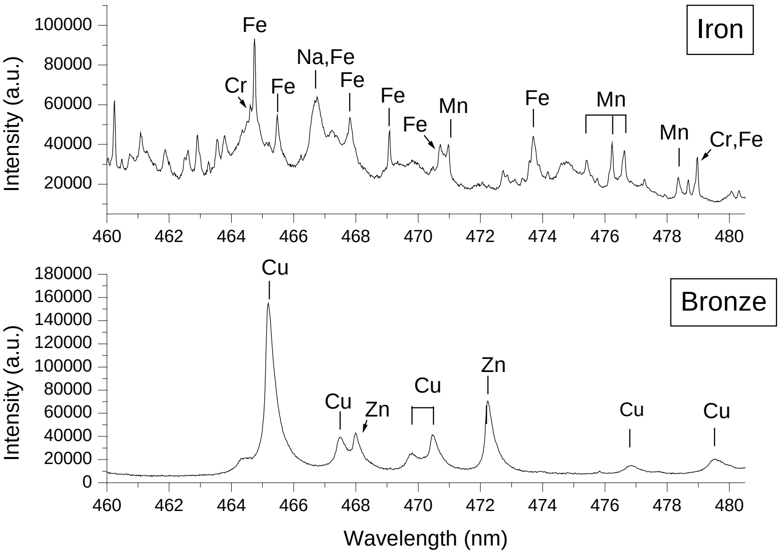

Figure 3 - Recognition of alloys by means of double pulse LIBS in artificial sea-water. 20 shot spectra collected after the second pulse. Laser and acquisition parameters as in figure 2.

The same wavelength range resulted also suitable to identity bronze and to sort it from iron. It can be verified in figure 3, where a quaternary bronze sample, made of copper, tin, bronze and lead, is compared with a commercial C40 iron containing also chromium and manganese as impurities. Both figures show that no impurity from the alkali metals usually present in sea water (Na, K, Mg, Ca) is interfering with the analysis in the selected wavelength range.

Quantitative analyses of copper based alloys are of importance for dating archaeological findings. Former results [3] indicated that the double pulse technique in water could improve the performances of LIBS on this kind of samples which suffer of fractionation problems related to non stoichiometric laser evaporation. Therefore we performed quantitative LIBS chemical analysis on two submerged quaternary alloy samples, after generating calibration of curves by using corresponding standards. Copper calibration was done by the line (465 nm) normalisation on nearby background emission, while other elements were normalised on Copper. As an example the calibration curve obtained for lead is reported in figure 3, while the results are listed in Table 1 together with the corresponding results of SEM-EDX analysis performed on dried sample examined in vacuum. Although the agreement is not completely satisfactory for sample #2, quantitative data could be obtained without removing the sample for its artificial sea-water solution.

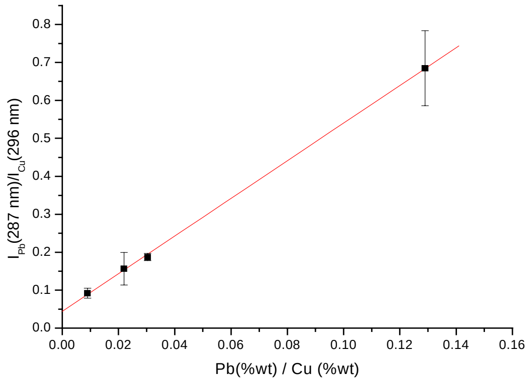

Figure 3 – Calibration curve for lead in quaternary Bronze (λ = 1064 nm, E1=52 mJ, E2=140 mJ, delay 800 ns, gate 1000 ns, 20 shots

		EDX	LIBS
Sample 1	Cu (%)	82.6	81
	Sn (%)	5.82	5.8
Sample 2	Cu (%)	50.9	53
	Zn (%)	31.8	23*
	Pb (%)	4.88	1.5**

Table 1 – Comparison of LIBS underwater analysis of a quaternary bronze with conventional SEM-EDX results on the same samples. (*) out of calibration range, (**) inhomogeneous distribution in this sample.

References

1. R.E.Russo, X.Mao, H.Liu, J.Gonzalez, S.S.Mao (2002) Laser ablation in analytical chemistry—a review, *Talanta* **57**, 425–451.
2. R. Sattmann, V.Sturm, R.Noll, (1995), Laser induced breakdown spectroscopy of steel samples using multiple Q-switch Nd:Yag laser pulses, J.Phys D, 28, 2181-2187.
3. A. De Giacomo, M. Dell'Aglio, F. Colao, R. Fantoni (2004) Double pulse laser produced plasma on metallic target in seawater: basic aspects and analytical approach, *Spectrochimica Acta B,* 59, 1431-1438.
4. P. K. Kennedy, D. X. Hammer, B. A. Rockwell (1997) Laser-induced breakdown in aqueous media, Prog. Quant. Electr. **21**, 155-248.
5. V. Lazic, F. Colao, R. Fantoni, V. Spizzichino, "Laser Induced Breakdown Spectroscopy in water: improvement of the detection threshold by signal processing", Spectrochimica Acta Part B **60**, 1002 – 1013 (2005).
6. V. Lazic, F. Colao, R. Fantoni, V. Spizzichino, "Recognition of archeological materials under water by Laser Induced Breakdown Spectroscopy", Spectrochim. Acta Part B **60**, 1014 – 1024 (2005).

Radical-Radical Reaction Dynamics

Jong-Ho Choi

Department of Chemistry and Center for Electro- and Photo-Responsive Molecules,
Korea University, 1, Anam-dong, Seoul 136-701, Korea (jhc@korea.ac.kr)

ABSTRACT

The reaction dynamics of ground-state atomic oxygen [O(^{3}P)] with a series of hydrocarbon radicals (RH: propargyl, allyl, t-butyl) have first been investigated by applying a combination of high-resolution spectroscopy in a crossed-beam configuration and *ab initio* calculations. The nascent rovibrational state distributions of OH products (Fig. 1) were examined.[1-9]

$$O(^3P) + RH \rightarrow OH + R$$

We also performed *ab initi* (Fig. 2), RRKM (Rice-Ramsperger-Kassel-Marcus) and *prior* calculations to characterize the observed distributions to understand the reaction mechanisms and energy partitioning. We hope this work sheds some light on the gas-phase radical-radical dynamics at the molecular level, which until now have remained unexplored..

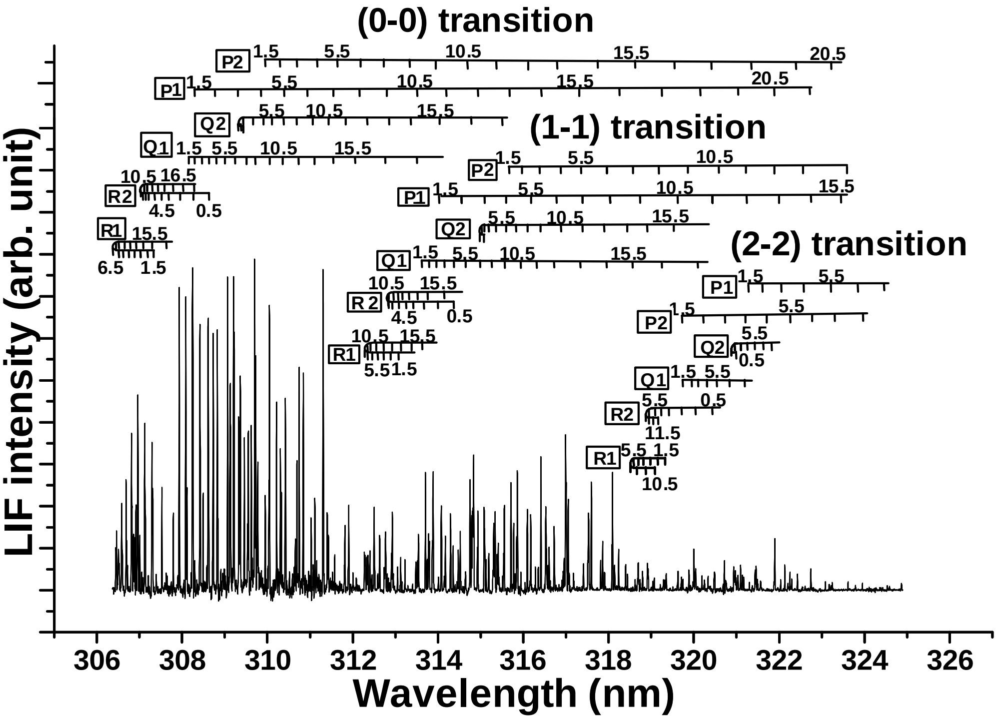

Fig. 1. LIF spectra of nascent OH ($A\,^2\Sigma^+ \leftarrow X\,^2\Pi$) products in the reaction of O(^3P) with t-C_4H_9.

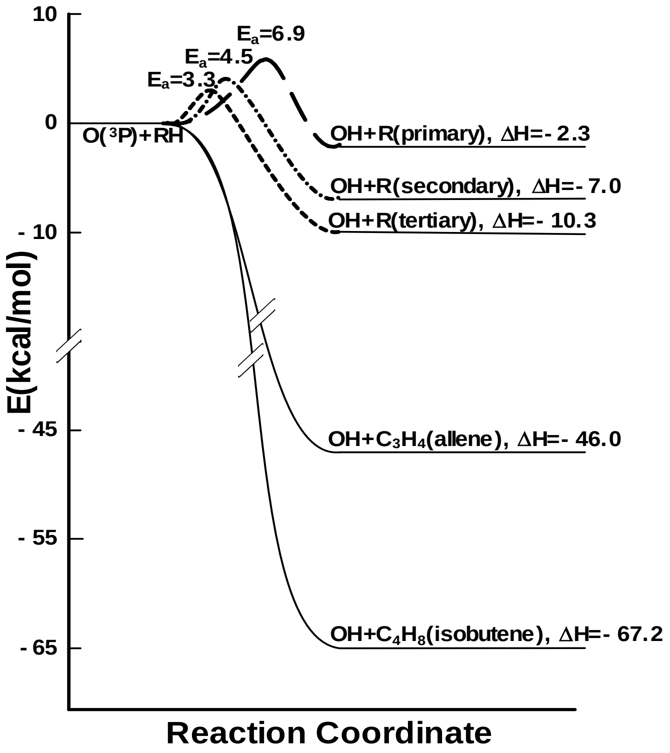

Fig. 2. The energy profile for the H-atom abstraction processes in the reactions of O(^{3}P) with a series of hydrocarbons.

REFERENCES

[1]. H.C. Kwon, J.H. Park, H. Lee, H.K. Kim, Y.S. Choi, and J.H. Choi*, *J. Chem. Phys. (Communications)* **116**. 2675 (2002).

[2]. J.H. Park, H. Lee, H.C. Kwon, H.K. Kim, Y.S. Choi, and J.H. Choi*, *J. Chem. Phys.* **117**.. 2017 (2002).

[3]. J.H. Park, H. Lee, Y.S. Choi, and J.H. Choi*, *J. Chem. Phys.*. **119**, 8966 (2003).

[4]. H. Lee, S.K. Joo, L.K. Kwon, J.H. Park, Y.S. Choi, and J.H. Choi*, *J. Chem. Phys. (Communications)* **119**, 9337 (2003).

[5]. H. Lee, S.K. Joo, L.K. Kwon, and J.H. Choi*, J. Chem. Phys. **120**, 2215 (2004).

[6]. S.K. Joo, L.K. Kwon, H. Lee, and J.H. Choi*, J. Chem. Phys. **120**, 7976 (2004)..

[7]. M.J. Nam, S.E. Yoon, L. Li, and and J.H. Choi*, *J. Chem. Phys. (Communications)* in press (Dec. 2005).

[8]. H. Lee, M.J. Nam, and J.H. Choi*, submitted to J. Chem. Phys.

[9]. L.K. Kwon, S.K. Joo, M.J. Nam, H. Lee, and J.H. Choi*, submitted to J. Chem. Phys.

Resonance Energy in Methyl Chloride

P. Mach[1], **V. Staemmler**[2], **J. Urban**[1]

[1]*Department of Nuclear Physics and Biophysics, Faculty of Mathematics Physics and Informatics, Comenius University, Bratislava, Slovakia Pavel.Mach@fmph.uniba.sk*

[2]*Department of Chemistry, Ruhr University Bochum, Germany*

ABSTRACT

The electron attachment reaction to methyl chloride

$$e + CH3Cl \rightarrow (CH3Cl^*)^{\cdot\cdot} \rightarrow Cl- + CH3\bullet$$

is a resonant process proceeding via formation of transient negative ion $(CH_3Cl^*)^-$ and the dissociation of this transient negative ion leads to the formation of CH_3 radical and stable Cl anion. The resonant character of the reaction means that the cross section for the electron attachment reactions depends strongly on the energy of the electrons. This is in strong contrast to most other chemical reactions. Electron attachment to this molecule has been the subject of many experimental studies [1-7] performed by swarm and beam techniques yielding the cross sections, thermal attachment rates as well as resonance width.

Theoretical contributions to the dissociative electron attachment to methyl halides [8-14] are mostly based on the using of semi empirical calculations (combination of the R-matrix theory with ab intio calculations) [5, 9-11]. The correct treatment of temporary anions cannot be done by means of standard quantum chemical methods. Since these states are resonances embedded in the continuum of scattering states, plain application of standard techniques will inevitably lead to a neutral molecule plus a free electron. This is the reason why many theoretical papers based on standard methods failed in the calculation of vertical electron affinities of halogenated molecules A rigorous treatment of anion resonances needs, of course, quantum mechanical scattering methods. However, it has been shown that it is also possible to employ quantum chemical approaches, originally designed for bound states, to describe resonances quite reliably. One such possibility has been proposed by Nestmann and Peyerimhoff [15,16], where the small increase in nuclear charge (perturbation by positive value) is able to transform the discrete component of a resonance state into a true bound state. The aim of the contribution is to calculate the vertical attachment energy as well as the resonance width of the methyl chloride molecule. In the frame of Nestmann's approach, the molecule has been treated as the quasi-diatomic by using of two approaches easy implemented for standard quantum chemical calculations. The vertical attachment energy has been obtained either as the negative ionization potential of stabilized

anion by OVGF method [17] or by using the static exchange approximation. The latter approach has also been used for the calculation of the resonance width. In the work also some technical details connected with different extrapolation schemes. For the larger interatomic distances dissociation curve was also calculated by means of standard quantum chemical methods. The shallow minimum in this region was examined in details, calculating also vibrational contribution with both harmonic and anharmonic treatment.

References

[1] P. G. Datskos, L. G. Christophorou, and J. G. Carter, Chem. Phys. Lett. 168 (1990) 324
[2] G. A. Gallup, K. Aflatoni, and P. D. Burrow, J. Chem. Phys. 118 (2003) 2562
[3] K. Aflatoni, and P. D. Burrow, Int. J. Mass Spect., 205 (2001) 149
[4] K. Aflatoni, G. A. Gallup, and P. D. Burrow, J. Phys. Chem. A 104 (2000) 7359
[5] D. M. Pearl, P. D. Burrow, I. I. Fabrikant, and G. A. Gallup, J. Chem. Phys. 102 (1995) 2737
[6] S. C. Chu, and P. D. Burrow, Chem. Phys. Lett. 172 (1990) 17
[7] P. D. Burrow, A. Modelli, N. Chiu, and K. D. Jordan, J. Chem. Phys. 77 (1982) 2699
[8] G. A. Gallup, J. Phys. B: At. Mol. Opt. Phys. 26 (1993) 759
[9] I. I. Fabrikant, J. Phys. B: At. Mol. Opt. Phys. 27 (1994) 4325
[10] I. I. Fabrikant, J. Phys. B: At. Mol. Opt. Phys. 24 (1991) 2213
[11] R. S. Wilde, G. A. Gallup, and I. I. Fabrikant, J. Phys. B: At. Mol. Opt. Phys. 33 (2000) 5479
[12] I. I. Fabrikant, and R. S. Wilde, J. Phys. B: At. Mol. Opt. Phys. 32 (1999) 235
[13] X. Shi, V. K. Chan, G. A. Gallup, and P. D. Burrow, J. Chem. Phys. 104 (1996) 1855
[14] T. N. Rescigno, A. E. Orel, and C. W. McCurdy, Phys. Rev. A 56 (1997) 2855
[15] B. Nestmann and S.D. Peyerimhoff, J. Phys. B 18 (1985) 615
[16] B. Nestmann and S.D. Peyerimhoff, J. Phys. B 18 (1985) 4309
[17] W. von Niessen, J. Schimer, and L. S. Cederbaum, Comp. Phys. Rep. 1 (1984) 57

Ionization reactions of selected amino acids

Š. Matejčík[1], P. Mach[2], J. Urban[2]

[1] *Department of experimental Physics, Faculty of Mathematics Physics and Informatics, Comenius University, Bratislava, Slovakia* *Stefan.Matejcik@fmph.uniba.sk*

[2] *Department of Nuclear Physics and Biophysics, Faculty of Mathematics Physics and Informatics, Comenius University, Bratislava, Slovakia*

ABSTRACT

L-alanine belongs to the simplest α-amino acids and is often considered as a model system for properties of more complex systems, particularly in the case of ionizing radiation. Alanine has attracted attention due to its radiation dosimetric properties and has been formally accepted as a secondary standard for high-dose and transfer dosimetry. The interaction of ionizing radiation with matter tends to the production of secondary reactive species along the track of the radiation. These secondary species may undergo subsequent reactions with the medium. The energy of the secondary electrons is sufficient to induce the electron impact ionization and dissociative electron impact ionization. These reactions are responsible for formation of the positive ions and radicals in the gas and aggregate phase and may play important role in the radical formation in the alanine. Our contribution covers the experimental and theoretical study on the electron impact ionization (EII) to L-alanine. The present electron impact ionization study has been carried out using the high-resolution crossed electron – molecule beams technique Using this technique we have measured the appearance energies of the ions formed via electron impact ionization and dissociative electron impact ionization (DEII) to alanine in the gas phase:

$$e + Ala \rightarrow (Ala^{+})^{*} \rightarrow fragment\ ion^{+} + neutral\ fragment \qquad (1)$$

In order to elucidate the studied reactions we have supported the experiment with high level ab initio calculations of the reaction enthalpies for particular reaction channels. These calculations are very helpful in the assignment of the measured ions to particular ionic structures. Using the mass spectroscopic technique the ions with given mass to charge ratio are measured as a function of electron energy. However, as the size of the molecule increases, several fragment ions may have the same mass to charge ratio and the mass spectroscopic technique can not identify the nature of the ion unambiguously. In this case the comparison of the measured appearance potential with the calculated ab initio reaction enthalpies could give indication on the nature of the ion.

The electron impact ionization of alanine in the gas phase leads to the formation of a large number of positive ions. In this contribution we present the appearance energies of the principal ions in the mass spectra with mass to charge ratio 89, 74, 55, 44, 42, 28, 18 and 15. The values of the appearance energies and the calculated energies are presented and discussed.

Recognition of asymmetric systems in the isolated state

A. Giardini[1,2], A. Paladini[1], F. Rondino[1], S. Piccirillo[3], M. Satta[4], D. Catone[1], M. Speranza[5]

[1]*Dipartimento di Chimica, Università di Roma "La Sapienza", pl. A. Moro 5, 00185 Roma, Italy, anna.giardini@uniroma1.it*

[2]*CNR-IMIP (sezione Istituto Materiali Speciali), 85050 Tito Scalo (Pz), Italy*

[3]*Università di Roma "Tor Vergata", Dipartimento di Scienze e Tecnologie Chimiche, Via della Ricerca Scientifica, 00133 Rome, Italy*

[4]*CNR- ISC (Istituto dei Sistemi Complessi), 00185 Roma, Italy*

[5]*Facoltà di Farmacia, Dipartimento di Studi di Chimica e Tecnologia delle Sostanze Biolog. Attive, Università di Roma "La Sapienza", pl. A. Moro 5, 00185 Roma, Italy*

1. Introduction

The discovery of abiogenic sources of homochirality and the understanding of the underlying principles are important steps towards the explanation of the origin of life. Chirogenesis usually leads to racemates, but spontaneous symmetry breaking has been achieved through only a handful of methods. One of them is acknowledged as the "chiral enrichment mechanism" and is based on the preferential destruction of one enantiomer of a racemate by interaction with a chiral agent, whether a circularly polarized photon or a massive species. In the latter case, diastereomeric clusters are involved which are held together by noncovalent interactions. The stronger are such interactions, the larger are the changes in the properties of the components of the complex. These changes are important for monitoring the formation itself of clusters and for evaluating their stability and reactivity. Diastereomeric clusters have proved to be ideal systems for modeling chiral recognition phenomena, and their applications in many scientific fields interlock the physical and life sciences [1].

The recognition process in some molecular and supramolecular asymmetric systems in the isolated state, has been performed by our group in the past [2,3]. Intermolecular interactions among the individual components of neutral and ionic clusters have been efficiently studied by mass resolved laser spectroscopy and mass spectrometry, respectively [2,3]. In the last years, third generation synchrotrons are intense circularly polarized light (CPL) sources used for investigating the intrinsic properties of chiral molecules in the isolated state [4].

The present paper reports examples on the most recent results of experimental and computational studies carried out with these methodologies on (R)- and (S)-3-hydroxytetrahydrofuran (**Th**$_\mathbf{R}$ and **Th**$_\mathbf{S}$) and clusters of (*R*)-(+)-1-phenyl-1-propanol (**P**$_\mathbf{R}$) with (R)- and (S)-methyl lactate (**L**$_\mathbf{R}$ and **L**$_\mathbf{S}$).

2. Experimental

Circularly polarized synchrotron radiation. A Circular Dichroism Angular Distribution (CDAD) experiment is based on photoionization spectroscopy of chiral molecules [5]. The dependence of the photoelectron intensity $I(\theta,\omega)$ on the emission angle θ is then expressed by the equation : $I(\theta,\omega) = \sigma(\omega)\,[1 - 0.5\ \beta(\omega)\ P_2(\cos\theta) + m\ D(\omega)\cos\theta] / 4\pi$, where $\sigma(\omega)$ is the energy-dependent cross-section, $\beta(\omega)$ is the asymmetry parameter, $D(\omega)$ is the dichroism parameter, and m = ±1 is the light helicity [6]. The P_2 term refers to the second-order Legendre polynomial and θ is the scattering angle between the photoelectron momentum and light propagation. The helicity of the circularly polarized light is defined according to the value m = +1 (left circular polarization) or m = -1 (right circular polarization) of the projection of the photon spin along its momentum. Accordingly, the electric vector describes a positive (right-handed) or negative (left-handed) screw. For a chiral molecule, the photoelectron intensity along the θ direction shows different values not only in case of a change of the light helicity (m = ± 1) but also when, for fixed value of m, the photoelectron intensity is measured in a forward/backward geometry, showing an asymmetry also in angular distribution [the cos(θ) dependence of the last term of the equation].

Resonant two-photon ionization spectroscopy with time-of-flight detection (R2PI-TOF). The experimental setup to produce the molecular clusters and to perform R2PI spectroscopy has been described in detail in previous publications [7]. The experimental set up combines a supersonic molecular beam with a home built time of flight (TOF) mass spectrometer. The supersonic expansion is produced by a General valve pulsed nozzle (timing from 120 to 180 microseconds, internal Ø 400 microns). In the heated valve a carrier gas (Ar, stagnation pressure from 2 to 4 atm) is mixed with a selected chromophore and a solvent molecule. Clusters are formed in the adiabatic supersonic expansion and the concentration of the seeding molecules is maintained low enough to minimize the production of larger clusters. The skimmed supersonic jet (1mm skimmer Ø) enters into a second chamber equipped with a TOF mass spectrometer. Molecules and clusters in the beam intersect one or two tuneable dye lasers and are excited and ionised. The detection of the ionised species is performed through a channeltron, and the signals recorded and averaged by a digital oscilloscope are stored and processed in a PC. 1cR2PI experiments involve electronic excitation of the species of interest by absorption of one photon hν1 and ionisation by absorption of a second photon hν1.

3. Results and discussion

CDAD experiments. **Th** is a floppy chiral molecule which can be seen as a prototypical building block of living matter, because of its similarity to the furanose rings of nucleotides. Like many other five-membered rings, the R and S enantiomers of **Th** may assume several ring-puckering conformations [6]. Among these, the structure C_4 endo is the global minimum at the MP2 level of theory using a modified 6-31G* basis set, whereas structure C_2 endo is only 1.34 kcal mol^{-1} less stable [6]. This stability difference is in substantial agreement with that calculated by us at the QST2-MP2-6-31G* level of theory, ΔE=1.28 kcal mol^{-1} [5].

The photoelectron valence spectrum of the $\mathbf{Th_{R/S}}$ enantiomers is characterized by two bands whose binding energies are shifted by about 1.8 eV with respect to the corresponding orbitals, HOMO, HOMO^{-1}, HOMO^{-2}, computed by the Koopmans theorem. An unresolved manifold of bands is observed at higher energies. The relative intensity of the two spectra, taken with circularly polarized light, differs only by less than a few percent. Opposite dichroic spectra are observed at the magic angle for the $\mathbf{Th_{R/S}}$ enantiomers and for the same enantiomer with the two analysers [5].

The photoionization dichroic *D* parameters of $\mathbf{Th_R}$ and $\mathbf{Th_S}$ have been measured for the HOMO, HOMO^{-1} and HOMO^{-2} orbitals, and their values discussed in the light of LCAO B-spline DFT predictions [5]. Figure 1 reports the dependence of the *D* factor as a function of the kinetic energy of the electron photoemitted from HOMO, showing a good agreement with theoretical predictions for the most stable C_4-endo [6]. The present study sheds light on a new potentiality of photoemission dichroism which appears to be sensitive not only to electronic factors, but also to structural, conformational, and vibrational factors.

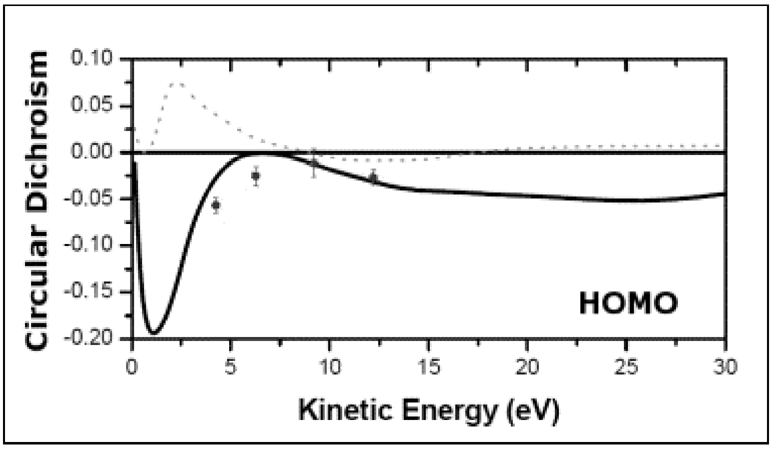

Figure 1. Dependence of the *D* factor on the kinetic energy of the photemitted electron from the HOMO. The solid curve refers to the computed D factor for the C_4 endo conformer of **Th**, while the broken curve refers to the computed D factor for the C_2 endo one.

Enantiodiscrimination by R2PI spectroscopy. The band origin region of the excitation spectrum of the bare $\mathbf{P_R}$ displays a peak at 37577 cm^{-1} (A) and two other major peaks at 37618 cm^{-1} (B) and at 37624 cm^{-1} (C). This triplet of bands have been assigned to the 0_0^0 electronic $S_1 \leftarrow S_0$ origin of three stable conformers of the chromophore, obtained by rotation around its C_α-C_β bond placed quasi-perpendicular to the aromatic ring [2]. In particular, the most intense band B is associated with the most stable *anti* rotamer, whereas the less intense bands A and C to the two *gauche* conformers.

The 1cR2PI excitation spectra of the isomeric complexes of $\mathbf{P_R}$ with various α-substituted carboxylic esters have been performed. Their spectral patterns are characterized by an ensemble of bands red- or blue-shifted relative to the 0_0^0 electronic $S_1 \leftarrow S_0$ origin of the most populated *anti* conformer of the bare chromophore $\mathbf{P_R}$ (peak B at 37618 cm^{-1}). The most intense band for each cluster is separated from the peak B of the bare chromophore by a $\Delta\nu$ value. A red shift (negative $\Delta\nu$) is due to an increase of the complex bonding in going from the S_0 ground state to the S_1 excited state. A blue shift (positive $\Delta\nu$) is due to a decrease of the complex bonding by the same excitation process. The magnitude of the $\Delta\nu$ values is somewhat related to the variation of bonding efficiency in the π and π* states.

The bathochromic shifts of the 0_0^0 electronic $S_1 \leftarrow S_0$ origin, observed when $\mathbf{P_R}$ is associated with an alcoholic partner, is phenomenologically related to the increase of the electron density on the oxygen center of the chromophore hydrogen bonding with the O atom of the solvent [2]. Similarly important are dispersive interactions between the aliphatic chain of the solvent and the π-system of the chromophore, which are mainly responsible of the different spectral shifts observed in diastereomeric complexes involving chiral moieties [2].

This general behavior is further corroborated by the 1cR2PI absorption spectra of the homochiral [$\mathbf{L_R}$•$\mathbf{P_R}$] and heterochiral [$\mathbf{L_S}$•$\mathbf{P_R}$] complexes (Figure 2a and 2b, respectively), obtained by monitoring the ion signal at the ethyl loss fragment mass (m/z 211). Similar spectra have been obtained by monitoring the parent ion signal at m/z 240. Their spectral patterns are characterized by the presence of five intense bands all red-shifted relative to the band origin B of the bare chromophore $\mathbf{P_R}$. No blue-shifted signals were observed for these 1:1 complexes. Concerning the nature of these five signals, it is well established that association of $\mathbf{P_R}$ with bidentate partners, like the selected esters, can markedly unbalance the relative population of the A-C rotamers of the chromophore to the point that only one $\mathbf{P_R}$ conformer predominates [2]. This view is further confirmed by DFT calculations of the most stable diastereomeric [$\mathbf{L_R}$•$\mathbf{P_R}$] and [$\mathbf{L_S}$•$\mathbf{P_R}$] isomers. Among the DFT computed structures, we have tentatively assigned the ones corresponding to the least and more red-shifted band of Figure 2a and 2b. The least red-shifted band correspond to structures characterized by the alcoholic OH bond pointing to the π-system of $\mathbf{P_R}$ at relatively short O-H•••π equilibrium distances (O-H•••π distance = 3.25 Å for the heterochiral and 4.16 Å for the homochiral structure) [8]. The more red-shifted bands correspond to structures, which show an intramolecular O-H•••Y interaction between the functional groups of **L**, in analogy with complexes of $\mathbf{P_R}$ with 2-butanol [2].

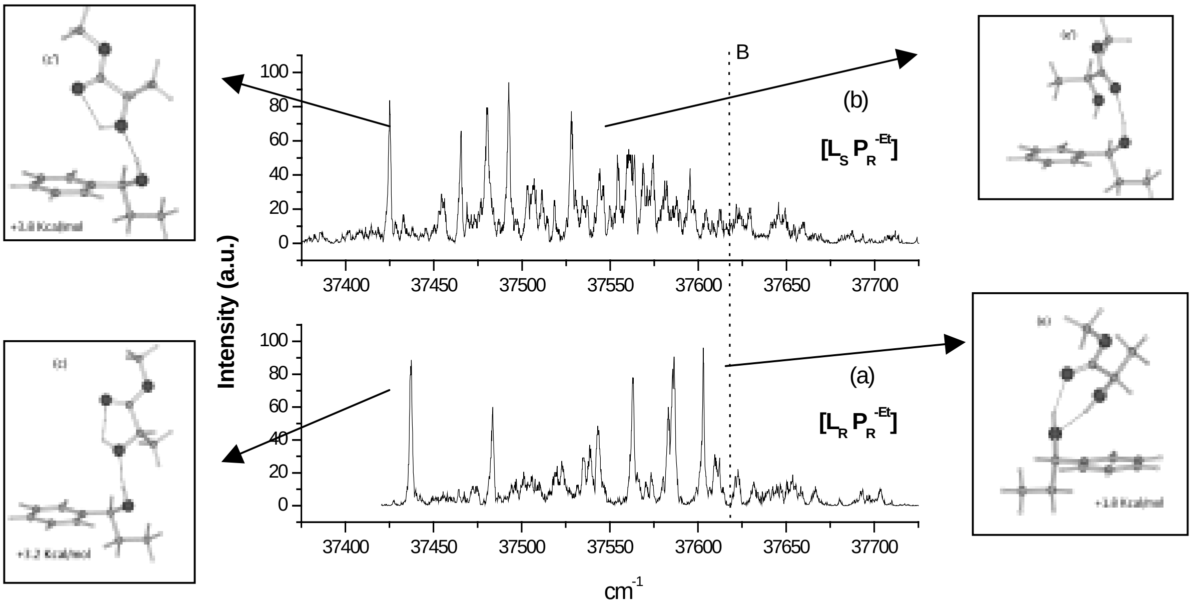

Figure 2. 1cR2PI excitation spectra of $\mathbf{P_R}$ complexed with $\mathbf{L_R}$ (a) and $\mathbf{L_S}$ (b). The dashed line refers to the peak B at 37618 cm^{-1} of bare $\mathbf{P_R}$. Calculated structures at the B3LYP/6-31G level.

4. Conclusions

The study of intrinsic properties of chiral molecules and their recognition processes has been extensively applied in our group by using different techniques, such as the Circular Dichroism in the Photoelectron Angular Distribution and the Resonant Two Photon Ionization spectroscopy coupled with Time of Flight Mass Spectrometry. These methodologies have been proven to be ideal to investigate at molecular scale the specific interactions governing the biological processes. In this short review, we have shown that the reported methodologies together with ab initio calculations, can provide a link connecting the structures and conformations of chiral molecules and their clusters in gas phase.

References

1. E. G. Robertson, J. P. Simons. Phys. Chem. Chem. Phys. 2001, 3, 1-18.
2. Latini, M. Satta, A. Giardini, S. Piccirillo, M. Speranza. Chem. Eur. J. 2000, 6, 1042-1049.
3. A. Paladini, D. Scuderi, A. Laganà, A. Giardini, A. Filippi, M. Speranza. Int. J. Mass Spectrom. 2003, 228, 349-358
4. B. Ritchie. Phys. Rev. A 1976; 13: 1411-1415
5. A. Giardini, D. Catone, S. Stranges, M. Satta, M. Tacconi, et al. Chem. Phys. Chem 2005, 6, 1164-1168.
6. R. J. Lavrich, R. L. Rhea, J.W. McCargar, M.J. Tubergen. J. Mol. Spectr. 2000, 199, 138-143; R. J. Lavrich, C. R. Torok, M.J. Tubergen. J. Phys. Chem. A 2001, 105, 8317-8322.
7. D. Consalvo, A. Van der Avoird, S. Piccirillo, M. Coreno, A. Giardini, et al. J. Chem. Phys. 1993, 99, 8398
8. A. Giardini, A.Paladini, F. Rondino, S. Piccirillo, M. Satta, M. Speranza, Org. Biomol. Chem. 2005, 21, 3984-3989.

Trajectory simulation of the interaction of CsCl and RbJ in cross molecular beams at high collision energies

V.M. Azriel, L.Yu. Rusin

Institute of Energy Problems of Chemical Physics RAS, Leninskiì prospect 38, Bldg.2, Moscow 119334, Russia, e-mail: Vladimir.Azriel@sunchem.ru

Mathematical simulation of experimental data on scattering of molecular beams allows to restore in some cases a potential energy surface (PES), adequate to investigated elementary process. In this case there is an opportunity in details to investigate dynamics of elementary process, including in the conditions which are beyond experiment. The success of restoration of PES essentially depends on character of the experimental dynamic information, and in particular on differential and double differential cross sections of scattering of products, and also on excitation functions of products of interaction. Excitation functions give especially a lot of information about the dynamics of endothermic processes, including information about possible channels of interaction and dynamics of each channel of such processes as collision-induced dissociation (CID) [1,2].

We represent here the results of trajectory simulation of collision-induced dissociation in the system CsCl+RbJ at collision energies ranging from 1 eV to 200 eV. The method of trajectory simulation is described in details in [3].

The PES used in calculations is constructed as additive function of pair ionic interactions of all included ions, and the excitation functions of formation of positively charged ionic products calculated on the base of this PES are in the quantitative agreement with experimental data obtained at the collision energies ranging from 1 eV to 10 eV [4].

The interaction of two molecules with ionic bond can proceeds via 12 channels:

1. $\mathrm{CsCl} + \mathrm{RbJ} \rightarrow \mathrm{CsCl} + \mathrm{RbJ}$
2. $\rightarrow \mathrm{Cs}^+ + \mathrm{Cl}^- + \mathrm{Rb}^+ + \mathrm{J}^-$
3. $\rightarrow \mathrm{Cs}^+ + \mathrm{Cl}^- + \mathrm{RbJ}$
4. $\rightarrow \mathrm{Rb}^+ + \mathrm{J}^- + \mathrm{CsCl}$
5. $\rightarrow \mathrm{CsJ} + \mathrm{Rb}^+ + \mathrm{Cl}^-$
6. $\rightarrow \mathrm{RbCl} + \mathrm{Cs}^+ + \mathrm{J}^-$
7. $\rightarrow \mathrm{CsJ} + \mathrm{RbCl}$
8. $\rightarrow \mathrm{CsClRb}^+ + \mathrm{J}^-$
9. $\rightarrow \mathrm{CsClJ}^- + \mathrm{Rb}^+$
10. $\rightarrow \mathrm{CsJRb}^+ + \mathrm{Cl}^-$
11. $\rightarrow \mathrm{RbJCl}^- + \mathrm{Cs}^+$
12. $\rightarrow \mathrm{CsClRbJ}$

Neutral products are formed in the channel 1 including elastic and inelastic interaction, the channel 7 corresponding exchange reaction, and the channel 12 with formation of products through the long-living intermediate complex stabilized by rotation. All other channels correspond to formation of experimentally measured ionic products, and the channels (2)-(4) represent typical collision-induced dissociation with disintegration on ions of one or both molecules of reagents, while in channels (5), (6) and (8) - (11) simultaneously with dissociation of reagents there is a formation of new products.

In a range of collision energies 0-200 eV the excitation functions of channels (2) and (12) are monotonous, and the first one increases from a threshold equal to the sum of dissociation energies of both molecules CsCl and RbJ, reaching saturation at high collision energies (fig.1). Despite of strong endothermicity the excitation function has no precisely expressed threshold that is characteristic for the formation of only atomic products. The similar threshold behaviour and saturation of excitation function was observed for three-atomic systems [5,6]. The behaviour of cross section of the channel (12) completely corresponds to dynamics of the process proceeding through a long-living intermediate complex, i.e. falls exponentially up to zero with growth of collision energy from 0 up to 0,4 eV.

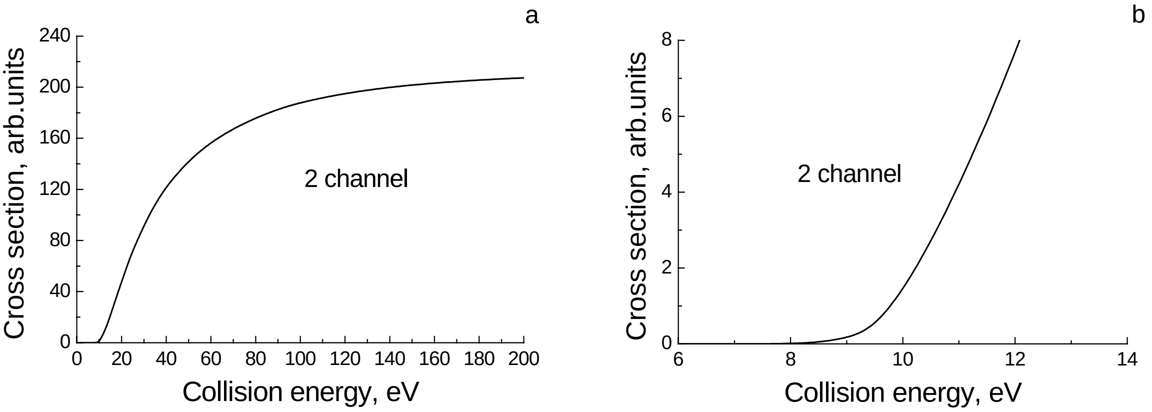

Fig.1. The excitation function of the channel (2) at the full range of collision energies (a) and near threshold (b).

The excitation functions of channels (3)-(11) possess strongly expressed threshold behaviour and have bell-like shape. They differ with values of thresholds and positions of maxima. Threshold energies of channels (3) and (4) correspond to collision energies 3,5-4 eV, then excitation functions grow till the values of energy approximately 30 eV, and then decrease slowly at further increase in collision energy. The cross sections of channels (3) and (4) correspond approximately as 3:1 in all investigated range of energies (fig.2).

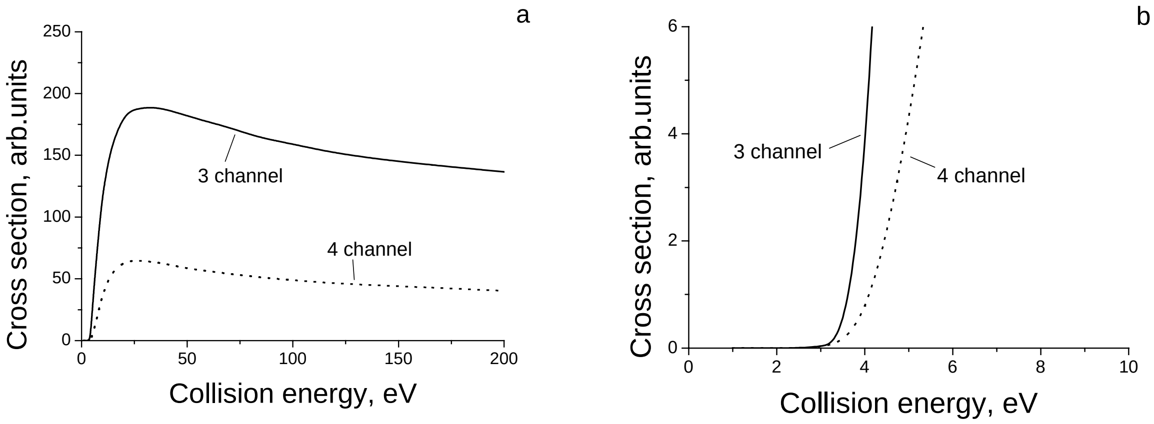

Fig.2. The excitation function of the channels (3) and (4) at the full range of collision energies (a) and near threshold (b).

Excitation functions of channels (5) and (6) have the same values of threshold energies, as considered above, but they reach a maximum at much smaller collision energies and decrease more quickly at the further growth of energy. The maximal value of cross section of the channel

(5) exceeds similar value for the channel (6) in 1,5 times and is reached at a bit smaller collision energy, but in a range of high energies the excitation function of the channel (5) falls more quickly, than the channel (6) (fig.3). At small collision energies heavier molecule CsJ in the channel (5) is formed with greater cross section probably because of heavy ions leave from each other more slowly. In the range of higher energies it is more difficult to stabilize such molecule, since their equilibrium distance is more, and bond energy is less in comparison with molecule RbCl. Absolute value of the maximum of excitation function of the channel (5) in 2 times smaller than the maximal cross section of the channel (4).

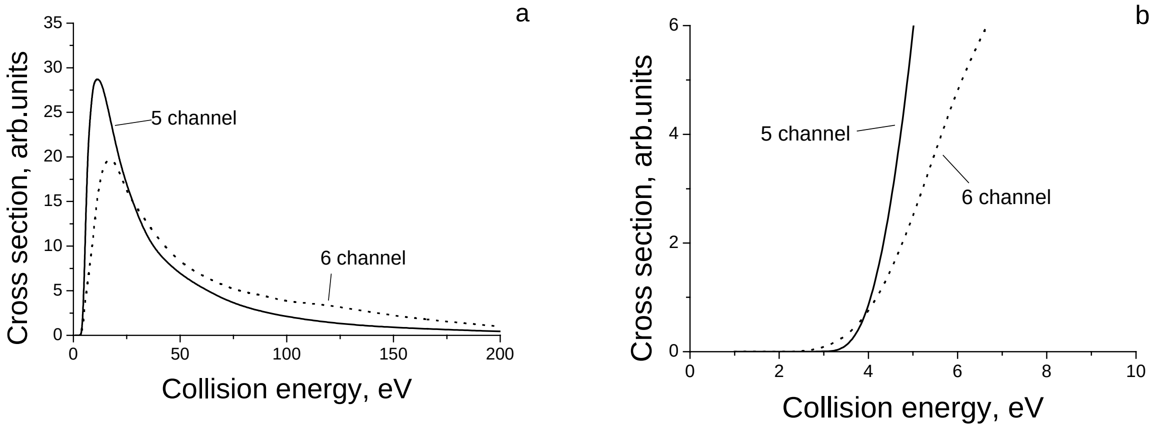

Fig.3. The excitation function of the channels (5) and (6) at the full range of collision energies (a) and near threshold (b).

Channels (8) - (11) form very narrow, practically symmetric excitation functions decreasing up to zero already at collision energy 20 eV. The maximal value of cross section of the channel (10) associated with the formation of the heaviest ionic complex approximately on the order exceeds similar values for three other channels.

References

[1] - V.M. Akimov, V.M. Azriel, L.Yu. Rusin. // Dynamics of collision-induced dissociation in four-atom systems. In: 12-th European Conference on Dynamics of Molecular Collisions (MOLEC XII), Bristol, U.K., 1998, p.28.
[2] - V.M. Azriel, L.Yu. Rusin. // Branching in the ion pairs formation in the collisions of CsCl and RbJ for the energy ranging from 0,1 to 25 eV. In: 20-th International Symposium on Molecular Beams, Portugal, Lisbon, 2003, p.139 (P9A).
[3] - V.M. Akimov, V.M. Azriel, L.Yu. Rusin, M.B. Sevryuk. // J.Chem. Soc., Faraday Trans.,1996, v.92, p.1683.
[4] - V.M. Azriel, V.M. Akimov, L.Yu. Rusin. // Russian J.Chem.Phys., 2002, v.21, p.18.
[5] - Wexler S., Parks E.K. // Ann.Rev.Phys.Chem., 1979, v.30, p.179.

[6] - Parks E.K., Pobo L.G., Wexler S. // J.Chem.Phys., 1984, v.80, p.5003.

Dynamics of ionic recombination in the system $Cs^+ + Br^- + R \rightarrow CsBr^* + R$, where R=Hg, Xe and Kr

V.M. Azriel, L.Yu. Rusin

Institute of Energy Problems of Chemical Physics RAS, Leninskiì prospect 38, Bldg.2, Moscow 119334, Russia, e-mail: Vladimir.Azriel@sunchem.ru

Despite of a greater role which plays recombination of atoms and radicals in the mechanism of chemical reactions and, especially, in nonequilibrium conditions, we know very little about dynamics of recombination processes [1]. In chemical kinetics three mechanisms of recombination are considered:

- direct three-body recombination, proceeding in one stage

$$A + B + C \rightarrow AB + C \qquad (1)$$

- Lindeman mechanism with transfer of energy from excited intermediate state to the third body

$$A + B \leftrightarrow AB^* \qquad (2a)$$

$$AB^* + C \rightarrow AB + C \qquad (2b)$$

- three-stage mechanism including formation of an intermediate complex of one reagent with the third body with its subsequent reaction with other partner of recombination

$$B + C \leftrightarrow BC^* \qquad (3a)$$

$$BC^* + C \rightarrow BC + C \qquad (3b)$$

$$A + BC \rightarrow AB + C \qquad (3c)$$

Without research of recombination dynamics it is very difficult to attribute this or that mechanism to concrete reaction, because the general kinetic laws of all three mechanisms are indistinguishable. Leaving in the party essential experimental difficulties of such researches, we should note absence of the enough adequate potential energy surface (PES), that allows to investigate dynamic characteristics of recombination processes of neutral and charged particles.

In [2,3] we informed on attempt to simulate the recombination dynamics of ions Cs^+ and Br^- with atoms Xe as the third particle by quasiclassical trajectory technique on the PESs that describe quantitatively reverse process of collision-induced dissociation. We represent bellow some results of the investigation of dynamics of reaction $Cs^+ + Br^- + R \rightarrow CsBr^* + R$, where R=Hg, Xe and Kr.

Movement of three particles through a potential energy surface was described by the equations of Hamilton and the task was solved in the center of mass system. Ions Cs^+ and Br^- were in the beginning of a trajectory on distance 250 atomic units from each other, and third particle R - on distance 100 atomic units from the center of mass of pair Cs^+ - Br^-. It was possible to change both this parameters. Further all three particles started to move in a direction to the general center of mass of system. Velocities of ions Cs^+ and Br^- were defined by the set value of relative energy of rapprochement of ionic pair. As on the basic part of a trajectory interaction of ions was defined by long-range coulomb part of potential, then the time through which they will meet in the center of mass can be calculated analytically. Simultaneously a particle R should reach a point of the center of mass of all system, that unequivocally defines the value of initial velocity of this particle in the assumption, that on the basic part of a trajectory this velocity does not vary in view of weak interaction of neutral atom with ions on greater distances. Changeable values were also impact parameter of atom relatively the center of mass of ionic pair and angle between vectors of relative velocity of ionic pair and atom R. The equations of movement were integrated by method of Adams of 6-th order, initial steps for which were calculated by Runge-Kutta procedure. The step of integration on time got out to equal 50 atomic units that provided conservation of full energy and an impulse on all extent of a trajectory no worse then 10 in minus 6 degree from their initial values.

Criterion of the termination of the trajectory leading to recombination, the condition was, that the distance between ions Cs^+ and Br^- does not exceed 30 atomic units, full energy of this pair is negative, and distances from both ions of a molecule up to the third atom more than 100 atomic units. In the end of a trajectory in case of formation of molecule CsBr its internal state was defined, i.e. values of vibration and rotation quantum numbers were calculated.

Calculations show, that for all three systems in case of non-collinear configurations of rapprochement the trajectories are direct, i.e. distances from atom R up to both ions decrease, and, having reached the minimal values, start to increase at once. For collinear configurations both from cesium, and from bromine sides after the first impact with atom the corresponding ion due to the received energy approaches with the second ion, ricochet and again collides with atom, then last leaves from the formed molecule. Thus the molecule possesses very high vibration energy corresponding in case of R=Hg to vibration quantum numbers above 200, and higher vibration energy corresponds to interaction of atom of mercury with an ion of cesium. The typical trajectories for both configurations are represented on fig.1.

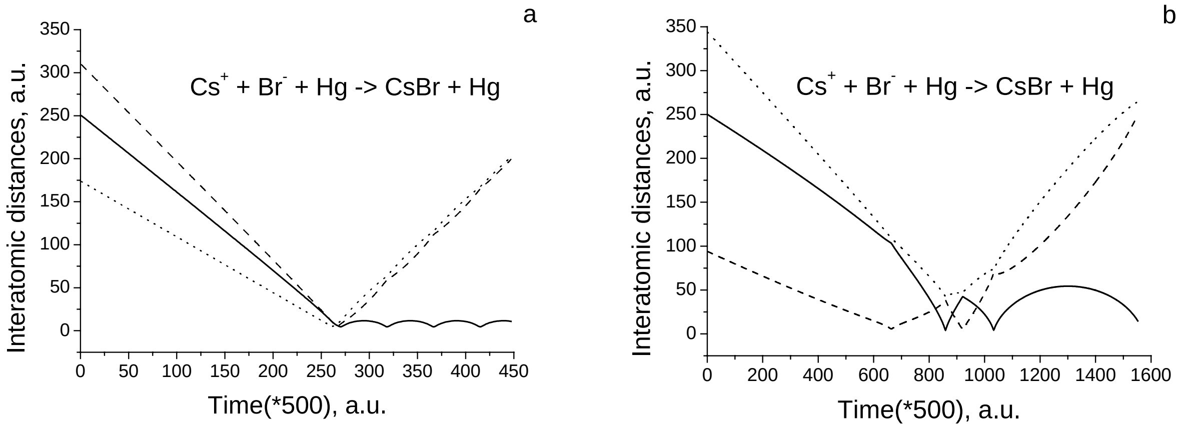

Fig.1. The schematic representation of a trajectory for non-collinear (a) and collinear (b) configurations of rapprochement for recombination of ions Cs^+ and Br^- at presence of atom Hg. Changes in time of three paired distances are shown, and the solid line corresponds to distance in pair Cs^+ - Br^-, and dashed lines - in pairs Cs^+ - Hg and Br^--Hg.

For all systems the probability of recombination in very strong degree depends on a configuration of three-body collisions. Recombination with the presence of atom Hg proceeds with the maximal probability in case when the vector of its velocity is perpendicular to the line of rapprochement of ionic pair. In case of xenon the collinear configuration is the most preferable one, when atom Xe catches up with ion Br-; in this case recombination occurs in very wide range of relative energies of rapprochements of ionic pair from 0 up to 28 eV and not so strongly depends on velocity of atom Xe. For a perpendicular configuration of collision the admissible range of relative energies of ionic pair is narrowed up to values 0-10 eV, and at collinear collision from the side of cesium the recombination occurs only at very small velocities of all three particles (fig.2). In case of atom Kr recombination proceeds in one range of energies of rapprochements both for a perpendicular configuration of collision, and for collinear configuration from the side of ion Br^-, while the collinear configuration of collision from a heavy ion of cesium does not lead to recombination at all.

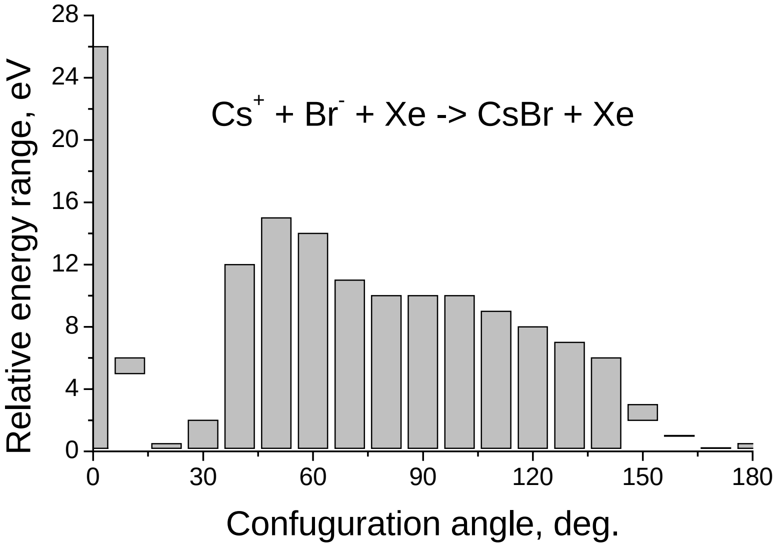

Fig.2. An admissible range of relative energies of rapprochements of ionic pair at recombination Cs^+ and Br^-at presence of atom xenon.

The range of admissible impact parameters of atom R relatively the center of mass of pair Cs^+ - Br^- is considerably narrowed with growth of collision energy, but at all energies zero value of impact parameter, i.e. when all three particles simultaneously come to the general point of the center of mass, is optimum. So, for a perpendicular configuration of collision in case of atom Xe the range of impact parameters at which the recombination of ionic pair is realized, makes from -7 up to +8 for energy of rapprochement 0,2 eV, from -2 up to +3 for energy 3 eV, and at energy of rapprochement 10 eV recombination occurs only at zero value of impact parameter (fig.3).

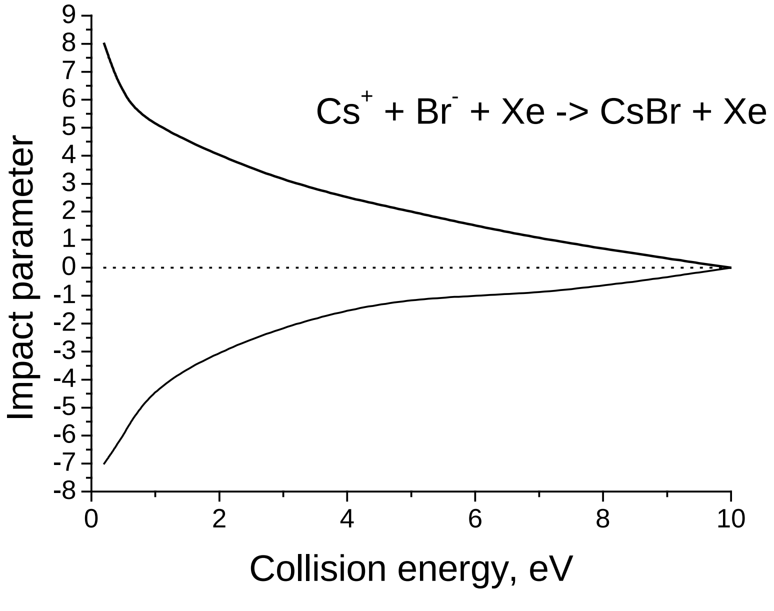

Fig.3. Dependence of admissible values of impact parameter on relative energy of rapprochement of pair Cs^+ - Br^-.

Dependences of total cross sections of recombination on relative energy of rapprochement of pair Cs^+ - Br^- are calculated in the assumption that atom R moves perpendicularly to line of rapprochement of ions, and both its impact parameter and velocity are chosen by a method of Monte-Carlo. The excitation functions received thus are represented on fig.4, from which it is clear, that in all cases the probability of recombination decreases exponentially with growth of collision energy, but the higher the mass of third atom the higher the absolute values of cross sections of recombination.

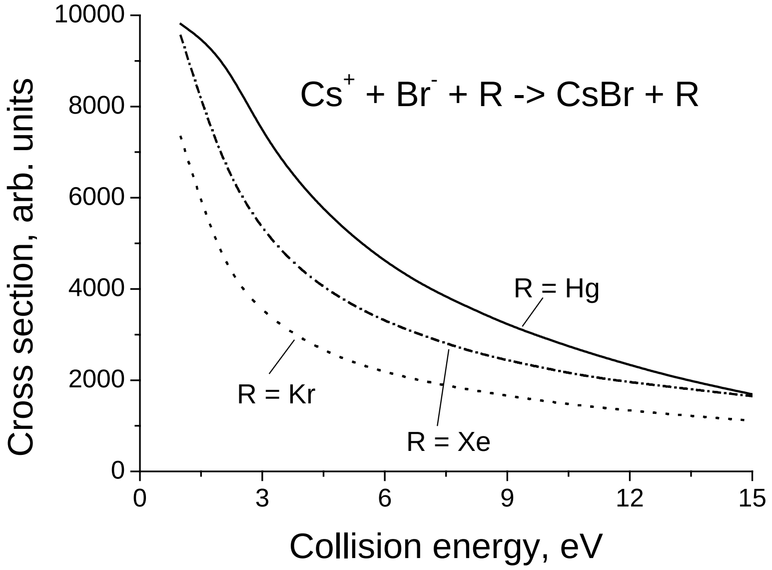

Fig.4. Cross sections of recombination in the system $Cs^+ + Br^- + R \rightarrow CsBr^* + R$, where R=Hg, Xe and Kr.

Distributions of rotation quantum numbers of formed molecules CsBr are qualitatively identical for all systems, and corresponding distributions of vibration quantum numbers vary significantly from system to system due to, possibly, the mass effects in efficiency of transfer of energy.

References

[1] – F.T. Smith. // In: Kinetic Processes in Gases and Plasmas, edited by A.R.Hochstim (Academic, New York, 1969), pp. 321-381.
[2] - V.M. Azriel and L.Yu. Rusin. // Trajectory simulation of the recombination reaction $Cs^+ + Br^- + Xe \rightarrow CsBr + Xe$. In: 14-th Symposium on Atomic, Cluster and Surface Physics (SASP 2004), Italy, La Thuile, 2004, PC-4.
[3] - V.M. Azriel, L.Yu. Rusin. // Influence of energy of approach of ionic pair on internal excitation of a formed molecule in reaction of recombination $Cs^+ + Br^- + Xe \rightarrow CsBr^* + Xe$. In: 21-th International Symposium on Molecular Beams, Hersonissos, Crete, Greece, 2005, p.52 (P09).

Recombination of atomic Hydrogen physisorbed on low-temperature Surfaces

Thomas R. Govers

Aecono Consulting, 59, rue de Prony, 75017, France,
E-mail: thomas.govers@wanadoo.fr

Molecular beam experiments that use low-temperature bolometers as (energy-) detectors are well suited to the study of physisorption and recombination of hydrogen on low-temperature surfaces. Experiments where this technique is combined with mass spectrometry to examine atoms and molecules released from the surface are summarised and reviewed with reference to astrophysical implications. Hydrogen atoms physisorbed on polycrystalline water ice are shown to be sufficiently mobile to recombine efficiently even at surface temperatures as low as 3 K. Molecules are formed with substantial internal energy, probably of the order of 35000 K, and are immediately released when formed. Coverage by molecular hydrogen plays an important role in determining overall recombination efficiency and may self-regulate recombination in interstellar clouds: on hydrogen-free grains recombination is limited by the low sticking coefficient of hydrogen atoms, while on grains covered by molecular hydrogen the binding energy is reduced so that recombination is limited by the rapid evaporation of physisorbed atoms.

Explosives detection by low energy electrons

Philipp Sulzer[1], **Flaminia Rondino**[2], **David Kilgour**[3], **Verena Grill**[1], **Sylwia Ptasinska**[1], **Paul Scheier**[1], **Tilmann D. Märk**[1]

[1]*Institut für Ionenphysik, Leopold-Franzens-Universität Innsbruck, Technikerstr. 25,*
A-6020 Innsbruck

[2]*Universita di Roma, La Sapienza, Dipartimento di Chimica*

[3] *Defence Science and Technology Laboratory (Dstl), Fort Halstead, Sevenoaks, Kent,*
TN14 7BP

ABSTRACT

Mass spectrometry is a potentially useful technology for the detection of explosives in security screening applications [1]. The ability to detect different classes of explosives in public places like airports, subways or buses is an important and valuable contribution to infrastructure security. Many different explosive detection techniques have been developed over the years with differing degrees of success. Positive ion mass spectra, upon electron or photon impact, exhibit a multitude of fragment peaks that may make an unambiguous identification of volatile explosives in ambient air a difficult task. In contrast dissociative electron attachment is a resonant process and leads to the formation of (fragment) anions only at specific electron energies. In the present work the attachment cross sections of all major product anions formed by free electron attachment to various gas phase explosives are measured with the aim of identifying key anions that can act as fingerprints for all commonly used explosives.

All explosives studied so far show impressively large cross sections for electron attachment when they interact with free low energy electrons [2]. NO_2^- turns out to be a major anion for all NO_2 containing molecules, such as Trinitrotoluene (TNT) or Pentaerythritol Tetranitrate (PETN). However, the positions of the resonances depend strongly on the composition and structure of the neutral precursor molecule. This dependence could provide an unambiguous identification of the explosive. In the case of Nitrotoluene even the different isomers can be assigned to a characteristic anion yield of the NO_2^-.

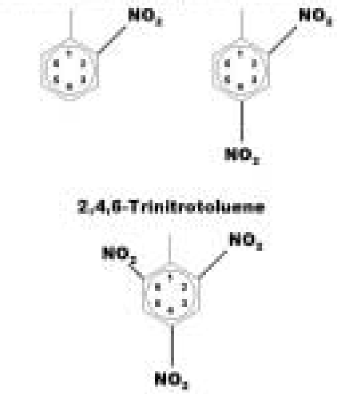

Fig. 4: Nitrotoluenes

Our measurements are performed utilizing a high resolution hemispherical electron monochromator that enables the investigation of positive and negative ion formation processes with a typical energy resolution of ~60meV to ~100meV. The product ions are analyzed with a quadrupole mass filter and detected by a channeltron type secondary electron multiplier operated in the pulse counting mode (see Fig. 2). In the past this experimental setup was successfully used to investigate inelastic interactions of free electrons with gas phase molecules of biological relevance, such as DNA bases [3,4,5], sugar [6], amino acids [7,8] and nucleosides [9]. Head space vapours of the analytes were used for analysis. Analytes with high volatility (e.g. 4-MNT and 2,4-DNT) produce sufficient vapour pressures for detection at room temperature, but low volatility analytes (e.g. TNT and PETN) required additionally heating to raise the vapour pressure to useable levels.

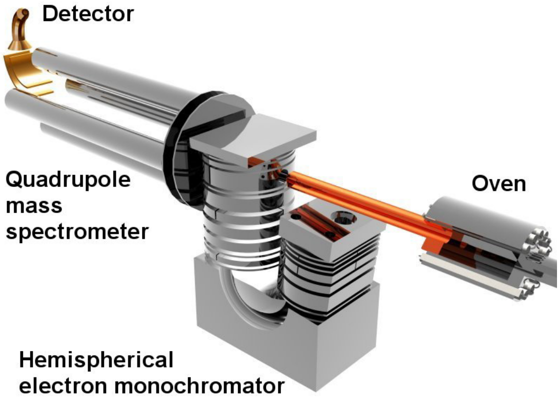

Fig. 2: Schematic view of the experimental setup

Results

In extension to earlier studies on DEA to explosives [10] the anion efficiency curves for all major anions were measured with high electron energy resolution (below 100meV). In order to achieve such a high resolution the collision region between the electrons and the neutral molecules must be free of electric fields. However, fragment anions that are formed in a field free ion source with an appreciable amount of kinetic energy in the dissociation process will reach the detector with reduced probability and will therefore be under-represented in the mass spectrum. In order to account for this effect, which may influence strongly the measured anion efficiency curves, the initial kinetic energy of all product anions is measured utilizing a beam deflection method that is described elsewhere [11]. Furthermore, autodetachment rates and unimolecular decomposition of parent anions are determined utilizing a highly sensitive sector field mass spectrometer.

Fig. 3 displays an anion mass spectrum at ~0eV for TNT. Dinitrotoluene (DNT) and Mononitrotoluene (MNT) have comparable spectra if one considers the different parent masses and replaces H by the additional NO_2 molecules. A common feature shared by Mononitrotoluene, DNT and TNT is a very strong anion yield at m/z 46 (NO_2, see also Fig. 1) at an electron energy above ~2eV.

Fig. 4 displays the NO_2^- anion yield as a function of the electron energy for TNT, 2,4-DNT and 2-NT. The anion efficiency curves of NO_2^- can be unambiguously assigned to the highly explosive TNT or to non-explosive 2-NT.

Another common feature of the investigated Nitrotoluenes is a narrow and intense zero eV resonance and no anion signal at higher electron energies for the parent anions (137amu for 2-NT, 182amu for 2,4-DNT and 227amu for 2,4,6-TNT). In contrast, no parent anion is found for electron attachment to PETN.

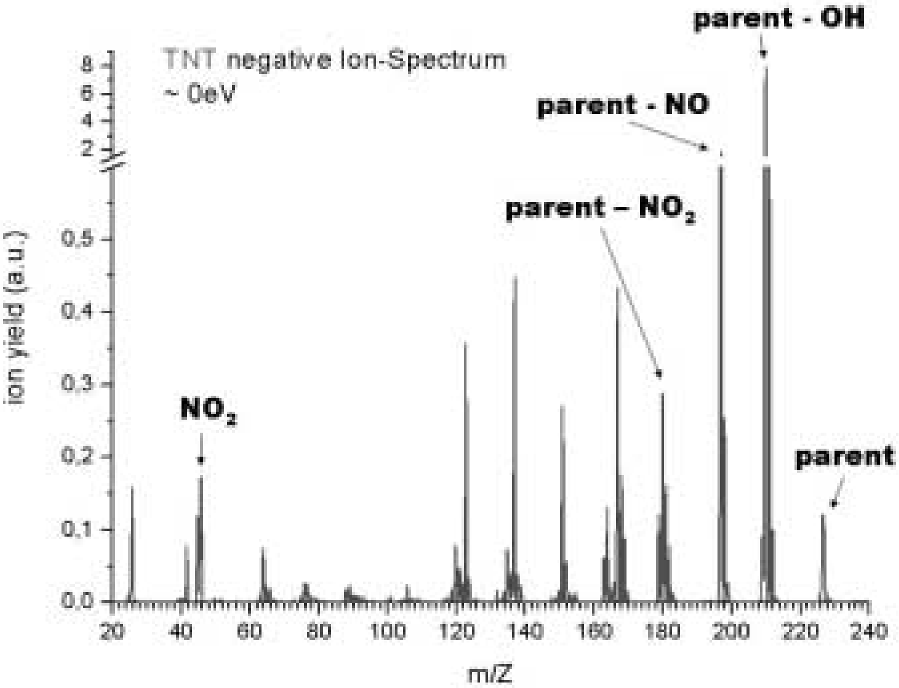

Fig. 6: TNT mass spectrum at ~0eV

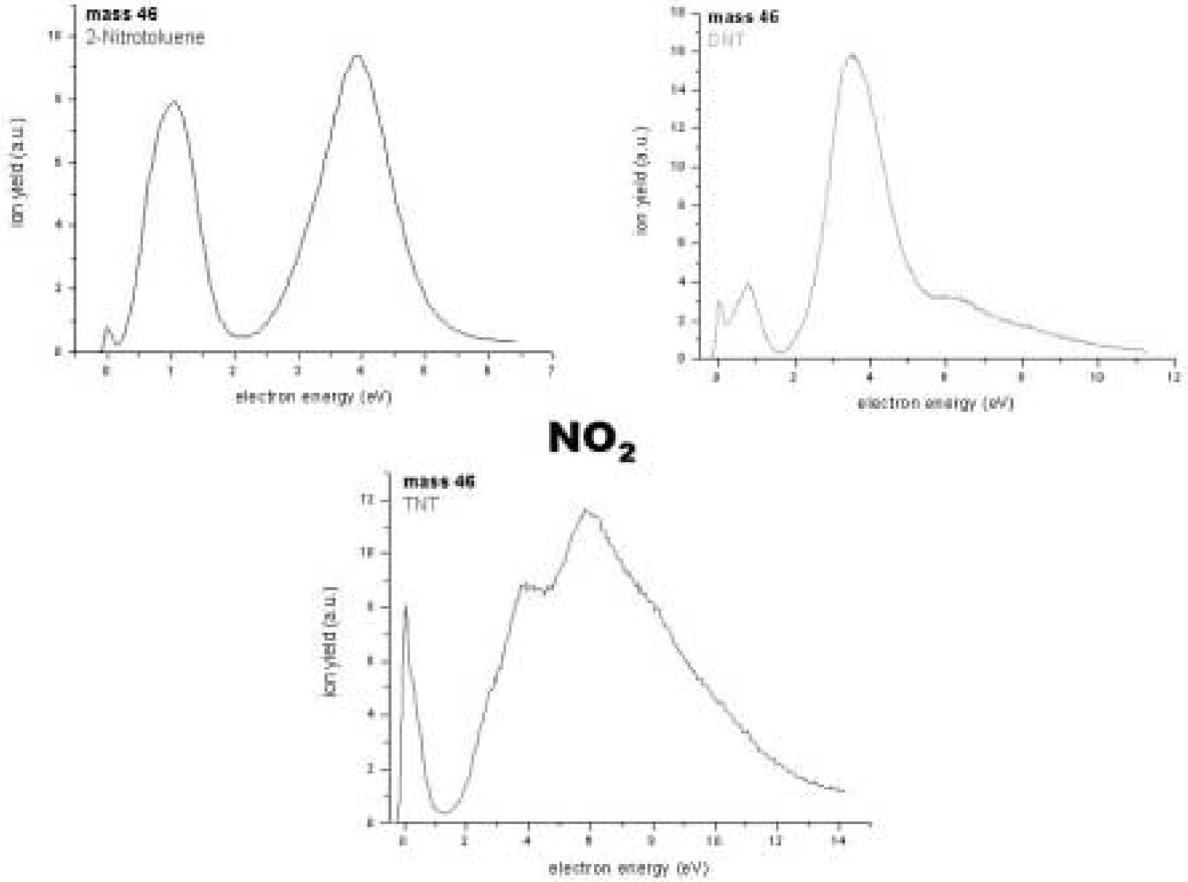

Fig. 7: m/z 46 anion efficiency curves of different Nitrotoluenes

Furthermore, the resonances are not only affected by the number of NO_2 groups attached to the aromatic ring, but also by the position with respect to the methyl group. Measurements of different isomers of MNT and DNT have been recorded. Fig. 5 displays the NO_2^- anion efficiency curve produced by dissociative electron attachment to 4- and 2-Nitrotoluene. For 4-NT the NO_2 group is located opposite to the methyl group and for 2-NT the NO_2 group is located next to the CH_3 group (see Fig. 1). Site dependent differences in the anion efficiency curves of isomeric forms of Nitrotoluene can also be observed at other masses. For instance the anion at a mass 107amu which corresponds to the loss of 30amu (NO) displays two resonances for 2-NT (one at ~1eV and one at ~4eV) and only one resonance for 4-NT (at ~4eV).

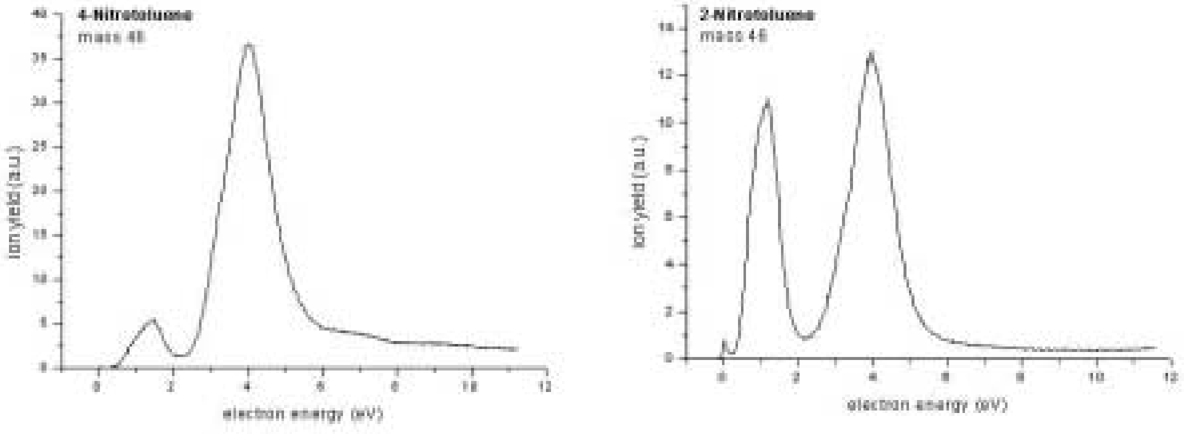

Fig. 8: Mass 46 from 4- and 2-NT

Acknowledgement

This work is partly supported by the FWF, Wien, the EU Commission, Brussels and the UK Ministry of Defence (MOD) through the Defence Science and Technology Laboratories (Dstl) contract RD031-011213 as part of the Electronics Systems Research Programme.

References

[1] National Research Council, ‘Opportunities to improve airport passenger screening with mass spectrometry’, National Academies Press, Washington DC, 2003.

[2] S. Boumsellek, S.H. Alajajian, A. Chutjian.; J Am Soc Mass Spectrom; 1992, 3, 243-247

[3] G. Hanel, B. Gstir, S. Denifl, P. Scheier, M. Probst, B. Farizon, M. Farizon, E. Illenberger, and T. D. Märk, *Phys. Rev. Lett.* **90** (2003) 188104 1

[4] S. Denifl, S.Ptasinska, M. Probst, J. Hrusak, P. Scheier and T.D. Märk, *J. Phys. Chem. A* **108** (2004) 6562

[5] S. Ptasinska, S. Denifl, V. Grill, T.D. Märk, P. Scheier, S. Gohlke, M.A. Huels and E. Illenberger, *Angew. Chem. Int. Ed.* **44** (2005) 1647

[6] S. Ptasinska, P. Limao-Vieira, S. Denifl, P. Scheier and T.D. Märk, *Chem. Phys. Lett.* **401** (2005) 227-231

[7] S. Ptasinska, S. Denifl, A. Abedi, P. Scheier and T.D. Märk, *Anal. Bioanal. Chem.* **377** (2003) 1115-1119

[8] S. Ptasinska, S. Denifl, P. Candori, S. Matejcik, P. Scheier and T.D. Märk, *Chem. Phys. Lett.* **403** (2005) 107-112

[9] S. Ptasinska, P. Candori, S. Denifl, S. Yoon, V. Grill, P. Scheier and T.D. Märk, *Chem. Phys. Lett.* **409** (2005) 270

[10] J.A. Laramee, M.L. Delnzer; Anal. Chem.; 1994; 66; 719-724

[11] Feil et al. IJMS (2004)

Probing and Controlling Gas/Surface Chemistry with Laser Radiation

Régis Bisson, Tung T. Dang, Plinio Maroni, Marco Sacchi, Rainer D. Beck and Thomas R. Rizzo

Laboratoire de Chimie Physique Moleculaire (LCPM), Ecole Polytechnique Fédérale de Lausanne (EPFL), CH-1015 Lausanne, Switzerland

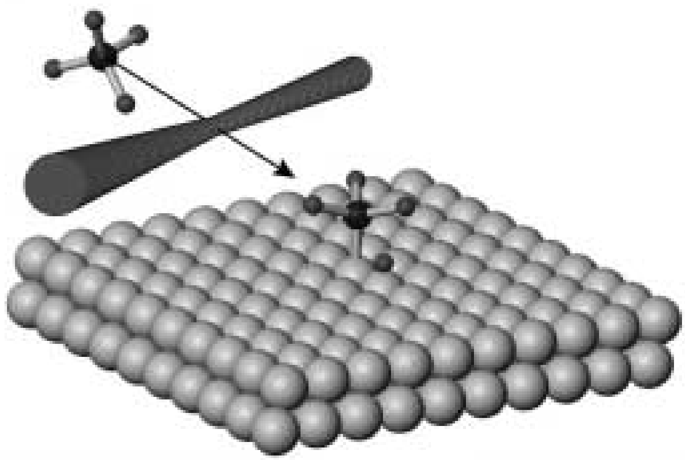

Laser light is an invaluable tool for detailed experimental studies of chemical reactions. The ability to prepare reagent molecules in specific quantum states and to resolve the quantum state distribution of reaction products using laser radiation has been key to the field of chemical reaction dynamics which studies chemistry at a fundamental microscopic level. This contribution reviews the methodology developed in our group at the EPFL for the quantum state resolved investigation of molecule/surface reactions using pulsed laser radiation, molecular beams, and single crystal surfaces in ultra-high vacuum. We present recent results for the dissociative chemisorption of methane on Ni(100), the rate-limiting step in steam reforming for hydrogen production, which provide clear evidence of mode-specific reactivity for this system invalidating statistical models of the reaction. Currently, we investigate the chemisorption of silane (SiH4) on nickel and silicon surfaces, the latter reaction being essential to semiconductor industry. In addition to explore the dynamics of this important reaction, the controlled deposition of isotopically pure silicon layers via isotope selective laser excitation is of interest to improve transport properties, such as thermal conductivity of silicon-based devices. We will present first results of this work in progress.

Stability of uracil and thymine cations

M. Beikircher[1], S. Ptasińska[1], S. Feil[1], M. Winkler[1], A. Bacher[1], W. Schustereder[2], O. Echt[3], T.D.Märk[1], P. Scheier[1]

[1]Institut für Ionenphysik,Universität Innsbruck, Technikerstraße 25, 6020 Innsbruck, Austria – manuel.beikircher@uibk.ac.at

[2]Max-Planck-Institut für Plasmaphysik, D-85748 Garching, Germany

[3]Department of Physics, University of New Hampshire, Durham, USA

ABSTRACT

Metastable decomposition of uracil and thymine cations is observed and the fragmentation of the positively-charged molecules is investigated down to the second generation. The dissociation of the parent cations via ring fragmentation is observed either in a single reaction window or sequentially following the loss of a hydrogen atom. The decay rates and the kinetic energy release of the dominant process are determined and, by using deuterated molecules, an assignment of the site where the H-loss occurs becomes possible.

1. Introduction

DNA and RNA can be damaged through ionising radiation (α, β, γ and heavy ions). Besides the direct collision of the fast projectiles with these macro molecules several secondary products such as ions, radicals and low energy electrons can induce further damage. In their pioneering work Sanche and coworkers [1] demonstrated that electrons with energies as low as 5 eV can effectively induce single and double strand breaks in dry plasmid DNA. Subsequent studies in the gas phase in Innsbruck showed that even electrons with kinetic energies below the threshold for electronic excitation can destroy the building blocks of DNA via dissociative electron attachment (DEA). Electrons with a kinetic energy < 20 eV are produced in large quantities along the trajectory of high energy particles (~40000/MeV).

Attachment of free electrons to uracil and thymine leads exclusively to the formation of fragment anions. The most abundant product are $(U-H)^-$ (Fig. 10) and $(T-H)^-$, respectively [1], [2]. However, in the positive ion mass spectrum no H-loss is observed (Fig. 11).
This is in contrast to electron impact ionization of hydrocarbons where H-loss is an important process. In the present study H-loss from excited uracil cations has been identified; the resulting ion $(U-H)^+$ is observed to decay quickly into more stable products upon ring dissociation.

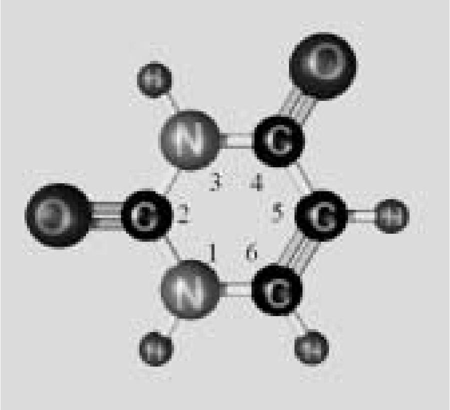

Fig. 9 – The uracil molecule

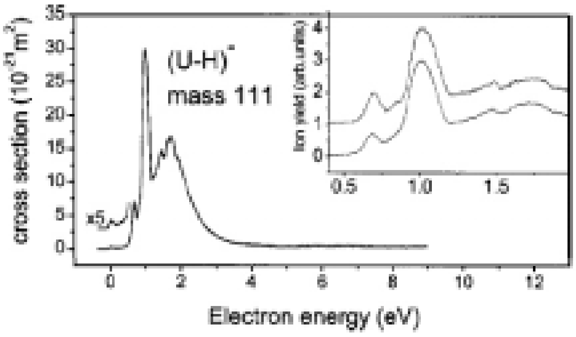

Fig. 10 – Cross section for formation of (U-H)$^-$ [3]

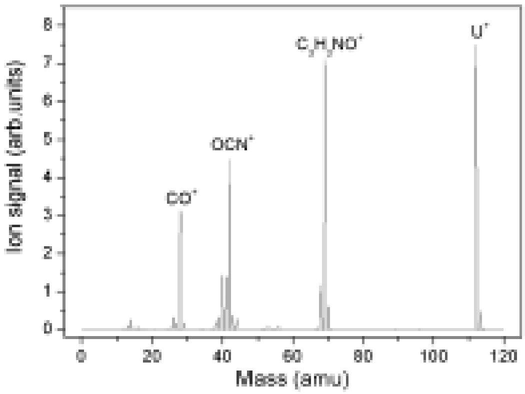

Fig. 11 – Positive ion mass spectrum of uracil

2. Experimental

The measurements are performed utilizing a modified VG-ZAB mass spectrometer in reversed geometry. Uracil and thymine are evaporated at a temperature of about 170°C and ionized by electron impact at 74 eV. The ions are then accelerated at different acceleration voltages, from 1 to 10 kV, resulting in different flight times to the detector. By decoupling the two sector fields, single decay processes are studied in two different time windows and the sequential decay of metastable uracil can unambiguously be identified.

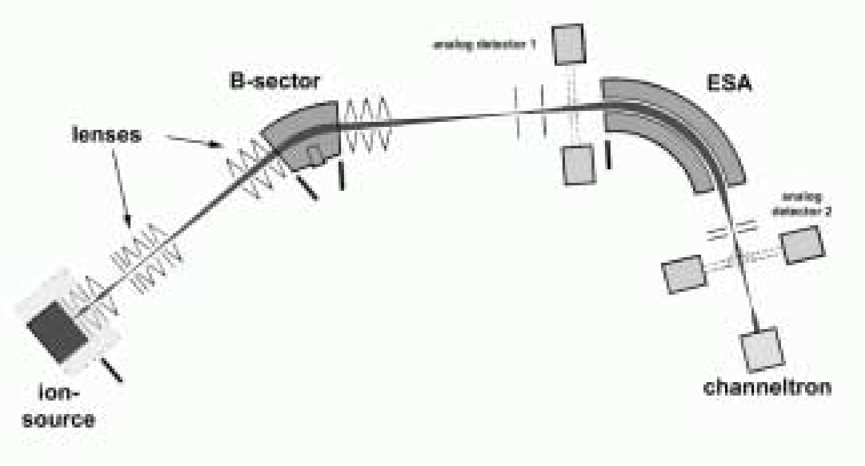

Fig. 12 – Schematic view of the experimental setup

For the present experiments intense primary ion beams are necessary in order to measure with sufficiently high accuracy the unimolecular dissociation reactions which have rather low decay rates.

3. Results

The most intense fragment ion with mass 69 amu is formed by two different reaction paths, (i) a dominant direct decay of 112 into 69 and (ii) a weak sequential decay starting with an H-loss and followed by a ring break-cleavage between the carbon and nitrogen atoms.

Fig. 13 – Sequential decay process of uracil

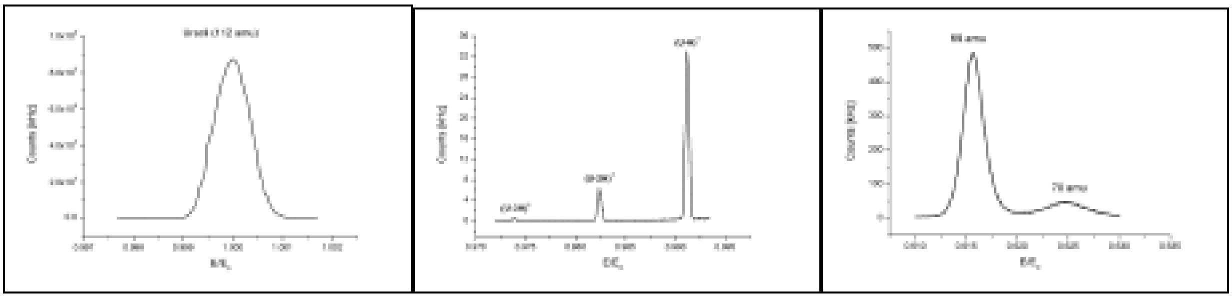

Fig. 14 – Uracil parent ion signal and product ion signals upon unimolecular dissociation

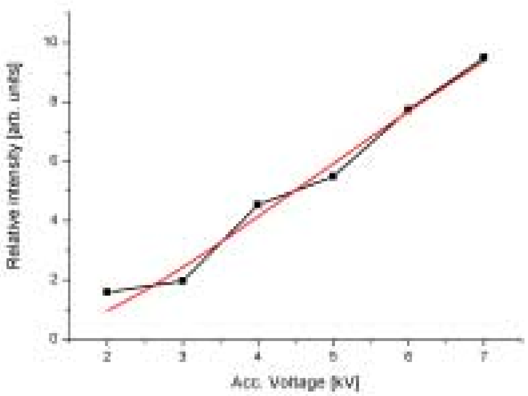

Fig. 15 – Ratio of 69 amu fragment to the 112 parent ion

To estimate the lifetime of U^+ the ratio of the fragment ion to the corresponding parent ion yield for the decay reaction $112^+ \rightarrow 69^+$ in the 2nd field free region was plotted versus acceleration voltage and fitted assuming a single exponential decay. This red line in Fig. 7 corresponds to a decay rate constant $k = 2.38\times10^5$ s^{-1} which corresponds to a mean life time of 4.2 µs.

The average kinetic energy that is released during the metastable unimolecular decomposition can be determined from the widths of the mass analyzed ion kinetic energy scans of the parent and fragment ions. We obtain an average kinetic energy release of 15 meV for the main fragment with mass 69 and about 1 meV for the neutral hydrogen loss.

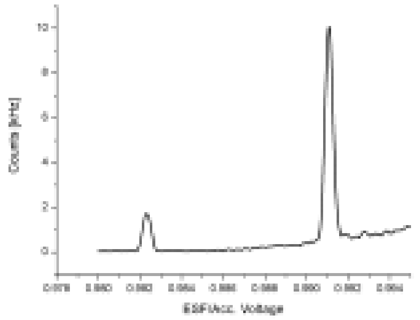

Fig. 16 – MIKE scan of undeutared uracil

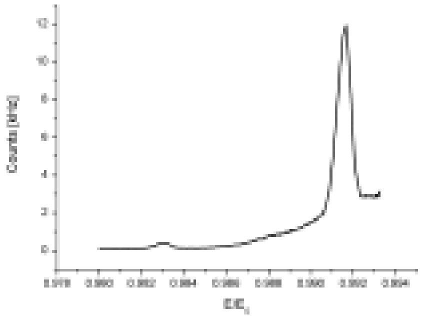

Fig. 17 – MIKE scan of 1,3 d-uracil

Partially deuterated uracil was used to distinguish between H-loss from the nitrogen and carbon sites of the molecule [4,5]. In the present study we used 1,3 d-uracil in which deuterium replaces the H-atoms at the N-sites, see first results given in Fig.8 and 9.
However, deuteration at the nitrogen positions of uracil is very critical since a fast hydrogen exchange with water will quickly replace D with H. Furthermore, a more complex exchange via water incorporation at the unsaturated bond enables D transfer from the N-sites to the C-sites.

4. Acknowledgment

The work was supported in part by the FWF Vienna and the European Commission Brussels.

References

[1] B. Boudaiffa et al., *Science* **287** (2000) 1658
[2] G. Hanel et al., *Phys. Rev. Lett.* **90** (2003) 188104
[3] S. Denifl et al., *J. Chem. Phys.* **120** (2004) 6557-6565
[4] S. Ptasinska et al., *Angew. Chem. Int. Ed.* (2005) in print
[5] S. Ptasinska et al., *Phys. Rev. Lett.* **95** (2005) 093201

Ion interactions with biomolecular clusters

Fresia Alvarado[1], Ronnie Hoekstra[1], Thomas Schlathölter[1], Bruno Manil[2], Jimmy Rangama[2], Bernd Huber[2]

[1] KVI Atomic Physics, Rijksuniversiteit Groningen, Zernikelaan 25, NL-9747 AA Groningen

[2] CIRIL-GANIL, rue Claude Bloch, BP 5133, F-14070 Caen Cedex 05

Ionization and fragmentation of DNA and its constituents is a primary step in biological radiation damage. When a charged particle crosses the cell, secondary particles such as low energy electrons, radicals and (singly/multiply charged) ions are formed within the track. The interaction of these secondary particles with biologically relevant molecules is responsible for a large fraction of the induced biological damage in the cell. The damage produced on the DNA molecule can be in the form of Single Strand Breaks (SSBs) or Double Strand Breaks (DSBs). In living organisms, SSBs are usually repaired without further consequences but DSBs can cause lethal lesions. Furthermore, multiple ionization events within the particles' track, those lead not only to DSB formation but also to more complex, less repairable lesions.

At the molecular level the induction of strand breaks remains to be understood. Our studies of the interaction of keV ions with isolated molecules (nucleobases) in the gas phase have revealed that fragmentation patterns and fragment formation are strongly influenced by the projectile and the target electronic structure. They provided a first step for our recent studies on biomolecular clusters.

In joint experiments at KVI/Groningen and GANIL/Caen we investigated the collision induced fragmentation of isolated purines and pyrimidines in the gas phase and in the cluster environment. It was shown that for uracil, adenine and thymine fragmentation channels not observed in the isolated molecules open up in the cluster case. For a deeper understanding of radiation damage to clusters, however, cluster formation mechanisms have to be understood and controlled. In first studies, we observed a structured spectrum of pyrimidine based clusters with magic numbers 7, 10 and so on. On the other hand, the adenine – cluster spectrum is structureless.

A very remarkable result was obtained with mixed clusters in the gas phase. Mixing nucleobases that in DNA form a Watson-Crick pair (hydrogen bonding between the DNA strands), we observed the preferential formation of mixed clusters (middle peaks in the sets of three peaks in left figure). Such mixed clusters are not formed if the constituents do not correspond to a Watson-Crick pair (see right figure).

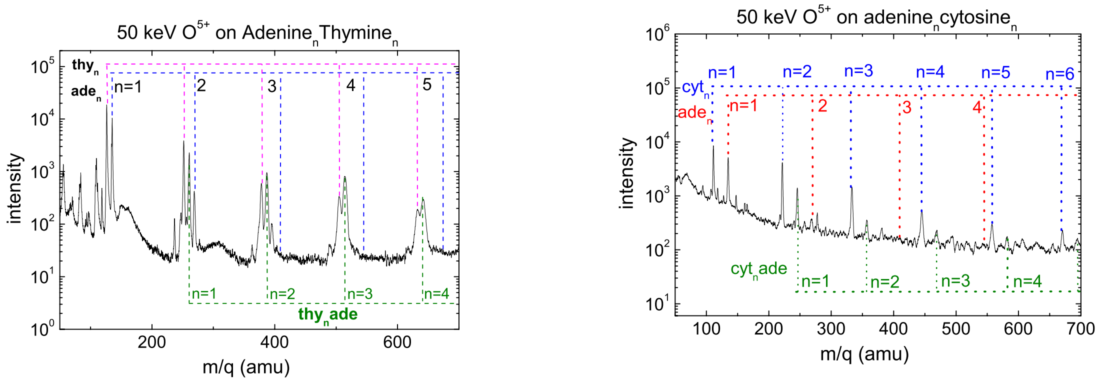

Mass spectra of cluster formation in mixing either adenine or thymine or adenine and cytosine.

Dissociative electron attachment to valine

D. Kubala[1], J. Kočíšek[1], O. Ingolfsson[2], Š. Matejčík[1]

[1]*Department of experimental physics, Comenius University, 84248 Bratislava, Slovakia*

[2]*Department of chemistry, Uiversity of Iceland, Reykjavik, Iceland*

ABSTRACT

Using a high resolution crossed electron molecule beams apparatus the electron attachment to the gas phase L-valine ($(CH_3)_2CHCH(NH_2)COOH$ - Val) was studied by means of mass spectrometric detection of the product anions.

1. Introduction

In this paper we present an experimental study of dissociative electron attachment (DEA) to the amino acid L-Valine (Valine Val – $(CH_3)_2CHCH(NH_2)COOH$, m/z=117) in the gas phase. This work is contribution to the better understanding of the mechanism of the negative ion and radical formation from this amino acid. The DEA to a molecule in the gas and condensed phase is a resonant process which proceeds via two steps:

$$e + \mathrm{Val} \rightarrow (\mathrm{Val}^-)^\# \rightarrow \text{negative ions + neutral fragments} \qquad (1)$$

The first step is the formation of the transient negative ion (TNI) $(\mathrm{Val}^-)^\#$ which may subsequently (in the second step) dissociate into negative ions and neutral fragments or radicals. The resonant character of the DEA reactions is represented by the form of the cross sections. The position and width of the DEA resonances are characteristic for the molecule and given ion. Using the crossed electron/molecule beams technique combined with the mass analysis of the negative ions we were able to measure the ion yields for the formation of particular negative ions.

Present work is according to our knowledge the first study on low electron energy interactions of the electrons with valine. Recently several studies on DEA to amino acids glycine and alanine [1,2,3] have been published. These studies revealed some characteristic dissociation patterns in the DEA. The dominant DEA channels in both molecules were the $(M-H)^-$ ions, where M denotes the glycine or alanine. According to these studies the $(M-H)^-$ ions have been formed via π * (COOH) resonance peaking at about 1.8 eV. The π*(COOH) resonance is typical feature for the molecules containing the COOH (carboxyl) functional group. The DEA studies of glycine and alanine [1,2,3] showed that besides the π* resonance additional resonances at higher electron energies (around 6 and 10 eV) exist.

2. Experimental setup

The experiment has been carried out using the crossed electron/molecule beams apparatus at Comenius University in Bratislava (Figure 1). The apparatus has been described in detail in [4] therefore we give only a brief description. The electron beam is formed by a trochoidal electron monochromator (TEM). The electron energy resolution of the electron beam in present experiment was about 140 meV. The resolution of the electron monochromator has been kept low in order to increase the electron current and to achieve sufficient ion yield. The calibration of the electron energy scale and the estimation of the electron energy resolution were performed through the measurement of the non dissociative electron attachment to SF_6.

The molecular beam was formed in a heatable effusive molecular beam source (EMBS). The beam of the molecule is formed by the effusion of the gas trough a channel (0.5mm diameter and 4 mm long) and an external aperture. The valine is under normal conditions in solid state. The sample was placed directly into the stainless steel container of the EMBS. The EMBS was resistively heated to temperatures of about 140°C in order to achieve sufficient vapour pressure. The negative ions formed in the intersection volume between the electron and the molecular beams are extracted by a weak electric field into the quadrupole mass spectrometer (QMS). The mass selected negative ions are detected as a function of the electron energy.

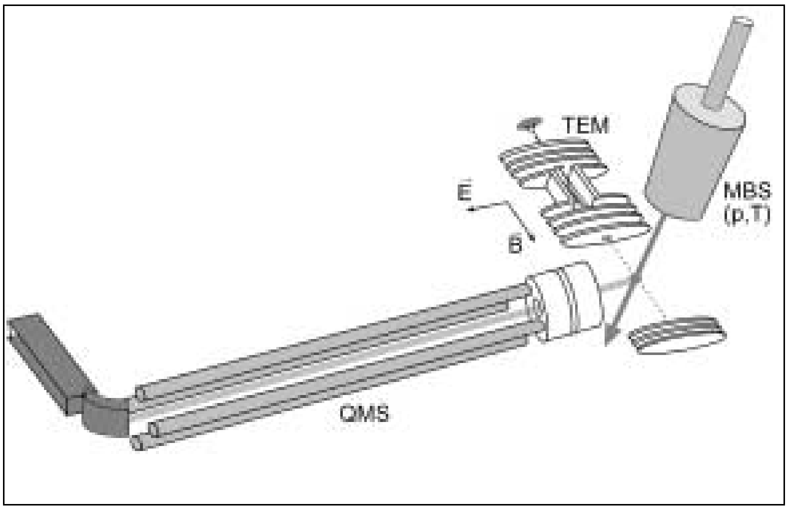

Figure 1. Schematic view of the crossed beams apparatus in Bratislava, MBS – molecular beam source, TEM trochoidal electron monochromator, QMS – quadrupole mass spectrometer.

3. Results and discussion

We have studied the energy dependency of the negative ion formation in dissociative electron attachment to valine in the electron energy range from 0-14 eV. In this energy range dissociative electron attachment to valine was found to leads to the formation of fragments with the mass to charge ratio (m/z) of 116, 100, 74, 56, 45 26 and 17. We attribute these mass to charge ratios to the fragment ions $(M\text{-}H)^-$, $(M\text{-}OH)^-$ $C_2H_4O_2N^-$, $C_4H_8^-$, $COOH^-$ CN^- and OH^-.

The most pronounced of these fragments is similarly to the previous studied amino acids the dehydrogenated molecular ion $(M\text{-}H)^-$ (Figure 2a) formed via reaction:

$$e + Val \rightarrow (Val^-)^{\#} \rightarrow (Val - H)^- + H \qquad (2)$$

This fragment is predominantly formed via a low energy π* resonance, reflected in the ion yield curve by an peak with a maximum at about 1.2 eV, second weaker resonance is present at about 5.5 eV and monotonic increase of the ion yield is observed up to the end of the measured ion yield at about 14 eV.

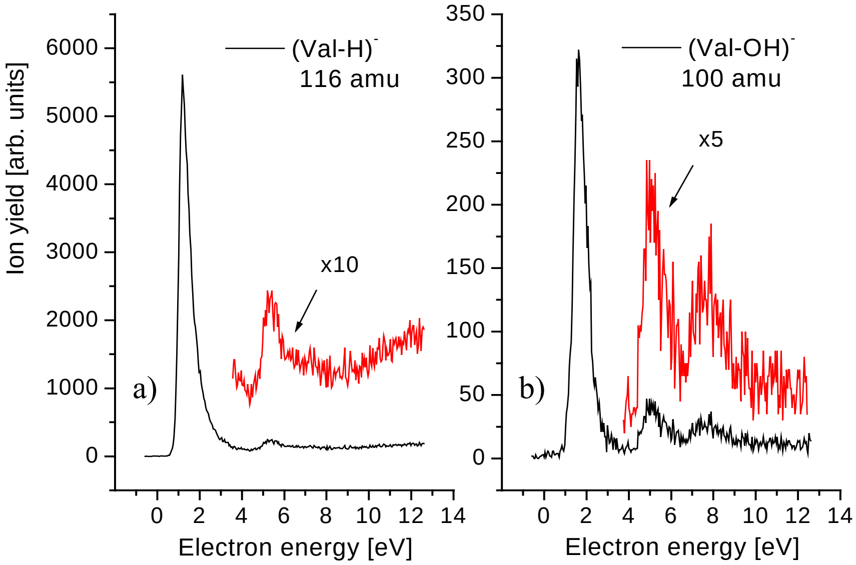

Figure 2. The ion yields for a) $(Val\text{-}H)^-$ m/z=116 b) $(Val\text{-}OH)^-$ m/z=100 ion formation via DEA to valine

In addition to M-H$^-$ the fragment ion M-OH$^-$ (Fig. 2 b) is formed at about 1.6 eV. The intensity of this peak is about one order of magnitude weaker in comparison to the M-H$^-$ ion. Pronounced resonances were also observed at 5.5 eV for both ions and at about 7.5 eV for the M-OH$^-$ ion.

The negative ions associated with the cleavage of the COOH group from the TNI have been observed (Val-COOH)$^-$ m/z=72 and COOH$^-$ m/z=45. The ion yields of these two ions are presented in the Figures 3a and 3b. Whereas the (Val-COOH)$^-$ ion is formed at high energy resonance at about 8 eV, the COOH$^-$ ion formation proceeds via several resonances some of them accessible already at low electron energies. Similarly also the OH$^-$ ion yield shows resonances at low energies, i.e. resonances at sub excitation energies located close to 2 eV.

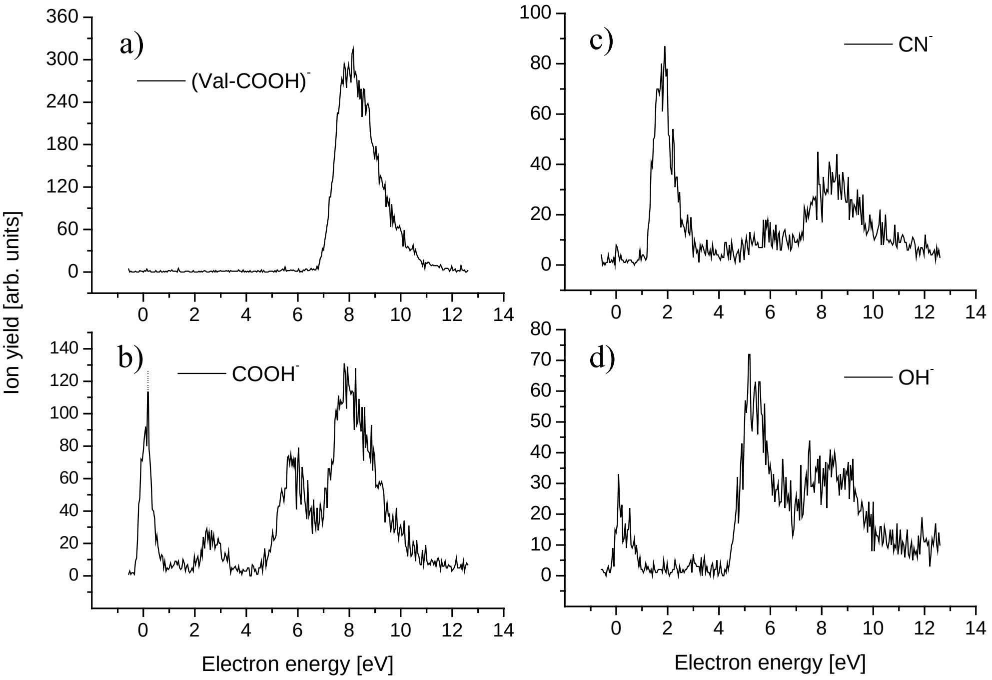

Figure 2. The ion yields for formation of the selected fragment ions from valine.

4. Acknowledgments

This work was supported by the Slovak Grant agency APVT project Nr. 20-007504

5. References

[1] S. Gohlke, A. Rosa, E. Illenberger, F. Brüning, M. Huels, J. Chem. Phys., 116 (2002)10164
[2] S. Ptasinska, S. Denifl, A. Abedi, P. Scheier, T. D. Märk, Anal. Bioanl. Chem., 377 (2003) 1115
[3] S. Ptasinska, S. Denifl, P. Scheier, T.D. Märk, S. Matejcik,Chem. Phys. Lett., 403 (2005) 107

Dissociative electron attachment to 1-chloro-3-bromo-propane and 1-chloro-2-bromo-propane

J. Kočišek[1], W. Barszcewska[2], Š. Matejčík[1], D. Kubala[1]

[1]Department of Experimental Physics, Comenius University, Mlynska dolina F2, 84248 Bratislava, Slovakia

[2]Department of Chemistry, University of Podlasie, ul. 3. Maja 54, 08-110 Siedlce, Poland

ABSTRACT

The dissociative electron attachment (DEA) to 1-chloro-3-bromo-propane and 1-chloro-2-bromo propane has been studied using a crossed electron/molecule beams apparatus. The negative ion yields in the electron energy range from about 0eV to about 9eV have been measured at different temperatures.

1. Introduction

The studies of the temperature dependence of the DEA to chloro and bromo substituted hydrocarbons is continuation of our previous work on DEA to chloro and bromo substituted methanes [1-4]. In that study we have observed strong dependence of the DEA cross sections on the temperature of the gas and also strong changes in the branching ratios between Br^- and Cl^- ions. In present work we have studied the DEA to 1-bromo-3-chloro-propane and 1-chloro-2-bromo-propane. The main interest of our investigation was the measurements of the ion yields of the negative ions formed in the DEA to the molecules. Moreover, we were interested in the competition of particular reaction channels of DEA reaction. The ion yields were measured ain the electron energy range from 0 to about 9eV. Additionally the negative ion mass spectra of the molecules at different electron energies have been studied.

2. Experiment

The experiment has been carried out using the crossed electron/molecule beams apparatus at Comenius University in Bratislava. The apparatus has been described in detail in [1]. The electron beam is formed by a trochoidal electron monochromator (TEM). The electron energy resolution of the electron beam in present experiment was about 80 meV. The calibration of the electron energy scale and the estimation of the electron energy resolution were performed through the measurement of the non dissociative electron attachment to SF_6. The molecular beam was formed in a heatable effusive molecular beam source (EMBS). The negative ions formed in the intersection volume between the electron and the molecular beams are extracted by a weak electric field into the quadrupole mass spectrometer (QMS). The mass selected negative ions are detected as a function of the electron energy.

3. Results

The DEA to 1-chloro-3-bromo-propane and 1-chloro-2-bromo-propane has been studied in the electron energy range from about 0 to 2 eV (Figure 1). The DEA to these molecules preferentially results into Br^- formation. In the case of 1-bromo-3-chloro-propan the Cl^-/Br^- ratio was about 1:100 but in the case of 1-chloro-2-bromo-propan the ratio was only 1:20. This kind of behaviour could be explained by the differences in the structure of the molecules. The differences in the efficiency of $ClBr^-$ and $HClBr^-$ negative ion formation have been observed for DEA to 1-bromo-3-chloro-propane and 1-chloro-2-bromo-propane. These molecular ions were formed with higher efficiency from 1-chloro-2-bromo-propane than from 1-chloro-3-bromo-propan. Possible explanation for this effect could be the fact that the distance between Br and Cl atoms in the 1-chloro-2-bromo-propane is smaller than in the 1-chloro-3-bromo-propane and thus the formation of the molecular ions is more probable.

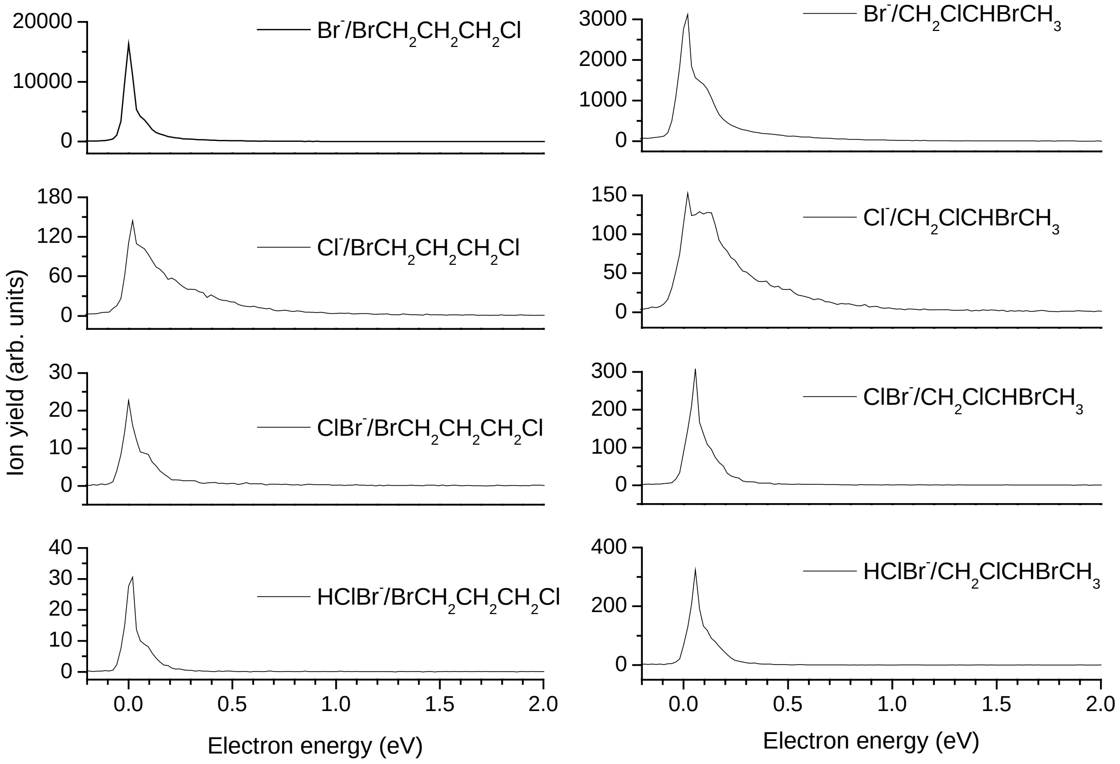

Figure 1. The ion yields for DEA to 1-chloro-2-bromo-propane and 1-chloro-3-bromo-propane.

4. Acknowledgments

This work was supported by the Slovak Grant agency APVT project Nr. 20-007504

References

[1] Matejcik S, Foltin V, Stano M and Skalny J D 2002 Int. J. Mass Spectrosc. 223/224 9

[2] Matejcik S, Ipolyi I, Illenberger E, 2003, Chem. Phys. Lett., 375 660

[3] Ipolyi I, Matejcik S, Lukac P., Skalny JD, Mach P., Urban J, 2004, Int. J. of Mass Spect., 233 193-197

[4] Ipolyi I, Stano M, Matejcik S, Acta Phys. Slov., in print

Superconducting MgB_2 thin films prepared by magnetron sputtering

R. Mičunek[1], A. Plecenik[1], P. Kúš[1], M. Zahoran[1], M. Tomášek[1], T. Plecenik[1], M. Gregor[2], M. Štefečka[2], V. Jacko[3], J. Greguš[1], B. Grančič[1], M. Kubinec[1], and M. Mahel'[1]

[1] Department of Experimental Physics FMFI, Comenius University, SK- 84215 Bratislava, Slovak Republic e-mail: Radovan.Micunek@fmph.uniba.sk

[2] Department of nanotechnology, BIONT, a.s., Karloveska 63, SK- 842 29 Bratislava, Slovak Republic

[3] Institute of Measurement Science, Slovak Academy of Sciences, Dubravska cesta 9, 841 04 Bratislava, Slovak Republic

Superconducting MgB_2 thin films are promising materials for preparation of cryoelectronic devices. On the one hand conventional superconductors have got a very low critical temperature. High temperature superconductors have got a higher critical temperature, but they are not stable enough and they have got a large anisotropy. On the other hand MgB2 has not such high critical temperature (it is only 39 Kelvin) but can be working with refrigerator in closed cycle. Several deposition methods for preparation of MgB_2 thin films were published and the promising results were obtained by MBE [1], by co-deposition of boron and magnesium from two resistive sources [2], pulsed laser deposition [3], magnetron sputtering [4], etc.

In our laboratory superconductor MgB_2 thin films with thickness 200 nm were prepared on various substrates by co-deposition of boron and magnesium from two independent magnetrons. Sapphire, silicon and glass were used as a substrate. In this paper we present properties of superconducting MgB_2 thin films on sapphire substrates.

We have prepared our samples in four steps. In the first step the substrates were cleaned, in acetone, isopropyl alcohol and distillates water. After cleaning we put the samples into vacuum chamber for magnetron deposition. This deposition method is based on magnetron deposition from two different sources. The magnetron with boron target was actuating by radio-frequency source at power 250 watt and magnetron with magnesium target was actuating by dc source at power 29 watt. Sample holder is rotating during the whole deposition. Deposition time was 40minutes. The vacuum chamber was evacuated by turbo-molecular pump to pressure 10^{-4} Pa and consecutively filled by argon to working pressure 7.4×10^{-2} Pa. The vacuum chamber was opened after the deposition process and samples were inserted to quartz tube in circular furnace. The quartz tube was evacuated to pressure 200 Pa and than filled with argon to pressure 10^5 Pa. Within the optimization process the annealing temperature was change in the range from 500 ^{o}C to 750 ^{o}C and time of annealing from 30 seconds to 600 seconds. Topography of annealed thin films was controlled by SEM microscopy (Fig.1)

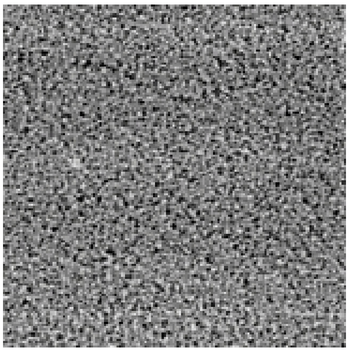

Fig.1 The morphology of superconducting MgB_2 thin film prepared by annealing of MgB at temperature 680 °C and time 2.5 minutes in Ar atmosphere. Scale bar is 5 μm.

Composition of MgB (before annealing) and MgB_2 thin films by Auger Electron Spectroscopy were controlled (see Fig. 2).

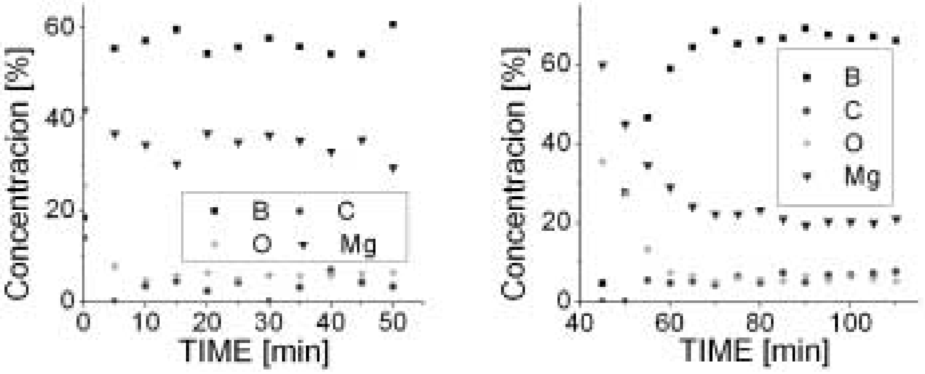

a) b)

Fig.2 The concentration profile of magnesium and boron in MgB thin film (before annealing (a)) and MgB_2 thin film (after annealing at temperature 690°C and time 2.5 minutes (b)) from Auger Electron Spectroscopy.

From a series of experiments an optimal time of annealing was found – for our thin films in the range from 2.5 minutes to 3 minutes. In Fig.3 one can see strong dependence of the R-T characteristics on the annealing temperature. The best results (the highest T_{con} and the narrowest transition to superconducting state ΔT_c) were obtained for the annealing temperature about 680 °C.

For measurement of critical current density the microstructures with defined dimensions were prepared by optical lithography with consequent etching in Ar^+ ion beam. After etching and removing the photo resist three micro strips (50 μm long and 5, 10 and 15 μm wide) were obtained (Fig.4 a).

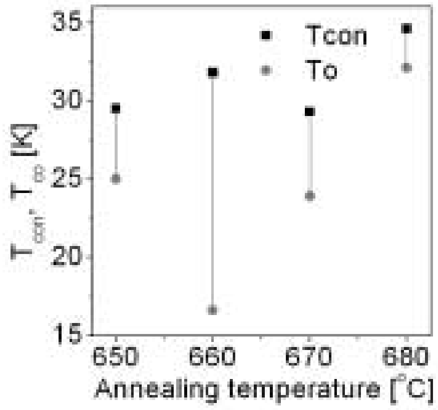

Fig.3 Dependencies of T_{con} and T_{c0} on the annealing temperature for MgB_2 thin films prepared by magnetron sputtering and ex-situ annealed at temperatures 650 °C, 660 °C, 670 °C, and 680 °C at 2.5 minutes.

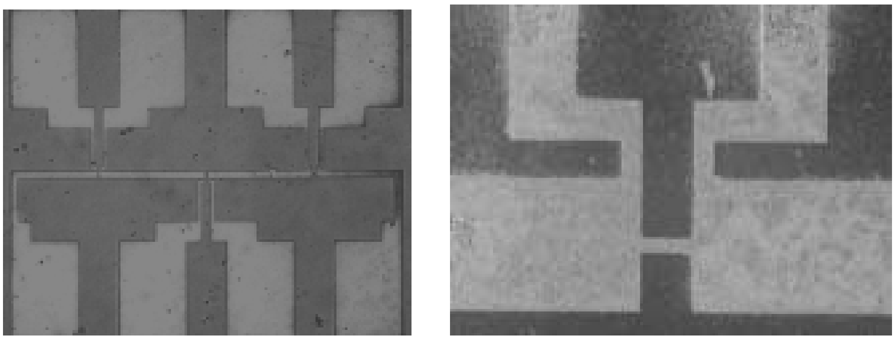

a) b)

Fig.4 The picture of the measured structures with 15 µm, 10 µm and 5 µm wide MgB_2 micro strips prepared by Ar^+ ion beam etching (a), detail of 10 µm wide strip (b)

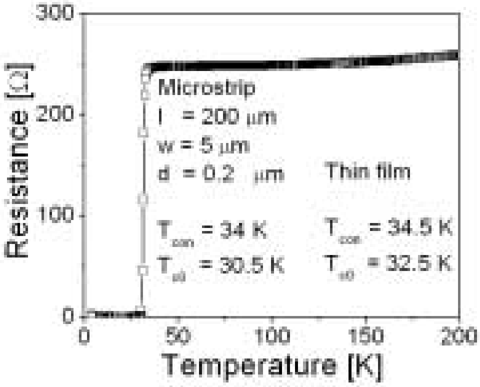

Fig.5 R (T) dependence measured on 10 µm wide micro strip shown in Fig.4.

In comparison with not patterned thin films, the depression of the critical temperatures was measured on micro strips. T_{con} decreased from 34.5 K (measured on simple MgB_2 thin film) to 34 K and T_{c0} from 32.5 K to 30.5 K (Fig.5). These changes are not significant and could be caused by various influences.

The V-I characteristics were measured on a micro strip with thickness d = 200 nm and width 5 µm at temperatures below T_c (see Fig.6 a). The hysteresis on V-I characteristics results from creation of hot spots and is typical for long bridges [5]. The critical current I_c for calculation of j_c was determined from the first jump to normal state. The highest critical current density j_c (4.2K) measured on the MgB_2 micro strips was lower than 10^6 A/cm^2 on this type of structures. The shape of the critical current density j_c vs. temperature is typical curve for long bridges contain SNS connections inside the strip (Fig.6 b) [6]. A "tail" near T_c is deflection from the predicted shape is caused by formation of a network of superconducting grains as described in the de Gennes - Werthamer - Clarke theory. Proximity bounded junctions inside the superconducting thin films can be fit as $J_C \sim (1-T^2)\exp(\alpha T^{0.5})$, where $\alpha = a_N/\xi$, a_N is the normal region size, ξ is the coherence length.

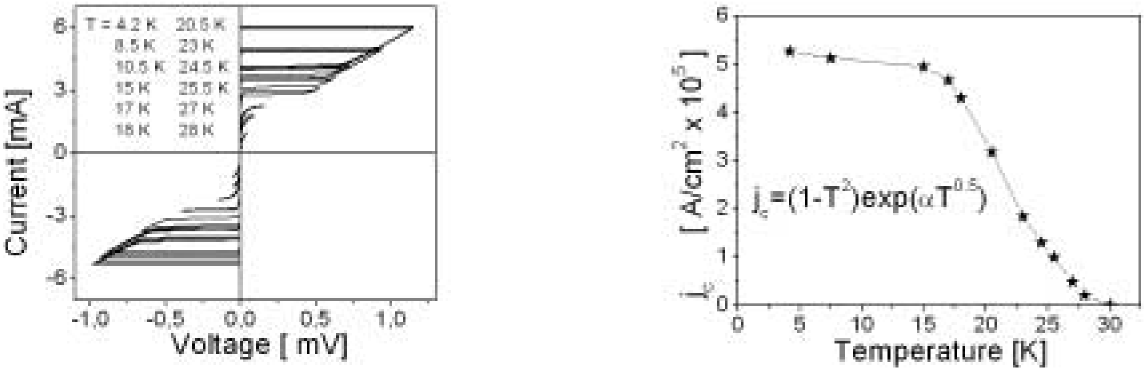

a) b)

Fig.6 V-I characteristics measured on the micro strip at indicated temperatures (a) and corresponding dependence of critical current density j_c vs. temperature (b).

The large value of α obtained from fitting procedure predicts very thin (several nanometers) normal regions between superconducting grains, and it should be the reason of lowered superconducting critical temperature ($T_{cmax} \leq 36$ K) in comparison with theoretical critical temperature $T_{c0} = 39$ K, and critical current density ($j_{cmax}(4.2\ K) \leq 10^6$ A/cm^2) in our MgB_2 thin films.

Acknowledgment

The authors thanks to the Ministry of Education of the Slovak Republic for support of the grant "Nanostructures for nanometrology, sensors and cryoelectronics". This work was also partially supported by the VEGA project No. 1/2011/05 and APVT project No. APVT-20/011804.

REFERENCES

[1] Y.Harada, M.Uduka, Y.Nakanishi, N.Yashimoto, and M.Yoshizawa. Physica C **412-414** (2004) 1383.

[2] A. Plecenik, L.Satrapinsky, P.Kúš, Š.Gaži, Š. Beňačka, I.Vávra, and I.Kostič, *Physica C* **386** (2001) 251.

[3] A.Brinkman et al., Physica C **353** (3301) 1.

[4] Z.Mori, T.Doi, Y.Ishizaki, H.Kitaguchi, M.Okada, K.Saitoh, and Y.Hakuraku, Physica C 412-414 (2004) 1371.

[5] A. Barone and G. Paterno, Physics and Applications of the Josephson Effect, John Willey & Sons, New York (1982).

[6] K.K.Likharev, Superconducting weak links, Review of Modern Physics **51** (1979) 101.

Research projects Department of experimental Physics FMPI Comenius University - TiB_2 buffer layer for superconducting MgB_2 thin films prepared by magnetron sputtering.

P. Kus, A. Plecenik

Department of Experimental Physics FMPI, Comenius University, SK- 84215 Bratislava, Slovak Republic, kus@fmph. uniba.sk

1. Introduction

Sputtering is one of the most commonly used methods for deposition of thin films. High melting point materials which are hard to deposit by evaporation techniques are easily deposited using sputtering. Sputtering techniques range from a simple dc glow discharge sputtering which is limited to the sputtering of conductive targets, to the rf sputtering where any target regardless of its conductivity can be sputtered. Sputtering is widely used in a wide range of application fields (in the micro and nano-electronics industry, basis materials research, manufacturing of sensors, optical devices, superconductors thin films, hard coating technology, etc). Its popularity stems from the simplicity of the physical processes involved, versatility of the technique, and flexibility for alteration and customization.

In our laboratories, at this time, we used this physical method for preparation of textured buffer layers TiB_2 for subsequent oriented growth of superconducting MgB_2 thin films (research project Superconductors for future technologies), for preparation of different types of hard coatings (TiB_2, TiB_2N, TiB_2Si, TiB_2SiN, TiAlN, TiAlSiN, etc, research project Nanocomposite coatings), preparation of nanostructured devices (Superconducting Single Photon Detector, Single Electron Tunneling Transistor and Sensors of gases) based on titanium and tungsten thin films (research project Nanostructures for cryoelectronics, sensors and metrology) and development of technology for preparation of superconducting solid state qubits for quantum computers. Because of wide research program on Department of experimental physics, we focus our attention in this contribution on the one specific program – preparation of TiB_2 buffer layers for superconducting MgB_2 thin films.

2. Experimental

TiB_2 thin film with thickness below 200 nm was deposited on (100) Si substrate in modified PVD system BALZERS BA k 550 using DC-magnetron sputtering in an inert Ar-atmosphere. A hot-pressed TiB_2 target with 50 mm in diameter and 5 mm in thickness was used. Target to substrate distance was 30 mm. Before deposition, substrates were ultrasonically cleaned in alcohol and distilled water. After pumping-down procedure (reached basic pressure was 10^{-4} Pa) the target was pre-sputtered during 10 minutes. Argon pressure during deposition was 0.2 Pa. Magnetron current and voltage was 0.1 A and 500 V. During deposition, the substrates were on floating potential. Deposition time was 5 minutes. After deposition, TiB_2 films were ex-situ annealed in vacuum furnace. Annealing process was hold in small Ar overpressure. Temperature was being held on 700°C during 10 minutes for TiB_2 layers and on 680°C during 3 minutes for MgB_x layers. MgB_x layers were prepared by means of simultaneous deposition from RF magnetron sputtering system equipped with boron target and a DC magnetron sputtering system equipped with magnesium target. Prior to the deposition the chamber was pumped-down to basic pressure of 10^{-4} Pa. The boron target was sputtered during the whole deposition process (deposition power was 250 W). The magnesium target was sputtered during 30 second cycles interrupted by 120 second ongoing pause (magnetron current was 0.1 A and magnetron voltage was 300 V). Target to substrate distance was 4 cm. Pressure of inert Ar atmosphere during deposition was 7.4x10^{-2} Pa.

3. Results

We focused our attention on the influence of the TiB_2 buffer layer on the superconducting properties of MgB_2 thin films. The MgB_2 thin films were prepared on the three different substrates: a) Si (100) without buffer layer, Si (100) buffered with unannealed TiB_2 buffer layer, c) Si (100) buffered with annealed TiB_2 buffer layer. Unannealed TiB_2 buffer layer exhibits no diffraction, however XRD measurements of annealed TiB_2 clearly exhibit diffraction at 27.6 degree correlated with creation of epitaxial TiB_2 layer with (001) orientation (Fig. 1). Superconducting MgB_2 thin films prepared on annealed TiB_2 buffered Si substrate exhibit onset temperature transition to superconducting state T_{con} at 33 K and zero resistance critical temperature T_{c0} at 30.2 K. The superconducting transition width obtained on MgB_2 thin films prepared with TiB_2 buffer layer is very sharp (Fig. 2).

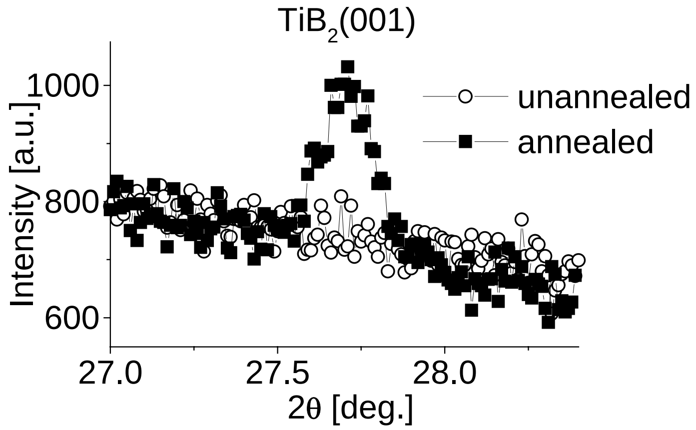

Fig.1 The XRD pattern of annealed and unannealed TiB_2 buffer layers.

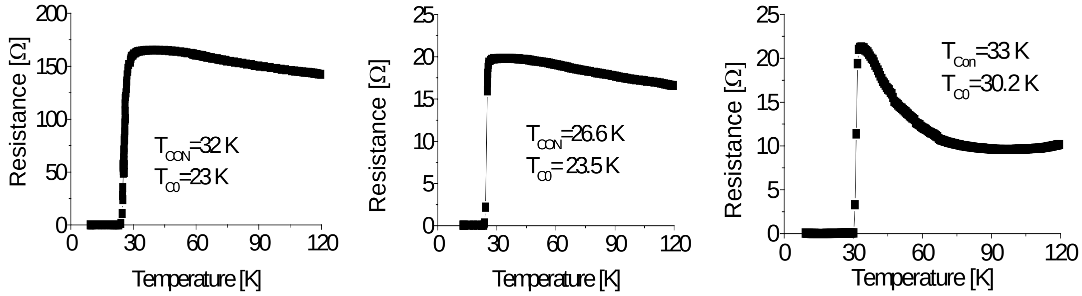

a) b) c)

Fig.2 R (T) dependences of annealed MgB_2 thin films prepared on Si substrate a), on Si substrate with unannealed TiB_2 layer b) and on Si substrate with annealed TiB_2 layer c).

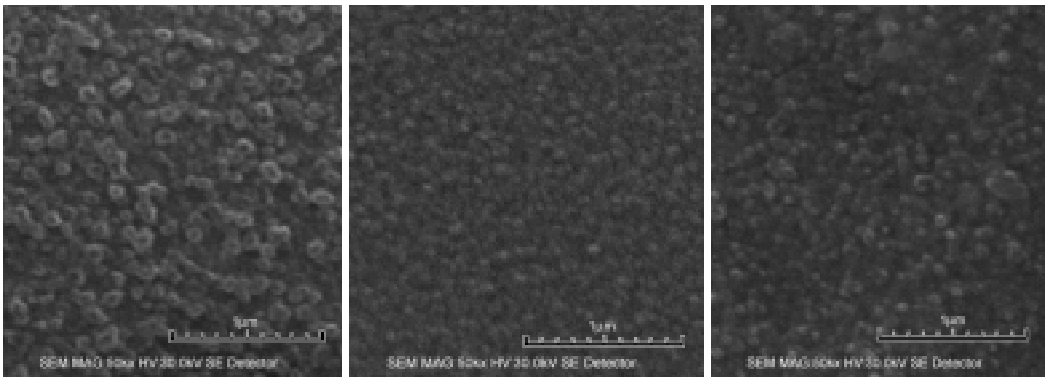

a) b) c)

Fig.3 The morphology of MgB_2 thin film prepared on Si substrate a), on Si substrate with unannealed TiB_2 layer b) and on Si substrate with annealed TiB_2 layer c).

Influence of TiB_2 buffer layer on the superconducting properties and morphology of MgB_2 thin films is clearly visible from Fig. 2 and Fig. 3. Insertion of the buffer layer makes the film surface considerably smoother and hence more suitable for patterning of the structures.

4. Conclusion

Oriented TiB_2 layers are expected to play an important role in silicon-superconductor technology and serve as an excellent buffer layer for subsequent growth of middle temperature superconductor MgB_2. Therefore it is necessary to investigate and optimize further the annealing process with TiB_2 buffer layer. This work is in the progress.

Acknowledgments

This work has been supported by research program sponsored by the Ministry of Education of the Slovak Republic, grants “Nanostructures for cryoelectronics, sensors and metrology” and ” Nanocomposite coatings” and supported by the Slovak Grant Agency for Science program No. 2/7199/20 and UK/341/2005. Special thanks to our colleagues and PhD. students for collaboration in these research activities.

References

[1] A.Plecenik, L.Satrapinsky, P.Kúš, et al. MgB2 superconductor thin films on Si and Al2O3 substrates, Physica C 363 (2001) 224.

[2] P.Kúš, A. Plecenik, L. Satrapinsky, et al. Supercoducting properties of MgB_2 thin films prepered on flexible plastic substrates, Appl. Phys. Lett. 81 (2002) 2199.

[3] B.Grancic, M.Mikula, L.Hruba, M.Gragor, M.Stefecka, A.Csuba, E.Dobrocka, A.Plecenik, P.Kus, The influence of deposition parameters on TiB_2 thin films prepared by DC magnetron sputtering, Vacuum 80 (2005) 174.

[4] F. Kunc, J. Musil, P. H. Mayrhofer and C. Mitterer, Low-stress superhard Ti-B films prepared by magnetron sputtering, Surf. Coat. Technol. 174 – 175 (2003) 744.

Superhard TiB_2 coatings prepared by DC magnetron sputtering

Branislav Grančič[1], Marián Mikula[2], Radovan Mičunek[1], Maroš Gregor[3], Miloslav Štefečka[3], Adrian Csuba[2], Miroslav Zahoran[1], Andrej Plecenik[1], and Peter Kúš[1]

[1]Department of Experimental Physics, FMPI CU, Mlynská dolina, Bratislava, Slovakia

[2]Institute of Materials and Machine Mechanics, SAS, Račianska 75, Bratislava, Slovakia

[3]Biont a.s. , Karloveská 63, Bratislava, Slovakia

Abstract

TiB_2 layers were prepared by balanced and unbalanced DC magnetron sputtering. Influence of substrate bias voltage on the properties of layers was observed.

Introduction

Bulk titanium diboride is a typical intrinsic hard material with hexagonal C32 crystal structure which is stable up to very high temperatures [1]. This material is suitable for preparation of hard coatings for wear resistance enhancement of cutting tools. These coatings are able, depending on the texture, to reach hardness more than 40 GPa [2]. By adding some content of nitrogen into the deposition atmosphere it is possible to prepare very perspective nanocomposite TiBN.

Experiment

Coatings were deposited onto substrates by means of balanced (50 mm in diameter) and unbalanced (100 mm in diameter) magnetrons using TiB_2 target (99.5%) in argon atmosphere. Tungsten carbide and stainless steel substrates were ultrasonically cleaned in acetone, isopropylalcohole and distilled water before deposition. After evacuation to initial pressure 10^{-4} Pa the chamber was filled with argon to 10 Pa. Additional cleaning of the substrates was done in plasma by application of voltage - 1000 V between the substrate holder and the electrode for 15 minutes. After cleaning of the substrates, deposition from the target was started at pressure of argon 0.5 Pa. Magnetron power was 100 W (balanced magnetron) and 700 W (unbalanced magnetron). Substrate distance was 40 mm (balanced magnetron) and 70 mm (unbalanced magnetron). Substrate voltage bias was changed from 0 V to – 500 V.

Chemical composition of deposited coatings was analyzed by Auger Electron Spectroscopy (AES) and Glow Discharge Optical Emission Spectroscopy (GDOES - LECO SA – 2000). Surface roughness and morphology was evaluated with Atomic Force Microscope (AFM - SOLVER P47) and Scanning Electron Microscope (SEM - TESCAN). X-ray Diffraction (XRD) in Bragg – Brentano geometry with CuK_α monochromator and TEM (JEOL JEM 100C) electron diffraction were used to evaluate the coating crystallinity and texture. Coating hardness and adhesion were measured by Vickers microindentor and scratch tester.

Results

Coating analysis was performed simultaneously in both cases - balanced magnetron A) and unbalanced magnetron B).

A) AES analysis showed that the Ti/B ratio in coatings deposited from balanced magnetron was nearly equal to ½. Also a small quantity of impurities (oxygen and carbon) was observed in coatings (Fig. 1). All coatings were very smooth with mirror-like surface. AFM showed that the coated substrates achieved low roughness $R_a = 4$ nm (Fig. 2). Cross section TEM confirmed that the coating roughness was influenced by substrate surface (Fig. 3). Deposited coatings were XRD amorphous which means that no diffraction peak was observed. However, the electron diffraction pattern confirmed presence of nanocrystalline structure in TiB_2 coatings (Fig. 4). Coating hardness was higher than 46 GPa (10 mN load)

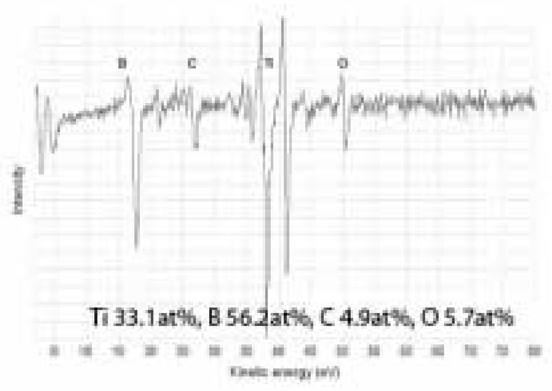

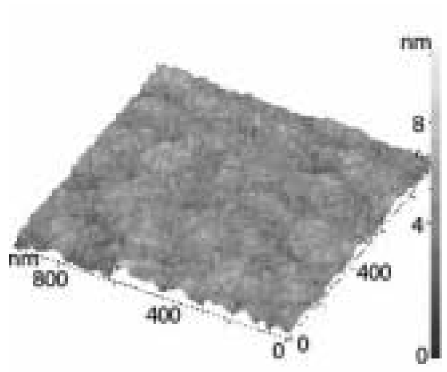

Fig.1 AES chemical anysis of TiB_2 coatings. Fig. 2 AFM analysis TiB_2 surface

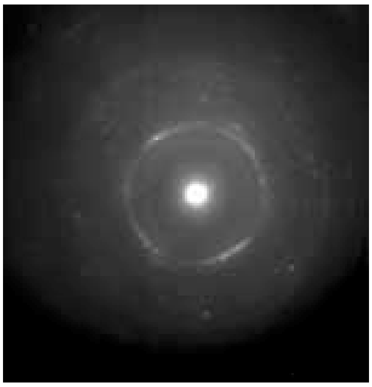

Fig. 3 TEM cross section of TiB_2 coating deposited on steel substrate.
Fig. 4 The electron diffraction pattern of TiB_2 coating.

B) Ion current density on substrates was approximately 1 mA/cm^2. GDOES analysis confirmed constant Ti/B ratio in each coating depth (Fig. 5). Small quantity of carbon present in surface region was decreased in higher coating depths. Depending on deposition time, the coating thickness was 1 μm – 5 μm. XRD analysis showed occurrence of TiB_2 (001) orientation depending on applied substrate bias voltage in the range from -150 V to - 400 V (Fig. 6). Outside this interval no coating diffraction peak was observed. Cross section SEM confirmed columnar character of

TiB_2 coatings (Fig. 7). Regardless to the deposition condition all coatings were harder than 40 GPa (10 mN load).

Conclusion

Both of the magnetron deposition methods (balanced and unbalanced) were able to produce coatings of TiB_2 harder than 40 GPa (10 mN load). TiB_2 coatings deposited by balanced magnetron exhibited nanocrystalline structure. Textured TiB_2 (001) coatings were prepared by unbalanced magnetron.

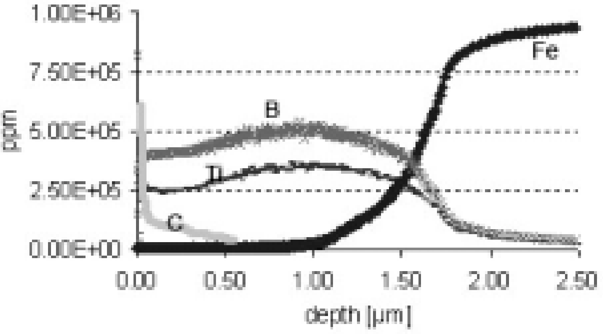

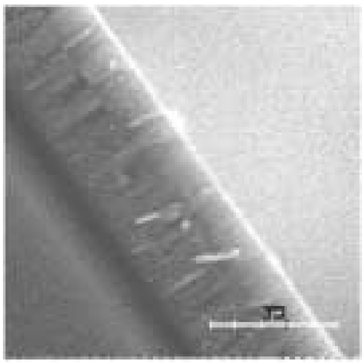

Fig. 5. GDOES depth profile of TiB_2 coating.

Fig. 7 SEM cross section of TiB_2 coating prepared by unbalanced magnetron sputtering

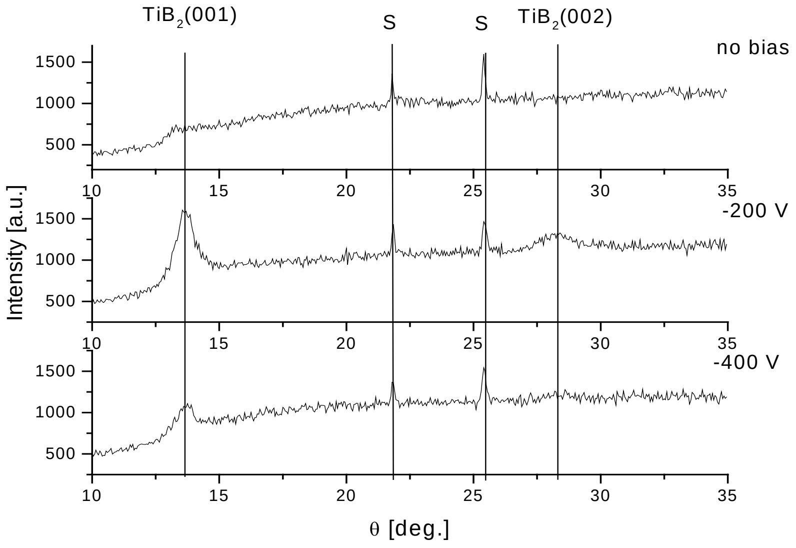

Fig. 6 XRD analysis of TiB_2 coatings deposited by different values of substrate bias.

Acknowledgment

This work was supported by following grants: UK/341/2005, VEGA 2/4165/04 and Applied Research Project Nanocomposite coatings for Technical Application.

Literature:

[1] R.G. Munro, J. Res. Natl. Inst. Stand. Technol. 105 (2000) 709 – 720.
[2] F. Kunc, J. Musil, P. H. Mayrhofer and C. Mitterer, Surf. Coat. Technol. 174 – 175 (2003) 744 – 753.

Tales of Glory: the Birth of Hydrogen Bond

David Cappelletti[1], Fernando Pirani[2], Vincenzo Aquilanti[2]

[1] *Dipartimento di Ingegneria Civile ed Ambientale, Università di Perugia, Perugia, Italy*

[2] *Dipartimento di Chimica, Università di Perugia, Perugia, Italy*

Intermolecular non-covalent interactions, in particular the hydrogen-bond, are central to various areas of chemistry and their role is crucial for modelling myriads of phenomena, ranging from biology to environmental science. In spite of almost a century of efforts, their detailed nature still awaits further experimental and theoretical attention at the basic level. The reported accurate measurements by molecular beam collision experiments of interaction forces between water and rare gases are delicate probes of incipient hydrogen–bond formation increasing along the series from He to Xe — as confirmed by accompanying *ab-initio* calculations — and thus yield quantitative indications for molecular dynamics simulations of non–covalently bound systems[1,2]. Further measurements have been addressed to characterize the H_2O-H_2, -CH_4, -N_2 and -O_2 weakly bound complexes, which are of species of interest for the radiation budget of the atmosphere[3]. For these systems the intermolecular forces are more complicated than in the case of rare gas containing complexes, and an interplay between experiments and theory is necessary to obtain some information on the features of potential energy surfaces. For the H_2O-H_2 complex the most recent ab-initio calculation[4] have been found in a relatively good agreement wit the experimental data, while for the other cases the work is still in progress.

1. V.Aquilanti, E. Cornicchi, M. Moix-Teixidor, N. Saendig, F. Pirani, D. Cappelletti, *Angew. Chemie Int. Ed.*, **44**, 2357 (2005)
2. D. Cappelletti, V.Aquilanti, E. Cornicchi, M. Moix-Teixidor, F. Pirani, *J. Chem. Phys.*, **123**, 024302 (2005).
3. *Water and weakly Interacting Species in Atmospheric Modelling*, a CECAM Workshops, Lyon, April 25-27 (2005), chair. D. Cappelletti.
4. M.P.Hodges, R.J.Wheatley, G.K.Schenter, A.H.Harvey, *J.Chem.Phys.*, **120**, 710 (2004).

The oxidation chemistry of benzene/air mixtures in atmospheric pressure plasma environments

D. Ascenzi, F. Casagrande, P. Franceschi, G. Guella, P. Tosi

Dipartimento di Fisica, Università di Trento, Via Sommarive 14, 38050 Povo (TN) Italy
(e-mail: ascenzi@science.unitn.it)

ABSTRACT

The chemistry of air-benzene mixtures in a plasma environment at atmospheric pressure has been investigated. Ionic products were detected by an Atmospheric Pressure Chemical Ionization Mass Spectrometer (APCI-MS) both in the positive and in the negative ion mode. Reactivity leading to neutral products was studied in a dielectric barrier discharge plasma with GC-MS off-line analysis of products. Even in the presence of trace amounts of O_2, several oxygenated products were observed. In particular, the positive APCI-MS ion spectra show intense peaks, which have been attributed to $C_6H_6O^+$ (phenol), $C_{12}H_{11}O^+$, $C_{12}H_{11}O_2^+$. In order to shed some light on the ionic mechanisms of benzene oxidation some of the relevant ion-molecule elementary processes were studied using a guided ion beam tandem mass spectrometer. Ab-initio calculations using density functional theory were carried out to characterize reaction energetics.

1. Introduction

The study of oxidation processes of aromatic compounds is of significant interest. Aromatics are mostly toxic and harmful to the environment and they are known to be formed to some extent in most combustion processes. To this purpose, benzene provides the simplest model to study the combustion processes of aromatic molecules [1, 2].

Plasma treatment has been proposed as an effective method for the decomposition of volatile toxic compounds and organic wastes [3]. Furthermore, the direct hydroxylation of benzene with molecular oxygen in a non thermal atmospheric plasma has been recently investigated as an alternative method for phenol synthesis [4, 5].

The chemistry within atmospheric pressure plasmas is dominated by multiple collisions among ions, radicals and neutral species both in the ground and excited states. The aim of our study is to understand the complex reaction mechanisms leading to benzene oxidation by detection of both ionic and neutral species. Ionic products from an Atmospheric Pressure Chemical Ionization source, which is a small size non thermal corona plasma, have been detected by on-line mass spectrometry. Stable neutral products from an atmospheric pressure Dielectric Barrier Discharge (DBD) plasma have been studied by gas chromatography coupled with mass spectrometric detection (GC-MS).

2. APCI-MS spectra: ionic products

APCI measurements on benzene were performed in the positive and negative ion mode using a Bruker Esquire-LCTM quadrupole ion-trap mass spectrometer (Bruker-Daltonics, Milano, Italy) equipped with an APCI interface (Hewlett-Packard/Agilent Technologies). Benzene was introduced either as liquid (injection flow 6ml/h) or as vapor by connecting the headspace over the liquid with the source environment and flushing with pure N_2. Pure dry nitrogen is also used as nebulizer and dry gas. Due to the geometry of the APCI source, some backstream of room air is always present in the surrounding of the corona needle, where the percentage of O_2 was estimated to be ~5 % by gas chromatography (GC) measurements. The amount of O_2 can be increased to 20% using air as nebulizer gas.

Positive ion mode APCI

The positive ion APCI mass spectra of benzene is relatively congested and show some remarkable features, among which:

- the parent ion $M^{+\cdot}$ attributable to the benzene radical cation is not the most abundant ion in the spectrum;
- ions containing one or more O atoms are detected with relevant intensities at m/z 94 ($C_6H_6O^+$), 171 ($C_{12}H_{11}O^+$) and 187 ($C_{12}H_{11}O_2^+$).
- other oxygen containing ions, although of smaller intensities, have been clearly detected at m/z 81 ($C_5H_5O^+$), 95 ($C_6H_7O^+$), 109 ($C_6H_5O_2^+$) and 203 ($C_{12}H_{11}O_3^+$).

Elemental formulas and some structural information of the O-containing products have been determined by deuterium labeling of benzene, MS^2 experiments and isotopical H/D exchange reactions observed after D_2O addition.

Similar oxygenated compounds have also been detected in the APPI (atmospheric pressure photoionization) spectrum of benzene [6, 7]. In particular, the authors have assigned the peak at m/z 94 to phenol molecular cation. In our experiment, the MS^2 spectrum of the ion at m/z 94 shows a facile primary loss of a neutral species of 28 amu (CO molecule). Furthermore, by addition of D_2O in the APCI source, a marked exchange reaction occurs which shifts the ion peak from m/z 94 to m/z 95. Both such results reasonably support the conclusion that ions at m/z 94 have a phenol-like structure, with the O-bound proton leading to facile scrambling with D_2O.

On similar basis, and following the results of other experiments performed with C_6H_5OH/air mixtures in APCI, we believe that the ions detected at m/z 171 ($C_{12}H_{11}O^+$) and m/z 187 ($C_{12}H_{11}O_2^+$) have most likely the structures of protonated diphenyl ether and protonated phenoxyphenol respectively.

The intensities of the oxygenated peaks in the APCI spectrum are enhanced when the amount of O_2 in the source is increased. The possible role of water (always present, in traces through residual humidity, in our APCI source) in the generation of oxygenated compounds, in particular of the $C_6H_6O^+$ ion, has been investigated by adding either H_2O or its isotopically labeled analogue $H_2{}^{18}O$ in the corona source region. In general water addition leads to an increase in the ratio $[C_6H_6O^+]/[C_6H_6^+]$ but when ^{18}O labeled water is used no substantial ^{16}O /^{18}O shift of the relevant ion peaks is observed, suggesting a minor participation of the oxygen atom of the water molecule in the generation of ions at m/z 94 (as well as of ions at m/z 171 and 187).

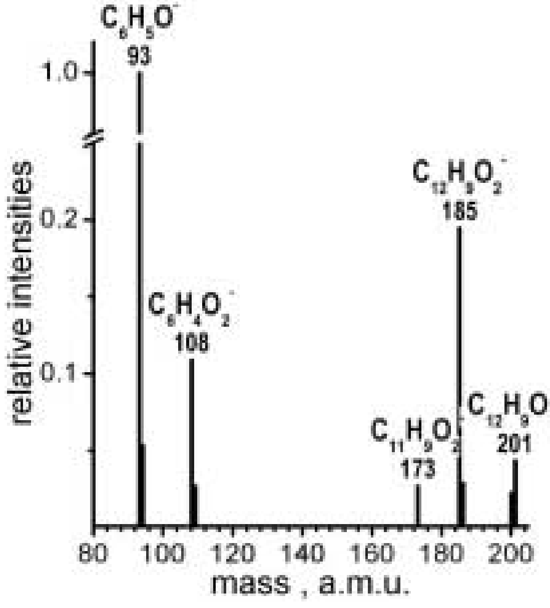

Figure 1: Negative ion mode APCI of a benzene/air mixture

Negative ion mode APCI

The negative ion APCI mass spectrum (shown in Fig. 1) is much clearer than the positive ion one. The most abundant species is the ion at m/z 93 ($C_6H_5O^-$). Such anion has been previously observed in a negative APCI-MS of benzene in N_2/N_2O carrier gas and attributed to the hydrogen radical displacement reaction by O^- ions on benzene [8]. Other oxygenated ions have been detected at m/z 108, 173, 185 and 201 and attributed to compounds with elemental formula $C_6H_4O_2^-$, $C_{11}H_9O_2^-$, $C_{12}H_9O_2^-$ and $C_{12}H_9O_3^-$ respectively.

GIB experiments

We have studied the possible ion-molecule reactions leading to $C_6H_6O^+$ in a home-built guided ion beam tandem mass spectrometer (GIB-MS) equipped with a RF octopole scattering cell for trapping of reagent and product ions. Pressure in the cell can be varied in the range 10^{-6}-10^{-3} mbar. When working in the high pressure range, conditions are similar to those operative in the CI (chemical ionization) source of any commercial analytical mass spectrometer. Therefore, with our GIB-MS experimental set-up it is possible to study the generation of secondary ions from selected ionic reagents, singled out from the total ionic population present in the CI source.

The generation of the ion $C_6H_6O^+$ in APPI spectra of benzene had been previously attributed [6, 7] to the attack of benzene radical cation $C_6H_6^+$ on molecular oxygen. In our GIB apparatus no evidence has been found of $C_6H_6O^+$ formation from the reaction of $C_6H_6^+$ with O_2, which leads essentially to collision induced dissociation of the projectile ion. Conversely, when phenylium ions $C_6H_5^+$ react with O_2 we observe the following product channels:

$$
\begin{aligned}
C_6H_5^+ + O_2 \quad &\rightarrow \quad C_4H_5^+\ (m/z=53) + 2CO \qquad (1)\\
&\rightarrow \quad C_5H_5O^+\ (m/z=81) + CO \qquad (2)\\
&\rightarrow \quad C_6H_5O^+\ (m/z=93) + O \qquad (3)
\end{aligned}
$$

Rate constants for channels (1) and (2) have been previously measured in SIFT experiments [9], whereas reaction (3), to the best of our knowledge, has not been observed before. Subsequent hydrogen abstraction of the $C_6H_5O^+$ produced via the ion-molecule process (3) from H_2O or C_6H_6 in the APCI source may result in $C_6H_6O^+$ formation. Ab-initio calculations of reaction energetics, using density functional theory, are currently carried out to investigate the relevance of such mechanism for the phenol cation formation.

O_2^+ and O^+ ions are known to be produced in a corona discharge in air by electron impact ionization. Flow tube experiments [10, 11] have already shown that the reactivity of these ionic species with C_6H_6 proceeds only by rapid non dissociative charge transfer ($k = 1.4*10^{-9}$ $cm^3 molecule^{-1} s^{-1}$ in the O_2^+ case and $k = 1.9*10^{-9}$ $cm^3 molecule^{-1} s^{-1}$ for O^+ [10]). Therefore, phenol cation synthesis from bond-forming reactions of oxygen ions can be excluded.

Further GIB experiments will be performed to elucidate other possible ionic mechanisms leading to further oxidation of phenol and diphenyl ether-like compounds.

3. Dielectric barrier discharge: GC-MS of neutral products

Benzene-N_2 mixtures with trace amounts of O_2 (3-4%) have been treated in an atmospheric pressure Dielectric Barrier Discharge (DBD) plasma reactor. Stable neutral products have been studied off-line by means of a GC-MS analyzer (Thermo-Finnigan Trace DSQ) as a function of the discharge parameters. The primary stable products were phenol (C_6H_5OH), biphenyl ($C_{12}H_{10}$) and products deriving from the subsequent oxidation of phenol or related compounds. In particular, *o*- and *p*-hydroxybiphenyl ($C_{12}H_{10}O$), diphenyl ether ($C_{12}H_{10}O$), 2- and 4-phenoxyphenol ($C_{12}H_{10}O_2$), 2,2'-dihydroxybiphenyl ($C_{12}H_{10}O_2$) have been observed.

4. Conclusions

In general, the production of ionic species under APCI conditions has been attributed to fast exothermic ion-molecule reactions (mostly charge exchange and/or proton transfer) of primary and secondary ions with the most abundant neutral species.

Mechanistic schemes based on the reactions of radicals (e.g. the hydroxyl radical OH or O atoms, which are the most important radicals generated in air plasmas) with abundant neutrals followed by post-ionization of products can usually be neglected due to the low ionization efficiencies of molecules. However, in the presence of relevant concentrations of highly reactive radicals, it can not be excluded that the chemistry of neutral species may influence the relative abundances of ionic products. Moreover, radical mechanisms most likely play a role in the production of neutral species. In particular, radical routes for the generation of phenol and other oxygenated compounds in benzene/O_2 plasmas have been proposed [12-14].

Simultaneous mapping of the ion population, of the major ionic reactions, and of the abundances of stable neutrals after plasma treatment is necessary to have a complete picture of the complex processes responsible for benzene oxidation.

Work is in progress in our laboratory to extend the investigation to other ionic reactions and to infer the role played by radicals.

5. References

[1] M. U. Alzueta, P. Glarborg, K. Dam-Johansen, Int. J. Chem. Kinet. **32**, 498 (2000).

[2] I. D. Costa, R. Fournet, F. Billaud, and F. Battin-Leclerc, Int. J. Chem. Kinet. **35**, 503 (2003).

[3] E. Marotta, G. Scorrano, C. Paradisi, Plasma Process. Polym. **2**, 209 (2005).

[4] D.-W. Lee, J.-H. Lee, B.-H.Chun, K.-Y. Lee, Plasma Chem. Plasma Process. **23**, 519 (2003).

[5] H. Sekiguchi, M. Ando, H. Kojima, J. Phys. D: Appl. Phys. **38**, 1722 (2005).

[6] M. Tubaro, E. Marotta, R. Seraglia, P. Traldi, Rapid Commun. Mass Spectrom. **17**, 2423 (2003).

[7] P. Traldi, E. Marotta, Adv. Mass Spectrom. **16**, 275 (2004).

[8] M. Annan, P. Vouros, Am. Chem. Soc. Mass Spectrom. **5**, 367 (1994).

[9] G. B. I. Scott, D. B. Milligan, D. A. Fairley, C. G. Freeman and M. J. Mc Ewan J. Chem. Phys. **112**, 4959 (2000).

[10] S.T. Arnold, S. Williams, I. Dotan, A.J. Midey, R.A. Morris, A.A. Viggiano, *J.* Phys. Chem. A **103**, 8421 (1999).

[11] P. Spanel, D. Smith, Int. J. Mass Spectrom. **1**, 181 (1998).

[12] T. Berndt, O. Böge, Z. Phys. Chem. **218**, 391 (2004).

[13] T. Berndt, O. Böge, Phys. Chem. Chem. Phys. **3**, 4946 (2001).

[14] M. Tezuka, T. Yajima, Plasma Chem. Plasma Process. **16**, 329 (1996).

Multidimensional tunneling dynamics in the prototype molecule NH_3

Frédéric Le Quéré, Roberto Marquardt* and Kenneth Sagui

Laboratoire de Chimie Théorique - Université de Marne-la-Vallée
F-77454 Marne-la-Vallée CEDEX 2 - *roberto.marquardt@univ-mlv.fr

ABSTRACT

Previous studies of the explicit time-dependent multidimensional quantum wave packet dynamics [1] have shown that, under laser excitation, ammonia undergoes ultrafast inversion in the sub-picosecond time domain and that this motion is governed by a multidimensional tunneling mechanism, even if the vibrational energy available after excitation largely exceeds the barrier for tunneling. For these studies, the time dependent Schrödinger equation was solved by expansion of a four-dimensional wave function in a large basis of spectroscopic states within the `URIMIR` program package [2]. In the present paper we review some of the previous results and report on ongoing, full-dimensional calculations using a new potential energy surface [3] and the multi-configurational time-dependent Hartree method (`MCTDH`) [4].

1. Introduction

Ammonia is a prototype molecule for large amplitude nuclear motion. Stereomutation in general and the inversion motion of ammonia in particular have been extensively studied for almost one century. While ammonia itself must be considered to have a completely delocalized and therefore non-classical molecular equilibrium structure, because of the fast tunneling in the vibrational ground state, its potential energy surface constitutes an ideal playground for studying the intramolecular kinetics of isomerization or racemization reactions under rather realistic conditions.

We might consider, for instance, a molecular structure that is initially localized on one side of the double well say, in the vibrational ground state (Figure 1). In the absence of external forces, such a structure will evolve periodically in time, because of the tunnel effect, with an approximate period of 48 ps.

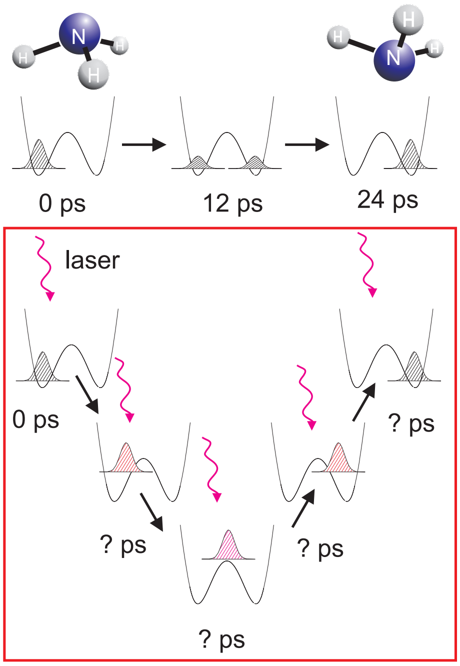

Figure 1: Laser-induced-inversion scheme

During this non-classical motion, planar molecular structures are hardly populated. In a previous work, we have inquired about the possibility of inducing a semi-classical motion over the inversion barrier by using an appropriate external driving field such as a laser [1]. Figure 1 suggests that, ideally, the wave packet would move coherently from one side of the double well to the other, while the molecule is absorbing sufficient energy from the laser field to overcome the barrier. Precise time scales and wave packet forms are fortiori unknown.

In [1] it was discussed that an appropriate means of inducing a semi-classical wave packet motion over the barrier should include multi-photon excitation of semi-classical vibrations that are somewhat orthogonal to the inversion manifold. Intramolecular vibrational redistribution (IVR) should then sooner or later drive the localized wave packet over the barrier. However, the wave packet was always found to undergo a very fast tunneling motion. A laser driven, semi-classical motion over the barrier, under substantial population of planar structures, seems difficult to be realized, if tunneling is the governing kinetic mechanism.

The calculations in [1] were done using global, full-dimensional, realistic analytical representations of the potential energy and dipole moment hyper-surfaces of ammonia [5]. However, the wave packet dynamics was calculated approximately in a reduced, four-dimensional space with the program package [2] because of computational constraints. Although the reduced space was chosen carefully such as to reduce errors arising from frozen dynamical coordinates, full-dimensional calculations are important for conclusive results. Furthermore, the representation of the potential energy surface used in [1] overestimates some tunneling splittings of excited NH stretching modes, which might as well contribute to artificially increasing the importance of the tunneling mechanism in the intramolecular kinetics. We are therefore currently carrying out investigations of this system using improved potential energy surfaces. The present work reports on ongoing calculations using the multi-configurational time-dependent Hartree method (`MCTDH`) [4] and the code developed in Heidelberg [6].

2. Theory

The `MCTDH` method is an approximative method for the iterative, self-consistent numerical integration of the time dependent Schrödinger equation. The method involves procedures for integrating non-linear differential equations and is therefore significantly more complex than the traditional method of expanding the time dependent wave function in a basis set of stationary states - and using linear algebra - to integrate the originally linear differential equation. Nevertheless, it has been proven to be very efficient for applications in large systems with many dimensions requiring many basis functions. For an extensive review see [4].

Molecular structures are described with poly-spherical coordinates $\vec{r}_i$ $(i = 1, \ldots, 3)$ of the Radau-type [7]. Configuration space is entirely covered by variation of three lengths $r_i = \mid \vec{r}_i \mid$ $(i = 3, \ldots, 1)$, which correspond essentially to the three NH bond lengths, two polar angles $\theta_i = \arccos((\vec{r}_i \cdot \vec{r}_3)/r_i r_3)$ $(i = 2, \ldots, 1)$ and one corresponding dihedral angle ϕ_1 (Figure 2, X=N, Y=H). The inversion motion is described by variation of ϕ_1, which becomes 180° at planarity. Equilibrium values corresponding to the equilibrium structure from [3] are $r_i \approx 99.8$ pm $(i = 1, \ldots, 3)$, $\theta_i \approx 108.7°$ $(i = 1, \ldots, 2)$ and $\phi_1^{\mathrm{L}} \approx 118°$, for instance, for the well on the left hand side, and and $\phi_1^{\mathrm{R}} \approx 242°$ for the well on the right hand side of Figure 1.

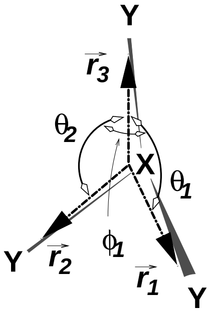

Figure 2: Definition of coordinates (see text and [7])

In `MCTDH`, initial conditions are given by defining the wave function in configuration space. In the following we shall concentrate on wave functions that are Gaussian distributions in each of the foregoing mentioned coordinates with variable centers c, widths w and phases p. While the variation of the center and width of the distribution allows to define spatially localized but vibrationally excited states, variation of the phase allows to monitor the initial linear momentum pertaining to that particular coordinate, and thus the initial amount of vibrational kinetic energy. With these studies we aim at investigating the effect of the variation of a minimal set of parameters needed to define spatially localized molecular structures on the subsequent quantum dynamics. It should be possible to generate such states with standard methods used in coherent control [8], but rather than discussing the excitation process itself, we shall concentrate here on the subsequent time dependent dynamics after excitation.

We consider here initially localized molecular structures where one particular NH bond is considerably elongated from its equilibrium value, while molecules are concentrated on the "left" well of Figure 1. Data analysis is done by inspection of the time evolution of reduced space vibrational and rotational probability densities

$$P_r(r,t) = \int |\psi|^2 d\tau_r \tag{1}$$

$$P_\phi(\phi,t) = \int |\psi|^2 d\tau_\phi \tag{2}$$

where r is the length of the Radau vector corresponding to the particular NH bond being elongated, $\phi = \phi_1$ is basically the inversion angular coordinate and $d\tau_r$, $d\tau_\phi$ are volume elements that exclude the coordinates r and ϕ, respectively. Integration is done over all coordinates except the one excluded. We shall also consider the kinetically relevant quantity

$$P_{\mathrm{L}}(t) = \int_0^{180^\circ} P_\phi(\phi,t) d\phi \tag{3}$$

which is proportional to the time dependent concentration of "left" species.

3. Results

Figure 3 shows wave packet and "left" species probabilities for two different initial conditions. Wave packet energies correspond to 12558 and 14115 cm^{-1} , respectively, for the upper and lower graphs. The zero point energy is calculated to correspond to 7436 cm^{-1} . The available vibrational energy after subtraction of the zero point energy corresponds hence to 5122 and 6679 cm^{-1} , respectively, which largely exceeds the energy to overcome the inversion barrier (1400 cm^{-1} , roughly, including variation of the zero point energy).

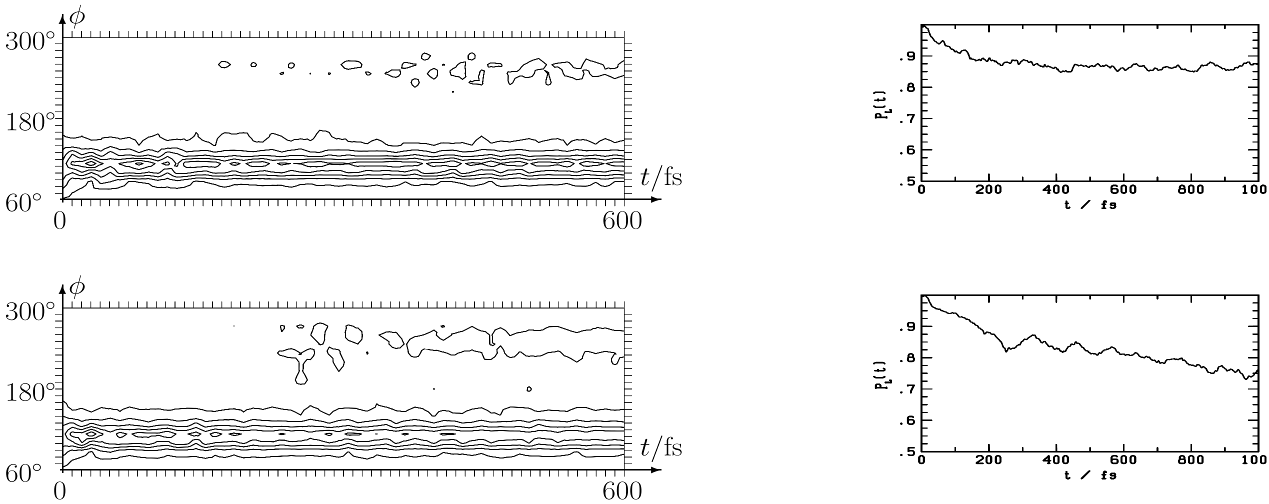

Figure 3: Time evolution of P_ϕ (left hand side) and P_{L} (right hand side) for initial conditions corresponding to Gaussian distributions centered at $< r_3 >= 114$ pm (top) and $< r_3 >= 124$ pm (bottom).

During inversion, the wave packet is simultaneously oscillating in the coordinate that is initially strongly displaced from equilibrium. Figure 4 shows the time evolution $P_r(r_3, t)$ following Eq. (1). Initially, this motion is semi-classical, but quantum-interference effects render the evolution highly delocalized after a few oscillations. The figure also invoke the occurrence of *semi-classical* windows discussed in previous work [9].

Inversion of vibrationally excited ammonia may thus occur on the sub-picosecond time scale, but this depends on the specific initial condition.

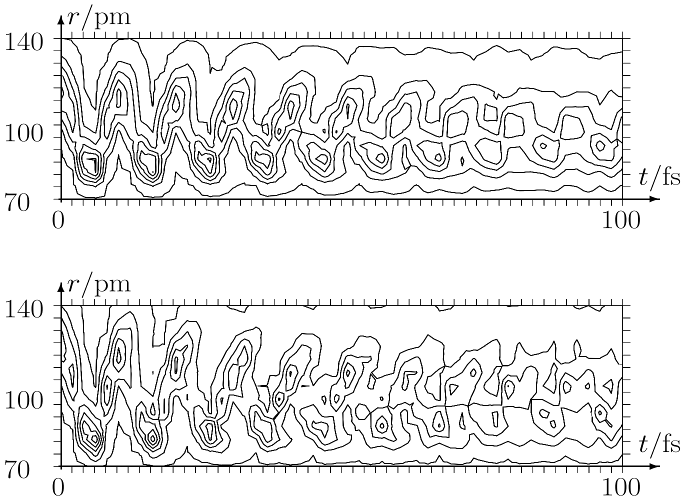

Figure 4: Time evolution of P_r (top and bottom graphs as in Figure 3).

4. Conclusions

The present results corroborate partially results from [1], where considerable inversion of up to 50% was found to occur in NHD_2 within the first 1000 fs under specific excitation conditions. The improved potential energy surface from [3] used in the present work leads to significantly smaller tunneling splittings of some excited vibrational states, which may indeed infer longer inversion times by tunneling. The formation of planar structures is not observed in the short time intervals considered here. Such structures should be observable, under two conditions: IVR is important as a driving mechanism for redistribution of the available vibrational energy into the inversion mode; IVR preserves the phase relation of the initial wave packet, such that tunneling becomes less important. The present results confirm previous findings qualitatively, but further investigations are needed, in particular, of the evolution of the projections of the wave packet on the set of spectroscopic states, which goes beyond the simple application of `MCTDH`.

References

[1] R. Marquardt, M. Quack, I. Thanopulos, and D. Luckhaus, J. Chem. Phys., **118**, 643–658 (2003).

[2] M. Quack and E. Sutcliffe, QCPE Bulletin, **6**, 98 (1986). R. Marquardt, M. Quack, and J. Stohner, to be published.

[3] R. Marquardt, K. Sagui, W. Klopper, and M. Quack, J. Phys. Chem. B, **109**, 8439–8451 (2005).

[4] M. H. Beck, A. Jäckle, G. A. Worth, and H.-D. Meyer, Phys. Rep., **324**, 1 (2000).

[5] R. Marquardt, M. Quack, I. Thanopulos, and D. Luckhaus, J. Chem. Phys., **119**, 10724–10732 (2003).

[6] M. H. Beck, A. Jäckle, G. A. Worth, and H.-D. Meyer. The MCTDH Package. Version 8.2, (2000).

[7] M. Mladenović, J. Chem. Phys., **112**, 1070–1081 (2000). F. Gatti, C. Muñoz, and C. Iung, J. Chem. Phys., **114**, 8275–8281 (2001).

[8] B. Kohler, J. L. Krause, F. Raski, C. Rose-Petruck, R. M. Whitnell, K. R. Wilson, V. V. Yakovlev, and Y. Yan, J. Phys. Chem., **97**, 12602–12608 (1993). D. G. Abrashkevich, I. S. Averbukh, and M. Shapiro, Annu. Rev. Phys. Chem., **101**, 9295–9302 (1994).

[9] S. Hervé, F. Le Quéré, and R. Marquardt, J. Chem. Phys., **116**, 3300–3308 (2002).

Paper for SASP 2006 in Obergurgl, Austria, 4-9 February 2006

RECENT RESULTS ON PARITY VIOLATION IN CHIRAL MOLECULES: CAMPHOR AND THE INFLUENCE OF MOLECULAR PARITY VIOLATION

Jürgen Stohner[1,2] and Martin Quack[2]
[1] Inst. for Chemistry and Biotechnology, Zürich University for Applied Sciences ZHW,
CH-8401 Winterthur; [2] Physical Chemistry, ETH-Zürich (Hönggerberg), CH-8093 Zürich

ABSTRACT

We report fully anharmonic vibrational frequencies for some selected fundamentals of totally 75 for camphor. The pure vibrational anharmonic frequencies have been obtained with a quartic force-field calculated by ab initio *or density functional (DFT) methods. A cut through the parity violating potential energy hyper-surface has also been determined as a function of reduced dimensionless normal coordinates* $\vec{q}$ *and fitted to a multi-dimensional polynomial expansion. This polynomial has been used to calculate parity-violation induced relative frequency shifts as expectation values using anharmonic vibrational wavefunctions for some of the fundamentals, which fall into the* CO_2*-laser emission range. Anharmonicity strongly influences the relative frequency shift as will be shown by comparison with calculations neglecting anharmonic couplings in camphor and some other molecules.*

INTRODUCTION

Quantum theory serves our current understanding of chemistry since the beginning of quantum mechanics. Early, mainly computational, limitations have been removed successfully and computational quantum chemistry proves useful over a wide range of applications. However, all advances made until recently relied on the foundations of quantum physics from about 1930 (for a recent review, see [1]). This changed in 1956 when parity violation was predicted and experimentally verified in particle physics [2, 3]. Our current understanding of fundamental processes in physics and chemistry is contained in the Standard Model of Particle Physics [4]. This is also of importance for molecular spectroscopy and dynamics: Due to a violation of space-inversion symmetry or parity, left- and right-handed molecules are no more energetically exactly equivalent. In the usual limiting case of molecular chirality (*de lege* symmetry breaking in the "high barrier" limit), the tunneling splitting for stereomutation between enantiomers is much smaller than the parity violating energy difference $\Delta_{\mathrm{pv}}E$ which then becomes a measurable quantity [5–7]. Early quantitative estimates of $\Delta_{\mathrm{pv}}E$ [8, 9] could be improved by orders of magnitude through progress in theoretical methodology [1, 10–12]. The Hamiltonian for parity violating potentials in chiral molecules [8–13] is given (in SI units) by

$$H_{\mathrm{pv}} \approx \frac{G_{\mathrm{F}}}{2\hbar\sqrt{2}m_{\mathrm{e}}c}\sum_a Q_a \sum_i \left[\vec{p}(i)\cdot\vec{s}(i), \delta^3(\vec{r}(i)-\vec{R}(a))\right]_+ \tag{1}$$

where nuclear spin effects have been neglected. The sums go over nuclei a and electrons i, m_{e} is the electron mass, c the velocity of light, $\hbar = h/2\pi$: Planck's constant h, G_{F}: Fermi-coupling constant, $\vec{p}(i)$: electron momentum, $\vec{s}(i)$: electron spin, $\delta^3(\vec{r}(i)-\vec{R}(a))$: Dirac delta distribution that confines the interaction to the positions of the nuclei, and $[\cdots]_+$ denotes the anti-commutator. The weak charge Q_a is approximately given by

$N_a - (1 - 4\sin^2\theta_\mathrm{W})\ Z_a$ with N_a: neutron number of nucleus a, Z_a: electric nuclear charge, θ_W: Weinberg angle. This Hamiltonian introduces an energy difference between left- and right-handed molecules, $\Delta_\mathrm{pv}E$, and the heat of reaction for stereomutation is (see Figure 1):

$$\mathrm{S} \quad = \quad \mathrm{R} \qquad\qquad \Delta_\mathrm{r}H_0^0 \approx N_\mathrm{A}\,\Delta_\mathrm{pv}E \tag{2}$$

$\Delta_\mathrm{pv}E = 2|E_\mathrm{pv}|$ where E_pv is the expectation value of H_pv with a spin-orbit perturbed ground state wavefunction (for more details, see [10, 11]). ΔE_pv might be observable directly in the time domain following the proposals in [5–7]. Another experiment to determine the influence of parity violation on molecular properties is to try to observe a shift of the vibrational frequencies between enantiomers [14, 15]. We have shown [16–18] that the current experimental accuracy still lacks three to four orders of magnitude for the measurement of the relative frequency shift between both enantiomers of CH(D)BrClF in the range of the CF-stretching fundamental at about 1078 cm^{-1}; an even higher accuracy would be needed to measure it in camphor which was the second example were early attempts have been undertaken to measure parity violation in molecules [19]. Table 1 shows an overview of molecular systems for which (relative) frequency shifts caused by parity violation have been calculated. The next section describes our theoretical approach briefly; more details can be found in [1, 10] (and references cited therein).

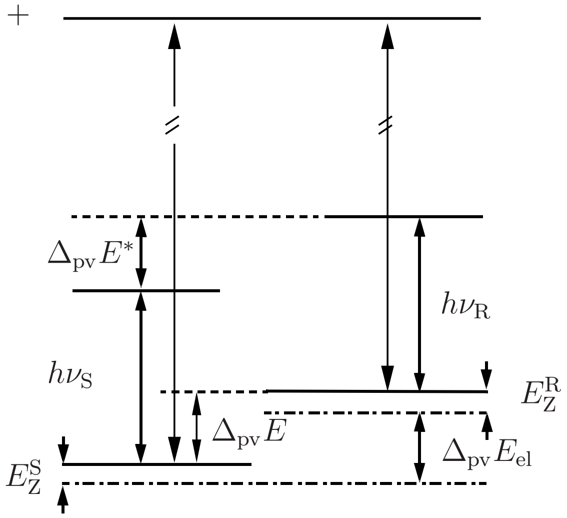

Figure 1: Energy level scheme (not to scale) for the stereomutation of an (S)- (left) and an (R)-Enantiomer (right).

THEORY

The parity violating potential V_pv of camphor has been determined using the RPA and MC-LR CASSCF ab initio method [10] along the reduced dimensionless normal coordinates $\vec{q}$ for all relevant vibrational degrees of freedom. In our early calculations [17, 18] we assumed $V_\mathrm{pv}(\vec{q})$ diagonal in q_i. $V_\mathrm{pv}(\vec{q})$ was then fitted to a polynomial expansion in q_i and the relative frequency shift has been determined on various levels of approximation: One-dimensional in the separable harmonic or anharmonic adiabatic approximation (SHAA or SAAA), or fully coupled by solving the multi-dimensional vibrational Schrödinger equation

Molecule	Year	Reference(s)
CHBrClF	1999/2000	[16, 17]
	2000	[20, 21]
CDBrClF	2000	[18]
	2003	[22]
CFXYZ (X,Y,Z=H,Br,Cl,I)	2002	[23]
F-oxirane (C_2H_3FO)	2001	[24]
BiHFBr, BiHFI	2003	[25]
PH_3AuCHFCl, ClHgCHFCl	2003	[26]
Camphor ($C_{10}H_{16}O$)	2004	[27]
$CBrClF^+$, $CBrClF^-$	2004	[28]
PHBrF, AsHBrF	2004	[29]

Table 1: Molecules for which (relative) frequency shifts have been calculated.

$$\widehat{H}_\mathrm{mol}(\vec{p},\vec{q}) = \widehat{H}^0_\mathrm{mol}(\vec{p},\vec{q}) + V_\mathrm{pv}(\vec{q}) \qquad \text{with} \qquad E_n \approx E_n^0 + \langle\Psi_n^0|V_\mathrm{pv}(\vec{q})|\Psi_n^0\rangle \tag{3a}$$

$$\Delta_{\rm pv} E_n = \left(E_n^{(\rm R)} - E_n^{(\rm R\,0)}\right) - \left(E_n^{(\rm S)} - E_n^{(\rm S\,0)}\right) \approx 2\,\langle\Psi_n^0|V_{\rm pv}(\vec q)|\Psi_n^0\rangle \tag{3b}$$

$V_{\rm pv}(\vec q)$ is expanded in a polynomial of $m^{\rm th}$ order, $\langle\Psi_n^0|V_{\rm pv}(\vec q)|\Psi_n^0\rangle$ is evaluated numerically.

$$\Delta_{\rm pv}\;\nu^{\rm ul}/\nu^{\rm ul} \approx 2\;[\langle\Psi_{\rm u}^0|\tilde V_{\rm pv}(\vec q)|\Psi_{\rm u}^0\rangle - \langle\Psi_{\rm l}^0|\tilde V_{\rm pv}(\vec q)|\Psi_{\rm l}^0\rangle]/(\tilde E^0_{{\rm u},j} - \tilde E^0_{{\rm l},j}) \tag{4}$$

In our current work we consider treatments where both the anharmonic parity conserving Born-Oppenheimer potential for vibrational motion and the parity violating potentials $V_{\rm pv}(\vec q)$ contain couplings between several normal modes [22,30]. $|\Psi_n^0\rangle$ is then the anharmonic eigenfunction to the eigenvalue $\tilde E_n^0$ of the complete (parity-conserving) vibrational molecular Hamiltonian ($\widehat H^0_{\rm mol}$) for the upper (u) or lower (l) molecular state, and the denominator gives the corresponding energy difference. The factor of 2 in eq. (4) arises from considering the difference between both enantiomers, which is twice the individual shift. More details can be found elsewhere [17,18,22].

Results and Conclusions

The reduced normal coordinate dependence of the parity violating potential energy has been used to determine relative frequency shifts for some selected fundamentals in camphor using a harmonic and anharmonic approximation. Table 2 shows that anharmonicity as well as anharmonic couplings are important to determine potentially observable relative frequency shifts. However, as our and other calculations performed on camphor have shown [27, 31, 32], current experimental accuracy is insufficient to experimentally verify the violation of the fundamental symmetry of space inversion or parity in this particular molecule. Table 2 displays the relative frequency shifts for various vibrational modes in camphor. It can be seen that for strongly anharmonically coupled modes (e.g. via Fermi-resonances (FR)) this coupling has a pronounced effect

		Relative Frequency Shifts $\Delta_{\rm pv}\nu/(10^{-20}\cdot\nu)$		
		Harmonic	Anharmonic	
Mode $\tilde\nu_i/{\rm cm}^{-1}$	i	1-dim	1-dim	3-dim (sp)
1009	29	−1.3	−1.3	
1038	30	−2.5	−2.3	
(1045)[1]			(+6 to +8)[1]	
1042	31	+18.1	+17.8	+12.4
1062	32	−15.6	−17.0	−16.5
1107	33	+0.7	+0.6	
1127	34	−0.1	−0.7	
1827	59	+7.2	+19.7	+20.4
Mode $\tilde\nu_i/{\rm cm}^{-1}$	i	1-dim	1-dim	2-dim (sp)
1321 (FR)	44	+2.26	+2.17	+3.16
3023 (FR)	66	+0.19	−2.37	−2.29

Table 2: Relative frequency shifts from one-dimensional harmonic and anharmonic calculations; the multi-dimensional calculations consider (vibrational) couplings: the shaded entries are from 3-dim. calculations (with rather weak couplings), whereas the entries marked FR are from calculations considering a strong Fermi-resonance between the two modes.[1] Previous calculations were carried out without considering anharmonic couplings [27,31].

on the frequency shifts calculated and can therefore not be neglected in a quantitative treatment [22].

REFERENCES

[1] M. Quack and J. Stohner, Chimia, **59**, 530 (2005).

[2] C. S. Wu, E. Ambler, R. W. Hayward, D. D. Hoppes, and R. P. Hudson, Phys. Rev., **105**, 1413 (1957).

[3] T. D. Lee and C. N. Yang, Phys. Rev., **104**, 254 (1956).

[4] M. Gaillard, P. Grannis, and F. Sciulli, Rev. Mod. Phys., **71**, S96 (1999).

[5] M. Quack, Chem. Phys. Lett., **132**, 147 (1986).

[6] M. Quack, Angew. Chem. Int. Ed. Engl., **28**, 571 (1989).

[7] M. Quack, Chem. Phys. Lett., **231**, 421 (1994).

[8] D. W. Rein, R. A. Hegstrom, and P. G. H. Sandars, Phys. Lett., **A71**, 499 (1979).

[9] R. A. Hegstrom, D. W. Rein, and P. G. H. Sandars, J. Chem. Phys., **73**, 2329 (1980).

[10] R. Berger and M. Quack, J. Chem. Phys., **112**, 3148 (2000).

[11] A. Bakasov, T. K. Ha, and M. Quack, J. Chem. Phys., **109**, 7263 (1998).

[12] A. Bakasov, T. K. Ha, and M. Quack. In J. Chela-Flores and F. Rolin, editors, *Proc. of the 4th Trieste Conference (1995), Chemical Evolution: Physics of the Origin and Evolution of Life*, pages 287–296, Dordrecht, (1996). Kluwer Academic Publishers.

[13] A. Barra, J. Robert, and L. Wiesenfeld, Phys. Lett. A, **115**, 443 (1986).

[14] C. Daussy, T. Marrel, A. Amy-Klein, C. Nguyen, C. Bordé, and C. Chardonnet, Phys. Rev. Lett., **83**, 1554 (1999).

[15] A. Bauder, A. Beil, D. Luckhaus, F. Müller, and M. Quack, J. Chem. Phys., **106**, 7558 (1997).

[16] J. Stohner, A. Beil, H. Hollenstein, O. Monti, and M. Quack. In *37th IUPAC Congress and 27th GDCh Meeting, Berlin, Germany, August 14-19, 1999, Frontiers in Chemistry: Molecular Basis of the Life Sciences*, page 525. ISBN 3-924763-82-8.

[17] M. Quack and J. Stohner, Phys. Rev. Lett., **84**, 3807 (2000).

[18] M. Quack and J. Stohner, Z. Physik. Chemie, **214**, 675 (2000).

[19] E. Arimondo, P. Glorieux, and T. Oka, Opt. Commun., **23**, 369 (1977).

[20] J. K. Laerdahl, P. Schwerdtfeger, and H. M. Quiney, Phys. Rev. Lett., **84**, 3811 (2000).

[21] R. Viglione, R. Zanasi, P. Lazzeretti, and A. Ligabue, Phys. Rev. A, **62**, 052516 (2000).

[22] M. Quack and J. Stohner, J. Chem. Phys., **119**, 11228 (2003).

[23] P. Schwerdtfeger, J. Laerdahl, and C. Chardonnet, Phys. Rev. A, **65**, 042508 (2002).

[24] R. Berger, M. Quack, and J. Stohner, Angew. Chem. Intl. Ed. (Engl.), **40**, 1667 (2001).

[25] F. Faglioni and P. Lazzeretti, Phys. Rev., **A67**, 032101 (2003).

[26] R. Bast and P. Schwerdtfeger, Phys. Rev. Lett., **91**, 023001 (2003).

[27] P. Schwerdtfeger, A. Kuhn, R. Bast, J. Laerdahl, F. Faglione, and P. Lazzeretti, Chem. Phys. Lett., **383**, 496 (2004).

[28] J. Stohner, Int. J. Mass Spectrometry, **233**, 385 (2004).

[29] R. Viglione, J. Chem. Phys., **121**, 9959 (2004).

[30] A. Beil, H. Hollenstein, O. Monti, M. Quack, and J. Stohner, J. Chem. Phys., **113**, 2701 (2000).

[31] P. Lazzeretti, R. Zanasi, and F. Faglioni, Phys. Rev. E, **60**, 871 (1999).

[32] J. Stohner and M. Quack, to be published.

Investigation of charged fullerenes in ion traps

Martin Arndt, Andreas Lassesson, Franklin Martinez, Gerrit Marx, Hagen Ritter, Lutz Schweikhard, Noelle Walsh

*Institute of Physics, Ernst-Moritz-Arndt University Greifswald, Domstraße 10a,
17489 Greifswald, Germany, Martin.Arndt@physik.uni-greifswald.de*

ABSTRACT

At the ClusterTrap experiment in Greifswald fullerene dianions have been created by electron attachment to monoanions in a Penning trap and investigated by collision induced dissociation. Recently, a radio-frequency-quadrupole (RFQ)-buncher has been built with the intention to use it as a preparatory trap for ions to be transferred to the Penning trap. Furthermore, a mobile Paul trap setup has been designed and assembled for the investigation of fullerene ions.

Introduction

Fullerenes are of particular interest for a number of reasons. Their structure and chemical bonding are different to that of metal clusters previously studied at ClusterTrap, they have a large number of degrees of freedom which makes them quite stable and they are particularly suitable for size-selected studies of the cluster properties. Creation of doubly negatively charged ions is possible due to the fact that the second electron affinity (EA2) of fullerenes containing more than 70 carbon atoms is positive.

The RFQ-buncher can trap a large number of ions due to the linear four electrode design. This makes it predestined to accumulate and select ions coming from a continuous ion source. The Paul trap offers the possibility to simultaneously store ions of both charge states and its small dimensions make it suitable for use at different experimental setups. A further advantage of the Paul trap setup is more accessible than the Penning trap where the ion storage volume is surrounded by a solenoidal superconducting magnet.

Experimental setup and results

Recent research projects at the ClusterTrap experiment were focused on the study of fullerene dianions in a Penning Trap. Fullerene dianions C_n^{2-} (n=70-90) have been created using the electron bath technique [1], which was originally developed for the production of multiply charged anions of metal clusters [2]. This technique involves the simultaneous storage of fullerene monoanions with low energy electrons for a certain reaction period. Some of these electrons may have enough energy to overcome the Coulomb barrier and attach to form dianions (Fig. 1) [1]. One outcome of our studies of fullerene dianion production is the confirmation that the relative dianion yield increases as a function of cluster size, as previously observed for the production of metal cluster dianions at ClusterTrap [3]. This behaviour can be explained by the height of the Coulomb barrier of the monoanion and the EA2 of the cluster. As for the Coulomb barrier, the larger the cluster, the lower the Coulomb barrier height and thus the more likely an electron has enough energy to overcome it and attach to the monoanion.

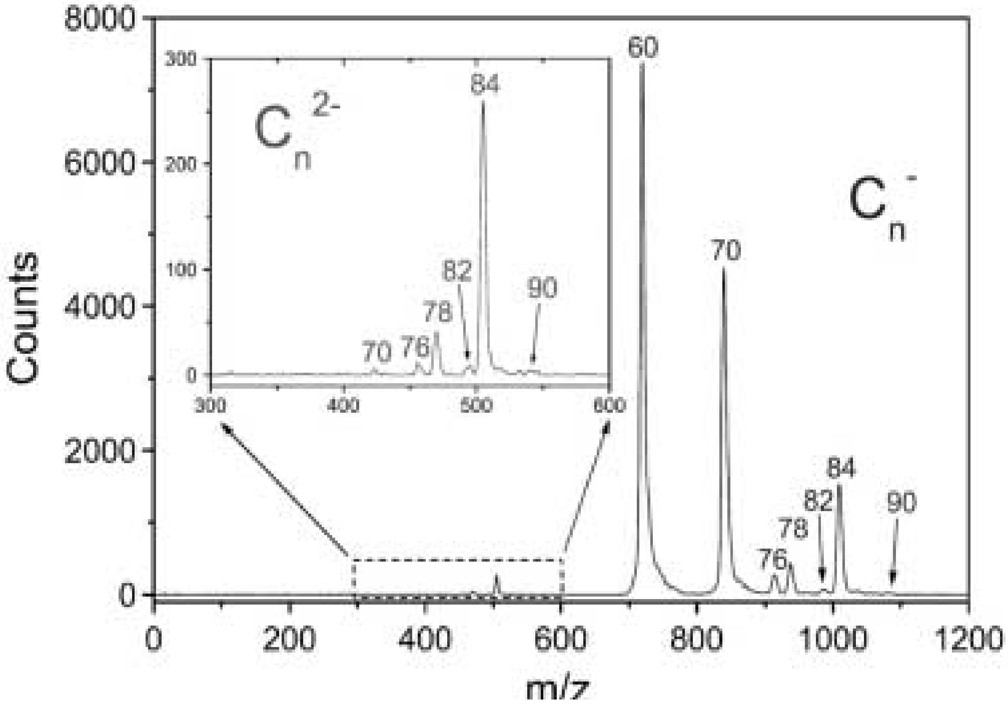

Fig. 1: Mass spectrum from the ClusterTrap after loading of negative fullerenes, C_n^-, and application of an electron bath.

Once attached, the electron may leave the cluster either by passing over the Coulomb barrier or tunnelling through it. Since the value of the second EA is more positive for larger clusters, it is found that larger clusters are more stable than smaller clusters with respect to loss of one of the two surplus electrons [1]. One of the possible experimental techniques that can be implemented at ClusterTrap is collisional activation with argon atoms in the trap (Fig. 2).

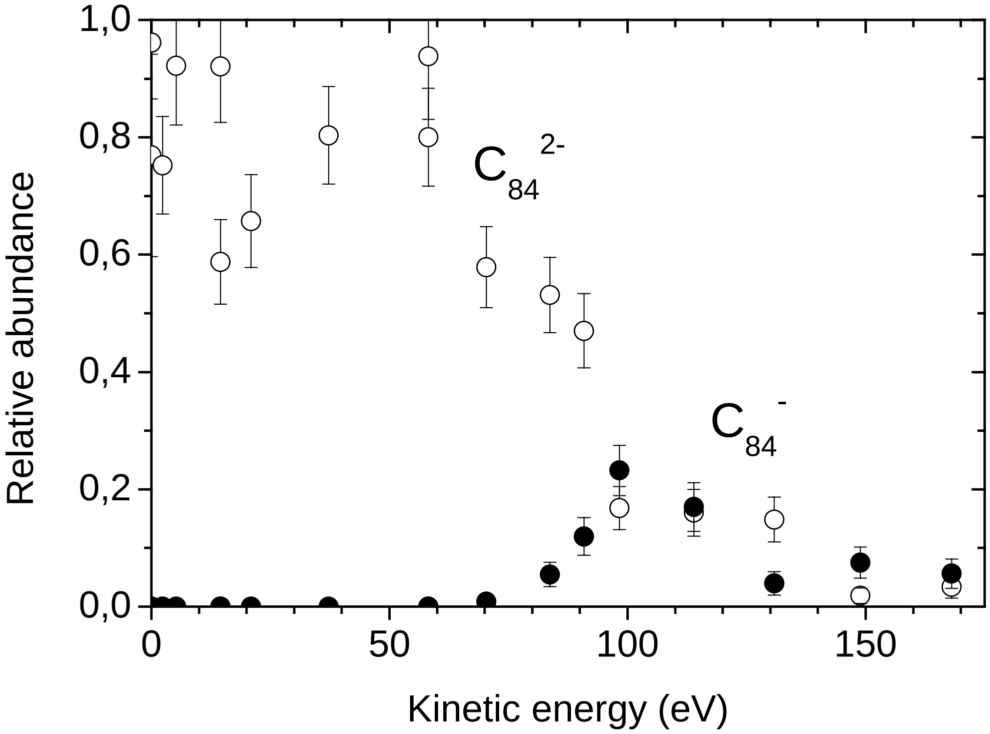

Fig. 2: Collisional activation of C_{84} dianions increases their internal energy and may result in delayed electron emission.

The current fullerene source [4] at the ClusterTrap experiment provides a continuous ion beam. An RFQ-buncher has been built and tested [5] to optimize the ion transfer to the Penning Trap (Fig. 3). It provides the possibility of ion accumulation, selection and cooling to form pulsed bunches of ions of a particular size distribution. The accumulation is realized by an additionally provided dc-potential-well in axial direction by use of segmented electrodes. The cooling is provided by a buffergas. Selection of the ions is achieved using two methods: The RFQ-buncher may be operated as a mass filter by use of appropriate AC and DC voltages. Alternatively, unwanted ions can be resonantly ejected by the application of additional radio-frequency voltages.

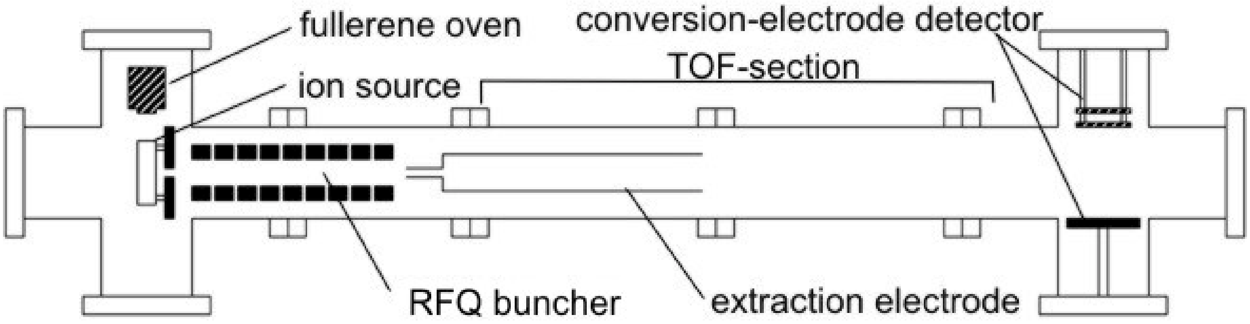

Fig. 3: The test setup of the RFQ-Buncher experiment.

In addition, a Paul trap has been assembled (Fig. 4) to investigate both anionic and cationic fullerenes simultaneously [6]. This can be achieved is possible in a Paul trap where the trapping is realized by an electric radio-frequency field, only. Different detection methods like the ramping of the guiding field amplitude and the time-of-flight method were used for initial studies. It is intended to investigate the stored cluster ions using photoactivation. Furthermore, it is foreseen that the Paul trap setup will be transported to DESY in Hamburg for measurements with the FEL.

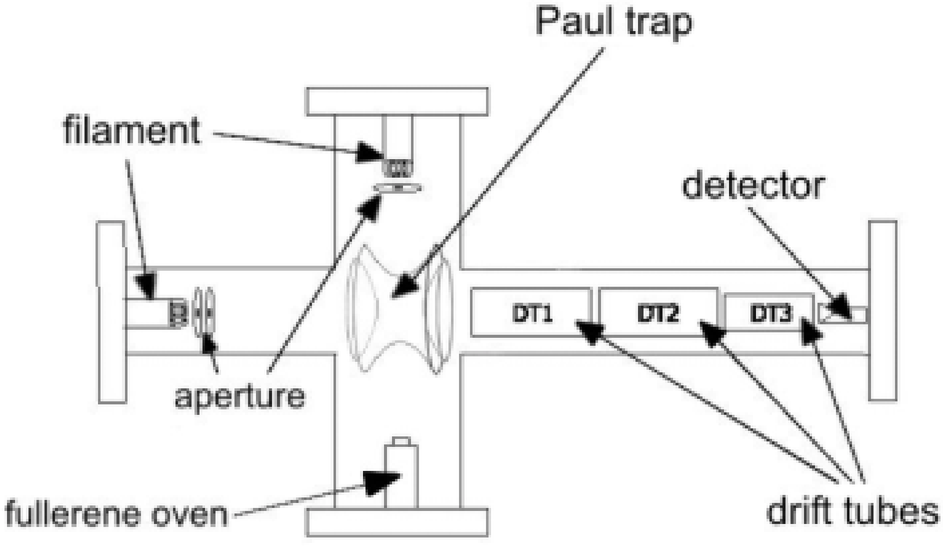

Fig. 4: Experimental setup of the Paultrap test experiment.

References:

[1] A. Lassesson, N. Walsh, F. Martinez, A. Herlert, G. Marx, L. Schweikhard, Eur. Phys. J. D 34 (2005) 73.

[2] A. Herlert, L. Schweikhard, Int. J. Mass Spectrom., 229 (2003) 19; A. Herlert, S. Krückeberg, L. Schweikhard, M. Vogel, C. Walther, Phys. Scripta, T80 (1999) 200.

[3] L. Schweikhard, K. Hansen, A. Herlert, G. Marx, M. Vogel, Eur. Phys. JD24, 137-143 (2003)

[4] F. Martinez, „Entwicklung und Test neuer Ionenquellen für die Clusterfalle“, diploma thesis (2004)

[5] M. Arndt, „Aufbau und Test eines Quadrupol-Ionen-Akkumulators“, diploma thesis (2005)

[6] H. Ritter, „Aufbau einer Apparatur zur Untersuchung von Clustern in einer Paulfalle“, diploma thesis (2005)

The Influence of Water Concentration on the Ozone Production in Corona Discharge Fed by Carbon Dioxide and Water

J. D. Skalný[1], J. Országh[1], N. J. Mason[2]

[1]*Department of Experimental Physics, Faculty of Mathematics, Physics and Informatics, Comenius University, Mlynská dolina F-2, Bratislava, SK*

[2]*Department of Physics and Astronomy, Open University, Milton Keynes, UK*

Experiment

Two cells containing identical coaxial cylindrical electrodes systems (stainless steel inner electrode of diameter 125 μm and stainless steel outer electrode of diameter either 16 mm), were prepared. Active part length of the discharge tube was 10 cm. Negative corona discharge was generated in one of them, the second being used as a comparative tube. Both were placed in a UV spectrometer and filled by mixture of carbon dioxide and water. Computer was used for recording optical transmittance of gas closed in cell containing the active electrode system by spectrometer. Using Lambert-Beer formula the ozone concentration in the discharge gap was calculated. The gas mixture was prepared by mixing two flows of gas. The gas flow from the cylinder was divided into two independent flows regulated by flow controllers. One of them stayed intact and another one was enriched by water vapours by flowing through the water closed in bubbler kept at constant temperature. These two flows were mixed together to gain required water concentration in CO_2 and the mixture was let into the reactor that was subsequently closed by two valves. Three values of humidity were mixed, 165 ppm, 305 ppm and 450 ppm of water in carbon dioxide. High voltage power supply unit was used to bring voltage to the electrodes. Two multimeters were used. One in the role of ampmeter and another one as a voltmeter in connection with high voltage probe. Ampmeter was connected to the computer as it was necessary to saved discharge current data every second. Three voltages were chosen for measurements 5.4 kV, 6.4 kV and 7,4 kV. The relative humidity of the ambient gas was 25 %. All experiments have been carried out at an ambient temperature (approx. 20°C) and at a pressure of ≈ 100 kPa.

Experimental results and discussion

Two different time dependent data were aquisited by PC during the measurement. The discharge current and the transmittance of the UV light through the reactor.

Discharge current

The onset voltage of the discharge was found to be at 4.95 ± 0.05kV and did not change significantly with the change of the amount of water vapours in the gas mixture. In contrast to this fact, the discharge current was influenced by the water. Figures 1, 2 and 3 show dependence of total discharge current on time during the measurement. From these it is possible to assume that the current gets lower with increasing amount of water in the mixture. It is evident especially in the first phase of the measurement when the total discharge current is high.

Ozone concentration

Figure 4, 5 and 6 show the dependence of ozone concentration on the time during the measurement. The concentration was calculated from measured transmittance. The effect of humidity on the ozone concentration is not well pronounced. The increase and the decrease of ozone concentration have been observed, depending on the voltage on electrodes. Peculiar effect requires further investigation.

If the amount of water rises then it also influences the presence of ions and more OH radicals are formed. Also probability of cluster formation is relatively high in the environment with high amount of water.

The following reactions are responsible for ozone formation and decomposition in the volume of the reactor:

$e + CO_2 \rightarrow CO + O + e$ $k_1 = f(E/N)$ (1) [1]

$O + O + CO_2 \rightarrow O_2 + CO_2$ $k_2 = 1.04 \times 10^{-32}\ cm^6 s^{-1}$ (2) [1]

$O + O_2 + M \rightarrow O_3 + M$ $k_3 = 5.85 \times 10^{-34}\ cm^6 s^{-1}$ (3) [1]

$e + O_3 \rightarrow O^- + O_2$ $k_4 = f(E/N)$ (4) [1]

$e + O_3 \rightarrow O_2^- + O$ $k_5 = f(E/N)$ (5) [1]

$O(^3P) + O_3 \rightarrow O_2 + O_2$ $k_6 = 8.5 \times 10^{-15}\ cm^3 s^{-1}$ (6) [1]

$O_3 + O_2(^1\Delta_g) \rightarrow O_2 + O_2 + O$ $k_7 = 4 \times 10^{-15}\ cm^3 s^{-1}$ (7) [1]

Acknowledgements

This research project was partially supported by Slovak Grant Agency VEGA under project 1/1267/04, the UK EPSRC (Grant GM/98944) EPS programs EIPAM and COST.

References

[1] Mikoviny T, Kocan M, Matejcik S, Mason N J and Skalny J D 2004 *J. Phys. D: Appl. Phys.* **64**

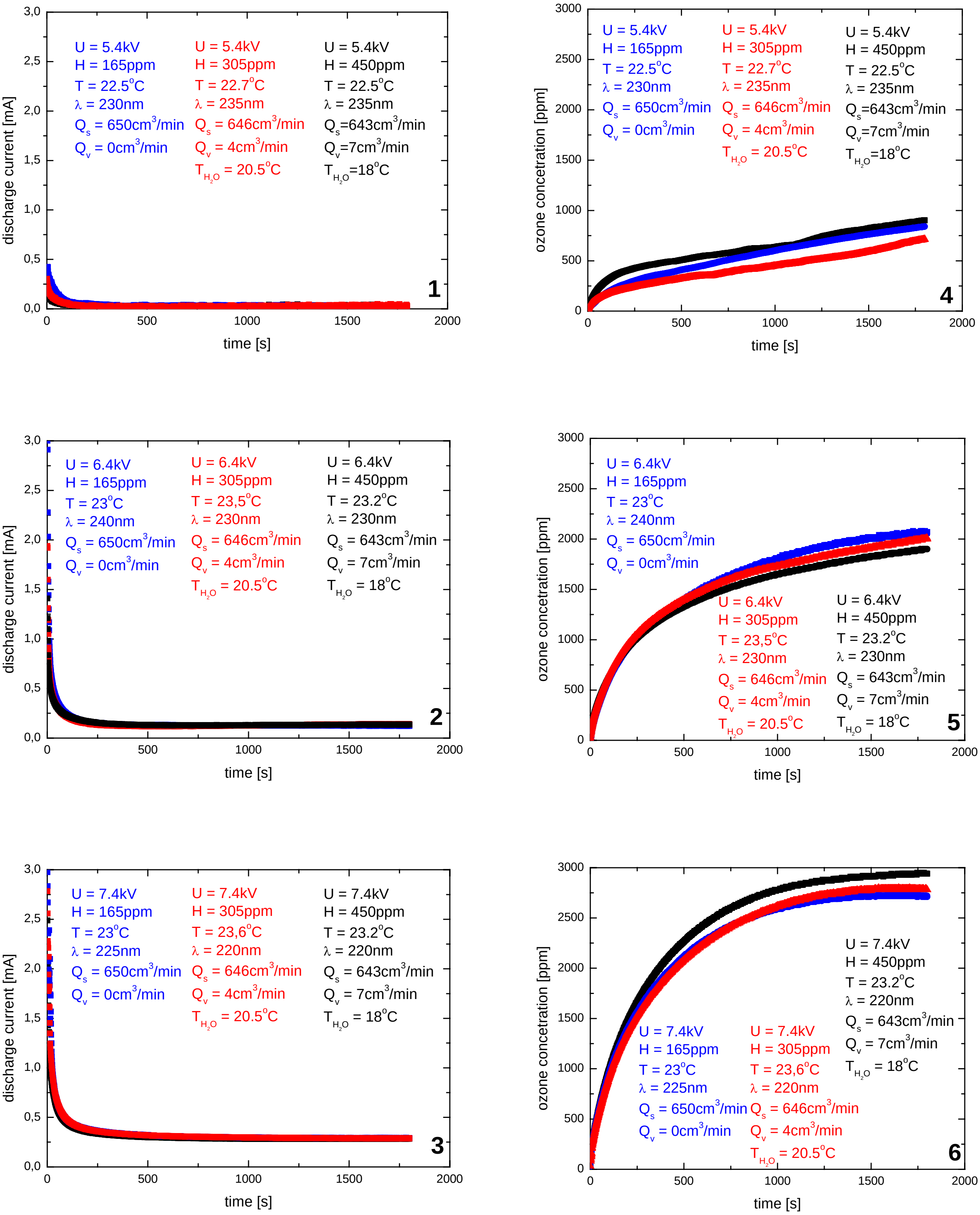
1
discharge current [mA]
time [s]
3,0
2,5
2,0
1,5
1,0
0,5
0,0
0
500
1000
1500
2000
U = 5.4kV
H = 165ppm
T = 22.5°C
λ = 230nm
Q$_s$ = 650cm^3/min
Q$_v$ = 0cm^3/min
U = 5.4kV
H = 305ppm
T = 22.7°C
λ = 235nm
Q$_s$ = 646cm^3/min
Q$_v$ = 4cm^3/min
T$_{H_2O}$ = 20.5°C
U = 5.4kV
H = 450ppm
T = 22.5°C
λ = 235nm
Q$_s$=643cm^3/min
Q$_v$=7cm^3/min
T$_{H_2O}$=18°C
4
ozone concetration [ppm]
time [s]
3000
2500
2000
1500
1000
500
0
0
500
1000
1500
2000
U = 5.4kV
H = 165ppm
T = 22.5°C
λ = 230nm
Q$_s$ = 650cm^3/min
Q$_v$ = 0cm^3/min
U = 5.4kV
H = 305ppm
T = 22.7°C
λ = 235nm
Q$_s$ = 646cm^3/min
Q$_v$ = 4cm^3/min
T$_{H_2O}$ = 20.5°C
U = 5.4kV
H = 450ppm
T = 22.5°C
λ = 235nm
Q$_s$=643cm^3/min
Q$_v$=7cm^3/min
T$_{H_2O}$=18°C
2
discharge current [mA]
time [s]
3,0
2,5
2,0
1,5
1,0
0,5
0,0
0
500
1000
1500
2000
U = 6.4kV
H = 165ppm
T = 23°C
λ = 240nm
Q$_s$ = 650cm^3/min
Q$_v$ = 0cm^3/min
U = 6.4kV
H = 305ppm
T = 23,5°C
λ = 230nm
Q$_s$ = 646cm^3/min
Q$_v$ = 4cm^3/min
T$_{H_2O}$ = 20.5°C
U = 6.4kV
H = 450ppm
T = 23.2°C
λ = 230nm
Q$_s$ = 643cm^3/min
Q$_v$ = 7cm^3/min
T$_{H_2O}$ = 18°C
5
ozone concetration [ppm]
time [s]
3000
2500
2000
1500
1000
500
0
0
500
1000
1500
2000
U = 6.4kV
H = 165ppm
T = 23°C
λ = 240nm
Q$_s$ = 650cm^3/min
Q$_v$ = 0cm^3/min
U = 6.4kV
H = 305ppm
T = 23,5°C
λ = 230nm
Q$_s$ = 646cm^3/min
Q$_v$ = 4cm^3/min
T$_{H_2O}$ = 20.5°C
U = 6.4kV
H = 450ppm
T = 23.2°C
λ = 230nm
Q$_s$ = 643cm^3/min
Q$_v$ = 7cm^3/min
T$_{H_2O}$ = 18°C
3
discharge current [mA]
time [s]
3,0
2,5
2,0
1,5
1,0
0,5
0,0
0
500
1000
1500
2000
U = 7.4kV
H = 165ppm
T = 23°C
λ = 225nm
Q$_s$ = 650cm^3/min
Q$_v$ = 0cm^3/min
U = 7.4kV
H = 305ppm
T = 23,6°C
λ = 220nm
Q$_s$ = 646cm^3/min
Q$_v$ = 4cm^3/min
T$_{H_2O}$ = 20.5°C
U = 7.4kV
H = 450ppm
T = 23.2°C
λ = 220nm
Q$_s$ = 643cm^3/min
Q$_v$ = 7cm^3/min
T$_{H_2O}$ = 18°C
6
ozone concetration [ppm]
time [s]
3000
2500
2000
1500
1000
500
0
0
500
1000
1500
2000
U = 7.4kV
H = 450ppm
T = 23.2°C
λ = 220nm
Q$_s$ = 643cm^3/min
Q$_v$ = 7cm^3/min
T$_{H_2O}$ = 18°C
U = 7.4kV
H = 165ppm
T = 23°C
λ = 225nm
Q$_s$ = 650cm^3/min
Q$_v$ = 0cm^3/min
U = 7.4kV
H = 305ppm
T = 23,6°C
λ = 220nm
Q$_s$ = 646cm^3/min
Q$_v$ = 4cm^3/min
T$_{H_2O}$ = 20.5°C

Fig. 1-6.

The photoionization and fragmentation of water in the EUV spectral region

C. A. Hunniford, R. Browning, S. W. J. Scully, K. F. Dunn and C. J. Latimer

Department of Physics and Astronomy, Queen's University Belfast, Belfast, BT7 1NN, UK

ABSTRACT

Photoion-pair formation in H_2O and D_2O have been studied using synchrotron radiation within the energy range 15-50eV. Superexcited states are shown to play an important role and exceptionally large isotope effects are observed.

1. Introduction

Ion-pair production is an extremely important method for the investigation of superexcited states in neutral molecules. In particular doubly excited Rydberg states, lying between the single and double ionization thresholds provide fundamental information on electron correlation. In addition investigations involving isotopic substitution can provide information on the decay dynamics of these states. Furthermore, in the case of water, radiolysis is known to be an important process causing cell mutations and death [1] with fragment negative ions playing an important role in bond breaking in DNA [2]. In this context there is a need for cross section data on fragmentation processes, including the following anion production channels:-

$$h\nu + H_2O \rightarrow \begin{array}{lcl} (H_2O)^* & \rightarrow & O^- + (2H)^+ \\ & \rightarrow & OH^- + H^+ \\ (H_2O^+)^* & \rightarrow & H^- + (OH)^+ \end{array} \qquad (1)$$

2. Experimental approach

These experiments were carried out at the Daresbury Laboratory (UK) synchrotron beamlines 3.1and 5D. The VUV photon beam was crossed by a narrow low pressure gas jet of target molecules. Cross sections for the production of both positive and negative ions were obtained by extracting them with an electric field and analyzing them using a triple quadrupole mass spectrometer [3]. The data was corrected for higher order radiation. The collision region was kept at a low pressure to avoid secondary collision effects (mainly electron capture) and the mass spectrometer was differentially pumped to reduce noise from stray electrons.

3. Results and discussion

The ions H_2O^+, OH^+, H^+, O^-, OH^- and H^- have been observed and all appear at their known thermochemical thresholds [4]. Figure 1 shows the cross sections for O^- production in the range 18 – 33 eV. The lines labeled T indicate the thermochemical thresholds. Two major features are apparent – a small one at ~19.5 eV and a large composite feature in the region 23 – 31 eV. The former shows only a small isotope effect which can readily be associated with the single-hole one-electron states built on the $(1b_2)^{-1}$ band of ion states centered at 18.5 eV. The large composite feature appears in a barren region in the photoelectron spectrum [4] and is clearly due to formation via doubly excited states. Two such states at ~25 and ~28 eV, as well as states built on the $(2a_1)^{-1}$ ion state at 32.3 eV, have recently been observed in the fluorescence spectra of fragment H atoms [5]. However fitting Gaussian functions to the present data clearly shows that there are at least three such doubly excited states at energies of 25.2, 27.1 and 29.0 eV. A strong isotope effect shows that the fragmentation process is being governed by autoionization. Interestingly relatively few O^- ions are observed to come from Rydberg states built on the $(2a_1)^{-1}$ ion core.

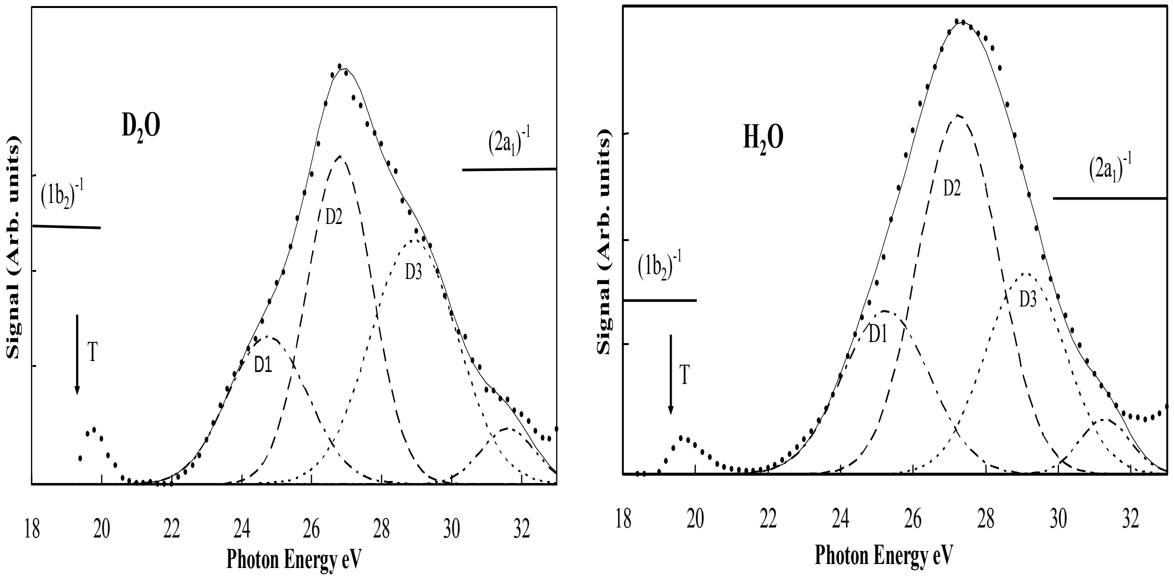

Figure 1 The formation of O^- in H_2O and D_2O. The lines labelled T indicate the thermochemical thresholds [3] and D1, D2and D3 are the doubly excited states observed in this work

The production of OH^- ions, shown in Figure 2 below, is found to be solely associated with excitation to known electronic states [6] in the energy region 17–20 eV converging on the $(1b_2)^{-1}$ ion states. The calculated series includes contributions from virtual orbitals as well as Rydberg states. Considerable vibrational structure is also observed, extending in the form of superexcited states, well into the continuum. As can be seen from equations (1) the OH^- production process is uniquely determined and is accompanied by the formation of an H^+ ion.

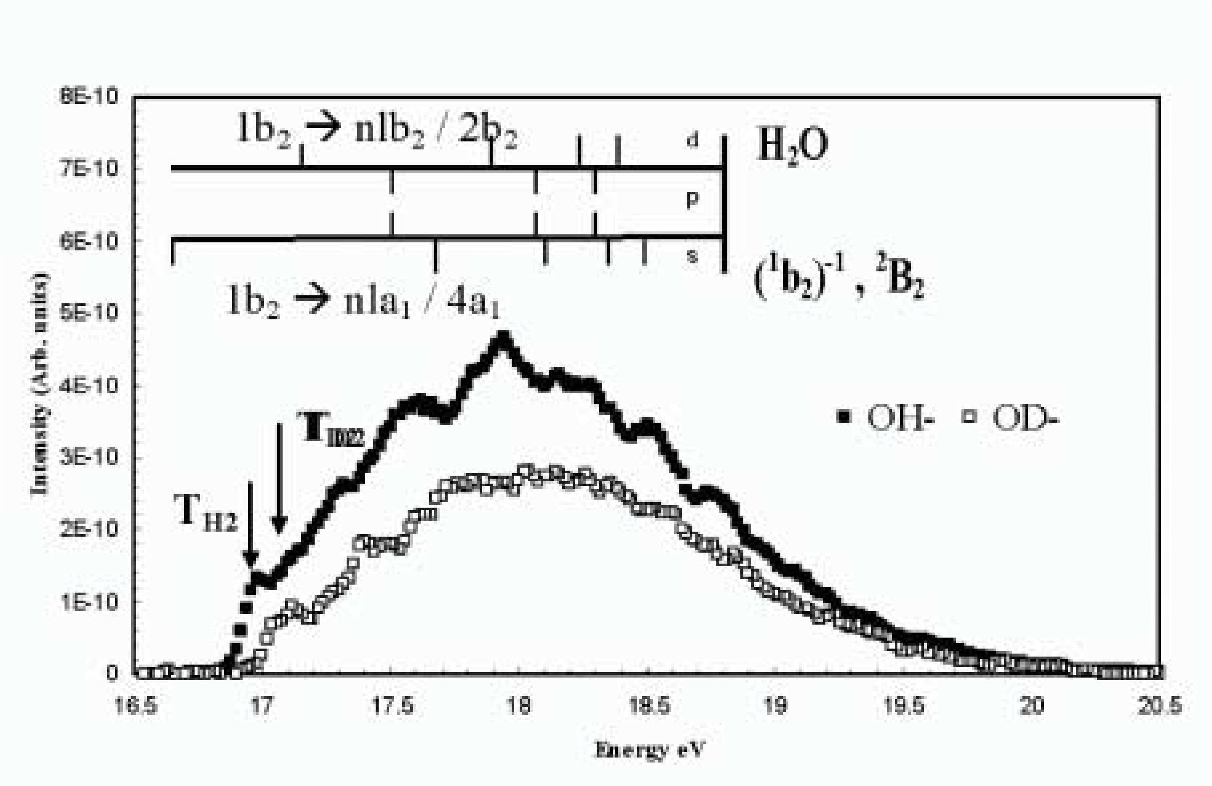

Figure 2 OH^- and OD^- formation in H_2O and D_2O. The thermochemical thresholds [3] and calculated energies of Rydberg states [6] are also shown.

The anions H^- and D^- were also observed in the 17-20eV energy region although in relatively small quantities and no isotope effects were seen. However above 25ev the cross section increases considerably as excitation to Rydberg states associated with the $(2a_1)^{-1}$ ion state at 32 eV becomes possible. As Figure 3 shows H^- production is found to further increase in the double ionisation region above 33.5 eV where 8 dication ion states are known [5]. In this region it is particularly interesting to note the exceptionally large isotope effect – the cross section ratio for $H^- / D^- \simeq 15$. Recently in a related investigation by Legendre et al [6] have investigated the double ionization of the HOD molecule by fast highly charged ions (10 MeV/u) and found a strong preferential cleavage, by a factor of 6.5,.of the O-H bond rather than the O-D bond. Semi-classical simulations of the dissociation dynamics of the ground dicationic state explain this effect as arising from initial position and momentum distributions.

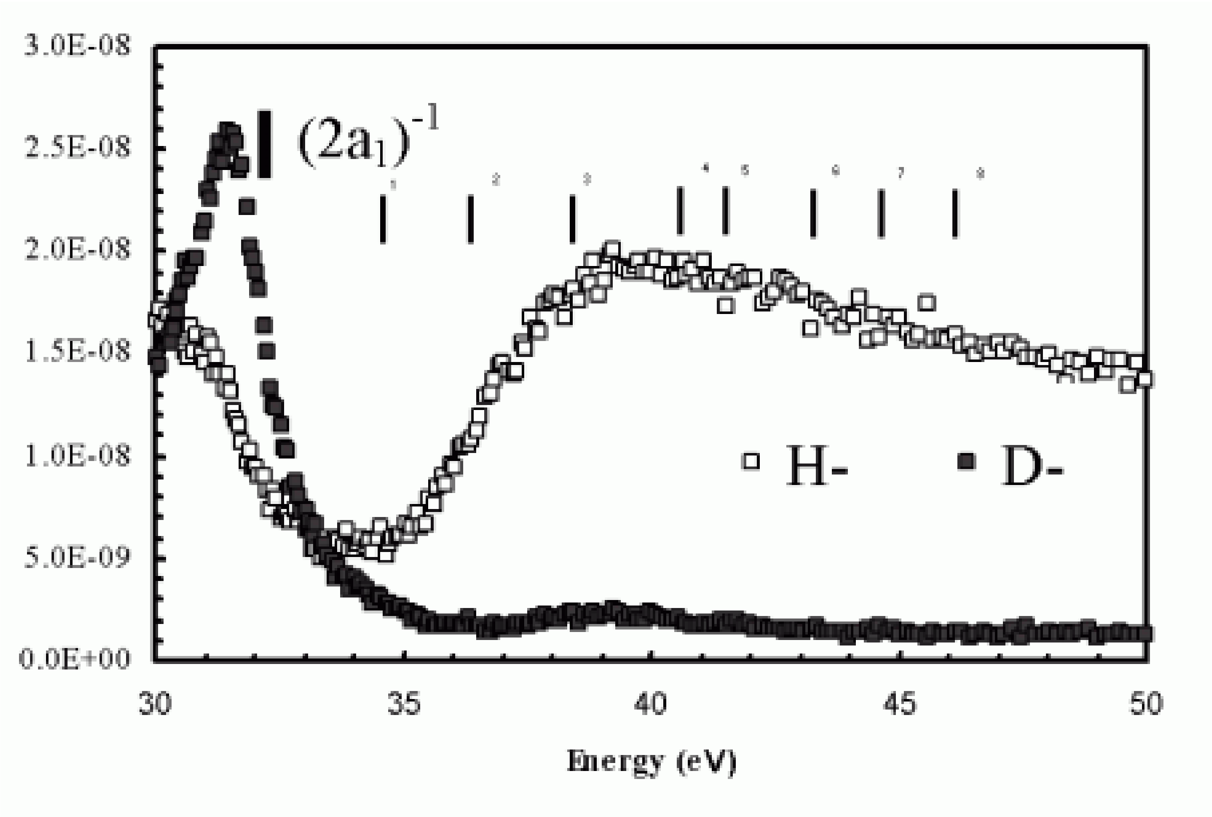

Figure 3 H$^-$ and D$^-$ formation in H_2O and D_2O above 30eV. The known energies of 8 dication states above the double ionisation threshold are also shown [7]

References

[1] G H Olivera et al Phys Med Biol 43 2347 (1998)
[2] X Pan et al Phys Rev Lett 90 208102-1 (2003)
[3] R A Mackie et al J Phys B 35 1061 (2002)
[4] J Berkowitz in VUV and Soft X-ray Photoionization, Eds U Becker and D A Shirley, Plenum Press, New York 1996
[5] M Kato, T Odagiri, K Kodama, M Murata, K Kameta and N Kouchi J Phys B 37 3127 (2004)
[6] G H F Dickerson et al J Chem Phys 76 1043 (1982)
[7] G C King et al to be published (2006)
[8] S Legendre, E Giglio, M Tarislen, A Cassini, B Gervais and L Adoui J Phys B L233 (2005)

Dynamics of l,c-C_3H and C_3 formation from the $C(^3P, ^1D) + C_2H_2$ reactions

F. Leonori[1], E. Segoloni[1], A. Bergeat[2], R. Petrucci[1], G. Capozza[1], N. Balucani[1], and P. Casavecchia[1]

[1] *Dipartimento di Chimica, Università di Perugia, 06123 Perugia, Italy, E-mail: piero@dyn.unipg.it*

[2] *LPCM, UMR5803, Université Bordeaux I, 33405 Talence Cedex, France*

The reactions of ground-state carbon atoms with unsaturated hydrocarbons are of basic chemical interest and of great relevance in areas which range from combustion to astrochemistry. Kinetic studies found them very fast ($k \approx 2\text{-}4\times10^{-10}$ cm^3 molecule^{-1} s^{-1}) down to very low temperature (15 K) and suggested that these are barrierless reactions dominated by long range attractive forces and that may have a critical role in the chemistry of the ISM.

We report on the investigation of the dynamics of the prototypical and perhaps most important C reaction, $C(^3P)$+acetylene, by using the crossed molecular beam (CMB)scattering technique with mass-spectrometric detection. We exploit the capability (a) of generating continuous supersonic beams of C atoms, (b) of crossing the reactant beams at variable angles (45°-90°-135°), and (c) of detecting the products by “soft” electron-ionization [1]. Angular distributions and TOF spectra at selected laboratory angles at *m/e* = 37 (C_3H) and 36 (C_3) were recorded in a wide range of collision energies (E_c~3.5-50 kJ/mol). Although C_3H still fragments to C_3^+ under soft EI, the two reaction pathways were unambiguously disentangled from differences in the *m/e* = 37 and 36 angular distributions and the observation of distinct peaks in the TOF spectra. We have identified the primary products (*l-,c*-C_3H and C_3), derived their center-of-mass angular and translational energy distributions, determined the branching ratios of the C_3H+H and C_3+H_2 forming channels, characterized the reaction micromechanisms, and obtained information on the potential energy surfaces (PESs). These studies extend significantly our previous investigation at E_c=29.3 kJ/mol [2] and earlier CMB studies with pulsed beams [3]. The data at E_c = 3.5 kJ mol^{-1} carry some fingerprint of the formation of the two C_3H isomers which appear to exhibit different dynamics, thus providing information on the *c*-C_3H/*l*-C_3H branching ratio and respective exoergicities. The branching ratio for C_3 production is higher at E_c = 3.5 kJ mol^{-1} than at E_c = 48 kJ mol^{-1} in agreement with the spin-forbidden nature of the $C(^3P_J) + C_2H_2(X^1\Sigma_g^+) \rightarrow C_3(X^1\Sigma_g^+) + H_2(X^1\Sigma_g^+)$ reaction which requires intersystem crossing between triplet and singlet potential energy surfaces and is thus favoured by a longer lifetime of the collision complex. Since our C beams contain, in addition to $C(^3P)$ atoms, also a significant concentration of excited $C(^1D)$ atoms, it has been possible to characterize the dynamics of C_3H and C_3 formation from the $C(^1D) + C_2H_2$ reaction as well, thanks to the capability of disentangling the $C(^3P)$ and $C(^1D)$ contributions in product angular and velocity distribution measurements [5]. We note that the reactions of $C(^1D)$ are of fundamental importance in comets. Notably, from measurements of EI efficiency curves of the reaction products down to very low electron energies, the first experimental estimate of the ionization energy (IE) of *l-,c*-C_3H radicals is also obtained (the experimental IE compare well with theoretical predictions [4]).

References

[1] P. Casavecchia *et al.*, *J. Phys. Chem. A* **109**, 3527 (2005).
[2] L. Cartechini *et al.*, *J. Chem. Phys.* **116**, 5603 (2002).
[4] R. I. Kaiser, W. Sun, A. G. Suits, and Y. T. Lee, *J. Chem. Phys.* **107**, 8713 (1997).
[4] R. K. Chaudhuri, S. Majumder, K. F. Freed, *J. Chem. Phys.* **112**, 9301 (2000).

Dynamics of radical-radical reactions in crossed beams: alkyl radicals (CH_3 and C_3H_5) + oxygen atoms

F. Leonori[1], E. Segoloni[1], N. Balucani[1], R. Petrucci[1], A. Bergeat[2], D. Stranges[3], and P. Casavecchia[1]

[1]Dipartimento di Chimica, Università degli Studi di Perugia, 06123 Perugia, Italy,
E-mail: piero@dyn.unipg.it

[2] LPCM, UMR5803, Université Bordeaux I, 33405 Talence Cedex, France

[3] Dipartimento di Chimica, Università di Roma "La Sapienza", 00185 Roma, Italy

While reactive differential cross sections (DCSs) have been measured using the Crossed Molecular Beams (CMB) scattering technique with "universal" electron-ionization mass-spectrometric detection for a large variety of radical-molecule reactions [1], little has been done so far on radical-radical systems despite their importance. This is mainly due to the difficulty of generating radical beams of sufficient intensity to carry out DCS measurements.

We report on the first direct measurements of product angular and velocity distributions for two important radical-radical reactions: $O(^3P) + CH_3$ (methyl) and $O(^3P) + C_3H_5$ (allyl), which are of great relevance in combustion chemistry. We generate *continuous* supersonic beams of $O(^3P)$ by a radio-frequency discharge beam source in a quartz nozzle, while *continuous* supersonic beams of the alkyl radicals are produced by flash-pyrolysis in a SiC nozzle beam source.

These reactions have been investigated extensively from the kinetic standpoint, and also theoretically [2, 3]; recently, OH product rovibrational distributions were determined by laser-induced-fluorescene for $O(^3P)$+allyl in pulsed jets [3]. In our CMB study, the primary products and their dynamics of formation are derived. Formaldehyde and acrolein are found to be the main products of the $O(^3P)$ reaction with methyl and allyl, respectively. By exploiting “soft” electron-ionization method for product detection [4], C-C bond fission channels have also been observed in the $O+C_3H_5$ reaction. The derived center-of-mass product angular and translational energy distributions reflect the geometry of the decomposing transition states and the energy partitioning, respectively; they are interpreted at the light of the available electronic structure calculations of the potential energy surfaces (PESs) [3, 5]. The results are expected to stimulate direct dynamics calculations on *ab initio* PESs for the prototypical radical-radical 5-atom reaction CH_3 + O.

References

[1] P. Casavecchia, *Rep. Prog. Phys.* **63**, 355-414 (2000); and references therein.
[2] W. Hack *et al.*, *Phys. Chem. Chem. Phys.* **7**, 1977 (2005), and references therein.
[3] S.-K. Joo, L.-K. Kwon, H. Lee, J.-H. Choi, *J. Chem. Phys.* **120**, 7976 (2004).
[4] See: P. Casavecchia, G. Capozza, E. Segoloni, F. Leonori, N. Balucani, G. G. Volpi, *J. Phys. Chem.* A **109**, 3527 (2005).
[5] T. P. Marcy, R. R. Diaz, D. Heard, S. R. Leone, L. B. Harding, S. J. Klippenstein, *J. Phys. Chem.* A **105**, 8361 (2001).

High Resolution Infrared Spectroscopy of Aromatic Compounds

Sieghard Albert and Martin Quack

Physical chemistry, ETH Zürich, CH-8093 Zürich, albert@ir.phys.chem.ethz.ch

ABSTRACT

The infrared spectra of pyridine, C_6H_5N, and chlorobenzene, C_6H_5Cl were measured with the Bruker IFS 125 HR Zürich Prototype (ZP) 2001 Fourier transform spectrometer at room temperature in a 3 m glass cell and in a White-type cell with effective optical path length between 9.3 and 19.6 m. The spectra were recorded with a resolution of 0.0008-0.0015 cm^{-1} in the range 600-1300 cm^{-1}. The pyridine spectra were analysed in the ν_{18a} and ν_{15} region using an effective Hamiltonian. A Coriolis resonance between the ν_{18a} and ν_{18b} states as well as between the ν_{15} and a dark state attributed to $\nu_4 + \nu_{16b}$ were detected and analysed. The spectrum of chlorobenzene was assigned in the ν_{10b} region. *C*-type transitions were identified.

1. Introduction

The analysis of the infrared spectrum of pyridine, a molecule with C_{2v} symmetry, has been of interest for over 60 years [1-5]. Recent submillimeter measurements up to 400 GHz yielded extended rotational constants of the ground state and first spectroscopic constants of five excited states [6-7]. The fully resolved infrared spectrum recorded in the region 600-1300 cm^{-1} with our Bruker IFS125 Spectrometer, made it possible to rovibrationally analyse the spectrum in the ν_4, ν_{11}, previously studied at lower resolution [8], and ν_{12} regions [9]. In this paper we present an analysis of the ν_{15} and ν_{18a} modes.

The vibrational spectrum of chlorobenzene (C_6H_5Cl), a molecule which also has C_{2v} symmetry, was first completely assigned by Whiffen [10]. Up to now there exists only one rovibrational analysis of the ν_{19a} band of chlorobenzene [11]. Here we present a preliminary assignment of the ν_{10b} band of $C_6H_5{}^{35}Cl$.

Pyridine is a prototype system for biologically relevant systems like the DNA bases. Chlorobenzene is a precursor in the combustion chemistry of polychlorinated biphenyls (PCB). An analysis of the rovibrational spectrum of pyridine might be the starting point for a better understanding of the spectra of DNA bases and their dynamics, and an analysis of the rovibrational spectrum of chlorobenzene might contribute to more insight into the combustion chemistry of PCBs.

Pyridine has 27 and chlorobenzene 30 normal modes. Among these, 10 (11) modes have A_1 symmetry, 9 (10) modes have B_2 symmetry, 5 (6) modes have B_1 symmetry and 3 (3) modes have A_2 symmetry (data of chlorobenzene in parentheses). All modes except the A_2 modes are infrared active. The A_1 modes show *a*-type transitions in the infrared spectra, the B_1 modes *c*-type transitions and the B_2 modes *b*-type transitions.

The infrared spectra of pyridine and chlorobenzene have been measured with the Bruker IFS 125 HR Zürich Prototype (ZP) 2001 [12] at room temperature in a 3 m glass cell and a White-type cell with an effective optical path length of 9.3-19.6 m. The spectra were recorded with a resolution of 0.0008-0.0015 cm^{-1} in the range 600-1300 cm^{-1}.

2. Analysis

The assignment of the observed rovibrational transitions belonging to a particular subband consisting of P and R branches has been carried out efficiently with an interactive Loomis-Wood assignment program [13] previously designed for linear molecules. This assignment program has been used successfully for several asymmetric top molecules: $CHClF_2$ [14], $CHCl_2F$ [15], CDBrClF [12] and C_2H_3DO [16]. In the following description the term ‘subband’ or ‘series’ describes the transitions belonging to one K_a or K_c value.

The rovibrational analysis has been carried out with Watson's A reduced effective Hamiltonian [17] in the III^r representation up to sextic centrifugal distortion constants. The spectroscopic data were analyzed using the WANG program described in detail in [18]. The spectroscopic constants of each band of pyridine were fitted separately according to the A reduction. All constants of the ground state of pyridine up to sextic distortion constants were fixed to the values of Ye et al. [7].

The ν_{18a} mode of pyridine

This mode of pyridine has A_1 symmetry. It was assigned in the spectrum as P and R branches for a-type transitions ($J < 60$, $K_a < 55$). The ν_{18a} band is perturbed by a z-Coriolis resonance between the ν_{18a} and ν_{18b} (B_2) states. The rotational, quartic and some sextic distortion constants of the ν_{18a} state were determined. The constants of the dark state ν_{18b} were fixed to the values of the ground state constants except for the rotational constants B and C. The Coriolis parameter ξ_z was determined to be 0.037 cm^{-1}. Figure 1 shows a comparison of the recorded band to a simulation using the fitted constants of an effective Hamiltonian. The upper trace shows the spectrum recorded in a 3 m cell with aperture 1.15 mm and a pressure of 0.8 mbar, the middle trace the spectrum recorded in a White-type cell with 9.6 m pathlength with aperture 1 mm and a pressure of 0.3 mbar, and the lower trace shows the simulation of the pyridine spectrum with a resolution of 0.0014 cm^{-1}. As one can see the reduction of the aperture and the pressure yields a slightly better resolved spectrum.

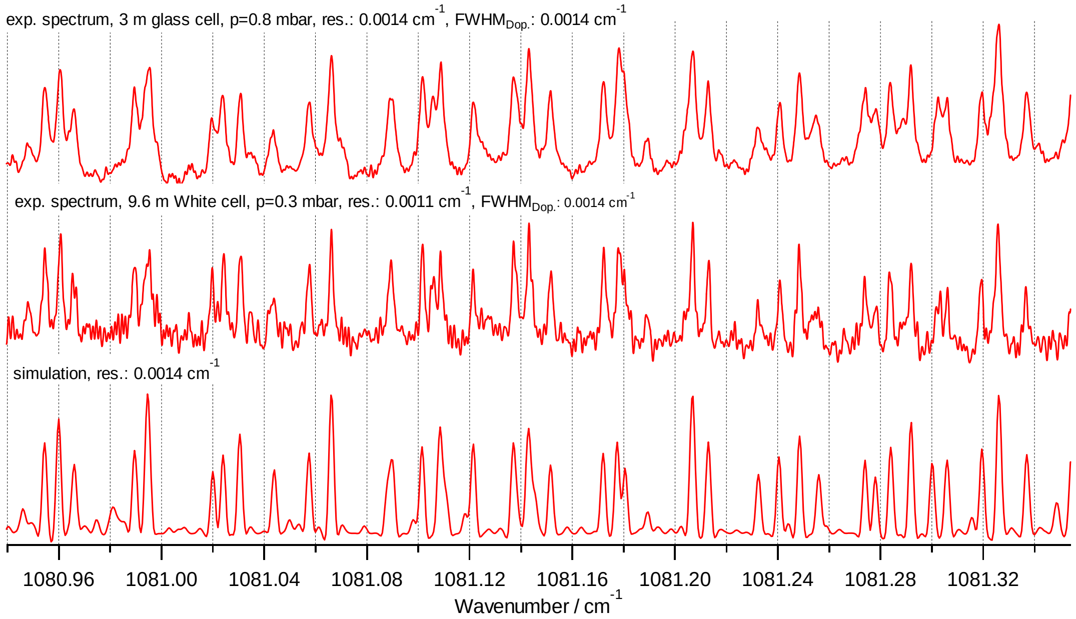

Figures 1: FTIR spectrum of the ν_{18a} band of pyridine compared to a simulation.

The ν_{15} mode of pyridine

This mode of pyridine has B_2 symmetry. It was assigned in the spectrum as P and R branches for b-type transitions ($J < 55$). The ν_{15} band is perturbed by a z-Coriolis resonance between the ν_{15} and ($\nu_4+\nu_{16b}$) (A_1) states. The rotational and quartic distortion constants of the ν_{15} state were determined. The constants of the dark state ($\nu_4+\nu_{16b}$) were fixed to the values of the ground state except for the rotational constant B. The Coriolis parameter ξ_z was determined to be 0.006 cm^{-1}. Figure 2 shows a comparison of the recorded band to a simulation using the fitted constants of an effective Hamiltonian.

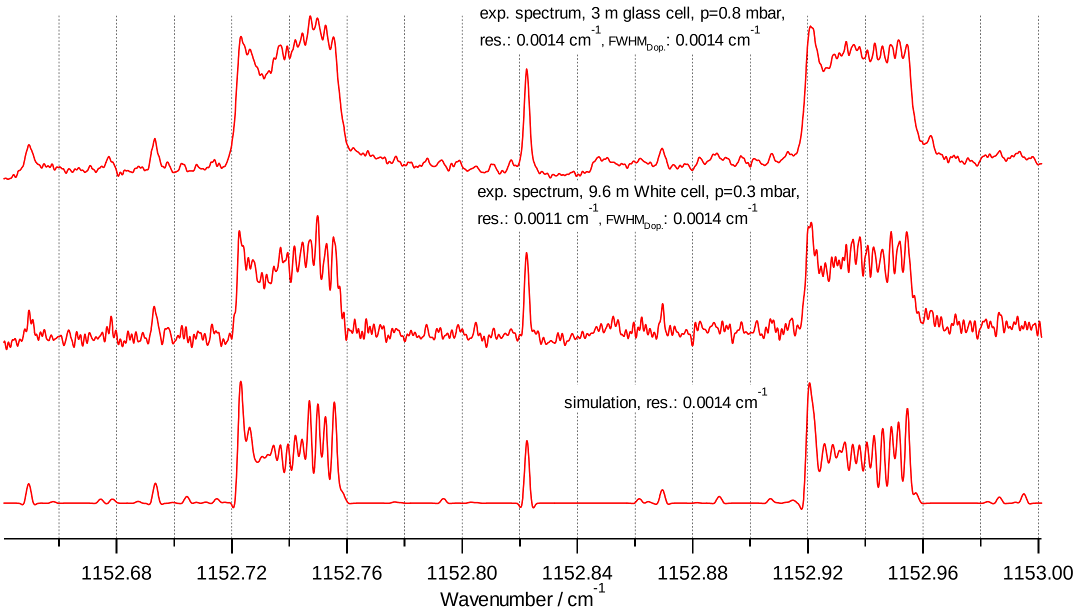

Figures 2: FTIR spectrum of the ν_{15} band of pyridine compared to a simulation.

The ν_{10b} mode of chlorobenzene

We have detected three bands of chlorobenzene in the region 650-1000 cm^{-1}, the ν_{10b} (B_1), ν_{12} (A_1) and ν_5 (B_1) bands. Among them, the ν_{10b} band has the highest intensity. According to the symmetry of the ν_{10b} band (B_1) it has *c*-type transitions which are clearly visible for the $C_6H_5{}^{35}C$ isotopomer in the Loomis-Wood diagram in Figure 3.

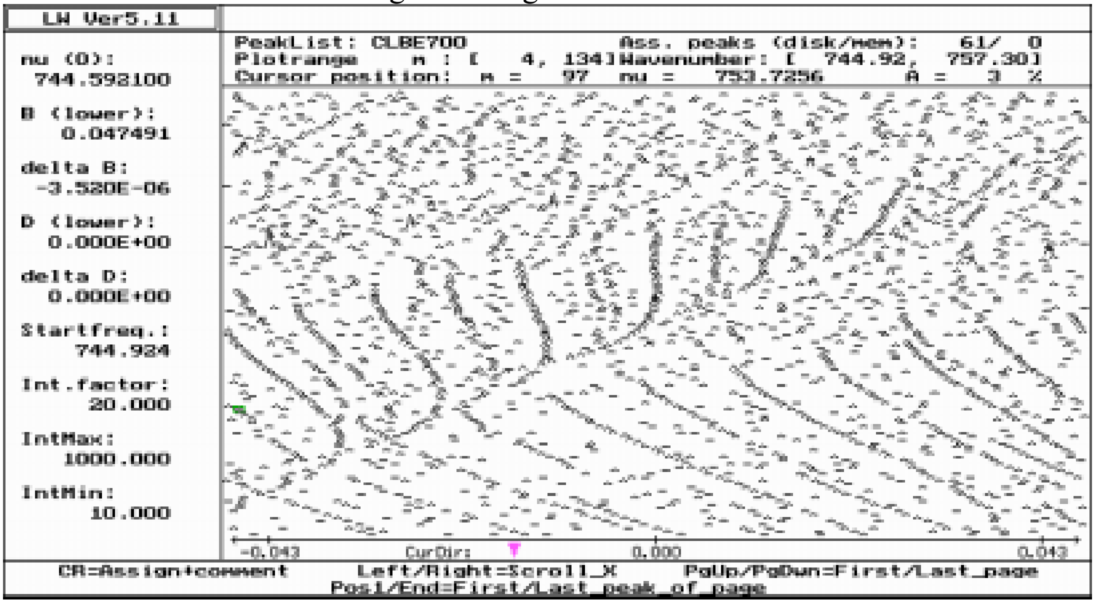

```
LW Ver5.11
nu (0):
 744.592100
B (lower):
  0.047491
delta B:
 -3.520E-06
D (lower):
  0.000E+00
delta D:
  0.000E+00
Startfreq.:
   744.924
Int.factor:
    20.000
IntMax:
  1000.000
IntMin:
    10.000

PeakList: CLBE700              Ass. peaks (disk/mem):   61/   0
Plotrange      m : [    4,  134]Wavenumber: [  744.92,  757.30]
Cursor position:  m =    97    nu =    753.7256        A =    3  %
```

Figure 3: Loomis-Wood diagram of the ν_{10b} band of chlorobenzene in the R branch region. The *c*-type transitions are clearly visible.

3. Conclusion

We were able to rotationally resolve the mid-infrared spectra of pyridine in the region 700 - 3600 cm^{-1} and chlorobenzene in the region 700-1000 cm^{-1}. All the bands of pyridine analysed so far are perturbed except the ν_4 band [9]. All the modes of pyridine with *B* symmetry are much weaker than those with *A* symmetry.

In the future, the region of pyridine around 1200 cm^{-1}, which is not unambiguously assigned, and the Fermi resonance bands of pyridine at 1500 cm^{-1} will be analysed. An analysis of the rovibrational spectra of the DNA bases should be possible based on the techniques developed here.

The *c*-type transitions of the ν_{10b} band (B_1) and *a*-type transitions of the ν_{12} (A_1) band of chlorobenzene $C_6H_5{}^{35}Cl$ have been positively identified and a complete analysis of these bands is underway.

References

[1] J. Turkevich and P.C. Stevenson, *J. Chem. Phys*. 11 (7), 328 (1943).
[2] H.D. Stidham and D.P DiLella, *J. Raman Spectrosc.* 8 (3), 180 (1979).
[3] K.N. Wong and S.D. Colson, *J. Mol. Spectrosc.* 104, 129 (1984).
[4] T.D. Klots, *Spectrochim. Acta* 54A, 1481 (1998).
[5] F. Partal Urena, M. Fernandez Gomes, E.A. Lopez Gonzalez and E. Martinez Torres, *Spectrochim. Acta* 59 2815-2839 (2003).
[6] S. Albert, D.T. Petkie, R.P.A. Bettens, S.P. Belov and F.C. De Lucia, *Anal. Chem.* 70, 719A (1998).
[7] E. Ye, R.P.A. Bettens, F.C. De Lucia, D.T. Petkie and S. Albert, *J. Mol. Spectrosc.* 232, 39 (2005).
[8] Y. Thiel, V.A. Walters, K.B. Wieberg and S.D. Colson, *Int. J. Quant. Chem*., 39, 423 (1991).
[9] S. Albert, K.K. Albert, M. Quack, R.P.A Bettens and F.C. DeLucia, *to be published.*
[10] H.D. Whiffen, *J. Chem. Soc*. 350 (1956).
[11] A. Uskola, F. J. Basterretxea and F. Castano, *J. Mol. Spectrosc*. 202, 262 (2000)
[12] S. Albert, K. Albert Keppler, and M. Quack, *Trends in Optic and Photonics* 84, 177 (2003).
[13] B.P. Winnewisser, J.Reinstädtler, K.M.T. Yamada, and J. Behrend, *J. Mol. Spectrosc*. 136, 12 (1989).
[14] S. Albert, H. Hollenstein, M. Quack, and M. Willeke, *Mol. Phys* 102, 1671 (2004).
[15] S. Albert, K. K. Albert and M. Quack, *J. Mol. Struct*. 695-696, 385 (2004).
[16] K. Keppler Albert, S. Albert, M. Quack, J. Stohner, O. Trapp, V. Schurig, *to be published.*
[17] J.K.G Watson, In J.R. Durig, editor, Vibrational Spectra and Structure, Vol. 6, pp. 1-89, Amsterdam, (1978). Elsevier.
[18] D. Luckhaus and M. Quack, *Mol. Phys*., 68, 745 (1989).

Large Amplitude Coupled Vibrations in the Hydrogen-Bonded Systems HF-H_2O, HF-H_2S, HCl-H_2O, and HCl-H_2S

M. Lewerenz, P. Asselin, B. Madebène, P. Soulard

Université Pierre et Marie Curie - Paris 6; CNRS, Laboratoire Dynamique Interactions et Réactivité, UMR 7075, Case 49, Place Jussieu, 75252 Cedex Paris, France

ABSTRACT

We present a combined experimental and theoretical study of the vibrational spectra of the hydrogen bonded complexes HF-H_2O, HF-H_2S, HCl-H_2O, and HCl-H_2S in the region of the donor (HF or HCl) stretching fundamental. Jet-FTIR spectra of HF-H_2S and HCl-H_2S show rotational resolution in spite of predissociation. Spectra recorded in a cooled cell exhibit pronounced hot band progressions due to low frequency intermolecular modes coupled with the donor stretch. The HF-H_2O spectrum indicates the presence of an extremely strong tunneling effect. The assignment of observed spectral features and the experimental coupling constants and trends in rotational constants are in excellent agreement with ab initio results obtained from potential surfaces at MP_2 and CCSD(T) levels and an adiabatic anharmonic variational calculation of the vibrational energy levels.

1. Introduction

Hydrogen bonding plays a major role for the structure of biomolecules and associating liquids. Infrared experiments carried out in our laboratory [1-4] and elsewhere have indicated the presence of a universal coupling scheme between the five soft intermolecular modes created by associating simple donors like HF and HCI with acceptors of the form R_2O or R_2S and the stiff donor stretching mode. This multidimensional coupling is an essential element in the correct prediction of the donor frequency shift, has immediate consequences for predissociation dynamics, and provides insight into the structure determining stiffness of hydrogen bonds. The present study is an extension of this work towards smaller complexes with R=H where rotational resolution can be achieved in the experiments and where high-level explorations of the potential energy surfaces are possible.

2. Summary of Results

Fig. 1 shows the vibrational spectrum of HF-H_2S observed in a free jet and in a cooled cell. The partially resolved K-structure indicates relatively slow predissociation even though we excite the donor stretch mode which is directly involved in the hydrogen bond. The low temperature provides an unambiguous assignment of the cold HF stretch transition which is 237 cm^{-1} red shifted with respect to free HF. At higher temperature hot bands appear which originate from complexes which carry one or more quanta of intermolecular excitation. Their position on the blue side of the cold transition indicates a stiffening of the intermolecular modes upon donor excitation. Similar trends are observed in the spectrum of HCl-H_2S. No rotational structure is resolved for HF-H_2O but a weak absorption remains about 19 cm^{-1} red shifted relative to the cold transition even in the free jet.

For all four complexes 2-dimensional cuts through the complete potential energy surfaces were computed for all combinations of the donor stretch mode with the five intermolecular modes at both MP2 and CCSD(T) levels with aug-cc-VTZ basis sets. The D_0 dissociation energies of all four complexes are found to lie below the donor stretching frequency thereby allowing predissociation. Vibrational energy levels were computed within an adiabatic variational approach, where the high frequency donor stretch problem is solved numerically for a large number of values of intermolecular coordinates R. The resulting eigenvalues $E(R;v)$ then provide adiabatic surfaces with parametric dependence on v on which the intermolecular problem is solved variationally, yielding eigenvalues $E(v_{inter};v)$ and wave functions from which expectation values can be computed.

The computed level structures show that the frequencies of most intermolecular modes increase with donor excitation and are in excellent quantitative agreement with experiment. The stiffening of the complexes upon donor excitation is also visible in the evolution of the B and C rotational constants which increase with excitation. The tightening of the complexes leads to an increase of the adiabatic barrier to inversion of the complexes, such that the huge tunneling splittings in HF-H_2O and HCl-H_2O undergo a major collapse (49 to 34 cm^{-1} and 64 to 48 cm^{-1}, respectively) which leads to a red-shifted satellite band for the donor stretch originating from the upper tunneling level. The computed position of this band is in excellent agreement with the observed position of the red-shifted hot band in HF-H_2O.

[1] M. Goubet, B. Madebène, and M. Lewerenz, Chimia 58, 618 (2004)
[2] P. Asselin, M. Goubet, M. Lewerenz, P. Soulard, and J. P. Perchard, J. Chem. Phys.121, 5142 (2004)
[3] M. Goubet, P. Asselin, P. Soulard, M. Lewerenz, and Z. Latajka, J. Chem. Phys.121, 7784 (2004)
[4] P. Asselin, M. Goubet, Z. Latajka, P. Soulard, and M. Lewerenz, Phys. Chem. Chem. Phys. 7, 592 (2005)
[5] P. Asselin, P. Soulard, B. Madebène, M. E. Alikhani, and M. Lewerenz, Phys. Chem. Chem. Phys. submitted (2005)

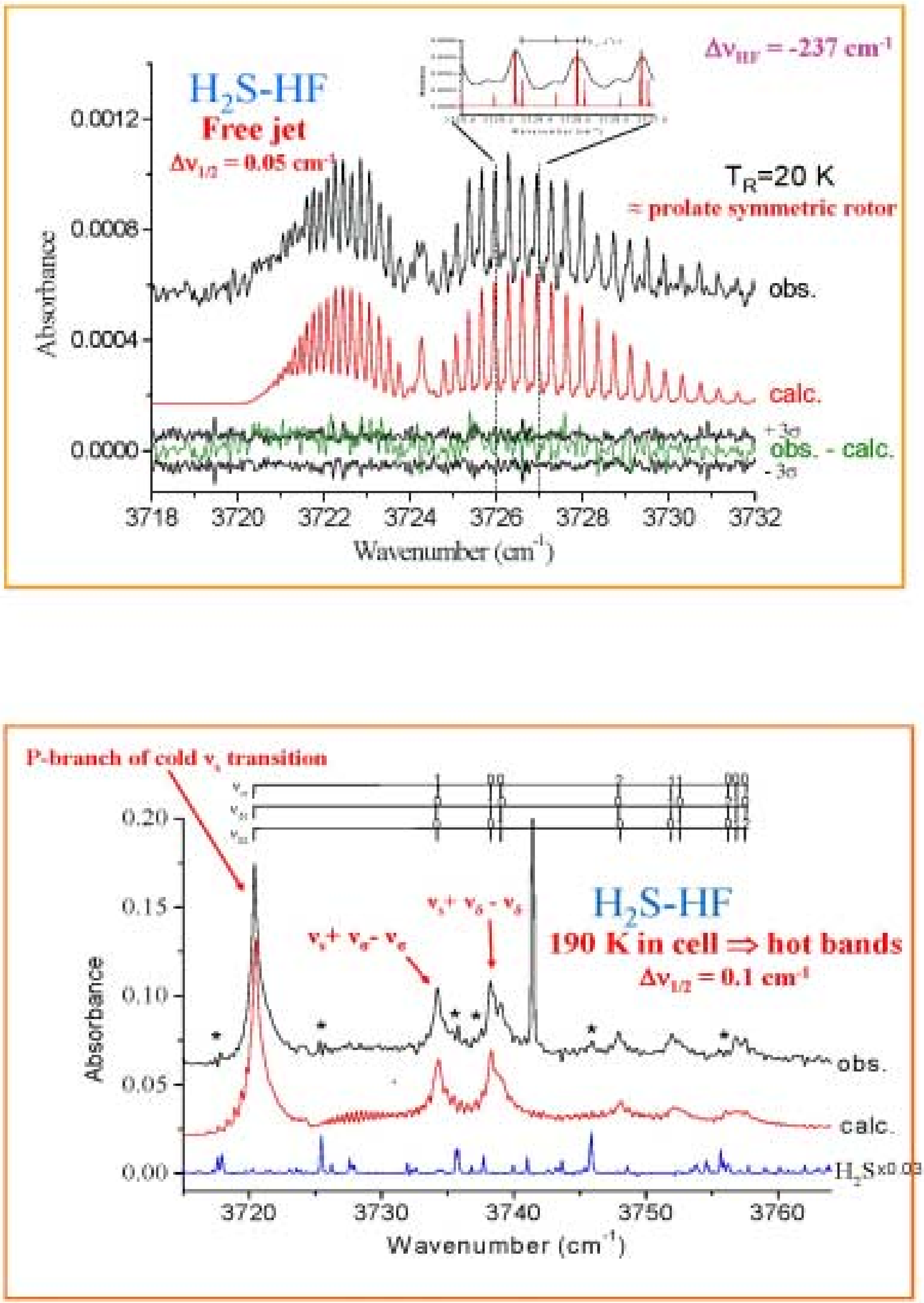

Fig. 1: Free jet (upper part) and cooled cell (lower part) spectra of the HF-H_2S complex. Note the partially resolved K-structure in the jet spectrum and the blue shifted hot bands at 190 K. The v_σ and v_δ labels give the quantum numbers of the intermolecular stretch and the two bending modes in the lower state of hot transitions. Asterisks indicate subtraction of H_2S monomer lines. The strong line near 3741 cm^{-1} is due to HF.

Collisional alignment of molecules in supersonic expansion probed by IR laser light absorption and molecular beam scattering

G. Demarchi[1,2], M. Scotoni[1], S. Iannotta[2], D. Bassi[1] , D. Cappelletti[3], M. Bartolomei[4], V. Aquilanti[4], F. Pirani[4]

[1] *Dept. of Physics, University of Trento, via Sommarive, 14, I-38050 Povo (TN)*
(presenting author email: demarchi@science.unitn.it)

[2] *CNR-IFN, Section of Trento, Via Sommarive ,18, I-38050 Povo (TN)*

[3] *Dept. of Civil and Env. Engineering, Via G. Duranti, 93a, I-06123 Perugia (PG)*

[4] *Dept. of Chemistry, University of Perugia, Via Elce di Sotto, 8, I-06123 Perugia (PG)*

ABSTRACT

The knowledge of the spatial orientation of molecules plays a fundamental role for the characterization of the physical, chemical and thus biological properties of a complex system. In the past few years the need for detecting, and afterwards controlling, the quantum state of an atomic or molecular system has increased a lot. In particular the rotational alignment of molecules obtained by supersonic expansion has received much attention[1-3], both from the theoretical and from the experimental point of view, because this technique has been recognized as a feasible way of preparing aligned molecules.

Discussion

In this work, recent results on alignment degree measurements of ethylene molecules, by means of polarized laser light absorption and molecular beam scattering, will be presented [4-5]. Those experiments have been carried out in two different molecular beam apparatuses, but with molecular beam sources operating under the same condition.

In the first apparatus a polarized pulsed IR laser provides the needed light source. A fast superconducting bolometer is used for the detection of the molecular absorption, using the TOF - optothermal technique. The scattering apparatus consists of a slotted disks velocity selector, a scattering cell (containing the target gas) placed along the molecular beam axis, and a quadrupole mass spectrometer as detector.

Rovibrational transitions of the molecules with suitable dipole moment bearing, with respect to the molecular spatial geometry, has been used as a probe of the preferential alignment of **J** (rotational angular momentum) in the spectroscopic experiment. The anisotropy parameter, defined as $R=2x(S_{para} - S_{perp})/(S_{para} + S_{perp})$ (S,absorption signal,for both laser light polarizations) has been determined under various experimental conditions (see Figure 1), and compared with the predictions of a simple theoretical model.

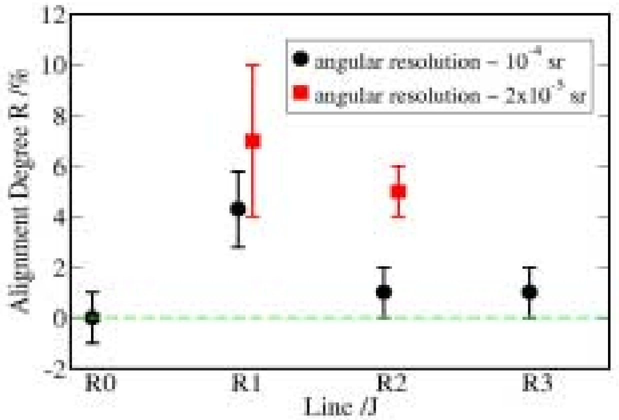

Figure 1: Anisotropy parameter, R, measured for various rotational angular states J, and for two diffent angular resolutions (only for J=1,2). There is a clear dependance both from the J value and from the solid angle sampled by the bolometer.

In the scattering apparatus, the integral cross section Q(v) of the seeded molecules with a gaseous target has been measured as a function of the beam velocity, and then compared with a model. If the projectile molecules change from a situation where **J** is randomly distributed to another one where **J** is aligned along some preferential direction, a change of Q(v) (see Figure 2), at the same v, is expected because of the modification of the intermolecular interaction.

Conclusions

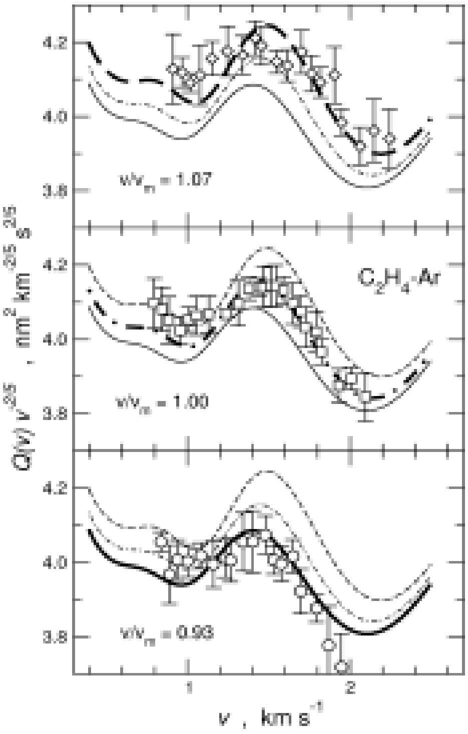

Figure 2: Scattering cross sections measured at various v/v_m ratios

The spectroscopic experiment clearly shows the dependence of the aligned molecules percentage from the rotational state. On the other side, the scattering experiment distinctly points out the relationship between aligned configuration of molecules and beam velocity. Some attractive applications for beams of aligned molecules have been recently presented, and the information provided by our experimental techniques in principle could be very useful for understanding the resulting surface obtained via molecular beam film growing[6]. Other preliminary results of work-in-progress experiments will also be presented.

References

[1] - V.Aquilanti, D.Ascenzi, D.Cappelletti, F. Pirani, *Nature* **371**, (1994) 399
[2] - S.Harich, A.M. Wodtke, *J.Chem. Phys.* ,**107**, (1997), 5983
[3] - F. Pirani, M.Scotoni, D. Bassi, D. Cappelletti *et al.*, *J. Chem. Phys.*, **119** (2003) 265
[4] - D. Cappelletti, F. Pirani, G. Demarchi, M. Scotoni *et al.*, *EPJD* (submitted)
[5] - D. Cappelletti, F. Pirani, G. Demarchi, M. Scotoni *et al.*, *Chem. Phys. Lett.* (submitted)
[6] - L. Vattuone, U. Valbusa, D. Cappelletti, F. Pirani *et al.*, *Angew. Chem. Int. Ed.,* **43**, 5200-5203 (2004)

Density functional theory for an accurate calculation of dispersion-dominated interactions in molecular clusters

B. Jeziorski[1], **R. Podeszwa**[2], **and K. Szalewicz**[2]

[1]Department of Chemistry, University of Warsaw, Pasteura 1, 02-093 Warsaw, Poland

[2]Department of Physics and Astronomy, University of Delaware, Newark, DE 19716, USA

It is well known and documented[1,2] that the local or gradient corrected density functionals developed thus far are unable to describe, even qualitatively, the dispersion interaction between two (or more) weakly interacting monomers. This problem severely limits the usefulness of the computationally efficient density functional theory (DFT). In particular, applications to clusters (or bulk phases) for which the total interaction energy is dominated by the dispersion interaction lead usually to very poor or nonsensical results.

On the other hand, the conventional wave function approach in the form the coupled cluster [CCSD(T)] or the symmetry-adapted perturbation theory (SAPT) has been shown to give very accurate description of the dispersion interaction and has provided intermolecular potentials which performed very well in numerous applications to spectroscopy and to simulation of bulk properties[3,4]. The high accuracy of CCSD(T) or conventional SAPT treatments comes, however, at the price of a very steep scaling of the computational effort which grows roughly as N^7, where N is the number of atoms. This steep scaling of the computational time with the system size makes applications to large polyatomic monomers unfeasible at the moment. These failures of the DFT and the conventional wave function approaches leaves a large class of weakly interacting polyatomic complexes without a possibility of an adequate theoretical treatment.

We have developed a method, referred to as SAPT(DFT), which solves the difficulty described above[5,6]. In this method, the dispersion part of the interaction energy is obtained from a generalized Casimir-Polder formula

$$E^{(2)}_{\text{disp}} = -\frac{1}{2\pi}\int_0^\infty \iiiint \alpha_A(\boldsymbol{r}_1, \boldsymbol{r}'_1|i\omega)\, \alpha_B(\boldsymbol{r}_2, \boldsymbol{r}'_2|i\omega) \frac{d\boldsymbol{r}_1 d\boldsymbol{r}_2}{|\boldsymbol{r}_1-\boldsymbol{r}_2|}\frac{d\boldsymbol{r}'_1 d\boldsymbol{r}'_2}{|\boldsymbol{r}'_1-\boldsymbol{r}'_2|} d\omega \tag{1}$$

evaluated with the frequency (ω) dependent density-density response functions $\alpha_A(\boldsymbol{r}_1, \boldsymbol{r}'_1|i\omega)$ and $\alpha_B(\boldsymbol{r}_2, \boldsymbol{r}'_2|i\omega)$ of monomers (A and B) computed using time-dependent DFT techniques. It has been proved essential that the monomer exchange correlation potentials $v_{xc}(\boldsymbol{r})$, employed in the calculations, are asymptotically corrected at large $|\boldsymbol{r}|$.

When the density fitting technique is used[7] to expanded $\alpha_X(\boldsymbol{r}_1, \boldsymbol{r}'_1|i\omega)$, X=A,B, in terms of products of auxiliary atomic orbitals (with coefficients forming matrices $\boldsymbol{C}_A$ and $\boldsymbol{C}_B$), Eq. (1) reduces to

$$E^{(2)}_{\text{disp}} = -\frac{1}{2\pi}\int_0^\infty \text{Tr}\, \boldsymbol{C}_A(i\omega)\, \boldsymbol{J}\, \boldsymbol{C}^T_B(i\omega)\, \boldsymbol{J}^T\, d\omega, \tag{2}$$

where $\boldsymbol{J}$ stands for the matrix of two-index Coulomb integrals and $\boldsymbol{X}^T$ denotes the transposition of matrix $\boldsymbol{X}$, When the matrices $\boldsymbol{C}_A$ and $\boldsymbol{C}_B$ are known (from monomer calculations) the evaluation cost of Eq. (2) scales as $M^3 I$, where M is the number of auxiliary orbitals (proportional to the number of atoms) and I is the number of ω-integration points (of the order of 10). The proposed method recovers the dispersion energies of He, Ne, Ar, H_2O, and CO_2 dimers to within 5% or better in the whole range of van der Waals minimum and for larger distances. The quality of the SAPT(DFT) dispersion energies appears to be so high that, except for the helium dimer, these energies may actually be more accurate than the results of the best wave function calculations.

To reconstruct the total interaction energy, the dispersion energy is combined with: (*i*) the electrostatic and first-order exchange interaction energies as defined in SAPT but computed using monomer Kohn-Sham determinants[8–10], (*ii*) the induction energy computed using the coupled Kohn-Sham static response theory[11], and (*iii*) the exchange-induction and exchange-dispersion energies computed using Kohn-Sham orbitals and orbital energies[6,12]. Employing the asymptotically corrected exchange correlation potentials for monomers is also essential in this case.

The resulting SAPT(DFT) potential energy curves turn out to be very accurate in the wide range of intermolecular separations. For the benzene dimer[13] the results are very close to those of the much more expensive CCSD(T) treatment. For systems of the size of the benzene dimer and for the triple-zeta quality basis sets, a SAPT(DFT) calculation (with density fitting) takes less time than a conventional supermolecular DFT calculation.

Due to the favorable computational scaling the SAPT(DFT) approach is applicable to much larger molecules than any method used thus far for a reliable calculation of dispersion-dominated interaction potential. Specifically, calculations for dimers involving over 40 atoms have already been performed using this approach.

References

1. X. Wu, M. C. Vargas, S. Nayak, V. L. Lotrich, and G. Scoles, J. Chem. Phys. **115**, 8748 (2001).
2. S. Tsuzuki and H. P. Lüti, J. Chem. Phys. **114**, 3949 (2001).
3. B. Jeziorski, R. Moszynski, and K. Szalewicz, Chem. Rev. (Washington D.C.) **94**, 1887 (1994).
4. B. Jeziorski and K. Szalewicz, in *Handbook of Molecular Physics and Quantum Chemistry*, edited by S. Wilson, Wiley, 2002, Vol. 3, Part 2, Chap. 8, pp. 37-83.
5. A. J. Misquitta, B. Jeziorski, and K. Szalewicz, Phys. Rev. Lett. **91**, 033201 (2003).
6. A. J. Misquitta, R. Podeszwa, B. Jeziorski, and K. Szalewicz, J. Chem. Phys. - in press.
7. R. Bukowski, R. Podeszwa, and K. Szalewicz, Chem. Phys. Lett. **414**, 111 (2005).
8. H. L. Williams and C. F. Chabalowski, J. Phys. Chem. A **105**, 646 (2001).
9. A. J. Misquitta and K. Szalewicz, Chem. Phys. Lett. **357**, 301 (2002).
10. A. Hesselmann and G. Jansen, Chem. Phys. Lett. **357**, 464 (2002).
11. G. Jansen and A. Hesselmann, J. Phys. Chem. A **105**, 11156 (2001); A. Hesselmann and G. Jansen, Chem. Phys. Lett. **362**, 319 (2002).
12. A. J. Misquitta and K. Szalewicz, J. Chem. Phys. **122**, 214109 (2005).
13. R. Podeszwa and K. Szalewicz, Chem. Phys. Lett. **414**, 488 (2005).

NIR spectroscopy of H_3^+, H_2D^+ and D_2H^+ in plasma

P. Hlavenka[1], R. Plašil[1], I. Korolov[1], G. Bánó[2], J. Glosík[1]

[1] Charles University, Faculty of Mathematics and Physics, Prague, Czech Republic (petr.hlavenka@mff.cuni.cz)

[2]Research Institute for Solid State Physics and Optics, HAS, Budapest, Hungary

ABSTRACT

Studies of H_3^+, H_2D^+, D_2H^+ ions in plasma at 100 and 300K are presented. The ions are generated in pulsed microwave discharge in He-Ar-H_2/D_2 gas mixture. Near infrared (NIR) second overtone transitions are used to identify the ions. The data were obtained using NIR Cavity Ringdown Spectroscopy (NIR-CRDS). Ion temperatures are obtained from Doppler broadening of absorption lines; ion number densities and their variations are obtained from CRDS signal.

1. Introduction

The ions H_3^+ and its deuterated isotopologues (H_2D^+, D_2H^+ and D_3^+) play important roles in the kinetics of media of astrophysical interest [1,2], planetary atmospheres and also in laboratory produced plasmas. Recent observations of the dense interstellar medium have shown that, in cold dense regions, deuterated molecular species are highly abundant. Also doubly and triply deuterated species were observed [3,4,5]. These observations stimulated an intensive search for H_2D^+ and D_2H^+ ions. The search was successful and H_2D^+ and D_2H^+ have been detected in cool dense interstellar clouds [3,4]. These observations have stimulated interest in further laboratory and theoretical studies of partially deuterated molecule ions. The kinetics of the formation of H_3^+, H_2D^+ and D_2H^+ ions in H_2/D_2 containing plasmas is well understood at laboratory temperatures [6,7,8]. The main challenge for future experiments is state-to-state description of ion molecule reactions of H_3^+ and its deuterated isotopologues at low temperatures corresponding to interstellar conditions. State selective studies of recombination are also required The motivation of the present study using overtone spectroscopy in low temperature plasma is the search for a tool available for simple *in situ* characterisation of the internal state of the reacting/recombining H_3^+, H_2D^+, D_2H^+.

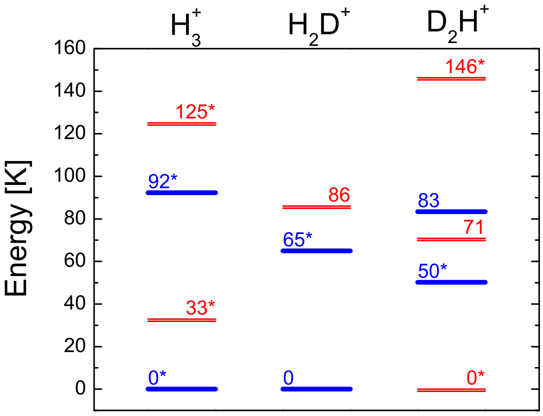

Fig. 1 Lowest energy levels of H_3^+, H_2D^+ and D_2H^+. The scale and values are both in K. Double line with value on the left represents the ortho states whereas single line with value on the right represents the para states of each species. The asterisk indicates the lover level of observed transition.

The low rotational energy levels of studied ions are plotted in Fig. 1, ortho and para states are indicated. Results of the present experiments will be used in parallel studies of laser induced ion-molecule reactions (LIR) carried out in a low temperature RF trap.

2. Experiment

In the present experiments ions were produced by a pulsed microwave discharge in He-Ar-H_2-D_2 mixture. **Fig. 2** shows a schematic diagram of the apparatus and indicates position of the mirrors of the optical cavity. A large flow of He was used to dilute possible impurities due to out gassing from the walls during the discharge, and to protect the surface of the mirrors from plasma-enhanced deposition. In order to minimize losses the UHV technology was used in Test Tube and gas handling systems.

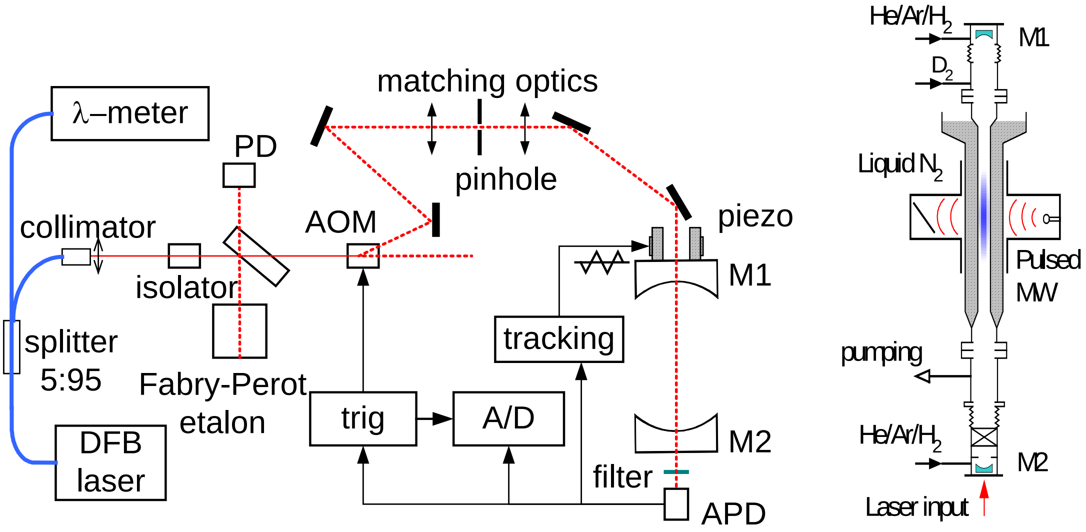

Fig. 2 Schematic diagram of the Test Tube apparatus and the continuous wave cavity ringdown spectrometer (cw-CRDS). The light from DFB diode laser is coupled into a high reflective cavity (M1,2). After reaching the threshold intensity, beam is switched off and the decay of light due to reflective losses and absorption of molecules is detected by a photodiode. Wavelength calibration uses Fabry-Pérot etalon and a wavemeter.

He ions and metastable atoms created during the microwave discharge are converted to H_3^+, (and deuterated analogues) by a sequence of ion-molecule reactions. The production scheme is well known. As the primary aim of this paper is the experimental determination of transition frequencies in NIR region, we focused on achieving high concentration of ions in lowest rotational states rather than kinetics studies of processes in plasma discharge. Once the transition frequencies are known, the discharge and ions population can be studied.

The physical principles of continuous wave cavity ringdown spectroscopy (cw-CRDS) have been described in numerous publications (see, for instance [9,10] and references cited therein). The present NIR-CRDS set-up is a modification of the version used in our previous work on H_3^+ recombination studies [11,12] where a detailed description of our NIR-CRD spectrometer could be found (see **Fig. 2** for details of actual set-up). The absolute wavenumber position at each wavelength was obtained from a wavemeter based on a Michelson interferometer. A Fabry-Pérot etalon was used to linearise the wavenumber scale. The spectra of H_2O and HDO were used to calibrate the system. We estimate the accuracy of the wavenumber measurement to be better than ± 0.005 cm^{-1}. The experiment was guided by the use of transition frequencies and integral absorptions predicted using the ultra-high accuracy *ab initio* model [13,14].

3. Results and discussion

3.1 H_3^+

Using He-Ar-H_2 mixture we first measured absorption spectra of H_3^+ ions at several buffer gas temperatures. We obtained second overtone transition frequencies corresponding to several low lying rotational energy states, both ortho and para. In **Fig. 3** the absorption line corresponding to transition $v_2 = 3 \leftarrow 0$ (P_{22}) is plotted, obtained transition frequency is 6877.546 cm^{-1}. The spectrum was measured during the microwave From the Doppler broadening the kinetic temperature of ions was obtained. In the same figure the decay of ion number density and corresponding ion temperature during an early afterglow (dominated by H_3^+) are plotted. From the plasma decay the recombination rate coefficient can be calculated [11].

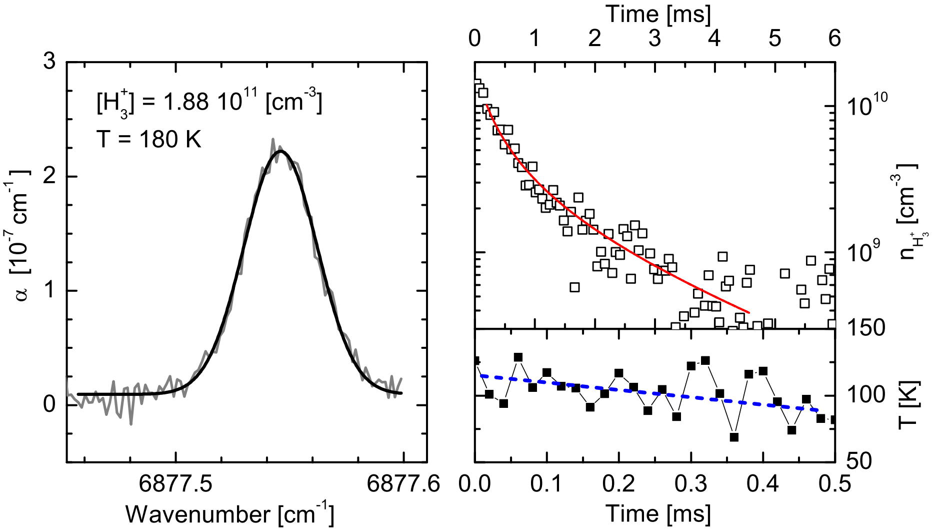

Fig. 3 Left: Second overtone absorption spectra of H_3^+ (ν_0 = 6877.546 cm^{-1}) recorded during microwave discharge in He/Ar/H_2 (flow ratio 800/1.2/0.8) in liquid N_2 cooled discharge tube, p = 6.5 mbar.

Upper right: The decay of H_3^+ concentration due to recombination and diffuse losses derived from absorption at the peak centre. Lower right: The kinetic temperature evolution derived from Doppler broadening of H_3^+ spectra in afterglow.

3.2 H_2D^+ and D_2H^+

Microwave discharge in a liquid nitrogen cooled mixture He-Ar-H_2-D_2 was used to produce deuterated $H_2D^+$and D_2H^+ ions. In **Fig. 4** there is a plot of absorption line corresponding to first excited para state of H_2D^+(v = 0). Measured transition frequency 6491.352(2) cm^{-1} is in very good agreement with theoretical value of Ramanlal and Tennyson. Again the ion kinetic temperature obtained from Doppler broadening is by 140 K higher than buffer gas temperature.

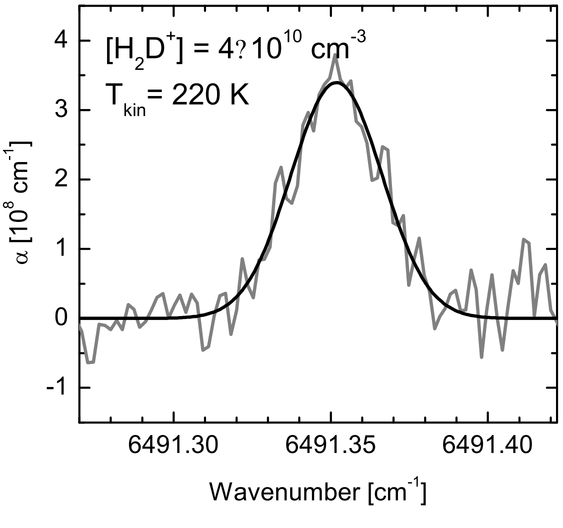

Fig. 4 Second overtone absorption spectra of H2D+ (ν_0 = 6491.352(2) cm^{-1}) measured in modulated microwave discharge in liquid N_2 cooled He/Ar/H_2/D_2 gas mixture, p = 7 mbar. With the assumption of the thermodynamic equilibrium with $T = T_{kin}$ = 220 K the number density [H_2D^+] = 4×10^{10} cm^{-3} was obtained.

Three absorption lines were observed for D_2H^+ ions. Example of measured line is plotted in **Fig. 5**. By tuning the laser to resonant frequency of transition the absolute number density of D_2H^+ ions in the discharge as a function of ratio of partial pressures of hydrogen and deuterium was measured, see right panel of **Fig. 5**. The calculation was made under assumption of thermodynamic equilibrium.

All measured transition frequencies for all three studied ions are in very good agreement with theoretical value calculated by Ramanlal and Tennyson [13,14].

Obtained transition frequencies are used in our study of Laser Induced Reactions at 10K in RF trap. Further studies of H_3^+, H_2D^+, D_2H^+ and D_3^+ ions are in progress.

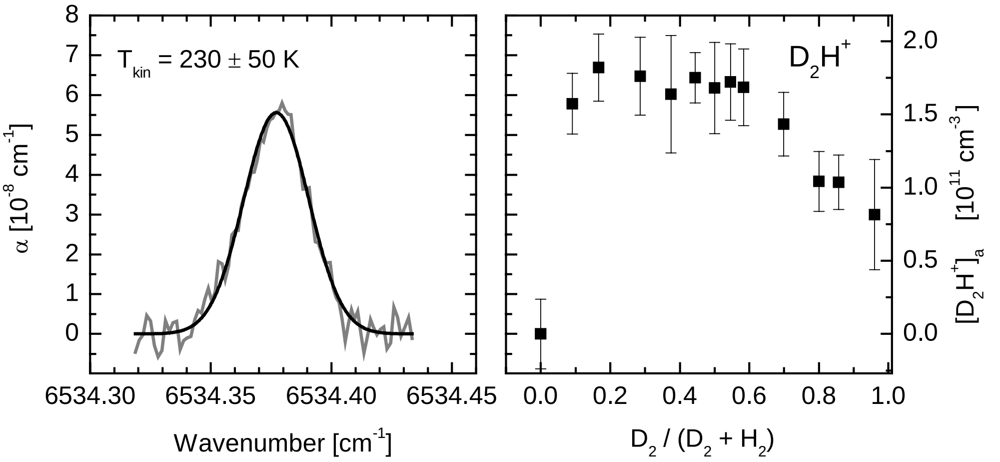

Fig. 5 Left: Second overtone absorption spectra of D_2H^+ ion (ν_0 = 6534.377(1) cm^{-1}). The obtained number density [D_2H^+]=1.5×10^{11} cm^{-3} (T = T_{kin} = 230 K). Right: The concentration of D_2H^+ in microwave discharge in $He/Ar/H_2/D_2$ mixture at different D_2/H_2 ratios, p = 7 mbar. The number density was calculated from the absorption at the central frequency.

Acknowledgments This work is a part of the research plan MSM 0021620834 that are financed by the Ministry of Education of the Czech Republic and partly was supported by Kontakt CZ-8/2004, GACR (202/03/H162, 205/05/0390, 202/05/P095), GAUK-278/2004 /B-FYZ/MFF, GAUK-226/2005 /B-FYZ/MFF

References

[1] T.R. Geballe, Phil. Trans. R. Soc. London A 358 (2000) 2503
[2] T.J. Millar, H. Roberts, A.J. Markwick, S.B. Charnley, Phil. Trans. R. Soc. London A 358 (2000) 2535.
[3] E. Roueff, Journal of Physics: Conference Series 4 (2005) 1
[4] C. Vastel, T.G. Phillips, H. Yoshida, Astrophysical Journal 606 (2004) L127.
[5] C. Vastel, T.G. Phillips, C. Ceccarelli, J. Pearson, Astrophysical Journal 593 (2003) L97.
[6] N.G. Adams, D. Smith, Astrophys. J. 248 (1981) 373.
[7] J. Glosík, Int. J. Mass Spectrom. Ion Proc. 139 (1994) 15.
[8] D. Gerlich, E. Herbst, E. Roueff, Planetary and Space Science 50 (2002) 1275.
[9] D. Romanini, A.A. Kachanov, F. Stoeckel, Chem. Phys. Lett. 270 (1997) 538.
[10] J. Morville, D. Romanini, A.A. Kachanov, M. Chenevier, Appl. Phys B 78 (2004) 465.
[11] P. Macko, G. Bánó, P. Hlavenka, R. Plašil, V. Poterya, A. Pysanenko, O. Votava, R. Johnsen, J. Glosík, Int. J. of Mass Spectrometry 233 (2004) 299.
[12] P. Hlavenka, R. Plašil, G. Bánó, I. Korolov, D. Gerlich, J. Ramanlal, J. Tennyson, J. Glosík, send for publication to Int. J. of Mass Spectrometry (2006)
[13] O.L. Polyansky and J. Tennyson, J. Chem. Phys. 110 (1999) 5056
[14] J. Ramanlal, J. Tennyson, Mon. Not. R. Astr. Soc. 354 (2004) 161

Paper for SASP 2006 in Obergurgl, 4-9 February 2006

Ultrafast Redistribution of Vibrational Energy After Overtone Excitation of CH_3I - Three Different Time Scales

Vitaly Krylov, Edouard Miloglyadov, Martin Quack, and Georg Seyfang

Physical Chemistry, ETH–Zürich, CH–8093 Zürich, Switzerland

Abstract

The redistribution of vibrational energy after overtone excitation was investigated for CH_3I in femtosecond pump-probe experiments by time delayed UV-absorption spectroscopy. Dependent on the near-IR excitation frequency three different relaxation times have been measured reaching from τ_1^{IVR} = 200 - 400 fs, τ_2^{IVR} = 4 - 6 ps to τ_3^{IVR} = 250 - 400 ps. This wide range of relaxation times is explained by different intramolecular coupling schemes for the initially excited vibrational levels.

Introduction

Already quite early it was realized in reaction rate theory that intramolecular vibrational energy redistribution (IVR) is essential for unimolecular reactions [1, 2, 3]. If the time scale for IVR is comparable to or slower than the time scale for the unimolecular reaction, mode selective chemistry may be expected. Two significantly different methods have been applied successfully to investigate the intramolecular redistribution of vibrational energy after near-IR overtone excitation: I. If a molecular Hamiltonian H_{mol} for the intramolecular couplings is derived from high resolution IR-spectra the time dependent dynamics of the initially excited vibrational levels can be obtained [3, 4, 5]. II. Intramolecular relaxation times can also be determined in femtosecond pump-probe experiments, where the population of the initial level, excited by the strong near-IR pump pulse, is followed by a time delayed weak probe pulse [6, 7, 8, 9].

For many molecules it has been shown that the Franck-Condon overlap integral from the excited XH-stretching vibration (X = C, N, O) in the electronic ground state to the lowest vibrational level of the electronically excited state is negligible. Only after relaxation of the initially excited level to the background states a significant 'hot-band' Franck-Condon factor is obtained. Generally, it is found that vibrationally excited molecules show an UV-absorption which is shifted to longer wavelengths. For CH_3I it has been found experimentally and was confirmed in theoretical calculations that this shift of the UV-absorption spectrum is related to the excitation of the CI-stretching vibraton. The technique of delayed UV-absorption has already been applied to study IVR after overtone excitation for different I-containing compounds in solution and in the gas phase [7, 9, 10, 11].

Experimental [9]

For our pump-probe experiments two identical optical parametric generators (OPG) (TOPAS, Light Conversion) are pumped by a femtosecond Ti:Sapphire laser (Clark CPA-1000) resulting in a pulse duration of 120 - 150 fs. The first overtone of the CH-stretching vibration around 5900 cm^{-1} is excited by the idler wave of one OPG, whereas the fourth harmonic of the output from the second OPG around 300 nm is used to probe the spectral changes in the UV-spectrum of the excited molecules. To measure the time evolution, the UV-pulse is sent through a variable delay line. For the near-IR a pulse energy of 30 - 40 μJ and a spectral width of 120 cm^{-1} are obtained. To reduce nonlinear intensity effects in the overlap region the UV-probe pulses are attenuated to pulse energies below 0.2 μJ. Both laser beams are focused with a f = 250 mm lens to the center of the sample cell (l = 200 mm) where they are overlapped under a small angle of 1-2 degree. To measure the change of the UV-absorption due to the near-IR excitation, the near-IR beam is modulated by an optical chopper. The relative pulse energy of the UV-beam is measured for every laser pulse before and behind the sample cell on two photodiodes D1 and D2. The difference of the ratio of the measured detector voltages U$_{D2}$/U$_{D1}$ for pump laser-on minus pump laser-off is calculated after transfer of the data to the computer to obtain the time dependent UV-absorption signal

$$\Delta_{UV} = \frac{U_{D2}/U_{D1}(\text{near-IR on}) - U_{D2}/U_{D1}(\text{near-IR off})}{U_{D2}/U_{D1}(\text{near-IR on}) + U_{D2}/U_{D1}(\text{near-IR off})} \tag{1}$$

Typically 3000 - 5000 laser pulses were averaged for each delay time between near-IR pump and UV probe pulse.

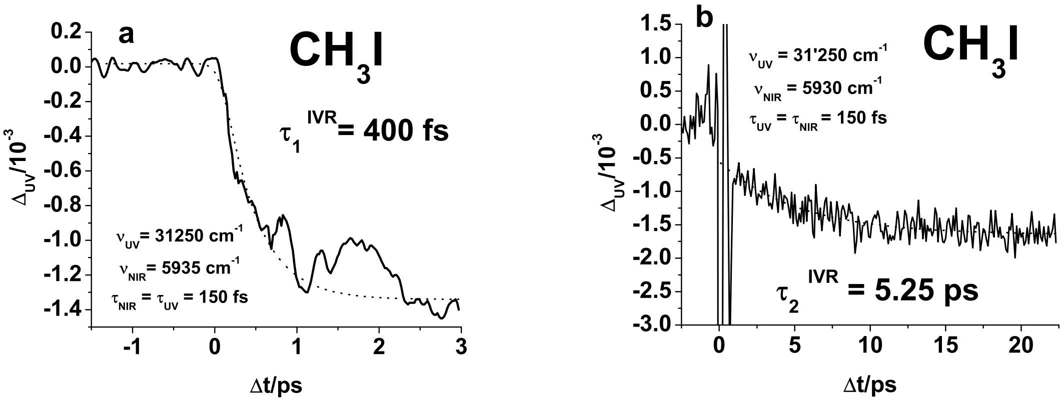

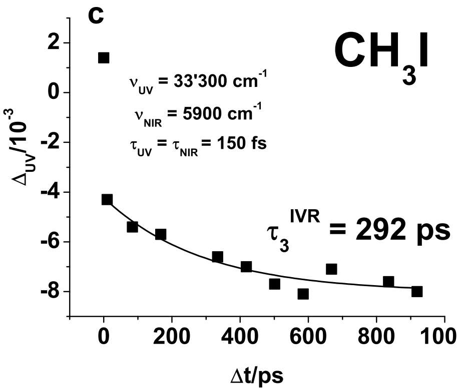

Figure 1: Three time scales for the redistribution of vibrational energy after overtone excitation of CH$_3$I, fast (a), medium fast (b) and slow (c). For every time scale an adjusted exponential decay function ($\cdots\cdots$) is shown. Three significantly different relaxation times τ_1^{IVR} = 0.2 - 0.4 ps, τ_2^{IVR} = 4 - 6 ps, and τ_3^{IVR} = 200 - 400 ps are obtained from the fit.

Results

The vibrational structure of the overtone of the CH-stretching vibration has been analyzed by J.L.Duncan et al.[12] The absorption spectrum between 5800 - 6200 cm^{-1} is dominated by the absorption of the four vibrational bands $2\nu_1$, $2\nu_4^0$, $2\nu_4^{\pm2}$ and $\nu_1 + \nu_4^{\pm1}$, where the last one is strongly coupled by a Fermi resonance to the $(\nu_4^{\pm1} + 2\nu_5^0)$-state. At room temperature the UV-absorption of CH_3I to the dissociative A-state shows its maximum around 38'000 cm^{-1} and extends down to 35'000 cm^{-1}. The variation of the UV-spectra due to vibrational excitation is detected in the spectral range from 31'000 - 35'000 cm^{-1}. In the experiments the photon energy of the pump laser is varied between 5800 - 6200 cm^{-1}. For a given excitation energy the measured relaxation times do not change significantly, if the probe wavelength is varied within the range given above.

For an excitation around 5900 cm^{-1} three different relaxation processes with relaxation times τ_1^{IVR} = 200-400 fs, τ_2^{IVR} = 4 - 6 ps and τ_3^{IVR} = 250 - 400 ps were found. Experimental decays for the three different relaxation processes are shown in figure 1. Due to experimental limitations the three relaxation processes had to be measured in different experiments and the relaxation times were obtained by fitting a single exponential decay curve separately in each experiment. It would be preferable to fit a combined model function to one single experiment with delay times reaching from 0 - 1000 ps. But as the relaxation times differ by 1-2 orders of magnitude, we think that our evaluation method is appropriate.

Within the experimental uncertainty the measured decay times for the three different relaxation processes do not depend on the precise photon energies of the near-IR pump and UV probe beam. If the pump laser is scanned across the near-IR absorption region only the relative magnitude of the signal amplitude of the three relaxation processes is changed. This is shown in figure 2, where the UV-absorption signal measured at 31'250 cm^{-1} is given for a delay time of 0.2, 20.0 and 1000 ps as a function the near-IR excitation energy. The dependence of the measured UV-signal upon the near-IR frequency for a delay time of 1000 ps follows, apart from a scaling factor, closely the absorption spectrum of the near-IR pump beam in a photo-acoustic cell.

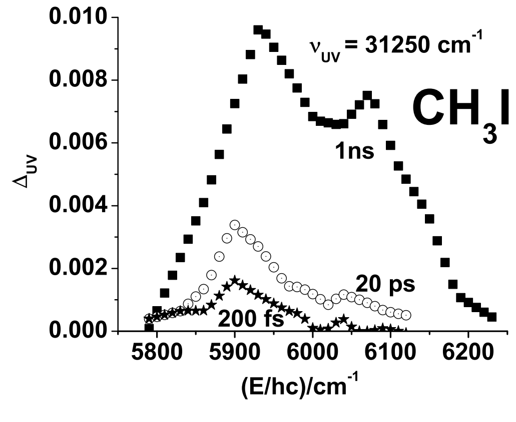

Figure 2: Energy dependence of the measured UV-absorption signal after near-IR excitation of CH_3I for different delay times between the near-IR pump and UV probe pulse Δt_1 = 0.2 ps ($\star$, fast process), Δt_2 = 20 ps ($\odot$, medium fast), and Δt_3 = 1000 ps (■, slow)

Discussion

From figure 2 it can be seen that the fast relaxation process is only measurable around 5900 cm^{-1}. Also the signal amplitude of the medium fast relaxation process is a factor of

3-4 larger in this spectral region compared to the range around 6100 cm^{-1}. An inspection of the IR-spectrum shows that the absorption in the low energy region is due to the vibrational states $2\nu_1$, $\nu_1+\nu_4^{\pm1}$, and $\nu_4^{\pm1}+2\nu_5^0$, where the latter two are only separated by 67 cm^{-1} and are coupled by a Fermi resonance with a coupling matrix element of $W_{155} = 46.8\ \mathrm{cm}^{-1}$ [12]. The region around 6100 cm^{-1} is dominated by the two $2\nu_4$-bands of A_1- and E-symmetry.

To obtain a 'hot-band' UV-absorption, observable by the time delayed probe pulse, the vibrational excitation has to migrate from the initially excited CH-chromophore to the lower lying background states, in particular to the CI-stretching vibration ν_3. A fast relaxation process is expected, if the initially populated level is directly, or only through a very small number of intermediate steps, coupled to the CI-stretchting vibration. To explain the frequency dependence of IVR in CH_3I a complete analysis of the vibrational couplings in the region of the first overtone of the CH-stretching vibration would be necessary. This analysis is not available yet. But some indications can be taken from the analysis of the fundamentals of the CH-stretching vibrations. In the analysis of the IR-spectrum around 2850 cm^{-1} a relatively strong coupling of the $2\nu_5^0$ state to the $(\nu_3+\nu_5^{\pm1}+\nu_6^{\pm1})$-state and from there to the $(2\nu_3+2\nu_6^0)$-state is found with coupling matrix elements of 10 to 12 cm^{-1} [13]. Thus, it may be justified to assume that the vibrational levels of CH_3I around 5900 cm^{-1} are efficiently coupled through the $(\nu_4^{\pm1}+2\nu_5^0)$-state to the CI-stretching vibration. This would explain the high contribution of the fast relaxation process in this spectral range. For the spectral range around 6100 cm^{-1} this route for an efficient excitation transfer does not exist, and only a slow relaxation process is measured.

Acknowledgement

Our work is supported financially by the ETH Zürich and the Schweizerischer Nationalfonds. We enjoyed discussion with and help from Sieghard Albert, Hans Hollenstein, Jürgen Stohner, and Martin Willeke

References

[1] M. Quack, and J.Troe *Theoretical Chemistry: Advances and Perspectives*, 6B:199–276, 1981

[2] M.Quack *Il Nuovo Cimento*, 63B:358–377,1981

[3] M.Quack in 'Femtosecond Chemistry', Manz, J. and Woeste, L., editors, *Verlag Chemie (Weinheim)*, pages 781–818 (1995)

[4] M.Quack *Annu. Rev. Phys. Chem.*, 41:839–874,1990

[5] J.Pochert, M.Quack, J.Stohner, and M.Willeke. *J. Chem. Phys.*, 113:2719, 2000

[6] D.Bingemann, M.P.Gorman, A.M.King, and F.F.Crim *J. Chem. Phys.* 107:661-664, 1997

[7] A.Charvat, J.Assmann, B.Abel, D.Schwarzer, K.Henning, K.Luther, and J.Troe *Phys. Chem. Chem. Phys.* 3:2230-2240, 2001

[8] T.Ebata, M.Kayano, S.Sato, N.Mikami *J. Phys. Chem A* 105:8623-8628, 2001

[9] V.Krylov, M.Nikitchenko, M.Quack, and G.Seyfang *Proc. SPIE* 5337:178-189, 2004

[10] D.Bingemann, A.M.King, and F.F.Crim *J. Chem. Phys.* 113:5018-5025, 2000

[11] C.G.Elles, M.J.Cox, and F.F.Crim *J. Chem. Phys.* 120:6973-6979, 2004

[12] J.L.Duncan, A.M.Ferguson, and S.Matthew *J. Chem. Phys.* 91:783-789, 1989

[13] F.Lattanzi *J. Chem. Phys.* 92:4380-4382, 1990

Investigation of stereomutation tunneling switching dynamics and parity violation in Chlorineperoxide

Martin Quack and Martin Willeke
Physical Chemistry, ETH–Zürich, CH–8093 Zürich, Switzerland
(willeke@ir.phys.chem.ethz.ch, martin@quack.ch)

Abstract

We present quantitative calculations on the stereomutation tunneling processes in the axially chiral chlorine isotopomers of Cl_2O_2 employing a quasiadiabatic channel reaction path Hamiltonian (RPH) approach and the corresponding parity violating potentials by means of quantum chemical calculations including our Multi Configuration-Linear Response (MC-LR) approach to electroweak quantum chemistry. The calculated ground-state torsional tunneling splittings $\Delta E_{\pm}$ for all isotopomers of Cl_2O_2 are much smaller than the parity violating energy differences $\Delta_{\mathrm{pv}}E$ between the enantiomers of these molecules and therefore parity violation is predicted to dominate the quantum dynamics of stereomutation at lower energies [1]. We propose a scheme using "tunneling switching" with vibrational excitation in order to carry out a measurement of time dependent parity violation in superposition states of initially well defined parity.

Introduction

Molecular parity violation has found renewed recent interest after our theoretical discovery [2-4] that the parity-violating effective potentials in polyatomic molecules and hence the parity-violating energy differences between enantiomers of chiral molecules are one to two orders of magnitude larger than anticipated on the basis of earlier theories [5]. Thus the proposed measurement of such energy differences [6] may be close to realization. Until now, no experimental effects of molecular parity violation have been observed, while qualitative suggestions of their importance in a variety of contexts e.g. homochirality observed in nature have been discussed in the literature (see e.g. reviews [7,8]). The experiments which are under current study fall in two categories. The first kind proposes to measure frequency differences e.g. in infrared spectra of chiral molecules (e.g. [9-11]) ($h\nu_R - h\nu_S$ in the scheme of Fig. 1). A drawback of such an experiment is that it only allows the determination of the *difference* of parity violating energy differences (e.g. $\Delta_{\mathrm{pv}}E^1 - \Delta_{\mathrm{pv}}E^0 = h\nu_R - h\nu_L$ (see Fig. 1)), which is an obvious limitation. The other approach is based on the use of optical transitions to intermediate excited states of well defined parity, which are accessible from both enantiomers, for example excited achiral electronic states, and some quantitative calculations for this case have been performed for 1–3–difluoroallene [12]. This means that $\Delta_{\mathrm{pv}}E$ can be measured either as a combination difference of spectral lines in the frequency domain or as a time dependent spectral change [6,7]. Another possibility is to carry out such experiments in the electronic ground state only [8], if one uses "tunneling switching" between a vibrational ground state satisfying $\Delta_{\mathrm{pv}}E^0 >> \Delta E^0_{\pm}$, where $\Delta E^0_{\pm}$ would be the tunneling splitting for a symmetrical (in this case hypothetical) parity conserving potential, and a vibrationally excited level satisfying $\Delta E^n_{\pm} >> \Delta_{\mathrm{pv}}E^n$, where therefore the energy eigenfunctions have essentially well defined parity. The aim of our paper is to present a theoretical proof of principle for such an experiment for the real, spectroscopically accessible [13], axially chiral molecule Cl–O–O–Cl.

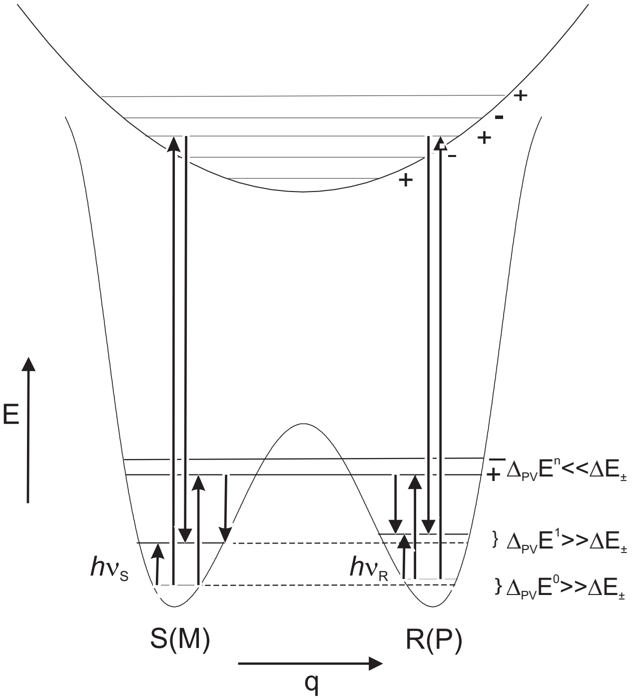

Fig. 1: Scheme for the generation of states of well defined parity in a chiral molecule with a substantial barrier for stereomutation in the ground state. In a first optical transition one generates a state of well defined parity (+) in either an electronically excited achiral state or a highly excited torsional state (with $\Delta_{\mathrm{pv}}E << \Delta E_{\pm}$). In a second induced transition a state (with $\Delta E_{\pm} << \Delta_{\mathrm{pv}}E$) with initially well defined (-) parity is generated in the ground state potential.

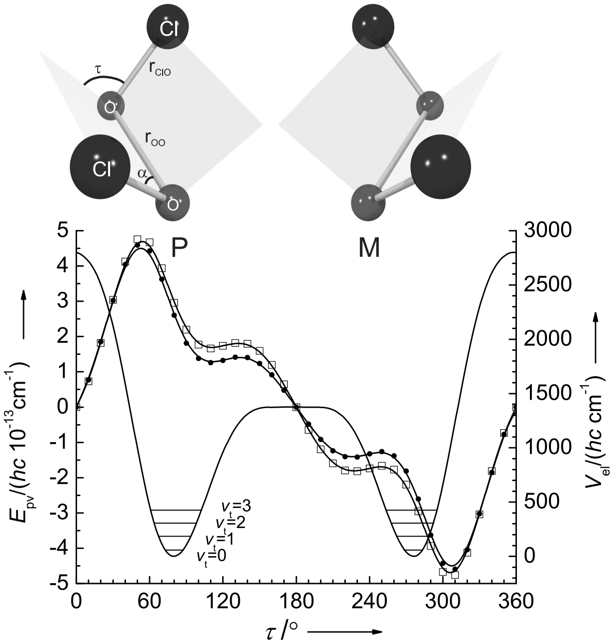

Fig. 2: Parity conserving torsional potential $V(\tau)$ plotted as a function of the dihedral angle τ and torsional energy levels for the first four torsional states ($v_t = 0...3$) and the corresponding parity violating potentials calculated with RPA/aug-cc-pVTZ (full circles) and RPA/6-311+G* (open squares). The calculations follow the reaction path in steps of $\Delta\tau = 10°$ with optimization of all structural parameters.

Theory and Methods of Calculation

The torsional tunneling dynamics were calculated with the quasi-adiabatic channel-reaction path Hamiltonian (RPH) approach described in detail in [14-18] using MP2/aug-cc-pVTZ calculations [1]. In short it treats the torsional motion anharmonically in detail and all remaining coordinates as harmonic (but anharmonically coupled to the reaction coordinate). The reaction path was calculated as a minimum energy path with the corresponding dihedral angle τ (Fig. 2) as leading coordinate. E_{pv} was determined within our MC-LR approach using the "random phase approximation" (RPA), as described in detail elsewhere (see [4,19-21] and refs. cited therein).

Results and Conclusion

Table 1 summarizes the results for the torsional tunneling splittings in the parity conserving potential $\Delta\tilde{\nu}_t = \tilde{\nu}\,(A^-) - \tilde{\nu}\,(A^+)$ of the first 14 pure torsional states (up to the trans barrier height) and the torsional wavenumbers $\tilde{\nu}(A^+)$ with respect to the corresponding zero point level and the corresponding band strengths G_t for transitions from the ground state of Cl_2O_2

isotopomers. The calculated tunneling splitting for the vibrational ground state is extremely small and on the order of $10^{-24}\mathrm{cm}^{-1}$. The calculated band strength G_t decreases by about an order of magnitude for each additional quantum of torsional excitation with the exception of states comparable in energy with the trans barrier height ($V_{\mathrm{trans}} = 1361\ \mathrm{cm}^{-1}$).

Tab. 1: Torsional tunneling splittings $\Delta\tilde{\nu}_t = \tilde{\nu}\,(A^-) - \tilde{\nu}\,(A^+)$ for pure torsional states $|v_t\rangle$ and band strengths G_t (in pm^2) for transitions from the rovibrational ground state $|v_0(A^+)\rangle$ to $|v_t(A^-)\rangle$ of $\mathrm{Cl_2O_2}$ (RPH, aug-cc-pVTZ). v_t is the torsional quantum number in high barrier notation. The corresponding $\tilde{\nu}\,(A^+)$ refer to the corresponding zero point level given in the line "0" as approximate wavenumber. Torsional level calculations without tunneling and using only the 1–dimensional torsional potential (CCSD(T)/ECP-TZDP//MP2/ECP-TZDP) are shown in parentheses [22]. All wavenumbers are given in cm^{-1}.

	^{35}Cl–O–O–^{35}Cl			^{37}Cl–O–O–^{37}Cl	
v_t :	$G_t(\nu_t(A^-) \leftarrow \nu_0(A^+))$	$\Delta\tilde{\nu}_t$	$\tilde{\nu}(A^+))$	$\Delta\tilde{\nu}_t$	$\tilde{\nu}(A^+))$
0	$-^a$	$6.7 \cdot 10^{-25}$	1504.64	$4.1 \cdot 10^{-25}$	1495.7
1	$6.8 \cdot 10^{-3}$	$5.1 \cdot 10^{-23}$	123.6 (122 [22])	$3.3 \cdot 10^{-23}$	121.4 (119 [22])
2	$1.4 \cdot 10^{-3}$	$2.0 \cdot 10^{-21}$	245.4 (242 [22])	$1.3 \cdot 10^{-21}$	241.1 (238 [22])
3	$9.1 \cdot 10^{-5}$	$5.0 \cdot 10^{-20}$	364.9 (361 [22])	$3.3 \cdot 10^{-20}$	358.6 (354 [22])
4	$4.6 \cdot 10^{-6}$	$9.3 \cdot 10^{-19}$	481.9 (478 [22])	$6.0 \cdot 10^{-19}$	473.8 (469 [22])
5	$2.9 \cdot 10^{-6}$	$1.4 \cdot 10^{-17}$	596.0	$8.7 \cdot 10^{-18}$	586.2
6	$1.1 \cdot 10^{-6}$	$1.7 \cdot 10^{-16}$	706.8	$1.1 \cdot 10^{-16}$	695.5
7	$1.4 \cdot 10^{-7}$	$2.8 \cdot 10^{-15}$	813.8	$1.5 \cdot 10^{-15}$	801.3
8	$3.4 \cdot 10^{-8}$	$6.1 \cdot 10^{-13}$	916.5	$2.0 \cdot 10^{-13}$	903.0
9	$6.5 \cdot 10^{-8}$	$3.1 \cdot 10^{-10}$	1014.0	$9.9 \cdot 10^{-11}$	999.9
10	$9.8 \cdot 10^{-9}$	$1.7 \cdot 10^{-7}$	1105.3	$5.2 \cdot 10^{-8}$	1090.8
11	$1.3 \cdot 10^{-10}$	$1.0 \cdot 10^{-4}$	1188.2	$3.0 \cdot 10^{-5}$	1174.1
12	$6.5 \cdot 10^{-11}$	$8.2 \cdot 10^{-2}$	1258.5	$2.2 \cdot 10^{-2}$	1246.3
13	$8.4 \cdot 10^{-10}$	12.6	1290.5	8.58	1287.6
14	$1.3 \cdot 10^{-10}$	19.5	1316.4	19.36	1307.3

The isotope effect on the tunneling splitting increases as the energies of the levels reach the energy of the trans barrier height with the largest effect for v_t=12. Our results for the torsional levels (up to $v_t = 4$) can be compared with the corresponding results of ref. [22] and show a good agreement. However, no tunneling splittings were reported in ref. [22].

The parity violating potential E_{pv} as a function of the torsional angle τ is shown in Fig. 2. The antisymmetry of E_{pv} about 180^o is clearly apparent in contrast to the symmetric parity conserving potential. Because of the antisymmetry of E_{pv} the absolute value of $\Delta_{\mathrm{pv}}E^{\mathrm{el}}$ is just twice the absolute value of E_{pv} of the P or M enantiomer at their equilibrium structure.

$$|\Delta_{\mathrm{pv}}E^{\mathrm{el}}| \;\; = 2|E_{\mathrm{pv}}(P-\mathrm{Cl_2O_2}, eq.)| \;\; \approx |\Delta_R H_0^{\ominus}/N_A| \approx (hc)6\cdot 10^{-13}\mathrm{cm}^{-1} \tag{1}$$

The result shows that $M-\mathrm{Cl_2O_2}$ is stabilized compared to $P-\mathrm{Cl_2O_2}$ by about $6\cdot 10^{-13}\mathrm{cm}^{-1}$ (RPA/6-311G(df); with a modest basis set dependence and only a small isotope effect). We conclude that $\Delta_{\mathrm{pv}}E$ is about 12 orders of magnitude larger than the vibrational ground state torsional tunneling splittings $\Delta E_{\pm}$. Thus tunneling is suppressed and all low lying eigenstates, for which $\Delta_{\mathrm{pv}}E >> \Delta E_{\pm}$ is valid (here up to $v_t = 7$, see Tab. 1) have a well defined chirality (P or M). "Tunneling switching" occurs at modest torsional excitation of about 1000 cm^{-1} or more. At higher levels, tunneling splittings dominate over parity violation and thus each level has a well defined parity. Excitation with a narrow band "pump" infrared laser in a frequency range above 1100 cm^{-1} thus would allow one to achieve a parity selection following the scheme of Fig. 1. It is clear that it would be very difficult to excite to high torsional overtone levels directly due to unfavorable transition band strengths (Tab. 1). However, one might choose a sequential excitation scheme or excite a low overtone of a higher frequency mode, searching for an "accidental" resonance coupling of such a level with a high overtone of the torsion. Then a stimulated emission caused by a subsequent infrared laser pulse generates a superposition state with initially well defined parity in an energy range where the dynamics is dominated by parity violation. This superposition state would evolve in time due to parity violation and change parity with $\tau_{\mathrm{pv}}/2 = h/(2\Delta_{\mathrm{pv}}E) \simeq 28\,\mathrm{s}$ and its initial time evolution in the ms range should be measurable with techniques described in [6]. All in all our exploratory calculations indicate that Cl_2O_2 [1,23] is a possible candidate for realizing such a "tunneling switching" scheme for a successful measurement of $\Delta_{\mathrm{pv}}E$.

Acknowledgement: We enjoyed fruitful discussions with Ľuboš Horný, H. F. Schaefer III, Achim Sieben and Jürgen Stohner. Our work is supported financially by ETH Zürich and Schweizerischer Nationalfonds.

References

[1] M. Quack and M. Willeke, *Proc. of the 19th Colloq. High Res. Molec. Spec., Salamanca*; 2005, pp. 224-225, *and to be published.*

[2] A. Bakasov, T. K. Ha, and M. Quack. In J. Chela-Flores and F. Rolin, editors, *Proc. of the 4th Trieste Conference (1995), Chemical Evolution: Physics of the Origin and Evolution of Life*, pages 287–296, Dordrecht, (1996). Kluwer Academic Publishers.

[3] A. Bakasov, T. K. Ha, and M. Quack, J. Chem. Phys., **109**, 7263 (1998).

[4] R. Berger and M. Quack, J. Chem. Phys., **112**, 3148 (2000).

[5] R. A. Hegstrom, D. W. Rein, and P. G. H. Sandars, J. Chem. Phys., **73**, 2329 (1980); S. Mason and G. Tranter, Mol. Phys., **53**, 1091 (1984).

[6] M. Quack, Chem. Phys. Lett., **132**, 147 (1986).

[7] M. Quack, Angew. Chem. Int. Ed. Engl., **28**, 571 (1989).

[8] M. Quack, Angew. Chem. Intl. Ed. (Engl.), **41**, 4618 (2002).

[9] V. S. Letokhov, Physics Letters A, **53**, 275 (1975).

[10] A. Bauder, A. Beil, D. Luckhaus, F. Müller, and M. Quack, J. Chem. Phys., **106**, 7558 (1997).

[11] C. Daussy, T. Marrel, A. Amy-Klein, C. T. Nguyen, C. J. Borde, and C. Chardonnet, Phys. Rev. Lett., **83**, 1554 (1999).

[12] M. Gottselig and M. Quack, J. Chem. Phys., **123**, 084305 (2005).

[13] M. Birk, R. Friedl, E. Cohen, H. Pickett, S. Sander, J. Chem. Phys., **91**, 6588 (1989).

[14] B. Fehrensen, D. Luckhaus, and M. Quack, Z. Phys. Chem. N. F., **209**, 1 (1999).

[15] B. Fehrensen, D. Luckhaus, and M. Quack, Chem. Phys. Lett., **300**, 312 (1999).

[16] M. Gottselig, M. Quack, and M. Willeke, Isr. J. Chem., **43**, 353 (2003).

[17] M. Quack and M. Willeke, Helv. Chim. Acta, **86**, 1641 (2003).

[18] R. Berger, M. Gottselig, M. Quack, M. Willeke, Angew. Chem. Intl. Ed., **40**, 4195 (2001).

[19] R. Berger, M. Quack, and J. Stohner, Angew. Chem. Intl. Ed., **40**, 1667 (2001).

[20] R. Berger and M. Quack, ChemPhysChem., **1**, 57 (2000).

[21] M. Quack and J. Stohner, Z. Physik. Chemie, **214**, 675 (2000).

[22] P. C. Gómez and L. F. Pacios, J. Phys. Chem., **100**, 8731 (1996).

[23] Ľ. Horný, M. Quack, H. F. Schaefer III, M. Willeke, *Proc. of the 28th Internat. Symp. on Free Radicals, Leysin*; J. P. Maier, ed., 2005, p. 110, *and in preparation.*

Measurements of edge plasma parameters in toroidal plasmas with probes

R. Schrittwieser[1], C. Ioniță[1], P.C. Balan[1], C.A.F. Varandas[2], H.F.C. Figueiredo[2], C. Silva[2], J. Stöckel[3], J. Adámek[3], M. Hron[3], J. Brotánková[3], M. Tichý[4], E. Martines[5], G. Van Oost[6]

[1]*Association EURATOM/ÖAW, Department of Ion Physics, Leopold-Franzens University, A-6020 Innsbruck, Austria (Roman.Schrittwieser@uibk.ac.at)*

[2]*Association EURATOM/IST, Centro de Fusão Nuclear, Instituto Superior Técnico, Lisboa, Portugal*

[3]*Institute for Plasma Physics, Association EURATOM-IPP.CR, Czech Academy of Sciences, Prague, Czech Republic*

[4]*Faculty of Mathematics and Physics, Charles University in Prague, Czech Republic*

[5]*Consorzio RFX, Associazione EURATOM-ENEA sulla Fusione, Padova, Italy*

[6]*Department of Applied Physics, Ghent University, Belgium*

ABSTRACT

We report on investigations of the edge plasma region of toroidal magnetised fusion experiments with electrostatic probes. Various methods and probe arrangements were used to determine the plasma potential, the electric field, the radial fluctuation-induced particle flux and the Reynolds stress. Investigations were undertaken mainly in ISTTOK (**I**nstituto **S**uperior **T**écnico **Tok**amak), Lisbon, Portugal, and CASTOR (**C**zech **A**cademy of **S**cience **Tor**us), Prague, Czech Republic.

1. Introduction

The phenomena in the edge plasma region of a magnetised toroidal fusion plasma are decisive for the radial transport and loss of plasma and energy, which leads to a reduction of the confinement time. The edge region consists of the density drop inside the **l**ast-**c**losed **f**lux **s**urface (LCFS) and of the so-called **s**crape-**o**ff **l**ayer (SOL). Radial particle transport is often due to large-scale electric field fluctuations in this region [1,2,3] and may account for a major part of the anomalous energy and particle losses observed [4,5,6,7,8,9,10]. The most important parameters are the electric field components in radial and poloidal direction, the density and the electron temperature. The simplest and most straightforward diagnostic tools are probes of various types by which the plasma potential can be measured directly. Such probes are (i) emissive probes [1,2,3,4] and (ii) ball-pen probes [5].For the measurement of electric field components and the electron temperature, various combinations of emissive or ball-pen probes and cold probes were used.

In the following the diagnostic tools and probe arrangements are presented. Also shown is an interesting result of a preliminary measurement of the radial fluctuation-induced particle flux Γ and the Reynolds stress R_e. These investigations were carried out in ISTTOK and CASTOR, which both are large aspect ratio tokamaks with similar dimensions, i.e., a major radius of 40 cm and a minor radius of 8 cm. They work with hydrogen and reach core densities of 10^{19} m^{-3} and electron temperatures of 100 - 200 eV.

2. Probes for direct measurements of the plasma potential

There are very few diagnostic tools to determine the plasma potential Φ_{pl} with sufficient accuracy and spatial and temporal resolution. The least expensive and most easily to handle tool is the cold plasma probe (Langmuir probe). Usually the current-voltage characteristic (*I-V* characteristic) of a cold probe is used to derive Φ_{pl} from the inflection point. However, this method is time-consuming and moreover electron drifts or electron beams might falsify the results of cold probes by shifting the entire *I-V* characteristic towards more negative values.

2.1. Emissive probes: To compensate this effect emissive probes can be used which emit an electron current into the plasma. Emissive probes are standard tools in laboratory plasmas (see e.g. [16,17,18,19,20]), but only a few years ago our group has started to use them also in fusion experiments at higher densities and temperatures [11,12,13,14,15]. The emission current from the probe into the plasma can be observed in the current-voltage characteristic as long as the potential on the probe surface is more negative than the plasma potential. Then the floating potential of such a probe equals the plasma potential.

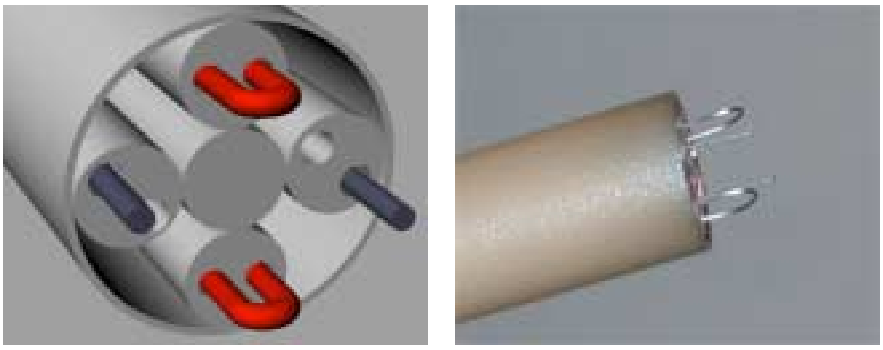

*Figure 1**:** An arrangement of two emissive wire probes and two cold probes for simultaneous measurements of the poloidal electric field, the ion density and the electron temperature.*

The usual technical realisation of an emissive probe consists of a small loop of tungsten wire with a diameter of about 0.2 mm, about 6 mm total length, inserted into a suitable double-bore ceramic or boron nitride tube. Fig. 1 shows an arrangement of two emissive wire probes and two cold probes. The probe is inserted in such a way that the two emissive probes measure Φ_{pl} at two positions on a poloidal meridian. From these values the poloidal electric field component can be calculated. One of the cold probes is biased negatively to measure the ion saturation current, from which the ion density can be derived. The other cold probe is swept and the electron temperature is calculated from the *I-V* characteristic [21].

2.2. Ball-pen probe: A ball-pen probe consists of a cylindrical collector with a conical tip of 2 or 4 mm diameter, which can be moved up and down inside a screening tube of boron nitride [15,22]. In the design shown in Fig. 3, an additional Langmuir probe ring is mounted near the top of the BN tube. This acts as conventional cold probe to deliver the value of the floating potential [23]. The parameter h indicates the position of the collector relative to the tube, with $h = 0$ meaning that the collector tip lies exactly in the plane of the mouth of the tube.

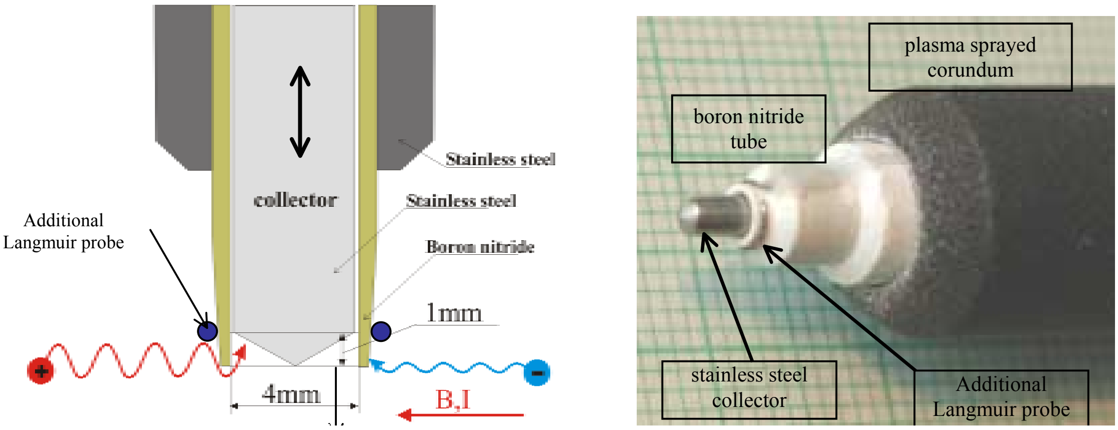

(a) (b)

Fig. 2: (a) Schematic of the ball-pen/cold probe combination. The conical collector can be shifted inside the boron nitride (BN) screening tube that acts as a shield for electrons. The Langmuir probe is made of 0.2 mm diameter tungsten wire. (b) Photo of the ball pen probe. In this case the ball-pen collector is fully exposed to the plasma.

The measurement of the plasma potential Φ_{pl} by means of the ball-pen probe utilises the difference between the electron and ion gyroradii in a magnetised plasma. Since the former are much smaller, they can be partly screened off by the BN tube, when the collector is withdrawn inside [24]. In our case, by shifting the collector inside the BN tube, the effective collection area of the electrons can be varied. Therefore, the electron current reaching the collector can be adjusted to the same magnitude as that of the ion current, with the effect that the floating potential becomes equal to the plasma potential Φ_{pl} similar to the emissive probe.

3. Results and discussion

In radial direction the fluctuation-induced particle flux is given by $\Gamma = \left\langle \tilde{n}_{pl} \tilde{v}_r \right\rangle$, where $\tilde{n}_{pl}$ are the density fluctuations and $\tilde{v}_r$ is the fluctuating radial velocity component. The frequencies of the strong electric field fluctuations in the edge region are usually well below the ion cyclotron frequency. In this case the radial velocity can be approximated by the ***E***×***B*** velocities, thus the flux becomes $\Gamma = \left\langle \tilde{n}_{pl} \tilde{E}_\vartheta / B_0 \right\rangle$.

A counteracting mechanism might be the Reynolds stress R_e, which is a measure of the anisotropy of turbulent velocity fluctuations. This produces a stress on the mean flow, which may cause a poloidal flow if the Reynolds stress has a radial gradient. Then the poloidal flow will be sheared, which should reduce the radial turbulent transport. The Reynolds stress of a turbulent plasma is given by $R_e = \left\langle \tilde{v}_r \tilde{v}_\vartheta \right\rangle$, where $\tilde{v}_\vartheta$ is the poloidal component of the fluid velocity. Assuming that the main fluctuations which lead to transport are purely electrostatic and that the transport is due to ***E***×***B*** drifts, R_e becomes: $R_e = \left\langle \tilde{E}_\vartheta \tilde{E}_r \right\rangle / B_0^2$.

Fig. 2 shows radial profiles of Γ (solid line) and of R_e (dashed line) in the edge region of ISTTOK. Also shown is $\partial R_e/\partial r$ (dotted line). The vertical line shows the position of the LCFS. Here it is interesting to note that the flux passes through a minimum around the position of the LCFS which is also there where the gradient of the Reynolds stress reaches a maximum. This is in keeping with theories that the Reynolds stress leads to a sheared poloidal flow, which is able to reduce the turbulent radial transport. The fact that the flux becomes negative in this region, i.e., inward, has to be clarified and still needs further thorough investigations.

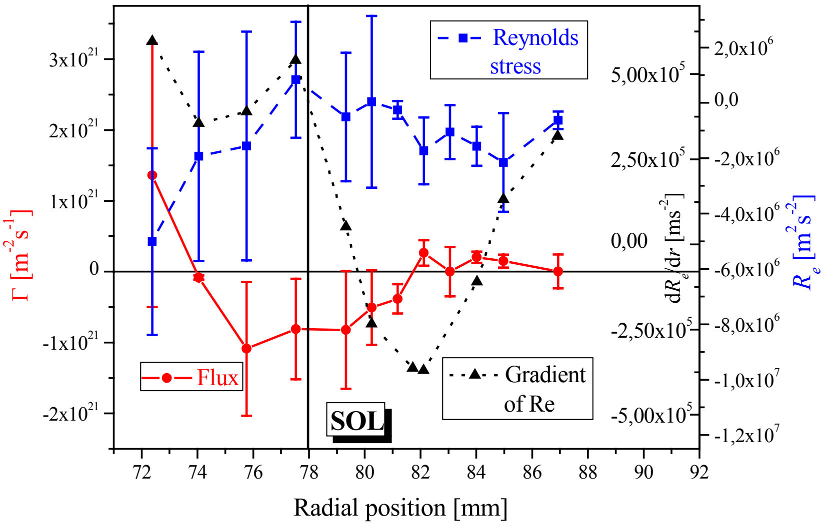

Fig. 3. Preliminary results of the measurements with a probe arrangement to measure the radial and poloidal electric field components and the density simultaneously: Radial profiles of the radial fluctuation-induced flux Γ *(red solid line), of the Reynolds stress R_e (blue dashed line) and of the gradient of R_e (black dotted line).*

Acknowledgement

This work has been carried out within the Associations EURATOM-ÖAW, EURATOM-IST, EURATOM-IPP.CR and EURATOM-ENEA. The content of the publication is the sole responsibility of its author(s) and it does not necessarily represent the views of the Commission or its services. The work performed at CASTOR was supported by the project 202/03/0786 of the Grant Agency of the Czech Republic.

References

[1] T. Huld, A.H. Nielsen, H.L. Pécseli, J. Juul Rasmussen, *Phys. Fluids B* **3** (1991), 1609.

[2] J. Bleuel, M. Endler, H. Niedermeyer, M. Schubert. H. Thomsen, W7-AS Team, *New J. Phys.* **4** (2002), 38.1.

[3] O. Grulke, T. Klinger, *New J. Phys.* **4**, (2002), 67.1.

[4] B.A. Carreras, C. Hidalgo, E. Sánchez, M.A. Pedrosa, R. Balbín, I. Garcia-Cortés, B. Van Milligen, D.E. Newman, V.E. Lynch, *Phys. Plasmas* **3** (1996), 2664.

[5] E. Sánchez, C. Hidalgo, M.A. Pedrosa, R. Balbín, B. van Milligen, I. García Cortez, *Contr. Fusion Plasma Phys.* **38** (1998), 93.

[6] B.A. Carreras, B. van Milligen, C. Hidalgo, R. Balbin, E. Sanchez, I. Garcia-Cortes, M. A. Pedrosa, J. Bleuel and M. Endler, *Phys. Rev. Lett.* **83** (1999), 3653.

[7] B. LaBombard, *Phys. Plasmas* **9** (2002), 1300.

[8] R. Trasarti-Battistoni, D. Draghi, C. Riccardi, H.E. Roman, *Phys. Plasmas* **9** (2002), 3369.

[9] D.L. Rudakov, J.A. Boedo, R.A. Moyer, S. Krasheninnikov, A.W. Leonard, M.A. Mahdavi, G.R. McKee, G.D. Porter, P.C. Stangeby, J.G. Watkins, W.P. West, D.G. Whyte, G. Antar, *Plasma Phys. Control. Fusion* **44** (2002), 717.

[10] V. Naulin, *New J. Phys.* **4** (2002), 28.1.

[11] R. Schrittwieser, C. Ioniță, P.C. Balan, Jose A. Cabral, H.F.C. Figueiredo, V. Pohoață, C. Varandas, *Contrib. Plasma Phys.* **41** (2001), 494.

[12] R. Schrittwieser, J. Adámek, P. Balan, M. Hron, C. Ioniță, K. Jakubka, L. Kryška, E. Martines, J. Stöckel, M. Tichý, G. Van Oost, *Plasma Phys. Contr. Fusion* **44** (2002), 567.

[13] J. Adámek, P. Balan, I. Ďuran, M. Hron, C. Ioniță, L. Kryška, E. Martines, R. Schrittwieser, J. Stöckel, M. Tichý, G. Van Oost, *Czechoslovak J. Phys.* **52** (2002), 1115.

[14] P. Balan, R. Schrittwieser, C. Ioniță, J.A. Cabral, H.F.C. Figueiredo, H. Fernandes, C. Varandas, J. Adámek, M. Hron, J. Stöckel, E. Martines, M. Tichý, G. Van Oost, *Rev. Sci. Instrum.* **74** (2003), 1583.

[15] J. Adámek, J. Stöckel, I. Ďuran, M. Hron, R. Pánek, M. Tichý, R. Schrittwieser, C. Ioniță, P. Balan, E. Martines, G. Van Oost, *Czechoslovak J. Phys.* **55** (2005), 235.

[16] R.F. Kemp, J.M. Sellen Jr., *Rev. Sci. Instrum.* **37** (1966), 455.

[17] R.W. Motley, *J. Appl. Phys.* **43** (1972), 3711.

[18] J.R. Smith, N. Hershkowitz, P. Coakley, *Rev. Sci. Instrum.* **50** (1979), 210.

[19] S. Iizuka, P. Michelsen, J.J. Rasmussen, R. Schrittwieser, R. Hatakeyama, K. Saeki, N. Sato, *J. Phys. E: Sci. Instrum.* **14** (1981), 1291.

[20] A. Siebenförcher, R. Schrittwieser, *Rev. Sci. Instrum.* **67** (1996), 849.

[21] P. Balan, J. Adámek, I. Ďuran, M. Hron, C. Ioniță, E. Martines, R. Schrittwieser, J. Stöckel, M. Tichý, G. Van Oost, *29th EPS Conf. Plasma Physics Contr. Fusion* (Montreux, Switzerland, June 17 - 21, 2002), *Europhys. Conf. Abstr.* **26B** (2002), 2.072.

[22] J. Adámek, J. Stöckel, M. Hron, J. Ryszawy, M. Tichý, R. Schrittwieser, C. Ioniță, P. Balan, E. Martines, G. Van Oost, *Czechoslovak J. Phys.* **54** (2004), C95.

[23] J. Adámek, C. Ioniță, R. Schrittwieser, J. Stöckel, M. Tichy, G. Van Oost, *32nd EPS Plasma Phys. Conf.* (Tarragona, Spain, June 27 - July 1, 2005), *Europhys. Conf. Abstr.* **29C** (2005), P-5.081.

[24] I. Katsumata, M. Okazaki, *Jpn. J. Appl. Phys.* **6** (1967), 123.

Investigating the role of geometrical structure in the reactivity of small gas-phase transition metal clusters

Stuart Mackenzie, Mark Ford

Department of Chemistry, University of Warwick, Coventry, UK
(stuart.mackenzie@warwick.ac.uk)

ABSTRACT

We report on progress towards elucidating the role played by geometrical structure in determining the reactivity of small gas-phase metal clusters. Our relatively young research program combines Fourier transform ion cyclotron resonance (FTICR) mass spectrometric studies with high resolution photoionization techniques such as mass analysed threshold ionization (MATI) in order to identify structural motifs which enhance reactivity towards small molecules. In particular we are pioneering the use of MATI as a means not only of learning about the spectroscopy of these systems but also as a way of generating cationic clusters in known structural (*i.e.*, isomeric) forms. Specifically, we report evidence for multiple isomeric forms in the reaction kinetics of $Rh_n^{+/-}$ and $Co_n^{+/-}$ (n = 5-30) with NO, N_2O and NO_2 and $Nb_n^{+/-}$ with N_2. We further demonstrate the use of MATI spectroscopy in the generation of known vibronic states of various small cationic clusters of vanadium, and niobium.

1. Introduction

It has long been recognised that clusters of metal atoms have properties that differ significantly from those of both individual atoms and bulk metals and that in effect these clusters represent a unique state of matter.[10,11] Beyond their inherent scientific interest, much of the research into the reactivity of small metal clusters has arisen from the tantalizing possibility that they provide tractable model systems for understanding heterogeneous catalysis. Many industrial catalysts use highly dispersed metal including nano-particulate metal. There is good reason for the use of small particles in such applications: 30 years of surface science has revealed that it is surface defect sites that often provide the active sites for interesting chemistry. Clusters of metal atoms, with no long range order whatsoever, exhibit maximum surface area and can be considered as the ultimate concentration of defect sites.

Following the development of the laser ablation cluster source, a rich chemistry rapidly emerged, particularly for the clusters, M_n (and $M_n^{+/-}$), of transition metals.[10,12] It was quickly discovered that many clusters exhibit dramatic size-dependence in their rates of reactivity towards small molecules with some cluster sizes reacting with rates differing from those of adjacent cluster sizes by as much as four orders of magnitude.[13] Most experimental studies have been mass-spectrometric in nature and thus are not inherently sensitive to different structures. Nevertheless, several studies have reported results which have been interpreted in terms of the presence of multiple isomeric forms which in some cases react at significantly different rates.[13,14,15,16] Other evidence for the existence of multiple isomeric forms comes

---

[10] P.B. Armentrout, *Annu. Rev. Phys. Chem.*, **52**, 423, (2001)

[11] S.J. Riley, 1996 in *Clusters and Nanostuctured Materials* ed P. Jena, S.N. Behera, Nova Sci. (New York)

[12] M.B. Knickelbein, *Annu. Rev. Phys. Chem.*, **50**, 79, (1999)

[13] *see, for example,* J.L. Elkind, F.D. Weiss, J.M. Alford, R.T Laaksonen and R.E. Smalley, *J. Chem. Phys.*, **88**, 5215 (1988)

[14] Y. Hamrick, S. Taylor, G.W. Lemire, Z.-W. Fu, J.-C. Shui and M.D. Morse, *J. Chem. Phys.* **88**, 4095 (1988)

from ion mobility[17] and photoionization studies.[18] The unambiguous determination of cluster structures, remains, however a major challenge to modern chemical physics although modern action spectroscopies show great promise.[19] Elucidating the links between structure and reactivity has, until recently, been little more than a pipe-dream.

We report here on progress towards integrating spectroscopic and reactivity techniques in a way designed to shed light on the role played by geometrical structure in determining the reactivity of metal clusters. Specifically we perform reactivity studies on metal clusters using a conventional laser ablation source and a 3-Tesla Fourier transform ion cyclotron resonance mass spectrometer.[16] In parallel, we are developing mass analysed threshold ionization both as a technique providing important spectral information simultaneously on neutral and ionic clusters, and as a means by which to generate cationic clusters in known structural forms.[20] Ultimately, the combination of these techniques will, it is hoped, provide a means to study the reactivity of cationic clusters as a function of geometrical structure.

2. FTICR reactivity studies

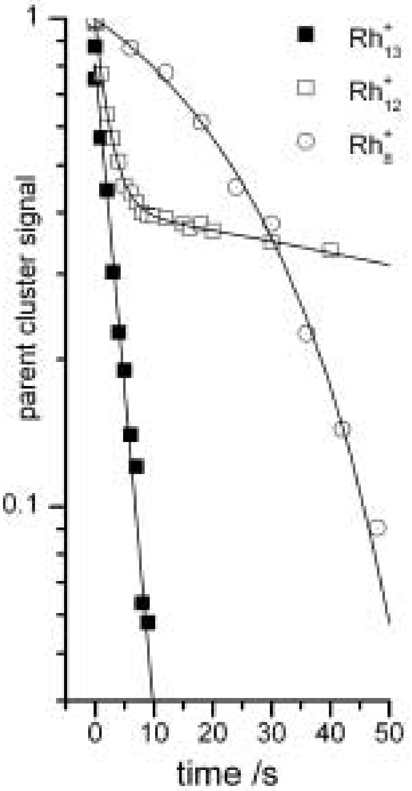

Figure 1: Kinetic plots for the reactions of several Rh_n^+ clusters with N_2O yielding Rh_nO^+. Non-linearity is interpreted as evidence for multiple low-lying isomeric forms with different reactivities.

Our approach to determining cluster reactivity is similar to that used previously by several groups.[13,15] A 532 nm laser ablation cluster source (a slightly modified version of the Bondybey cluster source[21]) generates both charged and neutral clusters the size regime n = 1-80. Charged clusters are guided by a series of ion optics into an ion cyclotron resonance cell within a 3-T magnetic field where they can be stored under UHV conditions for extended periods (several hours). Reaction kinetics are determined by exposing the clusters to low pressures ($< 10^{-8}$ mbar) of reactant gases and recording the mass spectra as a function of reaction delay. Due to its relevance to the automobile catalytic converter we have initially studied the reactivity of rhodium clusters with a range of N_xO_y family of molecules.[16,22] As well as determining the variation in reaction rate with cluster size we have concentrated on those cluster sizes whose kinetics deviate from pseudo first-order kinetics. Examples of such variations are shown in Figure 1 for the reaction of $Rh_n^+ + N_2O \rightarrow Rh_nO^+$. Rh_{13}^+ shows the expected straight line first order plot whilst Rh_{12}^+ and Rh_8^+ (and other cluster

---

[15] C. Berg, T. Schindler, M. Kantlehner, G. Niedner-Schatteburg and V.E. Bondybey, *Chem. Phys.* **262** 143 (2000)

[16] M.S. Ford, M.L. Anderson, M.P. Barrow, D.P. Woodruff, T. Drewello, P.J. Derrick and S.R. Mackenzie, *Phys. Chem. Chem. Phys.*, **7**, 975, 2005

[17] P.Weiss, T. Bierweiler, E.Vollmer and M.M. Kappes, *J. Chem. Phys.*, **117**, 9293, 2002

[18] M.B. Knickelbein and S. Yang, *J. Chem. Phys.*, **93,** 1476 (1990)

[19] A. Fielicke, C. Ratsch, G. Von Helden and G. Meijer, *J. Chem. Phys.*, **122**, 091105 (2005)

[20] M.S. Ford and S.R. Mackenzie, *J. Chem. Phys.,* **123**, 084308 (2005)

[21] C.Berg, T. Schindler, G. Niedner-Schatteburg and V.E. Bondybey., *J. Chem. Phys.*, **102**, 4870 (1995)

[22] M.A. Anderson, M.S. Ford and S.R. Mackenzie, *J. Phys. Chem. A.*, *submitted Nov 2005*

sizes) exhibit distinct non-linearity. This behaviour has previously been attributed to the existence of multiple isomers of the cluster in question each of which reacts at a significantly different rate[14,15,16] although the presence of states of different spin multiplicity cannot be ruled out. We report the results of extensive thermalisation experiments which appear to confirm this interpretation. Notably these "isomeric" effects are considerably more pronounced in the reactions of Rh_n^+ with the closed-shell N_2O than with either of the radicals NO or NO_2.

3. Mass Analysed Threshold Ionization for generating state-selected cluster ions

The low intensities of metal clusters generated by common techniques such as laser ablation make direct spectroscopic studies challenging except for the very smallest clusters. Only very recently with the advent of far infra-red action spectroscopies has it started to become possible to interrogate cluster structures effectively.[23] For small clusters, Hackett and Yang have pioneered the use of high resolution photoelectron spectroscopy in the form of zero-kinetic energy photoelectron spectroscopy (ZEKE) which, in tandem with DFT simulations has proven successful in characterizing both neutral and cationic states of small clusters such as V_3, Nb_3O, Nb_3N_2, *etc.*.[24]

We are developing mass analysed threshold ionization spectroscopy, MATI, which is similar to ZEKE but in which state-selected ions are detected rather than electrons, as a means both of studying the spectroscopy of small clusters and of generating significant numbers of fully characterized cationic clusters.[20] This technique makes use of pulsed field ionization of the meta-stable high principal quantum number Rydberg states which lie below and converge upon every ionization threshold. Coupled with a tuneable photoionization laser, peaks are observed in the generation of ions at every optically accessible ionization threshold (see Figure 2 for the MATI spectrum of Nb_3N_2). By understanding the spectrum it is possible to sit on a given spectral feature and selectively generate ions of a known isomeric (and indeed vibronic) form. We have started by concentrating on the systems in which the ZEKE spectra (and thus the IPs) are known and we demonstrate that, despite the technical difficulties involved, MATI can be used to generate large numbers (> 10^3) of structurally characterized cluster ions per laser pulse.

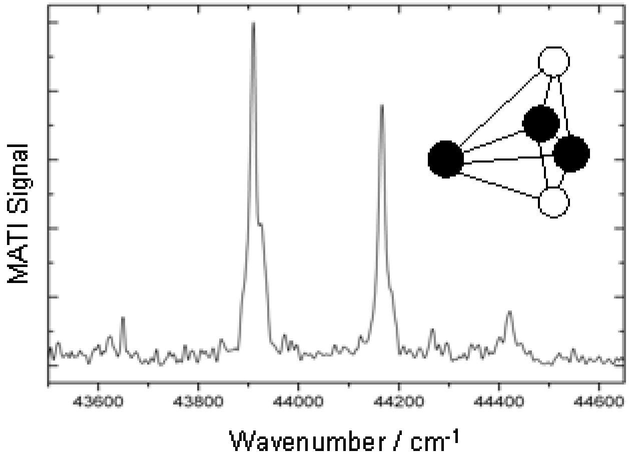

Figure 2: The mass analysed threshold ionization spectrum of Nb_3N_2 demonstrating the ability of MATI to generate isomerically selected cluster ions.

We believe that, ultimately, generating known isomeric forms of these clusters will permit the study of reactivity as a function of geometrical structure.

---

[23] A. Fielicke, A. Kirilyuk, C. Ratsch, J. Behler, M. Scheffler, G. van Helden and G. Meijer, *Phys. Rev. Lett.*, **93**, 023401 (2004)

[24] D.S. Yang and P.A. Hackett, *J. Electron. Spectrosc. Rel. Phenom.* **106**, 153 (2000)

Electron density measurements using a hairpin probe in plasma etching reactor

Eva Vasekova[1], **Jafar Al-Kuzee**[1], **N. St. J. Braithwaite**[1]

[1] *Department of Physics and Astronomy, The Open University, Milton Keynes, UK*
e-mail: e.vasekova@open.ac.uk

ABSTRACT

In this study, a plasma diagnostic technique using a microwave resonator probe is investigated in a low temperature plasma etching devices.

In order to examine the performance of the newly constructed hairpin probe in various plasma reactors; several sets of experiments have been performed. The electron density as a function of gas pressure and power coupled to the system has been measured in argon, oxygen, sulphur hexafluoride, *c*-C_4F_8 and in various mixtures of these gases. The measurements have been performed in CCP, ICP and magnetron plasmas.

1. Introduction

Microwave diagnostics of plasma utilizes the dependency of the plasma permittivity on the frequency of the electromagnetic field. If the plasma is located in a high frequency electromagnetic field with a frequencyω, while $\omega >> \upsilon$ (collision frequency in plasma), then the permittivity depends on the frequency as

(i)
$$\varepsilon = \varepsilon_0 (1 - \frac{\omega_p{}^2}{\omega^2}) \tag{1}$$

where ω_p is a plasma frequency

(ii)
$$\omega_p = \sqrt{\frac{e^2 n_e}{\varepsilon_0 m_e}} \tag{2}$$

where e, m_e are the electron charge and mass, respectively, ε_0 is permittivity of vacuum and n_e is the electron density. From equations (1) and (2) it is apparent that it is possible to determine electron density if the difference $(\varepsilon - \varepsilon_0)$ is known (measured).

(iii)
$$n_e = \frac{m\_\omega^2}{e^2}(\varepsilon - \varepsilon_0) \tag{3}$$

Plasma in a resonator causes detuning of the resonant frequency. The shift of the resonant frequency f_r corresponds to the change of the permittivity; therefore the electron density can be ascertained from the measured shift in f_r.

The hairpin probe used in this study is a quarter wavelength resonator designed and introduced by Stenzel [1] in 1975. It is a parallel-wire transmission line of U shape, open at one end and shorted at the other. The hairpin probe is coupled with alternating current from a small diameter loop situated near the lower part of the U. The AC is swept over a range of frequencies. The resonant frequency of the probe is given by the relation

(iv)
$$f_r = \frac{c}{4L\sqrt{\varepsilon_r}} \tag{4}$$

where c is speed of light, L is the length of the probe and ε_r is relative permittivity of the environment. If the probe is in vacuum, where $\varepsilon_r = 1$, then the resonant frequency is determined by the length of the probe

(v) $$f_0 = \frac{c}{4L} \tag{5}$$

If the probe is put into plasma the resonant frequency will change due to the change of permittivity. From equation (1) and (4) we can derive the relation for new resonant frequency

(vi) $$f_r^2 = f_0^2 + f_p^2 \tag{6}$$

From this equation and the relation for plasma frequency (2) we will get the electron density as a function of the shift of the resonant frequency

(vii) $$n_e = \frac{f_r^2 - f_0^2}{0.81} \tag{7}$$

where frequency is in GHz and the electron density n_e is in 10^{16} m^{-3}.

The hairpin probe used here is so called reflection probe, because the resonant frequency is determined from the signal reflected from the probe. Figure 1 is a sketch of the probe showing the coupling coaxial cable and the hairpin resonator. The coaxial cable ends with a small loop formed by the centre conductor. The hairpin is attached to the coaxial cable at the lower part of the U shaped structure, so that the plane of the loop is the same as the plane of the hairpin (see figure 1). The coaxial cable is made of copper wire (0.2 mm in diameter) and copper tube isolated by a glass tube. The hairpin structure is made of either tungsten or platinum wire. The dimensions of the hairpin are about 25 mm in length and 5 mm in separation. Exact dimensions vary slightly for each particular probe.

To determine the resonant frequency of the probe, the input loop is driven over a spectrum of frequencies with a sweep generator and the reflected signal is observed on an oscilloscope. The minimum in the reflected signal indicates the probe's resonant frequency.

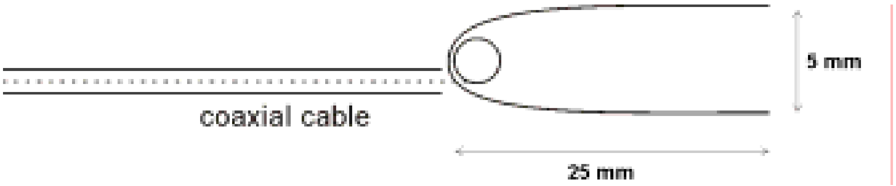

Figure 1 A diagram of the reflection hairpin probe.

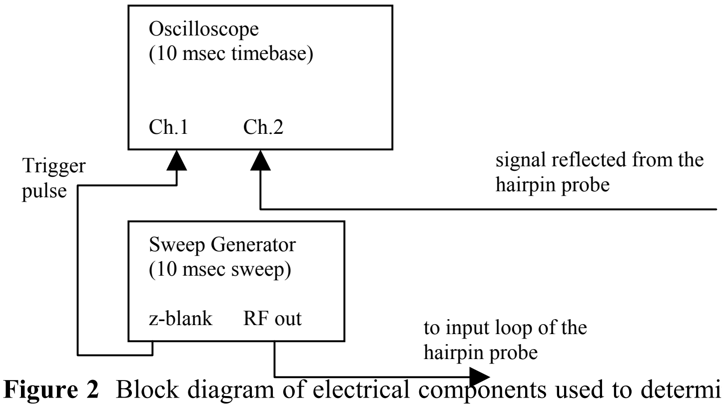

Figure 2 Block diagram of electrical components used to determine the resonant frequency of the resonator.

2. Results

The hairpin probe has been used to measure the electron density as a function of gas pressure and power coupled to the system. Several sets of measurements have been performened on CCP and ICP reactor. We found the electron density to rise with the increasing power coupled to the system in all investigated systems. However the dependency of electron density on the gas pressure differs in different plasmas. Figures 3 and 4 show the electron density measured in argon and oxygen in capacitively coupled plasma. While in argon plasma the electron density n_e monotinically increases with higher pressure, the dependancy in oxygen plasma is different. n_e is increasing until a certain value of the pressure. The pressure, at which the maximum n_e is produced, varies slightly for different input powers (80 – 100 mTorr). A further increase in pressure causes a steady decrease of electron density. Figure 5 shows the electron density measured in SF_6 and c-C_4F_8 ICP plasmas. In this case n_e falls monotonically with the pressure.

The duality in the n_e dependency on pressure can be explained by two tendencies going in opposite directions. With the increasing pressure, more molecules are available for the electrons to collide with and to generate a new electron – positive ion pair, which would increase the electron density. On the other hand the increase of the density of species decreases the mean free path of the electrons, so they gain less energy before collision which results in less production of electron – positive ion pairs. So we can assume, that the first increasing part of the dependency n_e(pressure) is due to increase of the number of the free electrons, while after reaching a certain pressure plasma density decreases due to more collisions.

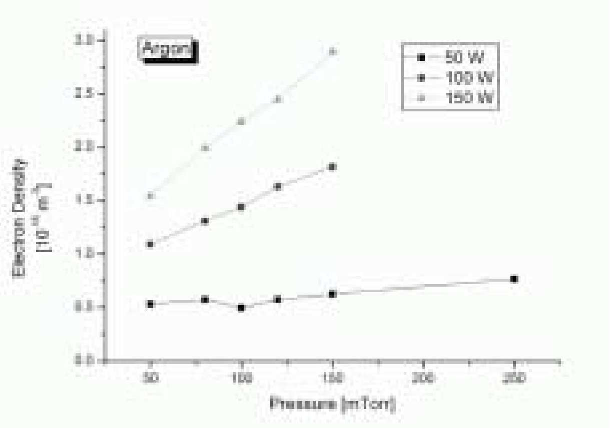

Figure 3 Dependency of the electron density n_e on the gas pressure for three different input powers. Common tendency in argon is that the n_e increases with the gas pressure.

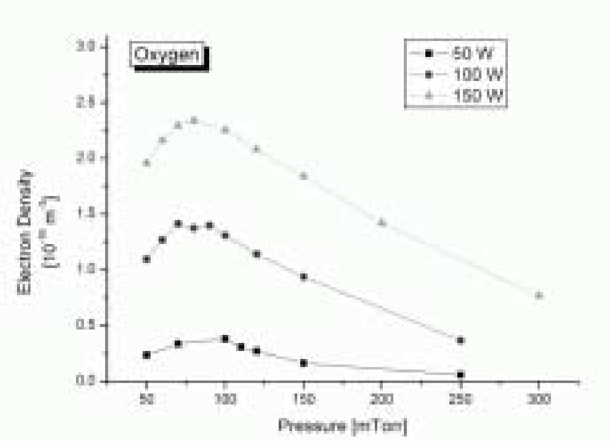

Figure 4 The dependency of n_e on pressure in oxygen plasma is different from that in an argon plasma. n_e is increasing until a certain value of the pressure. The pressure, at which the maximum n_e is produced, varies slightly for different input powers (80 – 100 mTorr). A further increase in pressure causes a steady decrease in electron density.

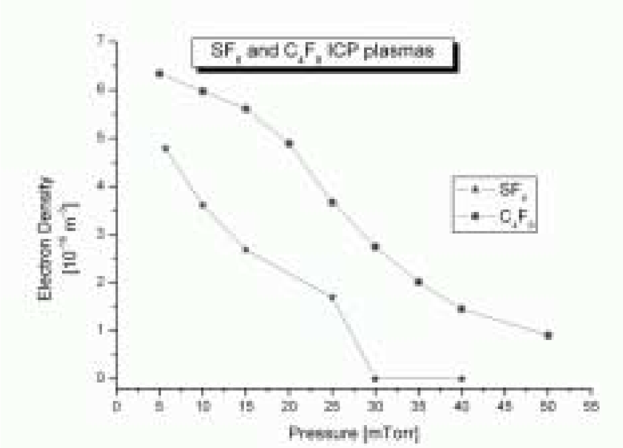

Figure 5 Electron density of ICP in SF_6 and *c*-C_4F_8 as a function of pressure.

Our observation regarding the etching of the probe in fluorine containig plasmas and deposition of material on the probe in magnetron plasma will also be shown. Several probes were used to ensure the reproducibility of the data.

References

[1] R.L. Stenzel, Rev. Sci. Instrum. 47, 603 (1976)
[2] R.B. Piejak, V.A. Godyak, R. Garner, B.M. Alexandrovich, N. Sternberg, 95, 7 (2004)

On the bending vibrations of linear carbon chains: Results of large-scale coupled cluster calculations

Peter Botschwina

Institut für Physikalische Chemie, Universität Göttingen, Tammannstraße 6, D-37077 Göttingen, Germany

Linear carbon chains are of considerable interest to the chemistry of combustion and astrochemistry (see [1, 2] for reviews). Since they have no permanent electric dipole moment, radio astronomy does not provide the appropriate technique to observe such species in the interstellar medium (ISM) or the circumstellar medium (CSM). However, astronomical observations of the first members of pure carbon chains in the infrared (IR) and visible region of the spectrum have been successful. C_3, which has a linear equilibrium structure and a very shallow bending potential (see, e.g., [3]), has been observed in the circumstellar envelope of the evolved carbon star IRC+10216 through its antisymmetric stretching vibration (ν_3) [4]. Through its bending vibrational transition (ν_2) in the far infrared (FIR) region at ca. 65 cm^{-1}, C_3 was found in the same astronomical source as well as in the direction of Sagittarius B2, making use of either the Infrared Space Observatory (ISO) [5] or the Kuiper Airborne observatory [6]. Rovibronic transitions of C_3 near 4050 Å have been known to astronomers since its detection in cometary tails as early as in 1881 [7]. The molecule was also observed in the same wavelength region in the atmosphere of cool stars (see [8] for a review) and even in the diffuse ISM [9, 10]. While the interstellar detection of linear C_4 in its $^3\Sigma^-$ electronic ground state must still be considered to be tentative [11], closed-shell linear C_5 was definitely observed in IRC+10216 through its antisymmetric stretching vibration of highest wavenumber, termed ν_3 [12]. Recently, a molecular band centered around 98 μm (102 cm^{-1}) was observed with ISO in the young planetary nebula NGC 7027. It was speculated that the band emission could arise from the lowest π_u bending vibrational modes of linear C_6 and C_5 [13].

The poster reports the results of large-scale coupled cluster calculations for the bending vibrations of linear carbon chains up to C_{15}. Only C_3 is a rather floppy species; all the other chains appear to behave like fairly normal semirigid molecules.

References

1 W. Weltner, Jr. and R. J. Van Zee, *Chem. Rev.*, 1989, **89**, 1713.

2 A. van Orden and R. J. Saykally, *Chem. Rev.*, 1998, **98**, 2313.

3 M. Mladenović, S. Schmatz and P. Botschwina, *J. Chem. Phys.*, 1994, **101**, 5891 and references therein.

4 K. H. Hinkle, J. J. Keady and P. F. Bernath, *Science*, 1988, **241**, 1319.

5 J. Cernicharo, J. R. Goicoechea and E. Caux, *Astrophys. J.*, 2000, **534**, L199.

6 T. F. Giesen, A. O. van Orden, J. D. Cruzan, R. A. Provencal, R. J. Saykally, R. Gendriesch, F. Lewen and G. Winnewisser, *Astrophys. J.*, 2001, **551**, L181; erratum ibid, 2001, **555**, L77.

7 W. Huggins, *Proc. R. Soc. London*, 1881, **33**,1; 1882, **34**,148.

8 U. G. Jørgensen, 1994, in Molecules in the Stellar Environment, ed. U. G. Jørgensen, Springer, Berlin.

9 J. P. Maier, N. M. Lakin, G. A. H. Walker and D. A. Bohlender, *Astrophys. J.*, 2001, **553**, 267.

10 T. Oka, J. A. Thorburn, B. J. McCall, S. Friedman, L. M. Hobbs, P. Sonnentrucker, D. E. Welty and D. G. York, *Astrophys. J.*, 2003, **582**, 823.

11 J. Cernicharo, J. R. Goicoechea, Y. Benilan, *Astrophys. J.*, 2003, **580**, L157.

12 P. F. Bernath, K. H. Hinkle and J. J. Keady, *Science*, 1989, **244**, 562.

13 J. R. Goicoechea, J. Cernicharo, H. Masso, and M. L. Senent, *Astrophys. J.*, 2004, **609**, 225.

Inelastic electron interaction (ionization/attachment) of biomolecules embedded in superfluid He droplets

S. Denifl[1], F. Zappa[1,2], I. Mähr[1], P. Scheier[1] and T. D. Märk[1]

[1] *Institut für Ionenphysik, Leopold-Franzens Universität Innsbruck, Technikerstr. 25, A-6020 Innsbruck, Austria (stephan.denifl@uibk.ac.at)*

[2] *UNESA – Rio de Janeiro - Brasil*

ABSTRACT

Since the pioneering experiments by Sanche and coworkers demonstrating that low energy electrons can damage plasmid DNA we have also carried out a series of measurements concerning inelastic electron interaction (ionization/attachment) with compounds of the DNA. First measurements were carried out with isolated biomolecules in the gas phase. We extend now these measurements by embedding the biomolecules in helium droplets which leads to the formation of bio-molecular clusters. We study the behavior of these clusters upon ionization and electron attachment using a double focusing mass spectrometer and compare the results with those from isolated gas phase molecules.

1. Introduction

Since the discovery of condensation in a helium nozzle expansion in 1961 [1] numerous works were dedicated to the study of helium clusters using different experimental and theoretical methods (see [2,3]). Beside the fundamental interest on these weakly bond Van-der-Waals clusters, which represent the intermediate between atom (molecule) and bulk, He clusters have unique properties raising special interest in the cluster science community. Helium has no triple point and solidifies only at pressures higher than 25 bar. At lower pressures helium remains liquid for $T \rightarrow 0$ K and shows superfluid behaviour with quantum nature [3]. Moreover, helium droplets are known to be the ultimate matrix for atoms and molecules due to their extremely low temperature, small matrix broadening and the possibility to create new molecular complexes [3]. One major disadvantage in the studies of the interactions of biomolecules with other particles in the gas phase is the necessity to heat up the samples. This can lead to significant excitation, structural change, or even fragmentation of the molecules of interest in the course of these studies. One way to circumvent this problem is to cool down the molecules formed via a standard effusive beam by collision with superfluid helium nano-droplets (pick-up).

Another reason why we choose simple biomolecules as pick up targets is the known fact, that the interaction of low energy electrons can damage DNA even at sub-ionization energies (by inducing single (SSBs) and double strand breaks (DSBs) which was recently shown by Sanche and coworker [4]). The yield of such DNA damage shows a resonant behaviour with respect to the electron energy which is an indication that electron attachment to a compound of the DNA may be an initial step. Indeed, the efficient resonant H^- production of the building blocks of DNA such as thymine, water and deoxyribose close to the above mentioned DSB resonance was recently demonstrated in experiments with thin layers [4] and in the gas phase [5].

2. Experimental apparatus

The apparatus used for the present measurements consists of a cluster source, a pick up cell with two ovens and a double focussing mass spectrometer (see Fig. 1) [6]. The neutral clusters are formed in the cluster source by an expansion of helium with a stagnation pressure of 10 - 20 bar at ~ 10 K through a 5 μm nozzle. After passing a differentially pumped chamber they enter 5cm further a pick-up cell containing the vapour of the biomolecules which is formed by heating the powders in the ovens. Afterwards the doped helium cluster beam enters the collision chamber of the Nier type ion source, where the interaction with the electron beam takes place. The ions produced are accelerated by 3kV and enter a double focusing mass spectrometer with reversed B-E geometry. The mass selected ions are detected by a channeltron. With this setup the ion yield of mass selected molecules and clusters can be recorded as a function of the electron energy. Alternatively it is possible to measure metastable decays of ions on the way to the detector in the μsec time regime [6].

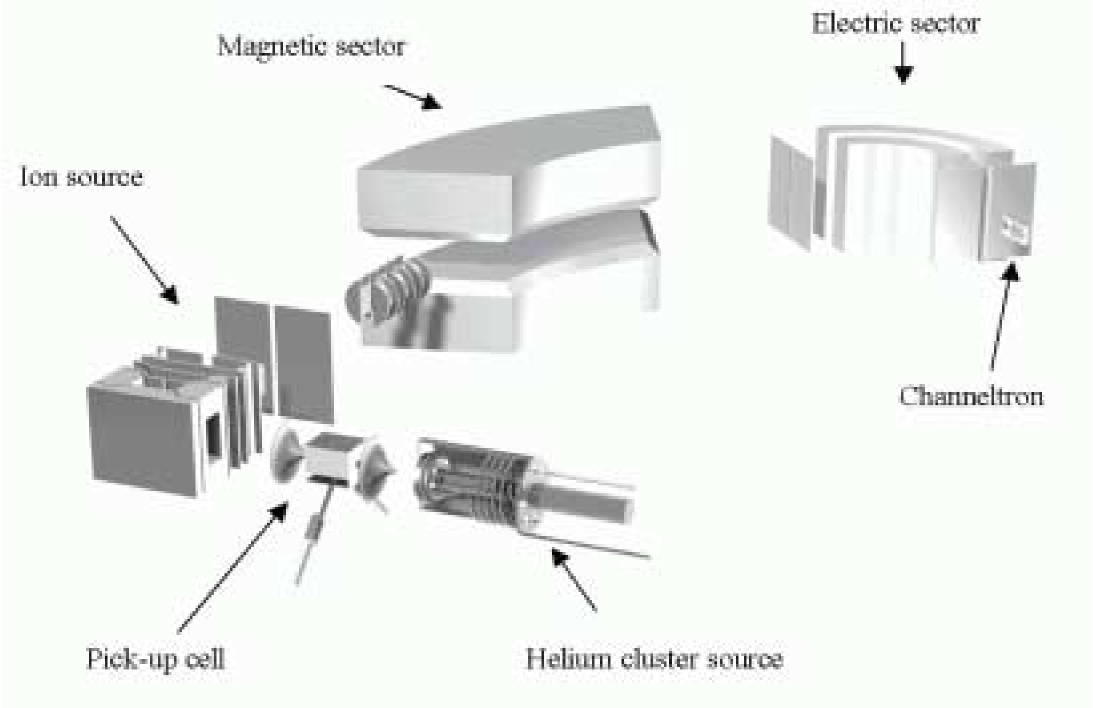

Fig. 1: Experimental set-up for the pick-up experiment: helium cluster source, pick-up region, ion source with two-sector-field mass spectrometer.

3. Results

Figure 2 shows as an example the positive mass spectrum recorded at the electron energy of 100 eV for helium cluster beam containing thymine molecules after the pick up. We can observe after ionization cluster ions of thymine up to a size of n = 8. Moreover, it turns out that protonated clusters are formed efficiently upon ionization. We also have performed measurements with simultaneously heating the ovens filled with adenine and thymine powder, respectively. In this experiment we are able to observe and study (appearance energies, stability,…) mixed cluster ions of adenine and thymine.

We will also present results concerning negative ion formation of biomolecules embedded in helium clusters (electron attachment studies). We can observe stable negative cluster ions up to the size of n = 3. Moreover, the dehydrogenated thymine anion can be observed with high abundance like in the gas phase. However, in contrast to the isolated gas phase, where this anion is formed efficiently only below 3 eV, the present results show the efficient formation also above 5 eV. A novel mechanism for the formation of these dehydrogenated anions will be presented.

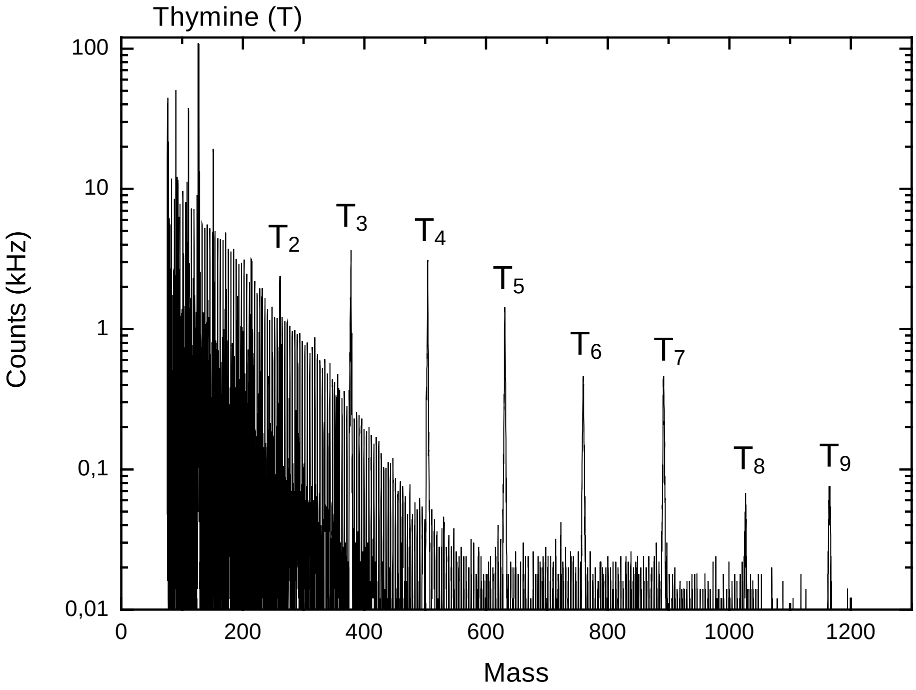

Fig. 2: Mass spectrum obtained after pick-up of thymine (from an effusive beam) by a helium cluster beam. Clearly visible is the presence of thymine clusters consisting of up to 8 molecules.

4. References

[1] E. W. Becker, R. Klingerhöfer, P. Lohse, *Z. Naturforschg.* 16a (1961) 1259

[2] J. Northby, *J. Chem. Phys.* **115** (2001) 10065

[3] J. P. Toennies, A. F. Vilesov, *Angew. Chem. Int. Ed.* **43** (2004) 2622

[4] B. Boudaiffa, P. Cloutier, D. Hunting, M. A. Huels and L. Sanche, *Science* **287** (2000) 1658

[5] S. Ptasinska, S. Denifl, V. Grill, T.D. Märk, P. Scheier, S. Gohlke, M. A. Huels and E. Illenberger, *Angew. Chem. Int. Ed.* **44** (2005) 1647

[6] K. Gluch, J. Fedor, S. Matt-Leubner, O. Echt, A. Stamatovic, M. Probst, P. Scheier and T.D. Märk, *J. Chem. Phys.* **118** (2003) 3090-3095

5. Acknowledgments

This work was supported by FWF (Wien), the EU commission (Brussels, through the EPIC network and the COST Action P9). F.Z gratefully acknowledges a post-doc grant from the Brazilian agency CNPq.

Coronene Clusters: Stability and Thermodynamics

Martin Schmidt, Albert Masson, and Catherine Bréchignac.

Laboratoire Aimé Cotton, CNRS, Bât 505, Campus d'Orsay, 91405 Orsay Cedex, France
email address: Martin.Schmidt@lac.u-psud.fr

Coronene $C_{24}H_{12}$ is polycyclic aromatic hydrocarbon molecule (PAH) with a highly symmetric structure. Due to its stability it is a common product of incomplete combustion of organic material. PAH molecules are also widely present in cosmic space as known due to their IR emission. The question of the synthesis of such molecules under cosmic conditions is one motivation of our studies [1].

The clusters are produced by gas aggregation and studied in the gas phase. They are excited either by a UV-laser in vacuum, by rare gas collisions at high energy, or thermally by a heat bath of helium. Fragmentations of clusters and molecules are studied.

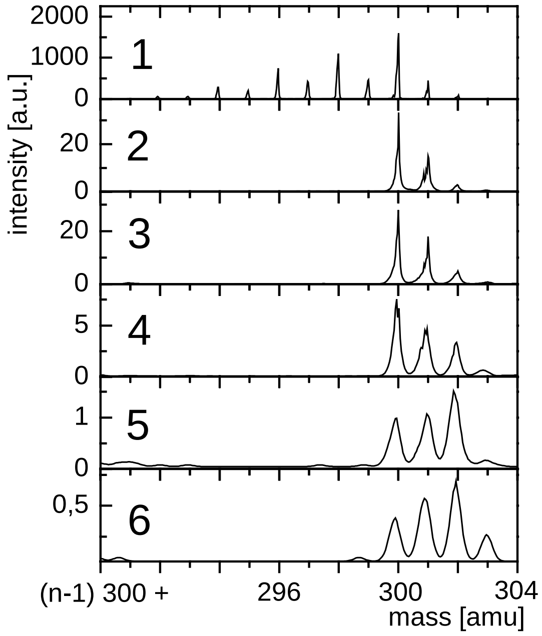

Fig. 18: Mass spectra of coronene and coronene *n*-clusters after strong laser excitation. of the range of *n*·300-10 to *n*·300+4 amu with *n* = 1-6. The intensities above *n*·300 correspond to the isotopic distribution due to the presence of ^{13}C. The peaks below 300 amu belong to dehydrogenation of the monomer. On the clusters the dehydrogenation is suppressed by the evaporative cooling of coronene subunits.

The fragmentation of coronene clusters and molecules occur in two well-separated energy and temperature regimes [2]. The evaporative ensembles of the coronene *cluster* ejecting coronene molecules and the coronene molecules ejecting hydrogen differ by a factor of 4 in temperature or a factor of 6 in energy. The corresponding thermodynamic regimes cannot mix in equilibrium. The coronene molecule dehydrogenates under sufficient heating by collisions or laser excitations. By contrast the cluster uses excess energy to evaporate coronene subunits. The resulting evaporative cooling effectively protects the single PAH-molecules in the cluster from dehydrogenation and suppresses in consequence inter-molecular reactions and the synthesis of bigger hydrocarbon species.

[1] Ph. Bréchignac, M. Schmidt, A. Masson, T. Pino, P. Parneix and C. Bréchignac, in press for Astronomy and Astrophysics **442**, 239 (2005).

2 Accepted for the Cluster Cooling Network special Issue of the International Journal of Mass Spectroscopy (2006).

Modelling Polarisation in Ion-Molecule Interactions

Marco Masia[1,2], **Michael Probst**[2] **and Rossend Rey**[1]

[1] *Departament de Fısica i Enginyeria Nuclear, Universitat Politecnica de Catalunya, Campus Nord B4B5, Barcelona 08034, Spain*

[2] *Institute of Ion Physics, University of Innsbruck, Technikerstraße 25, 6020 Innsbruck, Austria, michael.probst@uibk.ac.at*

ABSTRACT

Modeling accurately the interaction between ions and molecules is prerequisite in many areas of physics, chemistry and materials science. Therefore it is also at the center of attention in the development of the next generation of force fields for the simulations of clusters and molecular ensembles. This is mainly due to the fact that both in fundamental and in applied science it is increasingly important to be able to simulate very heterogeneous environments.

The proper inclusion of molecular and ionic polarizability is a basic requirement towards this goal but until now this is more or less restricted to quantum chemical and density functional methods which have their own limitations. In this presentation, we report our studies on the performance of several polarization models that model the interaction between ions and molecules without requiring quantum chemical calculations that are time-consuming and restricted to small systems.

1. Models and Methods

We show how the three most widely used polarization models perform on specifically chosen model systems. These models are:

(**a**) The point dipole model (PDM) which is defined by assigning a dipolar polarisability to atoms. The induced dipole moment is given by

$$\vec{\mu}_i = \alpha_i(\vec{E}_i^o + \sum_{j\neq i} T_{ij} \cdot \vec{p}_i)$$

where T is the dipole moment tensor

$$T = 3\frac{\vec{r}\vec{r}}{r^5} - \frac{I}{r^3}.$$

The electrostatic energy is then

$$U_p = - -\frac{1}{2}\sum_i \sum_{i\neq j} \vec{p}_i \cdot T_{ij} \cdot \vec{p}_j - \sum_i \vec{p}_j \cdot \vec{E}_i^0 + \sum_i \frac{p_i^2}{2\alpha_i}$$

and the implicit expression for the induced dipoles is normally solved iteratively:

$$p_i = \alpha_i[\vec{E}_i^0 + \sum_{j\neq i} T_{ij} \cdot \vec{p}_j]$$

(**b**) The shell model (also known as Drude oscillator) is based on a similar approach: Again, a polarizability is assigned to one or more sites. These sites are composed of two charges: one is fixed while the other is free to move, linked to the first one via a spring. The sum of both charges is equal to the charge of the atomic site. The spring constant is related to the charge on the moving shell and to the polarizability of the site:

$$k_D = \frac{q_D^2}{\alpha}$$

An advantage of this method is that it is easy to implement while an important drawback is that it increases the number of interaction sites and therefore the number of relative distances to be computed.

(**c**) In the chemical potential equalization method (CPE) variable charges are located on atomic sites within the molecule. Their value is computed by minimization of the electrostatic energy. This method is also known as the fluctuating charge method. For an isolated molecule, the molecular energy is expanded to second order in the partial charges:

$$U_{molec} = U_0(\{r\}) + \sum_{i=1}^{M} \chi_i^0 q_i + \frac{1}{2}\sum_{i=1}^{M} J_i^0 q_i^2 + \sum_{i=1}^{M}\sum_{j\neq i}^{M} J_{ij}(r_{ij}) q_i q_j$$

where $U(r)$ denotes the charge independent contribution. χ = atomic electronegativity and J = atomic hardness are in principle characteristic of the atomic site *i*, and $J_{ij}(r_{ij})$ is a screening function which is usually computed as the Coulomb integral of Slater *ns* atomic orbitals but can be viewed as an additional parameter. The equation above can be regarded as a convenient expansion of the molecular energy, with parameters to be fitted from molecular properties. The requirement is that the atomic electronegativities within the molecule ($\chi_I \equiv {}_I\, \partial\, U_{mol} / \partial\, q_i$) must equalize ($\chi_1 \equiv \chi_2 \equiv \ldots \equiv \chi_M$), while maintaining overall neutrality ($\sum q_i = 0$). This leads to the system of equations

$$\chi_i + J_i^0 q_i + \sum_{j\neq i}^{M} J_{ij} q_j - \partial \frac{\partial \vec{p}}{\partial q_i} \cdot \vec{E} = \chi\,, \quad \sum_j q_j = 0$$

from which the induced charges required to evaluate the molecular polarizability can be obtained. The first equation applies to each site in the molecule.

(**d**) The B3LYP density functional with the aug-cc-pVTZ basis set serves as a reference model. It is known that the error of this method and basis set for induced dipole moments is less than 3%.

2. Systems

H$_2$O: Regarding the systems selected, water is one obvious choice. It is undisputed that many-body effects effect a number of bulk water properties and can result in substantial structural changes in hydrated ion systems. For water a simple and reliable polarizable model is not yet available although a large number of polarizable models have been developed in the past and new ones are being developed at an increasing pace. The picture on the right side shows the interaction energy of a water molecule with a lithium ion (full lines) and the interaction energy if Li$^+$ is described as a point charge only.

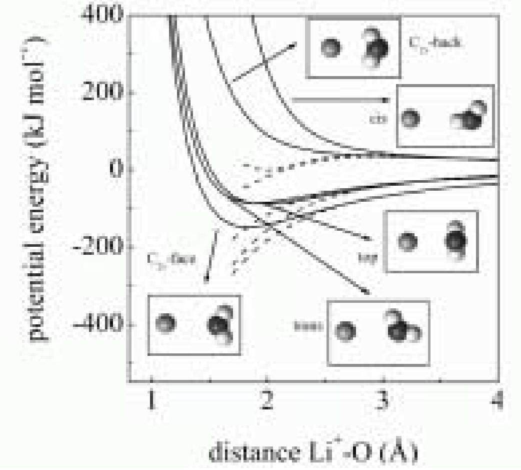

CCl$_4$: Water is a molecule with a permanent dipole moment and a rather low polarisability. As a complementary example of a highly polarizable molecule carbon tetrachloride, CCl$_4$ was chosen. This molecule displays a number of interesting features: its polarizability is almost one order of magnitude larger than the one of H$_2$O, it has no permanent dipole moment, and is highly anisotropic. Further, it is of great importance in technical processes and environmental issues. The picture on the right side of this paragraph

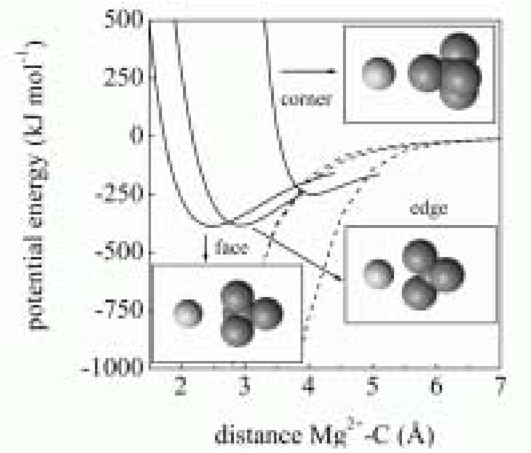

shows the interaction energy between CCl_4 and Mg^{2+} in the same way as it was depicted for H_2O and Li^+ in the last paragraph.

2. Results

At first, the three models are evaluated by calculating the induced dipole moment of a molecule interacting with a monovalent point charge. In the figure to the right five panels display the modulus of the total dipole moment of the water molecule for each of the chosen orientations. The last panel displays the *x* component of the induced dipole moment for the *top* configuration. Thick solid line are the reference values, thin solid lines the shell model results, dashed lines indicate the point dipole values and dotted lines the results from the fluctuating charges. Vertical dashed lines indicate the distance at which the potential energy profiles obtained for the ion or for a point charge are still indistinguishable. Regarding the performance of each method, the shell and point dipole method reproduce fairly well the *ab initio* profiles, the latter method coming even closer at the shortest distances. Already here the fluctuating charges are not as good. Another important conclusion is that, when compared with the *ab initio* results, no overestimations are observed for any of the polarization methods. Similar results are obtained for CCl_4.

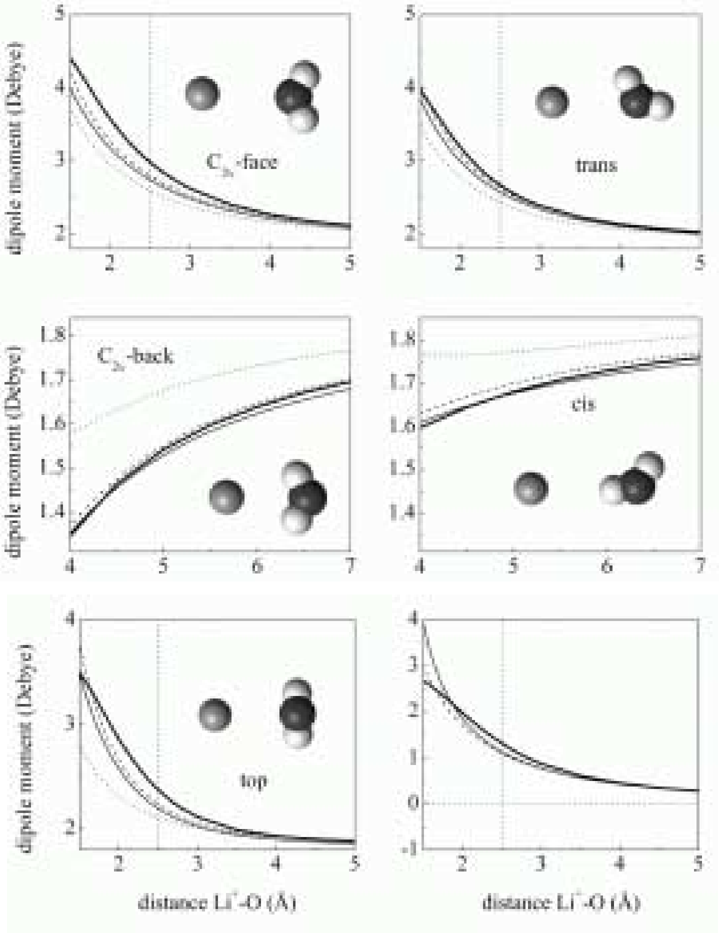

Turning to real ions as opposed to point charges, the limits of the linear polarization models become obvious. The figure to the right shows the results for various ions (only the C_{2v} geometry of the ion-water systems is shown). The thin solid line is the PDM result (a) which increases with decreasing distances. However, at separations close to contact the ab initio curves go through a maximum and then slightly decrease at the closest separations. This should be expected due to the overlap of electronic charge distributions. It can only be modeled by incorporating damping functions (dashed lines) into the PDM model. We have used the approach that both the electric field created by a fixed charge and that created by a point dipole are damped by functions $f_1(r)$ and $f_2(r)$:

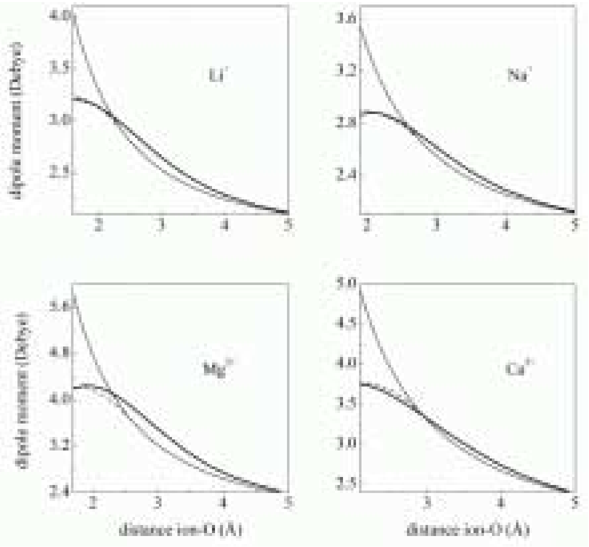

$$\vec{E}^{\,o} = f_1(r)\cdot q\,\frac{\vec{r}}{r^3} \qquad\qquad T = f_2(r)\cdot 3\frac{\vec{r}\vec{r}}{r^5} - f_1(r)\cdot\frac{I}{r^3}$$

The functions $f_1(r)$ and $f_2(r)$ are given as

$$f_1(r) = erf\left(\frac{r}{a}\right) - \frac{2}{\sqrt{\pi}}\left(\frac{r}{a}\right)e^{-(\frac{r}{a})^2}$$

$$f_2(r) = erf\left(\frac{r}{a}\right) - \frac{2}{\sqrt{\pi}}\left(\frac{r}{a}\right)e^{-(\frac{r}{a})^2}\left[1 + \frac{2}{3}\left(\frac{r}{a}\right)\right]$$

They show the proper asymptotic behaviour. The parameter *a* plays the role of the characteristic distance of maximum approach. It can be seen that the results are quite satisfactory.

We have also extended our approach to anions which are somewhat more complicated and to trivalent ions. To summarize, the main results or our investigation are:

- When reparametrized, the PD or SH models become the best ones that exist in the moment.
- The FQ model does not perform well and cannot be further optimized.
- In the case of 'real' ions the use of damping functions for the electrostatic interactions is needed. They have for the first time been applied to such situations and give excellent results.
- The same is also true for anions although they are somewhat more difficult to treat.

It seems that further research remains to be done in the following two areas:

- intramolecular details of the electron-density rearrangement upon polarization and
- extension of the models to nonlinear effects.

Some of our results are published in more detail in the following articles (same authors as this abstract):

- J. Chem. Phys. 121, 7362 (2004)
- Comp. Phys. Commun. 169, 331, (2005)
- J. Chem. Phys. 123, 164505/1-164505/13 (2005)
- Chem. Phys. Lett., in print (2005)

Temperature effects on dissociative electron attachment to HBr and DBr

M. Cingel[1], J. Fedor[1], J.D. Skalný[2], J. Horácek[3] , A. Stamatovic[4] , P. Scheier[1] and T.D. Märk[1]

[1] Institut für Ionenphysik und Angewandte Physik, Leopold Franzens Universität Innsbruck, Technikerstrasse 25, A-6020 Innsbruck, Austria (michal.cingel@uibk.ac.at)

[2] Department of Experimental physics, Comenius University, Mlynska dolina, 84245 Bratislava, Slovak Republic

[3] Institute of Theoretical Physics, Charles University, 18000 Prague, Czech Republic

[4] Faculty of Physics, P.O. Box 638, 11001 Beograd, Yugoslavia

Hydrogen halides constitute an ideal system for testing theoretical models for electron-molecule collisions. Corresponding cross sections (which can be compared to experimental results) include pronounced threshold peaks in the vibrational excitation cross section, step-like features (Wigner cusps) in the dissociative electron attachment (DEA) cross section and distinctly different shapes of the DEA cross section for different vibrational levels of the neutral molecule. The latter feature leads to clearly observable temperature effects.

In the present contribution we present measurements of the Br- ion yield following dissociative electron attachment to HBr and DBr. The effusive molecular beam was produced in a temperature controlled capillary heatable up to 400 ºC and perpendiculary crossed with an electron beam. Electrons were monochromatized in a trochoidal electron monochromator allowing to reach a kinetic energy resolution of about 35 meV. Anions produced were mass analyzed in a quadrupole mass spectrometer and deteced in a channeltron.

The ion yield spectra for HBr clearly show the growth of the resonance corresponding to the $\nu = 1$ vibrational level of the neutral molecule with increasing temperature. Furthermore, experimental results are in excellent agreement with the non-local resonance model calculations by the theoretical group of J. Horácek, Prague. We are also investigating presently the temperature effect on electron attachment to the DBr molecule.

Work supported by FWF, Wien and the EU Commssion, Brussels.

Kinetic energy distributions in metastable decay of rare gas dimer ions

J. Fedor[1], S. Matt-Leubner[1], K. Gluch[2], O. Echt[3] , F. Merkt[4] , P. Scheier[1] and T.D. Märk[1,5]

[1]*Institute for Ion Physics, Leopold-Franzens Universität, Technikerstrasse 25, A-6020 Innsbruck, (E-mail: juraj.fedor@uibk.ac.at)*

[2]*Institute of Mathematics, Physics and Informatics, Maria-Curie Sklodowska University, Lublin 20-031, Poland*

[3]*Department of Physics, University of New Hampshire, Durham, New Hampshire 03824*

[4]*Laboratorium fur Physikalische Chemie, ETH Hönggerberg, HCI, CH-8093 Zürich, Switzerland*

[5]*Also Adjunct profesor at: Department of Experimental Physics, Comenius University, 84215 Bratislava, Slovakia*

Metastable decay of rare gas dimer ions $Rg_2^+ \rightarrow Rg^+ + Rg$ (Rg = Ne, Ar, Kr, Xe) has been studied. Kinetic energy release distributions have been measured in the microsecond time regime using a three sector field mass spectrometer in the BEE geometry. Mass analyzed ion kinetic energy (MIKE) scan technique has been employed: parent ions were mass and energy selected by the magnetic and the first electric sector field, kinetic energy release of fragment ions was measured by scanning the second electric sector field. This high resolution technique enabled us to perform isotopicaly resolved measurements for Kr_2^+ and Xe_2^+ that were not possible with the conventional two sector field mass spectrometer.

Measured kinetic energy release distributions for different rare gas dimers are astonishingly different. The low kinetic energy parts in Ar_2^+ and Ne_2^+ MIKE spectra have been shown to originate from the metastable $II(1/2)_u \rightarrow I(1/2)_g$ bound-free transition [1]. Origin of the high kinetic energy part in the Ne_2^+ spectrum, absent in all other rare gases, is the non-radiative predissociation of the $II(1/2)_u$ electronic state [2].

Situation in Kr_2^+ and Xe_2^+ is utterly different. The low kinetic energy part of the MIKE spectrum cannot be explained by the $II(1/2)_u \rightarrow I(1/2)_g$ transition. The disagreement between measured and calculated kinetic energy distributions for this transition cannot be explained by inaccuracy of the potential energy curves. However, it turns out that the weakly bound $II(1/2)_g$ electronic state can accommodate a few bound vibrational levels in the heavier rare gas dimers [3]. Calculated lifetimes for the bound-free transitions from these vibrational levels into lower ungerade electronic states are in the order of microseconds. Thus in an exploratory study we have found that in Xe_2^+ three electronic transitions may contribute to the total signal: $II(1/2)_u \rightarrow I(1/2)_g$, $II(1/2)_g \rightarrow I(1/2)_u$ and $II(1/2)_g \rightarrow I(3/2)_u$. However, in Kr_2^+ the later transition is too weak to be observable. Calculated kinetic energy release distributions for these processes appear to agree with the experimental data. Further experiments and theoretical calculations will be carried out to confirm this interpretation.

Work partially supported by FWF, Wien and European Commission, Brussels.

[1] J. Fedor et al., Phys. Rev. Lett. **91** (2003) 133401
[2] S. Matt-Leubner et al., Phys. Chem. Chem. Phys. **7** (2005) 1043
[3] P. Rupper, O. Zehnder, F. Merkt, J.Chem.Phys.**121** (2004) 8279

Plasma characterization of reactive low voltage ion plating and correlation to film properties

D. Huber, A. Hallbauer, H.K. Pulker

Institut für Ionenphysik, Leopold Franzens Universität, Technikerstr. 25, A-6020 Innsbruck, Austria
daniel.huber@uibk.ac.at

ABSTRACT

The film deposition process studied in this work, i.e. reactive low voltage ion plating (RLVIP), is mainly used for applications in the field of precision optics. The coating material niobium pentoxide (Nb_2O_5) was chosen as a high refractive index material (n_{550}~2,40). It is particularly used for optical interference coatings. Different process settings concerning pressure conditions and plasma arc current, which are the main parameters of this coating process, were used and the resulting film properties compared with the arising plasma parameters. All depositions and plasma measurements were carried out in a Balzers BAP 800 (now Evatec BAP 800) ion plating plant. An increase of the arc current in the deposition process led to increasing densities of charged particles as well as to rising self-bias potential of the substrate holder. This means that higher energetic positive ions are deposited and bombard the growing film on the substrates, which leads to higher density and refractive index of the film (in this case Nb_2O_5), but also to high internal film stress. However, increasing the total gas pressure yields lower ion energies and particle densities in the substrate plane. Therefore refractive index and stress values of films produced at high pressure conditions are relatively low. The obtained plasma parameters, which were measured by a Langmuir probe, and the corresponding film properties are in good agreement.

1. Introduction

The quality requirements for thin films have strongly increased in the past years. For optical interference coatings [1], apart from their optical properties like reproducible stable refractive index and very low residual absorption, also the mechanical features are important for the application. Actually, the durability of a thin film system strongly depends on its resistance to environmental influences. In this context, the chemical stability, film density, internal film stress and surface morphological aspects have to be mentioned. Results that fulfill the high requirements can be obtained by physical vapour deposition techniques (PVD). Especially reactive low voltage ion plating (RLVIP) is suitable for the production of films with a high density. In this process high energetic positive ions of several tens of eV are provided to enhance film quality by bombardment during the deposition process [2]. Coatings obtained with this technique are characterized by bulk-like refractive index, high density and hardness. Furthermore, they exhibit a homogeneous amorphous structure and a nearly atomic-flat surface. The film properties are known to be very stable under changing temperature and humidity. But due to the ion bombardment also negative effects occur, i.e. a high compressive film stress and a relatively high optical absorption. However, they can be reduced by compensation layers and post depositional heat treatments on atmosphere, respectively.

2. Experimental

The coating plant used for this study was a Balzers BAP 800 (now Evatec BAP 800) ion plating plant. Fig. 1 shows a schematic of the plant, which was used to perform reactive low voltage ion plating. The coating material, i.e. 99,95% Nb_2O_{5-x} granulate, was melted and evaporated with a 270°-type electron beam gun. The electrons of a low-voltage-high-current plasma device were directed to the anodic melt in the crucible of the e-gun. Therefore the evaporated material and the added gas components (Ar and O_2) were effectively activated and ionized. The settings that were normally used for Nb_2O_5-coatings were the following: plasma arc current I_{arc}=50A; argon partial pressure $p_{Ar}=4*10^{-4}$mbar; oxygen partial pressure $p_{O2}=8*10^{-4}$mbar; deposition rate R=0,3nm/s. In order to minimize optical absorption caused by under-stoichiometry, the deposition rate was increased slowly from 0,05nm/s to 0,3nm/s.

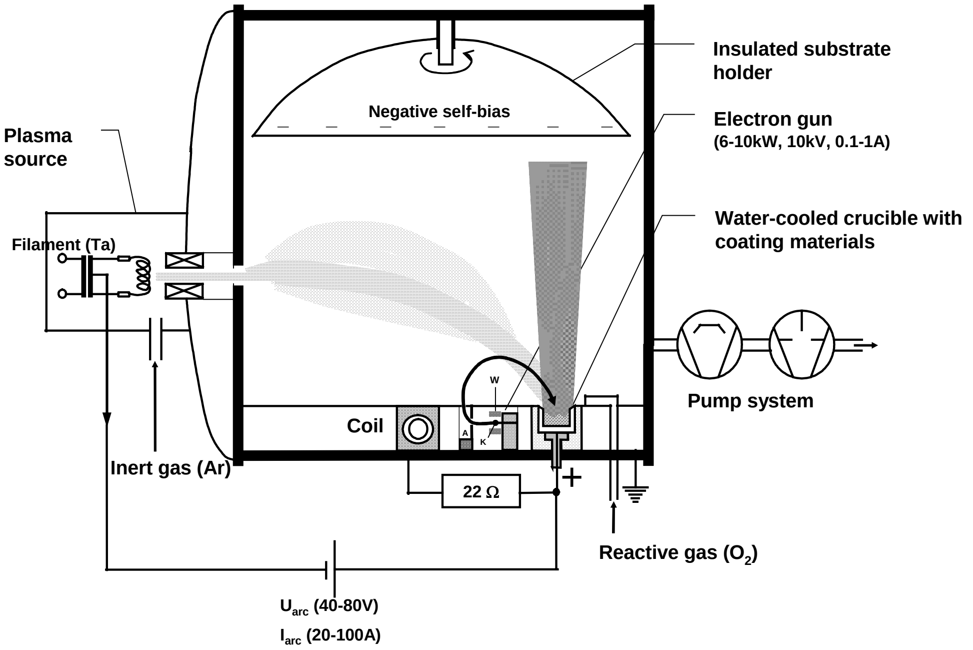

Fig. 1: Schematic of the ion plating device Balzers BAP 800.

For plasma characterization a Langmuir probe system (Smart probe – Scientific Systems) was used. The cylindrical Langmuir probe consisted of a 10mm long and 0,381mm thick tungsten wire, which was mounted in the substrate plane being approximately 70cm above the evaporation source. The probe current was measured at voltages between –95V and +95V in steps of 1V. The resulting current-voltage characteristic was analysed by "Smart Soft" of Scientific Systems (version 3.19). The refractive index of the films was calculated according to Swanepoel [3] from data obtained by spectrophotometric intensity measurements. The transmission spectra of the coated glass samples (Borofloat® samples) were measured in the range between 300 and 850nm by a Perkin Elmer Lambda 19 spectrometer.

3. Results

The two main process parameters, i.e. arc current and gas pressure, were changed in a wide range and their influence on the plasma characteristics and on the film properties were measured [4,5]. In the first series of measurements the arc current was varied between 20 and 80A while the total gas pressure was kept constant at $12*10^{-4}$mbar. The Langmuir probe results revealed that the electron and the ion density in the substrate plane were increasing nearly linearly with pressure as can be seen in Fig. 2. This means that higher numbers of bombarding ions are available. Furthermore, the self-bias voltage, which is responsible for the acceleration of the positive ions towards the substrates, increased from 8 to 13V within the studied arc current range. Therefore, besides the number of bombarding ions also their energy increased. This means that the total energy input into the growing film during the coating process was getting higher as the arc current was raised (see Fig. 3). These results were compared with the refractive index of the film, which is strongly correlated with the density. As shown in Fig. 4, the densification effect is rising obviously between 20 and 40A of arc current. In the range between 40 and 60A the densification effect is maximal, while the usage of higher energy input (I_{arc}>60A) leads to relaxation processes within the film, which reduce the refractive index.

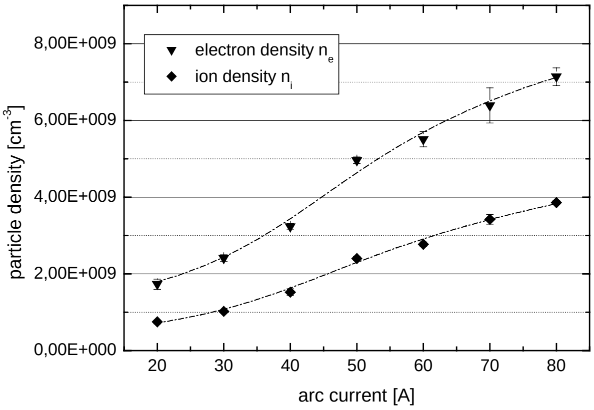

Fig. 2: Electron density n_e and ion density n_i depending on the arc current

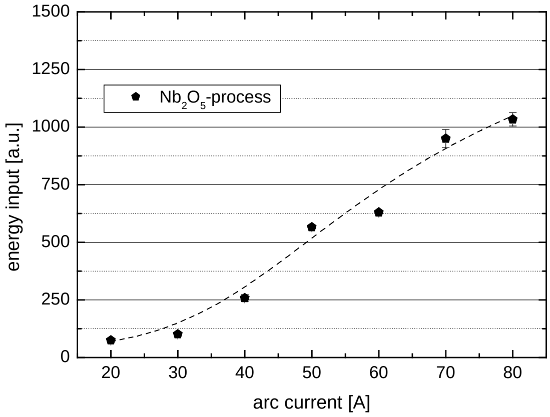

Fig. 3: Energy input of the ions measured in the substrate plane depending on the arc current

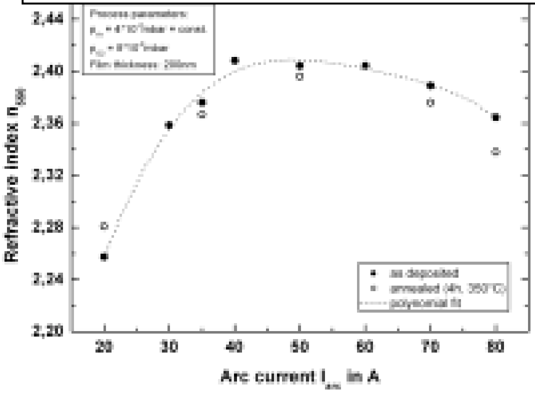

Fig. 4: Refractive index of RLVIP-Nb_2O_5-films as function of the arc current

In the second series of measurements the total gas pressure was varied by changing the oxygen partial pressure between $1*10^{-4}$ and $36*10^{-4}$mbar. Argon partial pressure ($4*10^{-4}$mbar) and arc current (50A) were kept constant. The Langmuir probe measurements showed a decrease of charged particle densities (see Fig. 5) as well as decreasing self-bias voltage, which goes down from 14 to 8V. As a consequence, the total energy available for the growth of the thin film decreased strongly with rising pressure as is displayed in Fig. 6. These results can be explained by increasing collisions in the gas phase. This implicates recombination processes, a reduction of the particle energy and a change of direction of the particles. As shown in Fig. 7, the refractive index of coatings produced under corresponding process conditions showed a decreasing characteristic when the pressure was raised – as could be expected from the plasma measurements.

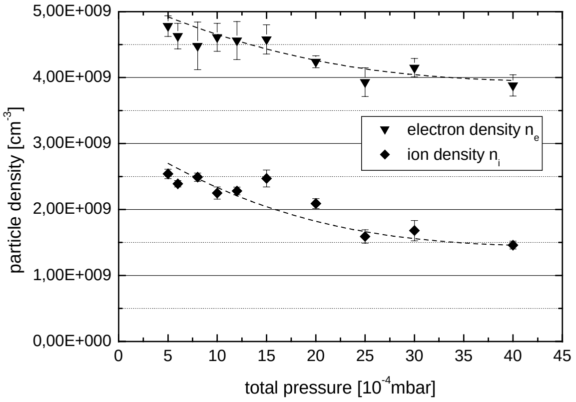

Fig. 5: Electron density n_e and ion density n_i depending on the total gas pressure

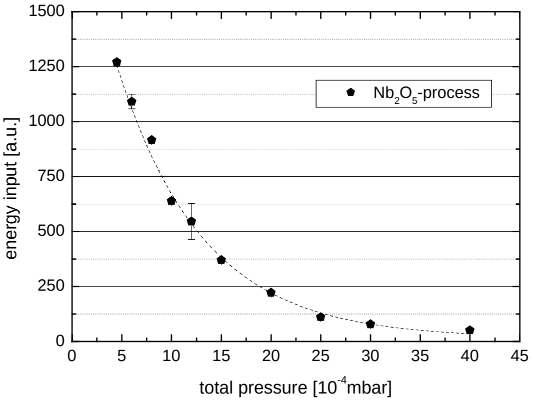

Fig. 6: Energy input of the ions measured in the substrate plane depending on the total gas pressure

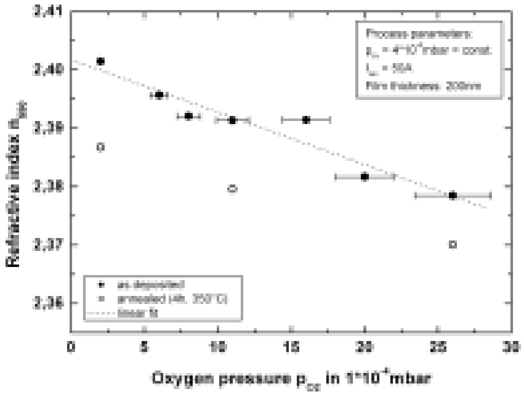

Fig. 7: Refractive index of RLVIP-Nb_2O_5-films as function of the oxygen partial pressure

4. Conclusion

The total energy input from the positive plasma ions into a growing film was found to increase in a nearly linear manner when the arc current was raised. This can be explained on the one hand by the higher number of ions and on the other hand by their energy. In contrast to that, increasing the total gas pressure had the opposite effect: a lower number of ions in the substrate plane and also lower ion energies. The total energy input of the ions decreased exponentially with rising pressure. The results of the plasma measurements correlate very well with the optical film properties, i.e. a low energy input leads to less densification and consequently to a low refractive index. However, using very high particle energies yields relaxation of the film structure and therefore a slight reduction of the refractive index and of the compressive stress.

References

[1] A.V. Tikhonravov, “Design of Optical Coatings”, Optical Interference Coatings, N. Kaiser, H.K. Pulker, 81-104, Springer, Berlin, 2003.

[2] E. Moll, H.K. Pulker, W. Haag, “Method and apparatus for the reactive vapour deposition of layers of oxides, nitrides, oxynitrides and carbides on a substrate”, United States Patent, Patent Number: 4.619.748, 1986.

[3] R. Swanepoel, “Determination of the thickness and optical constants of amorphous silicon”, J. Phys. E: Sci. Instrum., Vol. 16, 1986.

[4] D. Huber, A. Hallbauer, H.K. Pulker, „Plasma monitoring of the RLVIP-process with a Langmuir probe“, Proceedings of SPIE – Advances in optical thin films II, C. Amra, N. Kaiser, H.A. Macleod, Vol. 5963, SPIE, Bellingham, 2005.

[5] A. Hallbauer, D. Huber, H.K. Pulker, “Optical and mechanical properties of RLVIP Nb2O5-films”, Advances in Optical Thin Films II, Claude Amra, Norbert Kaiser, H. Angus Macleod, Vol. 5963, SPIE, 2005.

Ion-Surface collisions of ethane cations $C_2H_4^+$ and $C_2D_4^+$ on stainless steel and diamond surfaces

L. Feketeova[1], N. Endstrasser[1], V. Grill[1], P. Scheier[1], D. Steinmüller[2], T.D. Märk[1]

[1]*Institut für Ionenphysik und Angewandte Physik, Leopold Franzens Universität Innsbruck, Technikerstrasse 25, A-6020 Innsbruck, Austria*

[2]*RhoBest Coating Hartstoffbeschichtungen GmbH, Erlach 165, A-6150 Steinach, Tirol*

The compatibility between a reactor grade plasma and the first wall of the fusion reactor is one of the great challenges in fusion research, in particular for the design of ITER. The energetic particles, which are formed in the plasma, may strike the solid surface and erode and migrate the surface material. As some of the released particles are ionised these ions can afterwards be redirected to the walls and hit the surface again. In present fusion devices carbon is widely used as the plasma facing material due to its high thermal resistivity and low Z value despite its relatively large sputtering yield of hydrogenic species. To suppress carbon migration different surfaces are now under consideration for the design of ITER. In this study we have analysed the properties of different carbon surfaces, in particular different diamond surfaces. The use of a µm thick layer of nanocristalline diamond on a metal substrate renders this surface metallic and therefore a suitable wall candidate for a tokamak reactor.

By changing the final termination step during the production two different types of surfaces could be prepared, one terminated in a hydrogen gas environment, the other one terminated under air. In the first case the final functional atoms of the surface are -H, while for the air terminated surface the functional groups are -O or – OH. To allow for a comparison with data already published by different research groups, the surface collision data obtained after surface impact on the two diamond surfaces were compared with data obtained with a stainless steel surface, which was studied under similar conditions.

To study the influence of the terminal group on the secondary ion yield the projectile ions $C_2H_6^+$, $C_2H_4^+$ and $C_2D_4^+$ have been used. All of these ions were generated in a Nier type ion source by electron impact of deuterated or normal ethane vapour at an electron energy of about 100 eV and collided with the surface under study with varying collision energy. The collision energy was varied from almost zero collision energy up to about 50 eV collision energy. By using this energy range it is possible to vary the energy transferred to the projectile through the collision energy up to about 3 eV (approximately 6% of the collision energy is transferred to internal energy of the projectile during the collision). As this energy is in the range of normal bond dissociation energies, it is possible to induce extensive fragmentation in the projectile ion through the collision process. The mass spectra of the secondary ions as a function of collision energy have been recorded and summarized in so called collision energy resolved mass spectra (CERMS). These CERMS which have been measured for the stainless steel and the two diamond surfaces using $C_2H_6^+$ as projectile ion can be seen in Fig. 1.

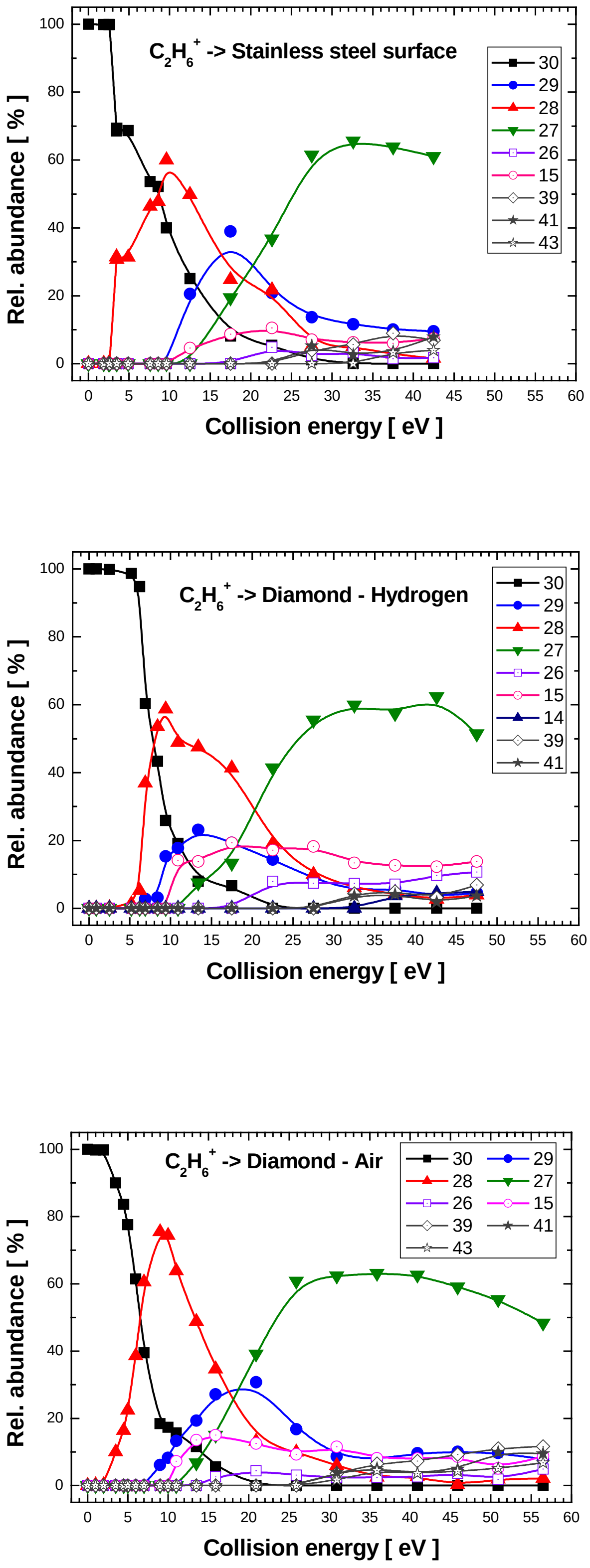

Fig.1: Collision energy resolved mass spectra after impact of $C_2H_6^+$ onto a stainless steel surface (upper panel), an hydrogen terminated diamond surface (middle panel), and an air-terminated diamond surface (lower panel). The different secondary ions are distinguished by their mass/charge number.

The comparison of these CERMS curves shows a clear difference between the two diamond surfaces in particular for the secondary ion at mass/charge = 28 Thomson. This ion, which corresponds to the fragment ion $C_2H_4^+$ produced from $C_2H_6^+$ by the loss of H_2, shows a completely different onset behaviour for the two diamond surfaces. In the case of the stainless steel and the air terminated diamond surface the onset was at about 2 eV collision energy, while in the case of the hydrogen-terminated diamond surface about 5 eV collision energy were necessary to induce this fragmentation. This change in appearance energy may be due to a different transfer of energy to the surfaces, i.e. the terminal group of the surface may change the energy balance of the collision process. To separate the effect of surface adlayers, which are present in any vacuum environment, from the effect of the terminal group, argon chemical sputtering was performed for all three surfaces. In Fig. 2 the collision energy resolved sputtering curves are shown for the diamond hydrogen surface.

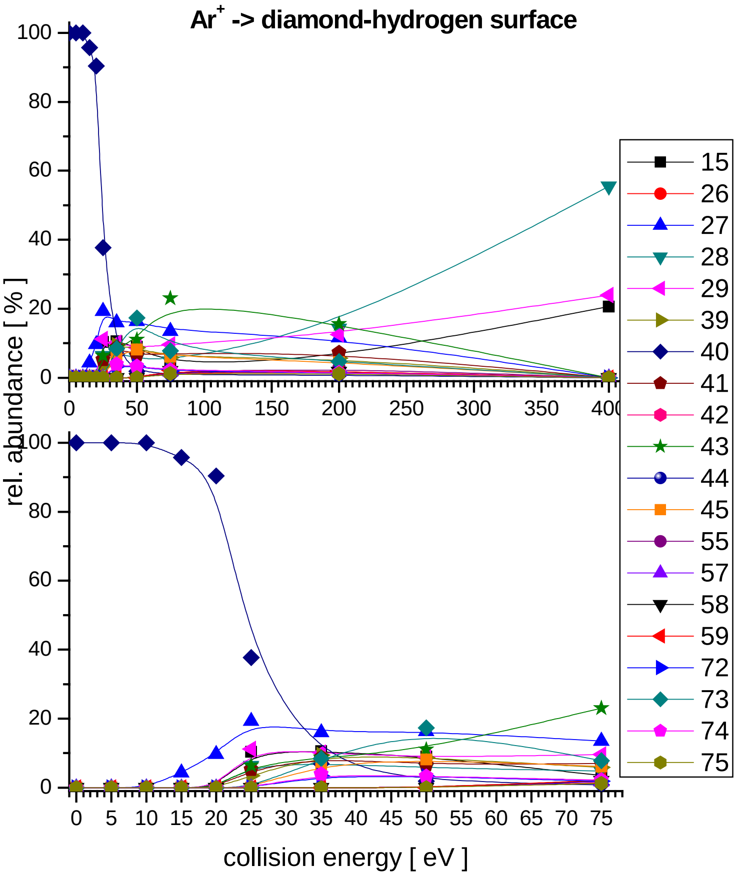

Fig. 2: *Collision energy resolved mass spectra after impact of* Ar^+ *onto a hydrogen terminated diamond surface. The different secondary ions are distinguished by their mass/charge number.*

The comparison of the Ar^+ CERMS for the three different surfaces showed that in the case of argon chemical sputtering, the hydrogen terminated surface behaved similar like the stainless steel surface, while the air-terminated diamond surface showed a significantly higher energy transfer to the surface. This different behaviour can be explained that for both diamond surfaces the sticking, i.e. the bonding of surface adlayers originating presumably from pump oil to the diamond surface, as well as the energy transfer from collision energy to internal energy of the projectile is different. Therefore both the terminal group and the surface adlayer have an effect on the collision energy balance.

To study the effect of the projectile ion on the collision process we performed similar experiments using $C_2H_4^+$ and $C_2D_4^+$ as projectile ions. The effect of the terminal group was less pronounced in these cases, but in particular for the $C_2D_4^+$ it was possible to distinguish between chemical sputtering by the projectile ion and surface induced dissociation. In Fig. 3 the survival probability of $C_2D_4^+$ ions, i.e. the yield of scattered parent ions divided by the total yield of all scattered ions is shown for the different surfaces. In this picture the effect of the terminal group on the work function of the surface can be clearly seen. The shift of about 6 eV in collision energy for the hydrogen terminated diamond surface in respect to the stainless steel and the air terminated diamond surface is in good agreement with the data obtained for the $C_2H_6^+$ projectile.

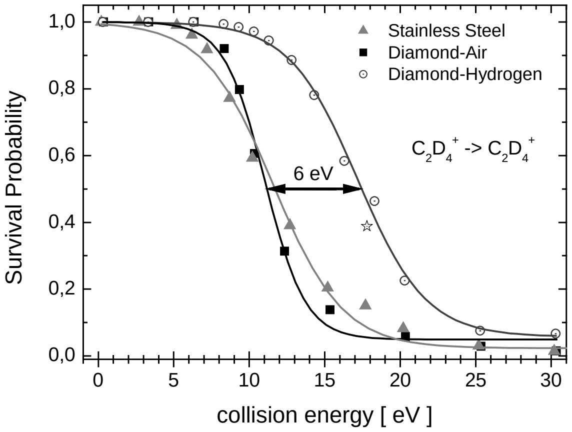

Fig.3: Survival probability of $C_2D_4^+$ ions, i.e. the yield of scattered parent ions divided by the total yield of all scattered ions. The solid line reflects a nonlinear least square fit with a sigmoidal function.

Acknowledgement:

This work has been carried out within the Association EURATOM- ÖAW. The content of the publication is the sole responsibility of its publishers and it does not necessarily represent the view of the EU Commission or its services. Work was also partly supported by the FWF, ÖAW and ÖNB, Wien, Austria.

Index of Authors